Abstract: This is the second in a series of reports concerning a series of tests
undertaken as part of the VELACS (Verification of Liquefaction Analyses by
Centrifuge Studies) Project. These tests were performed during the summer of 1991
using the geotechnical Centrifuge and the dynamic shaker at Rensselaer Polytechnic
Institute. The report is identical with a thesis submitted by Dr. Ting in Partial
fulfillment of requirements for the degree of Doctor of Philosophy. During his
studies, Dr. Ting served as a Graduate Research Assistant. Dr. Robert V. Whitman
(Professor of Civil and Environmental Engineering) was the principal investigator.
The VELACS project has been funded by the Earthquake Hazards Reduction program at
the National Science Foundation; Dr. Cliff Astill is the principal scientific
contact at NSF.

Report R93-13

DYNAMIC CENTRIFUGE TESTING OF A TILTING RETAINING WALL WITH SATURATED BACKFILL

2. ANALYSIS AND INTERPRETATION OF RESULTS

by

Nai-Hsin Ting
Robert V. Whitman

May 1993

Constructed Facilities Division
Department of Civil and Environmental Engineering
Massachusetts Institute of Technology
Cambridge, Massachusetts

PREFACE

This is the second in a series of reports concerning a series of tests undertaken as part of the VELACS (Verification of Liquefaction Analyses by Centrifuge Studies) Project. These tests were performed during the summer of 1991 using the geotechnical Centrifuge and the dynamic shaker at Rensselaer Polytechnic Institute. The previous report:

> Dynamic Centrifuge Testing of a Tilting Retaining Wall with Saturated Backfill, 1. Summary of Results and Preliminary Interpretation, by Ute K. Schran, Nai-Hsin Ting and Robert V. Whitman, February 1992. This is designated as Research Report R92-12 from the MIT Department of Civil and Environmental Engineering.

describes the design and development of the test and summarizes and discusses some aspects of the data. The current report contains all data, and presents a careful analysis and interpretation of these data - plus results from a "Class A" prediction using the residual strain method and the computer code CYCON.

This report is identical with a thesis submitted by Dr. Ting in Partial fulfillment of requirements for the degree of Doctor of Philosophy. During his studies, Dr. Ting served as a Graduate Research Assistant. Dr. Robert V. Whitman (Professor of Civil and Environmental Engineering) was the principal investigator.

ACKNOWLEDGMENTS

Page Intentionally Left Blank

TABLE OF CONTENTS

Page Intentionally Left Blank

LIST OF TABLES

LIST OF FIGURES

14

16

Page Intentionally Left Blank

CHAPTER 1

INTRODUCTION

This thesis is concerned with results from a series of centrifuge model tests simulating some important aspects of the behavior of waterfront retaining structures when shaken by earthquakes. The tests were undertaken to obtain data for use in two different ways:

- For use in verification of liquefaction analyses

- For development of a better understanding of the behavior of this complex soil-structure system, with the hope of improving and developing relatively simple rules for the analysis and design of such systems.

1.1   PROBLEM DEFINITION

The soils behind waterfront retaining structures are often cohesionless, and water tables are usually high in such soil backfills. During strong earthquakes, there is a strong possibility of pore pressure build-up and associated liquefaction phenomena. There have been numerous cases of failure or unsatisfactory performance of such structures.

Earthquake-induced problems with earth retaining structures have been studied for more than half a century (Okabe, 1926). Among various types of earthquake-induced damages, one major concern of geotechnical engineers is with the behavior of liquefiable

19

soils and of structures that retain the soils or those are built upon such soils. Up to the present time, a variety of techniques have been proposed for the analysis of earthquake-induced deformations of both the ground and the structures. Typically, many of these methods, employing numerical procedures, are used to assess the dynamic performance of soil and structures during earthquakes. Consequently, validation of these numerical techniques is required, by comparisons of the numerical predictions with observed soil behaviors. However, there are only few documented histories of the performances of both the soils and structures (pore pressure, acceleration and deformation data) during natural earthquakes. Even if many sites were instrumented to monitor these data, the use of field data to validate numerical methods would suffer from the following difficulties.

1. One cannot predict when and where an earthquake will take place. Field instrumentation would need to be installed in many sites. Both the capital and maintenance costs of such instrumentation would be prohibitively large. In addition, it might take decades, or even centuries, to obtain comprehensive field data for validating the numerical predictions.

2. It is difficult to determine the properties of field soils because of the inherent non-homogeneity of naturally deposited soil layers.

3. It is difficult to define the boundary conditions of field deposits.

Laboratory shaking table tests, as one alternative to field data, have been used to validate several numerical procedures (Yoshimi and Tokimatsu, 1978). The application of shaking table tests to validate numerical models is confined, however, to soils having much lower effective stresses than those in the field. Recently, one experimental technique has been employed to offer realistic full-scale stress states together with uniform soil and well-

20

defined boundary conditions. This technique is *dynamic centrifuge testing* (Schofield, 1981).

This research studies the behavior of a saturated sand and the retaining wall that supports it during earthquakes by dynamic centrifuge testing. One numerical model (CYCON) was employed to make predictions for the tests of the centrifuge. For the purpose of validating numerical models, a set of numerical criteria was established in this study to evaluate numerical predictions in a systematic fashion.

1.2   CLASS A PREDICTIONS

In the Thirteenth Rankine Lecture, Lambe (1973) examined the anatomy of predictions. He used an example of predicting the settlement of a building to illustrate the definitions of three types of predictions. A class A prediction of settlement would be made before construction and based entirely on data available at that time. A class B prediction would be made during the construction and might use data obtained during the

Table 1.1 Classification of predictions (*from* Lambe, 1973)

Prediction type	When prediction made	Results at time prediction made
A	Before event	-
B	During event	Not known
B_1	During event	Known
C	After event	Not known
C_1	After event	Known

initial part of the construction, such as measurements made during excavation, foundation construction, etc A class C prediction is one made after the settlement has occurred Table 1.1 summarizes the characteristics of the classifications.

A complete set of numerical analyses has been carried out to make "Class A" predictions for the outcomes of the centrifuge model tests. A numerical prediction for a dynamic centrifuge model test was performed based upon the soil properties, the geometry and boundary conditions of the test model, and the input motions applied to the model. Ideally, the prediction should be performed before the centrifuge test is conducted, according to the definition of class A predictions. However, it is impossible to make true class A predictions for such tests because the true acceleration applied to the model cannot be known in advance On the other hand, the acutal acceleration data must be used for making class A predictions for the purpose of verifying the numerical methods.

In this research, the soil properties were obtained from other independent laboratory tests performed by The Earth Technology Corp. (1992). The geometry and boundary conditions of the test model were determined before the tests were performed The only information from the test results used in the numerical predictions was the input acceleration. Therefore, the predictions are really "Class A" predictions The quotation marks around the term "Class A" denote that the numerical predictions were made, based on the author's honesty in not looking at the test results after the centrifuge tests had been performed That is, the predictions were made after the fact; however, the only information from the test data that was used in the predictions was the acceleration applied to each model.

The dynamic centrifuge model in this research was part of the original proposal for MIT's participation in the research program VELACS (Verification of Liquefaction

Analyses by Centrifuge Studies) sponsored by the National Science Foundation. When the program was modified to include the Class A Prediction exercise, MIT first proprsed to offer a similar experiment for that purpose (Figure 4.1a), but then withdrew from that exercise when it appeared that it was not possible to define well in advance test conditions that would yield results worthy of the effort of a prediction. The complex results presented in this thesis justify that decision. However, one set of "Class A" predictions were undertaken, as described herein, and the data are now available to everyone for the purpose of Class C predictions.

1.3 SCOPE OF RESEARCH

This research involves four major tasks to investigate the behavior of a retaining wall and a saturated sand behind the wall during earthquakes:

1. Centrifuge Check Test (Chapter 3)

   The check test was performed to evaluate the dependence of centrifuge liquefaction test results on the testing facility and experimenter. This is a part of a research project, *Verification of Liquefaction Analysis by Centrifuge Studies* (VELACS), sponsored by National Science Foundation, in which eight institutions performed similar tests using various geotechnical centrifuges.

2. Dynamic Centrifuge Model Testing (Chapter 4)

   This phase involved a series of dynamic centrifuge tests on a model retaining wall supporting a saturated sand. The wall was hinged at the base, and was supported by an elasto-rigid-plastic tie-back near the top. A plastic extension of the tie-back can occur during an earthquake if the load in the tie-back exceeds a yield load.

23

The plastic extension, which would cause a permanent tilt of the wall, was made possible by a slider in the tie-back system.

3. Numerical Analyses for the Centrifuge Model Tests (Chapter 5)

The primary objective of the numerical analysis is to investigate the applicability of one currently available analytical procedure to study liquefaction problems. A series of "Class A" predictions for the centrifuge model tests were performed using a finite element program, CYCON, which was developed at M.I.T. by Bouckovalas (1982) and Stamatopoulos (1989).

The second objective is to establish a systematic approach to rate the numerical predictions for dynamic geotechnical centrifuge tests. A reasonably strict set of numerical criteria was established to systematically evaluate analytical models for predicting seismic soil behaviors, by comparisons with observations. These criteria were employed to evaluate the numerical predictions with CYCON.

4. Analyses of the Centrifuge Model Tests (Chapters 6 and 7)

The centrifuge model tests were categorized into two types of tests based upon the behavior of the slider: non-slip tests and slip tests. The major aspects of behavior of the model during non-slip tests are earthquake-induced pore pressure changes in the soil and various thrusts acting on the wall from both the pore fluid and the mineral skeleton. Chapter 6 presents an extensive investigation of these tests. During slip tests, the major concerns are the characteristics of slippage and cyclic tilt of the retaining wall. A lumped-mass-sliding-block model was developed to analyze the slippage and the movement of the retaining wall during the slip tests. These analyses will be presented in Chapter 7.

Chapter 8 presents a summary of this research, recommended considerations for seismic design of earth retaining structures and suggestions for future study.

1.4   UNITS AND SCALES

Units:

The S.I. system of units is used throughout this thesis.

Scales:

- The centrifuge tests were performed at a centrifugal acceleration of 50g. Values of length and time in prototype scales are 50 times of those in model scale.
- All dimensions, accelerations, times and stresses are reported in prototype scales.
- Forces (in the tie-back) and spring constants discussed in Chapter 7 are reported in model scale [Newtons][1]. Prototype forces and spring constants would be 2,500 and 50 times larger, respectively.

1.5   DEFINITIONS OF SPECIAL TERMS IN THIS THESIS

Some special terms are used throughout this thesis to indicate some specific subjects related to the behavior of the soil-wall system. The definitions of these terms are described as follows:

- **Average Transient Thrust acting on a retaining wall**

The average transient earth thrust during an earthquake is the average earth thrust over time, in which the dynamic flutuations are smoothed out. Figure 1.1 shows a typical history of the earth thrust variation over time. The dashed curve in the figure shows the

---

[1] 1 Newton = 0.2248 pound.

average transient earth thrust which is obtained by connecting the averages of the peaks and valleys in the load history. Detailed discussions redarding the average transient earth thrust will be presented in Chapters 6 and 7.
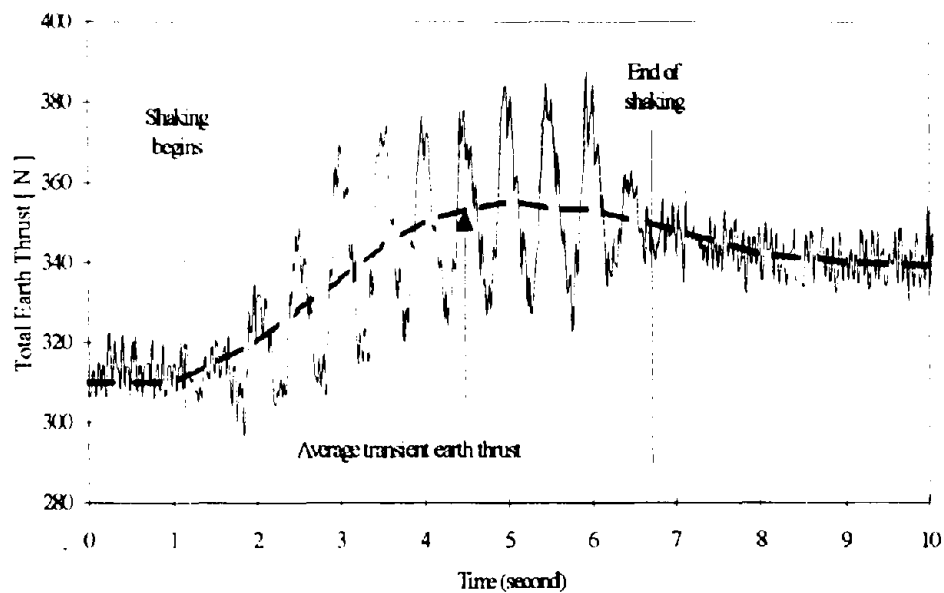
Figure 1.1: Average transient earth thrust in Test 1a

- **Plastic Tilt of a retaining wall**

The retaining wall may tilt as a result of increase of the thrust acting on it. During a weak earthquake that does not cause a yield of the tie-back system, the permanent tilt of the wall is a result of increase of the thrust acting on the wall, which in turn causes elongation of the spring in the tie-back system. At the end of an earthquake, the wall may tilt somewhat due to increased average transient thrust (accompanied by a pore pressure

build-up) The amount of tilt will decrease after the dissipation of the excess pore pressure. There is a residual tilt (compared to the pre-earthquake position of the wall) which is associated with the residual increment in the static earth thrust. The amount of this tilt is more or less proportional to the incremental static thrust and is refered as *elastic tilt*

During a strong earthquake, the wall's tie-back system may yield temporarily as a result excessive dynamic load (and the increased average transient thrust). The total amount of residual tilt of the retaining wall includes both elastic tilt and plastic tilt. The elastic tilt is due to the incremental static earth thrust. The plastic tilt is due to the yield of the tie-back system during the earthquake. In this research, the plastic tilt of the wall is a result of yield in a tie-back that supports the wall. Therefore, in this thesis, the term *plastic tilt* of the wall is directly related to the amount of elongation of the tie-back due to yielding.

Page Intentionally Left Blank

CHAPTER 2

BACKGROUND

The problem with the behavior of waterfront retaining structures during earthquakes is complicated. The major concern in this thesis is concentrated on the thrust acting on the wall during earthquakes. Section 2.1 reviews some analytical methods for dynamic lateral pressures on the wall from both the soil skeleton and pore fluid within the backfill.

Section 2.2 reviews previous studies on the retaining wall problem by dynamic centrifuge testing. These studies provide significant insight as to the designing of centrifuge models of earth retaining structures to simulate key behaviors of such structures during earthquakes.

Section 2.3 reviews the study of liquefaction potential of saturated sands, which is helpful in understanding the characteristics of the liquefiable backfill soil in this research.

Section 2.4 reviews some existing literatures about current numerical models that predict the behavior of soils during earthquakes. The cited numerical models were claimed to be effective in predicting some aspects of the soil behavior during earthquakes in some particular cases.

Section 2.5 reviews the background of sliding block models. The concept of sliding block model was applied in this thesis to help developing a lumped-mass-sliding-block

model to estimate the amount of plastic tilt in a model retaining wall during dynamic centrifuge tests

2.1 ANALYTICAL METHODS FOR DYNAMIC LATERAL PRESSURES ON RETAINING WALLS

2.1.1 Dynamic Earth Thrust on Retaining Walls

The earliest studies of dynamic lateral earth pressure on a retaining structure were presented by Okabe (1924) and Mononobe and Matsuo (1929). Their pseudo-static approach became known as the Mononobe-Okabe equation. The method was developed for dry cohesionless material. This method assumes that the wall tilts sufficiently to produce minimum active earth pressure during earthquakes. Under such a condition, a rigid soil wedge behind the wall may move with the wall during earthquakes. This is an extension of the Coulomb Sliding Wedge Theory modified to account for a lateral component of acceleration.

Many experiments have been performed on shaking tables to verify this pseudo-static approach. Shaking table and field experiments have been reported by Mononobe and Matsuo (1929), Ishii et al. (1960), Matsuo and Ohara (1960), and Richards and Elms (1979). Dynamic centrifuge tests have also been carried out of verify the Mononobe-Okabe equation by Steedman (1984), Zeng and Steedman (1988) and Anderson (1987). Seed and Whitman (1970) summarized previous experimental studies and commented that the lateral earth pressure coefficients computed for a cohessionless backfill using the Mononobe-Okabe equation are in reasonable agreement with the model test observations. They proposed a simplified Mononobe-Okabe equation as

$$\Delta P_{AE} \approx \frac{1}{2}\gamma H^2 \bullet \frac{3}{4}k_h \tag{2.1}$$

and $\qquad P_{AE} \approx \frac{1}{2}\gamma H^2\left(K_A + \frac{3}{4}k_h\right) \tag{2.2}$

where ΔP_{AE} and P_{AE} are the dynamic and total thrust acting on the wall at peak acceleration, respectively; γ is the unit weight of the backfill soil; H is the thickness of the backfill; and k_h ($= a_{max}/g$) is the coefficient of horizontal acceleration.

This force was originally assumed to act at 1/3 H from the base of the wall. However, various experimental shaking table tests on model retaining walls have shown the resultant force acts above the 1/3 point (Seed and Whitman, 1970). Seed (1969) has recommended that the dynamic component in the Mononobe-Okabe force be placed at 0.6 H above the base for design of vertical walls with horizontal dry backfill. This point of action of 0.6 H is a bit conservative for the purpose of designing a retaining wall. Sherif et al. (1981, 1982) performed a series of shaking table tests and concluded that the point of action of the earth thrust is at approximately 0.4 H above the base. Steedman and Zeng (1990) further showed that the point of action is above the 1/3 point when there is a phase change of the lateral acceleration in the backfill. Steedman (1984) assumed a height of 0.5 H. This height is more realistic in analyzing dynamic retaining wall problems.

2.1.2 Hydrodynamic Pressures on Retaining Walls

Westergaard (1933) developed a pseudo-static approximation for the change of water pressures during an earthquake for the case of a straight dam with a vertical up-stream face. The result of the Westergaard analysis is: the pressures are the same as if a certain body of water were forced to move back and forth with the dam while the

remainder of the reservoir is left inactive. A parabolic dynamic pressure distribution, p_{wd}, is proposed as

$$\Delta p = \frac{7}{8} k_h \gamma_w \sqrt{y_w H}$$ (2.3)

where y_w is the distance below the water table. The resultant hydrodynamic thrust is

$$\Delta P_u = \frac{7}{12} k_h \gamma_w H^2$$ (2.4)

acting at an elevation equal to 0.4H above the base of the pool.

The Westergaard approximation, Eq. (2.4), sometimes is used to estimate the thrust from pore water behind a vertical retaining wall[1] (Ebeling et al., 1992). However, due to the soil's permeability and inclination of the retaining wall, some modification to the Westergaard equation may be desirable (Matsuzawa et al., 1985).

Zangar (1953) presented an approximate solution for hydrodynamic water pressure against an inclined wall surface. Chwang (1978) developed an analytical solution that is close to Zangar's approximation as follows:

$$p_{wd} = C k_h \gamma_w H, \text{ with } C = \frac{C_m}{2}\left[\frac{y_w}{H}\left(2 - \frac{y_w}{H}\right) + \sqrt{\frac{y_w}{H}\left(2 - \frac{y_w}{H}\right)}\right]$$ (2.5)

in which C_m is a parameter related to the inclination angle and can be approximated as $C_m \approx \frac{3}{4}\frac{\alpha}{\pi 2}$, where α is the angle (in radians) between the backfill face of the wall and the horizontal base away from the backfill. When the wall is vertical, $\alpha = \pi/2$, Zangar's

---

[1] Christian (1993) indicated that a reduced (70%) hydrodynamic thrust in Eq. (2.4) is often used in practice.

approximation is about the same as the Westergaard's approximation between H/3 and 2H/3 above the base[2] and is slightly smaller elsewhere.

2.1.3 Dynamic Earth Pressures From a Saturated Backfill

Ishibashi and Madi (1990) proposed three methods to analyze the dynamic thrust acting on quaywalls based on case studies:

A. to use the traditional Mononobe-Okabe's dynamic lateral earth pressure

B. to use modified Mononobe-Okabe's in terms of the point of application of the resultant force depending upon wall movement modes and to use generalized apparent seismic coefficient and partial dynamic water pressure depending on the backfill soil's permeability

C. to apply dynamic liquid soil pressure against the backfill face of the wall.

They applied these analytical methods to study the stability of three types of quaywalls. Their case studies show that method (C) provided the lowest safety factors.

2.1.4 Influence of Phase on Earth Pressure Calculation

The results of dynamic centrifuge tests performed by Anderson (1987) showed clear phase changes in the lateral acceleration in the backfill soil as shear waves propagated from the base of the soil model towards the ground surface. Zeng (1990) also observed a similar pattern of phase change in the ground acceleration in their centrifuge model tests.

[2] Zangar's approximation is smaller than Westergaard approximation by an amount smaller than 5% between H/3 and 2H/3 from the base, and an amount of 5% ~ 15% elsewhere.

Steedman and Zeng (1990b) proposed an analysis that takes into account a finite shear wave velocity in the backfill, thus allowing for a phase change in a prototype structure. The phase change does not have a significant influence of the total earth pressure, but it has a marked effect on the distribution of the dynamic increment. The resultant pressure is shown to act at a point above one third of the height of the wall.

2.2 DYNAMIC CENTRIFUGE MODELING OF EARTH RETAINING STRUCTURES

Centrifuge testing of dynamic problems has been widely employed by geotechnical investigators in a variety of test configurations (Schofield, 1981). In recent years, centrifuge model tests have become extremely popular in the study of the behavior of soil deposits and structures supported by or retaining the soil. The centrifuge modeling technique has been shown to be a useful tool for development and verification of analytical models, especially in the subject of earthquake engineering where detailed field evidence is in shortage (Kutter, 1984).

Dynamic centrifuge testing has been applied to investigate the behavior of retaining structures during earthquakes (Steedman, 1984; Anderson, 1987; Pahwa et al., 1987; Kutter et al., 1990; Vucetic et al., 1993; Zeng, 1990). The techniques and experiences of modeling retaining structures developed in these dynamic centrifuge tests are valuable for the planning of subsequent tests.

2.2.1 Cantilever Retaining Wall

Steedman (1984) conducted a series of cantilever retaining wall experiments with dense, dry sand backfill on the Geotechnical Centrifuge in Cambridge, England The static deflections and bending moments of these walls were found to be consistent with a triangular stress distribution The lateral stress ratios indicated that the static rotations of the walls were sufficient to cause active failure Measured dynamic forces were found to be in agreement with the estimation using the Mononobe-Okabe equation The resultant height was assumed to be at 0.5H Plastic deformations of the retaining walls occurred with stronger earthquakes

Zeng (1990) performed 9 centrifuge tests on quay walls carried out at the Cambridge Geotechnical Centrifuge The tests involved models of free cantilever walls and anchored cantilever walls supporting dry or saturated backfills of Leighton-Buzzard 52/100 sand prepared at various relative densities (ranging from about 40% to about 90%). In saturated tests, the soil models were saturated or submerged with silicone oil that reduced the time scale for consolidation to 1/N during the centrifuge tests

Based on Zeng's saturated tests, Steedman and Zeng (1990a) showed that an initially stiff soil-wall system may deteriorate towards failure as strain softening is brought about by dynamic amplification or pore pressure build-up.

2.2.2 Tilting Retaining Wall

Anderson (1987) conducted a series of dynamic centrifuge tests on a model tilting gravity retaining wall with dry sand backfill Al-Homoud (1990) reviewed Andersons's

test results and and obtained some findings regarding the soil thrust acting on the wall during earthquakes. The major findings obtained from Anderson (1987) and Al-Homoud (1990) are summarized as follows:

I. Phasing

The most important observation is the phase relation between the ground accelerations and the dynamic earth thrust acting on the wall. Anderson's (1987) observations show that the earth force was about 180° out of phase with the lateral acceleration field tests with firm foundation soils, which is opposite to the assumption of the Mononobe-Okabe equation. Al-Homoud's (1990) finding shows that the measured earth thrust was approximately in phase with the wall movement: the minimum earth force occurred at the time of maximum outward tilt in the wall, while the maximum earth force occurred at the time of maximum inward tilt in the wall.

II. Dynamic Earth Thrust

The vertical position of the dynamic earth thrust was approximately 0.58 H above the wall base. This point of action was close to the value of 0.6 H suggested by Seed (1969).

III. Wall Movement

The rotational stiffness of the wall deteriorated with increasing outward tilt in the wall. This deterioration was due to the accumulation of outward wall tilt during successive cycles of strong shaking and the fact that there is an ultimate capacity of the resisting moment.

2.2.3 Amplification of Peak Acceleration

Much evidence (from both field and laboratory observations) show that the lateral ground acceleration is amplified as shear waves propagated from the base of the soil stratum. This information suggests that awareness should be paid to the amplification of ground acceleration in dynamic centrifuge tests. Some typical evidence from field observations and centrifuge model test results are listed as follows:

I. Field Observations

Seed and Lysmer (1980) presented data of maximum accelerations observed at different depths during the Tokyo-Higashi-Matsuyama earthquake of July 1, 1968. The data showed that the peak accelerations observed at the surface were about twice as large as those measured at a depth of about 10 m. Evidence from the Humbolt Bay Power Station during the 1975 Ferndale earthquake showed that accelerations at the surface were 2.3 times those at a depth of 24 m.

Seed et al. (1992) presented the strong motion data of the seismic response of soft and deep clay sites obtained during the 1989 Loma Prieta Earthquake. This article shows the ground surface acceleration data measured at various locations. The acceleration observed at Yerba Buena Island, a large, rocky outcrop near the center of the San Francisco Bay, was viewed as the input ground acceleration at the bed rock. The acceleration data obtained at four soft clay[3] recording sites showed amplified ground surface accelerations. The peak acceleration at the surface of soft clay was three to four times the peak acceleration of the bed rock.

---

[3] The soft clay at these sites is the San Francisco Bay Mud with various thicknesses ranging from about 8 meters to 30 meters.

II. Dynamic Centrifuge Test Results

Steedman (1984) demonstrated the evidence of amplifications of peak ground accelerations, at various depths in dry sand models during dynamic centrifuge tests. The amplifications of ground acceleration at surface in dry sands were also observed during the centrifuge tests conducted by Anderson (1987).

2.2.4 Belleville Disc Washers to Model Foundation Soils

The dynamic behavior of a realistic retaining wall is tangled with two types of interaction between the wall and the soil:

• the interaction between the wall and the backfill soil

• the interaction between the wall and the foundation soil

Clearly, the first one is the primary interaction. In the past few years, MIT's concentration was on the interaction between the wall and the backfill soil. Anderson (1987) used Belleville disc washers to model the stiffness of the foundation soils in his dynamic centrifuge tests, so that the interaction between the wall and the foundation soil was simplified.

The washers are conically shaped discs that can be stacked on top of each other. By varying the arrangement of these washers, one can obtain various load deflection characteristics of each stack of washers. In Anderson's model, the resistance to rotation of the wall was provided by two stacks of the disc washers. The load-deflection relationships of the washers are approximately linear.

The application of Belleville disc washers in centrifuge tests was an experimental advance in the field of dynamic centrifuge modeling. Disc springs function best under high load conditions in confined space. Springs composed of these disc washers are adequate for use in centrifuge testing. In this research, the author applied disc springs to provide both elastic and plastic[4] characteristics of a model retaining wall.

2.3   LIQUEFACTION POTENTIAL OF SATURATED SANDS

Dobry et al. (1981) showed that the liquefaction potential of a saturated sand depends on both the characteristics of the seismic shaking and of the soil. Their evidence indicated that overconsolidated sands have a larger resistance to liquefaction than normally consolidated sands. They reviewed a series of strain-controlled cyclic tests and showed the following:

1. There is a threshold cyclic shear strain for pore pressure build-up of $10^{-2}\%$ for normally consolidated sands. That is, there was no excess pore pressure in tests with cyclic shear strain smaller than $10^{-2}\%$.

2. Overconsolidation increases the value of the threshold strain from $10^{-2}\%$ to about $3 \times 10^{-2}\%$.

3. A heavily overconsolidated sand develops much less pore pressure at a cyclic strain, 0.05%, than the same sand when normally consolidated.

It was suggested that heavily overconsolidated sands subjected to ground accelerations of 0.15g will probably not liquefy because of the combined effects of larger

---

[4] The plastic behavior was provided with a slider in the tie-back system of the wall, in which four stacks of such spring washers were used.

shear modulus in the field, a larger threshold strain and a smaller pore pressure build-up for a strain somewhat above the threshold.

2.4 NUMERICAL MODELS FOR SANDS DURING EARTHQUAKES

Various numerical models for dynamic analysis of earth structures have been developed during the past fifteen years. There are wide variations in basic principles of these analysis procedures. Whitman (1992) made an extensive review of many of the numerical techniques. Some of these techniques and other currently available codes are described as follows.

2.4.1 Fully Coupled Analyses

The code DYNAFLOW developed by Prevost (1981) is based upon a constitutive model involving a concept of multi-yield surface plasticity, with a linearized hyperbolic backbone curve for the stress-strain relations during loading, unloading and reloading. Segments of the backbone curve are fitted to stress-strain curves observed in monotonic loading tests for the particular soil. Fundamental studies on soils were applied in establishing the shapes of yield surfaces. The flow rule associated with the yield surface provides the inelastic volume strain, and hence pore pressure changes. Validation has been achieved through comparisons between calculations and centrifuge test results, although this information is not generally available in the literature (Whitman, 1992).

Elgamal et al (1985) described an analysis based upon Prevost's constitutive model and applied it to the case of La Vallita Dam (Elgamal et al., 1990). The results suggest that dispersed plastic deformation is less important than concentrated slip

Another fully coupled analysis, DYSAC2 (Muraleetharan, 1990), was claimed to be successful in predicting the acceleration and pore pressure time-histories of level ground stratified soil deposits composed of a sand layer overlain by a silt layer (Arulanandan et al., 1992)

2.4.2 Partially Coupled Analyses

Finn et al (1977) developed a nonlinear dynamic effective stress response analysis for level ground condition The analysis was implemented in programs DESRA (Lee and Finn, 1975; 1978) and TARA The latest versions of the computer code TARA are known as TARA-3 and TARA-3FL (Finn et al., 1986) The soil response is modeled by combining the effects of shear and normal stresses. In shear, the soil is treated exactly as in the level ground analysis where it is considered as a nonlinear hysteretic material during unloading and reloading The shear stress-strain behavior is characterized by a tangent shear modulus which depends on the shear strain, the state of effective stress, and the previous loading history.

Siddharthan (1984) extended the Finn model to include the effects of initial static shear stress. The pore water pressure is computed in two steps First, the "apparent" plastic volume change is evaluated from the shear strain history of an element. The parameters (volume change constants) required to compute the pore pressures are estimated from the drained behavior of samples in a simple shear device The second step

is to estimate the rebound modulus and multiply it by the increment in volume change to determine the increment in pore water pressure.

Siddharthan (1984) reported a validation study on a series of seismic tests on centrifuge models. These tests were conducted on the Geotechnical Centrifuge at Cambridge University, England. Finn and Siddharthan (1984) showed that the recorded acceleration response and the response computed by the program TARA were in remarkable agreement.

2.4.3 Uncoupled Analyses

The Residual Strain Method (RSM) (Bouckovalas et al, 1984, 1991; Stamatopoulos and Whitman, 1987) is an uncoupled analysis that predicts the behavior of sands during earthquakes and earthquake-induced permanent deformations of foundations resting on sands. The program CYCON is an application of the RSM, a semi-empirical model, which computes the permanent strains and pore pressures from viscoelastic constitutive equations where time has been replaced by the number of load cycles (Bouckovalas, 1982). The constitutive parameters dependent upon the soil properties, the initial stresses and dynamic stress amplitudes, and they can be obtained from common static and cyclic laboratory tests on the particular soil. Computations focus upon displacements and pore pressures at the end of one or more load cycles.

The RSM was originally developed to analyze cyclic loading of offshore foundations on sands, under drained or undrained conditions (Bouckovalas et al., 1984, 1986). Recently, the method was extended to partially drained cyclic loading (Bouckovalas et al., 1991). In addition, research was invested to improve the accuracy of the semi-empirical

42

constitutive equations and fit the method to specific needs of earthquake-related applications (Stamatopoulos et al , 1991). CYCON was used in this research to predict the pore pressure behavior of a backfill behind a retaining wall as well as the tilt of the wall due to various earthquakes The results of the numerical prediction and the evaluation of the predictions will be presented in Chapter 5. A brief review of the residual strain method will also be described in Chapter 5.

2.5   SLIDING BLOCK MODEL FOR THE PERMANENT MOVEMENT OF A RETAINING WALL

Newmark (1965) first introduced the block-on-an-inclined-plane model to evaluate seismically-induced displacements along the slopes of earth dams The features of the Newmark's sliding block approach are as follows.

1. The permanent displacement induced during the seismic motion is accumulated through a series of slips along a well-defined yielding (sliding) surface in the soil. Slip starts when the inertia force of the upper soil wedge exceeds the shear strength along the sliding surface. When the relative velocity between the sliding wedge and the underlying dam body becomes zero, the slip ceases.

2. The material along the sliding surface is treated as rigid-plastic The occurrence of slippage is characterized by a yield acceleration (a limiting ground acceleration above which sliding takes place), A_c. Sliding takes place when the ground acceleration exceeds this limiting acceleration.

Makdisi and Seed (1978) employed Newmark's method and accounted for dynamic response of an embankment. They de-coupled the dynamic response phase from the sliding block phase in the system. The effect of this de-coupling on the estimated response

43

has been studied by Lin and Whitman (1983). This was accomplished by analyzing the response of a multi-degree of freedom mass-spring-slider system instead of calculating the response of an intact structure and then using that response as input to a mass-slider system. Newmark's sliding block approach has gained considerable popularity because of its simplicity. This approach will be used in Chapter 7 to analyze the seismically-induced tilt of a retaining wall with a tie-back that yielded temporarily during cyclic loading.

Richards and Elms (1979) used Newmark's sliding block concept to develop the first systematic approach to the seismic design of gravity retaining walls supporting dry cohesionless soils. The wall plus the soil wedge is treated as a rigid block, with the maximum transmittable acceleration determined by frictional resistance at the base of the wall plus the shear resistance along a failure plane through the soil. Whitman and Liao (1985) investigated factors affecting the choice of a suitable safety factor for use with the Richards-Elms method: errors in the use of a sliding block to represent a retaining wall and associated backfill, near-randomness in time-histories of earthquake ground motion and uncertainty in strength parameters. They developed a systematic approach for treating these uncertainties. Whitman (1990) developed new design rules for gravity walls based on the insights from the above analyses.

The above studies were concentrated on the outward sliding of a gravity wall. However, field observations suggest that, where there have been significant movements of gravity walls during earthquakes, rotations of the wall about their base has been important (Whitman, 1990). The behavior of tilting walls has, until very recently, received relatively little study.

44

CHAPTER 3

CENTRIFUGE CHECK TEST

The objective of the check test was to verify the consistency of dynamic centrifuge testing using at various geotechnical centrifuges. Similar (check) tests were carried out by eight institutions using various centrifuges. MIT undertook two tests as part of the check test program. These two tests were conducted on the geotechnical centrifuge at Rensselear Polytechnic Institute (RPI), with the assistance of RPI personnel to operate the centrifuge system.

The soil model in the test program consists of a saturated sand layer underlying a saturated silt layer. The soil model was spun up in the centrifuge to a gravity level of 50-g, and then excited by ten cycles of more-or-less sinusoidal input motions. Pore pressures and accelerations at various depths within both strata were measured. The testing program is described in Section 3.1.

Section 3.2 describes the sample preparation procedures developed for the check tests - because they were also used for the centrifuge model retaining wall tests (Chapter 4).

Section 3.3 reports the essential features of pore pressure responses, because the experience influenced the interpretation of the model retaining wall tests (Chpater 6).

Results of the two MIT tests have been reported through the VELACS documentation system (Ting et al , 1990). After reviewing the results from various experiment teams. Arulanadan (1991) concluded that generally consistent pore pressure behaviors were observed in tests performed at various geotechnical centrifuges

3.1   TESTING PROGRAM

Figure 3.1 shows the schematic of the test model   The model consists of two layers of soils: a 3.0m (prototype scale) thick layer of saturated fine sand underlying a 3.0m (prototype) thick layer of silt   The sand (Nevada sand) was supplied by Gordon Sand Company of Compton, California   The silt (Ottawa Silt No. 106) was supplied by U.S. Silica Corporation of Ottawa, Illinois   The properties of these two soils are documented in the VELACS Laboratory Testing Program Soil Data Report by The Earth Technology Corporation (1992)   Table 3.1 summarizes the properties of Nevada sand.

The sand was prepared by dry pluviation into the test container, followed by saturation with de-aired water   A 50% (by weight) silt-water slurry was placed on top of the saturated sand   The instrumentation was installed during the process of sample preparation   The saturated sample prepared with silt slurry was left for 24 hours prior to centrifuge testing   Detailed procedures for preparing saturated sand models are described in Section 3.2

The instrumentation scheme is shown in Figure 3.1   Pore pressures are measured at mid-depth in the silt layer, and at five depths in the sand layer: top, bottom and at each quarter depth   Horizontal and vertical accelerations are measured at the mid-depth in the

46

silt and at the sand-silt interface. Settlement data are measured at the silt surface and the sand-silt interface

Horizontal excitations were applied to the soil container at a centrifuge acceleration of 50g at the silt-sand interface. The sample was subjected to the steady centrifuge acceleration for 20 minutes (1000 min in prototype scale) or longer prior to inducing the earthquakes. The input ground motions consist of about 10 cycles of more-or-less sinusoidal horizontal motions (at 2 Hz) with a peak acceleration of 0.25g (all in prototype scales).

3.2 PREPARATION FOR SATURATED SAND STRATUM

3.2.1 Pluviation of Dry Sand

The sand layer was deposited using an existing MIT diffusive rainer[5] (Figure 3.2). The rainer consists of a thin-wall drum having a perforated base and an extended chimney downward to the container of the soil model. The chimney prevents the fine particles from escaping. Two sieves were placed in the chimney to diffuse the sand and distribute it into the shaking bin uniformly. The intensity of deposition is governed by four parameters: (1) the spacing and size of the openings in the perforated base; (2) the sizes of the openings of the screens; (3) the spacing between the screens and the raining drum; and (4) the spacing between the screens and the deposit surface. Al-douri, Hull and Poulos

---

[5]The rainer was initially designed for the pluviation of a courser sand. A No. 16 sieve is used to reduce the deposition rate, and therefore yield a denser condition for the fine Nevada Sand.

(1990) reported that this technique is effective to produce a uniform bed of sand sediment of a specified density

The sand was first laid in the drum of the raining device The bottom of the drum consists of a plate with equally spaced 3/4 inch holes and a trap door The expected relative density is obtained by calibrating the rainer, that is, by varying the rate of deposition and locations of the diffusing screens A screen equivalent to No. 16 sieve was placed on top of the perforated base of the drum to reach the appropriate deposition rate for Nevada sand with 60% relative density The dry density was evaluated by the net weight and volume of the sand deposition in a rectangular container in which the thickness[6] of the sand can be measured Consistent dry densities of 15.91 ± 0.08 kN/m^3, compared to a target of 15.95 kN/m^3 were obtained using this setup By using finer screens, the rainer could produce a Nevada sand with 75% relative density The dry density was 16.42 ± 0.12 kN/m^3, compare to a target density of 16.47 kN/m^3.

The process of pluviation was interrupted for instrumentation (e.g., the installation of pore pressure transducers and/or the accelerometers) To ensure the accuracy of installing the transducers, the sand is always over-pluviated by a few millimeters The extra amount of sand above the nominal location of the transducer is removed by vacuum, prior to installation Figure 3.3 shows the schematic diagram of the vacuum technique. The final thickness of the sand is reached by the same technique - over-pluviation followed by vacuuming away the over-pluviated sand

---

[6] The thickness of each deposition was made uniform with the vacuum technique (Figure 3.3).

3.2.2 Saturation Procedures

This section describes the detailed procedures for obtaining highly saturated sand specimens. The underlying concept is to saturate a porous media at an environment with very low absolute pressure (e.g., 0 ~ 10 mTorr). The low absolute chamber pressure guarantees the amount of air being minimum in the system.

In dynamic centrifuge tests measuring pore pressure responses, it is necessary to saturate the pressure transducer, in addition to saturating the sand. The requirement for saturating the pressure transducer is more stringent than that for saturating sand models. In centrifuge testing, the pore pressures are usually measured with miniature pressure transducers (e.g., Druck PDCR 81). Each pressure transducer has a protective porous stone (a ceramic filter) in front of its pressure diaphragm. The pores in the ceramic porous stone are much finer than the pore sizes of most sand skeletons. The saturation of the pressure transducer ensures the saturation of the sand skeleton. Based on the writer's experience, this low-pressure-saturation technique is extraordinarily effective for saturating ceramic porous stones with an air entry value of one bar.

The dynamic performances of the pressure transducers, saturated with the low-pressure technique, had been inspected prior to the centrifuge test program. The inspection was done in an independent cell specifically made for calibrating these miniature transducers. A saturated miniature pressure tranducer and a regular pressure transducer were installed in the cell which was filled with de-aired water. Then pressure pulses were applied to the cell. The output of both pressure transducers were recorded while pressure pulses were applied. The responses of both transducers are linear with each other, with R^2 values larger than 0.999 in linear regressions. The miniature transducers are also calibrated this way - based upon a (well-calibrated) regular pressure transducer.

49

A schematic diagram of the saturation process for the check test is shown in Figure 3 4 The sand is evacuated by vacuum pump No. 1. The absolute pressure in the soil container (the shaking bin) is monitored with a pressure guage connected to one outlet on the lid When the absolute pressure decreases to below 25 mTorr, the sand starts to be saturated with de-aired water. De-aired water enters the soil through an inlet of the bin near bottom (valve 6)

Under normal conditions, regular vacuum pumps in geotechnical laboratories can bring down the absolute pressure to about 50 to 125 Torr (corresponding to 94 to 84 kPa vacuum). Some vapor from the vacuum pump oil starts to migrate into the chamber at such pressures The oil vapor prevents further lowering of the pressure in the system. It is therefore necessary to connect an oil vapor trap between the vacuum pump (No. 1) and valve No. 1, in order to reduce the absolute pressure further. The vapor trap (not shown in the figure) is surrounded by liquid Nitrogen and catches the migrating oil vapor by crystallization at low temperatures. This trap prevents the oil vapor from entering the soil through the evacuation route. Such technique can effectively bring down the absolute pressure to less than 20 mTorr (0.02 Torr). The sand can be guaranteed to contain a minimum amount of air after several hours of evacuation.

The de-aired pore fluid (water) is allowed to fill the sand stratum after the bin is evacuated. However, at these very low absolute pressures, water will vaporize instantly when it starts to enter the dry sand. This instant vaporization at the water inlet would cause a piping damage to the sand stratum. The sand skeleton would then be destroyed by a strong water vapor flow due to the resulting large pressure gradient. One way to avoid such a disastrous condition is, prior to saturation, to bring up the absolute pressure in the sand container to a point above the vaporization pressure of water, without destroying the

soil skeleton   This is done by introducing a vapor pressure of water, 12 mTorr, above the sand surface (through Valve 3 at the top) prior to the saturation of sand from the bottom. The step-by-step procedures, referring to Figure 3.4, are listed as follows.

1. Put the top cover onto the sand container and seal the clearance.

2. Make all connections and seal properly.

3. Turn on vacuum pump No. 1 and open valve No. 1 slowly.

4. Monitor the absolute pressure with pressure guage connected to the vacuum tube. Let the vacuum process continue for at least 4 hours with the absolute pressure below 25 mTorr.

5. Turn on vacuum pump No. 2 and valves No. 2, No. 4 and No. 5.

6. Turn valve No 6 to the right to saturate the connection tube between flask No. 2 and valve No 6.

7. Turn valve No. 6 upward to stop the flow after the tube is saturated.

8. Close valve No. 2, open valve No. 3 slowly and wait for one minute.

9. Close valve No. 1.   Monitor the pressure guage and wait until the pressure increases to 12 Torr (vaporization pressure of water). Then open valve No. 2.

10. Turn Valve No 6 to the left slowly and let the distilled de-aired water flow into the sand container Make sure the flow rate is small.

The total time for saturating the check test model was about three hours.

3.3 IMPORTANT INFORMATION FROM CHECK TEST RESULTS

The results of the check test has been reported separately (Ting et al., 1990). The focus here is on the behavior of the pore pressures during the check tests.

The pore pressure in the soil model increases as a result of cyclic shaking. After reviewing the check test results from various institutions, Whitman et al. (1991) formed a theoretical profiles of pore pressure and effective stress in the soil model. This section describes the information as follows.

The expected pattern of behavior in the check test model is illustrated in Figure 3.5 (Whitman et al, 1991). The line OQB gives the variation with depth of the initial pore pressure u_0. The line PAD corresponds to the total vertical stress initially, during and after shaking. These lines are shown straight; actually they should be somewhat curved, due to the variation of gravity field within the total depth of the test model. The difference between PAD and OQB is the initial vertical effective stress σ'_{vo}.

Ideally, if (a) the sand is loose enough; (b) the shaking is strong enough; (c) the silt resists increase in pore pressure as a result of shaking; and (d) there is no movement of water vertically, then the pore pressure at the end of shaking is indicated by the heavy, solid line OQAD. That is, in the sand the initial vertical effective stress has been converted entirely into excess pore pressure, which is the difference between lines AD and QB.

Because of the low permeability of the silt above the sand, the excess pore pressure at the silt-sand interface is retained for some considerable time after the end of shaking.

52

Upward flow is established through the silt, and the pore pressure rises to the line PA. (There may be some delay in establishing this steady state flow through the silt; this delay is ignored in this argument.) On the other hand, because of the high permeability of the sand, the excess pore pressures within the sand readjust quickly and everywhere become equal to the excess pore pressure at the silt-sand interface. Thus, shortly after shaking the pore pressures within the sand are given by the line AC. (The excess pore pressure at this stage is the difference between lines AC and QB.) This decrease of excess pore pressure within the sand is accompanied by settlement of the sand and appearance of a thin layer of water at the interface.

Actually, some adjustment of pore pressure within the sand may occur during shaking. This would be expected if the consolidation time for the sand is similar to the duration of shaking. If this is the case, the pore pressure in the lower part of the sand may not increase all the way to line AD - owing to partial consolidation during shaking. This would mean that a thin layer of water forms at the interface during shaking, and hence accelerations could no longer be transmitted to the overlying silt. The pore pressures within the silt may increase somewhat as a result of shaking, and also because of response to the sudden increase in pore pressure at the base of the silt. This behavior is indicated by the lines intermediate between lines OQ and PA.

This postulated behavior of pore pressure in sand, based upon the check test results, is further confirmed by the centrifuge model tests (Chapter 4). This information will be used to develop the profile of pore pressure in sand, and the thrust on a retaining wall from the excess pore pressure, during centrifuge model tests in Chapter 6.

Table 3.1 Summary of Properties of Nevada Sand
(*from* The Earth Tech. Report, 1992)

Specific Gravity   =   2.67

Maximum Dry Density =   17.33 kN/m^3

(Minimum Void Ratio =   0.511)

Minimum Dry Density =   13.87 kN/m^3

(Maximum Void Ratio =   0.887)

Summary of Sieve Analysis:

Sieve Number	10	20	40	60	100	200
Sieve Size(x10^{-3}m)	2.000	0.850	0.425	0.250	0.150	0.075
Percentage Passing Through Sieve	100.0	100.0	99.7	97.3	49.1	7.7

Grain size curve is plotted in Figure 5.1.
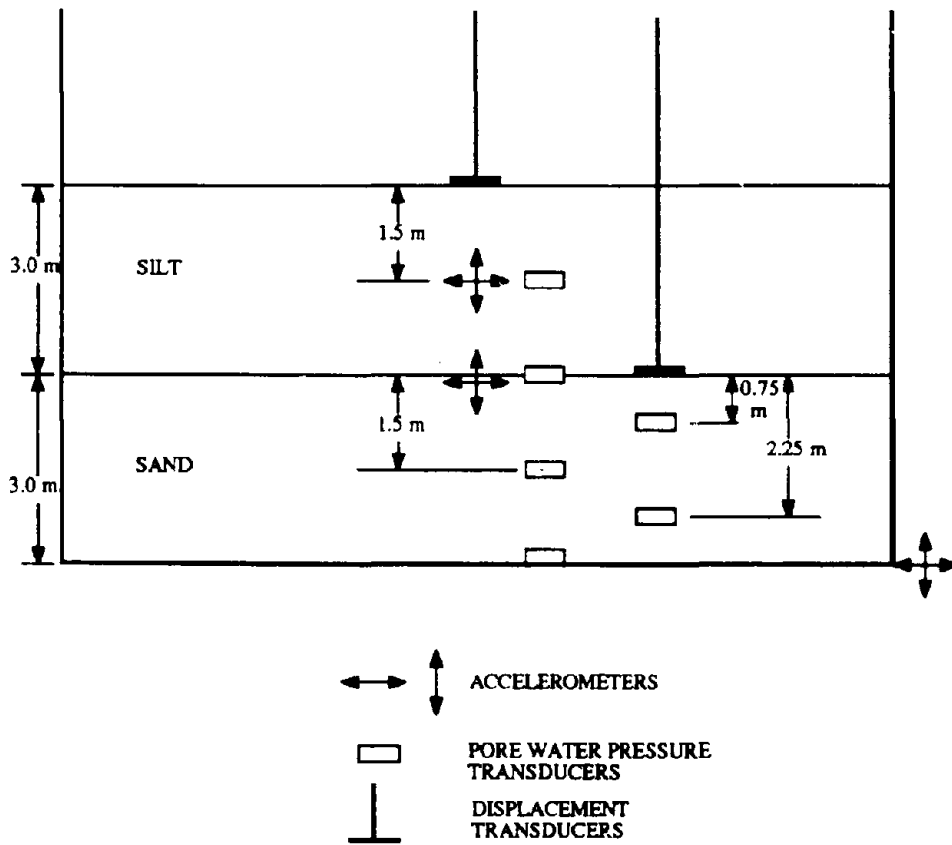
Figure 3.1: Check Test Model and Instrumentation
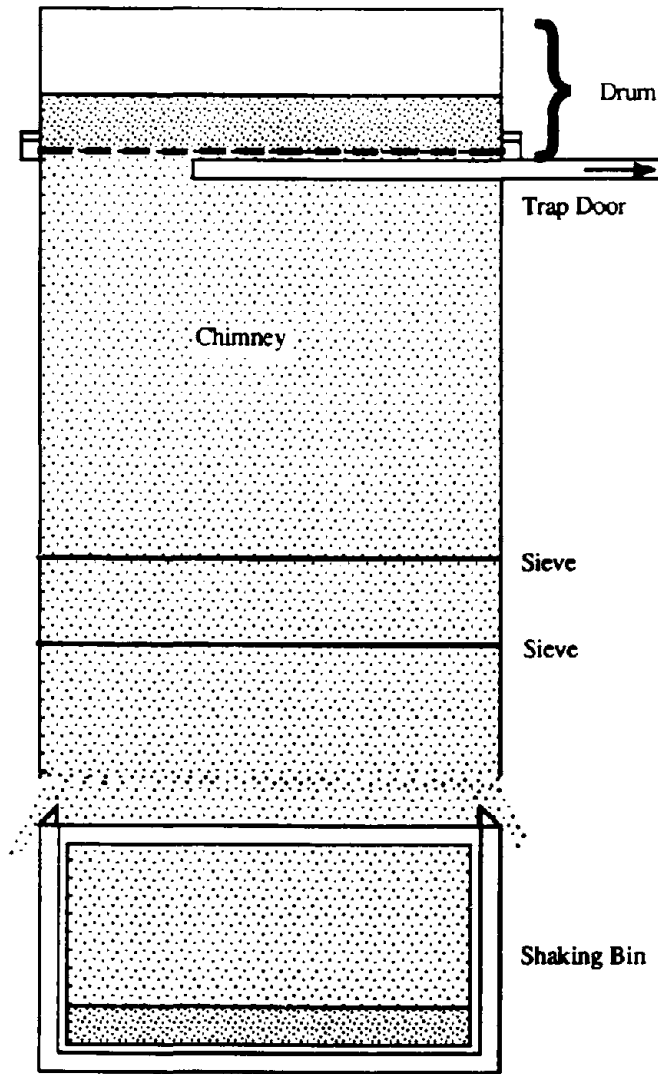
Figure 3.2: Sand Pluviation Device
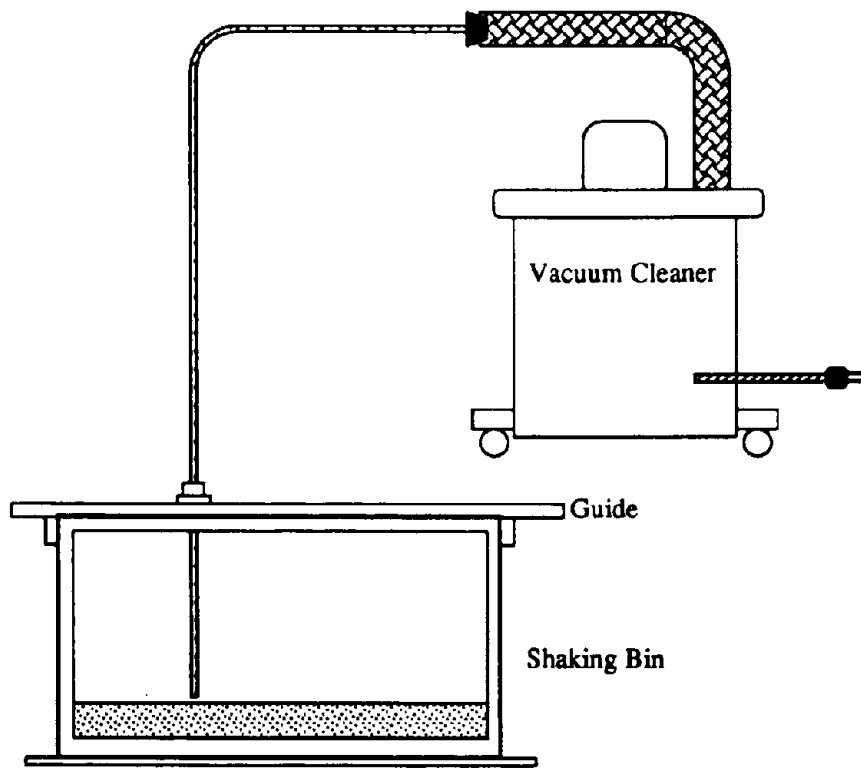
Figure 3.3: Removing over-pluviated sand with vacuum
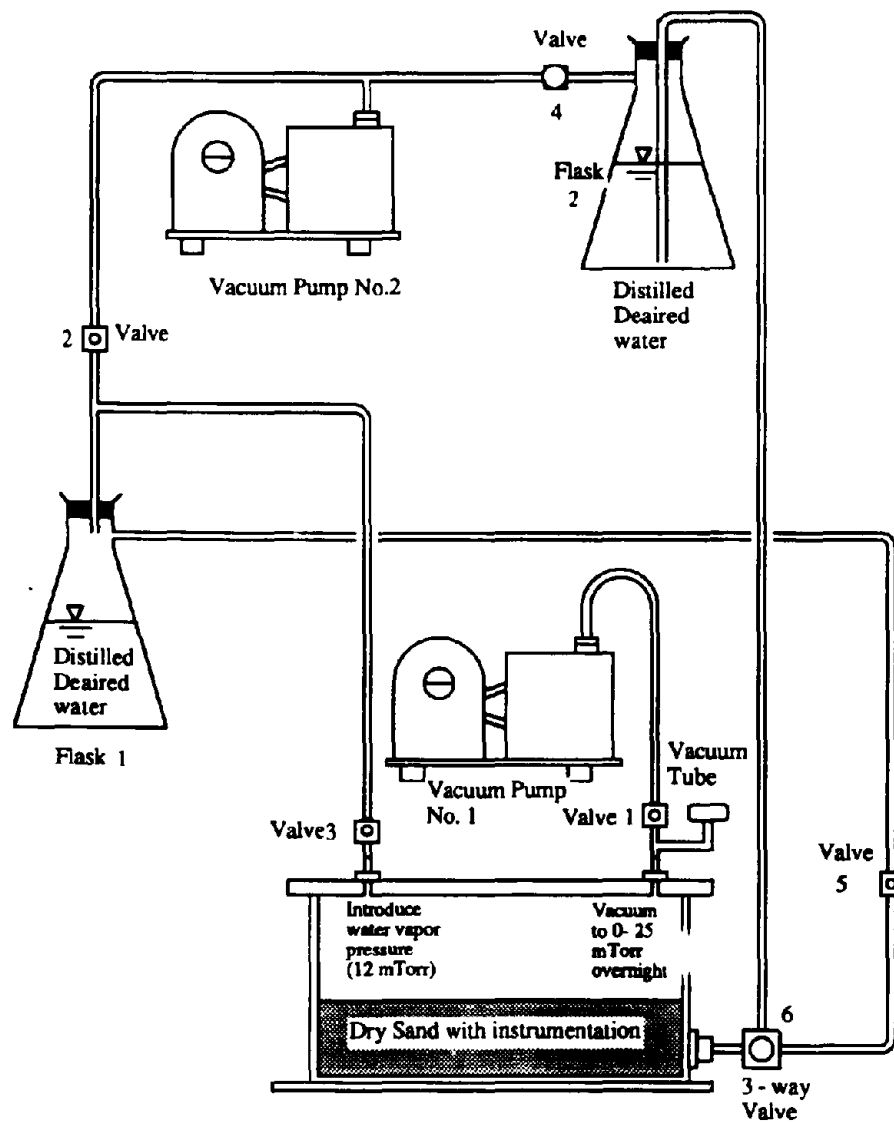
Figure 3.4: Saturation of Sand Sample and Pore Pressure Transducers

At end of shaking —————

Shortly after end of shaking

– – – –

O

P

A

Q

B C D

Pressure, stress

(a) Ideal Case

O

P

A

Q

B C D

Pressure, stress

(b) Typical Actual Case

SILT

SAND
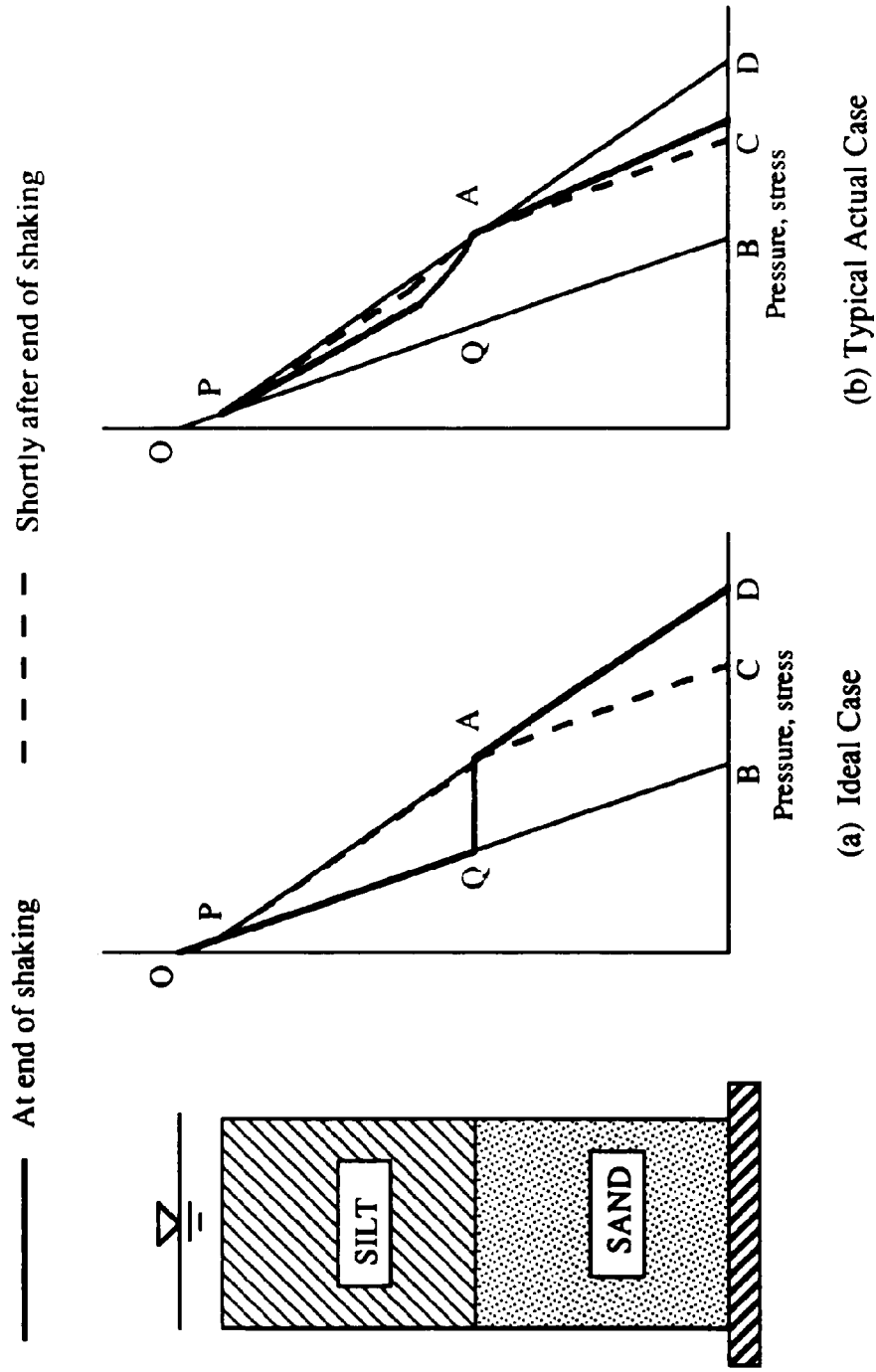
Figure 3.5: Pore pressure behavior during check tests

Page Intentionally Left Blank

CHAPTER 4

CENTRIFUGE MODEL TEST

The program of centrifuge model test was developed to investigate the behavior of a tilting retaining wall supporting a liquefiable backfill during earthquakes

Section 4.1 presents an introduction of the model retaining wall with a tie-back system, as well as the instrumentation. Section 4.2 presents the testing program and the procedures for performing the centrifuge model tests. Results of the model tests are presented in Appendix B. Section 4.3 presents the characteristics of the test results, as well as an evaluation of the load and displacement data.

4.1 INTRODUCTION

The experiment model is an idealized retaining wall supporting a saturated backfill of fine Nevada #120 sand as in the check tests (Chapter 3). This section presents an introduction of the model retaining wall and the instrumentation of the centrifuge model test.

4.1.1   The Model Retaining Wall and the Tie-Back System

Figure 4 1(a) is a conceptual configuration of the testing model. The wall is hinged at the base, and is supported by a system with an elasto-plastic force-displacement relationship. This arrangement resembles retaining walls only in a very rough way, but does contain important aspects of actual full-scale problems. In fact, the relative simplicity of the arrangement allows for straightforward interpretations of the results and for comparisons with theoretical predictions.

The same shaking bin for the check tests (Chapter 3) was used for the model tests. In order to satisfy the tilt characteristics required for the retaining wall model in Figure 4.1(a), the author used an elasto-plastic tie-back to support the tilting retaining wall. Figure 4.1(b) shows a modified design for the soil-wall system for the model test. This design maximizes the length of the backfill stratum in the existing shaking bin.

Figure 4.2 shows the actual assembly of the tie-back system. The spring provides the elastic behavior of the tie-back, and the slider makes the tie-back possible to deform plastically. Figure 4.3 shows the details of the slider. The side pieces are connected by a hinge to the load cell, which is rigidly connected to the shaking bin. The center piece is connected to the spring by a tie rod. The side pieces are compressed by an external load, exerted by the springs at both sides of the slider. The shear resistance between the center piece and the side pieces are controlled by the load applied in the spring. This load can be adjusted by changing the lengths of the springs. During dynamic tests, slip between the center piece and the side pieces is possible as the load in the tie-back exceeds the shear resistance of the slider which may be recognized as the yield load of the tie-back. During sliding, the center piece slides with the tie-back and the retaining wall, while the side

pieces do not. Therefore, the center piece may be viewed as the **sliding element** of the slider. The side pieces, and the springs are viewed as the **stationary element** of the slider.

The slider allows the tie-back to fail temporarily during each cycle of loading, when the load in the tie-back exceeds the shear resistance of the slider. The temporary failure during each load cycle is accompanied by a permanent slip at the slider. Such slip results in a plastic elongation of the tie-back, and hence a plastic tilt of the retaining wall.

Table 4.1 summarizes necessary information of the retaining wall model. The symbols will be used in later chapters. Detailed designs and properties of all parts of the retaining wall system are well documented by Schran (1992).

4.1.2 Instrumentation

Uniform sinusoidal pulses are used as input earthquake. The instrumentation measures the transient displacement at top of the wall, the force in the support, pore pressures at several points in the sand, and accelerations at base, on top of the wall, and near the surface of the sand.

Figure 4.4 shows the detailed arrangement of the centrifuge test model in prototype scale. The model scale is fifty times smaller[1]. The origin in this plot is located, in effect, at lower left center of the backfill. This figure also shows the nominal locations of the transducers. The actual locations of the transducers within the soil were measured after all tests were performed on each soil model. The instrumentation program planned for a total of 17 independent measurements to observe four types of information during the tests:

---

[1] The centrifugal acceleration was 50g in the testing program.

63

1. **Accelerations** - 6 measurements

   The horizontal accelerations were measured at base (A1), at the surface of the sand (A3), at load cell (A4), at the sliding layer of the slider (A5) and on top of the wall (A6) The vertical acceleration at base is measured (by A2) for the purpose of quality control for the input motion Results (in Appendix B) show that the peak vertical acceleration at base is less than 5% of the horizontal input acceleration.

2. **Pore Pressures** - 6 measurements

   Pore pressure within the backfill is measured at three depths near the retaining wall and near center of the backfill.

3. **Displacements** - 4 measurements

   The surface settlements are measured near the wall and near the center of backfill. The transient horizontal wall top displacement is measured using two displacement transducers (D3 and D4).

4. **Load** - 1 measurement

   The total load in the tie-back is measured by the load cell.

The details of the transducers are listed in Table 4.2. Due to the limited number (15) of available data logging channels of the centrifuge facility, not all 17 measurements were recorded in the testing program. Table 4.3 lists the channels not recorded or those that failed to record properly in all six series of tests.

The "effective mass" of the load cell in the axial direction was calibrated in the M.I.T. Geotechnical Centrifuge. The calibration was carried out to evaluated the inertia force associated with load cell in the centrifuge model setup during horizontal accelerations The load cell was installed vertically at the center of the centrifuge platform -- with the axial direction of the load cell pointing the center of the centrifuge during

spinning. Figure 4.5 shows the force measured by the load cell at various acceleration levels. The effective mass of the load cell is 300 grams from this figure.

4.2   TESTING PROGRAM

4.2.1   Testing Program

The test program includes 18 tests on 6 soil models. The primary factors that vary from test to test include:

- the relative density of the sand;
- the intensity of base shaking; and
- the permeability of the pore fluid.

Table 4.4 summarizes the test program. Each test involves one earthquake. Each earthquake involves ten cycles of sinusoidal motions at 100 Hz (2 Hz in prototype). Procedures of the model test are summarized in Section 4.2.2.

The test program aimed to perform liquefaction studies on medium-dense to dense sands. The models were prepared at two relative densities: 60% and 75%. The procedures for pluviating dry Nevada sand for a certain relative density are described in Chapter 3. Similar tests performed on samples with different relative densities may result in different responses in the backfill.

Various shaking intensities were used to quantify the relationships between the intensity and the dynamic responses in the backfill. Progressively stronger earthquakes

were applied to Models 1, 2 and 3. A strong earthquake followed by weaker shakings were applied to test Models 4, 5 and 6.

Model 3 used a different pore fluid. The permeability of the pore fluid is a key parameter of the soil in liquefaction studies. The purpose of using centrifuge to perform dynamic geotechnical test is to down-scale dimensions of the model. However, the permeability of the pore fluid in the model remains unchanged with scaling. In this test program, the pore fluid repl lresented a fluid 50 times more permeable in prototype scale. Therefore, one model (No. 3) was prepared using a pore fluid with smaller permeability, while water was used as the pore fluid for the remaining models. Tests 3a and 3b were performed on a model prepared with 55% glycerol solution as the pore fluid. This pore fluid is ten times less permeable than water. Nevertheless, results of the tests on the model saturated with glycerol solution have demonstrated substantial differences from similar tests performed on water saturated models. Other fluids, such as silicon oil, with much higher viscosity, can be potential candidates for much less permeable pore fluid. However, using such fluids would involve difficulties such as the procedures of saturating the model and the subsequent cleaning processes, especially during l lcleaning the delicate pore pressure transducers, each involving a fine porous stone in front of the pressure diaphragm.

4.2.2 Test Procedures

This section presents a brief summary of the procedures for the centrifuge model test. Critical steps are accompanied by remarks pertinent to this experiment. Detailed procedures are documented by Schran (1992).

I. Model Preparation

- **Pluviaton of dry sand**

  Transducers are embedded in the soil during this process, following the procedures in Section 3.2.1.

  Note that the wall is kept vertical while the sand is pluviated into the container. The wall is restrained from inward tilt by two permanent stops on the shaking bin, next to the inner face of the wall. During the raining process, the wall is restrained from outward tilt by a temporary strut between the shaking bin and the outer face of the wall.

- **Saturating the model**

  Follow the process in Chapter 3.

- **Install the tie-back**

II. Centrifuge Testing

- **Preload the tie-back**

  A preload of 100N ~ 200N was applied in the tie-back to prevent excessive tilting of the wall to avoid the active failure during spinning up the centrifuge. The preload prevented the wall from tilting at lower g-levels[2], say $10 \sim 20g$.

- **Mount the model on the centrifuge**

- **Remove the lateral support of the wall at the outward face**

  This step removed the constraint for the outward rotation of the wall. This allowed the wall to tilt during spinning up the centrifuge, due to increasing earth thrust.

---

[2]g-level is the gravity level in the centrifuge model, which is the vertical acceleration in the model normalized by the normal gravity out of the centrifuge.

67

• **Spin up the centrifuge**

Inspect all data log channels. Check if the transducer readings change properly during spinning up the centrifuge. Stop the centrifuge if necessary.

• **Shake the model**

Excite the model with 10 cycles of sinusoidal motion at 100 Hz (2 Hz in prototype earthquake).

• **Wait for full dissipation of excess pore pressure**

• **Check the amount of wall movement and get ready for another shake**

Check the amount of the residual wall movement. Make sure that the displacement transducer on the wall (DCDT#3) is within an effective range of extension. If the transducer has gone out of range, spin down the centrifuge and adjust the transducer location.

• **Shake the model**

Each model was excited by more than one earthquake. The centrifuge need not be spun down between each two subsequent earthquakes unless necessary, such as to adjust the displacement transducer.

• **Spin down the centrifuge**

• **Inspect the model and record the final thickness of backfill and depths of all embedded transducers**

4.3   TEST RESULTS

The data from the centrifuge model tests are presented in Appendix B. Table 4.5 summarizes the testing program, indicating whether slip occurred in each test. Two categories of tests are classified according to the outcomes of the tests:

68

• Non-slip tests

These tests do not involve slip at the slider. Two major behaviors of the model in these tests will be discussed:

      1) the earthquake-induced pore pressure change, and

      2) various thrusts acting on the wall from the earth pressures.

Chapter 6 will present an extensive investigation of the non-slip tests.

• Slip tests

For tests involving slip at the slider, the characteristics of the slippage are interesting. Chapter 7 will present the discussion of these tests first identifying the occurrence of slippage, and then presenting an explanation and estimations for the amount of slippage in each test, using a sliding block model.

Liquefaction of the soil is the most important feature of the dynamic tests on saturated sand. Section 4.3.1 discusses the meaning and nature of soil liquefaction in the tests.

Schran (1992) observed some significant features of data. Section 4.3.2 presents a summary of these features of data.

Section 4.3.3 presents a procedure to verify the load data and displacement data. The analyses calculate the horizontal wall displacement according to the observed load increments in the tie-back. Comparisons of the calculated incremental-load-induced wall movements and the observed wall displacements are made. Such comparisons offer an effective procedure to verify the validity of the independently measured displacement data and the load data.

69

4.3.1 Liquefaction of the Backfill Soil

The most important features of the dynamic centrifuge tests are those related to the liquefaction of the backfill. The liquefaction of soil can be indicated by two types of data: the pore pressure data and the data by the accelerometer in the backfill (A3).

The soil is defined as liquefied when excess pore pressure essentially reaches initial vertical effective stress. For the purpose of identifying liquefaction of soil, the excess pore pressure is usually converted to excess pore pressure ratio, which is the excess pore pressure normalized by the initial vertical effective stress of the soil. Appendix B reports the pore pressure data in both forms: the absolute excess pore pressure and the excess pore pressure ratio. Liquefaction is possible when excess pore pressure reaches 100%. Table 4.5 summarizes the occurrence of liquefaction in the testing program. The following observations characterize liquefaction using both acceleration data and pore pressure data.

1. **Liquefaction-Free** tests (peak input acceleration less than 0.07g):

   During weak earthquakes, the history of acceleration in the backfill is usually amplified and slightly distorted compared to that of the input accelerations. The excess pore pressure ratios do not reach 100% in these tests. The soil is **not liquefied** under such conditions. Figure 4.6 shows the acceleration histories in Test 1a as an example.

2. Tests involving **Liquefaction** of the soil (peak acceleration greater than 0.2g):

   The liquefaction of soil is defined as a soil, with zero effective stress, which can not transmit ground acceleration during earthquakes. When the earthquake is strong, the liquefaction front moves deeper in the backfill. The excess pore pressure ratios at the mid-depth also reaches 100%. The upper soil is really

liquefied and behaves like a fluid. Figure 4.7 shows the pore pressure acceleration data in Test 5a as an example. The ground acceleration can not be transmitted to the upper part of the soil after two cycles of shaking

3. Tests involving **Quasi-Liquefaction** of the backfill (peak acceleration between 0.07g and 0.20g)

Quasi-Liquefaction of soil is defined as a soil in which effective stress is zero at one or more times during a cycle, but can still transmit ground acceleration. During moderately strong earthquakes, the excess pore pressure ratios near the surface (P5 and P6) reach 100%. This is evidence of zero effective stress in the soil. However, the acceleration data (A3) show that the accelerations are still transmitted to the surface of the soil. Example of both characteristics are shown in Figure 4.8: data of excess pore pressure ratio and acceleration in Test 2c. The acceleration data show that the acceleration near the soil surface (A3) is distorted and amplified, compared to the input acceleration. Such acceleration data indicate that the soil skeleton is not fully destroyed and therefore the soil is not constantly fluidized during the cyclic shaking. The soil is recognized as *quasi-liquefied* in this test.

Figure 4.8 also shows the schematic diagram of effective stress path in the soil during one shearing cycle. In each shearing cycle, the sand experienced a cycle of dilation-contraction-dilation-contraction behavior. The pore pressure was minimum at points a and c, and was maximum at points b and d. The corresponding points during the seventh load cycle are also indicated in the histories of acceleration and pore pressure ratio records. At points b and d, the pore pressure ratio reached 100%. Temporary liquefaction was observed at these times, as indicated by the acceleration history (A3). The dilatancy was maximum at points a and c. Also, the effective stress was maximum at these times. On the other hand, the shaking bin was accelerating back and forth. The sand grains tended to "lock-up" at these times. This indicated by the large spikes in the acceleration history. The acceleration also indicates that the acceleration near the ground surface lagged from the input acceleration at the base.

71

The soil model No 2 was only quasi-liquefied in Tests 2b through 2f Progressive densification of the soil model prevented the model from liquefaction All other models are liquefied when the earthquake is stronger than 0.2g

4.3.2 Summary of Other Data Features

Schran (1992) observed some features of the test data, which are summarized as follows

1. **Accelerations**

   • The peak vertical acceleration at base is less than 5% of the peak horizontal acceleration at base.

   • The acceleration is amplified at load cell (A4) Figure 4 9 shows the trend of the amplification factor versus shaking intensity in test series 1 and 4 The container is not really rigid.

   • The major features of the acceleration in the backfill (A3) have been presented in Section 4 3 1.

2. **Wall Top Displacement**

   • Figure 4.10 shows a typical record of the horizontal wall top movement. A dynamic displacement amplitude fluctuates around an increasing mean value during shaking. The residual displacement decreases after the end of shaking.

   • The negative peaks during the first earthquake on each model are less than the value of static displacement during the spin up of centrifuge The wall does not

swing back against the stop pins[3] on the side wall of the shaking bin. This observation ensures the thrust applied to the backfill being smooth

- The dynamic displacement data are not quantitatively reliable. The responses of the displacement transducers degrade with frequencies of the dynamic displacements. The dynamic displacement data will be examined in Chapter 7.

3. Force in load cell

- The load cell data generally have similar features of the wall top displacement data in non-slip tests: a dynamic amplitude cycling around an increasing mean value during shaking, and a decrease of the residual load after the end of shaking

4. Pore pressure data

The behaviors of pore pressures during the tests are very interesting. Schran (1992) identified the following characteristics of the pore pressure data to describe behavior of pore pressure during the dynamic tests.

- the maximum value of excess pore pressure ratio;
- the trend of the mean excess pore pressure - i.e., the "average curve";
- the *visible* beginning of dissipation, i.e., decrease of the curve
- the dynamic amplitude during shaking;
- the existence of large negative excess pore pressure;
- the occurrence of higher frequency responses;

Schran (1992) made out six classes of pore pressure behavior based upon the above characteristics. The inferences of these characteristics will be covered in Chapters 5 and

---

[3]The pins keep the wall vertical in low g-levels during the centrifuge spin-up. They would prevent the wall from tilting (across the vertical line) into the backfill at any time.

6. The last two characteristics of dynamic pore pressure fluctuations are of particular interests. Chapter 6 will offer explanations for these features.

4.3.3 Incremental Earth Thrust and Tilt of the Retaining Wall

Having looked the behavior of the soil, the focus now is on the behavior of the retaining wall.

The retaining wall tilts as a result of increase of the earth thrust. The tilt of the retaining wall is quantified by the horizontal displacement at the top of the wall. It is worthwhile to verify the amount of the increase of the load in the tie-back and the horizontal wall displacement. This section presents investigation of the wall displacements and incremental loads during three periods: (1) during spinning up the centrifuge; (2) during earthquake; and (3) after the earthquake.

A. During spin up of centrifuge

The load in the tie-back increases while the centrifuge is spinning up. The tie-back was preloaded with a certain amount of force (100 ~ 200 N) prior to the spin-up of the centrifuge. The preload was applied by tightening the tie-back, which caused an initial deformation of the spring. During spin-up, the unit weight of the earth increased as gravity increased. Therefore, the static earth thrust on the wall increased during spin-up - owing to increasing horizontal earth pressure. The load, required in the tie-back to resist the static thrust, increased with the g-level of the vertical acceleration in the model. This load continued increasing during the period of spin-up, until the final g-level was reached.

During the period of spin-up, the wall started to tilt outward[4] when the static load reached the preload in the tie-back.

Table 4.6 presents the data of the load in the tie-back associated with each fresh soil model[5], prior to and after the spin-up of the centrifuge. F_i is the preload in the tie-back. F_o is the load in the tie-back after the centrifuge is spun up, prior to the earthquake. The dotted line in the figure, below the table, shows the load in the tie-back required to resist the static earth pressure, assuming K_o condition[6]. The actual load in the tie-back increased somewhat less rapidly with g-level than that indicated by the dotted line. This was due to the tilt of the retaining wall, which caused a decreasing coefficient of static earth pressure. The average rotation of the wall during spin-up was $0.186\% \pm 0.035\%$, corresponding to a horizontal wall displacement of 19.5 ± 3.7 mm in prototype scale. A typical rotation required to develop active condition ranges from 0.1%, for dense sands, to 0.5%, for loose sands. Therefore, the static earth pressure was close to active condition after spin-up, based on the empirical estimation.

Table 4.6 also presents the horizontal wall displacements calculated from the load increments, during spin up of the centrifuge. The calculated wall displacement is based on the deformation of the spring, due to the incremental load in the tie-back during spin-up. The deformation is calculated to be $50(F_0 - F_i) / k_2$, where $(F_0 - F_i)$ is the load increment during spin-up; k_2 is the spring constant (= 605 kN/m). The amplification factor of 50 puts the displacement in prototype scale. The calculated displacements are close to the

---

[4]Due to further deformation of the spring.

[5]A series of dynamic tests were performed on each soil model. A fresh model has no experience of any previous shaking.

[6]K_o = 1 - sinϕ = 0.41 (for Dr = 60%) or 0.364 (for Dr = 75%). The friction angles are presented in Table 5.1.

observed displacements. The agreement verifies the (static) wall displacements and the incremental (static) load in the tie-back during spin up of the centrifuge

B. During and after the earthquake

The average transient earth thrust on the wall increased during the earthquake and then decreased after the end of shaking. The change in the average transient earth thrust induced a variation in the load applied to the tie-back and a certain amount of wall movement. The amount of wall movement due to the change of average transient load during non-slip tests can be obtained directly, from the displacement data. Such movement cannot be determined from the displacement data in tests involving slip at the slider, since the amount of slip is included in the displacement data

Table 4.7 lists the changes of load in the tie-back, and observed wall movements associated with load changes, during non-slip tests. The load increments at the end of shaking (EOS) corresponded to the increase in the average transient earth thrust during the earthquake. The residual values represent the net increment of the average transient load due to each earthquake. Figure 4.11 shows a summary plot of the wall displacement versus load increment in non-slip tests. If all of the wall movement was the result of spring deformation, one can compute the incremental load in tie-back from the measured wall movement. The dashed line in Figure 4.11 shows the computed wall displacement from the incremental load, based on the amount of spring deformation. The good correlation indicates that there is little, if any, movement in the tie-back system other than in the spring.

Table 4.1   Information of the model retaining wall and tie-back

Masses:

	Symbols	
Wall	m_{wall}	1.156kg
Yoke+Screws	m_{17}	0.146kg
Spring	m_{16}	0.088kg
Connecting Rod	m_{15}	0.045kg
Sliding element of slider	m_{14}	0.075kg
Stationary element of slider	m_{13}	0.560kg
Connection to load cell	m_{12}	0.077kg
Effective mass of load cell	m_{11}	0.300kg

Dimensions:

	Symbols	
Height of Wall	H_{wall}	227mm
Height of tie-back	$H_{tie-back}$	210mm
Backfill Thickness	H	140mm
Width of backfill	w	190mm

Table 4.2   Instrumentation (see Figure 4.4 for transducer code)

Instrumentation Type	Code	Manufacturer	Model Type	Serial Number	Calibration Factor
					[mV/g]
Accele-	A1	PCB	303A03	23069	10.61
rometer	A2	PCB	303A03	23219	11.5
	A3	PCB	303A03	23220	11.77
size:	A4	PCB	303A03	22908	10.98
7.3mm(dia)	A5	PCB	303A03	22904	11.05
x 11.5mm	A6	PCB	303A03	22906	11.15
					[mm/V/V]
Displace-	D1	HP	7DCDT-100	KM	2.6146
ment	D2	HP	7DCDT-100	II	3.6487
Transducer	D3	COLLINS	SS-103	218163	2.3557
	D4	HP	7DCDT-250	HN	22.4683
					[kPa/V/V]
Pore	P1	DRUCK	PDCR 81	2087	19675.868
Pressure	P2	DRUCK	PDCR 81	1983	19627.154
Transducer	P3	DRUCK	PDCR 81	1054	9708.453
size:	P4	DRUCK	PDCR 81	5704	10442.31
6.5mm(dia)	P5	DRUCK	PDCR 81	5709	10336.821
x 11.6mm	P6	DRUCK	PDCR 81	5705	10296.908
					[N/V/V]
Load Cell	LC	Data Inst.	JP500	1391-0002	69926.027

Table 4 3: Channels not recorded or failed to record correctly in the testing program

Transducer Code	Test Series					
	1	2	3	4	5	6
A2	Failed in 1a					
A4		not recorded	not recorded		not recorded	not recorded
A5					Failed in 5a	
A6					Failed in 5a	
P1		not recorded	not recorded	not recorded	not recorded	not recorded
P2						Failed in 6a
P3	not recorded					
LC				Failed in 4a		
D1	not recorded					
D2				not recorded		
D3	Failed in 1c					
D4	not recorded					

Table 4 4 Summary of the Testing Program

Relative Density	Pore Fluid	Peak Input Acceleration					
		0 05g	0 10g	0 13g	0.25g	0 3g	0 35g
60%	Water	1a 4b	1b 4c		1c 4a		
75%	Water	2a	2b 5b	2c 6b	2d 6a	2e	2f 5a
	55% Glycerol Solution		3a		3b		

Table 4.5 Summary of occurrences of slip and liquefaction of the test program

Relative Density	Pore Fluid	Peak Input Acceleration					
		0.05g	0 10g	0 13g	0.25g	0 3g	0 35g
60%	Water	1a 4b	*1b* *4c*		**_1c_** **_4a_**		
75%	Water	2a	*2b* *5b*	2c *6b*	**_2d_** **_6a_**	*2e*	*2f* **_5a_**
	55% Glycerol Solution		*3a*		**_3b_**		

Note: **Bold** tests -   Slip-occurred tests
       Italic tests -   Soil is Quasi-Liquefied
       Underlined tests -   Soil is Liquefied
Descriptions of Quasi-liquefied and liquefied soils are presented in Section 4 3 1

Table 4 6: Incremental load in the tie-back and horizontal wall movement during centrifuge spin-up

Test No.	preload F_i (N)	load @ 50g F_o (N)	F_o-F_i (N)	Initial wall displ. (prototype)	
				$50(F_o$-$F_i)/k_2$ (mm)	Observed (mm)
1a	196	394	198	16.4	16.7
2a	205	399	194	16.0	16 2
3a	239	441	202	16.7	16.3
4a	145	382	237	19.6	20.1
5a	106	406	300	24.8	24.5
6a	108	386	277	22 9	23.1
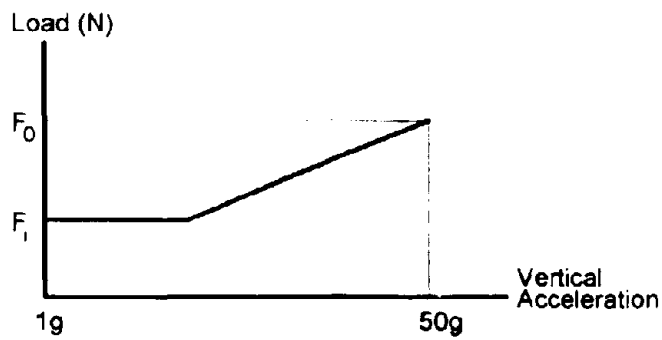
Note: k_2 (= 605 kN/m) is the spring constant

Table 4.7: Incremental load in the tie-back and horizontal wall movement during non-slip

tests

Test	Static load (N)			Load Inc. from initial		Wall top movement (mm)	
No.	Initial	@EOS	Residual	@EOS	Residual	@EOS	Residual
1a	394	431	419	37	25	3.1	2.85
2a	399	411	407	12	8	0.98	0.75
2b	408	478	443	70	35	5.66	4.35
2c	440	490	451	50	11	3.3	0.99
3a	441	544	520	103	79	9.08	8.15
4b	410	430	426	20	16	1.6	1.3
4c	423	470	450	47	27	4.2	2.7
5b	408	466	448	58	40	5.3	4.23
6b	384	469	440	85	56	7.05	4.95
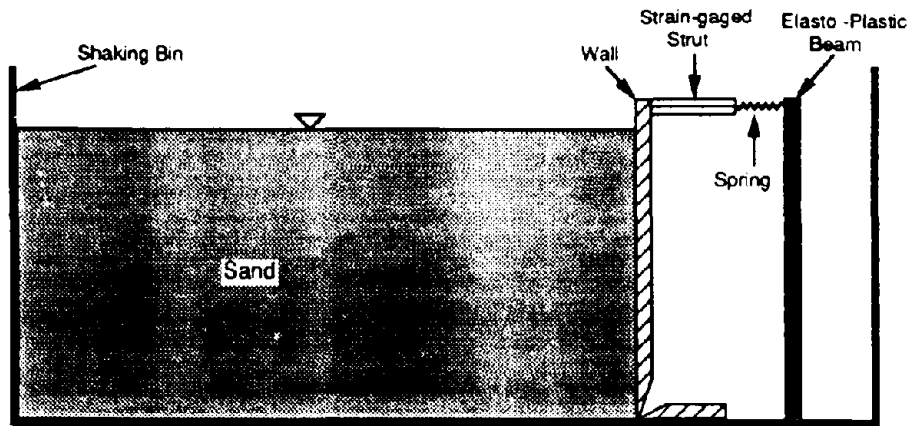
(a) Conceptual configuration of centrifuge test model
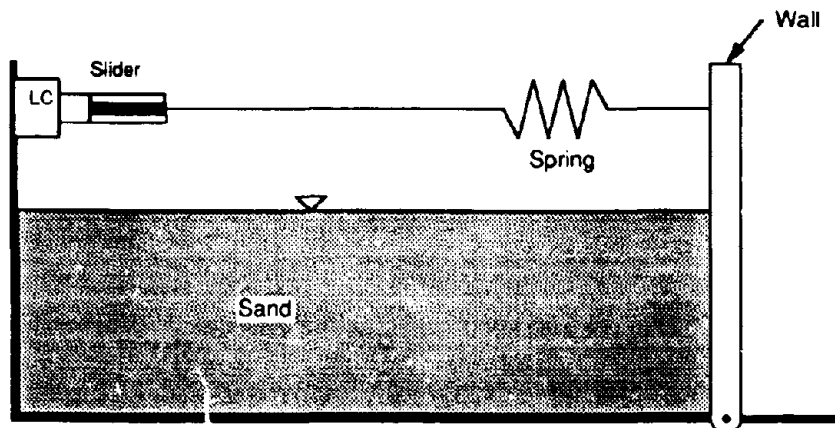
(b) Modified design for centrifuge test model

Figure 4.1: Concepts of designing the of centrifuge test model

Plain
View

Side
View
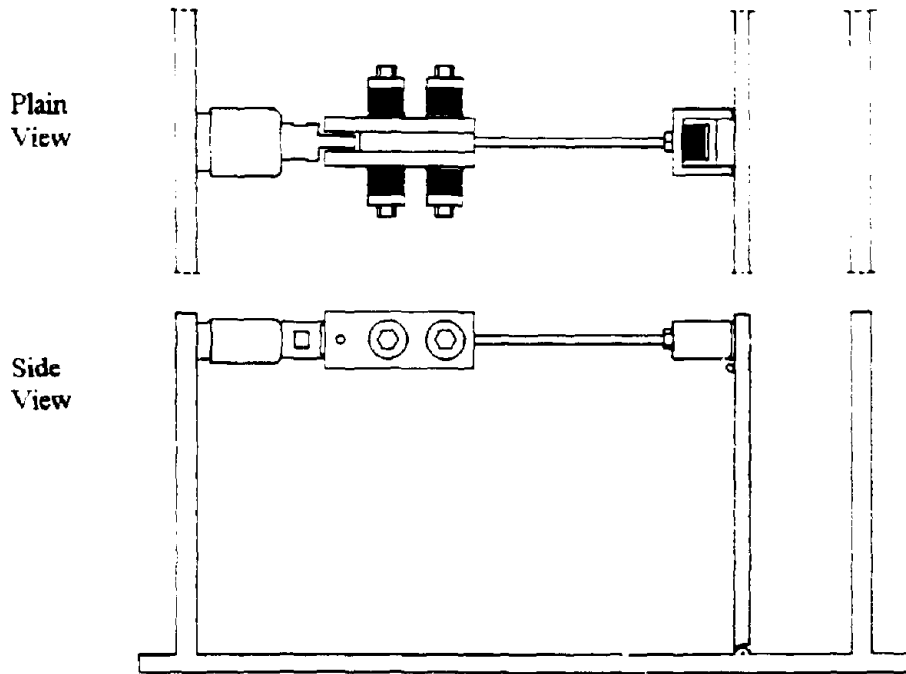
Figure 4.2: Complete assembly of the tie-back system
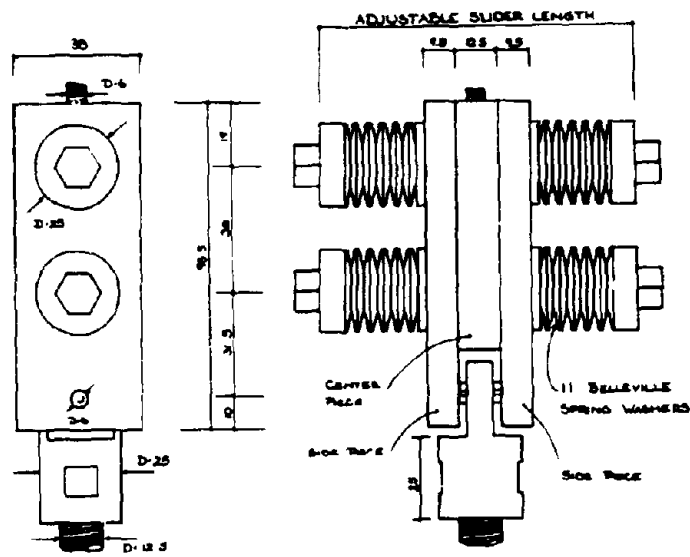
Figure 4.3: Detailed design of the slider

83

Locations of Instruments (Prototype)
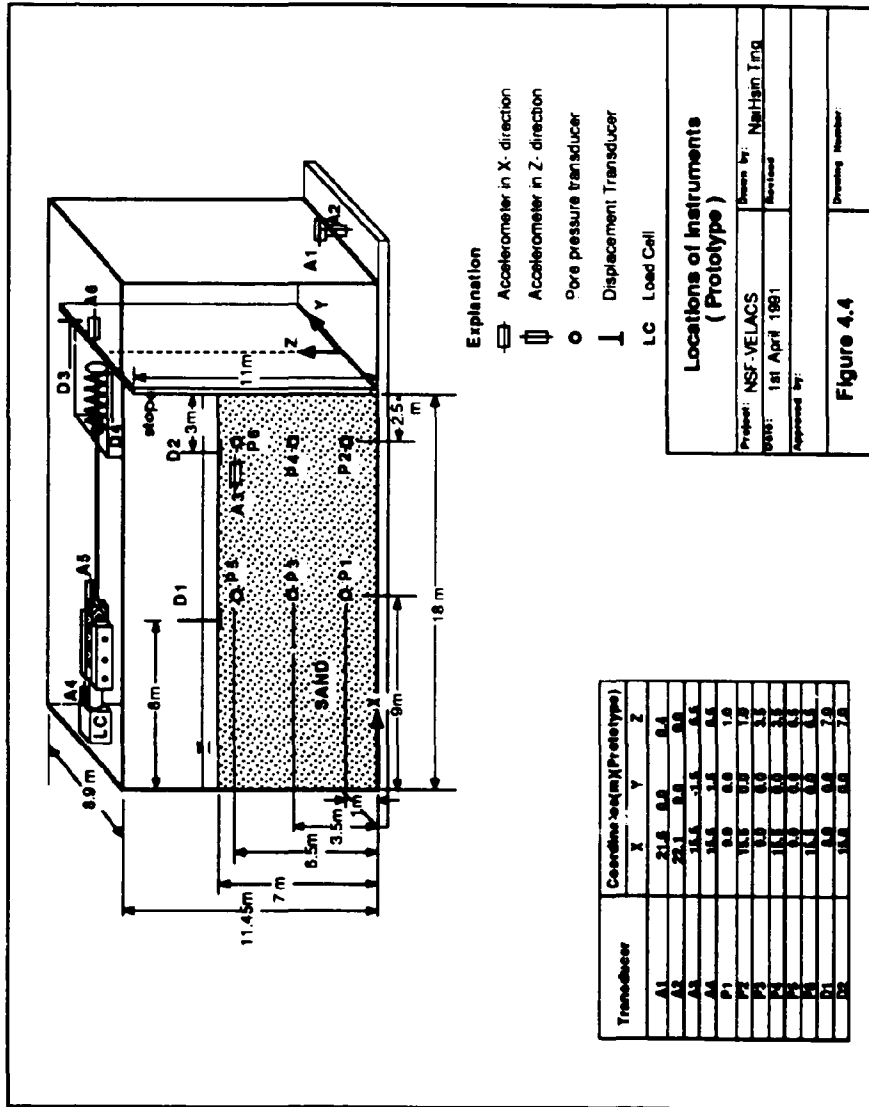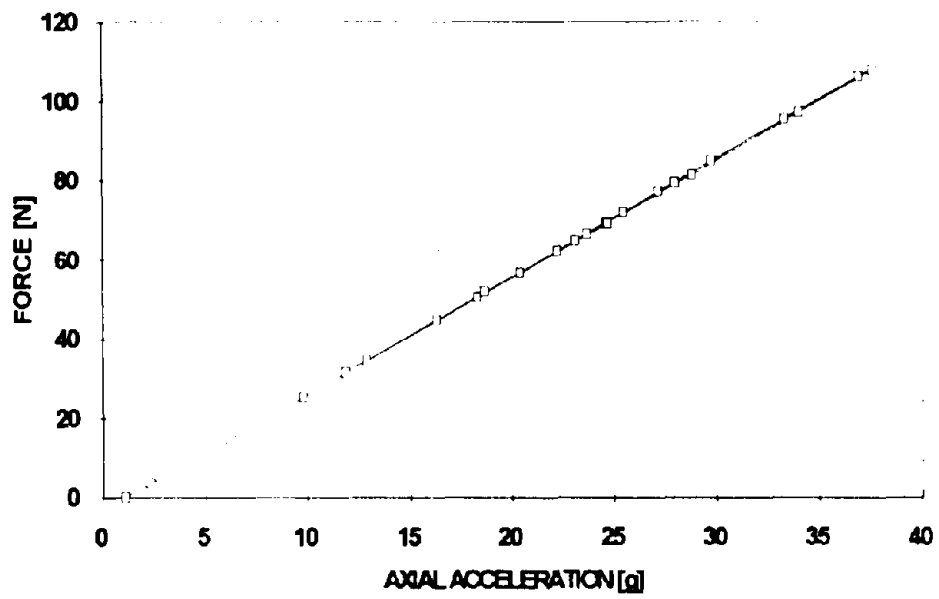
Figure 4.4

Figure 4.5: Calibration for effective mass of load cell
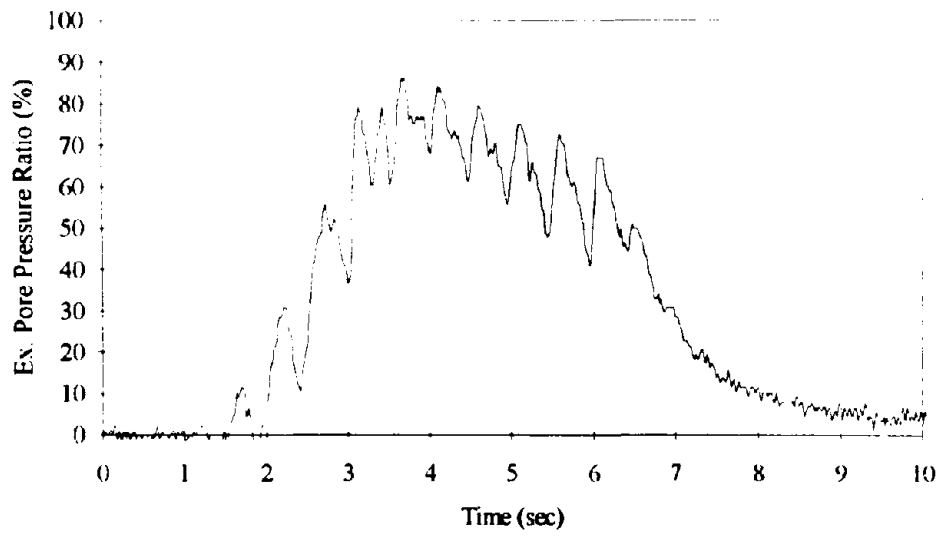
(a) Excess pore pressure ratio of P5
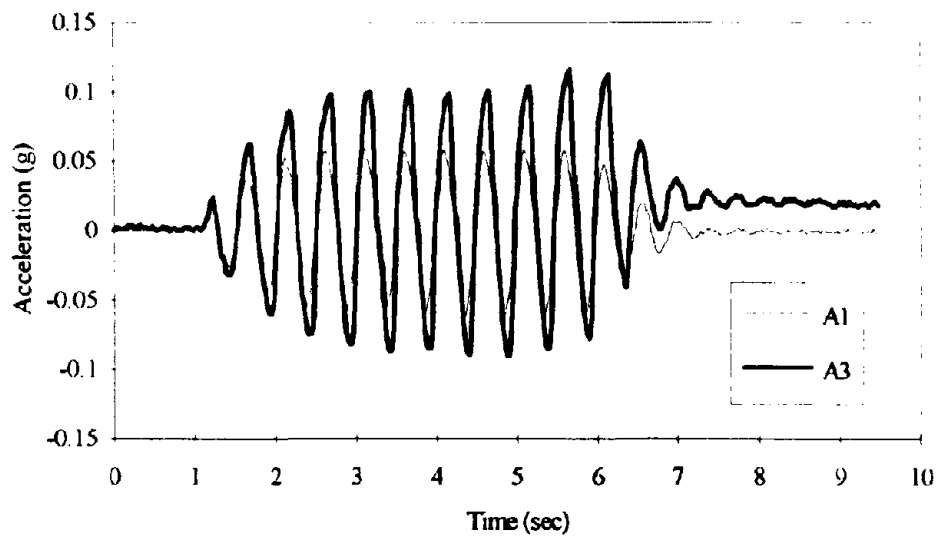
(b) Acceleration response in backfill versus input acceleration

Figure 4.6: Pore pressure ratio and acceleration response in backfill in Test 1a
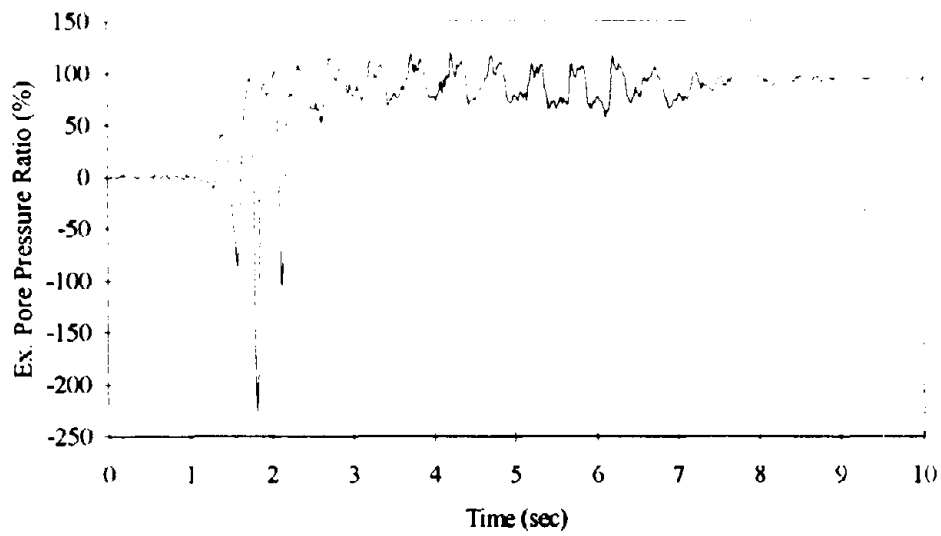
(a) Excess pore pressure ratio of P5
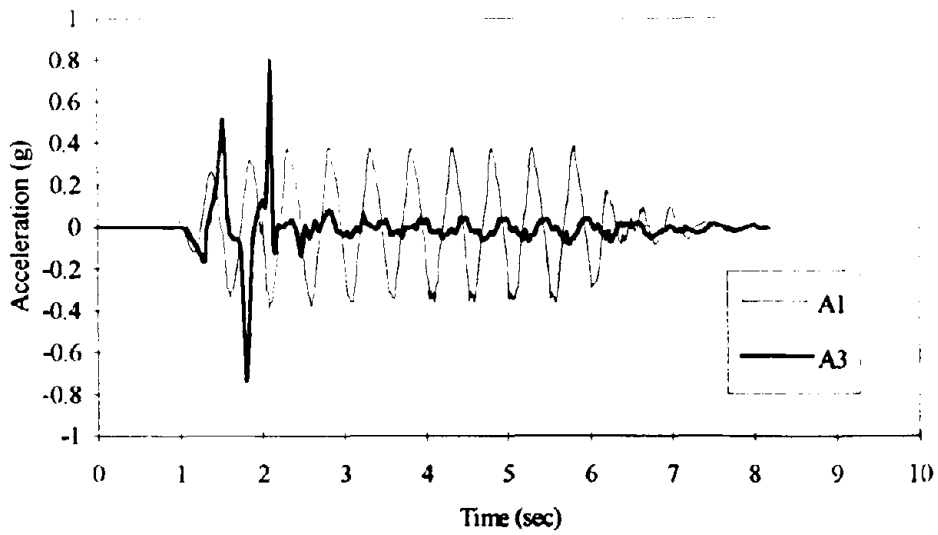
(b) Acceleration response in backfill versus input acceleration

Figure 4.7: Pore pressure ratio and acceleration response in backfill in Test 5a
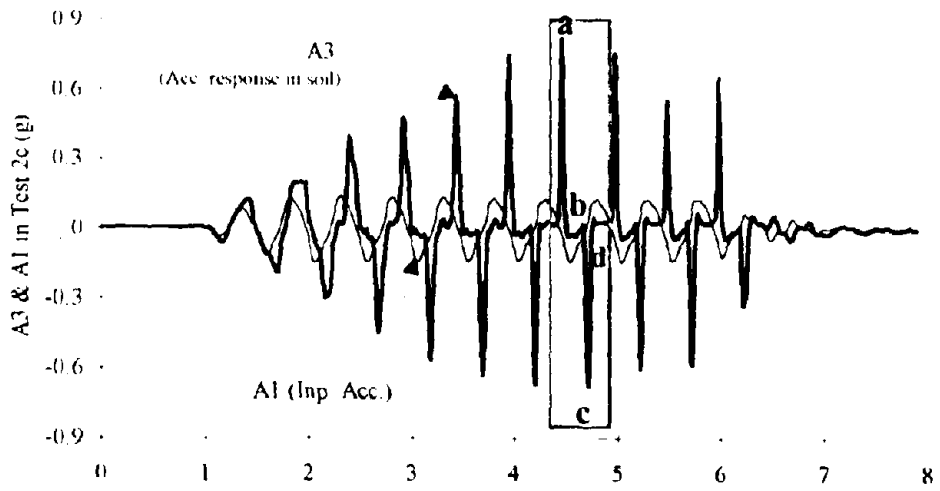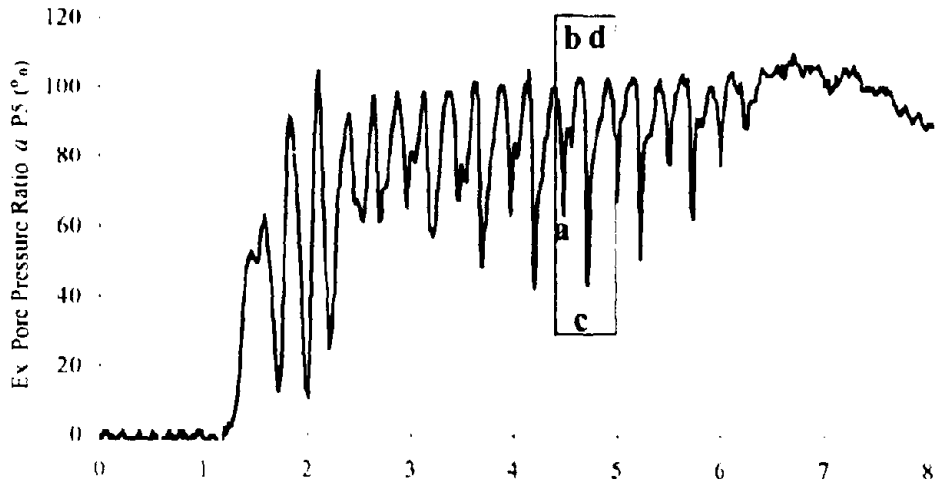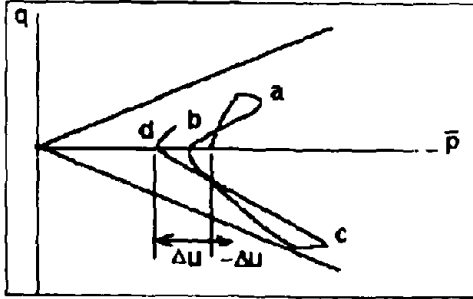
Figure 4.8: Pore pressure ratio and acceleration response in backfill in Test 2c
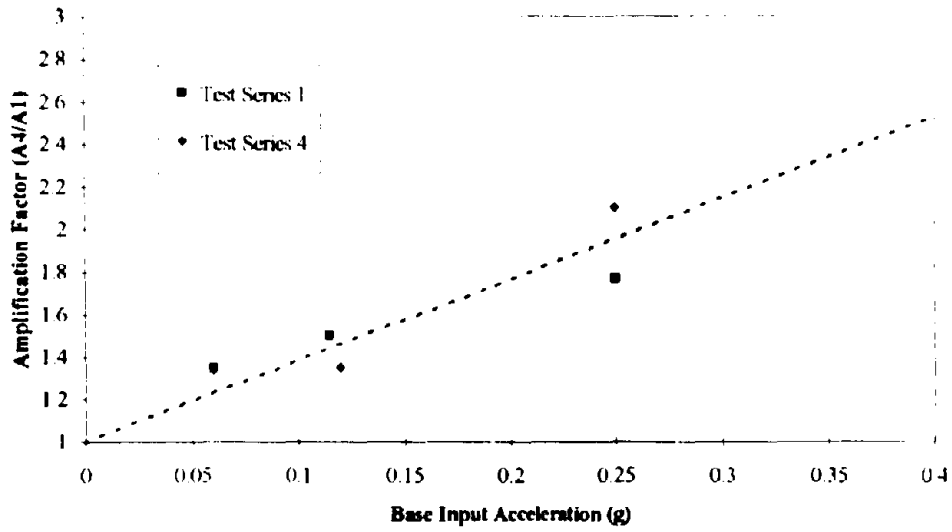
Figure 4.9: Factor of acceleration amplification at load cell (A4/A1)
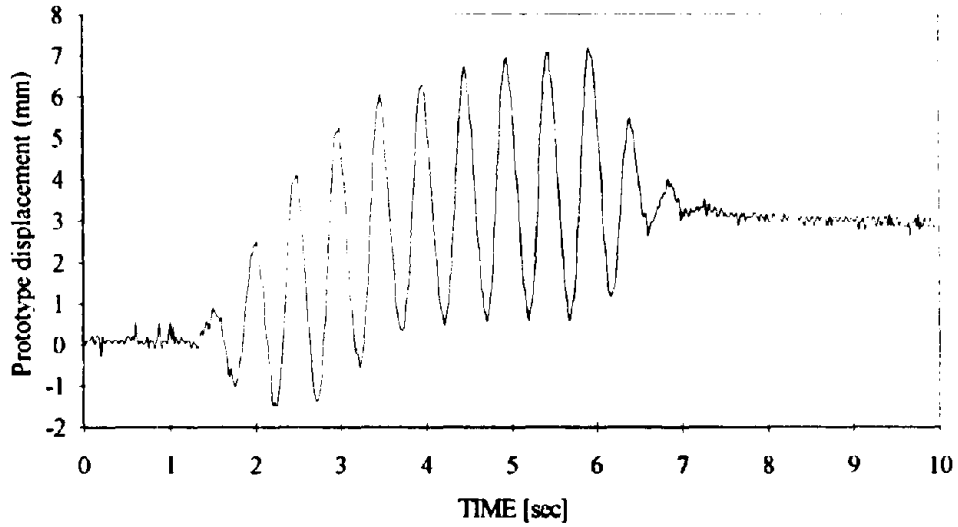
Figure 4.10: Horizontal wall movement (D3) in Test 1a
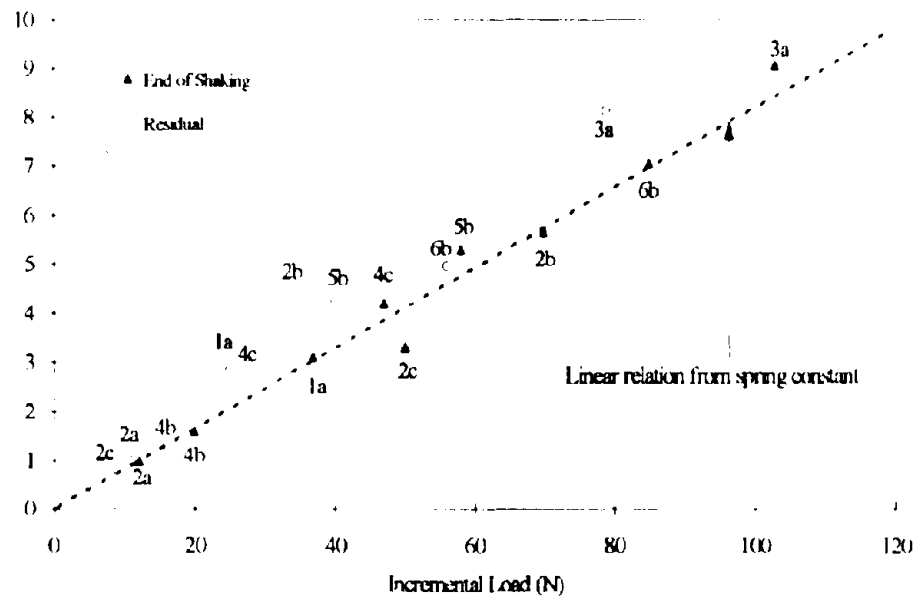
Figure 4.11: Static load increments and wall movements in non-slip tests

CHAPTER 5

NUMERICAL PREDICTIONS FOR MODEL TESTS

A complete set of numerical analyses has been carried out to make "Class A" predictions for the outcomes of the centrifuge model tests described in Chapter 4. The primary objective of these analyses in this research is to investigate the applicability of one currently available analytical procedure to study liquefaction problems.

To this extent, a novel and systematic approach is established to rate the numerical predictions for dynamic geotechnical centrifuge tests. The criteria in this approach are expressed in a general form and are potentially applicable for rating predictions for other centrifuge studies of soil liquefaction.

The quotation marks around the term "Class A" denote that the predictions were made class-A-like, based on the writer's honesty in not looking at the testing results after the centrifuge model tests had been performed. Although some information from the test data was used in making the predictions, the underlying spirit of Class A predictions was preserved throughout the process of predicting. The information from the test data taken into account for the predictions consists of the time history of input ground acceleration intensity and its amplification above the base, due to the flexibility of the soil-wall-container system. This observed acceleration information has been used as input data for predicting the response in the soil mass. Since all predictions were finalized before any comparison was made with the actual responses of the soil and the retaining wall in the

centrifuge tests, the predictions are essentially, although not formally, rated class A predictions

5.1 INTRODUCTION

In the testing program, each soil model experienced more than one series of shaking. Densification was applied to the soil model as a result of each earthquake. The properties of the soil may have been changed and the soil itself may have become non-uniform once it was shaken, especially when liquefaction was present. The changes in the soil after each earthquake are unknown. Therefore, predictions were made only for tests involving fresh soil models, i.e., responses associated with each soil model during and shortly after the first shaking.

The predictions were performed with the finite element program CYCON, based on residual strain method (RSM), a constitutive model in which accumulation of permanent strains is simulated by an analogy to visco-elasticity (involving semi-empirical relationships) for calculating accumulated permanent strains and pore pressures in a soil mass subjected to cyclic loadings. The principal interests involved in the model of the retaining wall with saturated backfill are the amount of excess pore pressure in soil and the permanent wall rotation associated with an earthquake. Some amount of permanent wall rotation is associated with each earthquake, as a result of temporary pore pressure increment behind the wall during the earthquake. However, with the setup of the centrifuge model, slippage at the slider may take place during strong earthquakes. The slippage may cause an extra amount of wall rotation. CYCON can predict the amount of wall rotation, without slippage at the slider. It does not predict this extra amount of

slippage-caused wall rotation. The estimation of amount of slippage is to be discussed in a later chapter in the thesis.

Section 5.2 presents a brief description of the constitutive relationships in RSM, as a convenient reference for later descriptions of the input parameters and how they were obtained. Detailed descriptions for RSM have been presented in many existing literatures, such as Bouckovalas (1984), Bouckovalas et al. (1984, 1986 and 1987, 1991), Stamatopoulos (1989), and Stamatopoulos et al. (1991). Section 5.3 describes the details of applying CYCON for making predictions: the determination and verification of model parameters; the finite element discretization; and the input shear stresses. Detailed procedures for obtaining and evaluating model parameters are presented in Appendix C. Section 5.4 summarizes the comparisons between the predicted test results and measured test data. General agreements in various important features were observed. The complete one-by-one prediction/measurement comparisons of excess pore pressures and horizontal wall top movements are presented in Appendix E.

5.2   THE FEM PROGRAM CYCON

5.2.1   INTRODUCTION

The computer code CYCON was utilized in this study to carry out the analysis of the pore pressures at various locations in the backfill and the horizontal wall movements due to the input ground motions. CYCON is the application of RSM with a finite element method. The RSM was originally developed to analyze cyclic loading of offshore foundations on sand, under drained or undrained conditions (Bouckovalas et al. 1984, 1986). Extensions and improvements of the original method included partially drained

93

cyclic loading due to drainage parallel to dynamic loading (Bouckovalas and Madshus, 1987). Partial drainage is the drainage condition in this liquefaction study. CYCON performs analyses in two dimensions (plane strain, plain stress or axisymmetric) under general boundary and loading conditions. The study in this exercise was performed as plain strain analysis.

The soil was modeled as a two-phase material, consisting of soil skeleton and the pore fluid. A non-linear relationship among effective stress-strain-number of load cycles governs the behavior of the soil skeleton, while the flow of the incompressible pore fluid is governed by Darcy's Law. Combination of this behavioral model with continuum mechanics theory yields a system of differential equations with respect to unknown displacements and pore pressures. An approximate solution of this coupled system of equations is achieved with the finite element method. A detailed description of the theoretical formulation of the problem and the solution algorithm is presented by Bouckovalas and Madshus (1987). The theoretical model for CYCON is based upon the residual strain method (Bouckovalas et al. 1984, 1986). A brief description of the constitutive relationships of the residual strain method (RSM) is presented here for convenience.

5.2.2 Constitutive Relationships of the Residual Strain Method (RSM)

The permanent strain increments due to cyclic loading are described by

$$d\varepsilon_{ij} = \frac{d\sigma'_{oct}}{K'} + d\varepsilon^o_{vol} \qquad (5.1)$$

$$de_{ij} = \frac{dS_{ij}}{2G'} + de^o_{ij} \qquad (5.2)$$

where K^t and G^t = the tangent bulk and shear moduli of the soil skeleton; $d\varepsilon^o_{vol}$ and de^o_{ij} represent nominal permanent strains that would accumulate in the case of constant average effective stresses ($d\sigma'_{oct} = dS_{ij} = 0$).

The tangent soil moduli K^t and G^t are described by simple hyperbolic relationships

$$K^t = AP_a \left(\frac{\sigma'_{oct}}{P_a} \right)^\alpha \tag{5.3}$$

$$G^t = G_0 \frac{(1-R^{\beta_s})^2}{1+(\beta_s - 1)R^{\beta_s}} \tag{5.4}$$

where P_a is the atmospheric pressure (= 100 kPa); R (= q/q_f) is the yield factor with respect to failure; q is the maximum difference in average principal stresses; q_f denotes q at failure; and G_0 is the shear modulus at very small shear strains ($\gamma < 10^{-5}$) estimated as:

$$G_0 = B_s P_a \frac{(2.973 - e)^2}{1+e} \sqrt{\frac{\sigma'_{oct}}{P_a}} \tag{5.5}$$

in which e is the void ratio; A, β_s, α and B_s are numerical constants to be determined from laboratory tests.

The nominal permanent strain increments $d\varepsilon^o_{vol}$ and de^o_{ij} in eq. (5.1) and (5.2) may be obtained directly from results of cyclic laboratory tests with constant average effective stresses ($d\sigma'_{oct} = dS_{ij} = 0$). Empirical expressions for permanent strains have been established based on results from drained cyclic triaxial tests on sand (Bouckovalas et al., 1991).

$$d\varepsilon^o_{vol} = C_1(1-Q^{-1})\gamma_{cyc}^{c2} N^{c3} dN \tag{5.6}$$

$$de^o_{ij} = C_2 Q^{c5} d\varepsilon^o_{vol} \tag{5.7}$$

95

where γ_{cyc} is the double amplitude cyclic shear strain, N is the number of cycles with uniform γ_{cyc}. The stress ratio Q is defined as

$$Q = \frac{q}{\sigma_{oct} M}$$

(5.8)

In (5.8) M is the slr $_{\downarrow}$ of a characteristic threshold (CT) line defined as

$$M = \frac{3 \sin \phi_{CT}}{3 - \sin \phi_{CT}}$$

(5.9)

In Eqn. (5.6) and (5.7), C_1 and C_2 are functions of volumetric density, and are to be determined from laboratory test data. The exponent constants c_1, c_2, c_3 and c_5 are practically constant for a wide range of volume and stress conditions (Stamatopoulos et al., 1991). All these parameters are to be either determined from the laboratory test data or obtained from other sands, with the adequacy of application to Nevada sand checked with test data.

Cyclic shear strain is related to cyclic shear stress by

$$\gamma_{cyc} = \frac{2\Delta q_{cyc}}{G_{0,cyc}} \frac{1}{1 - (2\Delta q_{cyc} / q_f)^{\beta_c}}$$

(5.10)

with $$G_{0,cyc} = B_c P_a \frac{(2.973 - e)^2}{1 + e} \sqrt{\frac{\sigma'_{oct}}{P_a}}$$

(5.11)

The exponent β_c is a parameter to be determined from laboratory cyclic tests. The parameter B_c is associated with the small strain cyclic shear modulus, $G_{0,cyc}$, which can be obtained through laboratory tests involving very small cyclic shear strains, such as resonant column tests.

96

5.3 ANALYTICAL SIMULATION OF CENTRIFUGE TESTS WITH CYCON

5.3.1 DETERMINATION OF CONSTITUTIVE MODEL PARAMETERS

The analysis with CYCON requires input model parameters that are related to the properties of the soil in the backfill. The Earth Technology Corporation has performed extensive series of static and cyclic laboratory tests on Nevada sand which were used for obtaining the model parameters for CYCON. Given the considerable experimental scatter of the data, the task of determining the model parameters involved significant intuition and judgement.

Explicit determination of the model parameters for CYCON requires a variety of laboratory tests involving a wide range of cyclic shearing strains. The laboratory tests on Nevada sands by The Earth Technology Corporation (1992) include various index tests, resonant column tests, monotonic and cyclic triaxial and direct simple shear (DSS) tests. A few model parameters can be extracted directly from the test data. Most others require more information. Information about two other similar sands (Oostershelde sand and Leighton-Buzzard sand) are used to help in choosing the parameters for Nevada sand. Comprehensive tests had been carried out on these two sands to determine the RSM model parameters (Bouckovalas, 1982; Pahwa et al. 1986).

In addition, the laboratory tests have been performed on Nevada sands with two relative densities 40% and 60%, while the centrifuge tests have been performed on sands with 60% and 75% relative densities. Many indirect interpretations are needed in choosing parameters for the sand with 75% relative density.

97

With the constitutive model currently implemented in CYCON, the mode of shearing may affect some of the model parameters determined from different types of laboratory tests (triaxial and DSS tests). In the centrifuge model test, the mode of shearing on the sand near the two end walls is similar to that in triaxial (TX) tests. For the sand near the middle part of the backfill and along the base, the shearing mode is similar to that in DSS tests. Therefore, two sets of model parameters (DSS and TX) for Nevada sands have been determined from DSS and triaxial tests, respectively. It is not practical nor possible to divide the soil backfill clearly into two regions: one using DSS parameters and the other using TX parameters, mainly because the exact boundaries of the two regions are not known with certainty. Parallel predictions were made based upon these two sets of parameters. The predicted results and instrumental observations will be presented in Section 5.4.

Table 5.1 summarizes the model parameters determined for Nevada sand. At first, the results of laboratory tests by the Earth Technology Corporation (1992) were re-compiled and evaluated in view of the general insight provided by RSM. Consequently, it is explored whether parameters obtained from the Oostershelde and Leighton-Buzzard sands are compatible with the experimental data for Nevada sand. This approach is justified due to the similarity among Nevada sand and these two sands which is confirmed by the grain size distribution curves (Figure 5.1). The parameters obtained for Nevada sand with Dr = 40% and 60% were verified through extensive comparison of the experimental data with the predicted DSS and triaxial test results using the RSM model and the chosen model parameters. After confirming these parameters for the looser sands, the final step is to estimate parameters for Nevada sand with Dr = 75%. The detailed procedure is outlined in Appendix C

5.3.2 Finite Element Discretization

The model of the retaining wall with saturated backfill is discretized into a total of 70 elements. The finite element mesh used in the analyses is presented in Figure 5.2. The mesh representing the sand is finer near the surface and/or near the retaining wall. The nominal locations of all transducers in all tests are also presented on the same plot. The numbering of the elements and coordinates of the nodal points are presented, with uniform sand elements, in Figure 5.3 for clarity.

Four materials are involved in the finite element discretization:
- a soil cushion (elements 1 and 2)
- the aluminum retaining wall (elements 3 to 7)
- a film of soil-wall interface (elements 11 to 16)
- the soil - Nevada sand (elements 17 to 70)

The imaginary soil cushion, with elasto-plastic deformation in the horizontal direction, represents the spring-slider assembly behind the wall, which gives the plastic rotation of the wall in the centrifuge model. The model parameters of the soil cushion were assessed to give an equivalent elastic stiffness and ultimate load associated with the rotation of the retaining wall, which had been controlled by the spring and slider in model tests. The assessments of the parameters were performed by independent calibrations. The aluminum retaining wall was assumed to be effectively rigid, with a very large Young's modulus. The thin soil-wall interface provides the possibility of slippage between the soil body and the wall. The properties of this interface are essentially the same as of the soil, except that its Young's modulus is set very large. This is to simulate a contact element that will slip after failure, but not deform perpendicular to the wall. The model parameters for all these four materials are summarized in Table 5.2.

99

5.3.3 Dynamic Shear Stresses

The cyclic shear stresses in each soil element (No. 11 through 70 in the finite element mesh) were obtained using the FEM program ABAQUS. The dynamic shear stresses in the soil come from the ground acceleration due to the input earthquake. The soil backfill in effect experienced an inertial horizontal (body) force during the earthquake. The peak cyclic shear stresses in the soil due to the peak ground acceleration, were estimated using ABAQUS, by applying a pseudo-static horizontal body force to plain strain elastic elements.

The body force may vary with the depth of each element in the soil to account for a non-uniform ground acceleration in the backfill. The applied horizontal body force is 20%[1] of gravity force at the base, 26.7% at the surface of the soil, with a linear variation in between. This non-uniform body force gives the soil a non-uniform horizontal ground acceleration, with 0.2g at the base, representing the input acceleration from the shaking table, and gradually larger horizontal accelerations above the base reflect which the amplification effects observed in t

On the other hand, the shear modulus was given in a way such that it was similar to what had been obtained from resonant column tests at various stress states. That is, the shear modulus was proportional to the square root of octahedral stress. This customized shear modulus corresponds closely to that of the tested sand under very small shear strains (in the range of 10^{-5} to 10^{-6}).

---

[1] The shear stresses associated with other levels of shaking intensities will be adjusted linearly in CYCON. The adjustments can be done with any time interval - cycle by cycle (or a fraction of a cycle).

The input file for analyzing the shear stresses with base horizontal acceleration of 0.2g using ABAQUS is presented in Appendix D. Table 5.3 lists the computed stresses at the centroid of each soil element. X and Y are the coordinates of each element as shown in Figure 5.3. S11, S22 and S12 represent the horizontal stress, vertical stress and shear stress in the X-Y plane respectively. These stresses are used as part of the input file for the analyses using CYCON. The input file for analyzing Test 1a with CYCON is also presented in Appendix D.

5.4 EVALUATION OF ANALYTICAL PREDICTIONS WITH CYCON

This section presents a series of the comparisons between the CYCON predictions and experimental measurements in the centrifuge model tests. In tests 1a, 2a and 3a, the soil did not liquefy. The amounts of reduction in moduli depend heavily upon the accumulated strains. Therefore, tests without liquefaction are the most severe cases for checking the predictive capability.

Complete results of CYCON predictions are presented in Appendix E. Records of experimental results are superimposed on these predictions as references. As stated earlier, the prediction model did not aim to predict the amount of the excessive horizontal wall movements due to slippage in slider at strong earthquakes. The large displacements due to sliding cannot be handled with the finite element algorithm currently implemented in CYCON. Thus the comparisons of analytical predictions with CYCON and test measurements are meaningful only for that part of shaking prior to slippage of the slider or for tests without any sliding at all.

101

5.4.1 Analytical Predictions of Pore Pressure Build-up

The estimation of excess pore pressure is of great interest for the broader understanding of the model behavior. The maximum excess pore pressure is generally viewed as the most important factor. However, some more features are also necessary to better evaluate the predictions in comparison with what have been measured in the centrifuge tests. Four features of pore pressure variation are used as criteria for the comparison of predictions and observations: peak excess pore pressure, rate of pore pressure rise, decay of excess pore pressure during the period of shaking, and rate of post-shake pore pressure decay. Comparisons based upon these features are performed on pore pressure response at particular transducer locations, except for P1 in Test 1a and P2 in Test 4a. These two measurement records are believed to have failed during testing because of the poor readings obtained (see Figures B.3 and B.47). Comparisons for all other predictions and observations are presented in the following subsections.

5.4.1.1 Peak Pore Pressure

The magnitude of the peak pore pressure is the most important feature among the four major criteria for evaluating the predictions for pore pressure against the observations. The results of comparisons show that CYCON is rated very good in predicting the peak pore pressures at various locations in the backfill during earthquakes.

Table 5.4 summarizes the ratios between the predicted and measured peak excess pore pressures at various locations (P1 through P6, as shown in Figure 4.1) in each test. The sequence of presentation for various tests follows the order of increasing earthquake intensities. Tests 1a and 2a involve weak earthquakes, 4a and 5a involve strong

102

earthquakes, while 6a involves a moderately strong earthquake. With similar earthquake intensities, the soil models in Tests 1a and 4a (D_r = 60%) would be expected to experience stronger responses than in 2a and 6a (D_r = 75%), because of the initially looser state. Test 3a is separated at the bottom of the table, due to the involvement of a different pore fluid and the consequent lower permeability. The numbering of the pore pressure transducers is slightly different in Test 1a. The pore pressure was not monitored at the location of P3 as in other tests. The pore pressures at the nominal locations P4, P5 and P6 were in fact recorded by transducers P3, P4 and P5. These are marked by parentheses in Table 5.4. The predictions for pore pressure response at P5 in test 2a and 1a are crossed out because the predicted responses are too low. These pore pressure responses are the worst predictions obtained by CYCON.

Generally speaking, agreement to a certain degree is found in most comparisons between the predicted peak excess pore pressures and the measurements. However, in reality, some pore pressure transducers may have settled (or floated) during earthquake, as a result of local soil liquefaction. The settlements of transducers during earthquakes may result in somewhat higher measured pore pressures than the expected (or predicted) values assuming no transducer settlements. Such observations are more frequent and obvious in cases associated with pore pressures at shallower locations, where local liquefaction is more likely to occur and a small transducer settlement can make a great difference! The prediction/observation ratios will be much lower than 100% if settlements are substantial. These ratios are marked by an asterisk in Table 5.4. Some pore pressure records show that the (time-wise) average excess pore pressure stayed at somewhat below the initial effective stress during the period of earthquake and jump to it at the end of shaking; these are marked by two asterisks in the table.

103

The effect of pressure transducer settlement upon the evaluation of predictions may be reduced by comparing the excess pore pressure ratios in which transducer settlements are considered. The excess pore pressure ratio is obtained by normalizing the excess pore pressure with the (final) vertical effective stress, based on the final depth of the transducer. The comparisons of excess pore pressure and excess pore pressure ratio for P5 in Test 5a are presented in Figures 5.4 and 5.5. The predicted/observed percentage ratios of peak excess pore pressure ratios for all cases are summarized in Table 5.5. Considerable improvements are obtained for cases marked by an asterisk in Table 5.4. The comparison ratios are brought closer to 100%

A summary of qualitative comparisons of peak excess pore pressure ratios based on Table 5.5 is presented in Table 5.6. Predictions with a certain degree of accuracy (within +/- 15% compared to the measurements) are presented in the shaded cells in Table 5.6. From Table 5.6 and the last column in Table 5.5, generally good agreement between the predicted and measured peak pore pressures is observed, especially for stronger shaking with water as pore fluid. Prediction/observation ratios are close to 100% in most cases. Except for only P5 associated with weaker shakings (1a and 2a), where significant underprediction occurs, the measured peak pore pressures are close to the predicted values using either DSS or triaxial parameters, or fall right in between (Test 3a).

5.4.1.2   Pore Pressure Rising Rate

A second feature of the pore pressure variation is the rate of pore pressure rise-up as a result of cyclic shearing. CYCON is successful in predicting (with DSS parameters) the time to reach peak pore pressure in Test 3a, with glycerin solution as the pore fluid, with which the prototype permeability is closer to water at 1g condition. Figure 5.6

104

shows the measured excess pore pressure history and the predictions of P4 in Test 3a.
However, for all tests using water as pore fluid, CYCON predicts a faster pore pressure
rise-up. Most predictions show that the pore pressure reaches its peak value within two
or three cycles of input acceleration, while the observations show a later time to reach
peak pore pressure. The case of P4 in Test 2a is shown in Figure 5.7 as an example.

Two criteria were used to check the rate of pore pressure rise-up: the time to reach
50% of peak pore pressure (from the start of earthquake); and the time rate of pore
pressure increment from 20% to 80% of peak pore pressure. Tables 5.7 and 5.8
summarize the comparisons between the predictions and observations based upon the
above criteria. In Table 5.7, a faster pore pressure rise-up is expressed by a time ratio
(predicted time against observed time to reach 50% peak pore pressure) less than 100%.
In Table 5.8, except for Test 3a, the predictions show a generally faster rise-up rate. For
tests with water as pore fluid, the rate of pore pressure rise-up is predicted 303%±87%
and 210%±70% faster than observations using parameters from DSS and triaxial tests
respectively.

A summary of qualitative comparisons of the excess pore pressure rising rates is
presented in Table 5.9. Based on this table and the last columns in Tables 5.7 and 5.8,
CYCON predicts the rate of pore pressure rise-up successfully for Test 3a with DSS
parameters. Predictions for all other tests, with either DSS or triaxial parameters, show a
tendency of faster pore pressure rise-up.

105

5.4.1.3 Decay of Excess Pore Pressure During Shaking

Decay of excess pore pressure during the period of shaking is present in most predictions and sometimes in measured pore pressure histories. A quantitative point of view falls upon the comparison between the predicted and measured excess pore pressure at the end of shaking. However, it may be inappropriate in cases for which the predicted peak pore pressure differs from the measurement. A closer examination compares the ratios of the excess pore pressure at EOS to peak excess pore pressure, from both the predictions and the measurements. The comparisons are summarized in Table 5.10.

Table 5.11 presents a summary of qualitative comparisons for the decay rate of excess pore pressure during shaking. The shaded cells in Table 5.11 express predictions with little or no decay during shaking. In Test 3a, in which glycerin solution is used as pore fluid, no decay of excess pore pressure is predicted using DSS parameters. This is similar to the test data (see Figure 5.6). In tests using water as pore fluid, CYCON predicts early decay during the periods of shaking with weak earthquakes while some recorded pore pressure histories show a later decay (see Figure 5.7). With strong earthquakes, CYCON successfully captures the feature that the pore pressure remains at the peak value until the end of shaking, although some minor decrement after peak is present. Figure 5.8 shows the measurements and predictions of P3 in Test 4a. This feature is captured better by predictions using triaxial parameters.

From Table 5.11 and the last column in Table 5.10, the decay of excess pore pressure is successfully predicted by CYCON with DSS parameters in Test 3a, with glycerin solution. For tests involving water as pore fluid, with weak earthquakes (1a and 2a), predictions using DSS parameters did a better job than those using triaxial

parameters; with strong earthquakes (Tests 4a, 5a and 6a), predictions using triaxial parameters better captured the fact that pore pressure stays high during shaking.

5.4.1.4   Post Shake Pore Pressure Decay

Two aspects are considered in evaluating the predicted post shake pore pressure decay behavior by CYCON: the rate of decay; and the time that decay starts. In some records, the decay of pore pressure starts during the period of shaking while some at the end of shaking (EOS), and others at some time after EOS (pore pressure remains at a certain level for a while after EOS). Comparisons between predictions and observations of the post shake decay in pore pressure variation are based primarily upon the rate of decay. The basis for comparing the predictions and test data is the time required to decay half of the excess pore pressure at EOS, although pore pressure may have decayed somewhat before EOS, especially in some predictions. This time period for the measured pore pressure history begins from the visual starting point of decaying if the pore pressure stays constant for some time after EOS. Table 5.12 summarizes the comparisons for all pore pressure histories. The average (predicted/observed) ratio of time for decay to half excess pore pressure at various locations for each test is listed in the last column in Table 5.12. The average ratios show that CYCON is good in predicting the post shake pore pressure decay with DSS parameters for weak earthquakes and with triaxial parameters for strong earthquakes.

A summary of qualitative prediction/observation comparison of post shake pore pressure decay is presented in Table 5.13. An excellent prediction for the dissipation of excess pore pressure is a prediction that follows more or less the test data. The predicted post shake pore pressure decay is rated excellent if the predicted rate of decay agrees with

107

the recorded data and the difference in the starting time of decay is within one second (less than two cycles of input acceleration). If agreement is present in the predicted and observed rates of decay after EOS, but not in the starting time, the prediction is rated good regarding the post shake pore pressure decay. The prediction is rated OK if the predicted rate of decay is within 50% ~ 200% of the observed decaying rate. A lot of judgment is involved in rating the predictions.

An example of predictions rated excellent is the prediction for P3 in Test 4a using triaxial parameters (Figure 5.8). This prediction is rated excellent because the prediction satisfies the two criteria for post shake excess pore pressure decay. Note that the basis for evaluating the rate of decay is the (predicted and/or observed) time to decay one half of the excess pore pressure at EOS, regardless of whether the predicted amount of excess pore pressure at EOS equals the measured data or not. In Figure 5.8, the data show a hold up of excess pore pressure at EOS before dissipation starts. This retained pore pressure is associated with the minor after-shock shakings observed from the input accelerations (Figure B.45). That is, the EOS is at t = 6.5 sec in the predictions, while the true EOS is at t = 7.5 sec in test data. Since both the prediction and data show same rate of decay, and both decay start directly at their EOSs (t = 7.5 sec and t = 6.5 sec), this prediction is rated as excellent in post shake excess pore pressure decay. Similarly, the prediction with triaxial parameters for P5 in Test 4a (Figure 5.9) is rated as good. It takes about the same amount of time (4.4 seconds) in both the observation and the prediction to decay one half of the predicted and/or measured excess pore pressures at EOS. In Table 5.13, predictions rated as excellent or good in post shake excess pore pressure decay are presented in shaded cells. This table shows that CYCON is good (with triaxial parameters) in capturing the post shake pore pressure decay associated with strong earthquakes.

108

5.4.2 Horizontal Wall Movements

The amount of horizontal wall movement (rotation of wall) as a result of earthquake is difficult to estimate. Any prediction may be claimed to be good if the accuracy is within a factor of two. In this study, CYCON was proven to be good in predicting the horizontal wall movement due to earthquakes. For tests with weaker input ground motions, in which no slippage at the slider occurred, most predicted wall movements are close to the observed movement within a factor of two. For tests involving strong earthquakes and slippage at the slider, the predicting of wall movement is beyond the current capability of CYCON.

The predictions for Tests 1a, 2a and 3a are presented in Figures 5.10 through 5.12. Measured displacement histories are also plotted on these figures as references. Comparisons of predicted horizontal wall top movements with measured results of these tests are summarized in Table 5.14. In general, predictions using DSS parameters are good for these tests involving weak shakings.

Prediction for Test 3a with DSS parameters is excellent since the trend of measured displacement change is more or less following the prediction (Figure 5.3). Predictions for Tests 1a and 2a show fast rise-ups in the first few cycles and then level off. Inspecting all these comparison figures reveals that both predicted and measured horizontal wall movements are heavily influenced by the excess pore pressure variations. In Test 3a, the predicted maximum displacement using triaxial parameters is about 45% of that using DSS parameters. In addition, the wall movement is both measured and predicted (with DSS parameters) to continue accumulating during the period of shaking and reaches its peak at the end. The same trends are observed in the excess pore pressure variations (see

Appendix E). The prediction of excess pore pressure using triaxial parameters also play an important role in the displacement prediction using the same parameters. In Tests 1a and 2a, rapid increments of wall displacements are accompanied by predicted fast excess pore pressures rise-ups. The predicted wall displacements stop increasing once the excess pore pressures start to decay at about the end of two to three cycles in the predictions. Particularly in Test 2a (Figure 5.2), the measured wall displacement continues accumulating as the excess pore pressures keep increasing in the measured histories.

5.4.3 SUMMARY

On the basis of the previous prediction/observation comparisons, CYCON is good at predicting the excess pore pressure (Table 5.6). The worst predictions for excess pore pressures are those for P5 in Tests 1a and 2a, in which soil did not liquefy. Predictions for these cases are too low compared with the observations. Except for these cases, CYCON is very good in predicting peak excess pore pressures. Analyses using either DSS or TX parameters offer very good predictions in peak excess pore pressures, especially for moderate to strong earthquakes. For post shake excess pore pressure decays, analyses using DSS parameters offer better predictions for tests with small earthquakes, while analyses with TX parameters give better predictions for tests with strong earthquakes (Table 5.13).

The amount of wall top movements is well predicted by CYCON, with DSS parameters. The accuracies of the predictions for tests without slip at slider are within a factor of 2 (Table 5.14). This agrees with the expectation that the global behavior of the model is similar to that in DSS tests. In fact, the predictions with TX parameters are not

too bad. The worst prediction for tests without slip at slider is the prediction for Test 3a, with an under prediction by a factor of only 2.5.

Although CYCON may be poor in some predictions, generally speaking, predictions by CYCON are good, given the uncertainties in determining the model parameters for analyses. Nevertheless, it is not the purpose of this thesis to decide why the predictions may have been poor and how the predictions may be improved.

Table 5.1: Model Parameters of Nevada Sand for Program CYCON

Dr	40%	60%	75%
ϕ_{max}	0.576	0.628	**0.6894**
c	0.0	0.0	0.0
ϕ_{CT}	0.488	0.488	0.488
S_u (kPa)	10000	10000	10000
e	0.73	0.656	**0.595**
e_{min}	0.50	0.50	0.50
$P\alpha$ (kPa)	100	100	100
B_c	265	265	265
β_c	0.70	0.90	**1.0**
B_s	---	23,46	**23,46**
β_s	40	40	40
A (TX)	490	263	**286**
A (DSS)	490	526	**572**
k (m/s)	0.0033	0.0028	0.0017
α	0.50	0.50	0.50
c_1	11	11	11
C_1	0.00685	0.00646	**0.00616**
c_3	0.40	0.40	0.40
c_2	1.26	1.26	1.26
C_2	12	12	12
c_5	3	3	3

Table 5.2: Model Parameters of All Materials Used in Program CYCON

Material	Soil Cushion	Aluminum Wall	Soil-Wall Interface	Sand Dr=60%	Sand Dr=75%
E	0.0	10^{10}	10^{10}	0.0	0.0
γ	285.71	26.46	10.3	10.3	10.3
ϕ_{max}	1.50	0.0	0.628,0.6894	0.628	0.6894
c	0.0	0.0	0.0	0.0	0.0
ϕ_{CT}	1.40	0.0	0.488	0.488	0.488
S_u (kPa)	100.0	0.0	1000.0	1000.0	1000.0
e	1.0	0.0	0.656,0.595	0.656	0.595
e_{min}	0.9	0.0	0.50	0.50	0.50
P_α(kPa)	100	100	100	100	100
B_c	2.5215	0.0	265	265	265
β_c	0.9	0.0	0.9,1.0	0.90	1.0
B_s	1.75	0.0	23,46	23,46	23,46
β_s	40	0.0	40	40	40
A (TX)	2.270	0.0	263,286	263	286
A (DSS)	2.270	0.0	526, 572	526	572
k (m/s)	0.00	0.00	0.0028, 0.0017	0.0028	0.0017
α	0.50	0.0	0.50	0.50	0.50
c_1	11	0.0	11	11	11
C_1	0.0	0.0	0.00646,0.00616	0.00646	0.00616
c_3	0.40	0.0	0.40	0.40	0.40
c_2	1.26	0.0	1.26	1.26	1.26
C_2	12	0.0	12	12	12
c_5	3	0.0	3	3	3

Table 5.3: Stresses and Coordinates at the centroid of each element

Element No.	X (m)	Y (m)	S11 (kPa)	S12 (kPa)	S22 (kPa)	Element No.	X (m)	Y (m)	S11 (kPa)	S12 (kPa)	S22 (kPa)
11	-0.015	-0.25	-30.900	0.082	-5.472	41	-6	-0.25	-8.977	0.590	-0.082
12	-0.015	-0.75	-31.490	0.027	-3.784	42	-6	-0.75	-8.709	1.757	-0.230
13	-0.015	-1.25	-31.710	0.028	-4.238	43	-6	-1.25	-8.427	2.921	-0.417
14	-0.015	-2.25	-35.150	0.043	-11.200	44	-6	-2.25	-9.380	5.300	-2.621
15	-0.015	-4	-31.140	0.071	-20.290	45	-6	-4	-8.063	10.120	-5.034
16	-0.015	-6	-41.700	-0.051	-29.370	46	-6	-6	-8.710	34.880	-5.273
17	-0.64	-0.25	-25.790	0.665	-1.901	47	-8	-0.25	-3.001	0.590	-0.052
18	-0.64	-0.75	-26.630	1.229	-0.847	48	-8	-0.75	-2.878	1.792	-0.085
19	-0.64	-1.25	-26.560	1.302	-0.597	49	-8	-1.25	-2.804	3.035	-0.196
20	-0.64	-2.25	-30.060	1.266	-7.019	50	-8	-2.25	-3.143	5.663	-0.989
21	-0.64	-4	-27.020	1.643	-16.370	51	-8	-4	-2.495	10.960	-1.557
22	-0.64	-6	-40.810	6.361	-28.860	52	-8	-6	-3.582	37.360	-2.588
23	-1.875	-0.25	-21.040	0.752	-0.368	53	-10.5	-0.25	4.513	0.577	0.051
24	-1.875	-0.75	-21.920	1.873	-0.529	54	-10.5	-0.75	4.373	1.786	0.167
25	-1.875	-1.25	-22.270	2.522	-0.660	55	-10.5	-1.25	4.132	3.008	0.213
26	-1.875	-2.25	-25.500	3.159	-5.934	56	-10.5	-2.25	4.521	5.594	1.296
27	-1.875	-4	-22.450	4.597	-13.220	57	-10.5	-4	4.240	10.850	2.819
28	-1.875	-6	-25.060	17.080	-14.010	58	-10.5	-6	3.699	36.880	2.222
29	-3.125	-0.25	-17.260	0.654	0.103	59	-13.5	-0.25	13.360	0.656	0.050
30	-3.125	-0.75	-17.450	1.818	-0.250	60	-13.5	-0.75	13.190	1.784	0.227
31	-3.125	-1.25	-17.470	2.756	-0.534	61	-13.5	-1.25	13.300	2.851	0.724
32	-3.125	-2.25	-20.150	4.199	-4.957	62	-13.5	-2.25	15.280	4.852	4.208
33	-3.125	-4	-17.750	6.972	-10.560	63	-13.5	-4	13.060	8.826	7.926
34	-3.125	-6	-19.340	25.060	-10.590	64	-13.5	-6	8.818	30.680	2.457
35	-4.375	-0.25	-13.700	0.611	0.074	65	-16.5	-0.25	22.390	0.652	0.711
36	-4.375	-0.75	-13.490	1.754	-0.176	66	-16.5	-0.75	22.820	1.649	0.075
37	-4.375	-1.25	-13.220	2.819	-0.415	67	-16.5	-1.25	22.440	2.144	-0.393
38	-4.375	-2.25	-15.000	4.785	-3.840	68	-16.5	-2.25	25.150	2.598	4.729
39	-4.375	-4	-13.090	8.687	-7.920	69	-16.5	-4	21.540	3.706	11.980
40	-4.375	-6	-14.190	30.560	-7.980	70	-16.5	-6	35.440	12.860	24.470

114

TABLE 5.4 : COMPARISON OF EXCESS PORE PRESSURE PREDICTIONS WITH MEASUREMENTS
- PEAK EXCESS PORE PRESSURE   (PREDICTED/OBSERVED)

TEST	Acceleration	Shearing Mode	P1	P2	P3	P4	P5	P6	Average
2a	0.05g	DSS		125%	105%	115%	~~18%~~	140%	125%
		TX		85%	75%	82%	~~14%~~	115%	90%
		Comment					Under Pred.		
1a	0.05g	DSS	-	105%		100%(P3)	~~14%(P4)~~	100%(P5)	102%
		TX	-	75%		65%(P3)	~~12%(P4)~~	75%(P5)	72%
		Comment	Failed Record				Under Pred.		
6a	0.25g	DSS			125%	122%	67%*	75%*	97%
		TX			120%	115%	67%*	75%*	94%
		Comment							
4a	0.25g	DSS		-	100%	100%	70%*	50%*	80%
		TX		-	95%	100%	70%*	50%*	80%
		Comment		Failed Record			Liquefied	Liquefied	
5a	0.35g	DSS		100%	100%	100%	50%*	50%*	75%
		TX		100%	95%	100%	50%*	50%*	75%
		Comment					DSS-Lqfd	Liquefied	
3a	0.08g	DSS		145%	150%	115%	NG	NG	137%
		TX		40%	40%	40%	NG	NG	40%
		Comment							

Note: * Will become closer to 100% if depth (settlement) is corrected

TABLE 5.5 : COMPARISON OF EXCESS PORE PRESSURE PREDICTIONS WITH MEASUREMENTS - P.P. RATIO

TEST	Acceleration	Shearing Mode	P1	P2	P3	P4	P5	P6	Average
2a	0.05g	DSS		125%	105%	115%	40%	140%	121%
		TX		85%	75%	82%	20%	115%	90%
		Comment					Bad Prediction		
1a	0.05g	DSS	-	105%		100% (P3)	25% (P4)	125%	110%
		TX	-	75%		65% (P3)	15% (P4)	100%	87%
		Comment	Failed Record				Bad Prediction		
6a	0.25g	DSS			100%	110%	100%	100%	100%
		TX			95%	100%	100%	100%	99%
		Comment							
4a	0.25g	DSS		-	100%	92%	100%	75%	89%
		TX		-	95%	90%	82%	75%	84%
		Comment		Failed Record			Liquefied	Liquefied	
5a	0.35g	DSS		120%	100%	100%	88%	64%	101%
		TX		115%	95%	100%	96%	60%	101%
		Comment					DSS-Lqfd	Liquefied	
3a	0.08g	DSS		145%	115%	98%	NG	112%	118%
		TX		40%	30%	33%	NG	115%	55%
		Comment							

TABLE 5.6 : QUALITATIVE COMPARISON OF PEAK EXCESS PORE PRESSURE RATIO

A QUALITATIVE SUMMARY FOR PEAK EXCESS PORE PRESSURE RATIO

TEST	Acceleration	Shearing Mode	P1	P2	P3	P4	P5	P6
2a	0.05g	DSS		OK	Excellent	Good	Small	Large
		TX		Good	OK	OK	Small	Good
1a	0.05g	DSS		Excellent		Excellent(P3)	Small(P4)	OK (P5)
		TX		OK		Small (P3)	Small(P4)	Excellent(P5)
6a	0.25g	DSS			Excellent	Good	Excellent	Excellent
		TX			Excellent	Excellent	Excellent	Excellent
4a	0.25g	DSS			Excellent	Good	Excellent	OK
		TX			Excellent	Good	OK	OK
5a	0.35g	DSS		OK	Excellent	Excellent	Good	Small
		TX		Good	Excellent	Excellent	Excellent	Small
3a	0.08g	DSS		Large	Small	Small		Good
		TX		Small	Small	Small		Good

Rating	Range of accuracy
Excellent	95% - 105%
Good	85% - 115%
OK	75% - 125%

SUMMARY OF CASE No.

CASE	DSS	TX
Excellent	11	9
Good	6	5
OK	4	5
Large	2	0
Small	3	7
Total	26	26

Cases of Good or
Excellent predictions

117

TABLE 5.7 : COMPARISON OF EXCESS PORE PRESSURE PREDICTIONS WITH MEASUREMENTS

- TIME TO RISE 1/2 PEAK EXCESS PORE PRESSURE   (PREDICTED/OBSERVED)

TEST	Acceleration	Shearing Mode	P1	P2	P3	P4	P5	P6	Average
2a	0.05g	DSS		38%	50%	48%	50%	40%	45%
		TX		40%	50%	53%	50%	40%	47%
		Comment							
1a	0.05g	DSS	NG	50%		55% (P3)	30% (P4)	30% (P5)	41%
		TX	NG	55%		60% (P3)	30% (P4)	30% (P5)	44%
		Comment	Failed Record						
6a	0.25g	DSS			50%	55%	65%	100%	68%
		TX			70%	80%	80%	100%	83%
		Comment							
4a	0.25g	DSS			60%	53%	-	75%	63%
		TX			75%	62%	65%	75%	69%
		Comment		Failed Record			Liquefied	Liquefied	
5a	0.35g	DSS		65%	60%	70%	68%	-	66%
		TX		75%	75%	85%	80%	-	81%
		Comment					DSS-Lqfd	Liquefied	
3a	0.08g	DSS		135%	150%	65%	NG	NG	117%
		TX		25%	40%	65%	NG	NG	43%
		Comment							

118

TABLE 5.8 : COMPARISON OF EXCESS PORE PRESSURE PREDICTIONS WITH MEASUREMENTS
- RATE OF PORE PRESSURE INCREMENT [kPa/sec]   (PREDICTED/OBSERVED)

TEST	Acceleration	Shearing Mode	P1	P2	P3	P4	P5	P6	Average
2a	0.05g	DSS		325%	300%	325%	-	450%	350%
		TX		280%	185%	190%	-	360%	254%
		Comment							
1a	0.05g	DSS	NG	250%		180% (P3)	- (P4)	144% (P5)	192%
		TX	NG	133%		100% (P3)	- (P4)	120% (P5)	118%
		Comment	Failed Record				Under Est.		
6a	0.25g	DSS			330%	450%	135%	NG	305%
		TX			300%	235%	115%	NG	217%
		Comment							
4a	0.25g	DSS			500%	300%	-	450%	417%
		TX			285%	267%	225%	400%	295%
		Comment		Failed Record			Liquefied	Liquefied	
5a	0.35g	DSS		225%	440%	160%	200%	-	256%
		TX		150%	220%	135%	150%	-	164%
		Comment					DSS-Lqfd	Liquefied	
3a	0.08g	DSS		110%	110%	110%	NG	NG	110%
		TX		40%	40%	50%	NG	NG	45%
		Comment							

NOTE : DSS rate ratio = 303% +/- 87% ;   TX rate ratio = 210% +/- 70%

TABLE 5.10 COMPARISON OF EXCESS PORE PRESSURE PREDICTIONS WITH MEASUREMENTS
- RATIO OF EXCESS PORE PRESSURE @ EOS / PEAK EXCESS PORE PRESSURE
[PREDICTED RATIO / OBSERVED RATIO]

TEST	Acceleration	Shearing Mode	P1	P2	P3	P4	P5	P6	Average
2a	0.05g	DSS		54%	40%	42%	-	27%	41%
		TX		91%	80%	87%	-	46%	76%
		Comment					Under Pred.		
1a	0.05g	DSS	NG	37%		40% (P3)	- (P4)	15% (P5)	30%
		TX	NG	76%		64% (P3)	- (P4)	28% (P5)	56%
		Comment	Failed Record				Under Pred.		
6a	0.25g	DSS			81%	80%	75%	-	79%
		TX			93%	93%	91%	100%	94%
		Comment							
4a	0.25g	DSS		-	82%	65%	-	100%	82%
		TX		-	95%	86%	96%	100%	94%
		Comment		Failed Record			Liquefied	Liquefied	
5a	0.35g	DSS		52%	93%	58%	100%	-	76%
		TX		78%	100%	80%	100%	-	90%
		Comment					DSS-Lqfd	Liquefied	
3a	0.08g	DSS		100%	100%	100%	NG	NG	100%
		TX		-	-	-	NG	NG	-
		Comment		DSS-OK	DSS-OK	DSS-OK			

120

TABLE 5.11 : QUALITATIVE COMPARISON OF RATE OF DECAY IN EXCESS PORE PRESSURE DURING SHAKING

A QUALITATIVE SUMMARY FOR DECAY IN EXCESS PORE PRESSURE DURING SHAKING

TEST	Acceleration	Shearing Mode	P1	P2	P3	P4	P5	P6
2a	0.05g	DSS		Fast	Fast	Fast	-	Fast
		TX		Excellent	Good	Good	-	Fast
1a	0.05g	DSS	-	Fast		Fast (P3)	- (P4)	Fast (P5)
		TX	-	OK		Fast (P3)	- (P4)	Fast (P5)
6a	0.25g	DSS			Good	Good	OK	-
		TX			Excellent	Excellent	Excellent	Excellent
4a	0.25g	DSS		-	Good	Fast	-	Excellent
		TX		-	Excellent	Good	Excellent	Excellent
5a	0.35g	DSS		Fast	Excellent	Fast	Excellent	-
		TX		OK	Excellent	Good	Excellent	-
3a	0.08g	DSS		Excellent	Excellent	Excellent		
		TX		-	-	-		

Rating	Range of accuracy
Excellent	90% - 100%
Good	80% - 90%
OK	70% - 80%

SUMMARY OF CASE No.

CASE	DSS	TX
Excellent	6	10
Good	3	4
OK	1	2
Fast	10	3
Slow	0	0
Total	20	19

Cases of Good or Excellent predictions

TABLE 5.12 : COMPARISON OF EXCESS PORE PRESSURE PREDICTIONS WITH MEASUREMENTS
- RATIO OF TIME TAKEN TO DECAY ONE HALF EXCESS PORE PRESSURE @ EOS
[PREDICTED / OBSERVED]

TEST	Acceleration	Shearing Mode	P1	P2	P3	P4	P5	P6	Average
2a	0.05g	DSS		120%	100%	100%	-	120%	110%
		TX		250%	200%	200%	-	120%	180%
		Comment							
1a	0.05g	DSS	NG	72%		150% (P3)	- (P4)	110% (P5)*	110%
		TX	NG	115%		200% (P3)	- (P4)	110% (P5)*	142%
		Comment	Failed Record				Under Est.		
6a	0.25g	DSS			38%	45%	50%	55%	47%
		TX			75%	100%	100%	100%	94%
		Comment							
4a	0.25g	DSS			45%	45%	55%	45%	48%
		TX			100%	108%	100%	100%	102%
		Comment		Failed Record			Liquefied	Liquefied	
5a	0.35g	DSS		50%	50%	35%	45%	50%	46%
		TX		100%	100%	90%	93%	90%	95%
		Comment					DSS-Lqfd	Liquefied	
3a	0.08g	DSS		120% **	133% **	133% **	NG	NG	129%
		TX		-	-	-	NG	NG	-
		Comment							

Note: * Predicted time for decay half from peak P.P. / Observed time to decay half from EOS (end of shaking)

** Time to decay half from peak P.P.

122

TABLE 5.13 : QUALITATIVE COMPARISON OF POST PEAK DECAY OF EXCESS PORE PRESSURE

A QUALITATIVE SUMMARY FOR POST SHAKE DECAY BEHAVIOR

SUMMARY OF CASE No.

TEST	Acceleration	Shearing Mode	P1	P2	P3	P4	P5	P6
2a	0.05g	DSS		OK	Good	Good	-	OK
		TX		OK	OK	OK	-	OK
1a	0.05g	DSS	-	OK		OK (P3)	- (P4)	Good(P5)
		TX	-	Slow		lower(P3	- (P4)	Good(P5)
6a	0.25g	DSS			Fast	Fast	OK	OK
		TX			Fast	Good	Good	Good
4a	0.25g	DSS		-	Fast	Fast	OK	OK
		TX		-	Excellent	Good	Good	Good
5a	0.35g	DSS		OK	OK	OK	Fast	OK
		TX		Good	Good	Good	Good	Good
3a	0.08g	DSS		OK	OK	OK	Slow	Good
		TX		Slow	Slow	Slow	Slow	Slow

CASE	DSS	TX
Excellent	0	1
Good	4	12
OK	15	4
Fast	5	1
Slow	1	7
Total	25	25

Cases of Good or Excellent predictions

Rating	Rate of decay within 90-110% accuracy	Time to start decay (Difference<1sec)	Rate of decay within 50-200% accuracy
Excellent	Yes	Yes	Yes
Good	Yes	No	Yes
OK	No	Yes/No	Yes

TABLE 5.14 : COMPARISON OF PREDICTED HORIZONTAL
WALL MOVEMENTS WITH MEASUREMENTS

TEST	Shearing Mode	Predicted/Observation Peak Displacement Ratio	Rating
1a	DSS	0.85	Good
	TX	0.6	Good
2a	DSS	0.5	Good
	TX	0.45	Marginal
3a	DSS	0.9	Excellent
	TX	0.4	Under Pred.

Predictions classified as Good or Excellent

124
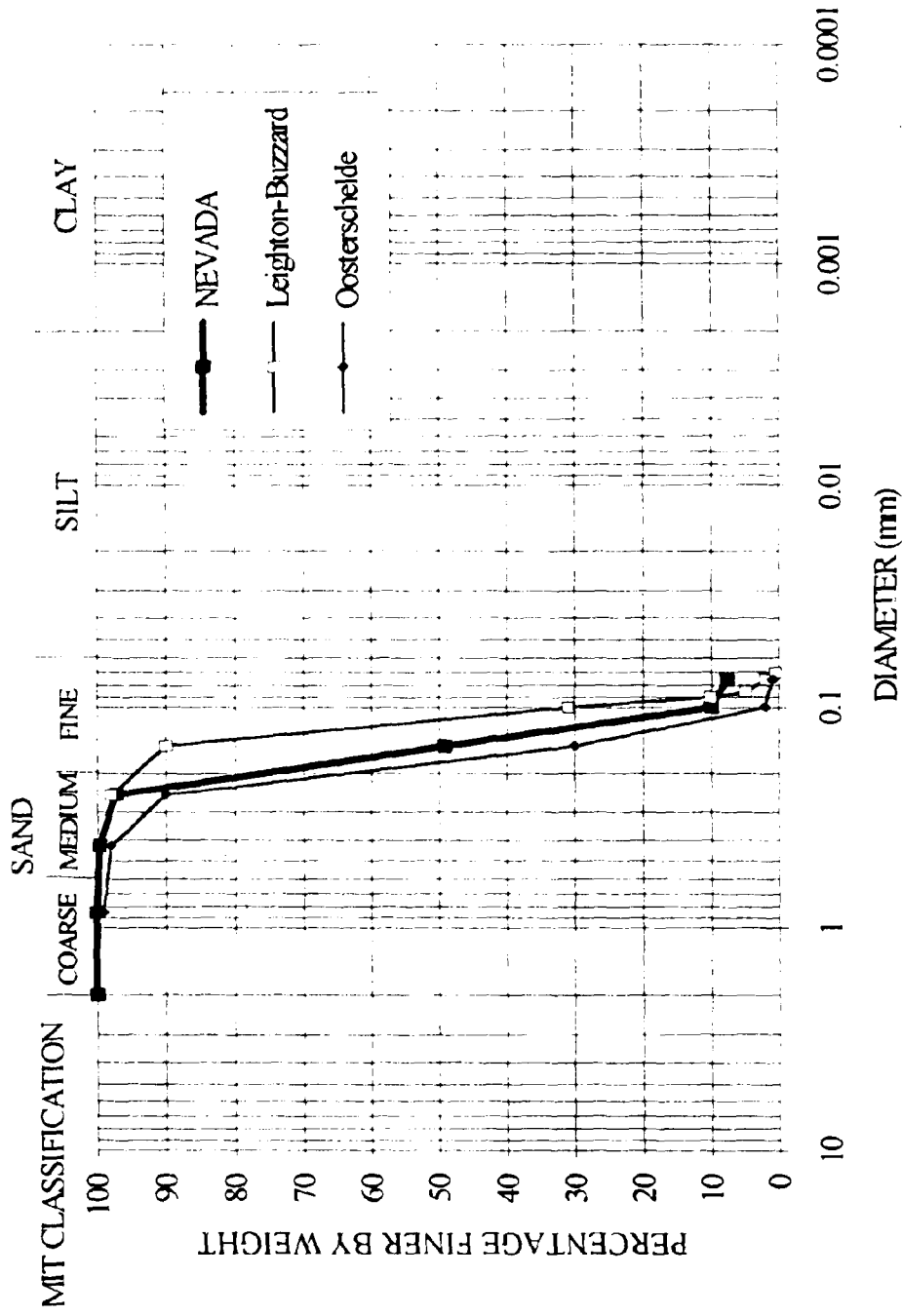
Figure 5.1: Grain size distribution curves of Nevada, Leighton-Buzzard and Oosterschelde Sands

125
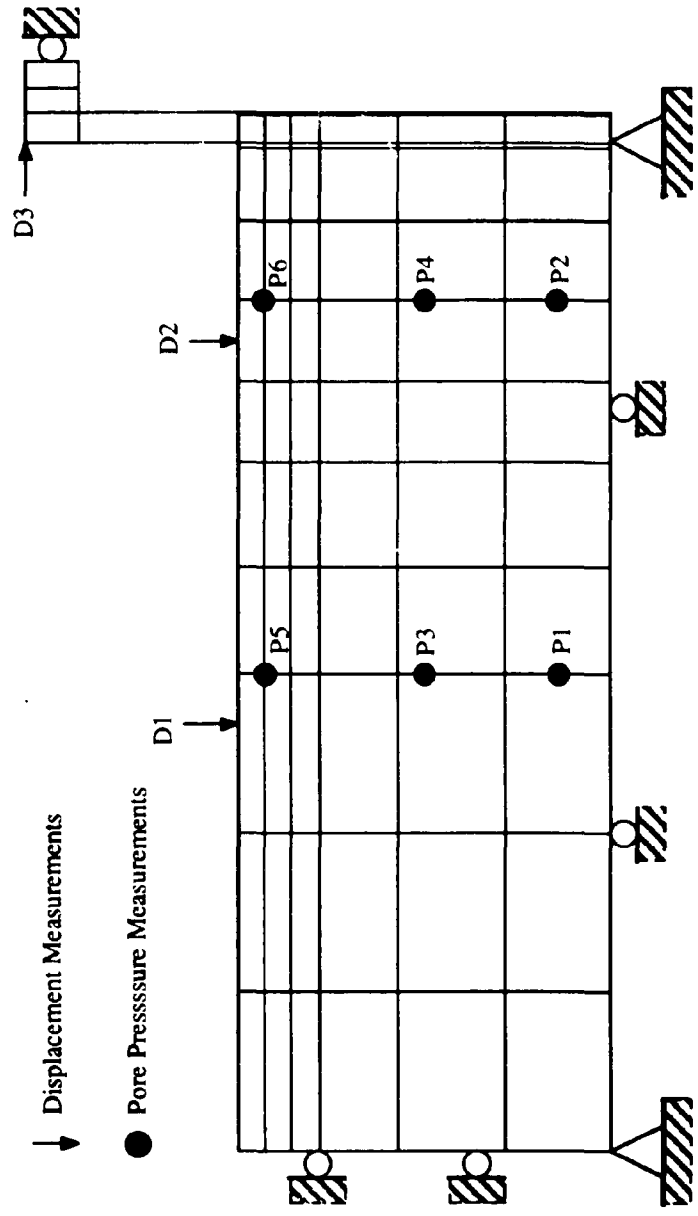
Figure 5.2: FINITE ELEMENT MESH
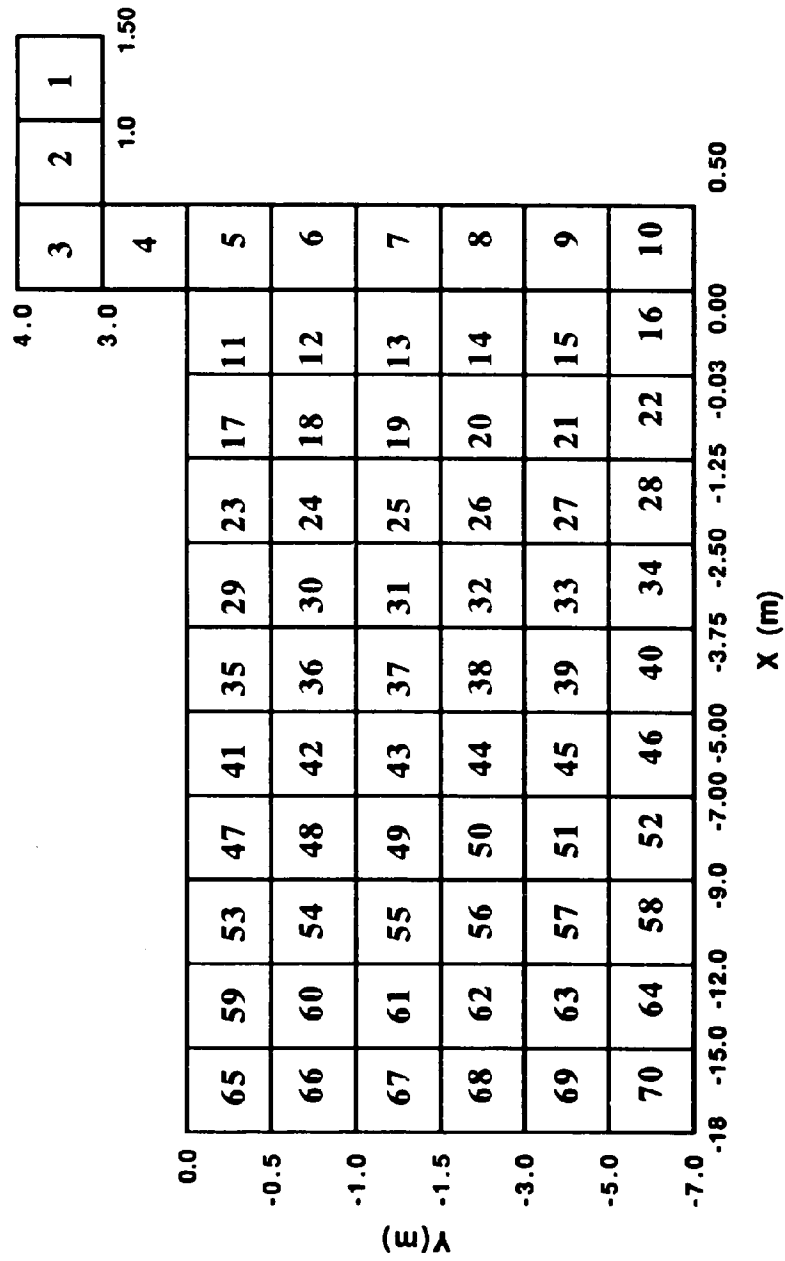
Figure 5.3: Numbering of Element and Periferal Coordinates of The FINITE ELEMENT MESH

127
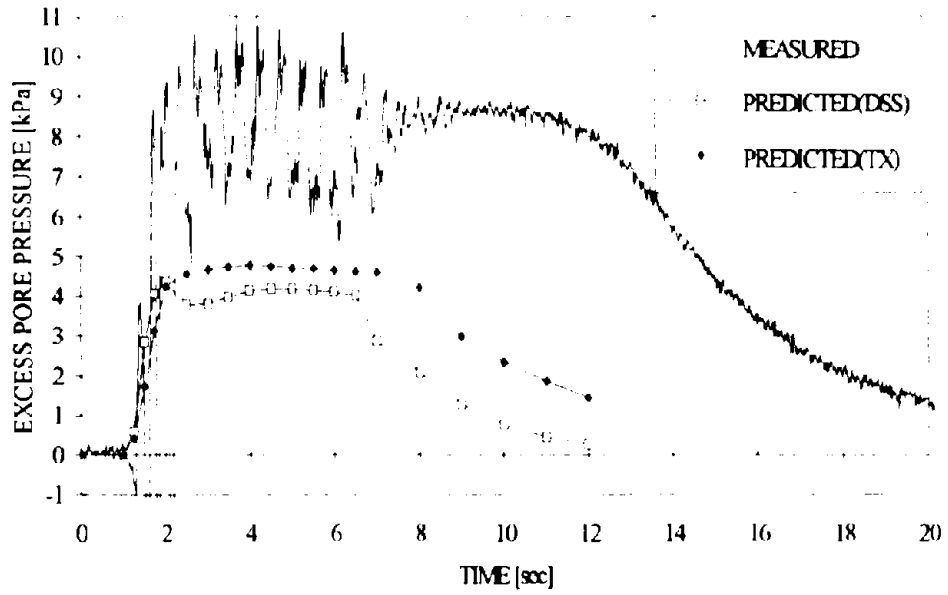
Figure 5.4 CYCON predicted and measured excess pore pressure at P5 in Test 5a
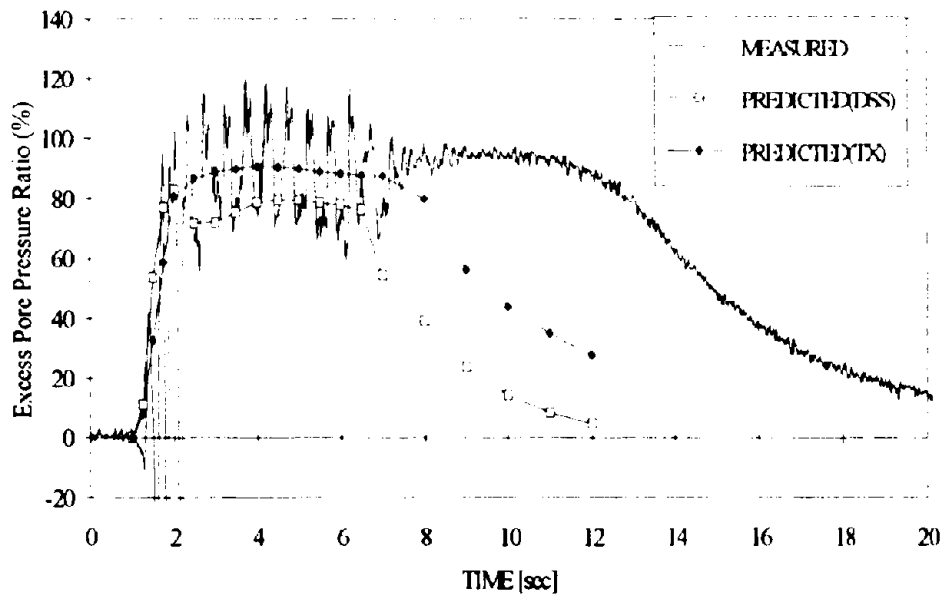
Figure 5.5 CYCON predicted and measured excess pore pressure ratio at P5 in Test 5a
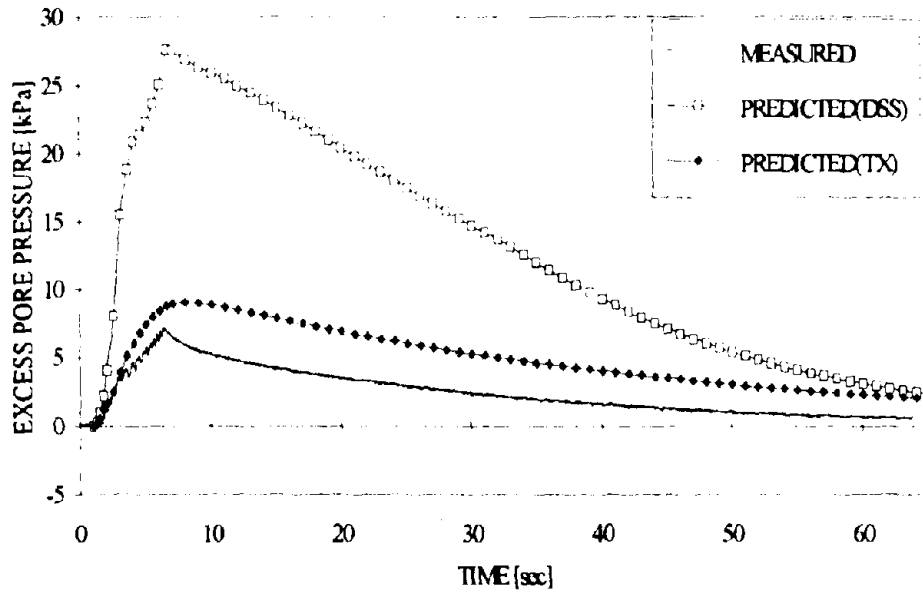
Figure 5.6: CYCON predicted and measured excess pore pressure at P4 in Test 3a
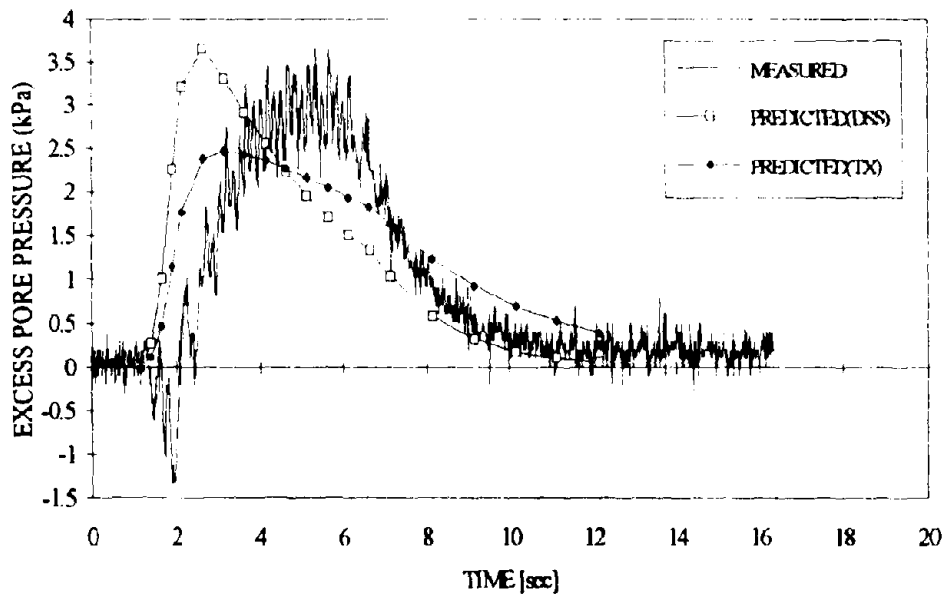
Figure 5.7: CYCON predicted and measured excess pore pressure at P4 in Test 2a

129
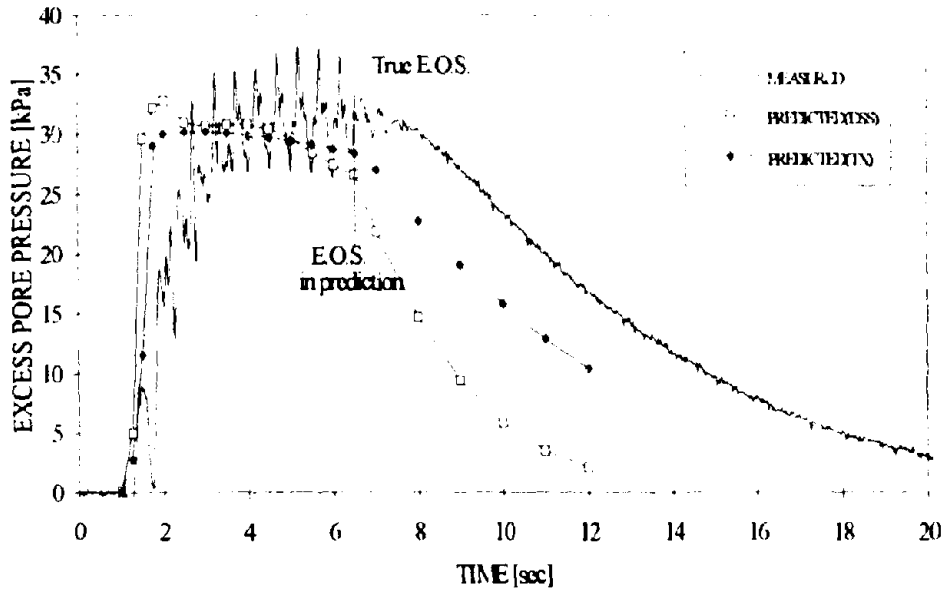
Figure 5.8: CYCON predicted and measured excess pore pressure at P3 in Test 4a
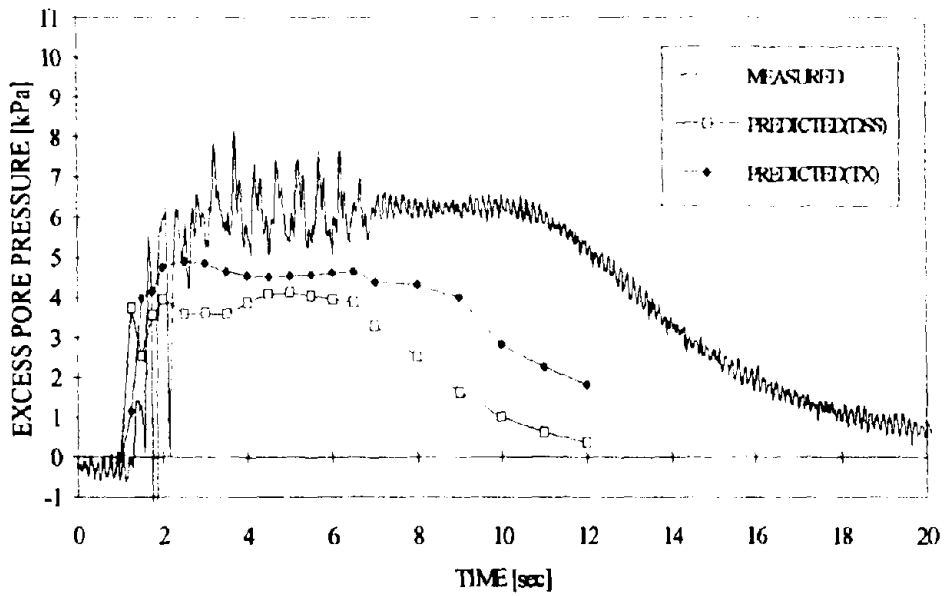
Figure 5.9: CYCON predicted and measured excess pore pressure at P5 in Test 4a

130
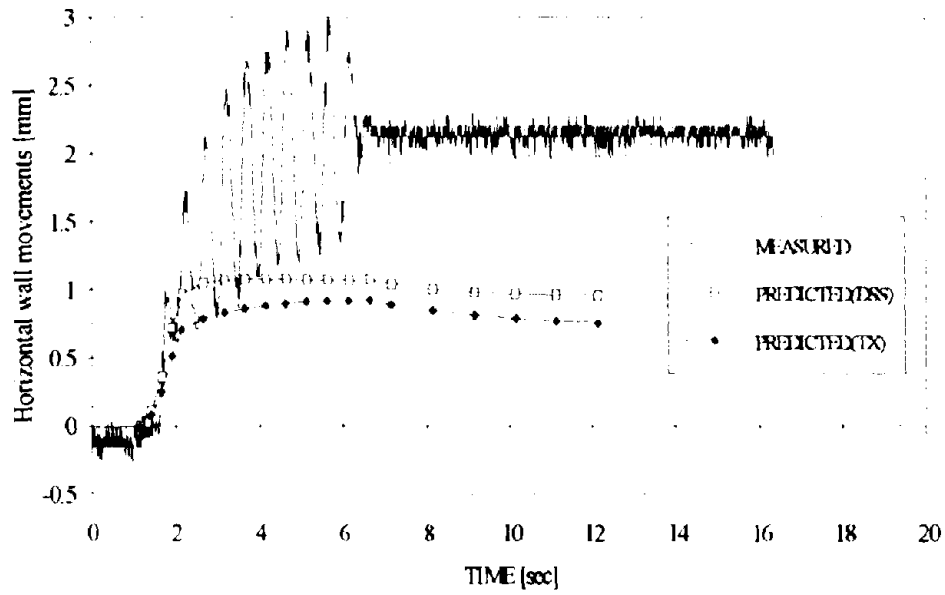
Figure 5.10: CYCON predicted and measured horizontal wall displacement at sand surface in Test 2a
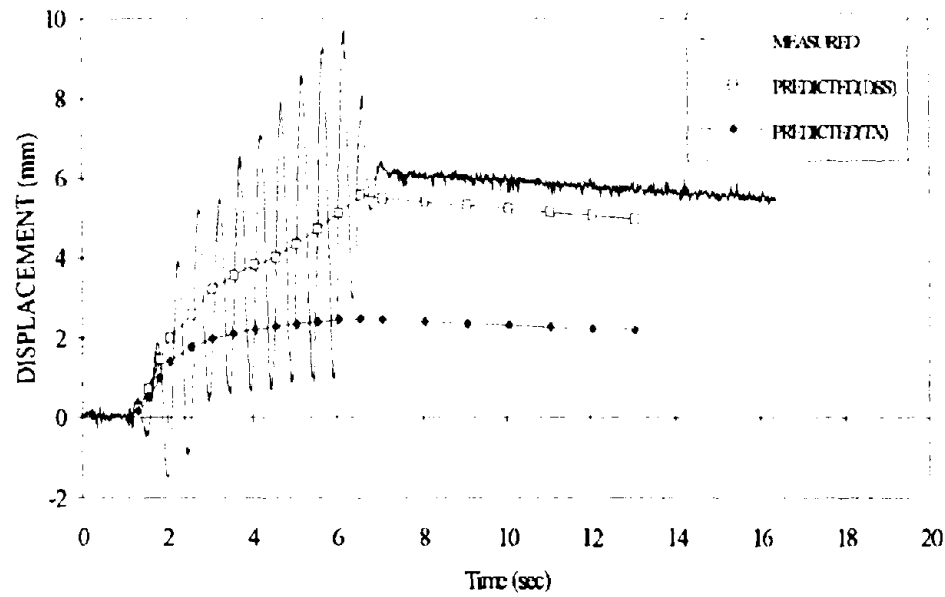
Figure 5.11: CYCON predicted and measured horizontal wall displacement at sand surface in Test 3a

131

Page Intentionally Left Blank

CHAPTER 6

BEHAVIOR OF THE SOIL-WALL SYSTEM IN
CENTRIFUGE MODEL TEST
(I) BEHAVIOR PRIOR TO SLIPPAGE AT SLIDER

This chapter presents the analyses of the general behavior of the soil-wall model in the non-slip tests (Table 4.5). These tests involved small to moderate earthquakes. Generally, the peak input acceleration was less than 0.15g. Stronger earthquakes would cause some plastic tilt of the retaining wall due to slip at the slider. The overall behavior of the model was characterized by variations in the thrusts acting on the wall due to the earthquakes. The investigations of the thrusts depend on the data of load measurement in the tie-back. During minor to moderate earthquakes, the dynamic load in the system was small enough to keep the total load in the tie-back below the yield load. During strong earthquakes, an excessive dynamic load brought the total load beyond the yield load of the tie-back. The tie-back failed temporarily during each cycle of shaking, as a result of the slippage at the slider. This chapter presents the analyses of the all thrusts acting on the wall prior to the slippage at slider. The characteristics of slippage at the slider during the model tests are presented in Chapter 7. Tremendous change in the system developed once slip occurred. The investigation of earth thrusts in such tests is much more complicated and is beyond the scope of this thesis.

During earthquakes, the variation of pore pressure in the backfill is important. Trends of pore pressure build-up and cyclic fluctuations were observed during earthquakes in the model test program. Section 6.1 presents the observations and

133

explanations of the net increase and fluctuations of the pore pressure during earthquake shaking.

Analysis of the earth thrusts[1] helps the understanding of the general behavior of the model test and improves the confidence in estimating similar problems in reality. A great deal of information from the test data is involved in the investigation of the earth thrusts. Section 6.2 describes the detailed schemes to obtain the earth thrusts from various data sets in the centrifuge model tests.

Section 6.3 presents the analyses of the thrusts on the retaining wall. During the earthquake shaking, the average transient pore pressure thrust increased due to pore pressure build-up which brought a special trend of the variation of average transient soil skeleton thrust: first decreasing during earthquake shaking and then recovering after the earthquake. The residual thrust from the soil skeleton was always larger than the initial thrust prior to shaking. During the period of shaking, the inertia effect of the retaining wall itself was significant. In addition to the inertia effect, the periodic rotation of the wall about its foot yielded a tremendous influence on cyclic fluctuations of the thrusts from the soil skeleton and pore fluid.

---

[1] The earth thrust and pore pressure thrust in this thesis are reported in model scales. The thrusts would be 2,500 times larger in prototype scales.

134

6.1   PORE PRESSURE VARIATIONS

The pore pressure within a cohesionless soil may rise under cyclic straining. A trend of pore pressure build-up during earthquake shaking was observed in the centrifuge model tests. Cyclic fluctuation of the excess pore pressure was also observed during each cycle of ground motion. This section presents the observations and explanations of the net increase (build-up) and fluctuation of the pore pressure during the earthquake.

6.1.1   Increase of the Average Transient Pore Pressure

The build-up of pore pressure within a cohessionless soil is commonly observed during cyclic tests. Figure 6.1 shows typical effective stress paths in a sand subjected to cyclic loading. The excess pore pressure, denoted by Δu, is the difference between the present octahedral stress and the initial octahedral stress. Note that there is a net decrease in effective stress at the end of the loading cycle. This is an indication for the accumulation of excess pore pressure, i.e., the increase of the average transient pore pressure.

The observed variations in the average transient pore pressures in the centrifuge models are due to two mechanisms of pore pressure change: the build-up of pore pressure due to cyclic shaking; and the dissipation of excess pore pressure during and after shaking. The actual change of the average transient pore pressure is a result of competition between these two mechanisms.

During moderate to strong earthquakes (peak input acceleration greater than 0.07g), the change in the average transient pore pressure was dominated by the cyclic strain

135

induced pore pressure build-up. The rate of decrease in pore pressure due to dissipation was overcome by the rate of pore pressure build-up. Therefore, the transient average pore pressure increased steadily or remained essentially constant during shaking and decreased only after shaking ceased.

During weak earthquakes (peak input acceleration less than 0.07g), the pore pressure built up less rapidly than the dissipation after a few cycles of shaking. In Tests 1a, 2a and 4b, the pore pressures increased initially during shaking. The dissipation of pore pressure took place as soon as the pore pressure was built up. The mechanism of pore pressure build-up in these weak earthquakes was not strong enough to overcome the dissipation. Figure 6.2 shows the history of the excess pore pressure at P2 in Test 1a as an example.

6.1.2 Cyclic Pore Pressure Variation

This section describes the mechanisms for the pore pressure fluctuations during earthquake shaking in the non-slip tests. Three causes for pore pressure fluctuation within a loading cycle are identified:

- inertia of the pore fluid
- cyclic shearing of the saturated sand
- periodic rotation of the wall.

In this test program, the geometry of the model allowed periodic wall rotations during shaking. The cyclic wall rotation had substantial influence on the pore pressure fluctuation. The influence of this effect will be presented in Section 6.3.2. This section

describes the first two mechanisms of the cyclic pore pressure fluctuations in the model during shaking

1. Inertia of the pore fluid

In the centrifuge model, the backfill, in some way, can be viewed as a two-phase material. The two phases are the mineral skeleton and the pore fluid. A tank for the pore fluid is composed of the shaking bin and the retaining wall. During cyclic shaking, the inertia of the pore fluid results in a fluctuation of the pore pressure. The fluctuation of the pore pressure yielded a cyclic change of the thrust acting on the retaining wall from the pore fluid. Westergaard (1933) developed an approximation for the dynamic water thrust during earthquakes on a straight dam with a vertical up-stream face. This approximation sometimes is used to estimate the thrust from pore water behind a vertical retaining wall:

$$\Delta P_u = \frac{7}{12} k_h \gamma_w H^2 \tag{6.1}$$

where w is the length of the wall; H is the depth of water above base; k_h is the coefficient of acceleration, the horizontal input acceleration normalized by the gravity acceleration.

2. The cyclic shearing of the saturated sand

Figure 6.1 presents typical stress paths of sand during undrained cyclic loading. The stress paths explain the pore pressure fluctuations due to the cyclic shearing. The pore pressure fluctuates twice within each cycle of loading. Therefore, the frequency of pore pressure fluctuation is twice the frequency of the cyclic loading. The amplitude of pore pressure fluctuation is small with low cyclic shear stresses (Figure 6.1a). Very large negative excess pore pressure may develop with high cyclic shear stresses (Figure 6.1b). The pore pressure fluctuation due to excessive shearing has two features:

137

- large negative excess pore pressure peaks
- "double cycling" of the excess pore pressure.

"Double cycling" means the shear induced pore pressure experiences two cycles of fluctuations during one cycle of shearing.

During weak earthquakes, the shearing-induced pore pressure fluctuation was less significant. The inertia of the pore fluid dominates the pore pressure fluctuation. Figure 6.2 shows the excess pore pressure record of P2 in Test 1a, with a small input acceleration (0.06g). With a weak shaking, the characteristics of the pore pressure fluctuation are: (1) the double cycling of the pore pressure fluctuation is not obvious; and (2) the fluctuations are more or less "symmetrical" about the average transient pore pressure.

During strong earthquakes, excessive shearing occurred, especially near the surface of the backfill. The shearing-induced pore pressure fluctuation was more substantial. Figure 6.3 shows the excess pore pressure history of P5 in Test 5a. The soil skeleton experienced severe shearing due to a strong input ground motion ($a_{max} = 0.35$ g). The soil liquefied and the slider started to slip after two cycles of loading. The pore pressure history demonstrates two features of pore pressure fluctuations, prior to slip and liquefaction, associated with high shearing stresses: the "double cycling" and large negative excess pore pressure.

These two features of excess pore pressure fluctuation at strong earthquake loading are not unique in the model tests. Similar features are also observed in laboratory triaxial and simple shear tests. Observations from both the centrifuge model tests and laboratory shearing tests are presented as follows. Interpretation for these features follows the observations.

138

Observations from Centrifuge Model Tests

- "Double cycling" and negative pore pressure were evident near the surface of the backfill in tests involving strong earthquakes (P5 and/or P6). These features were present until soil liquefaction was indicated (by A3).

- When negative pore pressure was present in the initial cycles, the double amplitude of the excess pore pressure before liquefaction was much greater than that after liquefaction (see Figure 6.3).

- When the average pore pressure reaches the initial vertical effective stress (σ'_{vo}), the local soil is recognized as liquefied. The liquefaction is indicated by the acceleration record of A3, the accelerometer at the same depth in the soil as of the pore pressure transducer. The record of A3 in Test 5a is presented in Figure 6.4. When liquefaction occurs, horizontal accelerations no longer can be transmitted upward through the fluidized soil.

Table 6.1 lists the appearances of "double cycling" of the excess pore pressures, at all six pressure transducers in the backfill during all tests. The locations of the pressure transducers are shown in Figure 4.4. The double cycling is not present in tests with weak earthquakes. As the intensity of the earthquake increases, double cycling is present in greater depth.

Observations from Laboratory Tests

The investigations of laboratory tests on Nevada Sand are based on the Earth Technology Report (1992). The pore pressure data of laboratory cyclic shearing tests show two features of the pore pressure fluctuations: the "double cycling" and large negative excess pore pressure. These features are consistent with the observations from the centrifuge model test data.

139

1. Evidence of Double Frequency

"Double cycling" of the excess pore pressure is evident in several cyclic triaxial and DSS test results. Figure 6.5 shows the records of a cyclic simple shear test on Nevada sand with 60% relative density (The Earth Tech Test No 60-04). The frequency of the pore pressure fluctuation is twice as large as that of the cyclic stress or the cyclic strain.

2. Evidence of Large Negative Excess Pore Pressure Ratio

Large negative excess pore pressure is observed in both CIUC and CIUE tests on Nevada sand. The result of a CIUC test on Nevada sand is presented in Figure 6.6 (The Earth Tech Test No. 60-12). In this test, a negative excess pore pressure of -720 kPa is observed when failure occurs.

Interpretations for
Double Frequency and *Large Negative Excess Pore Pressure Ratio*

The stress path in Figure 6.1 gives an explanation for the double frequency of the excess pore pressure fluctuation. Within a cycle of loading, the excess pore pressure experiences a cycle of plus-minus-plus-minus variation. This variation is the "double cycling" of the excess pore pressure. The double cycling of the excess pore pressure may be a consequence of the dilation-contraction-dilation-contraction behavior of cyclic shearing of the soil skeleton.

The shearing stress increases as the intensity of earthquake increases. Extremely large negative excess pore pressure can develop in the sand when the sand is strained close to failure. Figure 6.1 (b) demonstrates the stress path at this extreme. The amount of negative excess pore pressure is very sensitive to the shear stress, the relative density of the sand, and the initial stress state of each individual cycle of shearing. This figure shows that very large negative pore pressure change is developed during shearing when the shear

140

stress is large. However, the positive increment in pore pressure is limited during cyclic loading

Concluding Comments

Pore pressure fluctuation within a cycle of input ground motion in the centrifuge model tests consisted of two superimposed components:

- the inertia of the pore fluid due to the input horizontal acceleration
- the cyclic pore pressure variation due to shearing.

During weak earthquakes, the effect of shearing was not prominent, and therefore the pore pressure fluctuation mainly came from the pore fluid inertia. This is highlighted by the single cycling and the approximate symmetric pore pressure fluctuation as shown in Figure 6.2.

During strong earthquakes, the shearing induced pore pressure variation was significant due to the severe shearing accompanied by the large shearing stresses. The effect from shearing of the soil skeleton on the excess pore pressure fluctuation exceeded the effect of the pore pressure inertia. As shown by the initial cycles of pore pressure fluctuation in Figure 6.3 and the cyclic stress path in Figure 6.1 (b), the pore pressure fluctuation due to shearing of the soil skeleton is distinguished with its double frequency and large negative excess pore pressure.

With intermediate shaking and shearing, the pore pressure variation was subjected to a competition between the above two effects. Figure 6.7 presents an illustration. The contributions of both effects on the fluctuation of pore pressure were comparable. The

pore pressure fluctuated with a predominant frequency of 2 Hz, superimposed with a 4 Hz cycle having a slightly larger negative component.

Various patterns of pore pressure variations in the model test results are observed, varying with both the shaking intensity and the location within the sand (Schran, 1992). The resultant pore pressure variations may be complicated; however, they are generally based upon the above two effects and the periodic rotation of the wall (Section 6.3.2). The observed excess pore pressure variations come from various combinations of these three effects.

6.2   EARTH THRUSTS ACTING ON WALL

The analyses of the earth thrusts were performed based upon the measurements of the total force in the tie-back. Various data records are involved in the analyses. This section presents the procedures and results of these analyses.

The first step is to investigate all moments acting on the wall. The wall is hinged at base. Above the base, the wall is subject to an earth thrust from the backfill, and a pulling force from the tie-back. During earthquake shaking, the inertia of the wall itself was also acting on it. The total moment about the base, from the tie-back force, minus the inertial moment gives the moment from the total earth thrust. For convenience of comparison and presentation, all thrusts involved are converted to amounts of force in the tie-back. Section 6.2.1 presents the procedures of these analyses to obtain total earth thrust on the retaining wall.

142

Total earth thrust consists of thrusts from both the mineral (soil) skeleton and the pore water pressure. The thrust from mineral skeleton can be obtained by subtracting the pore pressure thrust from the total earth thrust. The pore pressure thrust involves thrusts from both hydrostatic pore pressure and excess pore pressure in the sand backfill. Hydrostatic pore pressure thrust is calculated directly from the hydrostatic pore pressure along the depth of the backfill. Interpretation of excess pore pressure thrust calls for an integration scheme using the measured excess pore pressure data. The integration scheme is presented in Section 6.2.2.

Section 6.2.3 presents the total earth thrusts and the thrusts from both the excess pore pressure and mineral skeleton in all tests (except for a few tests missing major data). The inertia of the retaining wall and input acceleration data are also presented in this section. Results show that the wall inertia is a substantial part of the total force acting on the wall.

6.2.1 Moments Acting on Wall During Shaking

The total load in the tie back was measured with a load cell at the fixed end. Prior to earthquake, the measured load is the restraining force required in the tie back to balance the static earth thrust acting on the wall. After the commencement of earthquake in each test, the inertia of the system became an important component involved in the load cell record. The first step in analyzing the earth thrust during shaking is to investigate all moments acting on wall.

143

A simplified configuration of the testing model is shown in Figure 6 8   The balance of moment about the wall's base is expressed in Eq. $(6.2)^2$

$$\left[F_{1c} + (m_{11} + m_{12} + m_{13})A4 + \left(m_{14} + m_{15} + \frac{m_{16}}{2}\right)A5 + \left(\frac{m_{16}}{2} + m_{17}\right)A6\frac{H_{uc\_back}}{H_{wall}} \right] \cdot H_{uc\ back}$$

$$+ \frac{1}{2}m_{wall}H_{wall}A1 + I_{wall}\ddot{\theta} - F_{soil}H_3 = 0 \qquad (6.2)$$

where $H_{tie-back}$ is the distance between the tie-back and base; m_{wall} and I_{wall} (= $\frac{1}{3}m_{wall}H_{wall}^2$) are the mass and moment of inertia of the wall; F_{LC} is the force recorded by the load cell; F_{soil} is the total earth thrust; H_3 is the height from base where the earth thrust acts; A1, A4, A5 and A6 are the accelerations at the base, load cell, the sliding element of the slider and at top of the wall, respectively; and all mass term representations are shown in Figure 6 8   Data for the various masses are given in Table 4.1. The angular acceleration ($\ddot{\theta}$) of the wall can be obtained from horizontal acceleration measured at both top and bottom

$$\ddot{\theta} = \frac{A6 - A1}{H_{wall}} \qquad (6.3)$$

Moments in Eq. (6.2) are positive when counter-clockwise.

In Eq. (6.2), the author must assume A4 is equal to A5 in some tests.   The acceleration A4 was not recorded in test series 2, 3, 5 and 6, due to the limited data logging channels   However, the accelerations should be essentially identical along the tie-back if there is no slip at the slider. Therefore, A4 and A5 are set equal to each other in

---

[2] The calculations for the thrust acting on the wall were made using an older version of Eq. (6.4), which was slightly different from the current equation. There was little, if any, difference between the calculated results using the slight different versions of Eq. (6.4). The difference was confirmed to be negligible after examining a few cases. These comparisons are not reported in this thesis.

144

non-slip tests. The validity of this assumption was confirmed in Test 1. (Figure 7.1 shows the data of A4 and A5 in Test 1a.)

The first term in Eq. (6.2) is the restraining moment provided by the force from the tie-back. The term in the bracket is the calculation for the force at the hinge between the tie-back and the wall, given a measurement by the load cell. This term involves several inertia forces in the tie-back. The sign convention of the acceleration is: positive towards the retaining wall; negative towards the backfill. A positive load cell force is tension, a positive soil force is an outward thrust, as shown in Figure 6.8.

The second term in Eq. (6.2) is the moment from the mass inertia of the wall itself. The third term is the moment of rotational inertia of the wall. Thus, the moment exerted by the wall itself is

$$M_{wall} = \frac{m_{wall}A1}{2}H_{wall} + I_{wall}\ddot{\theta} \tag{6.4}$$

$$= \frac{m_{wall}A1}{2}H_{wall} + \frac{m_{wall}}{3}H_{wall}^2\frac{A6-A1}{H_{wall}}$$

$$= m_{wall}H_{wall}\frac{A1+2A6}{6}$$

The moment from total earth thrust is obtained by adding the moments associated with the wall inertia to the restraining moment by the tie-back. The restraining force required in tie-back to withstand the total earth thrust is expressed in Eq.(6.5).

$$P_{earth} = F_{soil}\frac{H_3}{H_{tie-back}} \tag{6.5}$$

$$= \left[F_{LC} + (m_{11} + m_{12} + m_{13})A4 + \left(m_{14} + m_{15} + \frac{m_{16}}{2}\right)A5 + \left(\frac{m_{16}}{2} + m_{17}\right)A6\right]$$

145

$$+m_{wall}\frac{(A1+2A6)H}{6H_{tie-back}}$$

Comparisons among the __restraining forces__ in the tie-back required to balance various thrusts will be presented in Section 6.2.3.

6.2.2 Thrust from Excess Pore Pressure

The interpretation of excess pore pressure thrust involves a process of integrating excess pore pressures measured at various depths near the wall. Figures 6.9 shows three excess pore pressures at various depths near the wall (P2, P4, and P6) in Test 2b. Figure 6.10 shows a schematic distribution of pore pressure along the depth of the soil backfill (by the dashed line). Eq. (6.6) expresses an estimation of the moment exerted by the excess pore pressure thrust about the base. This estimation is based on a simplified profile of pore pressure distribution, shown by the solid line in Figure 6.10.

$$M_{u,ex}(t) = w[\frac{h_2^2}{2}u_{2e}(t) + h_4(h_2 + \frac{h_4}{2})u_{4e}(t) + \frac{h_6}{2}(h_2 + h_4 + \frac{h_6}{3})u_{6e}(t)] \qquad (6.6)$$

where w is the width of the wall. The terms in the bracket in Eq.(6.6) are defined in Figure 6.10. The restraining force in the tie-back due to excess pore pressure is estimated by Eq. (6.7).

$$P_{u,ex}(t) = \frac{1}{H_{tie-back}}M_{u,ex}(t) \qquad (6.7)$$

$$= \frac{w}{H_{tie-back}}[\frac{h_2^2}{2}u_{2e}(t) + h_4(h_2 + \frac{h_4}{2})u_{4e}(t) + \frac{h_6}{2}(h_2 + h_4 + \frac{h_6}{3})u_{6e}(t)]$$

146

In Figure 6 10, the excess pore pressure in the upper part of the soil reaches the initial effective stress In the model tests, soil never liquefied throughout the entire thickness During the period of moderate to strong earthquake shaking, liquefaction occurred only in the soil near the surface. There was a liquefaction front moving downward from the surface during earthquakes, which is shown by the line between h_6 and h_4 in Figure 6.10 However, the movement of the liquefaction front can hardly be measured practically In addition, the contribution of the excess pore pressure in the liquefied zone to the entire excess pore pressure thrust is small because of the relatively small absolute values of excess pore pressure in this zone.

It is necessary to use reasonable values for h_2, h_4 and h_6 to estimate the excess pore pressure thrust The values used are 2m, 3.5m, 1.5m in prototype scale and 40mm, 70mm, 30mm in model scale, respectively. The pore pressure thrusts calculated according to the above scheme are not sensitive to minor changes of the value of h_6. Figure 6.11 shows a comparison of the pore pressure thrust in Test 2b calculated using slight different values of h_4 (= 3.25m) and h_6 (= 1.75m) as an example. The differences produced by using different values of h_4 and h_6 are: the cyclic amplitude is reduced by about 13%, and the average transient thrust is reduced by 0.4%. These changes are practically insignificant.

6.2.3 Restraining Forces at Tie-Back From Various Thrusts on Wall

Prior to earthquake shaking, the restraining force in the tie-back came only from the soil thrust At this time, the thrust acting on wall contained only the thrusts from soil skeleton and from hydrostatic pore pressure After the horizontal input ground motion began, the inertia of the soil skeleton, pore fluid and the wall itself were involved.

147

Thrust from soil skeleton is obtained by subtracting the pore pressure thrust from the total earth thrust. The pore pressure thrust includes thrusts from both hydrostatic pore pressure and excess pore pressure. The hydrostatic pore pressure thrust is constant and can be calculated from the distribution of hydrostatic pore pressure along the wall. In the model tests, the hydrostatic pore pressure thrust is 961N (model scale) acting at one-third depth from base. This thrust corresponds a restraining force of 214N in tie-back.

Figures 6.12 through 6.21 demonstrate the restraining forces in tie-back due to various thrusts acting on the wall, in tests with no slippage at slider. Once slippage occurs, the force measurements are no longer valid in many dynamic aspects, and consequently the analyses of dynamic thrusts in these tests are not meaningful. An exception is Test 1b. The slider did not slip until after several cycles of shaking. The dynamic responses prior to the slippage are included in the analysis. The thrusts in these figures include the total thrust (the force in the tie-back at the wall), the thrust due to the wall inertia, total earth (soil) thrust, excess pore pressure thrust and mineral skeleton thrust. In these figures, the input accelerations are also included for reference. Figures 6.22 and 6.23 summarize the time histories of the thrust from soil skeleton and pore pressure, respectively, in all non-slip tests. In these figures, longer time are used to demonstrate the variation of the average transient thrusts over time during and after the earthquakes.

6.3   GENERAL OBSERVATION OF ALL THRUSTS ON WALL

This section presents a general picture of the behavior of the soil-wall system during the centrifuge tests. The investigation of all thrusts against the retaining wall during and after earthquake helps us to understand the overall behavior of the model. The investigation was performed on the thrusts in Figures 6.12 through 6.21.

Section 6.3.1 describes the analyses of the average transient thrusts during and after each series of earthquake shaking. The analyses include the increase and decrease of average pore pressure thrust during and after the earthquake shaking, and the average variation of the thrust from soil skeleton during and after shaking. Observations from the analyses of the time-wise average variations of these thrusts are presented in Section 6.3.1.

Section 6.3.2 presents the analyses of the cyclic fluctuations in the thrusts. As a result of cyclic ground motion, fluctuations of the thrusts are present due to the inertia of the backfill. Applicability of the Mononobe-Okabe equation and Westergaard equation for calculating the dynamic thrusts of soil skeleton and pore fluid are checked. For this model test program, the periodic rotation of the retaining wall has very significant influence in the analyses of the dynamic thrusts. The details of the analyses are described in Section 6.3.2.

Section 6.3.3 summarizes the observations obtained from the analyses in the previous two sections.

6.3.1 Variation of Average Transient Thrusts on Wall from Pore Pressure and Soil Skeleton

Generally, pore pressure in the backfill increased during the period of earthquake shaking (see Section 6.1). Therefore, the horizontal thrust on the wall from pore pressure increased during shaking. The effective stress of the soil skeleton decreased as a result of pore pressure build-up. Consequently, thrust on the wall from soil skeleton decreased during shaking. The dissipation of excess pore pressure was not obvious during earthquake shaking, although it may be occurring, since the pore pressure tended to increase due to earthquakes (Section 6.1). Average pore pressures at end of shaking (EOS) were generally as large as those during shaking. Therefore, the EOS values are good indicators of the effect of shaking. At the end of shaking, pore pressure stopped increasing. The subsequent variation of pore pressure came purely from the dissipation of excess pore pressure. Therefore, the pore pressure thrust decreased after the end of shaking.

After shaking, the thrust from the soil skeleton increased with time. In addition to the amount of the dissipated excess pore pressure, the horizontal stresses in the soil skeleton increased more after shaking. At the end of shaking, the effective stress of the soil skeleton was low. As a result of dissipation of excess pore pressure, the sand particles in the soil skeleton were re-arranged to a denser state and exerted a larger horizontal stress to the wall, compared to the initial soil skeleton prior to earthquake. This increased horizontal stress results in a larger residual earth thrust.

The above qualitative descriptions are learned from the observations of the thrusts obtained in Section 6.2. They are consistent with expectations. A quantitative summary in Table 6.2 lists the thrusts in tests without slippage at slider. It summarizes the forces at

slider due to the thrusts from pore pressure and soil skeleton, and total thrust on the wall at initial, end of shaking, and residual states. Some observations obtained from this table are the following:

1. The amount of increase in pore pressure thrust during shaking generally increased with the peak input acceleration. (Refer to the 11th column in Table 6.2.)

2. The amount of decrease in soil skeleton thrust during shaking generally increased with the peak input acceleration, but with more scattering about the trend. The decrease in skeleton thrust was considerably less than the increase in pore pressure thrust. (Refer to the 17th column in Table 6.2.)

3. The amount of increase in soil skeleton thrust after shaking generally increased with the peak input acceleration. (Refer to the 19th column in Table 6.2.)

4. In Test 3a, the increment in pore pressure thrust during shaking was large compared with other tests with similar intensity of shaking. This was due to the smaller dissipation of the excess pore pressure during shaking, as a result of low permeability of the pore fluid.

The second observation shows that the change of the skeleton thrust during earthquake is associated with two aspects:

- the decrease in effective stress (related to the increase in pore pressure)
- the increase in horizontal stress in the skeleton (related to the increase in relative density).

The resultant change in the skeleton thrust is a compromise between these two effects.

The above observations are consistent with what one might have expected. Some more observations help us better understand the dynamic responses of the model:

151

5. The amount of decrease in the soil skeleton increased faster than linearly with the input earthquake intensity. Figure 6.24 summarizes the results of the non-slip tests. A relation proportional to cubic earthquake intensity is suggested by all but one data point (from Test 6b). This outlier will be further discussed shortly.

6. The increment in pore pressure thrust was small when the earthquake was very weak. Figure 6.25 summarizes the test results. The trend of the increase of pore pressure increment during shaking with earthquake intensity is marked by the broken line. There is a threshold of earthquake intensity for the pore pressure thrust to increase during shaking. Regression[3] of the test data indicates a threshold intensity of about 0.04g in these tests. This threshold acceleration is less than what would be predicted by Dobry et al. (1981), who would predict a threshold acceleration of 0.07g for the backfill of saturated Nevada sand.

7. Pore pressure build-up was a result of cyclic shearing. Dobry et al. (1981) observed that there is a threshold strain for pore pressure build-up during cyclic shearing. Figure 6.26 shows their observations of pore pressure build-up of two saturated sands during strain-controlled cyclic triaxial tests. The sands were placed at a relative density of about 60% by a variety of compaction techniques, and isotropically consolidated to pressures σ_c' between 100 and 140 kPa with OCR = 1. The vertical axis is the pore pressure build-up normalized by the initial vertical effective stress. The threshold cyclic strain for pore pressure build-up in saturated sands was found to be 10^{-2} %, as indicated by this figure.

In this research, the increment of pore pressure thrust during earthquake was an integration of pore pressure build-up along the retaining wall. The average pore pressure ratio can be obtained by normalizing the incremental pore pressure thrust (column 11 in Table 6.2) by the thrust caused by the initial effective stress,

---

[3] The regression ignores the data of Tests 1a and 3a. The data of Test 3a is ignored because of the different pore fluid, as in observation 5. The data of Test 1a is ignored due to the lower relative density. The result of Test 1a is above the general trend in Figure 6.23, due to the larger earthquake response associated with the lower relative density. Other tests with lower relative density were included in the regression since the results were not significantly affected by them.

$$P_p = \frac{1}{2}\gamma_b wH^2 \frac{0.5H}{H_{tie-back}} = 326N$$ Figure 6.27 shows the normalized pore pressure

build-up versus cyclic shear strains in non-slip tests. The cyclic sheai strains were calculated from dynamic amplitudes of cyclic horizontal wall movements[4]. Test 3a involved a less permeable pore fluid and yielded a larger pore pressure build-up; test ?c was a third shaking on the model and yielded smaller pore pressure build-up. Other than these two tests, Figure 6.27 indicates a similar trend of pore pressure build-up with increasing cyclic shear strain as that in Figure 6.26. This figure also suggests a threshold cyclic shear strain of $10^{-2}\%$ for pore pressure build-up, which is similar to that indicated in Figure 6.26.

8. Figure 6.28 shows the increment of the average transient total earth thrust during each earthquake in the centrifuge model tests (non-slip tests[5] and slip tests[6]). Generally, the incremental thrusts are less than about 100 newtons (model scale) which is about one-quarter (25%) of the initial static earth thrust (from soil skeleton and hydrostatic pore pressure) prior to earthquakes. That is, one-quarter of the initial static earth thrust is an upper limit of the incremental average transient total thrust at the end of each earthquake in this research. Note that the average transient earth thrust was slightly larger during each earthquake than at the end of shaking (as shown in the figure), due to the dissipation of excess pore pressure during earthquake

9. The thrust from soil skeleton had increased more than that had decreased during shaking. Figure 6.29 compares the changes in the soil skeleton thrust during and after the earthquakes. The trend of decrease in the average transient soil skeleton thrust during earthquakes is marked by the dashed curve. The trend of post shake

---

[4] The observed dynamic amplitudes of the wall displacement were amplified by a factor of 1.67 to yield the actual amplitudes. This was due to the de-amplified dynamic response of the displacement transducer at high frequencies. Chapter 7 will discuss this effect in more detail.

[5] Results are listed in the fifth column in Table 6.2.

[6] These incremental thrusts are also shown in Figures 7.2 through 7.7 and 7.10 through 7.15.

increment is marked by the dotted line. The difference between these two curves is the trend for residual thrust increment as a result of each earthquake.

10. Figure 6.30 shows the observed residual thrust increments in the non-slip tests. The trend of incremental thrust versus the shaking intensity first increases with the peak acceleration and then decreases with it. This trend is similar to the difference between the two curves in Figure 6.30.

11. One outlier (result of Test 6b) in Figure 6.30 reveals that some uncertainties associated with the trends in Figures 6.24, 6.29 and 6.30 may exist. These trends are influenced by the procedures of conducting the centrifuge tests. These procedures influenced the trends of the soil skeleton thrust. However, the trend of pore pressure thrust in Figure 6.25 was not affected.

In a soil model experiencing a series dynamic tests in the centrifuge, the lateral stress increases test after test, as long as there is no spin-down of the centrifuge between any two tests. However, the potential for the incremental lateral stress becomes smaller and smaller after each shaking due to: (1) the soil is densified due to previous shaking, and (2) the existing lateral stress ratio[7] gets higher and higher after each shaking. Therefore, the residual thrust increment in Test 2c (involving a third shaking on the model) was small as shown in Figure 6.30.

In this testing program, the lateral earth pressure coefficient in a fresh soil model was about equal to K_a[8] after the centrifuge was spun up -- owing to the outward rotation of the wall (Chapter 4). The potential for lateral stress increment was large for the models during the first shaking. However, this potential was also larg for Tests 4b,

---

[7] $K = \dfrac{\sigma_h'}{\sigma_v'}$

[8] Active lateral pressure coefficient $K_a \approx \dfrac{1 - \sin\phi}{1 + \sin\phi}$.

154

5b and 6b, since the centrifuge was spun down[9] and then re-spun up prior to these tests. The residual thrust increased more-or-less with the shaking intensity in these tests. Therefore, the data point of Test 6b in Figure 6.30 was high. In Figure 6.30, the data point of Test 4c resides at an intermediate location since it was a second shaking after re-spin-up.

During an earthquake, the soil skeleton is somewhat loosened, especially near the surface. The loosening of the soil skeleton is mainly associated with the increased pore pressure. The earth thrusts are influenced more by what happens near surface than by what happens at depth. If the earthquake is weak, only the soil near surface is affected. The influence on the soil skeleton at greater depth is small. However, the influence on the deeper soil aggregates when the earthquake becomes stronger. The decrease in the soil skeleton thrust is a result of the integration of the earthquake influence over the entire depth. Therefore, the amount of decrease in the soil skeleton thrust during shaking should increase faster than linearly with the input earthquake intensity. This is confirmed by the fifth observation.

The loosening of soil skeleton is one kind of dynamic response in the backfill. It is difficult to quantify how much the soil is loosened everywhere in the backfill. However, it is reasonable to add some "imaginary" contours of dynamic response (loosening of the skeleton) in the profile of the soil backfill. The dynamic response is the amount of decrease in the strength of the soil skeleton.

Figure 6.31 shows the imaginary contours of the normalized dynamic response (amount of loosening) of the soil backfill during weak and strong earthquakes. The three curves marked by "L", "M" and "S" are the hypothetical contours of the normalized

---

[9] For adjusting the location of the displacement transducer (D3).

dynamic responses. They represent three levels of dynamic responses in the backfill. large, medium and small. The dynamic response is larger near the backfill surface and the tilting retaining wall.

These contours do not necessarily vary linearly with the depth in the soil, nor linearly with the earthquake intensity. For better understanding, the dynamic response is normalized by the earthquake intensity. The contours of normalized dynamic response should be in the same locations for weak and strong shakings if the dynamic response varies linearly with the earthquake intensity. Under such circumstances, the relation in Figure 6.24 should be linear with the peak ground acceleration.

However, the normalized contours penetrate into deeper soil when the earthquake is stronger. The normalized dynamic response at a given depth increases with the shaking intensity. In other words, the depths of the "imaginary" contours of normalized dynamic responses increase with the earthquake intensity, as shown in Figure 6.31. Therefore, the relation in Figure 6.24 increases faster than linear with the earthquake intensity. Nevertheless, the cubic relationship in Figure 6.24 can serve only as a conceptual index. Further tests with other conditions will help confirming and generalizing this concept.

6.3.2 Cyclic Fluctuations of Thrusts on Wall

In the centrifuge model tests, the cyclic fluctuation of the total thrust on the wall was influenced substantially by the inertia of the wall itself. The amounts of the thrusts from the wall inertia and from the soil backfill were comparable (see Figure 6.36). This very large wall inertia effect plays an important role in analyzing the thrust from the backfill.

During cyclic shaking, the wall rotated about its base due to its inertia. In these tests, the input accelerations were approximately sinusoidal excitations. When the input acceleration was negative, the model accelerated towards the backfill with respect to the wall. The inertia of the wall itself caused a cyclic rotation about its base during earthquake. Due to the cyclic rotation of the wall, the cyclic amplitude of the wall movement was larger at the top than at the base. The excess amplitude of the wall top movement is a result of the wall inertia.

The periodic rotation of the wall was also a major cause for the dynamic fluctuation of the backfill thrusts. The significance of the periodic wall rotation is revealed by investigating the phasing of various thrust fluctuations during earthquakes.

Based upon the analyses by Mononobe (1929) and Okabe (1926) for lateral earth pressures on the retaining walls, and Westergaard's (1933) analysis for water pressures during earthquakes, the maximum and minimum in the fluctuations of the thrust from the backfill soil are expected to be observed when the ground acceleration is at the negative and positive peaks, respectively. However, such expectations are not fulfilled in the analyses of the model test data. Table 6.3 summarizes the phase angles (with respect to the peak input acceleration towards the backfill) of the thrusts fluctuations and cyclic wall rotations in tests with no slip at the slider. These phase angles are obtained from the diagrams in Figures 6.12 through 21 and Figures 6.32 and 6.33. Note that there is uncertainty of at least 5 to 10 degrees in determining the phase lag for each test. More uncertainties are involved when there are two peaks near the maximums in some cases. Potential uncertainty in the average phase lags in the entries near the bottom of the Table 6.3 may be even larger.

Figure 6.34 presents a summary of the average phase lags relative to the peak inward input acceleration at base, as given in Table 6.3 It is possible to hypothesize two different explanations for thrusts on a retaining wall during earthquakes

1. Type I thrust ---- related to earth *inertia*

   This type of thrust is associated with the ground acceleration It is consistent with the Mononobe-Okabe's and Westergaard's approaches for dynamic thrusts from the soil skeleton and the pore fluid. The maximum thrust of this type occurs when the peak ground acceleration towards the backfill is reached

   It is interesting to compare the third and the tenth columns in Table 6.3. In weak earthquakes (peak acceleration less than 0.07g) the phase lags of the thrust from soil skeleton are consistent with the acceleration response of the soil skeleton. When the intensity of earthquake increases, the acceleration response of the soil skeleton lags more, and so does the thrust from the soil skeleton. However, the phase lags of the thrusts are generally less than those of the acceleration responses. This fact is consistent with the hypothesis associated with Figure 6.31 in the previous section. The acceleration response in the backfill probably tends to lag more near the surface, where A3 is measured, than at greater depth. Therefore, in Table 6.3, the phase lags in column [3] are somewhat larger than those in column [10].

2. Type II thrust -- related to the angular *velocity* of the wall rotation

   The periodic wall rotation produced a fluctuation in the earth thrust. Consider a cylinder filled with fluid and having a pervious boundary through which fluid can squeeze, as shown in Figure 6.35. One end of the cylinder there is a periodically moving piston. The fluid pressure at the loaded end is proportional to the velocity of the piston. The peak pressure in the fluid would occur when the piston is pushing the cylinder at the maximum velocity. Similar pressure change is expected

158

if the piston is hinged at base. Such a pressure change is similar to the pore pressure fluctuation in the backfill behind the periodic rotating retaining wall in the test model. The average phase lag of the inward angular velocity of the wall is about 150 degrees. This analogy apparently explains why the average phase lag of the pore pressure thrust fluctuation is 150 degrees.

The effect of cyclic wall rotation on the fluctuations of soil thrusts is also obvious in analyzing the magnitudes of the fluctuations, expressed by the extent of the double amplitudes of cyclic thrust variations. Table 6.4 lists the double amplitudes of cyclic fluctuations of the thrusts acting on the wall, in tests with no slippage at the slider. The double amplitude of the total earth thrust (including both pore pressure and skeleton thrusts) fluctuation is plotted in Figure 6.36 against the intensities of the input accelerations.

The double amplitude of the dynamic soil skeleton thrust can be estimated by the Mononobe-Okabe (M-O) equation with the simplified coefficient as proposed by Seed and Whitman (1970):

$$2\Delta P_p = \gamma_b w H^2 (\frac{3}{4} K_h) \tag{6.8}$$

with a height of the thrust acting at $0.5H$. The coefficient of horizontal acceleration (K_h) is the ratio of the input acceleration to the gravitational acceleration. The double amplitude of the dynamic pore pressure thrust due to inertia effect can be estimated using the Westergaard equation (Westergaard, 1933):

$$2\Delta U = 2 (\frac{7}{12} \gamma_w w H^2 K_h) \tag{6.9}$$

with a height of the thrust acting at $0.4H$.

159

Equations (6.8) and (6.9) are based upon an assumption of uniform horizontal acceleration throughout the sand stratum. The actual peak horizontal acceleration was, in effect, amplified along the vertical direction. The amplification ratio is assumed as

$$\eta = 1 + \alpha \frac{z}{H} \qquad (6.10)$$

where z is the distance above the base and α (= 2.5 K_h)[10] is a parameter that describes the amount of acceleration amplification, which is based on the amplification factor in Figure 4.9. The amplified acceleration not only increased the thrusts acting on the wall, but also raised the points of action on the wall. Consequently, the effects of acceleration amplification should be considered in calculating forces in the tie-back to balance dynamic mineral skeleton thrusts and hydrodynamic thrusts in this research. The force (in tie-back) corresponds to the dynamic skeleton thrust is [based upon the M-O equation in (6.8)]

$$2\Delta P_p = \frac{0.5H}{H_{tie-back}} \gamma_b wH^2 \left(\frac{3}{4}K_h\right) \bullet \left(1 + \frac{1}{2}\alpha\right) \qquad (6.11)$$

By modifing the Westergaard equation in (6.9) according to the amplified acceleration above the base, the hydrodynamic thrust is

$$\Delta U_\alpha \quad \left(\frac{7}{12}\gamma_w wH^2 K_h\right)\left(1 + \frac{2}{5}\alpha\right) \qquad (6.12)$$

where the subscript α indicates that the amplification of the ground acceleration is described by Eq. (6.10). The point of action associated with this thrust is obtained by integrating the moment along the wall from the pseudo-static water pressure. The thrust

---

[10] The amplification factor in Figure 4.9 is $\eta = 1 + \frac{H_{tie-back}}{H}\alpha$. For example, $\eta = 2.5$ at K_h = 0.4. This indicates that $\alpha = 2.5K_h$ in this study.

160

in Eq. (6.12) is acting on the wall at a height of $\left(1-\frac{\frac{3}{5}+\frac{6}{35}\alpha}{1+\frac{2}{5}\alpha}\right)H$ above the base. Therefore, the double amplitude of the dynamic force in the tie-back is

$$2\Delta P_{u_\alpha} = \frac{2}{H_{tie-back}}\left(\frac{7}{12}\gamma_w wH^2 K_h\right)\left(1+\frac{2}{5}\alpha\right)\bullet\left(1-\frac{\frac{3}{5}+\frac{6}{35}\alpha}{1+\frac{2}{5}\alpha}\right)H \qquad (6.13)$$

The total dynamic moment acting on the wall from the backfill soil is

$$\Delta M_{soil} = \Delta M_{\bar{p}} + \Delta M_u \qquad (6.14)$$

$$= \frac{1}{2}\gamma_b wH^2\left(\frac{3}{4}K_h\right)\left(1+\frac{1}{2}\alpha\right)\frac{H}{2} + \left(\frac{7}{12}\gamma_w wH^2 K_h\right)\left(1+\frac{2}{5}\alpha\right)\left(1-\frac{\frac{3}{5}+\frac{6}{35}\alpha}{1+\frac{2}{5}\alpha}\right)H$$

If there is no amplification of ground acceleration in the backfill ($\eta = 1$ and $\alpha = 0$), then Eq. (6.14) is reduced into

$$\Delta M_{soil} = \frac{1}{2}\gamma_b wH^2\left(\frac{3}{4}K_h\right)\frac{H}{2} + \left(\frac{7}{12}\gamma_w wH^2 K_h\right)(0.4H) \qquad (6.15)$$

The double amplitude total earth thrust fluctuation at the tie-back is estimated as

$$2\Delta P_{earth} = 2\Delta P_{\bar{p}} + 2\Delta P_u \qquad (6.16)$$

The estimation is also plotted in Figure 6.36. The curve is non-linear because the amplification of acceleration increases with k_h.

Figure 6.36 indicates that the estimations of total dynamic earth thrust with the Mononobe-Okabe-Westergaard equation, Eq. (6.16), are close to observations. However, neither (6.11) nor (6.13) is applicable to predict the dynamic mineral skeleton thrusts or the hydrodynamic thrusts. Figure 6.37 shows both the observations and estimations for these thrusts.

The reason that Eq. (6.16) works for dynamic amplitudes of total earth thrust is because it gives results similar to using Mononobe-Okabe equation with γ_t, the total unit weight of soil (shown by a dashed line[11] in Figure 6.36); that is, the water is accelerating more or less with the mineral skeleton.

The reason that Eqs. (6.11) and (6.13) do not work is due to the interaction between the pore fluid and the mineral skeleton. Because the soil was so permeable, the pore fluid was pushed through the soil as the wall moved. The interaction between the pore fluid and the mineral skeleton caused an effect for skeleton thrust different from the M-O effect, and hence cause the observed skeleton thrusts to differ from the estimations with the M-O equation -- (6.11). On the other hand, the rate of flow is related to the wall movement, the largest pressure (so as to give largest gradient) occurs when the velocity of the pushing by the wall is largest. The magnitude of the hydrodynamic pressure is influenced by the velocity of the wall movement and hence differs from the estimation with the Westergaard equation -- (6.12).

6.3.3 Summary

The general observations obtained from the analyses of the decomposed thrusts acting on the wall are summarized as follows.

A. Variation of Average Transient Thrust

---

[11] This line is obtained as $2\Delta P_P = \dfrac{0.5H}{H_{tic-back}} \gamma_t wH^2 \left(\dfrac{3}{4}k_h\right) \bullet \left(1 + \dfrac{1}{2}\alpha\right)$. That is, the amplification of acceleration is considered.

162

1. The trends of change in the average transient soil skeleton thrust and the average transient pore pressure thrust during earthquakes generally agree with the expectations The pore pressure thrust increased during shaking and then decreased after shaking as a result of consolidation. The thrust from the soil skeleton decreased during shaking and then recovered afterwards.

2. The amount of change in these thrusts increased with the intensity of shaking

3. The amount of decrease in the soil skeleton thrust during shaking increased faster than linearly with the earthquake intensity.

4. The residual earth thrust after earthquake was larger than the initial thrust The incremental earth thrusts were generally proportional to the earthquake intensity

B. *Cyclic Fluctuations of the Thrusts*

5. The magnitude of the inertial loading on the wall in these tests is comparable with the total dynamic earth thrust.

6. The cyclic fluctuation of the pore pressure thrust is heavily influenced by the periodic rotation of the wall

7. The Mononobe-Okabe and Westergaard equations are not applicable for estimating, separately, the magnitudes of the fluctuations of the thrust due to the soil skeleton and pore fluid in this test program However, the total earth thrust fluctuations are reasonably estimated by Eq. (6.13), an equation combining both the Mononobe-Okabe equation and the Westergaard equation.

163

Table 6.1: Presence of "Double Cycling" of excess pore pressure fluctuation in all tests

Test No	Peak inp. Acc. (g)	P1	P2	P3	P4	P5	P6
Tests with no slippage at slider							
2a	0.05	-					
4b	0.06	-					
1a	0.06			-		X	X
3a	0.085	-				X	X
5b	0.09	-				X	X
2b	0.1	-				X	X
1b	0.115			-	X	X	X
4c	0.12	-				X	X
6b	0.13	-				X	X
2c	0.135	-		X	X	X	X
Tests with slippage at slider							
2d	0.2	-	X	X	X	X	X
3b	0.22	-	X	X	X	X	X
4a	0.25	-		X	X	X	X
1c	0.25		X	-	X	X	X
6a	0.25	-	-	X	X	X	X
2e	0.28	-	X	X	X	X	X
5a	0.35	-	X	X	X	X	X
2f	0.36	-	X	X	X	X	X

Note: " - " means the pressure transducer data are not recorded or a failed record.

Table 6.2 : Force in Tie-Back due to Total Thrust and Thrusts from Pore Pressure and Soil Skeleton at initial, end of shaking and residual states ---- in Tests where slippage did not occure

Test No.	Peak Base Acc. (g)	initial	Total Thrust (N) @ E.O.S.		Residual			initial	Thrust from Pore Pressure (N) @ E.O.S.		Residual			initial	Thrust from Soil Skeleton (N) @ E.O.S.		Residual		
			@ EOS	Inc. fr. initial	@ resid.	Increase from EOS	initial		@ EOS	Inc. fr. initial	@ resid.	Increase from EOS	initial		@ EOS	Inc. fr. initial	@ resid.	Increase from EOS	initial
[1]	[2]	[3]	[4]	[5]	[6]	[7]	[8]	[9]	[10]	[11]	[12]	[13]	[14]	[15]	[16]	[17]	[18]	[19]	[20]
2a	0.05	399	411	12	408	-3	9	214	236	22	214	-22	0	185	175	-10	194	19	9
1a	0.06	313	350	37	336	-14	23	215	265	50	215	-50	0	98	85	-13	121	36	23
4b	0.06	410	430	20	423	-7	13	215	235	20	215	-20	0	195	195	0	208	13	13
3a	0.085	441	544	103	475	-69	34	214	360	146	214	-146	0	227	184	-43	261	77	34
5b	0.09	408	476	68	444	-32	36	215	300	85	215	-85	0	193	176	-17	229	53	36
2b	0.1	408	495	87	440	-55	32	217	330	113	217	-113	0	191	165	-26	223	58	32
1b*	0.115	336	405	69	342	-63	6	211	345	134	211	-134	0	125	60	-65	131	71	6
4c	0.12	423	490	67	450	-40	27	213	333	120	213	-120	0	210	157	-53	237	80	27
6b	0.13	384	489	105	440	-49	56	214	339	125	214	-125	0	170	150	-20	226	76	56
2c	0.135	440	515	75	446	-69	6	216	361	145	216	-145	0	224	154	-70	230	76	6

* Slippage took place after 6 cycles of earthquake

Table 6.3: Phase Angle between cyclic thrust fluctuations and inward input accelerations

| Test No. [1] | Peak Input Acceleration (g) [2] | Phase Angles (in degrees) | | | | | | | |
		Acc. resp. in backfill (ACC3) [3]	Hor. Acc @ top of wall (ACC6) [4]	Rotation of wall (from) Rotational Acc. (A6-A1) [5]	Total Thrust [6]	Wall Inertia [7]	Thrust from Total soil Backfill [8]	Pore Pressure [9]	Soil Skeleton [10]
2a	0.05	45	43	45	45	40	100	-	-
1a	0.06	40	53	55	50	28	120	160	40
4b	0.06	45	25	25	40	30	110	-	45
3a	0.085	75	55	55	55	40	90	200	60
5b	0.09	85	45	50	60	30	120	170	60
2b	0.1	95	52	55	60	30	90	140	65
1b	0.115	90	65	65	60	30	90	120	90
4c	0.12	72	25	30	60	50	100	120	90
6b	0.13	125	50	50	60	40	90	155	110
2c	0.135	100	53	55	60	40	90	140	60
Average		77	52	54	55	36	100	151	69

Note: 1. Phase lags of thrusts are relative to INWARD input acceleration.
2. The outward acceleration is positive, and the inward acceleration is negative.
3. Phase lags of rotatinal accelerations in Tests 4b and 4c are stricken due to the small amounts of rotation

166

Table 6.4: Summary of Double Amplitude of Cyclic Fluctuations of All Thrusts on Wall in Tests with no Slippage at Slider

Test No. [1]	Peak Inp. Accel. (g) [2]	Total Thrust (N) [3]	Thrust from wall inertia (N) [4]	Total Earth Thrust (N) [5]	Pore Pressure Thrust (N) [6]	Soil Skeleton Thrust (N) [7]
2a	0.05	87	51	59		59
1a	0.06	92	73	60	15	75
4b	0.06	79	57	42		42
3a	0.085	166	103	118	37	155
5b	0.09	156	74	103	58	142
2b	0.1	217	153	120	37	156
1b	0.115	295	161	184		180
4c	0.12	305	156	168	67	124
6b	0.13	268	178	160	47	113
2c	0.135	294	186	235	55	260

167
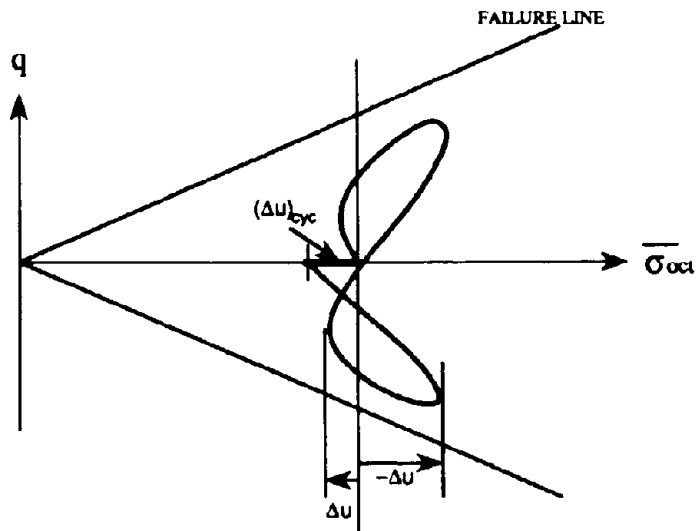
(a) Stress path at low to moderate shear stress
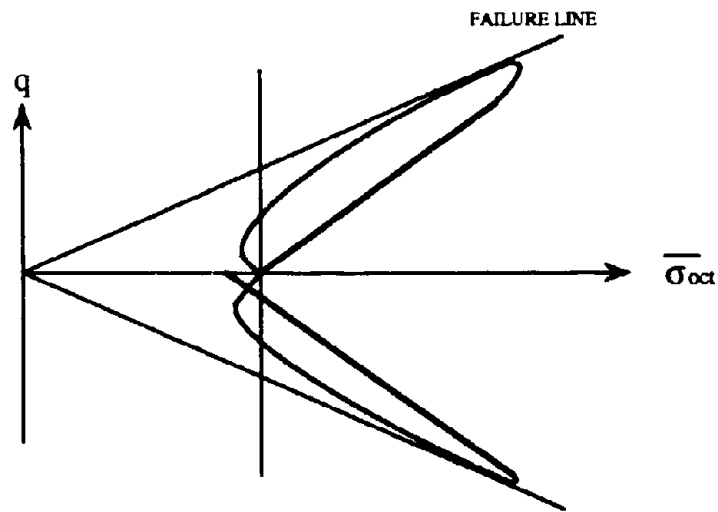
(b) Stress path at high shear stress

Figure 6.1: Typical Effective Stress Path of Sand During Undrained Cyclic Loading
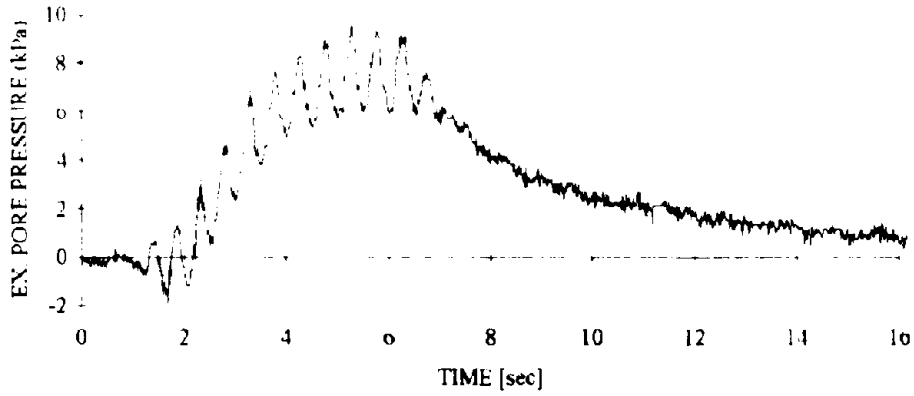
Figure 6.2: Excess Pore Pressure Record of P2 in Test 1a
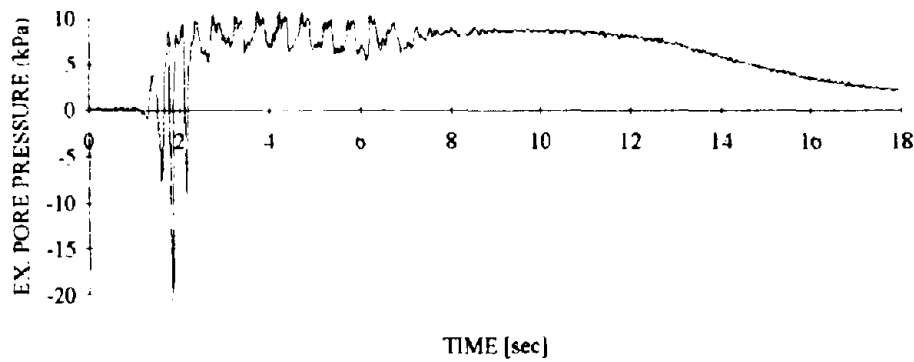
Figure 6.3: Excess Pore Pressure Record of P5 in Test 5a
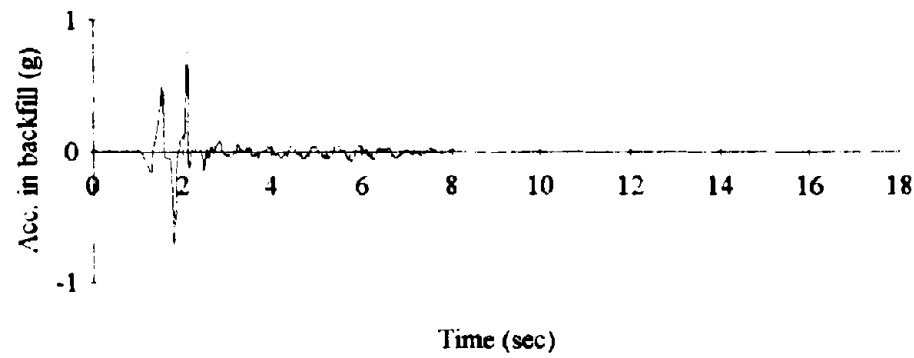
Figure 6.4   Acceleration Response in Backfill in Test 5a
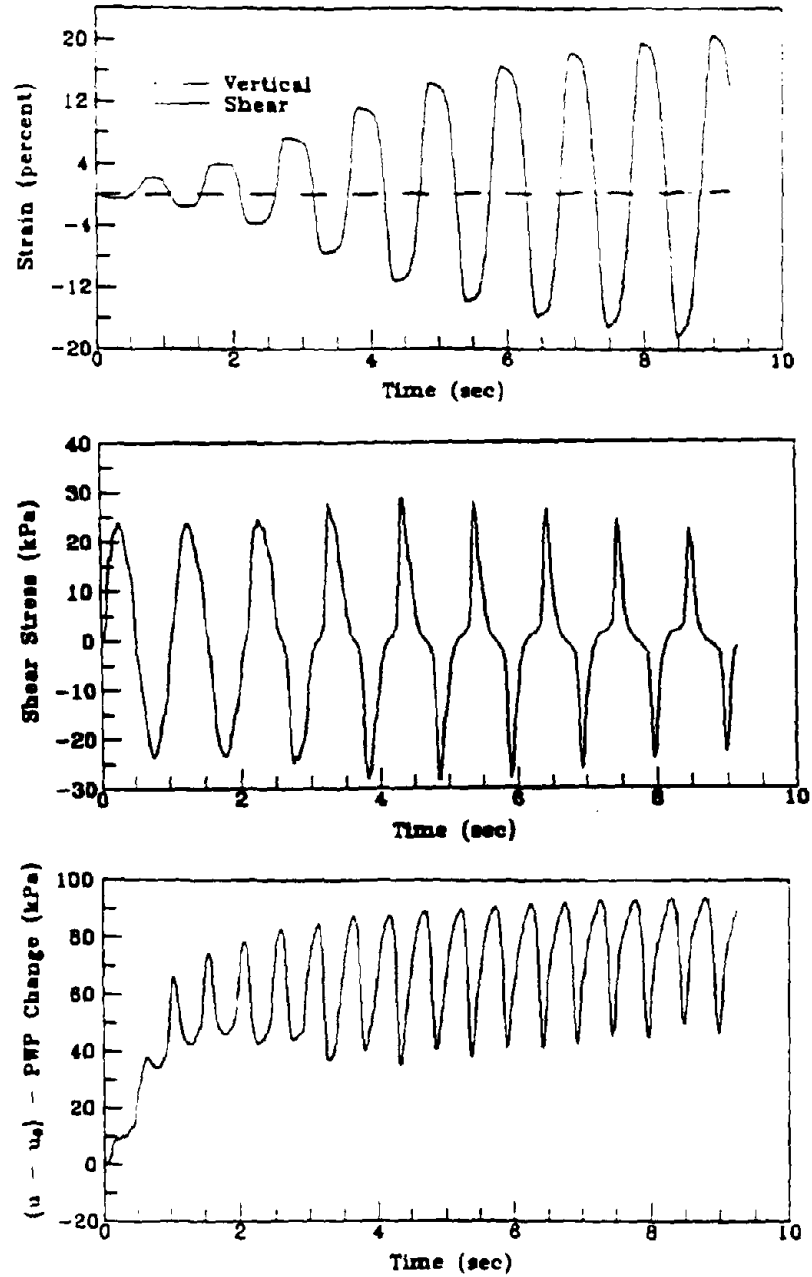
Figure 6.5: Results of Cyclic Simple Shear Test on Nevada Sand (Test No. 60-04)
(Reproduced from The Earth Technology Report)

170
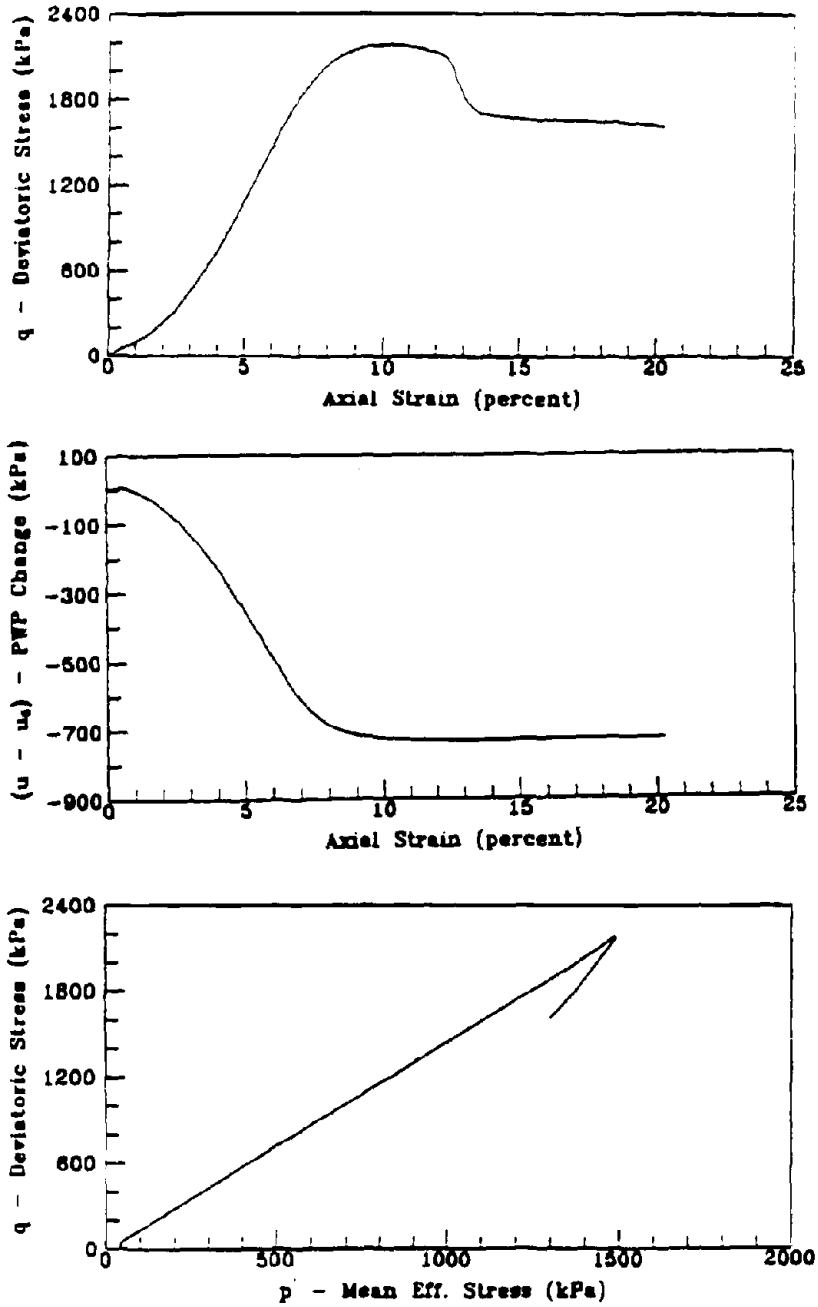
Figure 6.6: Results of CIUC Test on Nevada Sand (Test No. 60-12)
(Reproduced from The Earth Technology Report)
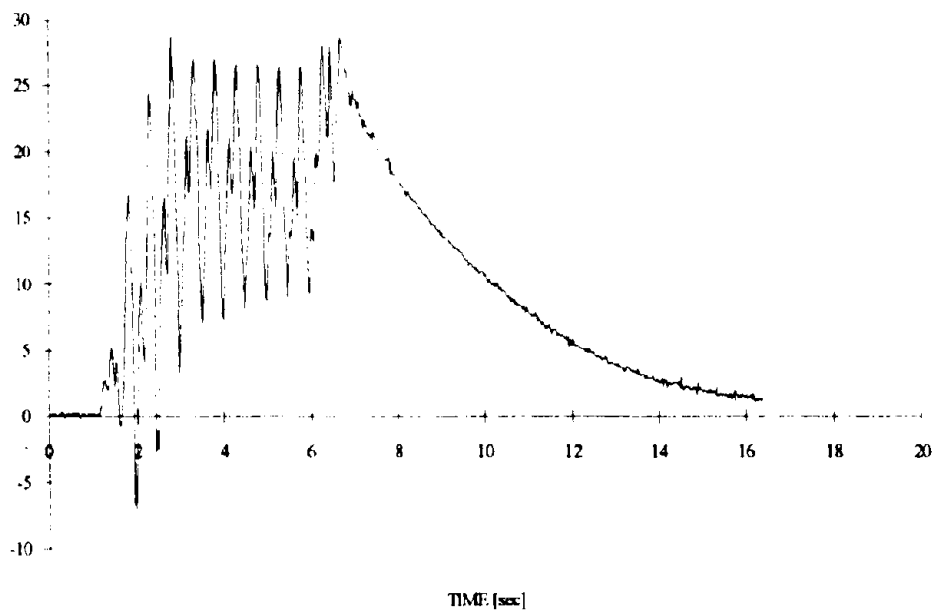
Figure 6.7   Excess Pore Pressure Record of P4 in Test 2d

Figure 6.8: A simplified configuration of the testing model
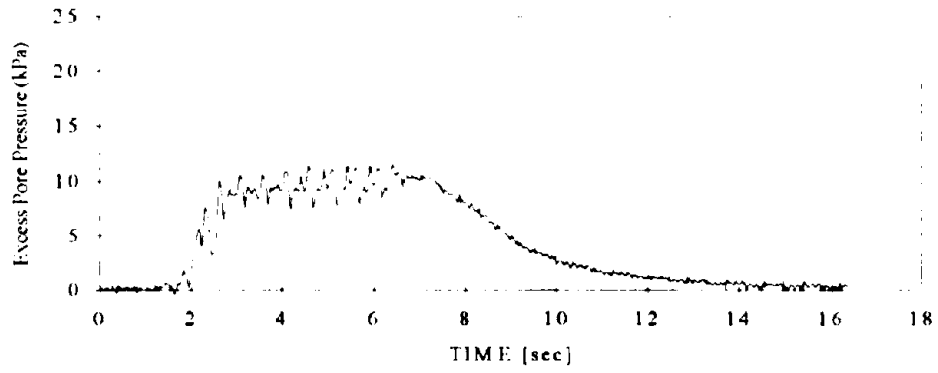
(a) Excess pore pressure at P6
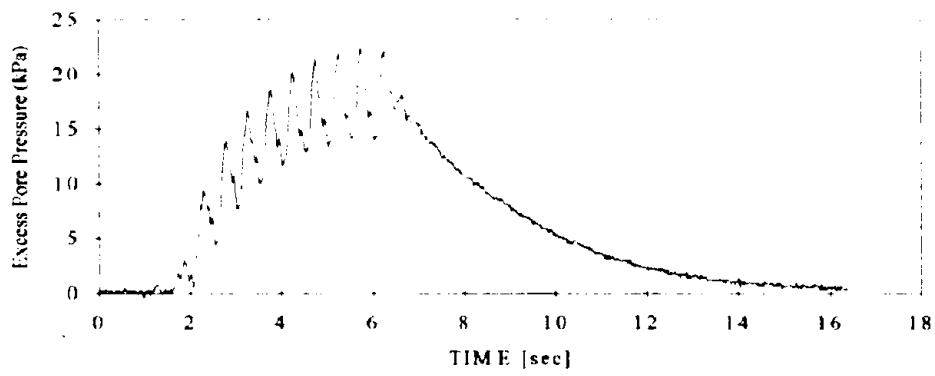
(b) Excess pore pressure at P4
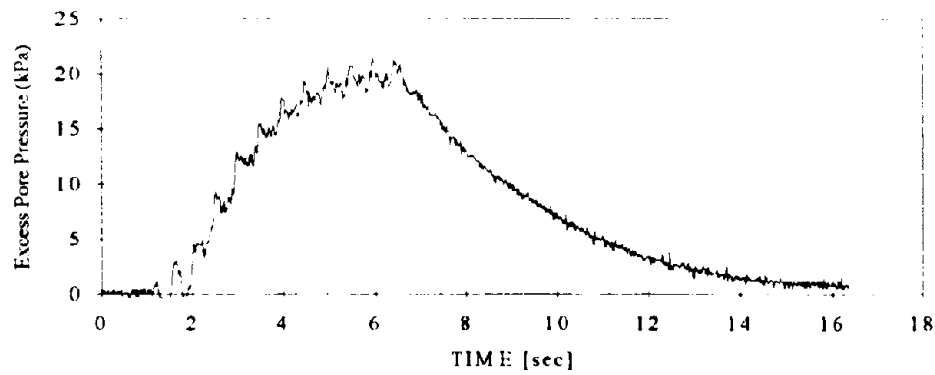
(c) Excess pore pressure at P2

Figure 6.9   Excess Pore Pressure of PPT2, PPT4 and PPT6 in Test 2b
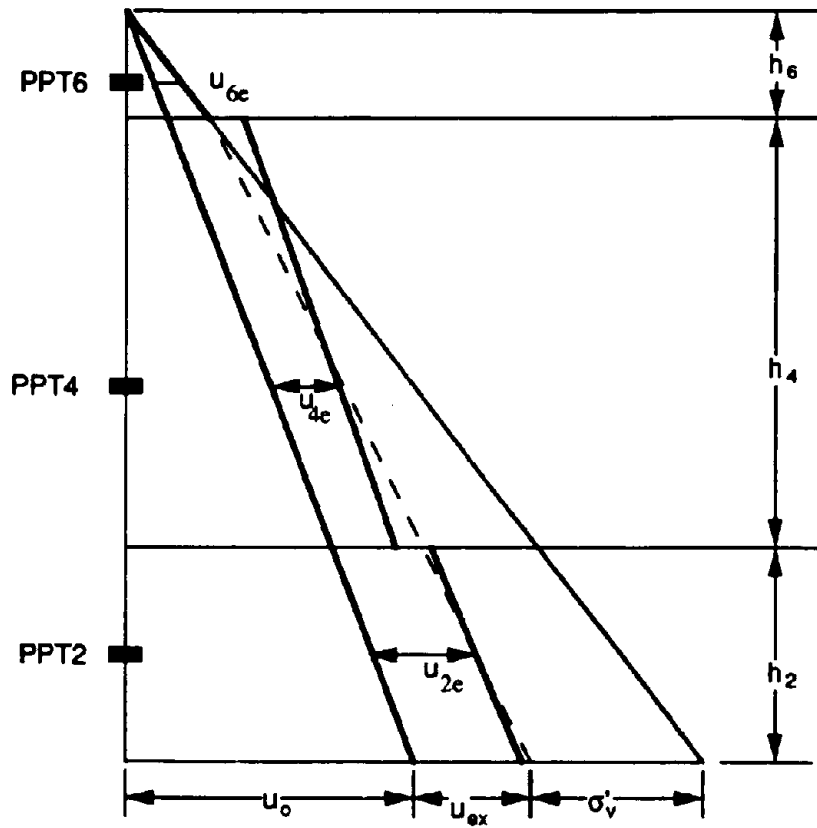
Figure 6.10: Schematic pore pressure distribution during centrifuge test
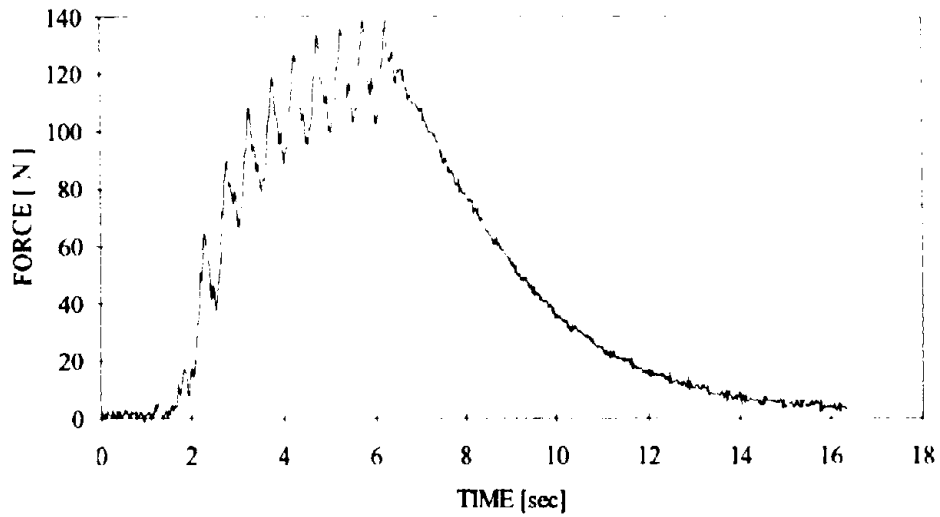
(a) $h_2 = 2m$, $h_4 = 3.5m$ and $h_6 = 1.5m$
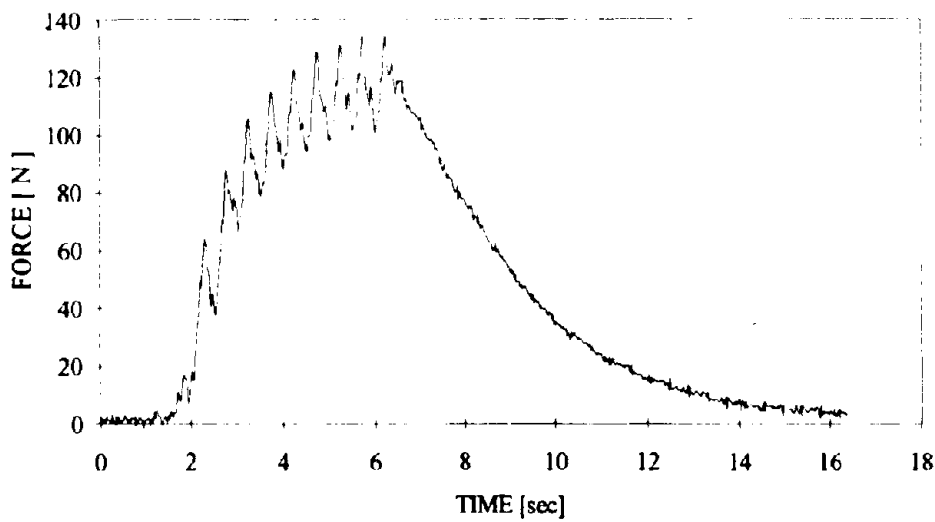
(b) $h_2 = 2m$, $h_4 = 3.25m$ and $h_6 = 1.75m$

Figure 6.11: Pore pressrue thrust calculated from P2, P4 and P6 in Test 2b

Time (sec)
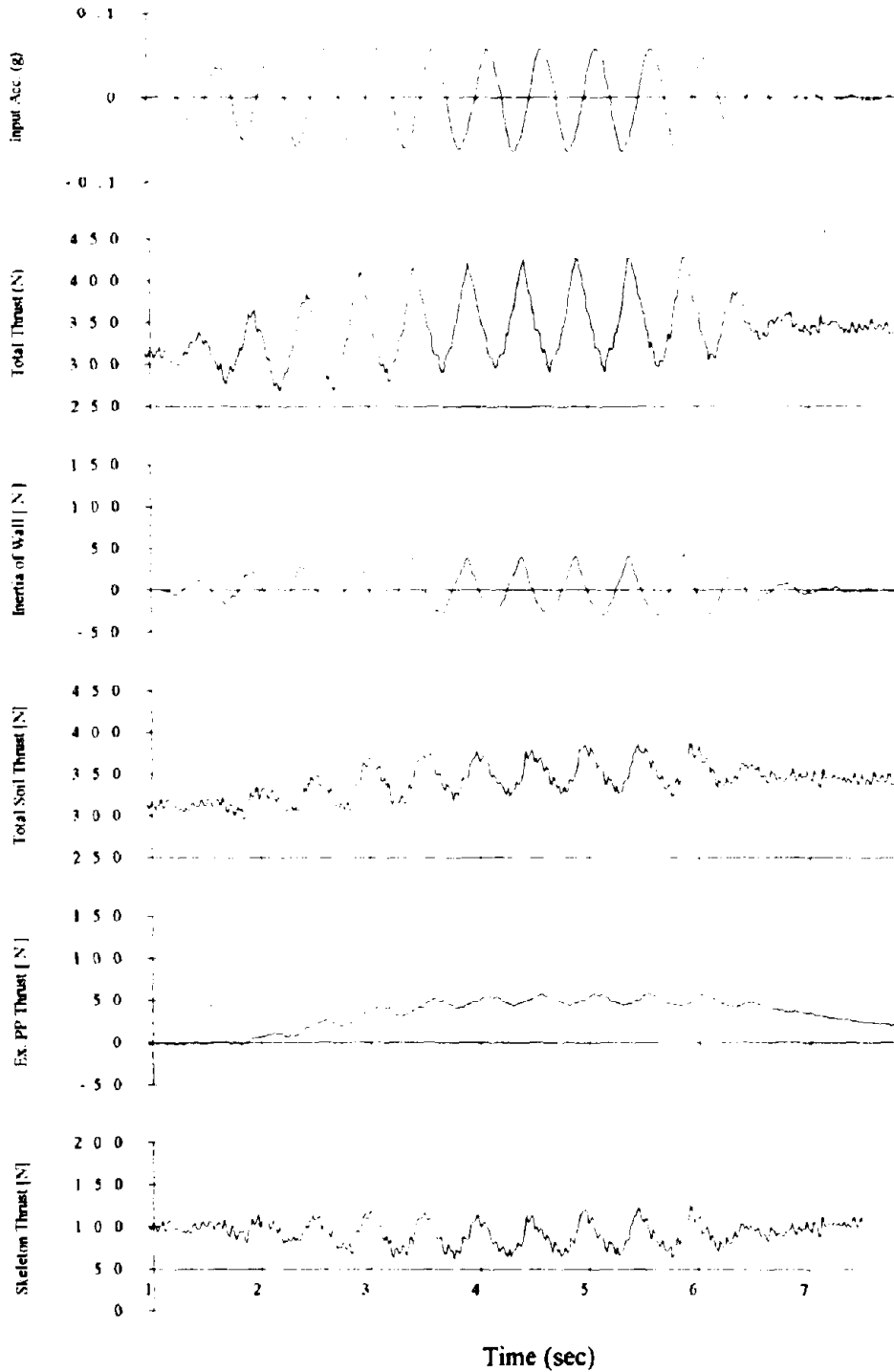
Figure 6.12: Earth Thrusts and Thrust from Wall Inertia in Test 1a

177
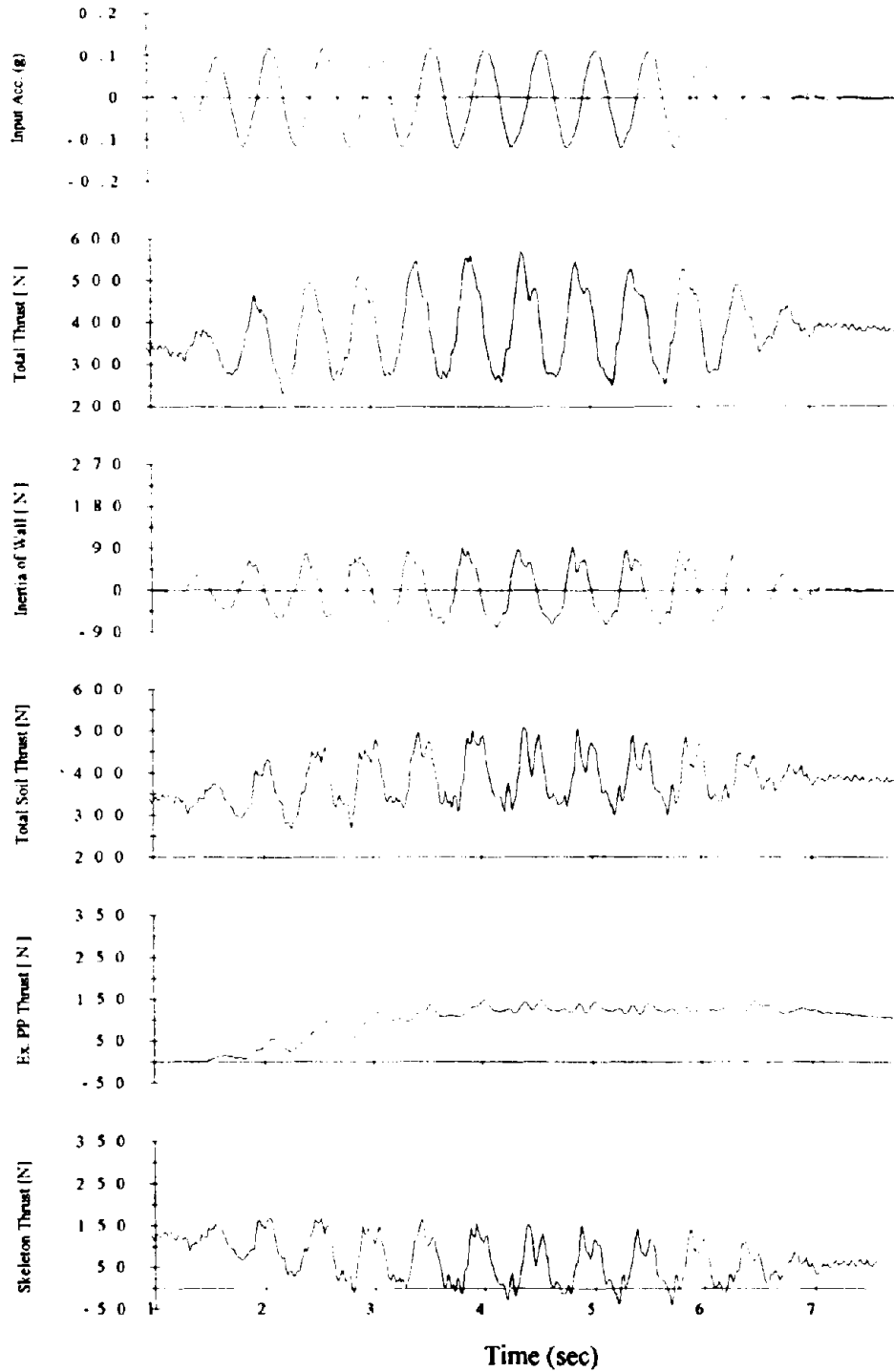
Figure 6.13: Earth Thrusts and Thrust from Wall Inertia in Test 1b

Time (sec)
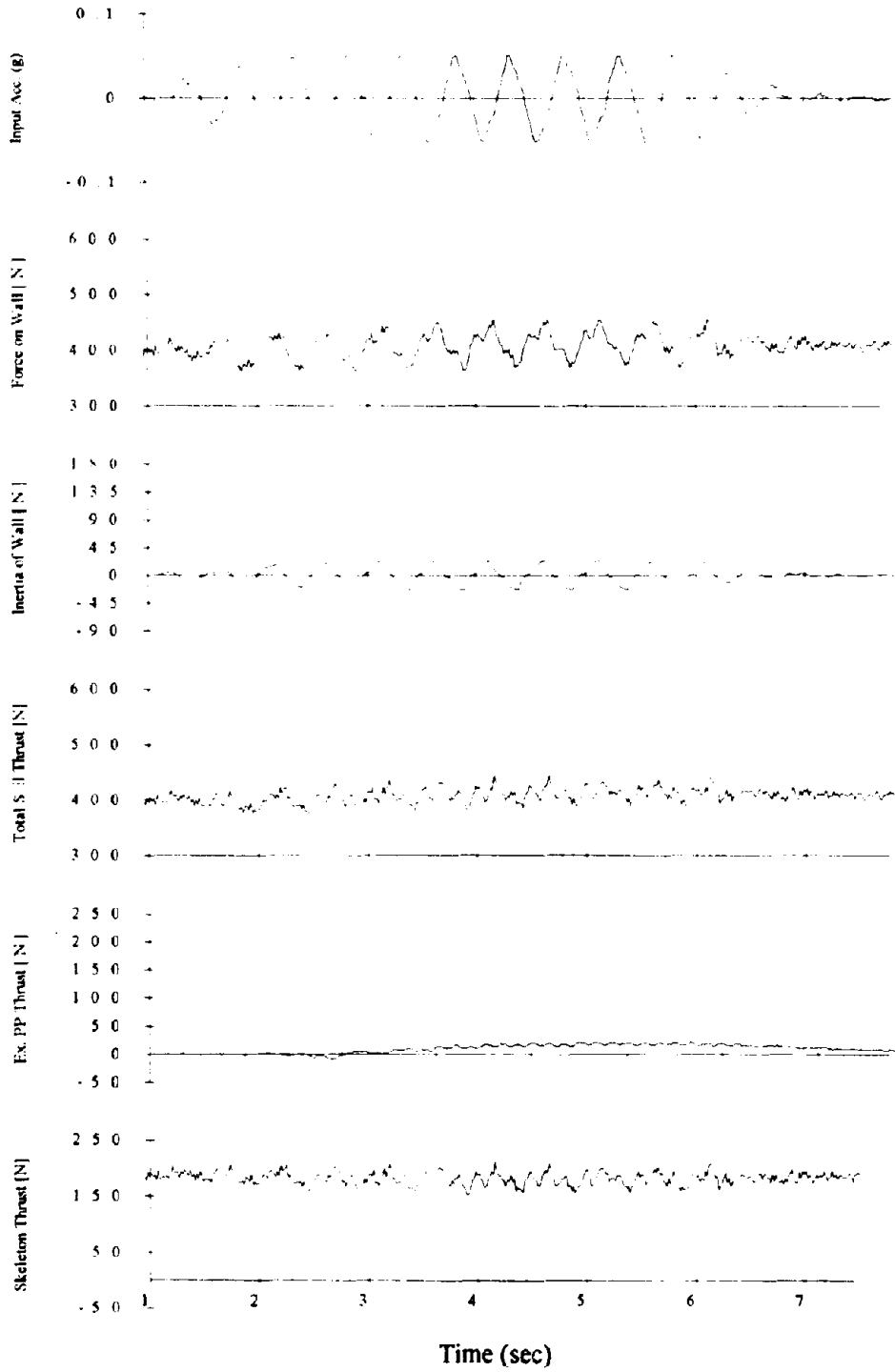
Figure 6.14: Earth Thrusts and Thrust from Wall Inertia in Test 2a

179
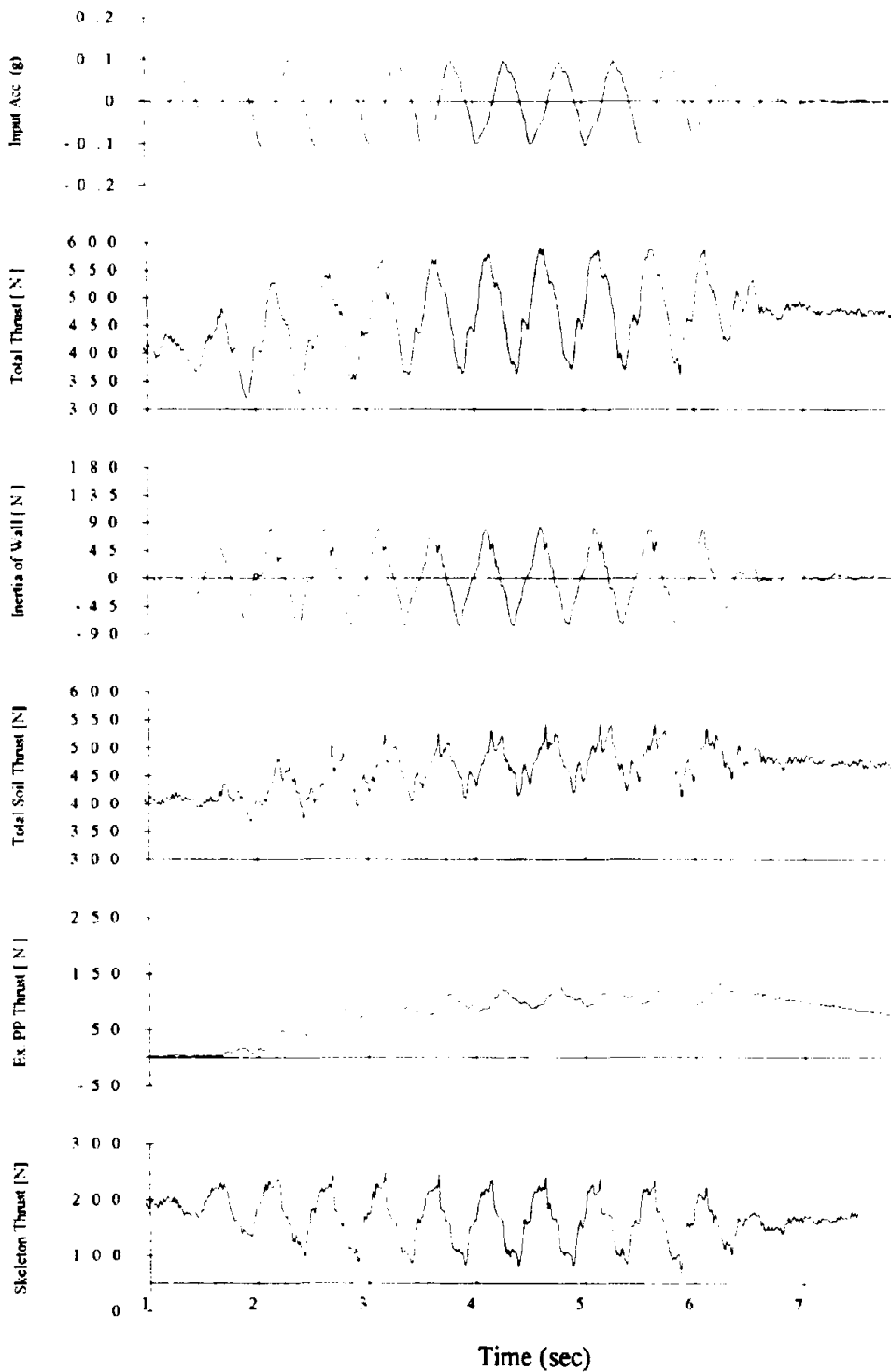
Figure 6.15: Earth Thrusts and Thrust from Wall Inertia in Test 2b

180

Time (sec)
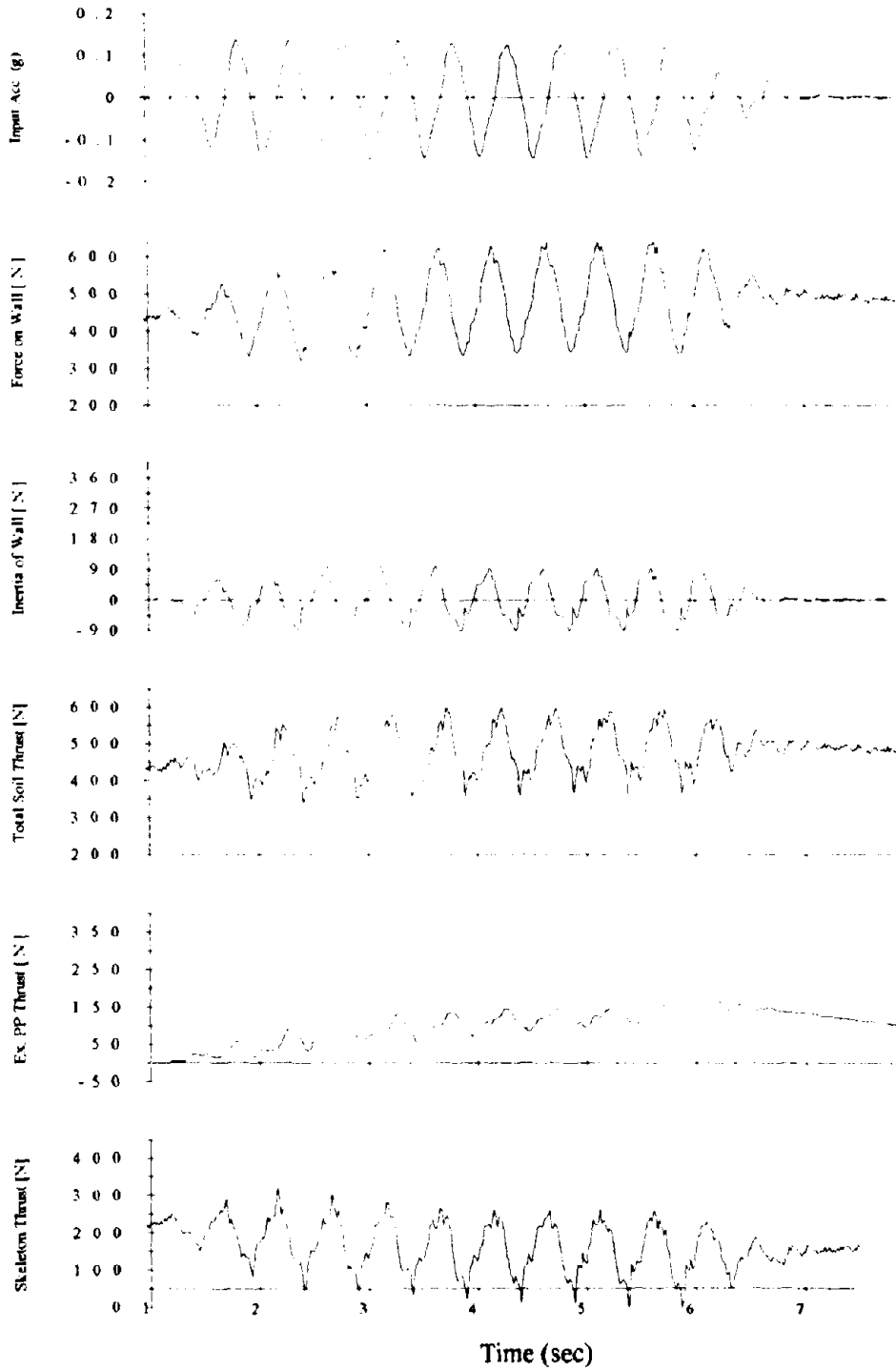
Figure 6.16: Earth Thrusts and Thrust from Wall Inertia in Test 2c

181

Time (sec)
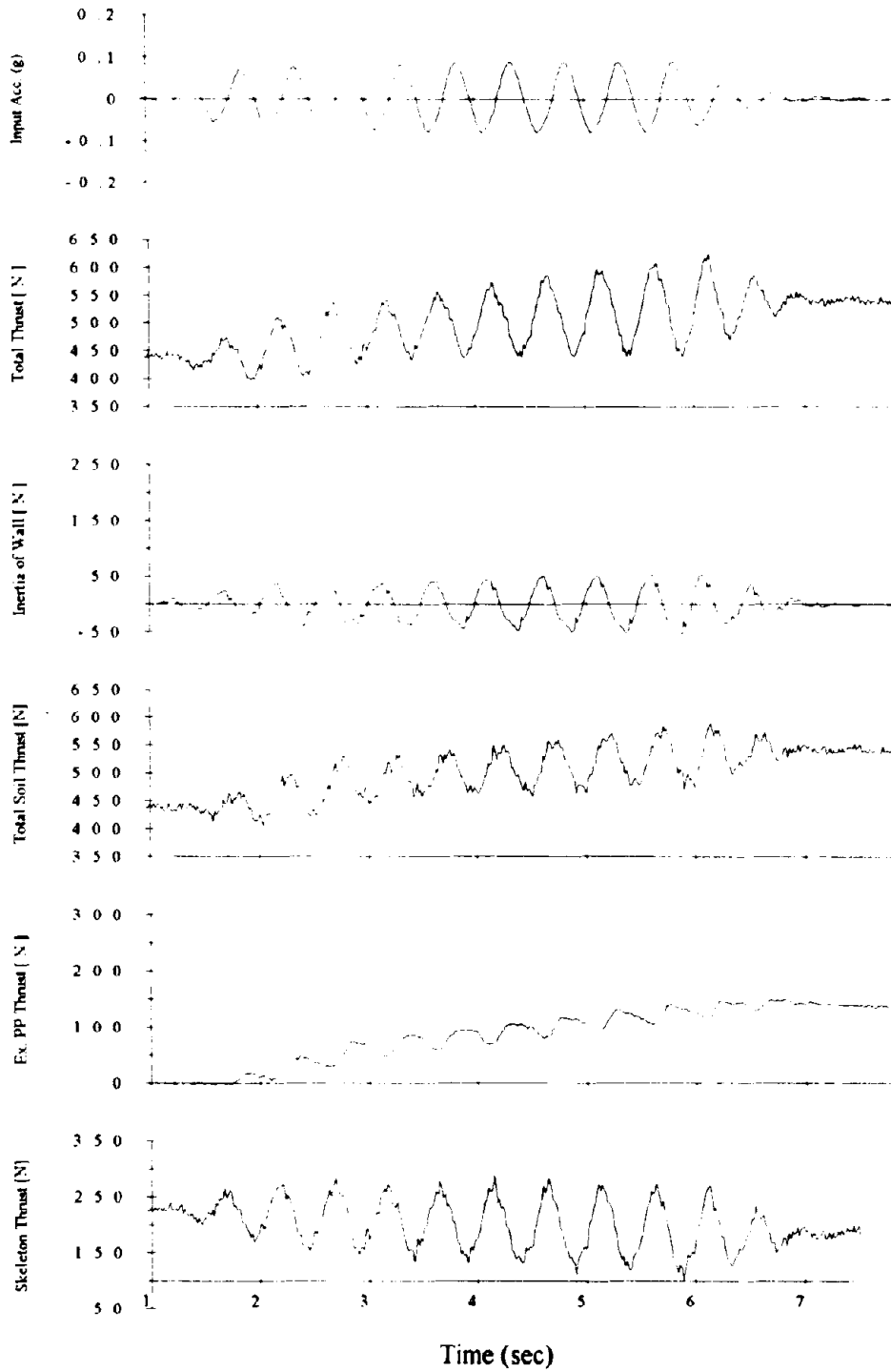
Figure 6.17: Earth Thrusts and Thrust from Wall Inertia in Test 3a
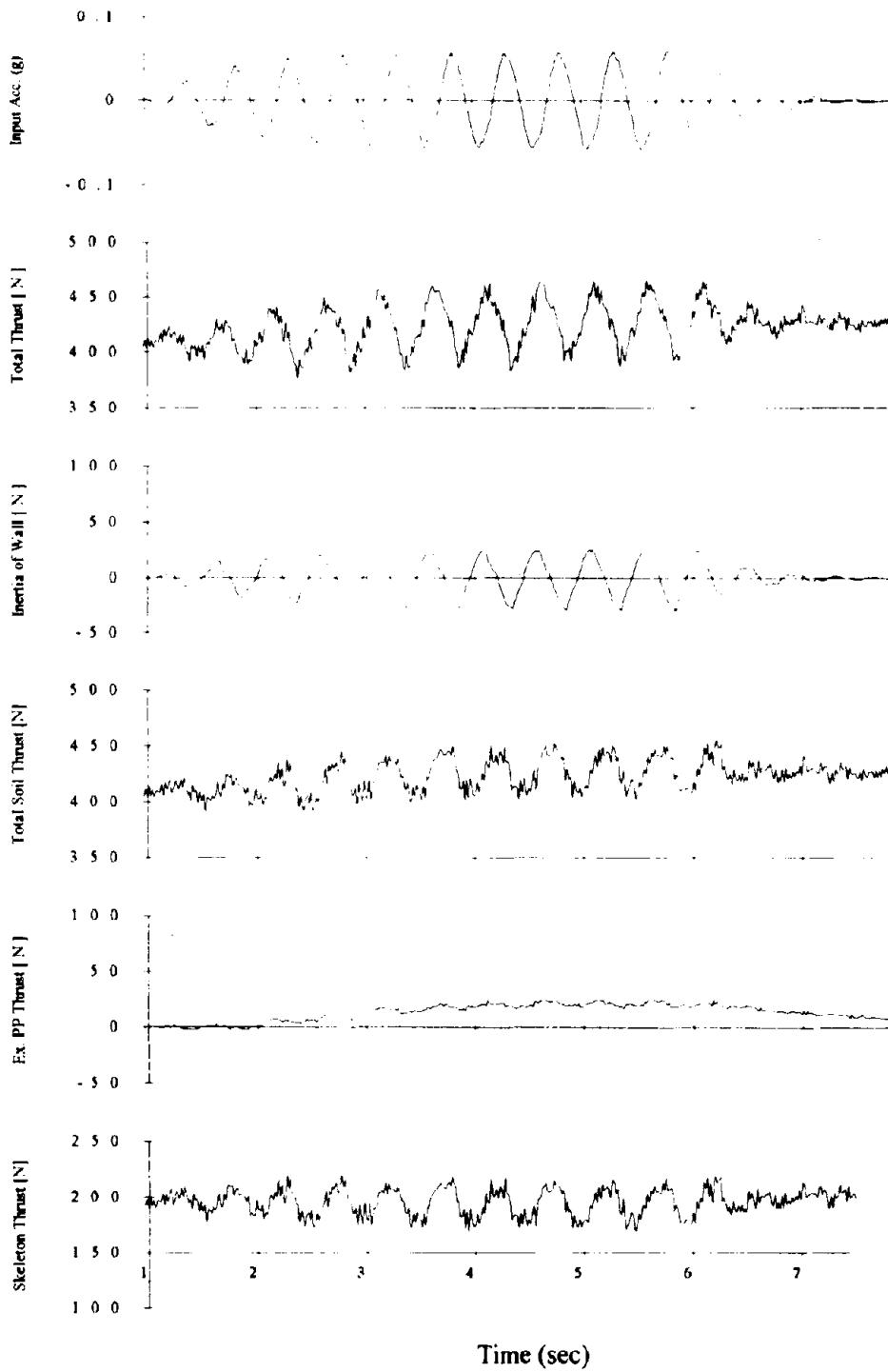
Figure 6.18: Earth Thrusts and Thrust from Wall Inertia in Test 4b

Time (sec)
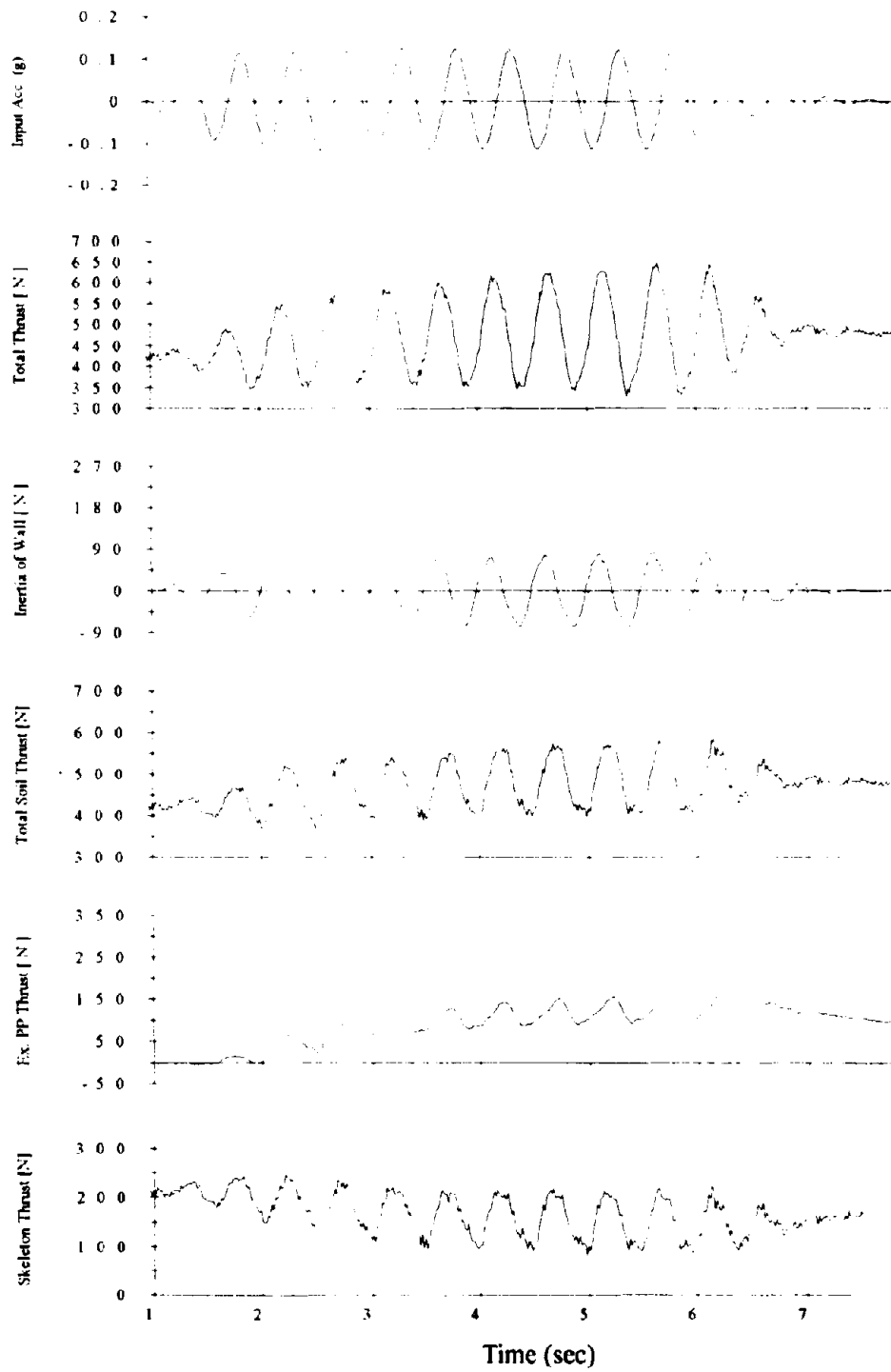
Figure 6.19: Earth Thrusts and Thrust from Wall Inertia in Test 4c
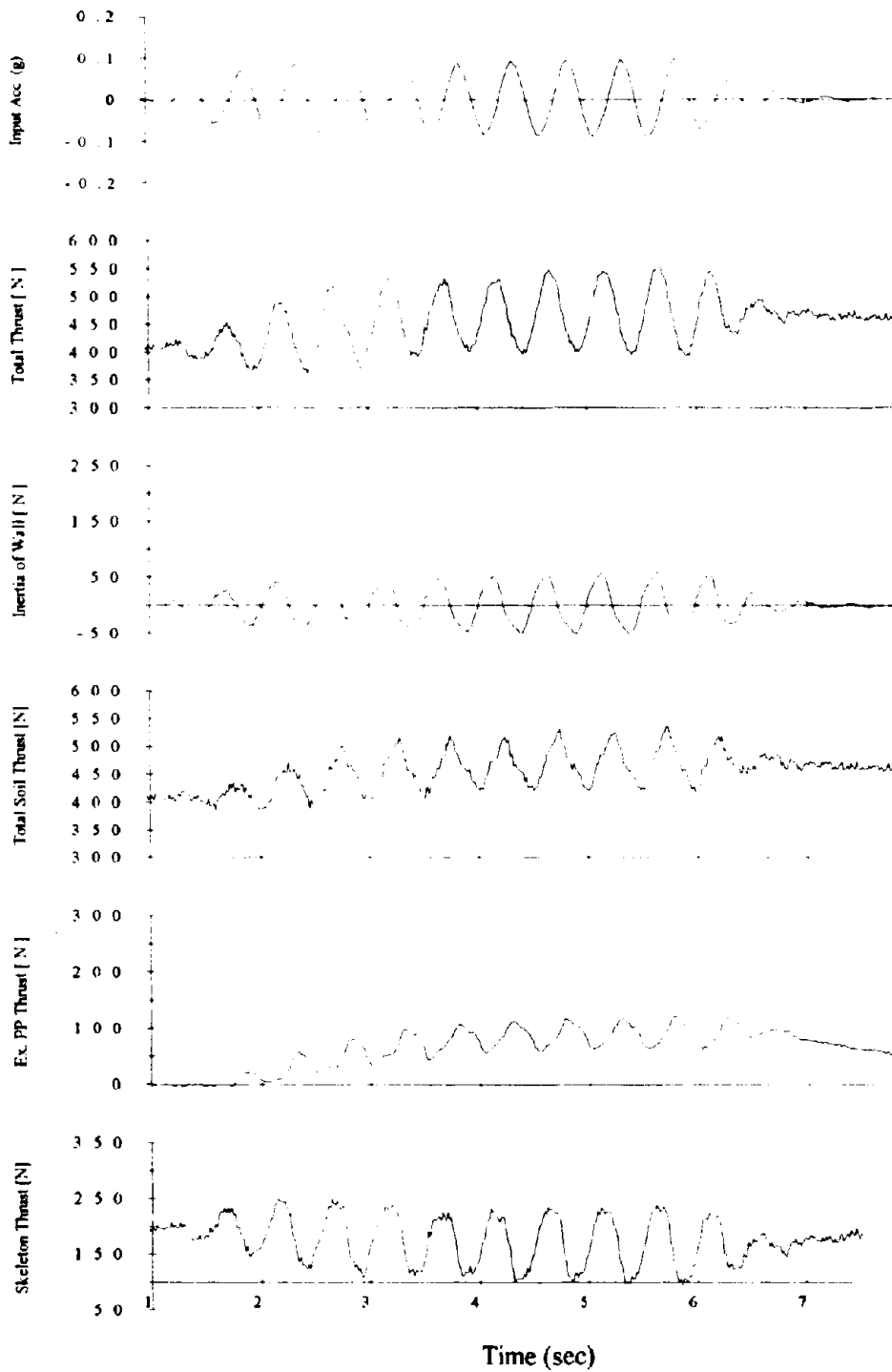
Figure 6.20: Earth Thrusts and Thrust from Wall Inertia in Test 5b
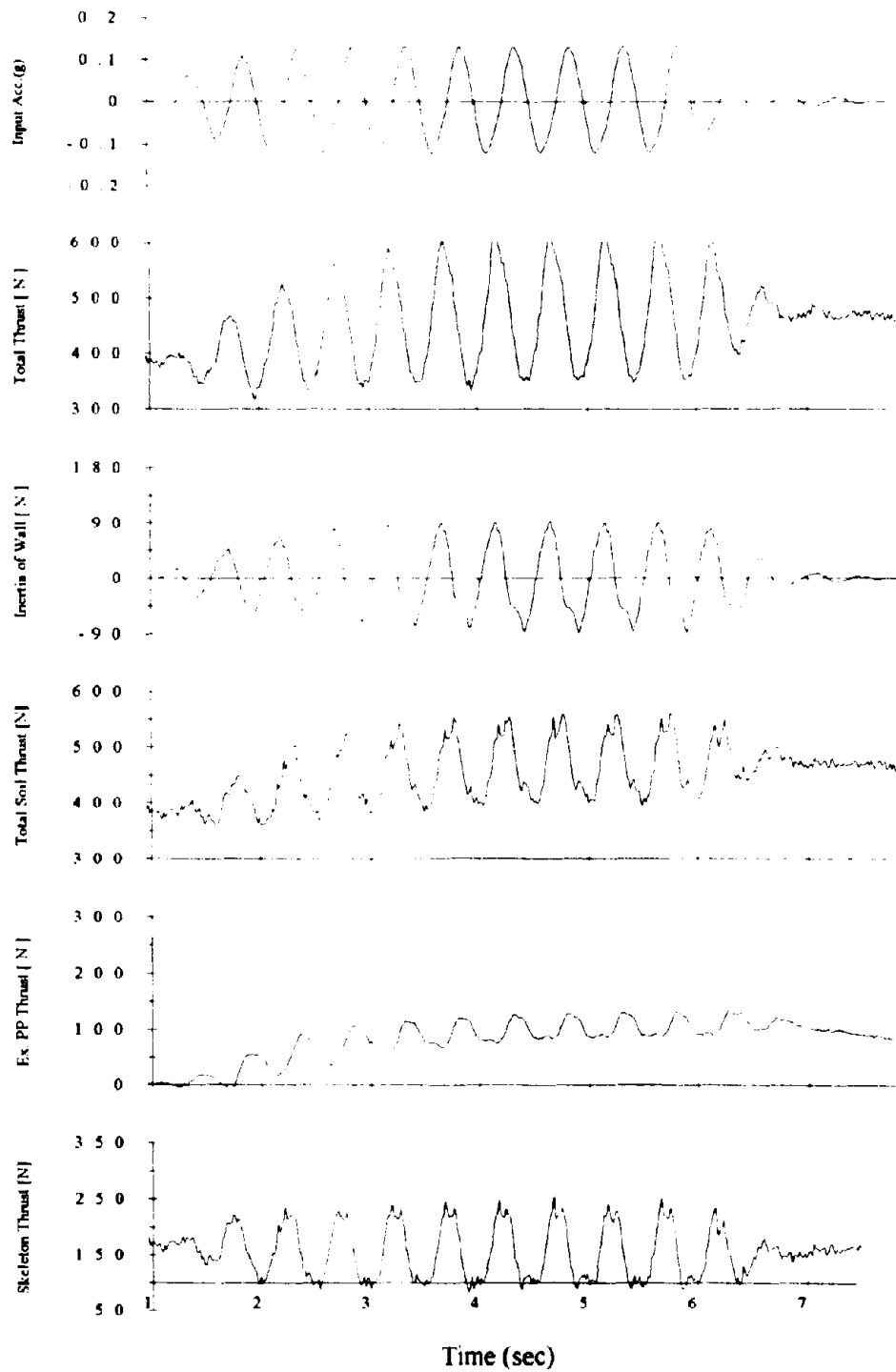
Figure 6.21: Earth Thrusts and Thrust from Wall Inertia in Test 6b

186
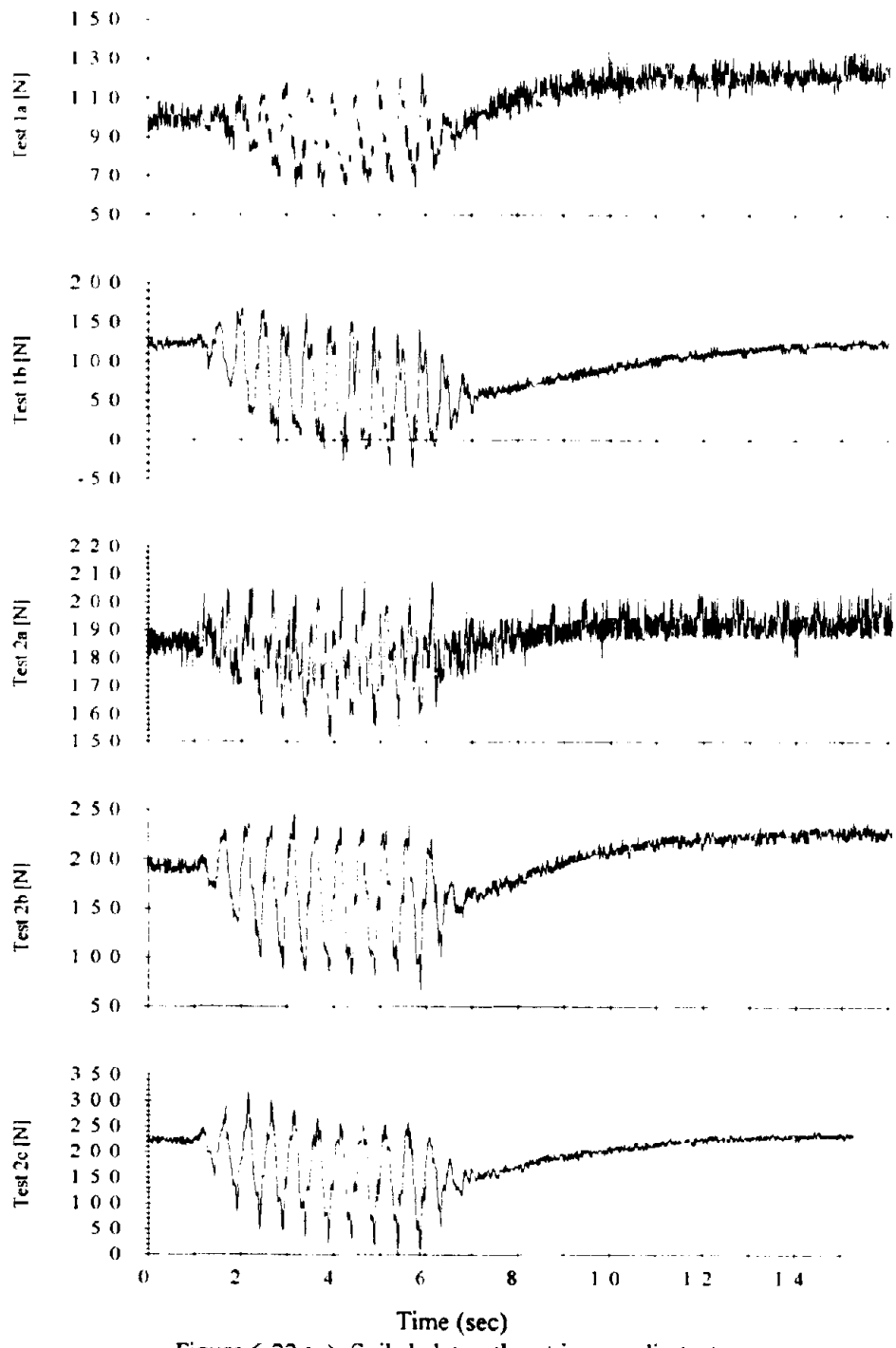
Figure 6.22 (a): Soil skeleton thrust in non-slip tests

187
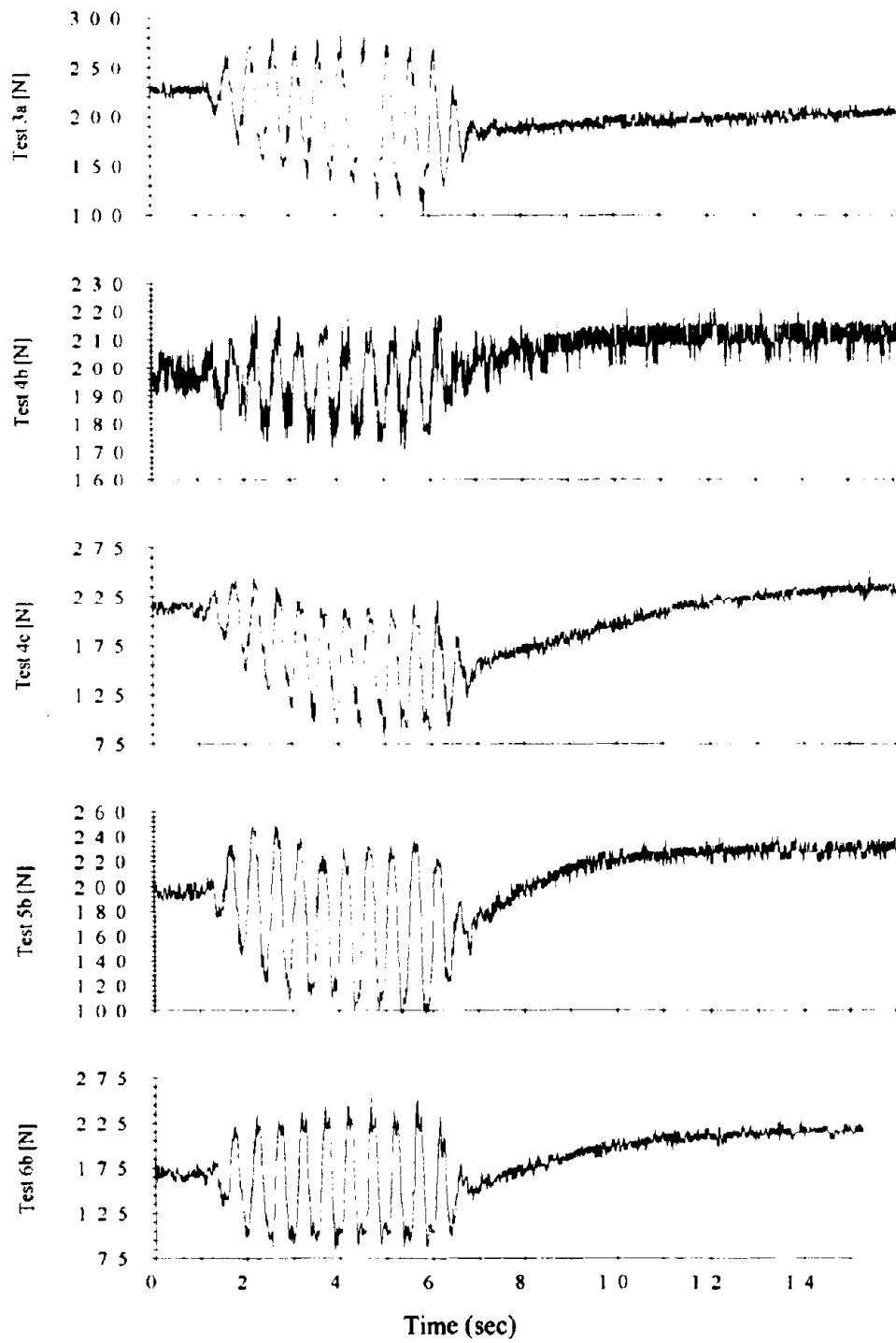
Figure 6.22 (b): Soil skeleton thrust in non-slip tests
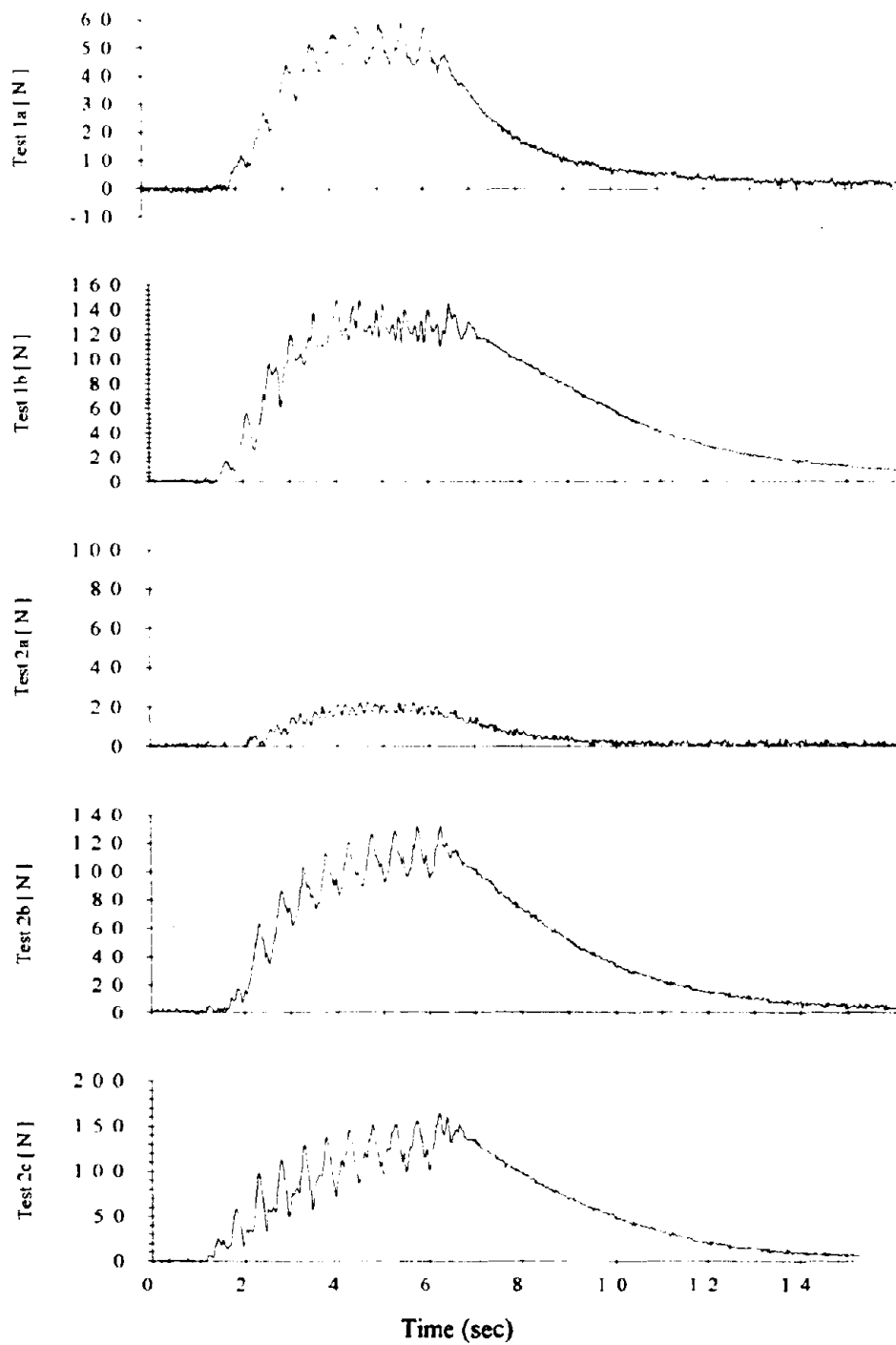
Figure 6.23 (a): Pore pressure thrust in non-slip tests
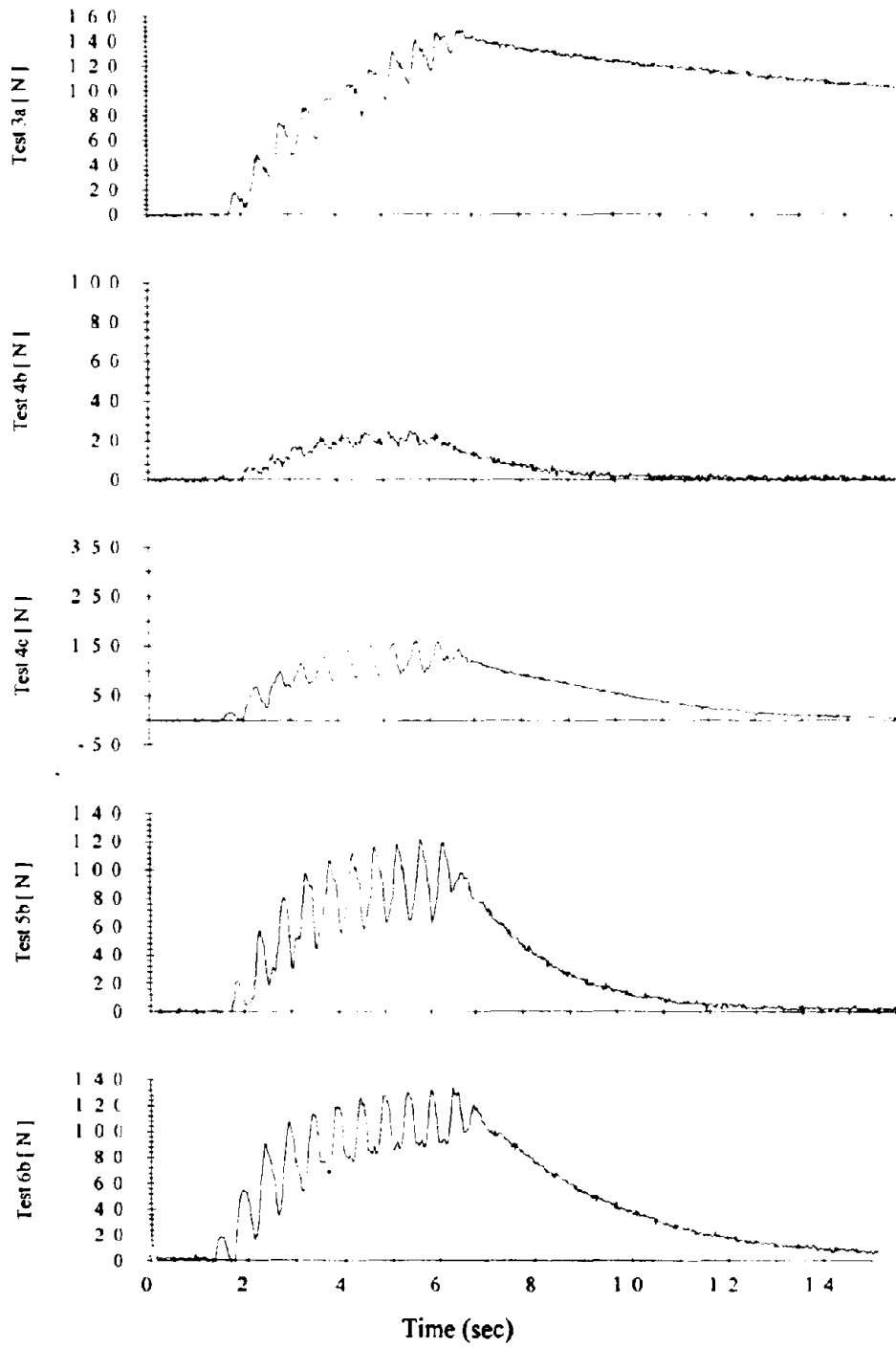
Figure 6.23 (b): Pore pressure thrust in non-slip tests

190
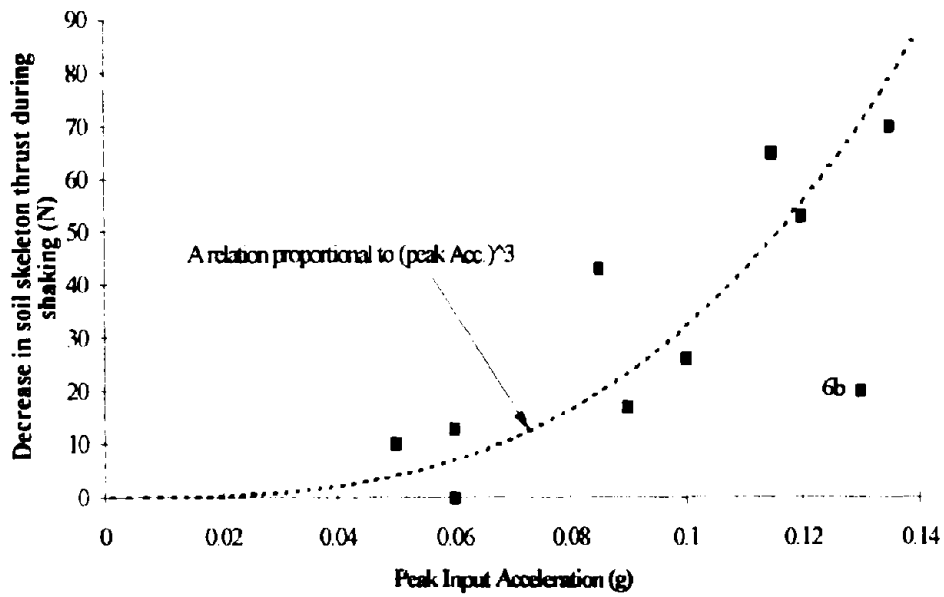
Figure 6.24: Decrease in Soil Skeleton Thrust during shaking in non-slip tests
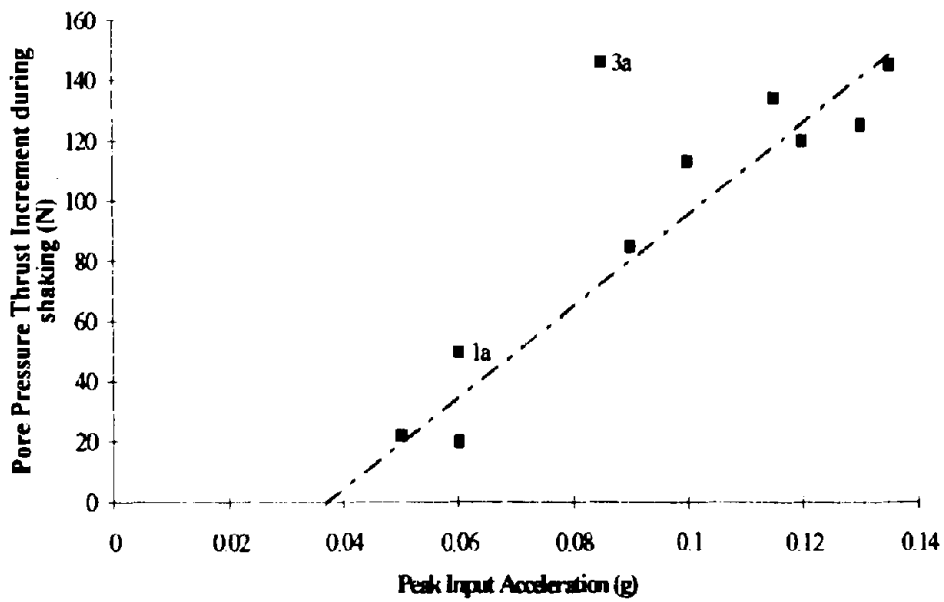
Figure 6.25: Pore Pressure Thrust Increment during shaking in non-slip tests

Soil	Specimen Preparation	σ_c' (PSI)	Symbol
Crystal Silica No 20 Sand	Dry Vibration Fresh Sample	14	O
	Wet Rodding Fresh Sample	14	△
	Dry Vibration Staged Sample	14	▲
Sand No 1	Moist Tamping Staged Sample	10	▽
	Staged Sample	20	▼

$n_c = 10$ cycles
$D_r \cong 60\%$
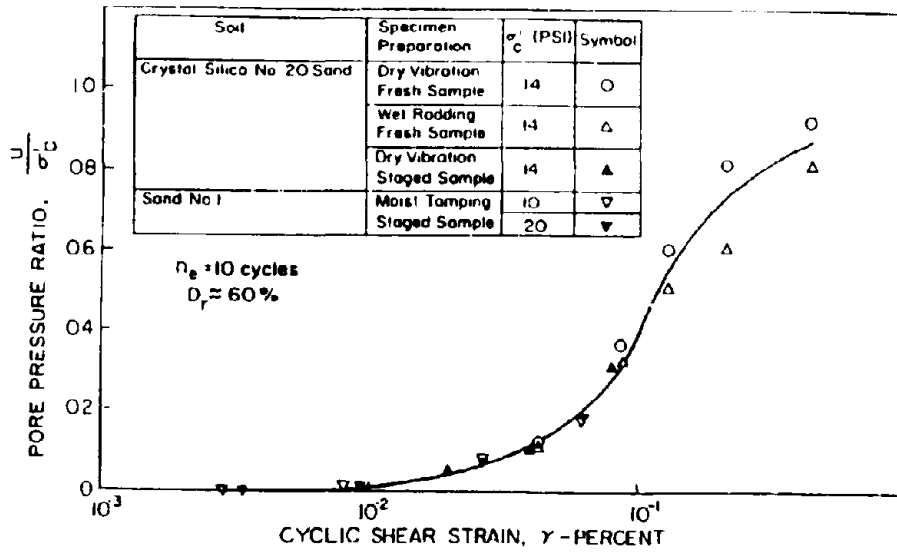
Figure 6.26 Pore Pressure Build-up of saturated sands in cyclic triaxial tests
(from Dobry et al., 1981)
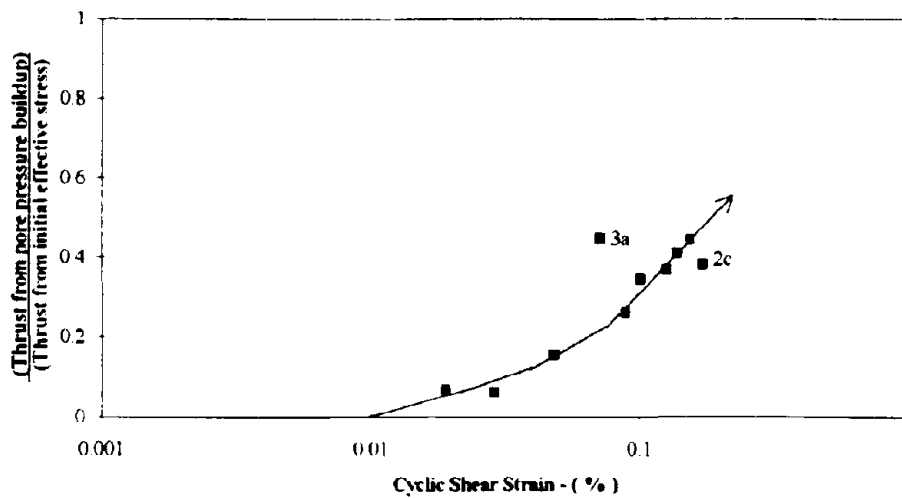
Figure 6.27 Pore Pressure Build-up versus cyclic shear strain in non-slip tests

192
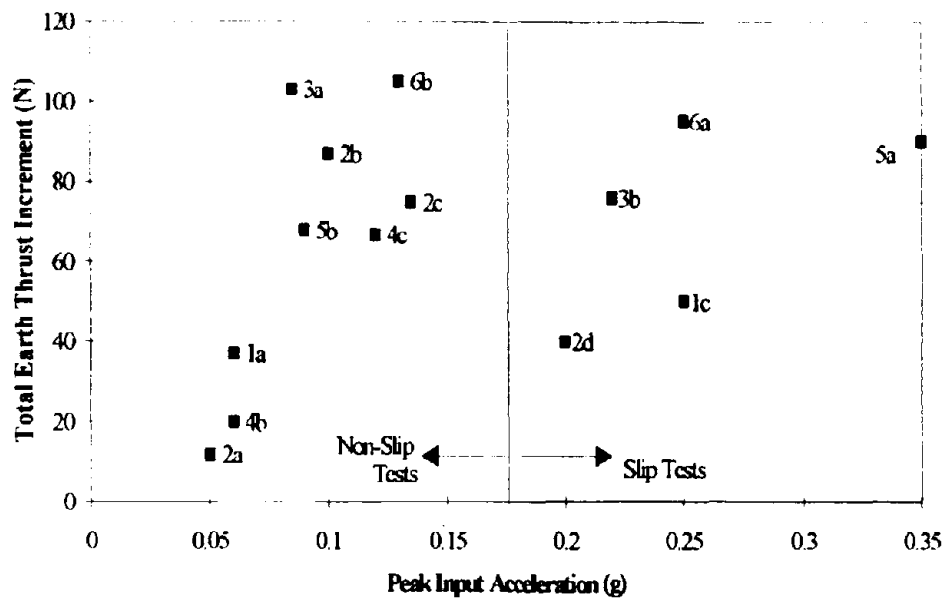
Figure 6.28: Incremental earth thrust at the end of shaking in centrifuge model tests
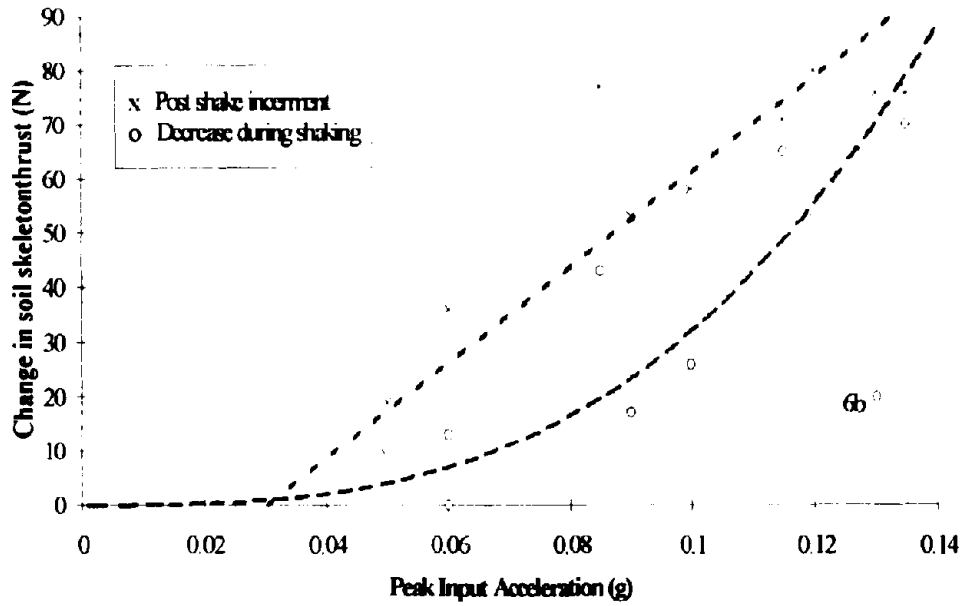
Figure 6.29: Post Shake Soil Skeleton Thrust Increment in non-slip test
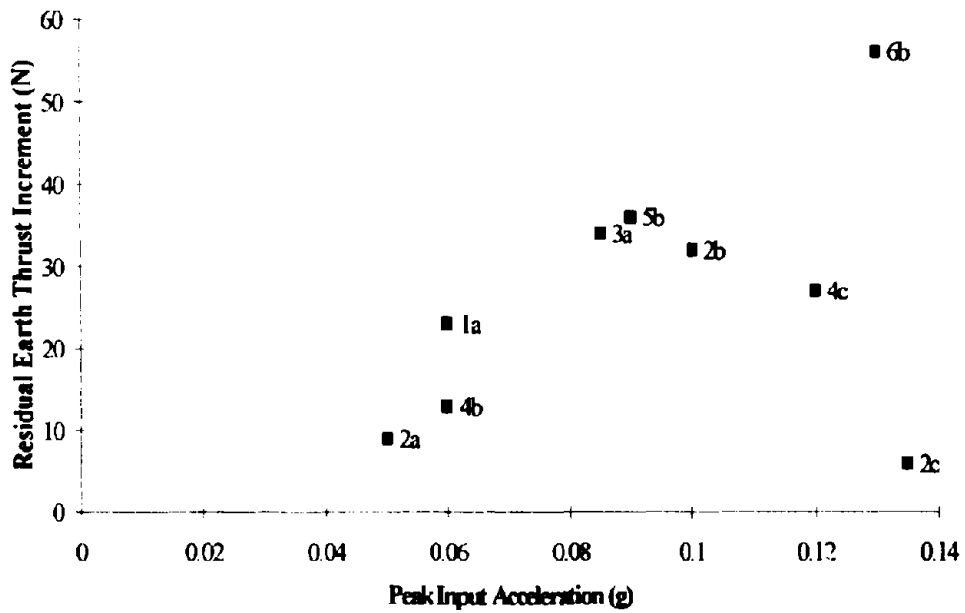
Figure 6.30: Residual Earth Thrust Increment after earthquakes in non-slip tests
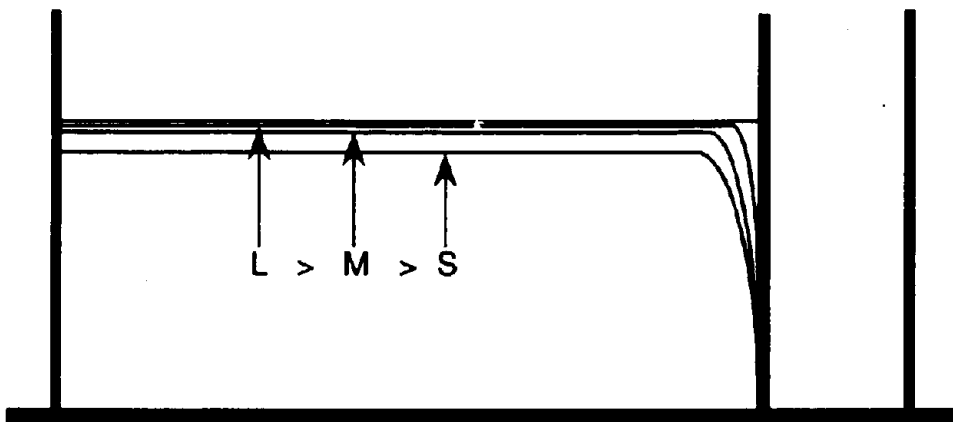
(a) at weak earthquake
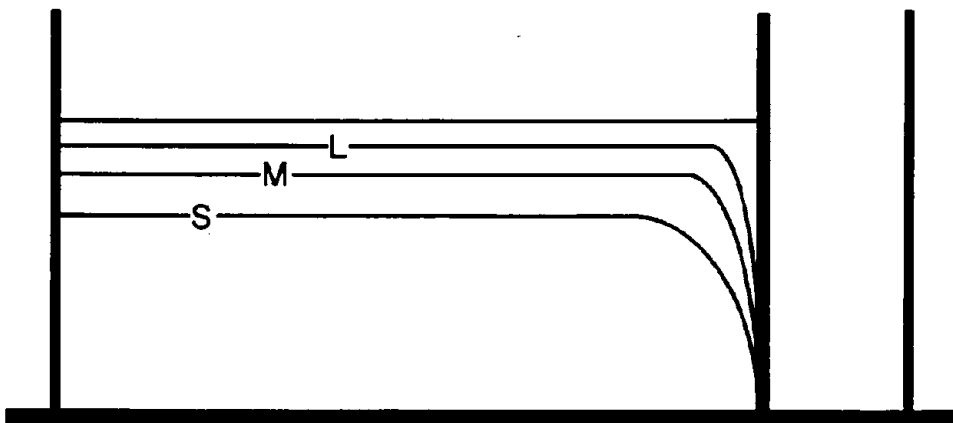
(b) at strong earthquake

Figure 6.31   Hypothetical contours of normalized dynamic response in soil backfill
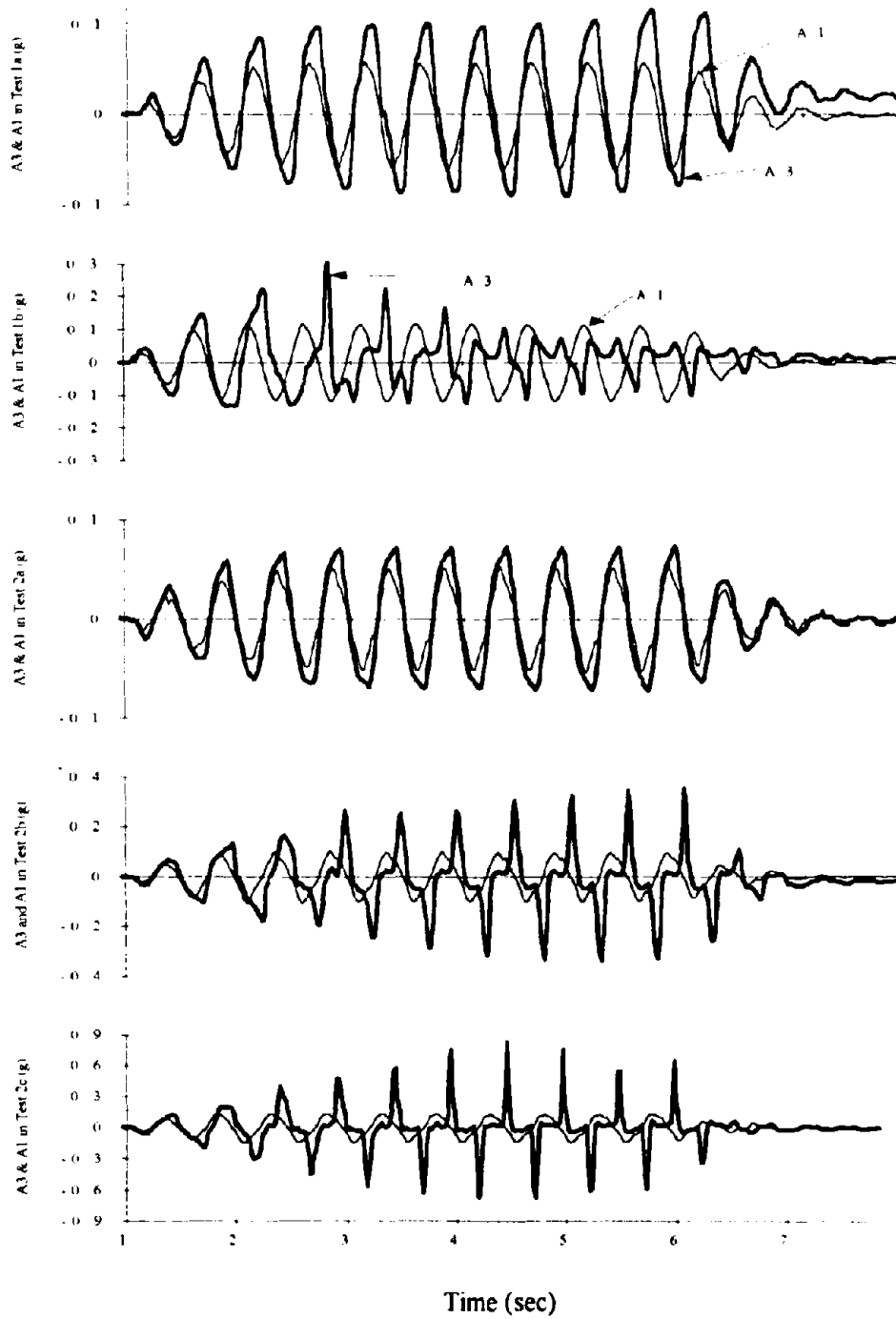
Figure 6.32: (a) Acceleration responses in soil (A3) and input accelerations (A1) in non-slip tests
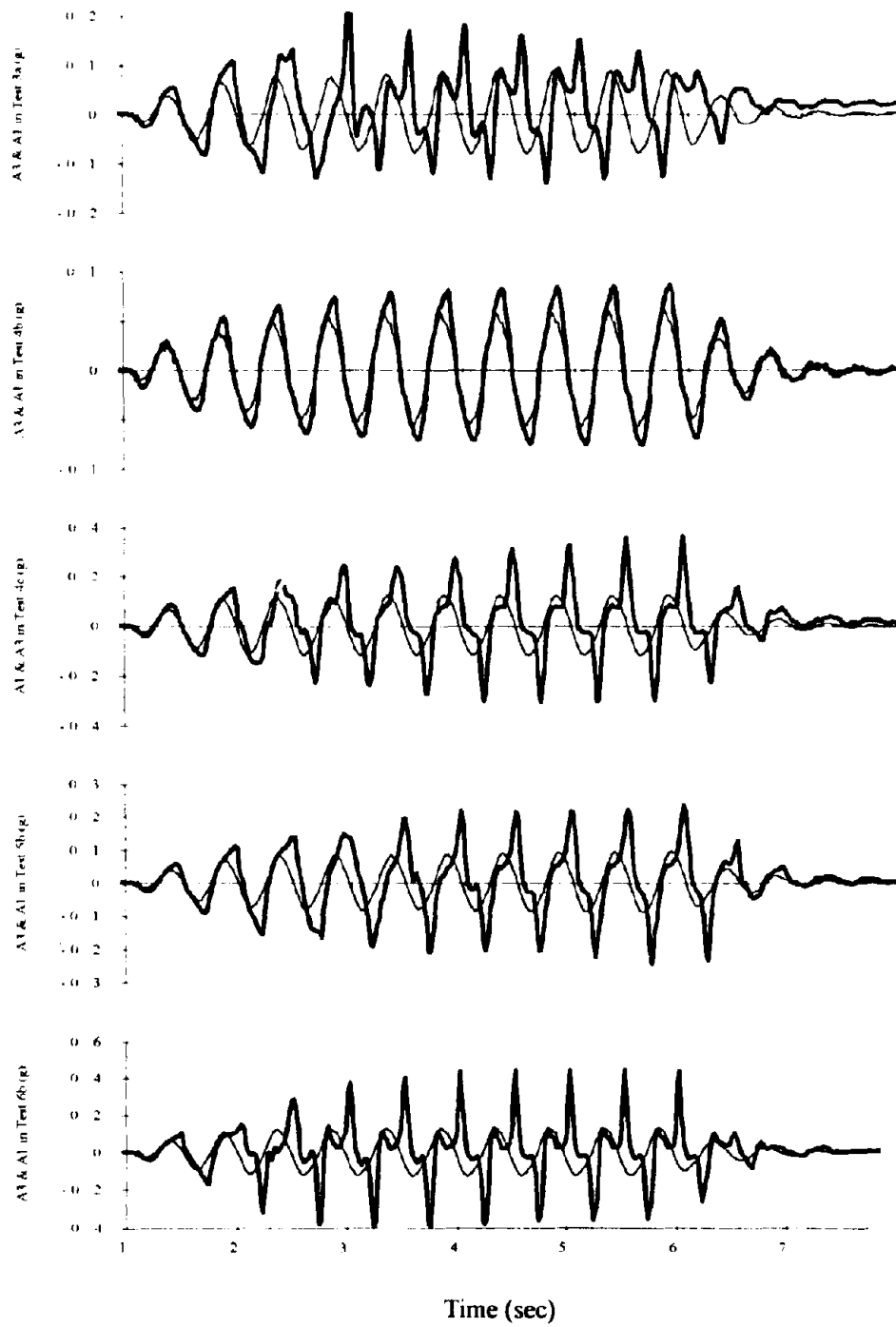
Figure 6.32 (b) Acceleration responses in soil (A3) and input accelerations (A1)
in non-slip tests
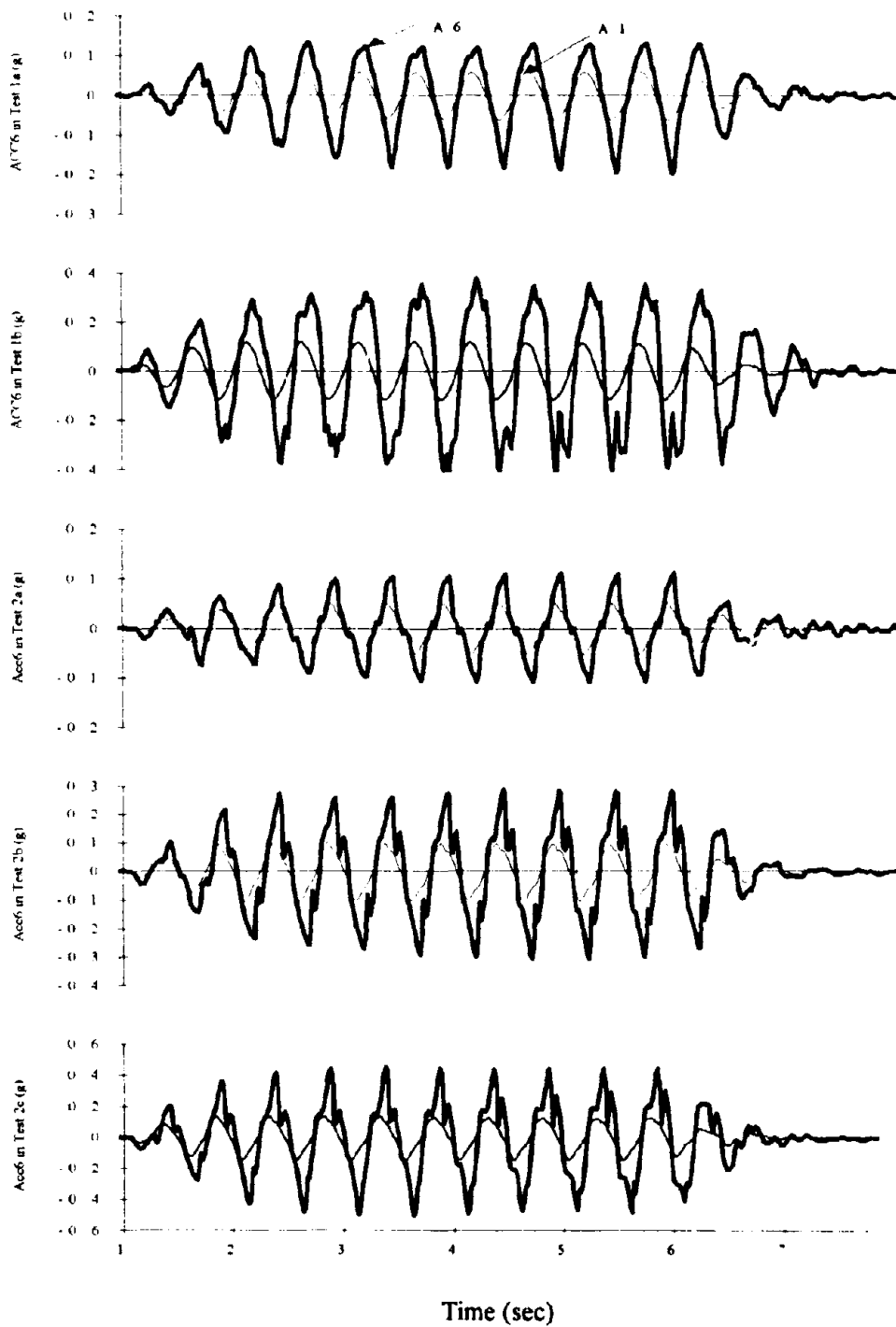
Figure 6.33 (b) Acceleration at top of retaining wall (A6) and input accelerations (A1) in non-slip tests

198

Figure 6.33 (b) Acceleration at top of retaining wall (A6) and input accelerations (A1) in non-slip tests

PHASE LAG
to peak
Inward Input
Acceleration

0

Wall Inertia
(36°)

θ_{max}
Peak Outward
Rotation
(~ 60°)

Maximum
thrust from
soil skeleton
(~ 69°)

(max. A3)
Max. Acc. response
in backfill
(~ 77°)

90

Maximum
Total Earth
thrust
(~ 100°)

180

Maximum
Pore Pressure
thrust
(~ 150°)

$-\dot{\theta}_{max}$
Peak inward angular
VELOCITY of rotation
(~ 150°)

270

$-\theta_{max}$
Peak Inward
Rotation
(~ 240°)
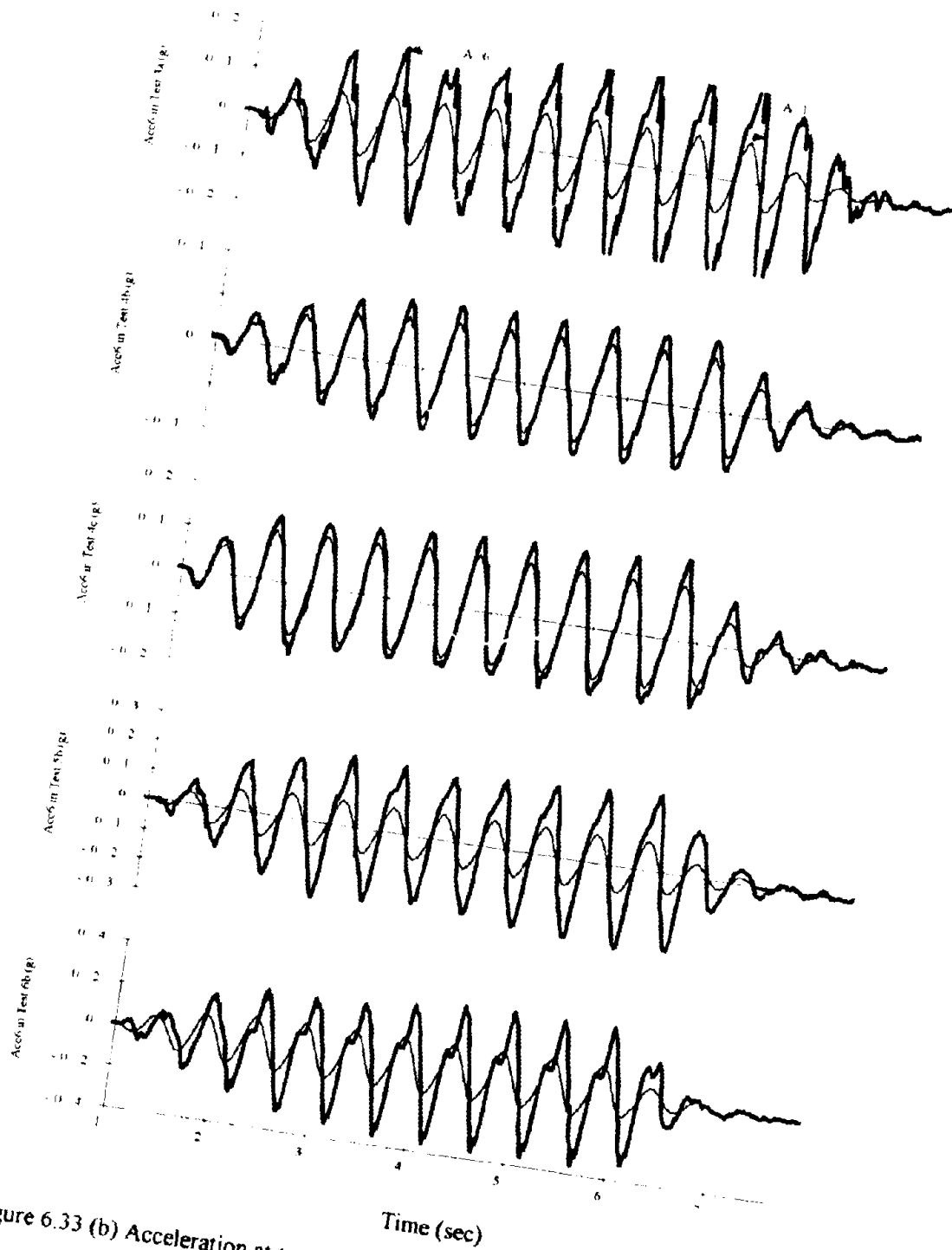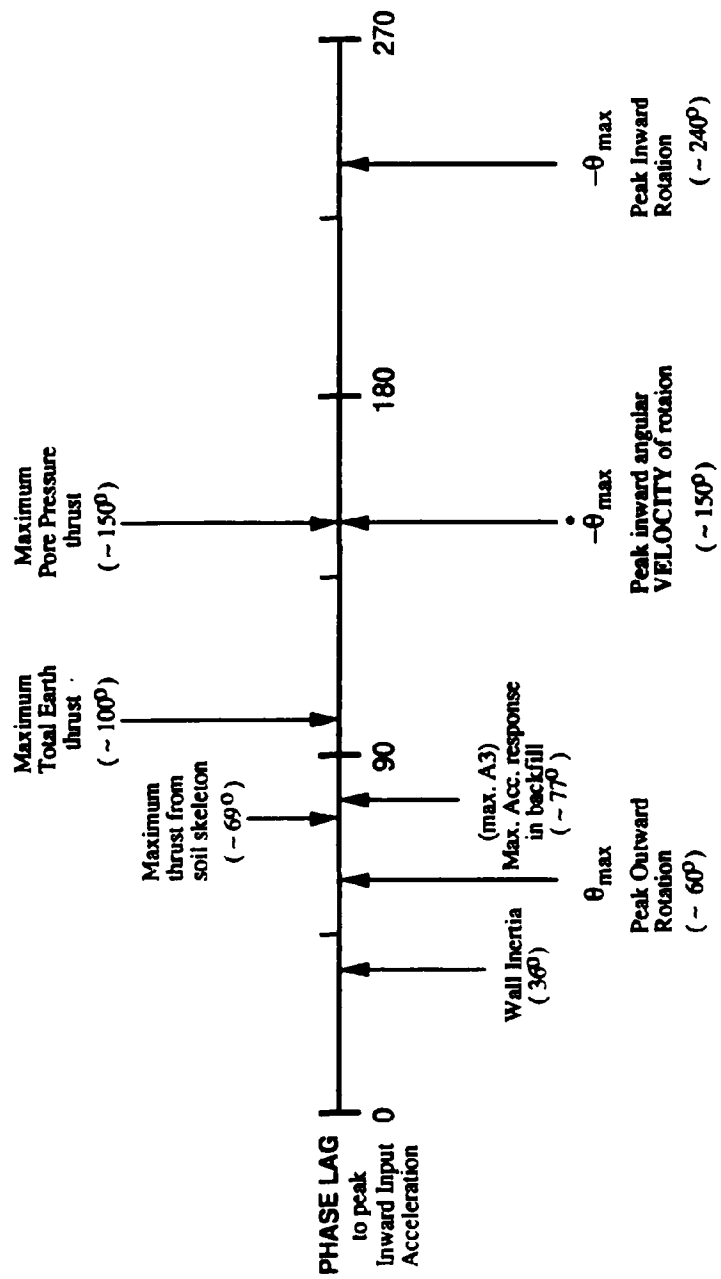
Figure 6.34 : Phase lags of various thrusts and wall rotations to the peak inward input acceleration

200
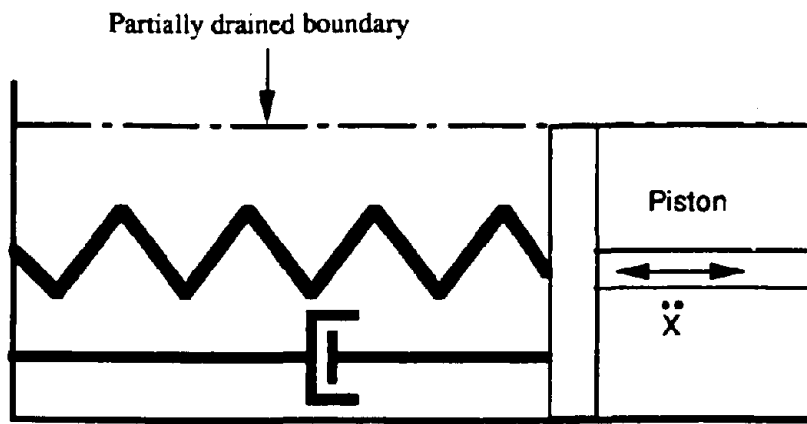
(a) Piston moves periodically in horizontal direction
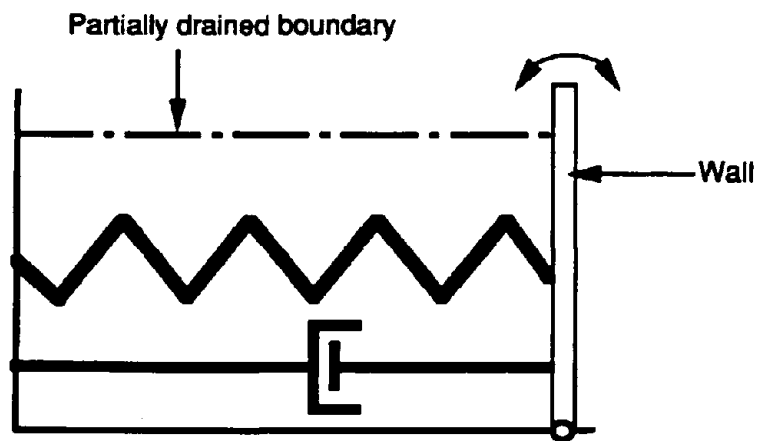
(b) Wall rotates periodically

Figure 6.35 : Hypothetical model for dynamic pore pressure fluctuation
due to periodic rotation of retaining wall
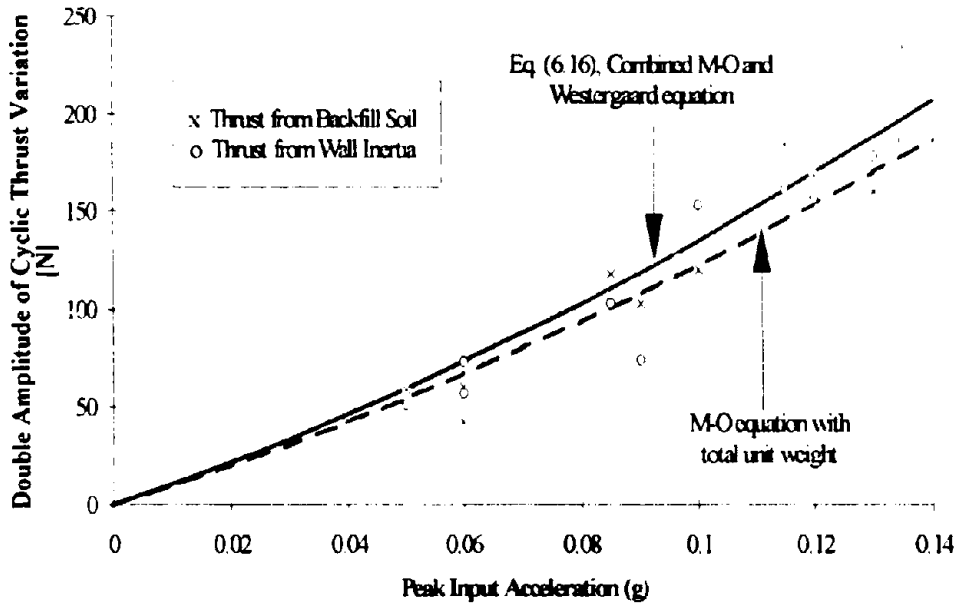
Figure 6.36: Double amplitude of cyclic thrust variation of thrusts from wall inertia and soil backfill in non-slip tests
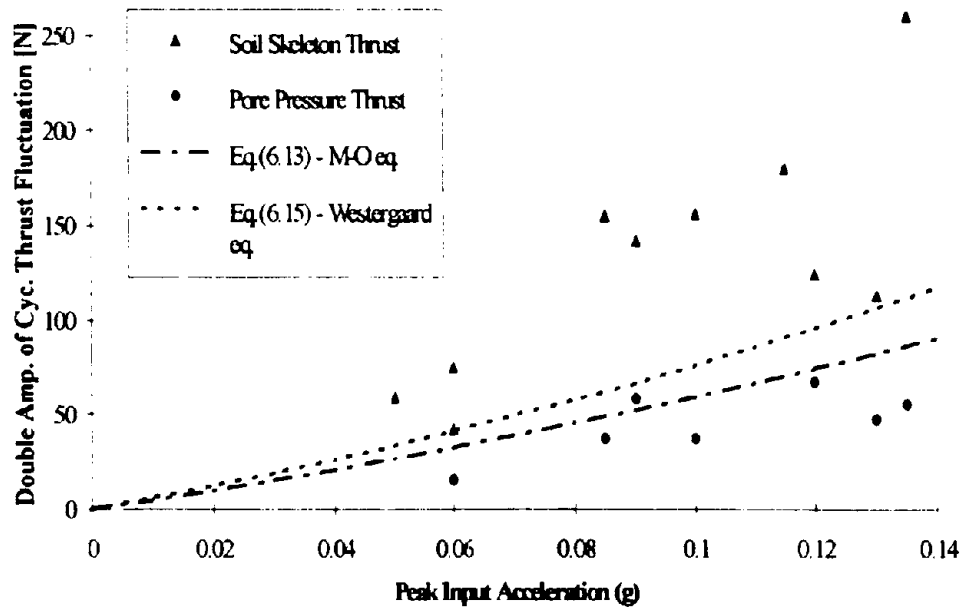
Figure 6.37: Double amplitude of cyclic thrust variation of thrusts from pore pressure and soil skeleton in non-slip tests

CHAPTER 7

BEHAVIOR OF THE SOIL-WALL SYSTEM IN CENTRIFUGE MODEL TEST (II) EARTHQUAKE-INDUCED PLASTIC TILT OF THE RETAINING WALL

Earthquakes caused large permanent tilts of the retaining wall in the centrifuge model in some tests. There were two types of permanent tilt: (1) elastic tilt -- due to the increased earth thrust and a consequent spring elongation; and (2) plastic tilt - due to the slip at the slider in the tie-back. One way to identify the occurrence of slippage is to investigate the loads at the two ends of the slider. Section 7.1 presents the analyses for these loads using different approaches.

The approach to investigation of the slip at the slider was to try a reasonable model with best estimates for parameters and inspect how well it does. A lumped-mass-sliding-block model was developed to estimate the amount of slippage. Section 7.2 describes this model. This model contains two lumped masses that represent the soil-wall system during earthquakes: one representing the mass of the wall and an equivalent soil mass that moves with the cyclically rotating wall; the other representing the sliding element of the slider plus the tie-back, which is viewed as sliding block along a frictional plane. With proper estimates for the model parameters (based on the results of non-slip tests), this model offers a reasonable estimation for the amount of slippage during the centrifuge model tests.

203

7.1 LOAD AND SLIP AT SLIDER

The load at the slider is the key parameter that governs the occurrence of slippage. Slip is possible when it reaches the yield load. However, this load was not measured directly. This section presents the analyses for the load at the slider during the dynamic centrifuge model tests, based on other available data.

The test model is shown in Figure 4.4. Figure 6.8 shows a schematic diagram of the retaining wall with the tie-back. The retaining wall is hinged at the base. All moments acting on the wall are resisted by the tie-back. The load in the tie-back is transmitted to the shaking bin through a slider (Figures 4.2 and 4.3). Under normal conditions, the load in the tie-back is entirely resisted by the frictional force between the two parts of the slider. Slip occurs when the load in the tie-back reaches the shear resistance of the slider.

The slip at the slider was controlled by the frictional force at the potential sliding surfaces between the sliding element and the stationary elements of the slider. This friction force will be referred to as the "load at slider". Two approaches were employed to investigate the load at slider. Section 7.1.1 presents an analysis of the load resisted by the slider, i.e., the load at the fixed elements of the slider. Section 7.1.2 presents an analysis of the load in the tie-back, i.e., the load applied to the sliding element of the slider.

The second approach interprets the load in the tie-back based upon the amount of rotation of the wall. The increase of the load at slider is proportional to the outward rotation of the wall. In non-slip tests, the loads obtained from both approaches should be consistent. However, in slip tests, the apparent load at slider obtained in Section 7.1.2 will be larger than that in Section 7.1.1, due to the incresed length of the tie-back as a result of

slip during the earthquake shaking. The discrepancy between the two analyses indicates the occurrence of slip. Section 7.1.3 presents the comparisons of the interpreted loads via both approaches. The comparisons provide a manner to verify the slippage at slider.

7.1.1 Load at The Fixed Support of Slider

This approach obtains the load at slider from the measured load data by the load cell, by taking off all involved inertia. The expression for the load at the fixed part of slider is

$$F_{slider}(t) = F_{LC}(t) + (m_{11} + m_{12} + m_{13})A4(t) \tag{7.1}$$

where A4(t) is the acceleration measured at the load cell; F_{LC} is the force measured by the load cell, and F_{slider} is the load at slider. The relative locations of the masses are shown in Figure 6.8. The mass terms include the fixed part of the slider ($m_{13} = 560g$), the connector between the slider and the load cell ($m_{12} = 77g$), and the "effective mass" of the load cell ($m_{11} = 300g$ from Figure 4.5).

Note that A4 was not recorded in some tests (series 2, 3, 5, and 6) due to the limited number of data log channels. In non-slip tests, data of A5 (acceleration at the sliding element) are used as a substitute for A4, since they are practically equivalent in these tests. Figure 7.1 illustrates the records of A1, A4 and A5 in Test 1a. An amplified input acceleration (A1) was used as A4 in slip tests in the analyses. The amplification factor varies with the earthquake intensity. It is estimated based on the trend in Figure 4.9. For example, an amplification of 1.75 was used for Test 2d, and a factor of 2.35 for Test 5a.

205

Results of the analyzed load at the fixed part of slider will be presented in Section 7.1.3.

7.1.2 Load at The Sliding Layer of The Slider

The second alternative computes the load at the sliding layer of the slider. This load is calculated based on the extension of the spring in the tie-back.

Two forces are acting on the sliding layer of the slider. One comes from the fixed support, as calculated in Section 7.1.1. The other comes from the force in the tie-back. This load is linear with the deformation of the spring. The spring deformation is practically equal to the horizontal wall displacement at tie-back, if there is no slip at slider. The deformation of the rest of the tie-back system is very small compared to the spring deformation. The horizontal displacement of the wall at tie-back is measured by two displacement transducers (DCDT No. 3 and No. 4). The spring force is calculated from the displacement data and spring constant.

The force at the sliding part of the slider is equal to the spring force plus the inertia of the system (see Figure 6.8). The system inertia is the product of the acceleration at the sliding layer (A5) and the masses of the sliding layer (m_{14}), the connection rod (m_{15}) and one half of the spring mass (m_{16}). Equation (7.2) expresses the load at slider based on this approach.

$$F_{slider}(t) = F_{LC,t=0} + k_2[D_3(t) - D_{3,t=0}] - (m_{14} + m_{15} + 0.5m_{16})A5(t) \qquad (7.2)$$

The first term at right is the initial static load measured by load cell prior to earthquake. The second term is the load variation calculated from the spring deformation (wall displacement); k_2 is the spring constant (= 605 kN/m), and D_3 is the measured

206

horizontal wall displacement near the spring. The last term in Eq. (7.2) is the inertia effect of all involved masses.

Results of the analyzed force at slider from the spring side (sliding part) of the slider are presented in Section 7.1.3.

7.1.3 Verification of Slip at Slider

The occurrence of slip can be indicated by comparing the loads at slider obtained from the above two approaches. Ideally, the loads calculated by Eqs.(7.1) and (7.2) should be identical in non-slip tests. Once slippage occurs, the accumulated amount of slip is included in $D_3(t)$ in tests with slip at the slider. As a result, the load obtained by Eq.(7.2) will be too large. The amount of the increased load is proportional to the amount of slippage.

Figures 7.2 through 7.7 demonstrate the comparisons of loads at slider obtained from both approaches in most tests. The heavy curves are the load histories obtained from the first approach -- Eq. (7.1). The lighter curves are the loads obtained from the second approach -- Eq. (7.2). The characteristics of these curves in non-slip tests and slip tests are discussed as follows.

I. Non-Slip Tests -- 1a, 2a, 2b, 2c, 3a, 4b, 4c, 5b and 6b

Three observations are drawn from the comparisons in Figures 7.2 through 7.7.

207

1. The leads indicated by the two curves, calculated from Eqs. (7.1) and (7.2), are similar to each other except during the earthquake period in each test.

2. The dynamic fluctuation of the load calculated by Eq. (7.2) lags from that by Eq. (7.1).

3. The dynamic amplitude of the load calculated by Eq. (7.2) is smaller.

The first observation indicates that the static performance of the displacement transducer (D3) was good, while the other two observations indicate that the dynamic performance of the displacement transducer was poor.

The second and the third observations are associated with the nature of the displacement transducer. At high operating frequency, the transducer has a phase lag and a de-amplification of the dynamic response. Figure 7.8 shows the nominal frequency response of the displacement transducer DCDT#3 (data from the manufacturer). The phase lag in degrees is shown by the curve with square data points. The decrease in amplitude is shown by the other curve. The definition of Db is

Amount in Db = 10 log (dynamic output / static output).

In the centrifuge test program, the frequency of all input acceleration was 100 Hz (2 Hz in prototype). A response ratio of 60% and a phase lag of 40° were the nominal frequency responses of the transducer at 100 Hz. These characteristics explain the second and third observations quantitatively.

II.   Slip Test -- 1b, 1c, 2d, 3b, 4a[1], 5a and 6a

---

[1] Figure 7.5 does not show the data of Test 4a due to failed load measurement.

Comparisons in Figures 7.2 through 7.7 clearly indicate that slippage occurred in these tests. In these tests, the load curve computed by Eq. (7.2) departs from the curve by Eq. (7.1) at the commencement of slip. For example, slippage occurred during the seventh cycle of load in Test 1b, and the second cycle in Test 1c.

One important feature of the load curves from Eq. (7.1) is that the positive peaks are of more-or-less uniform height once slip begins. This feature reveals that there was an upper limit to the load transmitted from the sliding element to the fixed elements in the slider. This is characterized by a flat head in the load history. The upper limit is the shear resistance of the slider. The feature of flat head is not obvious in some tests, such as 3b and 6a in Figures 7.4 and 7.7. The poorly defined shear resistance is likely to be a result of using an amplified A1 as a substitute for A4 (Section 7.1.1). This substitution is not exact. Three potential inaccuracies are associated with it:

1. The estimation of the amplitude of the acceleration may not be correct.
2. The shape of the A4 history, if recorded, might differ from the sinusoidal A1.
3. There may be a phase angle between A1 and the acceleration at the location of A4.

The slip at slider is clearly indicated in Figures 7.2 through 7.7. The analyses for load at slider also set forth the dynamic load fluctuation and yield load of the slider. This information will be used to explain the slip using the Lumped-Mass-Sliding-Block model in the next section.

209

7.2   LUMPED-MASS-SLIDING-BLOCK MODEL

7.2.1   The Model for The Stick-Slip Tilting Retaining Wall

A lumped-mass-sliding-block model is developed to investigate the slip at the slider during earthquakes. The dynamic motion of the tilting retaining wall model in the centrifuge test program is also analyzed by this model. Figure 7.9 shows the schematic lumped mass model for the actual centrifuge test model. The lumped mass "m_1" includes the masses of the retaining wall and the effective mass of soil that moves with the wall during rotation. The block "m_2" includes the sliding element of the slider and the part of the tie-back between the actual spring and the slider. The resistance of the soil backfill to the motion of the wall is represented by the spring constant k_1 and the damping coefficient c. The constant of the spring in the tie-back is k_2. The ground acceleration is marked by "$\ddot{s}$". Note that the acceleration at the sliding interfaces is larger than the input acceleration (Figure 4.9). The acceleration at this point is an amplified base input acceleration. The amplification factor increases with the intensity of shaking, following the trend shown in Figure 4.9.

The slip at the sliding element is represented by relative movement between m_2 and the "ceiling". Sliding is possible when the shear force exceeds the frictional resistance of the slider. The amount of slip may be analyzed using Newmark's (1965) approach to the dynamic response of a block-on-a-plane.

The equations of the motion in this lumped mass system are:

$$m_1 \ddot{x}_1 + C(\dot{x}_1 - \dot{s}) + k_1(x_1 - s) + k_2(x_1 - x_2) = 0 \qquad (7.3)$$

210

$$m_2 \ddot{x}_2 - k_2(x_1 - x_2) + F_{slider} = 0 \qquad (7.4)$$

Using the relative displacement between the masses and the frame ($y = x - s$), the above equations become:

$$m_1 \ddot{y}_1 + C \dot{y}_1 + k_1 y_1 + k_2(y_1 - y_2) = -m_1 \ddot{s} \qquad (7.5)$$

$$m_2 \ddot{y}_2 - k_2(y_1 - y_2) = -m_2 \ddot{s} - F_{slider} \qquad (7.6)$$

where F_{slider} is the friction force applied to m_2 from the frame, which is the load at slider as described in the previous section. Slip starts when the force on the sliding block is larger than the friction resistance of the slider (F_{cr}). The force at slider, F_{slider}, remains equal to F_{cr} during sliding, until the velocities of the block and ground motion coincide, i.e., $\dot{x}_2 = \dot{s}$ or $\dot{y}_2 = 0$.

The equations of the 2-DOF system can be written as,

$$M \ddot{U} + C \dot{U} + KU = R \qquad (7.7)$$

where $U, \dot{U}, \ddot{U}$ are the vectors of displacement, velocity and acceleration relative to the frame; R is the vector of external load;

$$M = \begin{bmatrix} m_1 & 0 \\ 0 & m_2 \end{bmatrix} ; \ C = \begin{bmatrix} c & 0 \\ 0 & 0 \end{bmatrix} ; \text{ and } K = \begin{bmatrix} k_1 + k_2 & -k_2 \\ -k_2 & k_2 \end{bmatrix} .$$

The mass "m_2" (= 0.2 kg) is the sum of the masses of the sliding layer, the rod between the slider and the one half of the mass of the physical spring. The mass "m_1" (= 2.0 kg) is estimated as

$$m_1 = \frac{1}{2} \frac{H_{wall}}{H_{tie-back}} m_{wall} + \frac{\Delta M_{soil}}{H_{tie-back}} + \frac{m_{spring}}{2} \qquad (7.8)$$

211

The second term is the effective mass of the soil "attached to the retaining wall" that moves with the wall during dynamic rotation. In Eq. (7.8), ΔM_{soil} is the dynamic moment exerted to the wall by the backfill soil as expressed by Eq. (6.14).

$$\Delta M_{soil} = \frac{1}{2}\gamma_b wH^2 \left(\frac{3}{4}k_h\right)\left(1+\frac{1}{2}\alpha\right)\frac{H}{2} + \left(\frac{7}{12}\gamma_w wH^2 k_h\right)\left(1+\frac{2}{5}\alpha\right)\left(\frac{\frac{3}{2}+\frac{6}{35}\alpha}{1+\frac{2}{5}\alpha}\right)H \quad (6.14)$$

where α (= 2.5 k_h) is a parameter describing the amplification of acceleration defined in Eq. (6.10). In most slip tests, input accelerations were about 0.25g. Therefore, m_1 = 2.0 kg is estimated using Eq. (7.8), with an assumption of α = 0.625 in Eq. (6.14)

Eq. (7.8) ignores the rotational inertia of the tilting wall, mainly owing to the complications related to the accelerations. The rotational inertia of the wall, I_{wall} = $\frac{1}{3}m_{wall}H^2_{wall}$, included in Eq. (6.4), is considered as a component of dynamic moment acting on the wall. This inertia would cause a force of 0.19(A6-A1) newtons in the tie-back during rotation. The effective mass associated with the rotational inertia should be 0.19(A6-A1) / A4. Figure 7.10 shows the acceleration histories of (A6-A1) and A4 in Tests 1c and 4a. At the positive peaks of A4, which are the times crucial from the standpoint of sliding, (A6-A1) is usually equal to one half of A4. Hence, the additional mass due to the rotational inertia is about 5% of the total mass, m_1. Moreover, the involvement of the differential acceleration (A6-A1) complicates the estimation procedures[2]. Therefore, the additional mass due to the rotational inertia of the tilting retaining wall is ignored in Eq. (7.8).

---

[2] The differential acceleration (A6-A1) is not sinusoidal and there is a phase lag between (A6-A1) and A4 (the input acceleration at the tie-back level, $\overset{\bullet\bullet}{s}$).

In Eq. (7.8), the concept of using an effective earth mass to account for the dynamic earth thrust is obtained from the insights of the pseudo-static Mononobe-Okabe and Westergaard equations for the dynamic thrusts from the soil skeleton and water. The effective mass multiplied by the ground acceleration gives a sufficient estimate for the dynamic earth thrust. The adequacy of estimating the effective earth mass using Eq. (7.8) has been verified in Section 6.3.2 (Figure 6.36).

The spring constant k_2 was calibrated to be 605 kN/m. The spring constant k_1 (=723 kN/m) and damping coefficient C (= 1485 kg/sec) are estimated based on the results of non-slip tests in Chapter 6. In tests with no slip at the slider, the relative displacement y_2 equals zero all the time. Therefore, Eq. (7.5) is reduced to

$$m_1 \ddot{y}_1 + C\dot{y}_1 + (k_1 + k_2)y_1 = -m_1 \ddot{s} \tag{7.9}$$

In non-slip tests, the acceleration terms $\ddot{s}$ and $\ddot{y}_1$ are the input acceleration at the tie-back level and the relative acceleration at top of the wall respectively, i.e., $\ddot{s}$ = A4 and $\ddot{y}_1$ = A6 - A4. Assume both A4 and A6 are sinusoidal with time; then $\ddot{s}$, $\ddot{y}_1$, $\dot{y}_1$ and y_1 can be written as follows.

$$\ddot{s} = A*\sin(\Omega t) \tag{7.10}$$

$$\ddot{y}_1 = -B*\sin(\Omega t - \alpha) \tag{7.11}$$

$$\dot{y}_1 = \frac{B}{\Omega}\cos(\Omega t - \alpha) \tag{7.12}$$

$$y_1 = \frac{B}{\Omega^2}\sin(\Omega t - \alpha) \tag{7.13}$$

where α is the phase lag between $\ddot{y}_1$ and $\ddot{s}$; Ω (= 200π) is the frequency of the input pulses. Substituting Eqs. (7.10) through (7.13) into (7.9), then Eq. (7.9) becomes

213

$$-m_1 B \sin(\Omega t - \alpha) + \frac{c}{\Omega} B \cos(\Omega t - \alpha) + \frac{k_1 + k_2}{\Omega^2} B \sin(\Omega t - \alpha)$$

$$= -m_1 A \sin(\Omega t) \tag{7.14}$$

Rearranging the terms in Eq. (7.14),

$$\left[\frac{k_1 + k_2}{\Omega^2} - m_1 \right] \sin(\Omega t - \alpha) + \frac{c}{\Omega} \cos(\Omega t - \alpha) = -m_1 \frac{A}{B} \sin(\Omega t) \tag{7.15}$$

Eq. (7.15) suggests the following relationships:

$$\tan \alpha = \frac{\dfrac{c}{\Omega}}{\left[\dfrac{k_1 + k_2}{\Omega^2} - m_1 \right]} \tag{7.16}$$

$$\left(m_1 \frac{A}{B} \right)^2 = \left(\frac{c}{\Omega} \right)^2 + \left[\frac{k_1 + k_2}{\Omega^2} - m_1 \right]^2 \tag{7.17}$$

In Eq. (7.16) and (7.17), the numerical values of all parameters other than k_1 and c can be determined independently (will be described shortly). Therefore, k_1 and c can be obtained through solving Eqs. (7.16) and (7.17) -- by substituting $\dfrac{c}{\Omega} = \tan \alpha \left[\dfrac{k_1 + k_2}{\Omega^2} - m_1 \right]$ from Eq. (7.16) into Eq. (7.17).

Table 7.1 summarizes the information determining the numerical values of k_1 and c. In equations (7.15) and (7.17), $\dfrac{B}{A}$ equals to $\dfrac{(A6 - A4)_{max}}{(A4)_{max}}$ in each test. In non-slip tests, the acceleration ratio $\dfrac{(A6 - A4)_{max}}{(A4)_{max}}$ is 1.365 ± 0.223. The dynamic fluctuation of the load in the tie-back lags about $50^\circ \sim 60^\circ$ from the input acceleration (see Table 6.3). The phase lags associated with stronger earthquakes tends to be constant at 60° (Table 7.1). The author decided to use a phase lag (α) of 60° in tests with stronger earthquakes, instead of the average value of 55°, for tests involving slip at the slider.

214

In Table 7.1, the information from Test 4b is discarded because of its small damping coefficient. Test 4b involved a relatively weak earthquake (a_{max} = 0.06g) applied to a model that had been densified previously with a strong earthquake in Test 4a (a_{max} = 0.25g). The cyclic shear strain (2.5×10^{-2}%) was small in this test compared with the cyclic strains in other tests, e.g., 0.16% in Test 6b. The small cyclic strain may have caused a small damping ratio and hence a small damping coefficient. Therefore, the information from Test 4b is omitted when considering the tests involving slippage in which the earthquakes were strong.

As listed in Table 7.1, the conclusive values of k_I and c were obtained using the average acceleration ratio of 1.365 and a phase lag of 60°. The final estimations of k_I and c are 723 kN/m and 1485 kg/s. The corresponding damping ratio (0.32) is a reasonable value for sands with large cyclic shear strains[3]. The back-calculated spring constant is verified to be a rational residual spring constant[4] of the Nevada sand. Appendix F describes the detailed verification process, in which the Winkler spring constant of Nevada sand at small strains is estimated using the method proposed by Scott (1973).

7.2.2 Horizontal Wall Displacements at The Tie-Back Level During Earthquakes

The lumped-mass-sliding-block model is applied to analyze the amount of slip. This model also analyzes the horizontal wall displacement (at the tie-back level) which includes

---

[3] The typical damping ratio of a sand with large cyclic strain is between 0.25 and 0.35.

[4] The cyclic shear strains ($2 \sim 5 \times 10^{-1}$%) were large enough to bring down the shear modulus to its residual value.

the amount of slip. This displacement is the relative displacement $y_1(t)$ in Eqs. (7.5) and (7.6). Figures 7.11 through 7.16 present the calculated y_1 with the model for tests in which slip occurred.

The numerical procedure uses the Newmark integration method with a time step of 0.00032 second in model scale (or 0.016 sec in prototype scale). This time step is the interval of time in each data set of observation. The analyses use the same k_j and same c values for all tests with slip at the slider. These values are considered to be the residual values at large strains.

The model first analyzes the dynamic load fluctuation at the slider based on an amplified input base acceleration (from the test data). The total load was obtained by summing up the initial static load and the dynamic load. Slip during each load cycle starts when the load in the spring exceeds the shear resistance at the sliding interface, and stops when the differential velocity ($\dot{y}_1$) reduces to zero. In the centrifuge tests, the average transient thrust increased during each earthquake (Section 6.3.1). The incremental thrust influenced the amount of slip in each load cycle. However, this load increment is not inherent in the lumped-mass-sliding-block model. Extra efforts were employed in the analyses to adjust the average transient load during earthquakes. Data of most test results show that the average transient total earth thrusts[5] increased very rapidly during the first few cycles of ground motion. The time-wise average loads in the tie-back remained more or less constant in the later periods of earthquakes. Therefore, two cases were considered to analyze the slip:

---

[5] The average transient soil skeleton thrust plus the average pore pressure thrust.

1. **Case I** ---

The average transient (total) earth thrust increases very rapidly when an earthquake starts. The total incremental load in the tie-back during an earthquake is added to the initial load at the commencement of the earthquake.

2. **Case II** ---

The average transient load increases linearly during the shaking period.

Figures 7.11 through 7.16 present the predicted horizontal wall displacements (at the tie-back level), $y_1(t)$; and the histories of the load at slider based on the above two cases. The observed displacement and load histories[6] are also included as references. Note that the amplitudes of the observed dynamic displacement are too small -- due to the frequency response of the displacement transducers (Section 7.1.3). The shear resistance of the slider was set, before each test, to various values according to the planned shaking intensity by adjusting the lengths of the compression springs (Figure 4.3). However, because of the short lengths of the springs and the very large spring constants, it was difficult to exert precise compression on the slider. Hence, due to the difficulty of knowing the exact shear resistance of the slider in advance, the yield loads at the sliding surfaces in the model were obtained from the observed load histories

Comparisons of the modeled and observed displacements in Figures 7.11 through 7.16 were made (see Table 7.2). The comparisons employed two criteria: (1) the amount of slip per load cycle; and (2) the residual horizontal wall displacement. The analyzed amount of slip per cycle in case I is rather uniform throughout the load cycles. The amount of slip during each load cycle in case II generally increases cycle by cycle. For the purpose of consistency, the modeled amount of slip per cycle is determined by averaging

---

[6] The observed histories of the load at slider, by Eq. (7.1), are obtained from Figures 7.2 through 7.7.

the amount of slip during the last six load cycles. In some tests, the slider did not slip during the first few cycles. The observed slip per cycle is determined by averaging the slip during the slip-occurring load cycles

This model is generally good at analyzing the earthquake-induced tilt of the retaining wall. Most test data fall between the analyzed amounts of displacement of cases I and II. Table 7.2 summarizes some numerical quantities to evaluate the analyzed displacements based upon these comparisons. The test-by-test reviews are described as follows:

1. Test 1b (Figure 7.11)

This test is the most interesting one among the slip tests. Slip did not occur until the seventh load cycle in this test. The shear resistance of the slider was not reached until the fifth load cycle. However, the slider did not slip in this load cycle even though the load exceeded the shear resistance of the slider. Both the load and the displacement histories showed that the sliding began during the seventh load cycle. It is very interesting to find that the commencement of sliding occurred at about $t = 4.4$ sec. The load history shows that the slider did not slip until the load reached 583N, 43N higher than the yield load, in the seventh load cycle. As soon as the sliding started, the load dropped down to the shear resistence, 540N.

The model does not assume the above behavior of the slider. The analyzed slip started during the second (Case I) or the third (Case II) cycle of load. Therefore, the total amount of slip is overestimated by the model. However, the analyzed amount of slip per cycle is acceptable, 9.4mm (Case I) and 7.5mm (Case II) versus 6.8mm in observation.

2. Test 1c (Figure 7.12)

The displacement transducers failed to work in this test. The displacement data in the curve marked by "observed" were obtained by integrating the acceleration data (A6-A4). The numerical values of this integrated curve are reliable during the first few

cycles. The curve is less reliable in the later cycles, due to potential accumulated numerical errors, particularly the residual displacement. The real displacement history should reside between the two analyzed curves of cases I and II.

Both the displacement and load data show that slip occurred during the second load cycle. The history of the load at slider shows that the shear resistance of the slider increases slightly cycle by cycle. This increase makes the amount of slip per cycle decrease cycle after cycle in the lower diagram.

3. Test **2d** (Figure 7.13)

There was apparent stick-slip behavior of the slider in this test. During the third through the fifth load cycles, the (observed) load at the slider exceeded the shear resistance -- as indicated by the later load cycles. The load history reveals that the load was entirely resisted by the slider without slippage in the first five load cycles. That is, slip did not occur until the sixth cycle. This is confirmed by the displacement history. Slip began to occur during the sixth cycle of load. The model assumes that slip occurs whenever the load in the tie-back reaches the shear resistance of the slider. Therefore, the analyzed slip starts in the third load cycle according to Case I. This analysis is reasonable, although different from what really happened.

In addition, the soil model in this test had experienced three previous earthquakes. Substantial densification of the backfill may increase the stiffness of the soil, and hence reduce the amount of slip per cycle. This may explain why the observed amount of slip per cycle was smaller than the analyzed values with both Cases I and II.

4. Test **3b** (Figure 7.14)

The shear resistance of the slider is poorly defined by the load history in this test. This is presumably due to the inaccuracies in the acceleration data of A4(t) in Eq. 7.1. The analysis of load involves an amplified base acceleration, $2.0A1(t)$, as a substitute of A4(t) in Eq. 7.1. This substitution may not be exact, and hence the resultant history of the load at slider is not likely to

219
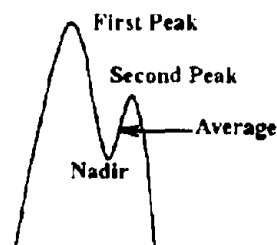
be accurate. The shear resistance of the slider is determined by judgment. There are two positive peaks in each cycle of the "observed" load history after the fifth load cycle. The first peak is believed to be associated with the error of the substitution of the acceleration terms. The average of the second peak and the nadir between the two peaks gives a reasonable estimation for the shear resistance of the slider.

5. Tests **5a** and **6a** (Figures 7.15 and 7.16)

The shear resistances of the slider in these tests are determined following similar procedures as in Test 3b. The model provides adequate estimations of the displacements.

Table 7.2 presents the numerical evaluations of the analyzed displacements based on the assumptions of Cases I and II. Several arguments are provided to help understand the analyses better. Note that the residual displacement data of Tests 1b and 1c are not included in the average modeled/observed ratios, due to the complicated situations described in the above reviews.

1. The average transient earth thrust increased gradually during the earthquake. However, Case I assumes an instantaneous load increment at the beginning of each earthquake. This assumption predicts the start of sliding to occur in earlier load cycles in the analyses associated with weaker earthquakes (1b and 2d). This results in an overestimate of the residual tilt of the wall. In addition, the amounts of slip during the intermediate load cycles are also overestimated. The peak load in such cycles is smaller than that during later cycles, due to the slower rising rate of the average transient (static) load.

2. The model (with Case I) provides good estimations of the permanent tilt (both elastic and plastic tilts) of the retaining wall associated with strong earthquakes ($A_{max} > 0.2g$). The average ratio of the modeled/observed residual displacement

220

for Tests 3b, 5a and 6a is 1.18 ± 0.15. Tests with weaker earthquakes (1b and 2d) involve slower build-ups of excess pore pressures, and hence slower increments in the average transient earth thrusts. Case II provides a better assumption of static load increment associated with weaker earthquakes.

3. The analyzed amount of slip per cycle associated with Case I is slightly conservative. The ratio between the modeled and observed slip is 1.27 ± 0.34. The model underestimates the slip per cycle according to the assumption of Case II. The modeled/observed slip ratio is 0.65 ± 0.28 with Case II.

4. The model overestimates the residual wall displacement (at the tie-back), with Case I. Case II yields underestimations of the residual displacements. The average ratios of the modeled/observe residual displacements are 1.55 with Case I, and 0.58 with Case II. Nevertheless, both estimations are within a reasonable range of accuracy of 50~200%.

5. Both the slip per cycle and residual slip are overestimated, with Case I, to a larger degree for tests involving weaker earthquakes (Tests 1b and 2d). The estimations for tests involving strong earthquakes are close to observations.

6. The magnitude of the observed displacement fluctuation is smaller than that analyzed by the model. The de-amplification ratio is about 60%, which is consistent with the frequency responses of the displacement transducer (at 100 Hz) in Figure 7.8. That is, the estimation of the dynamic amplitude of the wall displacement (at the tie-back level) is really about right. The phase lags of the displacement fluctuations are not compared due to the influence of slip during shaking.

221

7. The error of estimated residual tilt of the retaining wall may vary from test to test due to additive or compensating errors. The errors include

- the error in estimated amount of slip per cycle;
- the tilt due to the earthquake-induced static load increment;
- the error of modeled slip in the early load cycles.

7.2.3 Summary

The tilt of the retaining wall was well estimated by the lumped-mass-sliding-block model. The analyzed dynamic tilt and plastic tilt per cycle due to slip at slider are reasonably close to observations. However, some important issues associated with this model should be considered:

1. The spring constant and the damping coefficient of the soil backfill

   These parameters are back-calculated from results of non-slip tests in this study. Uncertainties associated with other situations may increase.

2. The assessment of the yield load of the system.

   The analysis of the amount of slip per cycle is heavily influenced by the yield load of the slider. The input yield load for the sliding-block model in this study is obtained from the observed load at slider in each test. Dramatic change in predicted slip may occur if the yield load is not reasonably assessed.

3. The influence of static (average transient) load increment during an earthquake.

   The increase in the static load during an earthquake has significant influence on the residual tilt of the wall. Case I ignores the process of static load increase

222

during an earthquake. Case II assumes a linear static load increase during its entire duration. Compared to Case II, the assumption in Case I has the following effect on the analysis of the tilt in the retaining wall:

- the additional computed slip in the early load cycles prior to the occurrence of real slippage; and

- the overestimation of slip during intermediate load cycles.

These influences have compensating effects on the residual tilt of the wall. However, the first effect is far more important than the other.

This chapter presented a lumped-mass-sliding-block model to investigate the plastic tilt of the retaining wall during the slip tests. The estimations are reasonably close to the observations. This model is potentially applicable to estimate the tilt or displacement of a retaining wall during true earthquakes. Improvement for the predictability of this model is beyond the purpose of this research. However, two suggestions for improving this model are presented as references for future study:

1. Implement relationships for damping coefficient and spring constant as functions of shear strains

2. Include the actual (or numerically predicted) incremental average transient earth thrust during load cycles.

223

Table 7.1 : Interpreted spring constant and damping coefficient of the soil-wall assembly in Tests with no Slippage at Slider

(Mass of the assembly = 2.0 kg)

Test No	Peak Inp. Accel (g)	Phase Lag (degrees)	$\frac{(A6-A4)max}{(A4)max}$	Spring Const k1 (kN/m)	Coeff. of Damping C (kg/s)	Damping Ratio β
2a	0.05	45	1.157	831	1030	0.206
1a	0.06	50	1.020	702	984	0.214
4b	0.06	40	0.876	714	709	0.153
3a	0.085	55	1.299	773	1340	0.278
5b	0.09	60	1.153	640	1258	0.287
2b	0.1	60	1.443	754	1574	0.331
1b	0.115	60	1.706	858	1860	0.367
4c	0.12	60	1.691	852	1843	0.365
6b	0.13	60	1.371	726	1495	0.320
2c	0.135	60	1.449	756	1580	0.332
Average		55	1.366	803	1367	0.287
use		60	1.365	723	1486	0.319

Table 7.2: Summary of horizontal wall displacement in prototype scale using Lumped-Mass-Sliding-Block Model

Test	Peak Input (g)	Yield Load (N)	Load cases in model	Slip per cycle modeled[1] (mm)	Slip per cycle observed[2] (mm)	Slip per cycle modeled/observed	Residual Displacement modeled (mm)	Residual Displacement observed (mm)	Residual Displacement modeled/observed	Dyn Amp observed/modeled
1b	0.1	540	Case I	9.4		1.38	78.4	30.0	2.61	0.615
			Case II	7.5	6.8	1.10	61.9		2.06	0.615
2d	0.2	770	Case I	15.2		1.88	135.5	51.6	2.63	0.580
			Case II	8.0	8.1	0.99	45.2		0.88	0.580
3b	0.22	830	Case I	29.8		1.06	193.5	180.5	1.07	0.643
			Case II	13.7	28.0	0.49	101.6		0.56	0.643
1c	0.25	635	Case I	41.8	[3]	1.24	371.0	[4]	0.87	- [3]
			Case II	27.3	33.6	0.81	235.1	425.8	0.55	- [3]
6a	0.25	775	Case I	31.5		1.31	254.0	186.5	1.36	0.586
			Case II	8.8	24.0	0.37	73.4		0.39	0.586
5a	0.35	1080	Case I	54.0		1.04	461.3	408.0	1.13	0.615
			Case II	21.1	51.7	0.41	195.1		0.48	0.615
Average			Case I			1.27			1.55 [5]	0.608
			Case II			0.76			0.58 [5]	0.608

Note: [1] Average for the last 6 load cycles
[2] Average slip during slip-occurred load cycles
[3] The observed displacement is obtained by integrating the acceleration data.
    The displacement data are not applicable.
[4] The residual displacement obtained by integrating acceleration data is not reliable
[5] Tests 1b and 1c not included

225
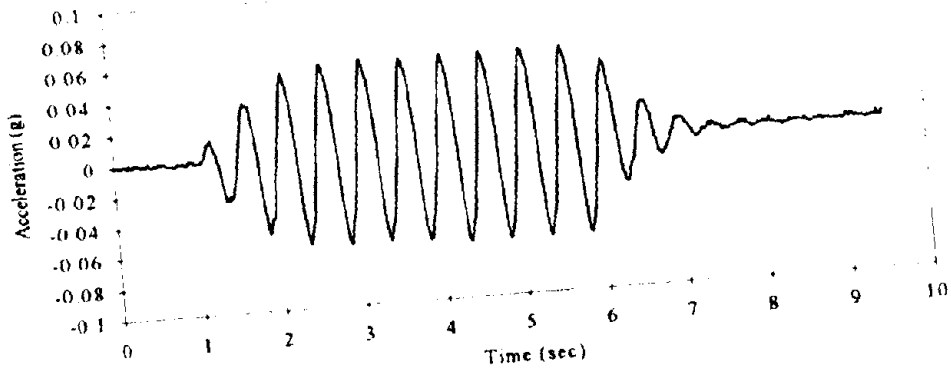
(a) Input acceleration at base (A1)
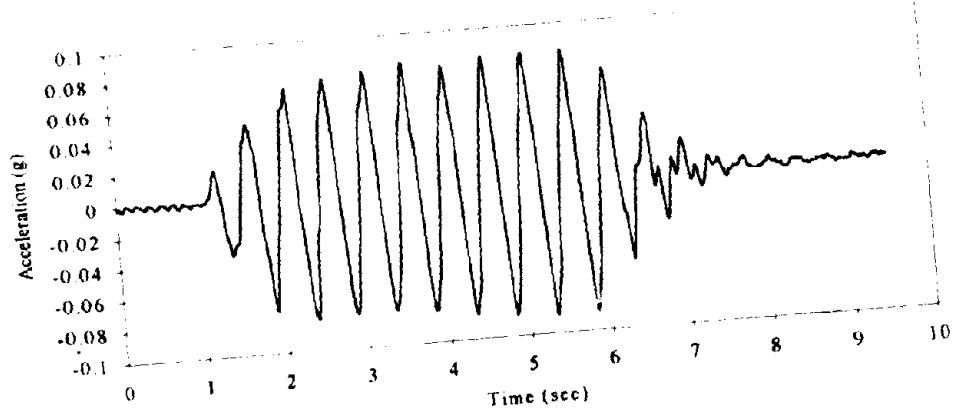
(b) Acceleration at load cell (A4)
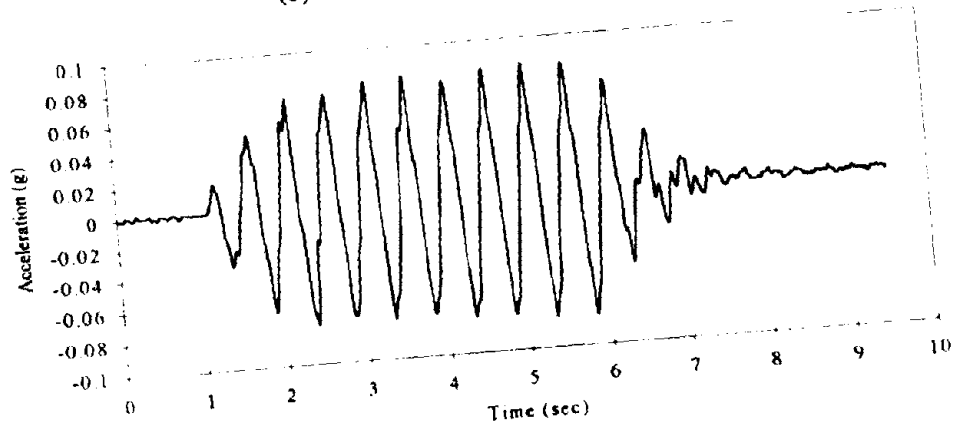
(c) Acceleration at slider (A5)

Figure 7.1: A1, A4 and A5 in Test 1a

226
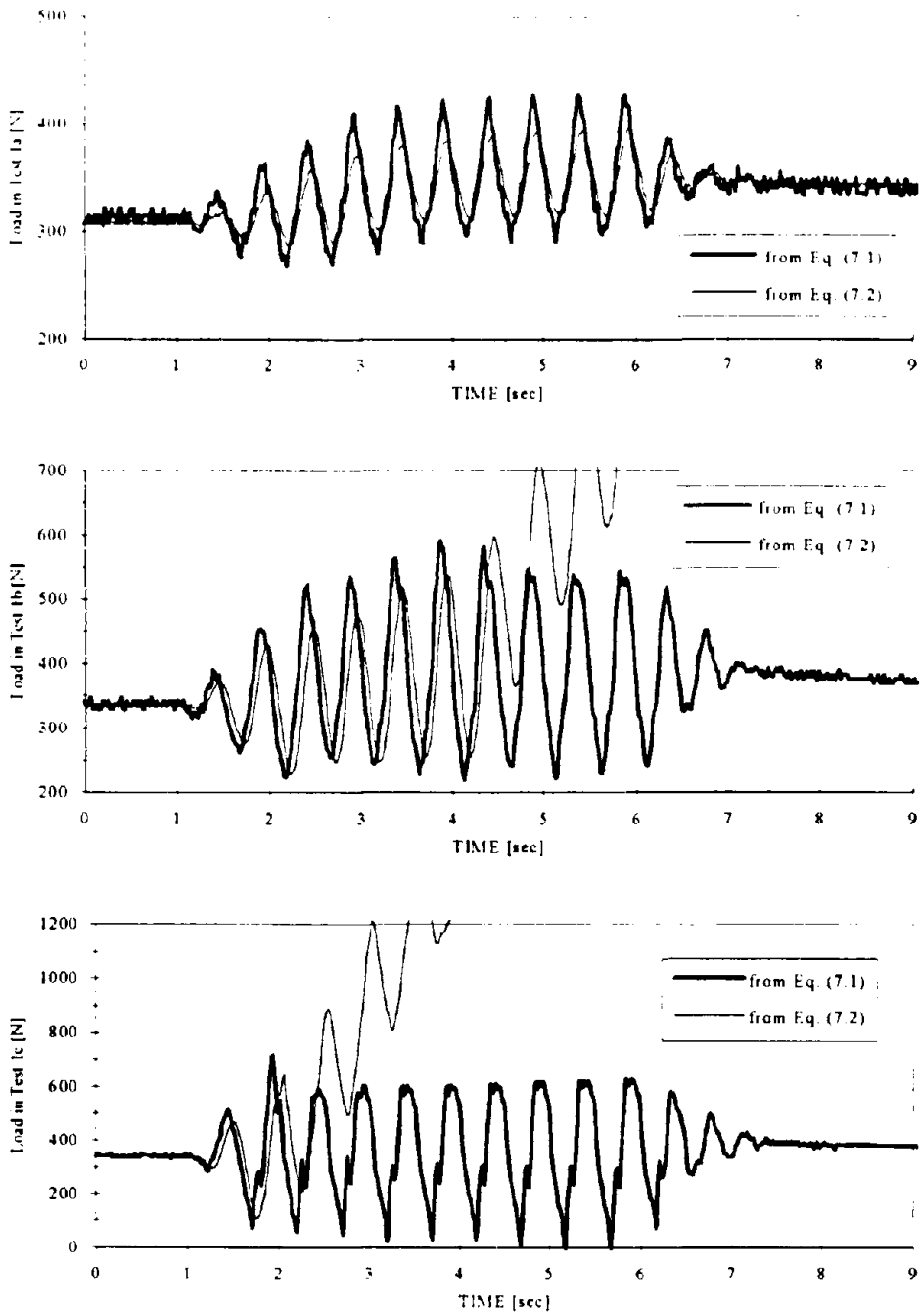
Figure 7.2:   Load at Slider in Tests 1a, 1b and 1c
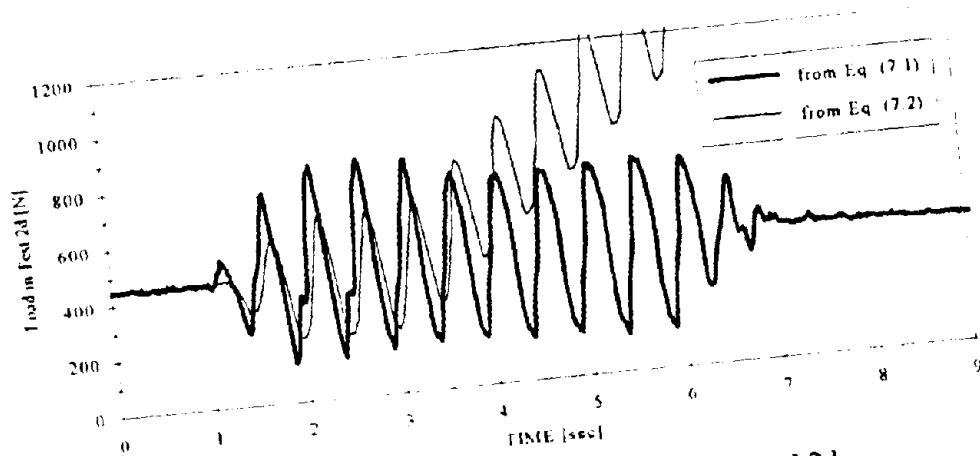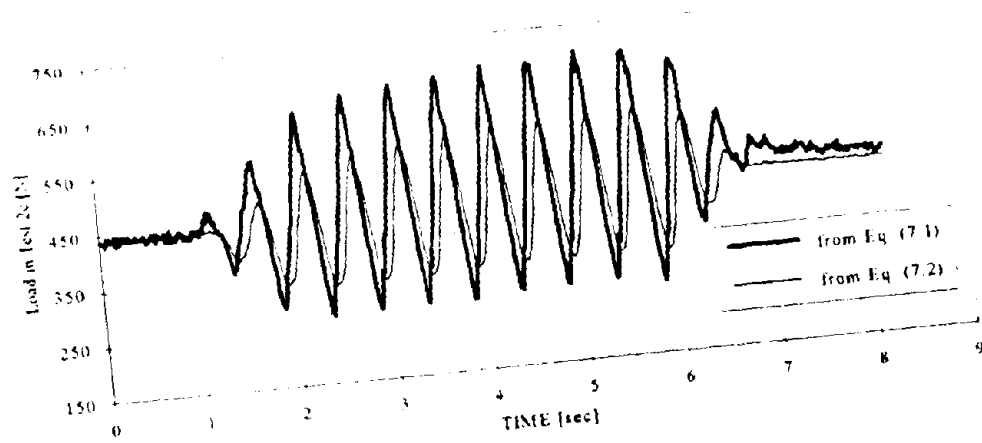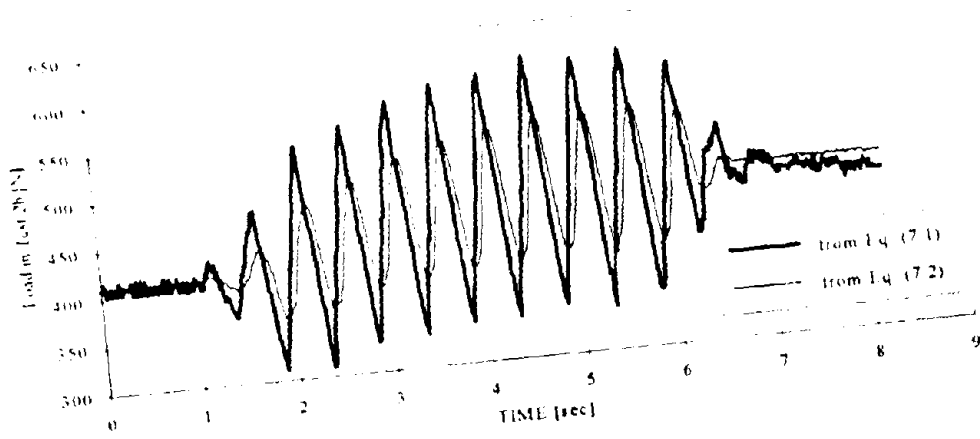
Figure 7.3:   Load at Slider in Tests 2b, 2c and 2d

228
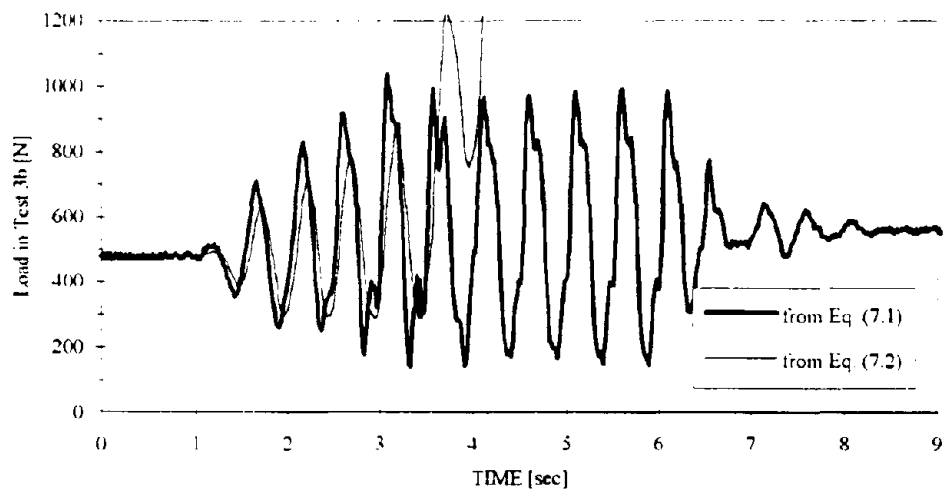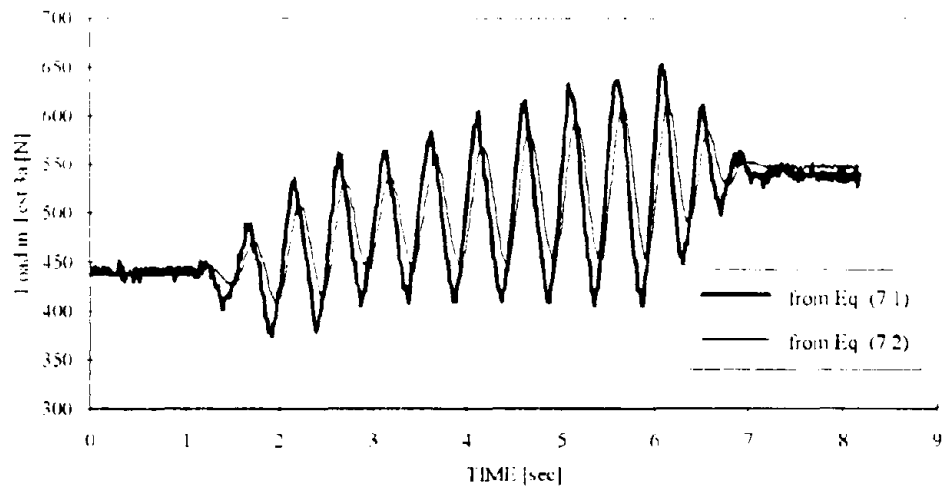
Figure 7.4:   Load at Slider in Tests 3a and 3b
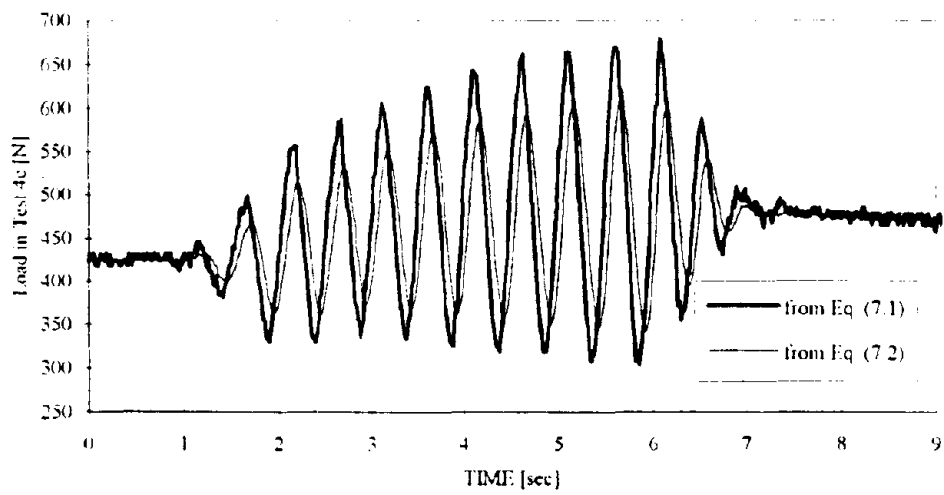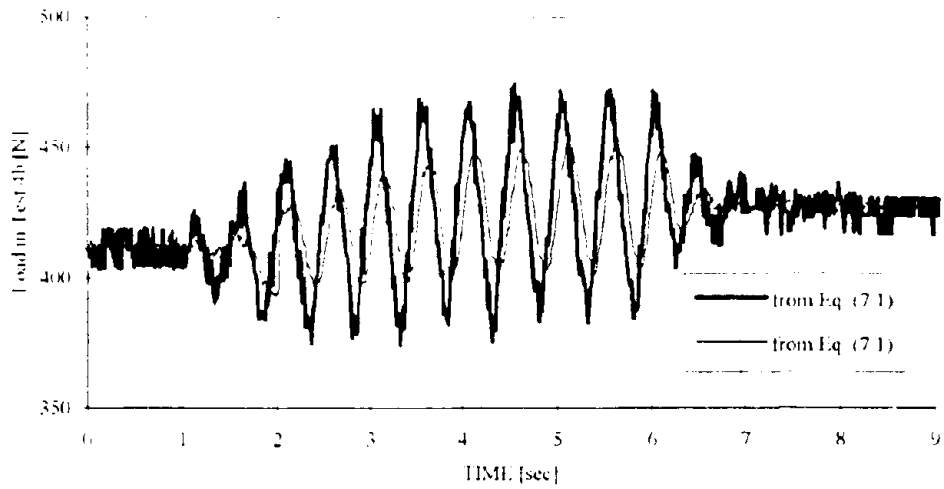
Note Record of load cell in Test 4a was failed

Figure 7.5:   Load at Slider in Tests 4b and 4c
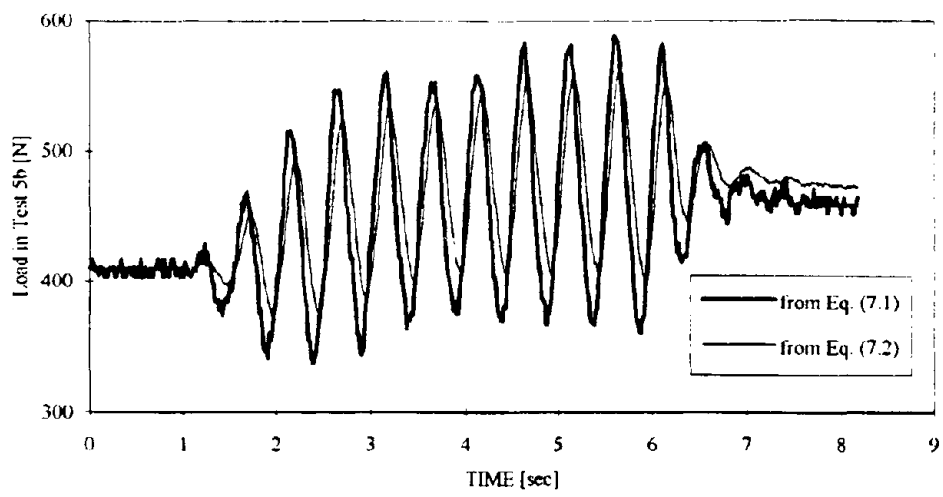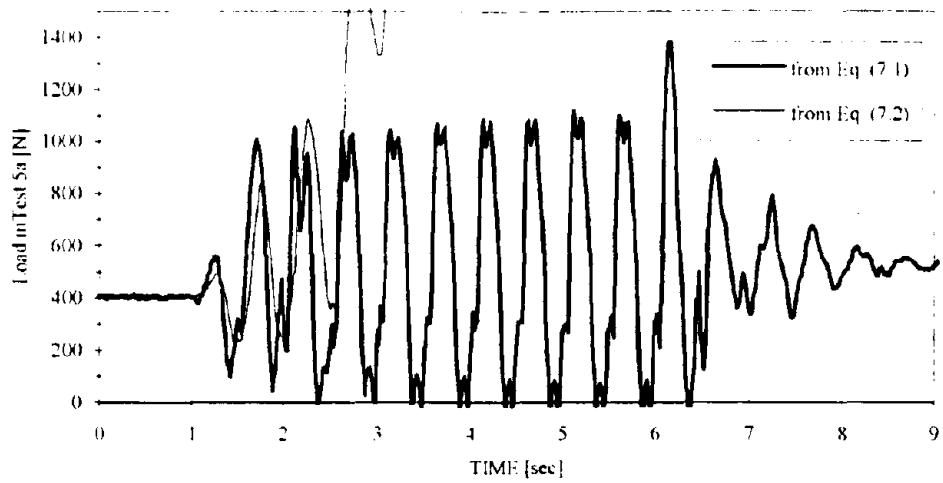
Figure 7.6:   Load at Slider in Tests 5a and 5b
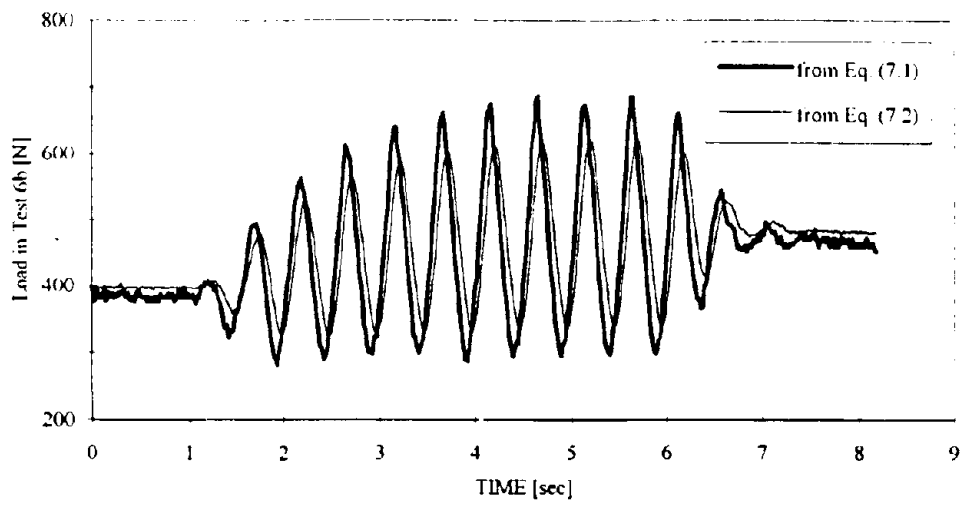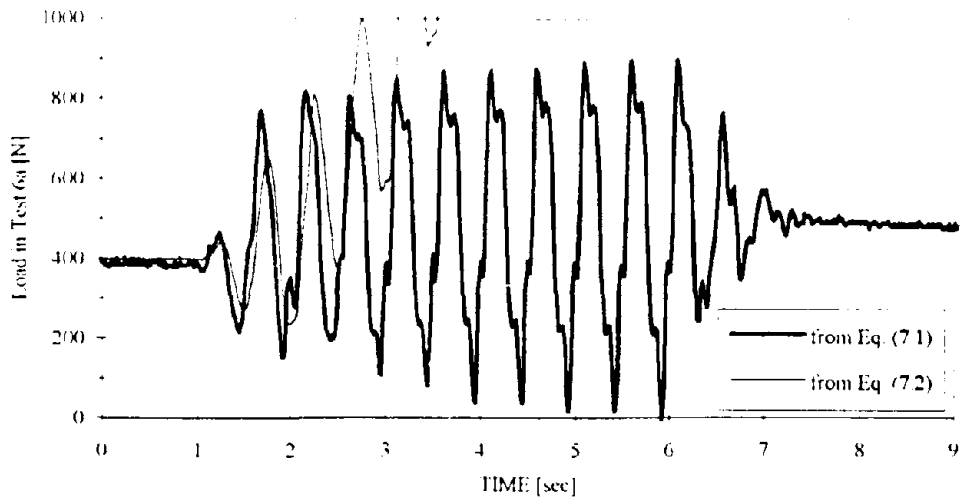
Figure 7.7: Load at Slider in Tests 6a and 6b
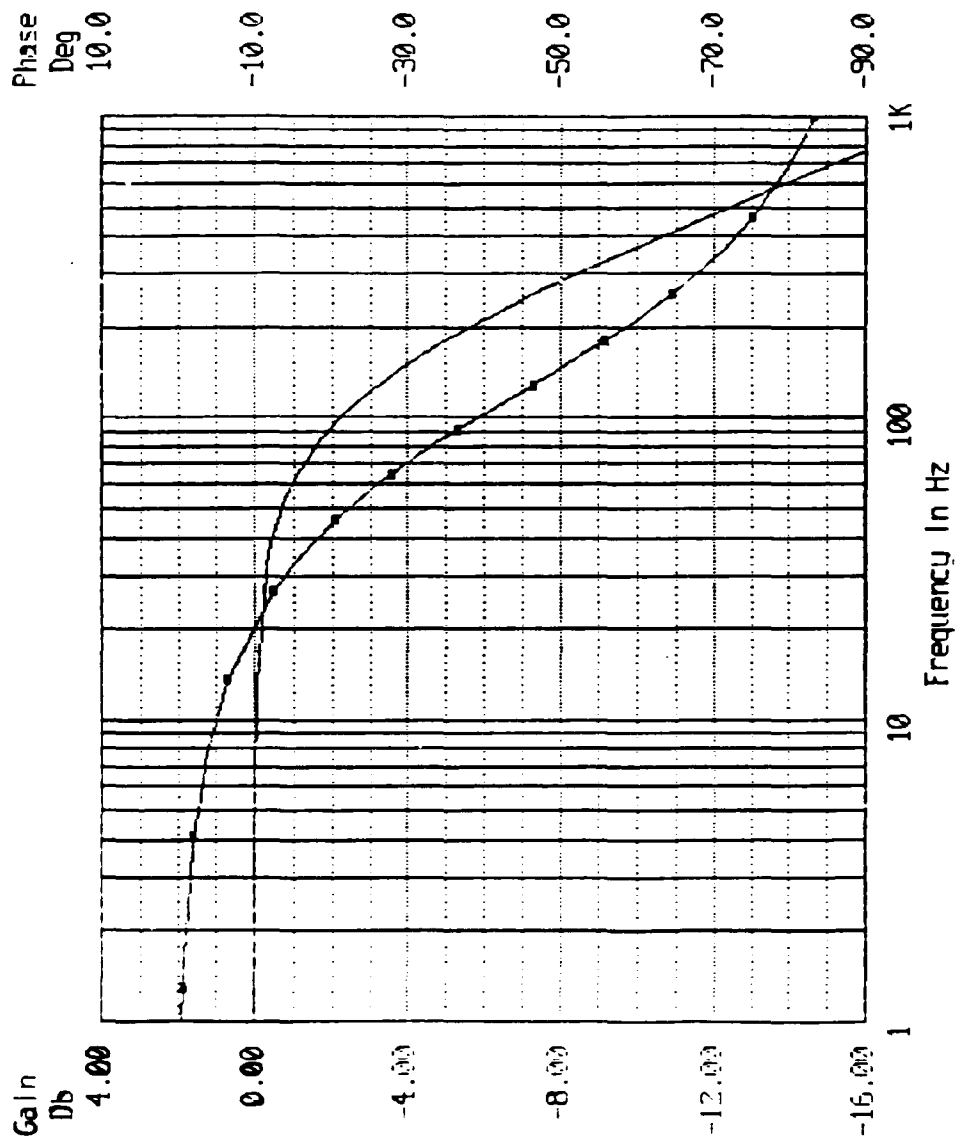
Figure 7.8   Frequency Response of Displacement Transducer
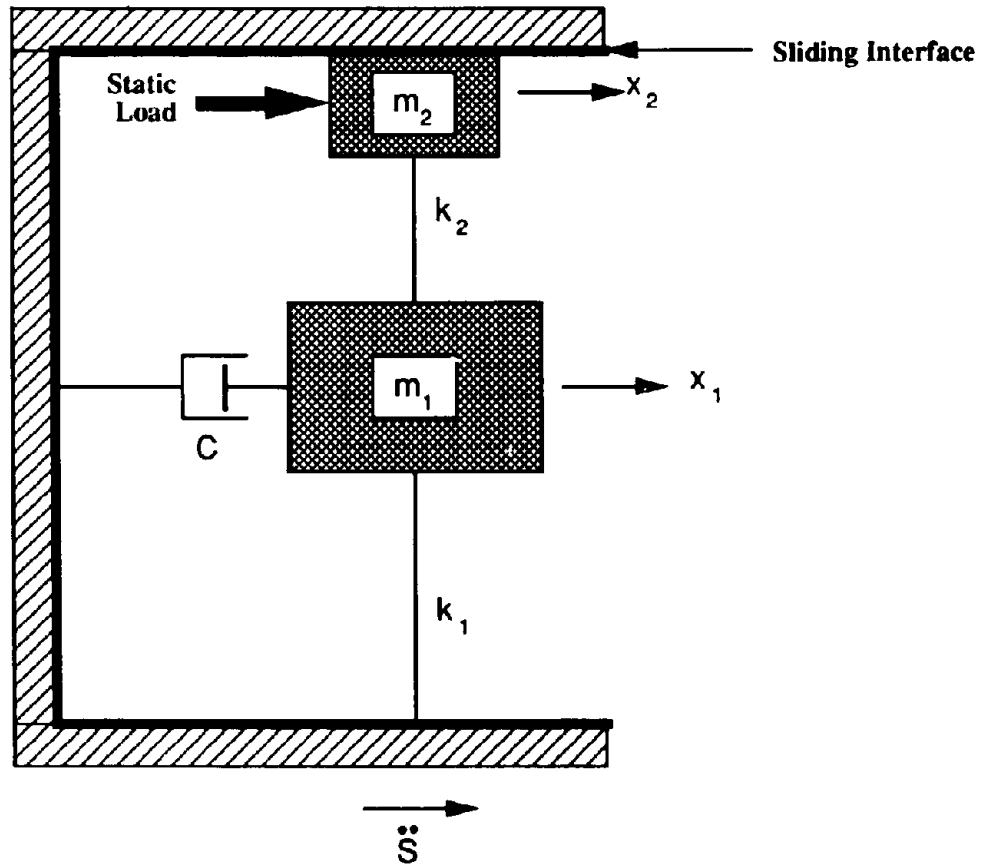
Figure 7.9: The Lumped-Mass-Sliding-Block Model

234
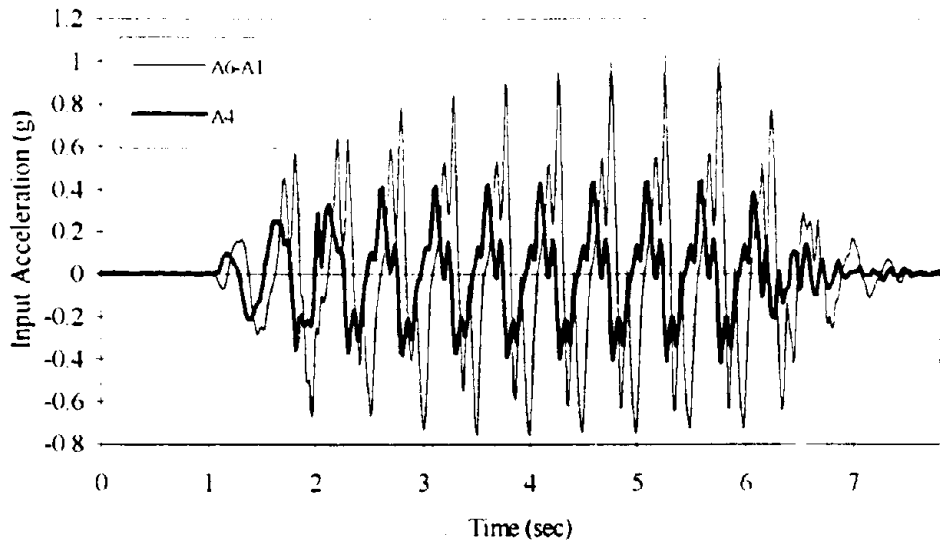
(a) Test 1c
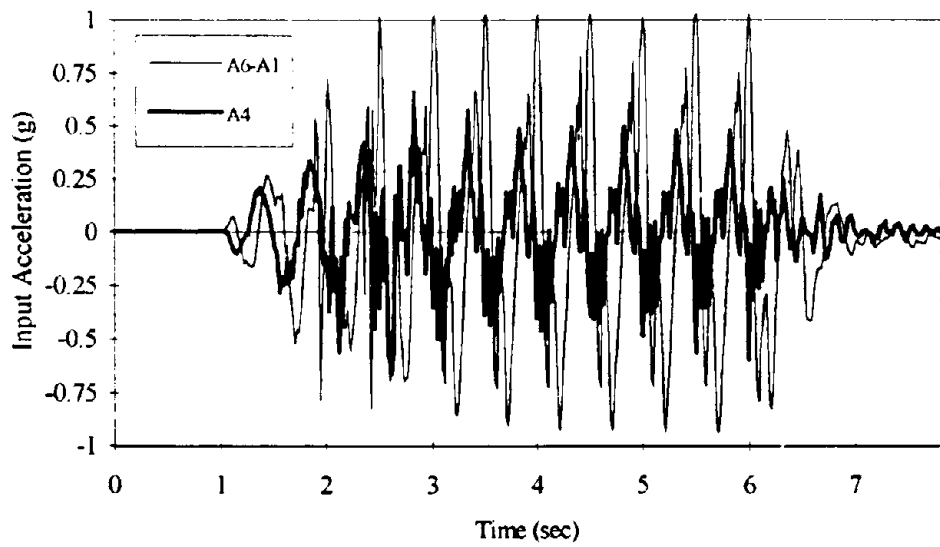
(b) Test 4a

Figure 7.10: (A6-A1) and A4 in Tests 1c and 4a
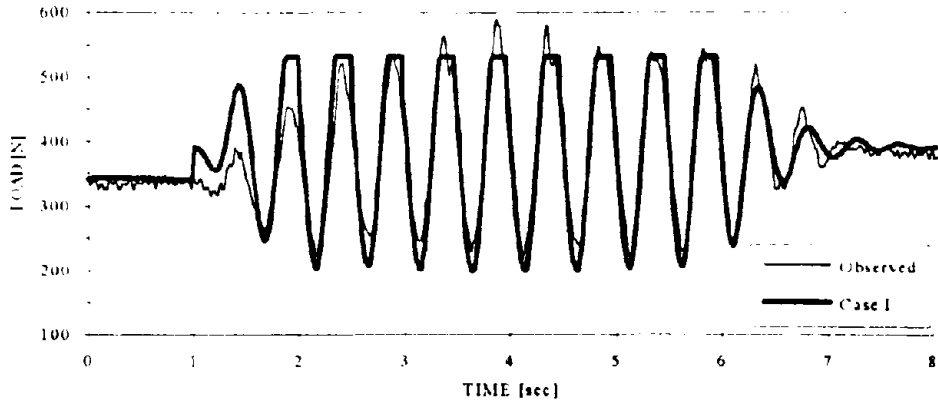
235

(a) Force at slider -- Case I
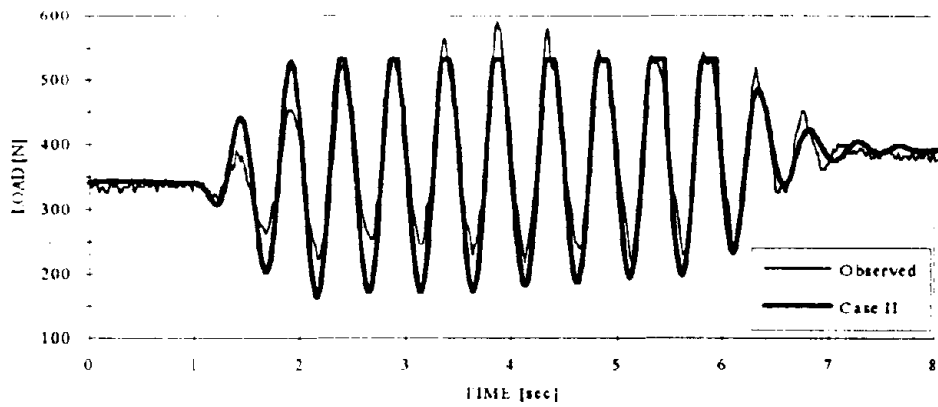
(b) Force at slider -- Case II
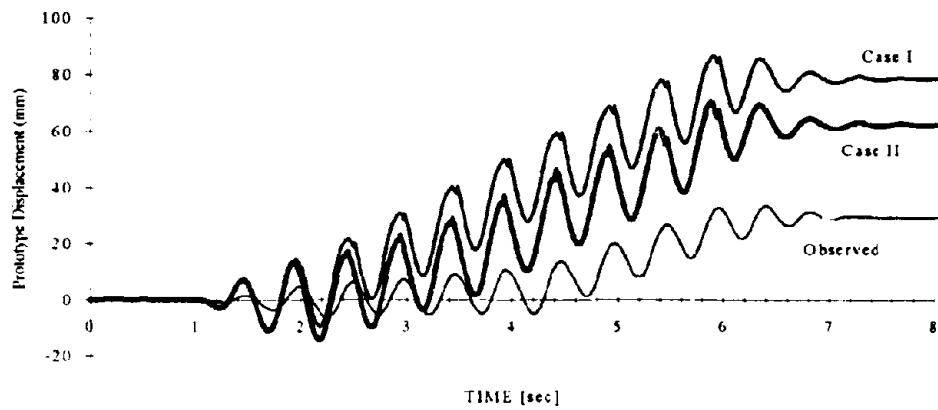
(c) Horizontal wall top displacement

Figure 7.11: Force at slider and horizontal wall top displacement in Test 1b
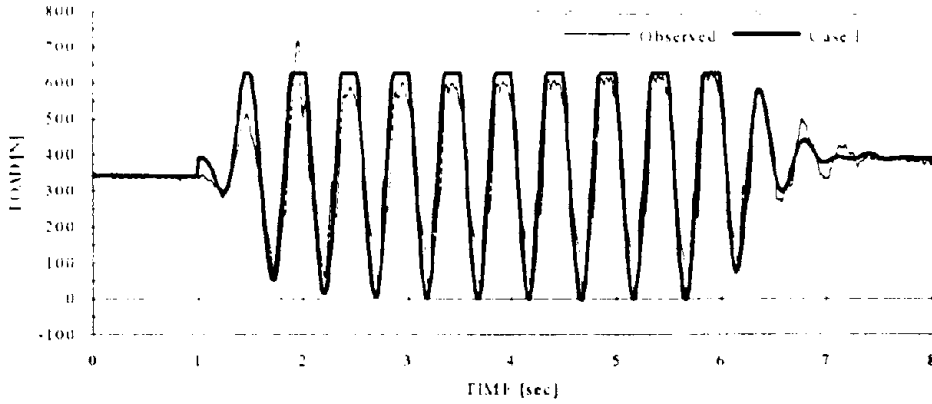
(a) Force at slider -- Case I
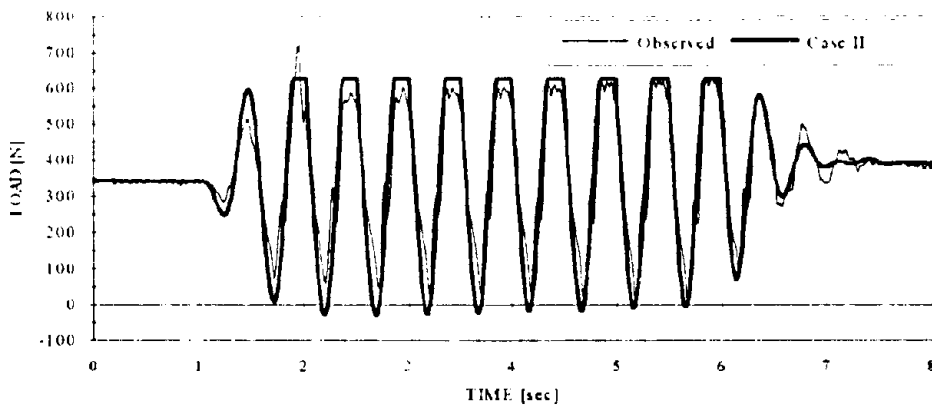
(b) Force at slider -- Case II
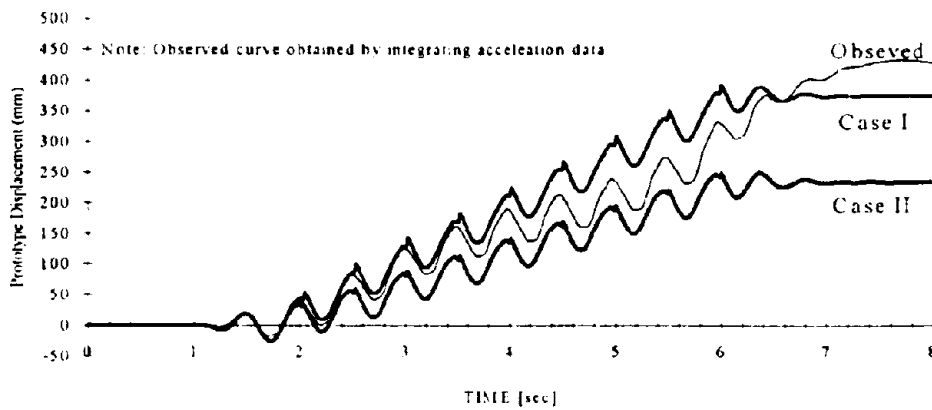
(c) Horizontal wall top displacement

Figure 7 12 Force at slider and horizontal wall top displacement in Test 1c
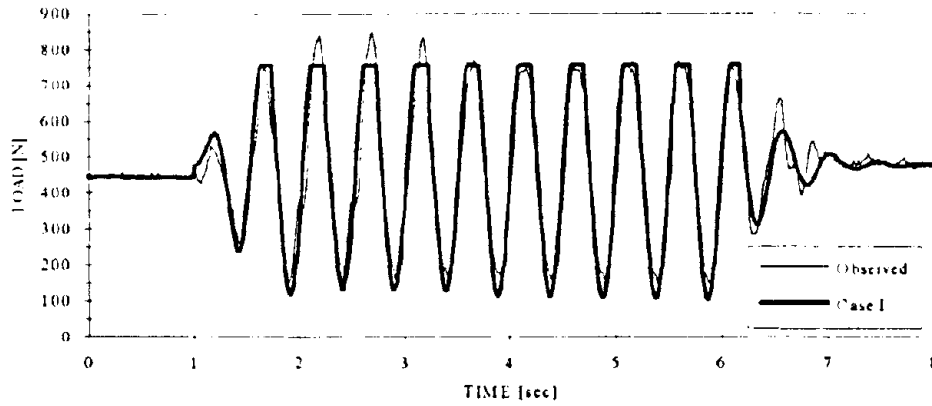
(a) Force at slider -- Case I
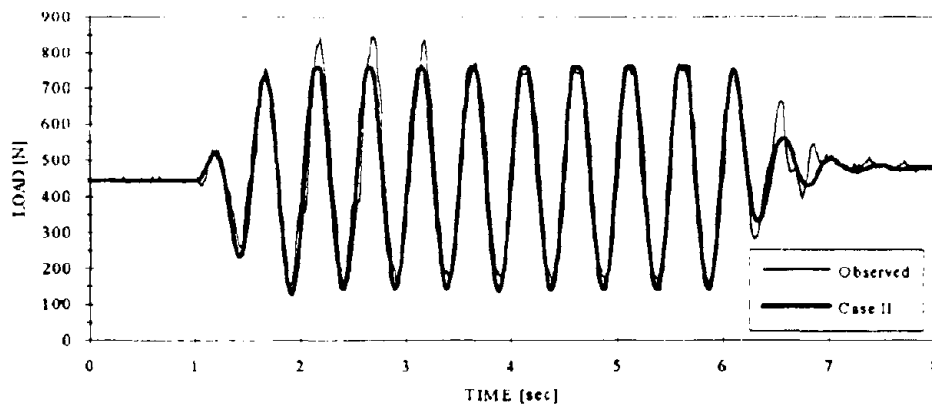
(b) Force at slider -- Case II
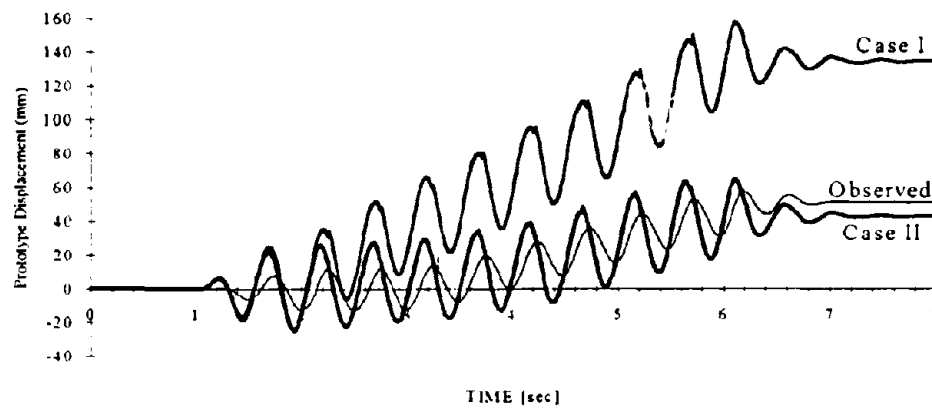
(c) Horizontal wall top displacement

Figure 7.13: Force at slider and horizontal wall top displacement in Test 2d
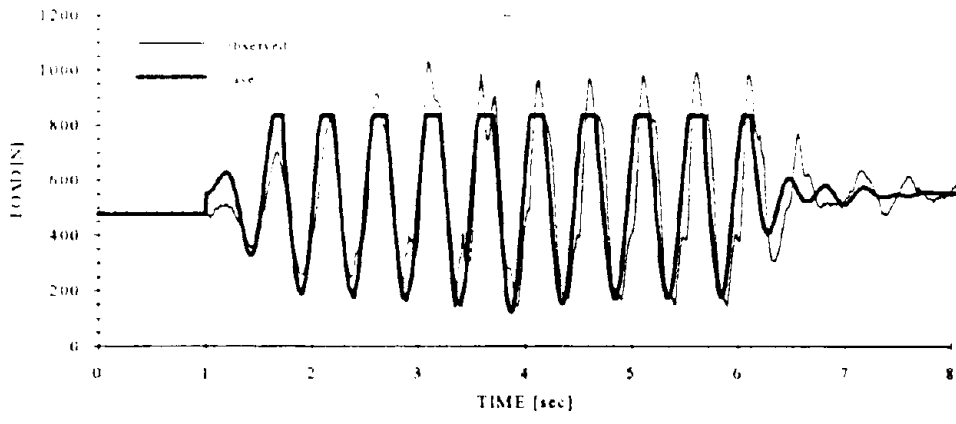
(a) Force at slider -- Case I
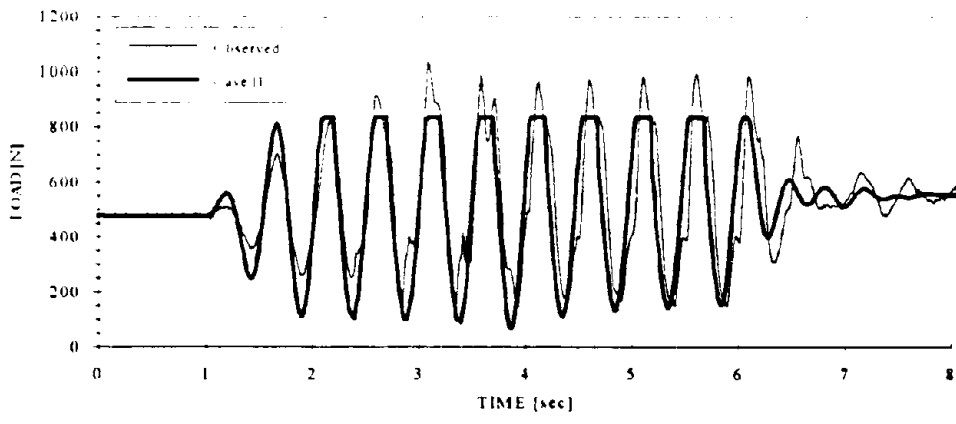
(b) Force at slider -- Case II
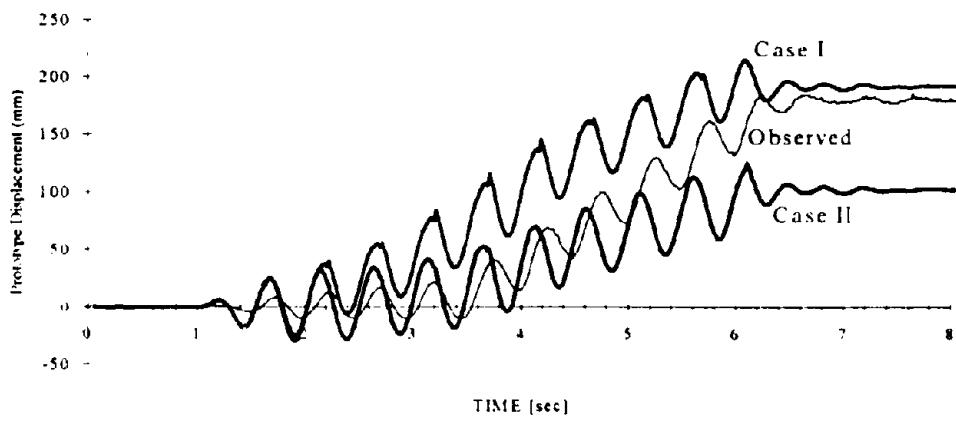
(c) Horizontal wall top displacement

Figure 7.14: Force at slider and horizontal wall top displacement in Test 3b
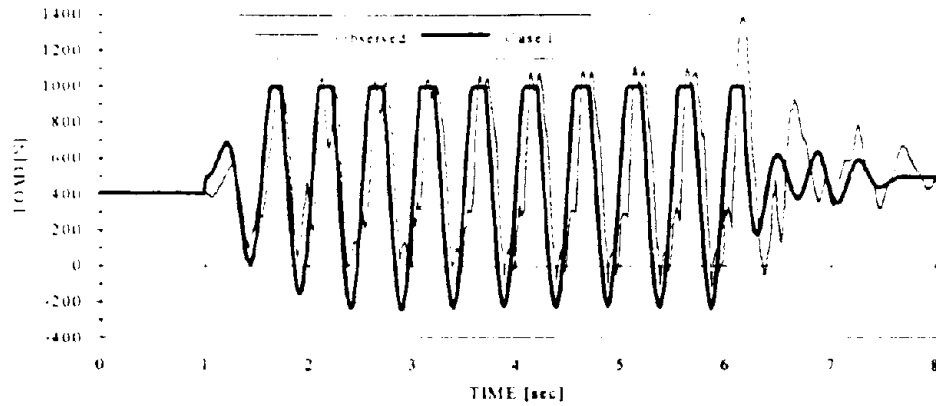
239

(a) Force at slider -- Case I
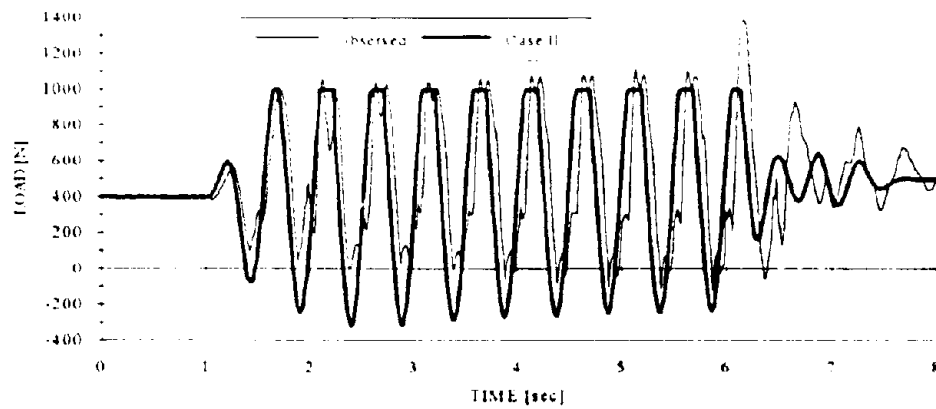
(b) Force at slider -- Case II
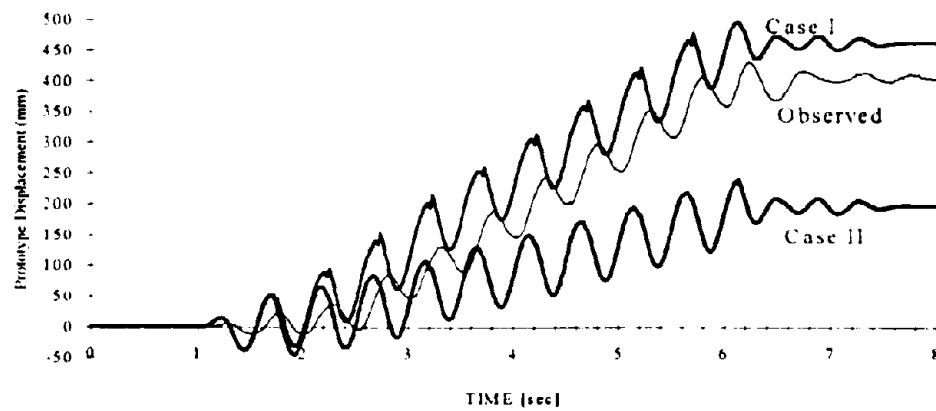
(c) Horizontal wall top displacement

Figure 7.15 Force at slider and horizontal wall top displacement in Test 5a
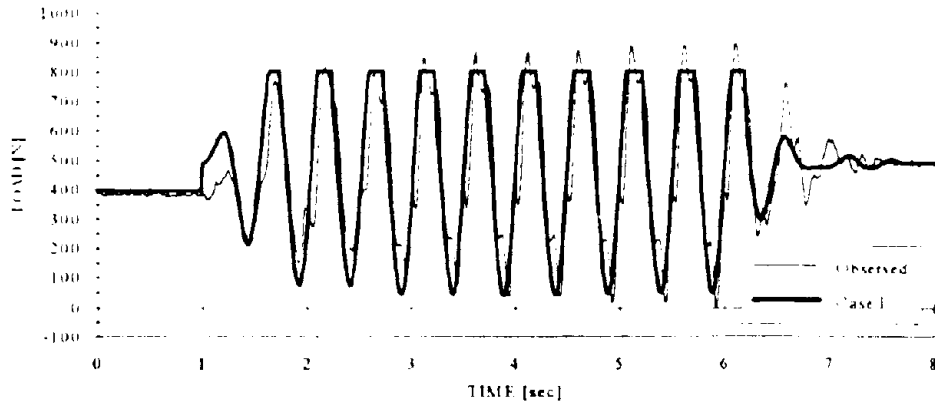
(a) Force at slider -- Case I
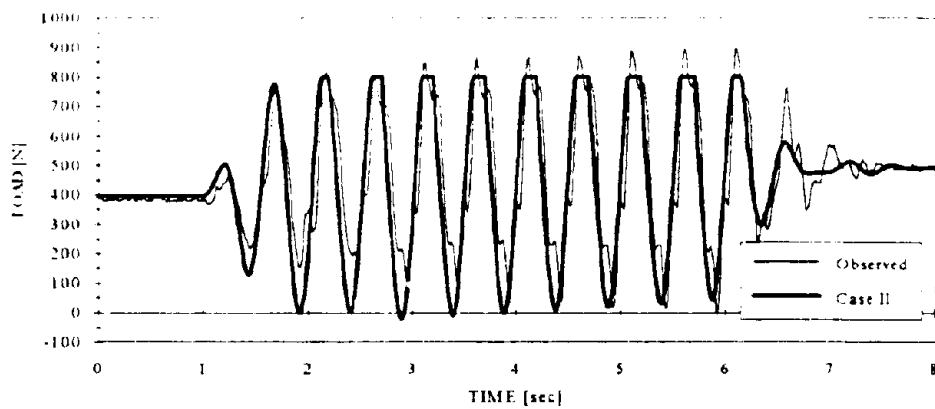
(b) Force at slider -- Case II
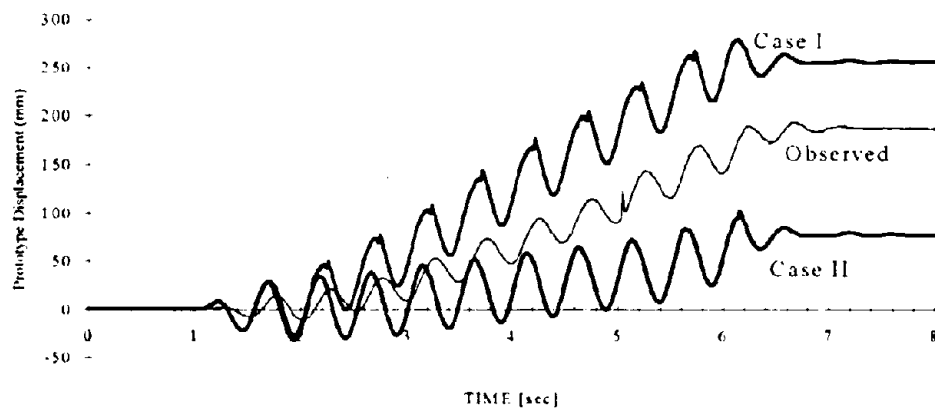
(c) Horizontal wall top displacement

Figure 7.16 Force at slider and horizontal wall top displacement in Test 6a

241

Page Intentionally Left Blank

CHAPTER 8

SUMMARY AND CONCLUSIONS

8.1 PURPOSE AND SCOPE OF RESEARCH

The primary objective of the research was to investigate the behavior of a retaining wall supporting a liquefiable backfill -- both the response of the backfill soil and its interaction with the wall. The secondary objective was to verify the capability of a particular numerical model for predicting the behavior of a liquefiable soil during earthquakes. These two objectives were carried out by performing: (1) dynamic tests on a specially designed centrifuge model involving a retaining wall and a saturated sand backfill; and (2) numerical predictions for the behavior of the model during the dynamic centrifuge tests, followed by extensive evaluations of the numerical predictions.

Dynamic centrifuge tests were performed on a saturated sand (Nevada #120) backfill supported by an idealized retaining wall that was hinged at the base and supported by an elasto-plastic tie-back near the top. The plastic behavior of the tie-back was provided by a slider that could slip and result in an elongation of the tie-back when the load exceeded the shear resistance of the slider. Eighteen tests were carried out on six models prepared at two relative densities: 60% and 75%. Artificial earthquakes were applied to these models with ten cycles of more or less sinusoidal excitation at various intensities (0.05 ~ 0.35g). The tie-back failed temporarily during strong earthquakes

(horizontal peak acceleration greater than about 0.20g)[1]. The failure in the tie-back was characterized by the slippage at the slider that caused an extension of the tie-back and a consequent plastic tilt of the retaining wall.

The centrifuge model tests were divided into two groups depending on whether slippage occurred: slip tests and non-slip tests. Chapter 6 discussed the major behavior of the model in non-slip tests -- (1) the earthquake-induced pore pressure changes; and (2) the earth and water thrusts acting on the wall during and after earthquakes. Chapter 7 discussed the major behavior of the model in slip tests -- the amount and characteristics of slippage at the slider.

The centrifuge model tests were carried out with quality controlled procedures. The results were reliable for the purpose of verifing numerical techniques. A series of "class A" predictions for the centrifuge model tests were made using a finite element code, CYCON, developed by Bouckovalas (1982) and Stamatopoulos (1989) at M.I.T. The investigation of numerical predictions was presented in Chapter 5.

To summarize, this research accomplished the following achievements regarding the centrifuge testing phase and the numerical prediction phase:

I. Centrifuge testing phase (dynamic model testing and analysis of the test results):

1. Developing a technique for preparing highly saturated sand models for dynamic centrifuge testing -- Chapter 3

---

[1] The input accelerations in the centrifuge model tests were either smaller than 0.135g (in non-slip tests) or greater than 0.2g (in most slip tests).

2. Building an idealized retaining wall and performing dynamic centrifuge tests on it -- Chapter 4

3. Classification of liquefaction conditions (liquefaction, quasi-liquefaction and liquefaction-free) -- Chapter 4

4. Studying the interaction between the retaining wall and the soil backfill -- Chapter 6

5. Characterizing the cyclic pore pressure variation within saturated sand during cyclic shearing -- Chapter 6

6. Evaluating the pore pressure build-up during cyclic shearing -- Chapter 6

7. Evaluating the earthquake-induced changes in earth and water thrusts acting on the retaining wall -- Chapter 6

8. Verification of the estimations of dynamic earth and water thrusts using Mononobe-Okabe and Westergaard equations -- Chapter 6

9. Establishing a lumped-mass-sliding-block model to analyze the amount of extension of the tie-back during strong earthquakes -- Chapter 7

II. Numerical prediction phase:

10. Performing a set of "class A" predictions (using CYCON) for the behavior of the saturated backfill behind the model retaining wall during centrifuge testing -- Chapter 5

11. Establishing a set of quantitative criteria to evaluate numerical predictions for the behaviors of soils during dynamic centrifuge tests in a systematic fashion -- Chapter 5

12. Evaluating the CYCON predictions with the quantitative criteria -- Chapter 5

The results show that the numerical code CYCON is good at predicting both the tilt of the retaining wall (in non-slip tests) and the excess pore pressures in the saturated

Nevada sand. The tilt of the retaining wall was better estimated by CYCON using parameters obtained from cyclic DSS tests than by using parameters from triaxial test data (Table 5.14).

Based upon the above analyses, this research disclosed some "scientific" findings regarding the response of a liquefiable backfill behind a retaining wall and the interaction between the soil and the wall during earthquakes. These scientific findings are summarized in the following section.

8.2   SUMMARY OF SCIENTIFIC FINDINGS

This research included three variables in the testing program: relative density of the sand, earthquake intensity and permeability. Two soil models[2] were prepared at a relative density of 60% and four models[3] were prepared at a relative density of 75%. One model[4] was saturated with a glycerol solution. The permeability of this model was smaller than other models using water as pore fluid by one order of magnitude. The testing results indicated that the lower permeability has a significant effect on pore pressure build-up (Chapter 6). However, this effect of permeability was not investigated throughly[5]. The test results did not show a significant effect of the relative density of the soil. The effect of earthquake intensity is significant. Some findings were made as to the behavior of a retaining wall supporting a saturated sand backfill, based on the effect of the earthquake intensity. They are summarized as follows:

---

[2] No. 1 and 4.

[3] No. 2, 3, 5 and 6.

[4] No. 3.

[5] The test data were not enough to identify the effect of pore fluid permeability quantitatively, due to limited test data.

I. Liquefaction and ground acceleration:

A liquefied soil has two major characteristics:

   (1) the excess pore pressure reaches the initial vertical effective stress

   (2) the ground acceleration cannot be transm itted through such a soil.

The soil models in this research never fully liquefied throughout the entire thickness. Local liquefaction near the surface of the backfill was observed in some tests with strong earthquakes. However, the test data show that the soil, in some cases, could still transmit the ground acceleration even though the excess pore pressure reached the initial vertical effective stress (σ'_{vo}). Therefore, the three conditions of a liquefiable soil during an earthquake are classified as follows in Section 4.3.1:

Soil conditions	Δu	Able to transmit ground acceleration	Peak input base acceleration[6]
Liquefaction-free	$< \sigma'_{vo}$	Yes	$< 0.07g$
Quasi-liquefaction	$= \sigma'_{vo}$	Yes	$0.07g \sim 0.20g$
Liquefaction	$= \sigma'_{vo}$	No	$> 0.20g$

The accelerations in the final column apply only to Nevada sand in the given configuration in this thesis

II. Threshold acceleration for pore pressure build-up:

Section 6.3.1 and Figure 6.25 indicate that there is a threshold ground acceleration for the pore pressure build-up. That is, there is no pore pressure build-up during weak earthquakes with peak ground acceleration less than the threshold acceleration. In this research, the threshold acceleration (at the base of the soil) for pore pressure build-up in Nevada sand is found to be 0.04g.

---

[6] These accelerations are applicable to the initial shaking of a soil model. In some tests involving a soil densified by several previous shakings, such as 2e and 2f, the soil was quasi-liquefied even though the peak accelerations were larger than 0.2g

247

III. Threshold strain for pore pressure build-up:

Figure 6.27 shows that there is a threshold cyclic shear strain for the pore pressure build-up. This threshold strain is 10^{-2}% for Nevada sand, which is similar to a value for two other sands found by Dobry et al. (1981) (Figure 6.26). The relationship between the amount of pore pressure build-up and cyclic shear strain is similar for Nevada sand and the other two sands in Figure 6.26.

IV. Loosening of soil skeleton versus earthquake intensity

Figure 6.24 reveals that the amount of soil skeleton loosening increases at a greater rate than peak input ground acceleration (Section 6.3.1). A set of hypothetical contours of normalized (to earthquake intensity) dynamic response of the soil skeleton is postulated in Figure 6.31 according to this observation.

V. Phase relations between the ground acceleration and the dynamic earth and water thrusts

A. Phase lags related to soil skeleton

Figure 6.32 shows clearly that the phase of the lateral acceleration in the backfill soil had changed as shear waves propagated from the base of the soil model. The phase lag of the ground acceleration affected significantly the phase of the dynamic earth thrust acting on the retaining wall. Figure 6.34 shows that the soil skeleton thrust was approximately in phase with the ground acceleration near the surface.

B. Phase lags related to hydrodynamic pressure

As a result of soil-wall interaction, the hydrodynamic pressure was significantly affected by the retaining wall. Figure 6.32 indicates that the hydrodynamic pressure was almost in phase with the peak angular velocity of the inward tilting of the retaining wall.

VI. Estimations for dynamic earth thrusts:

As indicated by the above observation and Section 6.3.2, the Mononobe-Okabe (M-O) and Westergaard equations, (6.13) and (6.15), did not work in estimating the dynamic thrusts from the soil skeleton ($\Delta P_{\bar{p}}$) and the pore fluid (ΔP_u) (Figure 6.37).

This is believed to result from the interaction between the backfill soil and the retaining wall: the cyclic tilting of the wall affected the fluctuation of the pore pressure thrust, which further affected the thrust from the soil skeleton. However, Eq. (6.16), an equation combining the M-O and Westergaard equations provides good estimates of the total dynamic earth thrust (ΔP) as demonstrated in Figure 6.36. This estimation is also effective for the one test with a lower permeability.

VII. Estimation of slip at the slider (amount of "yielding" of the tie-back):

Chapter 7 demonstrates that the amount of slip at the slider can be estimated with a lumped-mass-sliding-block model that involves two lumped masses: one representing the mass of the retaining wall plus a partial mass of the soil; and the other representing the part of tie-back that may slip during strong earthquakes. With reasonable model parameters, the lumped-mass-sliding-block model offers good estimates for the amount of slip.

8.3   FACTORS AFFECTING THE PLASTIC TILT OF A RETAINING WALL

The model retaining wall in this research generally resembled an idealized anchored sheet pile wall, although the mass associated with the wall was large compared to that of sheet piling. This section discusses the conditions related to the tilt of a retaining wall based upon the results of the centrifuge model tests. Base failures of earth retaining structures are also important; however, the investigation of such situations was beyond the scope of this research. Nevertheless, the fundamental characteristics of a retaining wall and of the backfill included in the following discussion are helpful to understanding the characteristics of actual retaining structures.

Earthquake-induced failures of retaining walls generally result from excessive plastic tilting or displacements of the walls. This research demonstrated that the amount of plastic tilting of a retaining wall was related to both the strength of the wall and tie-back system and to the transient total thrust acting on the wall during an earthquake. The

model retaining wall tilted plastically during strong earthquakes as a result of temporary yielding of the tie-back. The amount of the plastic tilt was directly related to the transient total thrust on the wall, the strength of the wall (the shear resistance of the slider), and the number of cycles in which the transient force exceeded the shear resistance.

The transient total thrust acting on a retaining wall during an earthquake is related to the static and dynamic earth and water thrusts (Mononobe-Okabe and Westergaard thrusts), the build-up of pore pressure, and the inertial thrust related to the wall itself. The dynamic thrusts and wall inertia are functions of the earthquake intensity. The major factor that controls the amount of plastic tilt of a given retaining wall during a predefined earthquake is the pore pressure build-up during the earthquake. Generally, the build-up of pore pressure causes a gradual increase of the average transient thrust acting on the wall[7]. Chapter 7 demonstrated that the amount of plastic tilt of the retaining wall is heavily affected by the increment of average transient thrust during an earthquake. During the non-slip centrifuge model tests, the average transient thrust increment caused by the pore pressure build-up ranged from 3% to about 25% of the initial static thrust[8], while the intensity of the earthquake ranged from 0.05g to about 0.13g, respectively (from Table 6.2). The significance of the pore pressure build-up increased during stronger earthquakes. When the soil is fully liquefied, as in an extreme case, the pore pressure build-up might cause an increment of static thrust of about 50 ~ 60% of the initial static thrust and consequently, result in a substantial amount of plastic tilt of the wall.

---

[7] In addition, the pore pressure build-up may decrease the strength of the retaining wall when an anchor is embedded in the liquefiable backfill. However, this point was not explicitly investigated in this research.

[8] The incremental average transient pore pressure thrust (due to pore pressure build-up) was about twice as large as the increment of the average transient total earth thrust. This was due to the decreased soil skeleton thrust during an earthquake - owing to the smaller effective stress.

The build-up of pore pressure in a saturated sand backfill during an earthquake depends on both the characteristics of the seismic shaking, the retaining structure and the soil. The seismic shaking is often characterized by the intensity, frequency and number of cycles. More specifically, for a given backfill material, the pore pressure build-up depends on the following factors: (1) the cyclic shearing strain and number of straining cycles, (2) the relative density of the backfill soil; and (3) the permeability of the pore fluid. The cyclic strain depends on the seismic shaking intensity, the stiffness of the retaining wall, and the relative density as well as the stress state in the soil. The magnitude of permeability will influence the dissipation of excess pore pressure during shaking. Chapter 5 shows that the pore pressure build-up was high in a model using a glycerol solution[9] as pore fluid. Therefore, the following factors should be considered when estimating the pore pressure build-up and the plastic tilt of the retaining wall:

1. permeability

2. the characteristics of the earthquake

   (the intensity, frequency and number of cycles of the seismic shaking)

3. the strength and stiffness of the retaining wall

4. the relative density of the backfill.

8.4 RECOMMENDED CONSIDERATIONS FOR SEISMIC DESIGN OF EARTH RETAINING STRUCTURES

Based on the analyses in Chapters 6 and 7, the following simple tools are tentatively suggested for the seismic design of earth retaining structures. Further investigation will be required to ascertain the limits upon the applicability of these suggestions.

---

[9] The permeability of the soil saturated with this solution is equal to 10% of the permeability of water (Chapter 4).

I. Maximum earth thrust on the retaining wall without yielding --

The maximum earth thrust can be calculated by summing up the following:

1. the initial static earth thrust

2. the incremental average transient thrust

3. the peak dynamic earth thrust

The incremental average transient earth thrust may be very large -- 50% of the initial static earth thrust if the soil is liquefied entirely throughout the thickness of the backfill. In this research, as shown in Figure 6.28, the incremental thrusts were generally below 25% of the initial static thrusts since the backfill soil never liquefied entirely (the soil only liquefied near the surface). This observation may well not apply to backfills with smaller permeability.

The dynamic earth thrust will cause a fluctuation in the moment exerted on the wall around the base. The moment due to the peak dynamic earth thrust may be estimated, based on the Mononobe-Okabe Westergaard equation as in Eq. (6.17), using Eq. (8.1)

$$\Delta M_{soil} = \frac{1}{2} \gamma_b w H_s^2 \left(\frac{3}{4} k_h \right) \frac{H_s}{2} + \left(\frac{7}{12} \gamma_w w H_s^2 k_h \right) (0.4 H_s) \qquad (8.1)$$

where w and H_s are the width and the height of the backfill; and k_h is the coefficient of peak horizontal acceleration at the ground surface ($= a_{max}/g$).

II. Modeling the earth's contribution to the dynamic load in the tie-back --

The earthquake-induced tilt of the retaining wall is the result of an excessive dynamic load applied to the supporting system, e.g., a tie-back and an anchor, due to ground acceleration. The two major components of the total dynamic load are from: (1)

252

the wall itself (inertia force); and (2) the backfill earth. The inertia force of wall was important in this research. However, the contribution of the wall inertia towards the total dynamic load applied to the tie-back may vary from site to site. The earth's contribution can be modeled using a lumped-mass-sliding-block model as described in Chapter 7. This model is potentially applicable to estimate the earth's contribution to the plastic tilt of a retaining wall in a general site. The following paragraphs summarize the procedures to estimate the earth's contribution.

Eq. (7.7) is an equation describing a multi-DOF system during cyclic shaking. For analyzing the plastic tilt of a retaining wall, the system can be simplified into a 2-DOF system involving two lumped masses (see Figure 7.9): one (m_1) representing the soil and a partial (or total) mass of the wall, and the other representing a sliding block (m_2) which is a partial (or total) mass of the wall.

The earth's contribution to the mass term m_1 can be estimated from the Mononobe-Okabe-Westergaard equation in Eq. (8.1). Eq. (8.2)

$$\left(m_1\right)_{earth} = \frac{1}{H_{app}}\left[\frac{1}{2}\rho_b wH_s^2\left(\frac{3}{4}k_h\right)\frac{H_s}{2} + \left(\frac{7}{12}\rho_w wH_s^2 k_h\right)\left(0.4H_s\right)\right] \quad (8.2)$$

where H_{app} is the height where $\left(m_1\right)_{earth}$ is applied.

In this model, the spring constant of the soil (k_1) can be estimated following the procedures in Appendix F. The damping coefficient of the soil (c_1) can be estimated from the spring constants and an assumed damping ratio at large cyclic strains (e.g. $\beta = 0.30$) --
$c_1 = 2\beta\sqrt{m_1(k_1 + k_2)}$.

8.5   RECOMMENDATIONS FOR FUTURE RESEARCH

Although the problem of the seismic behavior of a structure retaining a liquefiable backfill has been studied for decades, understanding of the behavior of both the wall and the soil during earthquakes is still limited. This research studied some essential aspects regarding this problem by performing dynamic tests on saturated sand models supported by an idealized retaining wall. Although this research developed approaches to investigating these key aspects, more work is needed to refine the simplified soil-wall models, such as the numerical predictions for sand behavior without yielding of the wall, the analysis of the plastic tilt of the retaining wall, etc. Yet still more information is needed on the behavior of realistic earth retaining structures. The following works are recommended as future research on the seismic behavior of structures retaining liquefiable backfills

8.5.1   More Investigation on the Existing Centrifuge Model Tests

This research has investigated some crucial features of the behavior of the soil-wall models during the dynamic tests. However, some other important aspects still need thorough study using the available data. The most important aspects include (1) the earth thrusts acting on the wall during slip tests; and (2) the features of surface settlements.

In Chapter 6, a hypothetical model was proposed that explained the phase lag of hydrodynamic thrust was related to the cyclic rotation of the wall during earthquakes. However, a complete theoretical work is needed to explain the interaction between the retaining wall and the soil, which should be modeled as a two-phase (soil skeleton and pore fluid) material

254

This research demonstrated that the effect of permeability on the pore pressure behavior was significant (Chapter 6). It is recommended that permeability be a major variable in future testing programs.

In order to improve the existing centrifuge model, the following recommendations are suggested:

1. Changing the location of the load cell to better record the load in the tie-back

   As shown in Figure 8.1, it is recommended to install the load cell between the spring and the slider (or between the wall and the spring). This design allows for direct measurement of load in the tie-back, minimizing interpretation of test results.

2. Improving the slider to better define the shear resistance

   It was difficult to pre-define the shear resistance of the slider in this study, because of the characteristics of the compressive springs in the slider. In order to better define the shear resistance of the slider, it is recommended to use springs with more appropriate deflection-compression relations (softer springs) in the slider.
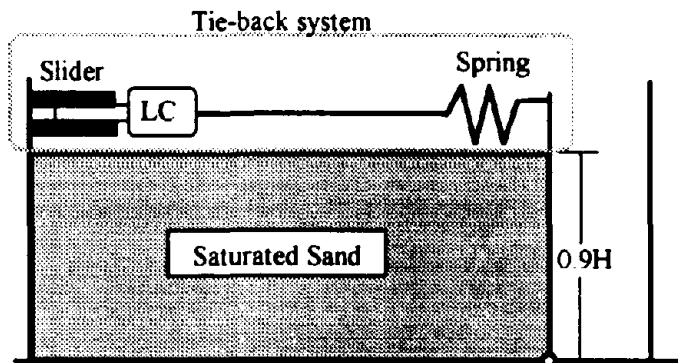
Figure 8.1: Improved configuration of the centrifuge model for future research

3. Minimizing the wall's contribution to the dynamic load in the tie-back

The wall's contribution to the total dynamic load in the tie-back was large (compare to the earth's contribution) in this research. It was large because (1) the wall's mass was large; and (2) the thickness of the soil backfill was small compared to the height of the wall. It is recommended to reduce the wall's contribution in future researches through two manners: (1) to use a thinner wall[10]; and (2) to increase the thickness of the backfill. A thinner wall will cause a smaller dynamic load because of the smaller inertia force. In this research, the backfill's thickness was equal to about 60% of the wall height - owing to the space required for installing the tie-back piece by piece (Chapter 4). The percentage of the earth's contribution to the amplitude of the total dynamic load would be larger if the thickness of the backfill were larger. Consequently, the percentage of the wall's contribution would be reduced.

The tie-back system was installed above the backfill in this research due to the dimensions of the existing shaking bin - owing to the limited space between the outer face of wall and the end wall of the shaking bin (Chapter 4). It is recommended to use a longer shaking bin in future researches such that the tie-back can be installed on the other side of the retaining wall, as shown in Figure 8.2.

---

[10] The wall's thickness was large in this research because of the current design of the hinge at the wall's base. An improved design of the base hinge is required for a thinner retaining wall.

256
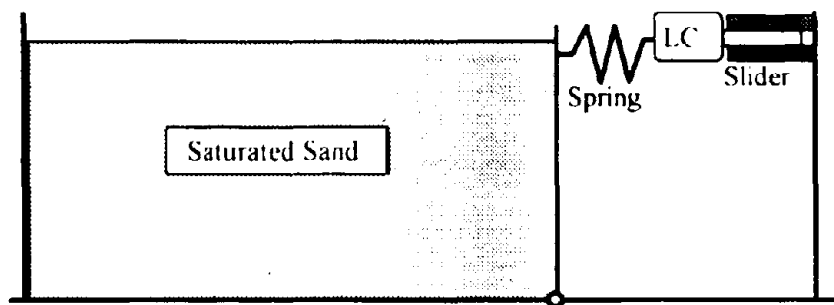
Figure 8 2 Recommended configuration of the centrifuge model for future research

However, if the same container is to be used, it is recommended that the tie-back system (see Figure 8 1) be assembled prior to installation, as the space required between the tie-back and the sand surface would be minimized This process will maximize the thickness of the sand to be about 90% of the wall height

4 Using better displacement transducers

Due to the frequency response, the dynamic performance of the displacement transducers (DCDT) was not satisfactory in this research It is recommended to use other types of displacement sensors, such as proximity sensors, in similar tests In addition, because of the small linear range of the dsiplacement transducer (for more acurate measurement) the centrifuge was usually stopped after each slip tests to adjust the location of the displacement transducer for subsequent tests This action caused a change of the stress state in the soil model when the centrifugal acceleration changed back and forth

4 Better locating pore pressure transducers

In this research, the locations of the embeded pore pressure transducers were determined by direct measurement during excavation after a series of tests on the model The transducer might have settled or levitated during each test One

option to locate the transducers at the end of a particular test is to inspect the model using X-ray. However, one must justify if is worthy to stop the centrifuge or not, since the stress state in the soil may be changed.

8.5.2 Analytical Work on the Dynamic Centrifuge Model Tests

The following efforts are recommended to refine and complete numerical predictions. They will also improve the lumped-mass-sliding-block model that predicts the amount of the retaining wall's plastic tilt resulting from of temporary yielding during an earthquake.

I. Numerical predictions

1. More laboratory tests (to better define the cyclic behavior of Nevada sand):

   In order to bring the analytical model RSM (with a computer code CYCON) into full predicting power, more laboratory tests are required to better quantify the model parameters. The recommended tests are strain-controlled cyclic triaxial and DSS tests on Nevada sand with relative densities of 60% and 75%.

2. "Class A" predictions for other centrifuge tests (with CYCON):

   With the model parameters determined in this research, CYCON can be applied to predict the behavior of Nevada sand during dynamic tests performed by other institutions[11] under different test conditions. The systematic procedures established in Section 5.4 are recommended for evaluating the predictions.

3. Evaluation of other numerical models:

---

[11] In the VELACS project.

It is recommend that the predictive capability of all numerical models be examined following the general type of systematic evaluation procedure described in Chapter 5.

II. Improving the lumped-mass-sliding-block model

From the engineering point of view, the amount of earthquake-induced tilt in the retaining wall is important. This study used a slider to simulate an anchor at the end of a tie-back that supports a model retaining wall near its upper edge. The plastic tilt in the wall resulted from the slip at the slider during strong earthquakes. This thesis developed a lumped-mass-sliding-block model to estimate the amount of slip at a slider in the tie-back for the retaining wall, based on insight concerning behavior during tests in which slip did not occur. This thesis has demonstrated that this model is effective in estimating the earthquake-induced plastic tilt in the model retaining wall. This model is potentially applicable to estimate the amounts of permanent tilt of other retaining walls. It is worthy to refine this model and make it available as a simple tool for estimating the amount of tilt of a retaining wall, as a result of temporary yielding of the wall and its anchoring system, during an earthquake.

The following two procedures are recommended for improving the lumped-mass-sliding-block model to better predict the plastic tilt of a retaining wall resulting from temporary yielding in the tie-back.

1. Implement relationships for the damping coefficient and spring constant of the soil as functions of shear strains.

2. Include the actual (or numerically predicted) incremental average transient earth thrust during load cycles.

8.5.3 Investigations of More Realistic Waterfront Structures

The following dynamic centrifuge tests are recommended for future study of the behavior of sand supported by more realistic retaining structures:

1. Repeat the centrifuge test in this thesis, but with the water table below the sand surface.

   The major points of interest are the pore pressure build-up, the behavior of the dry sand above the saturated sand, and the interaction between the sand and the wall

2. Dynamic tests with a flexible[12] cantilever retaining wall.

   This wall will be an idealized sheet pile wall with a base rigidly connected to the shaking bin Of major interest are the earthquake-induced changes of the earth thrust, deformation of the retaining wall, phase angles between the input acceleration and various thrusts of the soil-wall system, cyclic shear strain and pore pressure build-up

3. Dynamic tests with a stiff retaining wall hinged at base and supported with an embedded anchor.

   This wall will be similar to the wall in this research but supported by an embedded anchor Three series of tests are recommended:
   - (1) the water table is at the sand surface
   - (2) the water table is below the sand surface and the anchor is in dry sand
   - (3) the water table is below the sand surface and the anchor is in the saturated sand

   Attention should be paid to the effects of pore pressure build-up on the strength reduction of the anchor.

Better understanding of the seismic behavior of a waterfront structure is expected through the above recommended centrifuge studies. Nevertheless, a true "class A" numerical prediction is highly recommended prior to each detailed design of the above centrifuge models -- an effective estimate of pore pressure build-up will assist in the designing of the centrifuge model.

---

[12] If the wall is stiff, then it will be similar to the wall in this research.

REFERENCES

Al-Homoud, A. S. (1990): *Evaluating Tilt of Gravity Retaining Walls During Earthquakes*, Ph.D. Thesis, Department of Civil Engineering, M.I.T., Cambridge, Mass., June, 1990.

Anderson G. R. (1987): *Tilting Response of Centrifuge-Modeled Gravity Retaining Wall to Seismic Shaking*, M.S. Thesis, Department of Civil Engineering, M.I.T., Cambridge, Mass., June, 1987.

Al-douri, R.H., Hull, T., and Poulos, H.G. (1990): *Preparation And Measurement of Uniform Sand Beds in the Laboratory*, Research Report No. R609, March 1990, The University of Sydney, Department of Civil and Mining Engineering.

Arulanandan, K. (1991) : *Comparisons of Check Test Results*, Internal communication for the VELACS project. January 23, 1991.

Arulanandan, K. and Taghizadeh-Manzari, M. (1992): *Liquefaction Analysis of Stratified Soil Layers: A Verification of Coupled Stress-Flow Approach*, Proc. 10th World Conference on Earthquake Engineering, July 24, 1992, Madrid, Spain.

Bouckovalas, G. (1982) : *An Analytical Method for Predicting Permanent Deformation of Foundations Under Cyclic Loads*, Sc.D. Thesis, Department of Civil Engineering, M.I.T., June, 1982.

Bouckovalas, G., Whitman, R. V., and Marr, W. A. (1984): *Permanent Displacement of Sand with Cyclic Loading*, J. Geotech. Engrg., ASCE, 110(11).

Bouckovalas, G., Marr, W. A., and Christian, J.T. (1986): *Analyzing Permanent Drift from Cyclic Loads*, J. Geotech. Engrg., ASCE, 112(7). 579-593.

Bouckovalas, G. and Madshus, C. (1986): *Foundation Engineering Criteria for Gravity Platforms: Pore Pressure Build up and Dissipation, Permanent and Cyclic Displacements for Gravity Platforms on Sand*, NGI Report 40013-33

Bouckovalas, G. and Madshus, C. (1987): *Permanent Displacement and Pore Pressure from Partially Drained Cyclic Loading*, Proc. Sixth Int. Conf. on Offshore Mechanics and Arctic Engineering Symp., Houston, Texas, March 1-5, 1987

Bouckovalas, G., Stamatopoulos, C. A., and Whitman, R. V. (1991): *Analysis of Seismic Settlements and Pore Pressures in Centrifuge Tests*, J. Geotech. Engrg., ASCE, 117(10). 1492-1508.

Bucky, P. B. (1931): *Use of Models for the Study of Mining Problems*, Am. Inst. Mining and Metallurgical Engineers, Tech Pub. No. 425, pp. 3 - 28.

Christain, J. T. (1993): Personal Communication during Ph.D. Thesis Committee meeting on March 12, 1993, MIT

Chwang, A. T. (1978): *Hydrodynamic Pressures on Sloping Dams During Earthquakes, Part II, Exact Solution*, Journal of Fluid Mechanics, Vol. 87, Part 2, pp. 343-348.

Dobry, R., F. Y. Yokel, R. M. and R. S. Ladd (1981): *Liquefaction Potential of Overconsolidated Sands with Moderate Seismicity*, pp. 643 - 664 in Earthquakes and Earthquake Engineering: The Eastern United States, J. E. Beavers, ed., Ann Arber Science Publishers, Ann Arber, Michigan.

Ebeling, R. M, Ernest, E. M. Jr., Whitman, R. V., and Finn, W. D. L. (1992): *The Seismic Design of Waterfront Retaining Structures*, US Army, Technical Report ITL-92-11, US NAVY Technical Report NCEL TR-939.

Elgamal, A-M. M., Abdel-Ghaffar, A. M., and Prevost, J. H. (1985): *Earthquake-induced Plastic Deformation of Earth Dams*, Proc. Second Int. Conf. Soil Dynamics and Earthquake Engrg.

Elgamal, A-M. M., Scott, R. F, Succarieh, M. F., and Yan, L. (1990): *La Vallita Dam Response during Five Earthquakes Including Permanent Deformation*, J. Geotech. Engrg, ASCE Vol. 116 (GT10), pp. 1443-1462.

Finn, W. D. L., Lee, K. W., and Martin, G. R.(1977): *An Effective Stress Model for Liquefaction*, Journal of Geotechnical Engineering Division, ASCE, Vol. 103, GT6, 1977, pp. 517 - 533

Finn, W. D. L., Yogendrakumar, M, Yoshida, N., and Yoshida, H. (1986): *TARA-3: A Program for Non-Linear Static and Dynamic Effective Stress Analysis*, Soil Dynamic Group, Department of Civil Engrg, University of British Columbia, Vancouver, B. C.

Finn, W. D. L. and Siddharthan, R. (1984): *Seismic Response of Caisson-Retained and Tanker Islands*, Proceedings, 8th World Conference on Earthquake Engineering and Soil Dynamics, Sand Francisco, August 1985, pp. 751 - 757.

Ishibashi, I. and Madi, L. (1990): *Case Studies on Quaywalls' Stability with Liquefied Backfills*, Proc. 4th US National Conference on Earthquake Engineering, May 20-24, 1990, Palm Springs, California, Vol. 3 pp. 725-734

Ishii, Y., Arai, H, and Tsuchida H. (1960): *Lateral Earth Pressure in an Earthquake*, Proc. Second World Conference on Earthquake Engineering, Tokyo, pp. 211-230.

Kutter, B. L. (1984): *Earthquake Deformation of Centrifuge Model Banks*, J. Geotech Engrg., ASCE, 110(12) 1697-1714.

Kutter, B. L., Casey, J. A., and Romstad, K. M. (1990): *Centrifuge Modeling and Field Observations of Dynamic Behavior of Reinforced Soil and Concrete Cantilever Retaining Walls*, Proc. of 4th US National Conference on Earthquake Engineering, Palm Springs, pp. 663-672, May 20-24, 1990.

Lambe, T. W. (1973): *Predictions in Soil Engineering: 13th Rankin Lecture*, Geotechnique, London, England, 23(2), pp. 149 - 202.

Lambe, T. W. and Associates (1977): *Cyclic Triaxial Tests on Oosterschelde Sands*, Document L-39, prepared for Rijkwaterstaat, Deltadienst, the Hague, Netherlands, September, 1977.

Lambe, T. W. and Whitman, R. V. (1969): *Soil Mechanics*, John Wiley & Sons, Inc., New York, Chapters 13 and 23.

Lambe, P. C. (1981): *Dynamic Centrifugal Modeling of a Horizontal Sand Stratum*, Ph.D. Thesis, Dept. of Civil Engng. M.I.T.

Lee, M. and Finn, W-D Liam (1975): *DESRA-1: Program for the Dynamic Effective Stress Response Analysis of Soil Deposits Including Liquefaction Evaluation*, Report No. 36, Soil Mechanic Service, Department of Civil Engrg, University of British Columbia, Vancouver, B. C.

Lee, M. and Finn, W-D Liam (1978): *DESRA-2: Dynamic Effective Stress Response Analysis of Soil Deposits with Energy Trsmitting Boudary Including Assessment of Liquefation Potential*, Report No. 38, Soil Mechanic Service, Department of Civil Engrg, University of British Columbia, Vancouver, B. C.

Lin, J. S. (1982): *Probabilistic Evaluation of the Seismically-Induced Permanent Displacements in Earth Dams*, Research Report No. R82-21, Department of Civil Eng., M.I.T., Cambridge, Mass.

Lin, J. S. and Whitman, R. V. (1983): *Decoupling Approximation to the Evaluation of Earthquake-Induced Plastic Slip in Earth Dams*, Earthquake Engineering and Structural Dynamics, Vol. 11, pp. 667 - 678.

Makdisi, F. I. and Seed H. B. (1978): *Simplified Procedure for Estimating Dam and Embankment Earthquake-Induce Deformations*, J. of the Geo. Eng. Div., ASCE, Vol. 104, GT7, pp. 849 - 867.

Matsuo, H. and Ohara, S. (1960): *Lateral Earth Pressure and Stability of Quay Walls During Earthquakes*, Proc. Second World Conference on Earthquake Engineering, Tokyo, pp. 165-187.

Matsuzawa, H., Ishibashi I. and Kawamura M. (1985): *Dynamic Soil and Water Pressures of Submerged Soils*, J. of Geotech. Engng., ASCE, Vol. 111, No. 10, pp. 1161-1176.

Mayne, P. W., and Kulhawy, F. H. (1982): K_0-*OCR Relationships in Soil*, J. Geotech. Engrg. Div., ASCE, 108(6), pp 851-872.

Mononobe, N., and Matsuo, H. (1929): *On the Determination of Earth Pressures During Earthquakes*, Procedings, World Engineering Congress, Vol. 9, 1929.

Muraleetharan, K. K. (1990): *Dynamic Behavior of Earth Dams*, Ph.D. Thesis, University of California at Davis, Davis, CA.

Newmark, N. M. (1965): *Effect of Earthquakes on Dams and Embankments*, Geotechnique, London, England, Vol. 25, No. 4, pp. 743 - 761.

Okabe, S. (1924): *General Theory of Earth Pressure and Seismic Stability of Retaining and Dam*, Japan Society of Civil Engineering Journal, Vol. 10, No. 6, 1924

Pahwa, A., Germaine, J. T., and Whitman R. V. (1986): *Cyclic Triaxial Testing of Leighton-Buzzard 120 200 Sand*, Research Report R86-24, Department of Civil Engineering, M.I.T., September, 1986

Pahwa, A., Whitman, R. V. and Germaine J. T. (1987): *Seismic Design of Retaining Walls - Quick RElease Tests on Centrifuge of Wall Retaining Saturated Sand Backfill*, Research Report R87 - 18, M.I.T., June 1987.

Prevost, J. H. (1981): *DYNAFLOW: A Non-linear Transient Finite Element Analysis Program*, Report No. 81-SM-1, Dept. of Civil Engrg., Princeton University, Princeton, NJ

Richards, R., and Elms, D. G. (1979): *Seismic Behavior of Gravity Retaining Walls*, J. Geotech. Engng., ASCE, Vol 105, GT4, pp. 449-464.

Schofield, A. N. (1981): *Dynamic and Earthquake Geotechnical Centrifugal Modelling*, Proc. Int. Conf. on Recent Advances in Geotechnical Engrg. and Soil Dynamics, Univ. of Missouri, Rolla, MO., 3.

Scott, R. F. (1973): *Earthquake-Induced Earth Pressures on Retaining Walls*, Proceedings, 5th World Conference on Earthquake Engineering, Rome, Italy

Seed, H. B. (1969) *Dynamic Lateral Pressures on Retaining Structures*, Lecture presented at University of California at Berkeley, California

Seed, H. B. and Lysmer (1980) *The Seismic Soil-Structure Interaction Problem for Nuclear Facilities*, Report to Lawrence Livermore Laboratory, Seismic Safety Margin Research Program

Seed, H. B. and Whitman, R.V. (1970) : *Design of Earth Retaining Structures for Dynamic Loads*, 1970 ASCE Specialty Conference on Lateral Stresses in the Ground and Design of Earth Retaining Structures, Cornell University, Ithaca, NY, State of the Art Papers, 103-147.

Seed, R. B., Dickson, S. E., Rau, R. K., White, R. K. and Mok, C. M. (1992): *Observations Regarding Seismic Response Analyses for Soft and Deep Clay Sites*, Proc. NCEER/SEAOC/BSSC Workshop on Site Response during Earthquakes and Seismic Code Provisions, Nov. 18-20, 1992, Univ. of S. California, Los Angeles.

Sherif, A., Ishivashi, I. and Lee C. D. (1981): *Dynamic Earth Pressures Against Retaining Walls*, Soil Engineering Research Report No. 21, University of Washington, Seatle, WA, Jan., 1981.

Sherif, A., Ishivashi, I. and Lee C. D. (1982): *Earth Pressures Against Rigid Retaining Walls*, ASCE J. of the Geotechnical Engrg. Division, Vol. 108, No. GT5, pp. 679-695.

Siddharthan, R. (1984): *A Two-Dimensional Nonlinear Static and Dynamic REsponse Analysis of Soil Structures*, Ph. D. Thesis, University of British Columbia, Canada

Stamatopoulos, C. A. (1989) : *A Method Predicitng Earthquake-induced Permanent Deformations of Foundations*, Ph.D. Thesis, Department of Civil Engineering, Massachusetts Institute of Technology, 1989.

Stamatopoulos, C. A. and Whitman, R. V. (1987): *Computation of Earthquake-Induced Permanent Deformations of Foundations on Liquefaction-Susceptible Sand*, M.I.T. Research Report R87-05, Department of Civil Engineering.

Stamatopoulos, C. A., Bouckovalas, G. and Whitman, R. V. (1991): *Analytical Prediction of Earthquake-induced Permanent Deformations*, J. Geotech. Engrg., ASCE, 117(10) pp. 1471 - 1491.

Steedman R. S. (1984): *Modeling of the Behavior of Retaining Walls in Earthquakes*, Ph. D. Thesis, Engineering Department, Cambridge University, Cambridge, England

Steedman, R. S. and Zeng, X. (1990a): *The Seismic Response of Waterfront Retaining Walls*, Proc. of the ASCE Specialty Conference on Design and Performance of Earth Retaining Structures, Geotechnical Special Publication No. 25, pp. 872-886.

Steedman, R. S. and Zeng, X. (1990b): *The Influence of Phase on the Calculation of Pseudo-Static Earth Pressure on a Retaining Wall*, Geotechnique, Vol. 40, No. 1, pp. 103-112.

Ting, N.H., Iglesia, G. R. and Whitman, R. V. (1990): *MIT Check Test for the VELACS Project*, Report to the Project Coordinators, December, 1990 - unpublished.

Timoshenko, S. P. and Woinowsky-Krieger, S. (1959) : *Theory of Plates and Shells*, McGraw-Hill.

Timoshenko, S. P. and Gere, J. M. (1972) : *Mechanics of Materials*, D. Van Nostrand.

Vucetic, M., Tufenkjian, M., and Doroudian M. (1993): *Dynamic Centrifuge Testing of Soil Nailed Exacavations*, Accepted for Publication in ASTM Geotech. Testing Journal (to be published in) June, 1993.

Westergaard, H. M. (1933) *Water Pressures on Dams during Earthquakes*, Transactions, ASCE, Vol. 98, 418-472.

Whitman, R. V. (1988) *Notes for Soil Dynamics* (MIT Course 1.331), unpublished

Whitman, R. V. (1990): *Seismic Design and Behavior of Gravity Retaining Walls*, Proc. ASCE Special Conference on Design and Performance of Earth Retaining Structures, Geotechnical Special Publication No. 25, pp. 817-842.

Whitman R. V. (1992) *Predicting Earthquake-caused Permanent Deformations of Earth Structures*, Proc. Wroth Memorial Symposium on Predictive Soil Mechanics, Oxford University, July 27-29, 1992. pp. 573-584

Whitman, R. V. and Liao, S. (1985):*Seismic Design of Retaining Walls*, Miscellaneous Paper GL-85-1, US Army Engineer Waterways Experiment Station, Vicksburg, MS

Whitman, R. V., Ting, N. H., Schran, U. and Germaine, J. T. (1991), *VELACS PROJECT - COMMENTS RE CHECK TESTS*, Internal communication for the VELACS project. February 19, 1991.

Yoshimi, Y. and Tokimatsu, K. (1978): *Two-Dimentional Pore Pressure Changes in Sand Deposits During Earthquakes*, Proc. Second International Conf. on Microzonation for Safer Construction - Research and Applications, Vol. 2, National Science Foundation, Washington, D.C.

Zangar, C. N. (1953): *Hydrodynamic Pressures on Dams Due to Horizontal Earthquakes*, Proc. Experimental Stress Analysis, Vol. 10, No. 2, pp. 93-102.

Zeng, X. and Steedman R. S. (1988): *Seismic Design of Retaining Walls*, Research Report No. R88-07, Dept. of Civil Engng, MIT.

Zeng, X. (1990): *Modelling of the Behavior of Quay Walls in Earthquakes*, Ph.D. Thesis, Cambridge University, Cambridge, England

Cyclic Triaxial Tests on Oosterschelde Sands, Department of Civil Engineering, M.I.T.,R 79-24, order 646, June 1979.

Verification of Liquefaction Analyses by Centrifuge Studies Laboratory Testing Program Soil Data Report, Prepared for The National Science Foundation, The Earth Technology Corporation, Irvine, California, March, 1992.

Page Intentionally Left Blank

Appendix A

DEFINITIONS OF TERMS

A: A RSM model parameter

a_c: Resistance acceleration (at which the wall will begin to slip)

a_{max}:   Peak ground acceleration

A1:   Horizontal acceleration measured at base

A3:   Horizontal acceleration response in backfill

A4:   Horizontal acceleration measured at load cell

A5:   Horizontal acceleration measured at the sliding sheet of the slider

A6:   Horizontal acceleration measured at top of the retaining wall

B_s: RSM model parameter, describing the shear modulus at small shear strains

B_c: RSM model parameter, describing the shear modulus at small cyclic shear strains

C: Damping matrix in the lumped mass model

c: Damping coefficient of the soil backfill for the lumped mass of earth and wall

$C_1, C_2, c_1, c_2, c_3, c_4, c_5$: RSM model parameters

D_3:   Wall top displacement measured by displacement transducer #3

$D_{3,t=0}$:   Initial wall top displacement before shaking

Dr: Relative density

DCDT: Displacement transducer

DSS: Direct simple shear test

E: Young's modulus

e: Void ratio of a soil

e_{max}:   Maximum void ratio

e_{min}:   Minimum void ratio

F_{LC}:   Force recorded by the load cell

F_{slider}:   Load at slider

G: Shear modulus

G^t: Tangent shear modulus

269

G_o: Shear modulus at very small shear strains

$G_{o,cyc}$: Shear modulus at very small cyclic shear strains

g: Gravitational acceleration, $g = 9.81$ m/sec^2

H: Total thickness of backfill

H_3: Height from base where total earth thrust acts on retaining wall

$H_{tie-back}$: Height of the tie-back above the base

H_{wall}: Height of the retaining wall

h_2, h_4, h_6: Heights of pore pressure transducers from base

I_1: Rotational inertia of the retaining wall

K: Bulk modulus

K^t: Tangent bulk modulus

K: Lateral earth pressure ratio, $K = \sigma_h' / \sigma_v'$

K_a: Active stress ratio

K_o: Lateral stress ratio for one-dimensional strain

K: Stiffness matrix in lumped mass model

k_1: Spring constant of the soil backfill for the lumped mass of earth and wall

k_2: Constant of the spring in the tie-back

k_h: Coefficient of peak horizontal acceleration ($= a_{max}/g$)

kPa: Kilo Pascals

LC: Load Cell

M: Slope of the characteristic thrsehold line in a effective stress path diagram

M: Mass matrix in the lumped mass model

ΔM_{soil}: Dynamic moment acting on retaining wall from soil backfill

m_1: Lumped mass of soil and wall in Section 7.2

m_2: Lumped mass of sliding block in Section 7.2

$(m_1)_{earth}$: Earth's contribution to m_1 (Section 8.4)

m_{11}: Effective mass of LC

m_{12}: Mass of connector between LC and slider

m_{13}: Mass of fixed part of the slider

m_{14}: Mass of sliding part of the slider

m_{15}: Mass of the rod between slider and spring

m_{16}: Mass of the spring in tie-back

m_{17}: Mass of the yoke and screws that connect the spring to the wall

m_{fluid}: Partial mass of pore fluid moving with wall during dynamic rotation

$m_{mineral}$: Partial mass of soil skeleton moving with wall during dynamic rotation

270

m_{wall}	Mass of the retaining wall
N	Scale factor in centrifuge modeling, number of cyclic load cycles
n	Porosity
P	Thrust acting on the retaining wall
P_a	Atmospheric pressure (= 100 kPa)
P1, P2, P3, P4, P5 and P6	Pore pressure at various locations in backfill - see Figure 4.4
P_{AF}	Peak earth thrust acting on a retaining wall
ΔP_{AF}	Peak dynamic earth thrust acting on a retaining wall
P_{earth}	Resistance in tie-back due to total earth thrust
$2\Delta P_{earth}$	Double amplitude of dynamic earth thrust on the retaining wall
$2\Delta P_p$	Double amplitude of dynamic soil skeleton thrust on the retaining wall
$2\Delta P_u$	Double amplitude of hydrodynamic thrust on the retaining wall
$2\Delta P_{u_a}$	Double amplitude of hydrodynamic thrust on the retaining wall when ground acceleration is amplified above the base
p_{wd}	Water pressure acting on a dam or a retaning wall
P_{wd}	Water thrust acting on a dam or a retaning wall
Q	Shear stress ratio - Eq (5.8)
q	Shear stress
Δq_{cyc}	Cyclic shear stress
q_f	Shear stress at failure
R	Yield factor with respect to failure (R = q/q_f)
R	External load vector of the lumped mass model
S_u	Undrained strength of a soil
TX	Triaxial test
$\ddot{s}$	Ground acceleration in the lumped mass model
$U, \dot{U}, \ddot{U}$	Vectors of relative (to frame) displacement, velocity and acceleration in the lumped mass model
$2\Delta U$	Double amplitude of hydrodynamic thrust on retaining wall
ΔU_α	Hydrodynamic thrust if horizontal ground acceleration is amplified along the wall
u_{ex}	Excess pore pressure
u_{2e}, u_{4e}, u_{6e}	Excess pore pressure measured at three depths next to the wall
V	Peak ground velocity
w	Width of the backfill/retaining wall

271

α:	A RSM model parameter	
α:	A parameter describing the amount of increase of horizontal acceleration along the vertical direction - in Eq. (6.10)	
β:	Damping ratio	
β_c	A RSM model parameter describing cyclic shear stress-strain relations	
β_s:	A RSM model parameter describing shear stress-strain relations	
ϕ:	Friction angle of soil	
ϕ_{CT}:	Angle between the characteristic threshold line and the horizontal axis in an	

effective

stress path diagram

γ:	Unit weight; shear strain	
	γ_b:	Buoyant unit weight of soil
	γ_d:	Unit weight of dry soil
	γ_d:	Total unit weight of soil
	γ_w:	Unit weight of water
	γ_{cyc}:	Double amplitude of cyclic shear strain
η:	amplification ratio of horizontal acceleration along the vertical direction	
θ:	Relative rotational angle of the wall with respect to the position with zero wall top displacement	
σ:	Total stress	
σ':	Effective stress	
	σ_h':	Horizontal effective stress
	σ_v':	Vertical effective stress
	$\bar{\sigma}_{oct}$:	Octahedral effective stress

Appendix B

CENTRIFUGE MODEL TEST RESULT
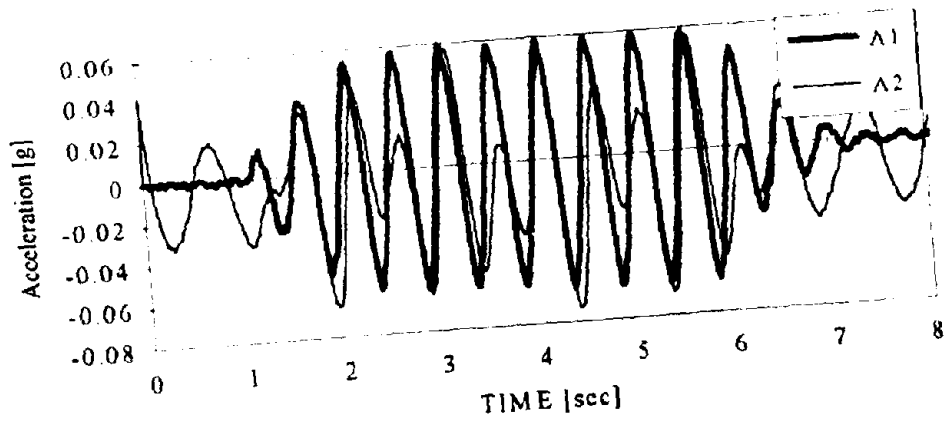
(a)   A1 and A2
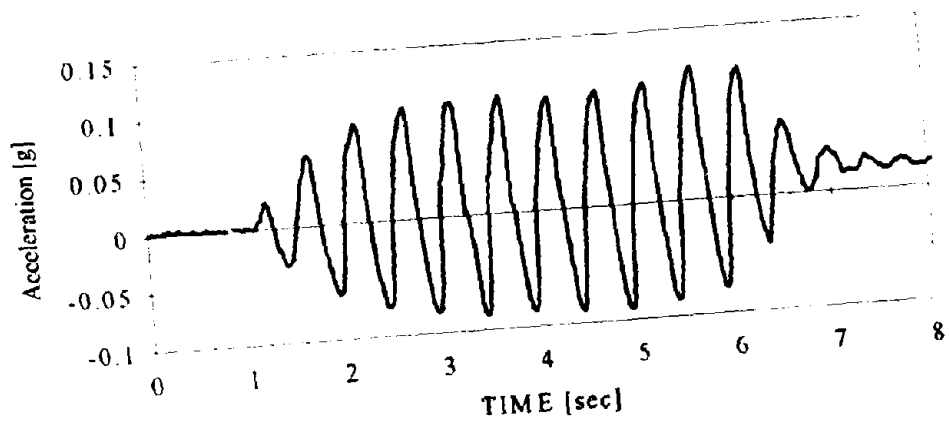
(b)   A3

Figure B.1: Acceleration data in Test 1a
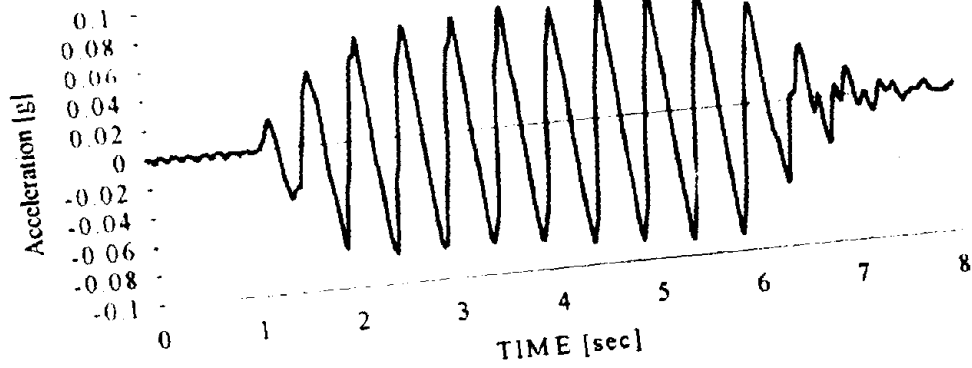
(c)   A4
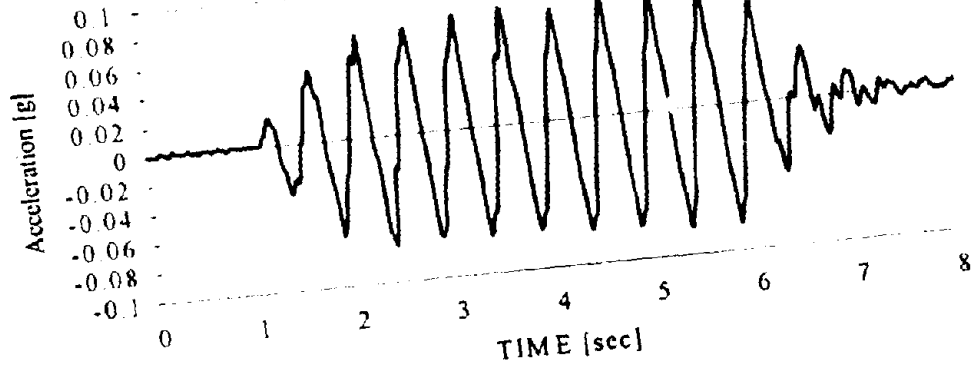
(d)   A5
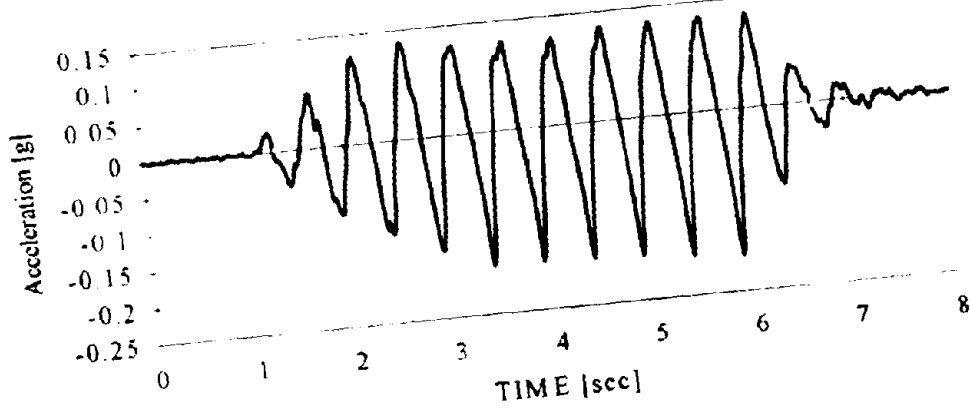
(e)   A6

Figure B.1: Acceleration data in Test 1a
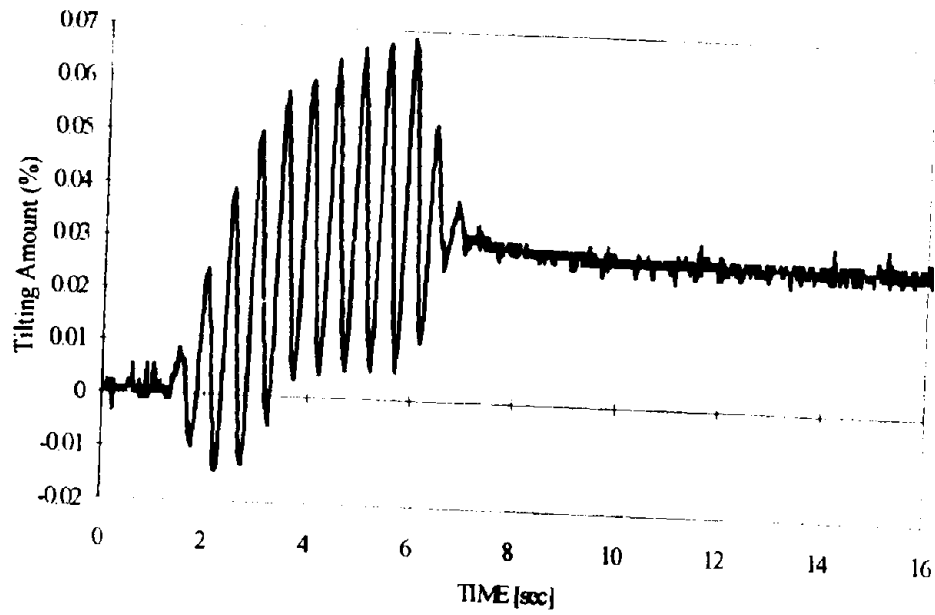
(a) Amount of tilt in wall (δ/H) - data of D3
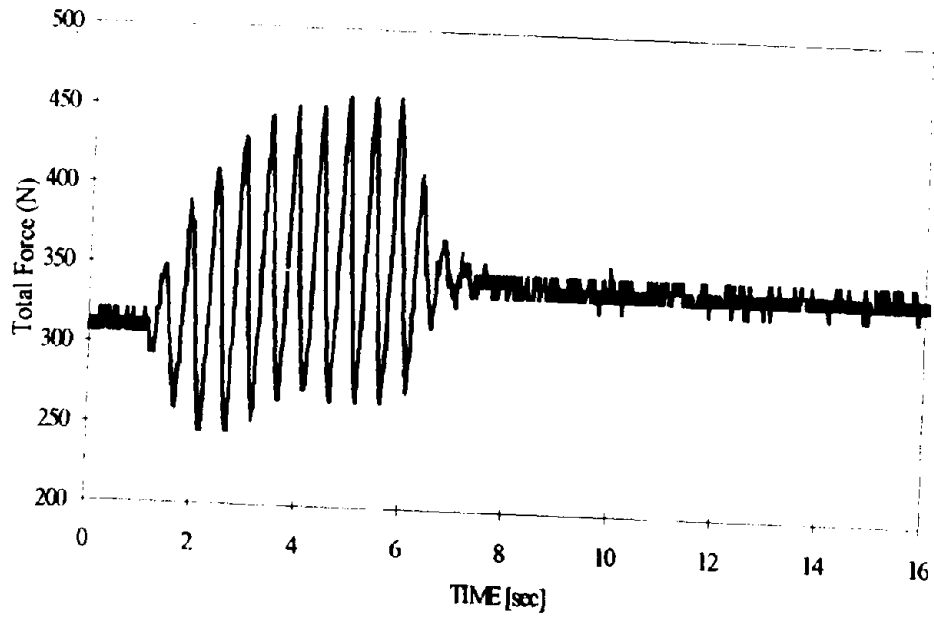
(b) Load data (in model scale)

Figure B.2: Displacement and load data in Test 1a
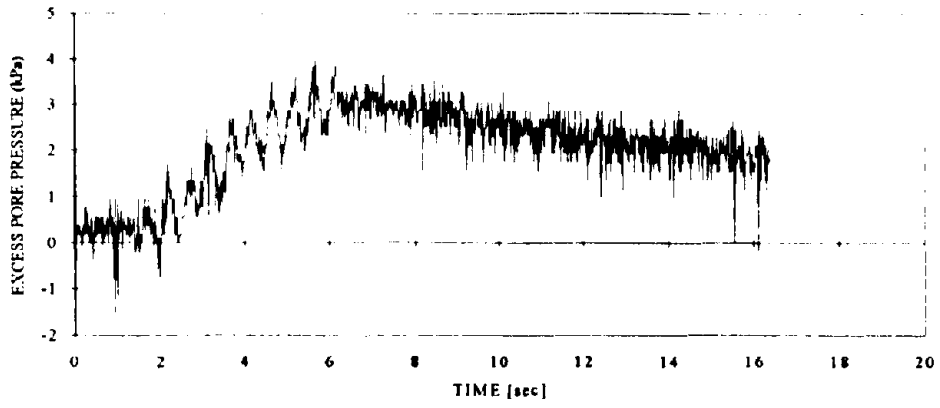
(a)   P1
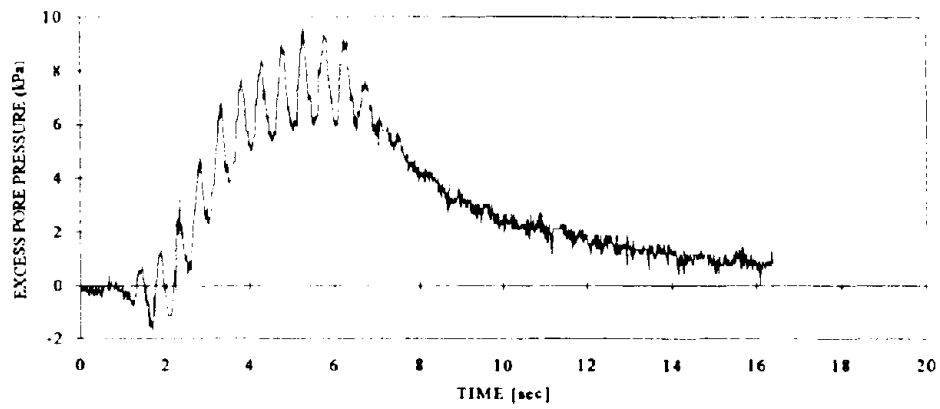
(b)   P2
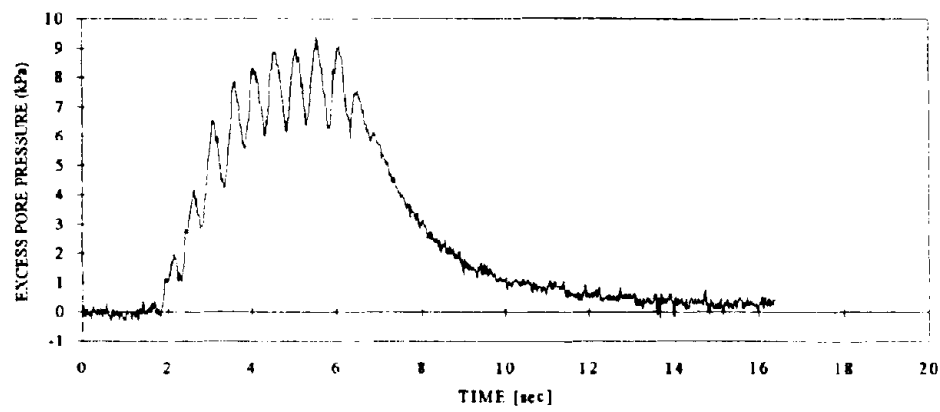
(c)   P4

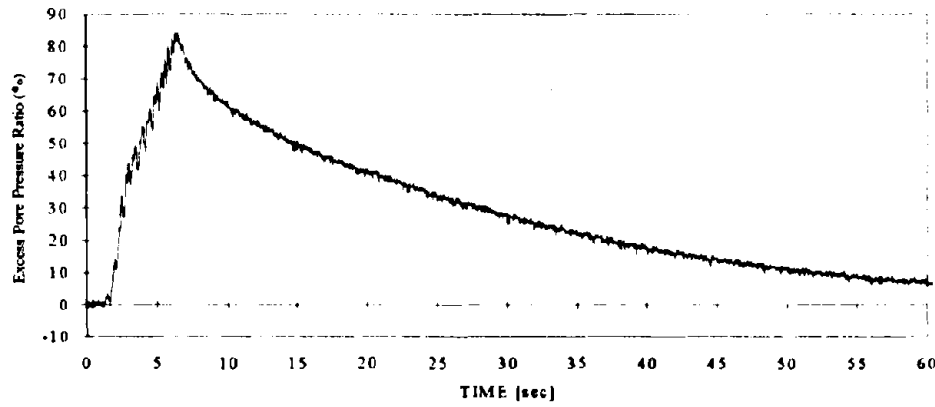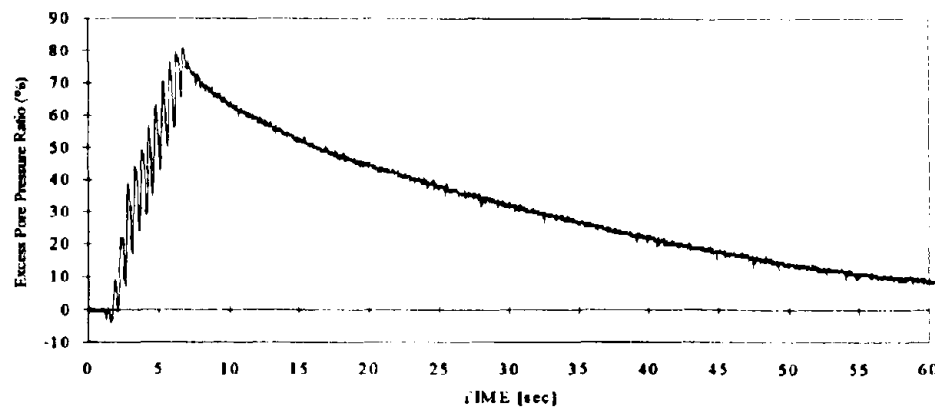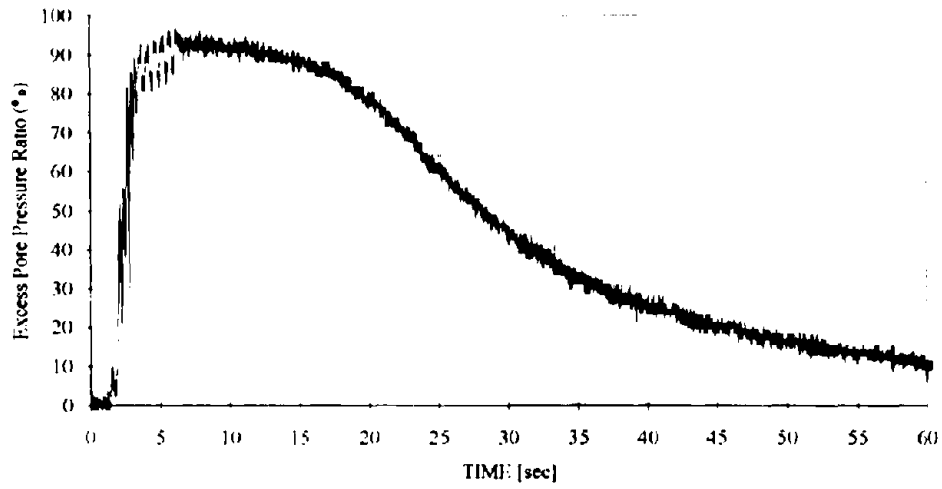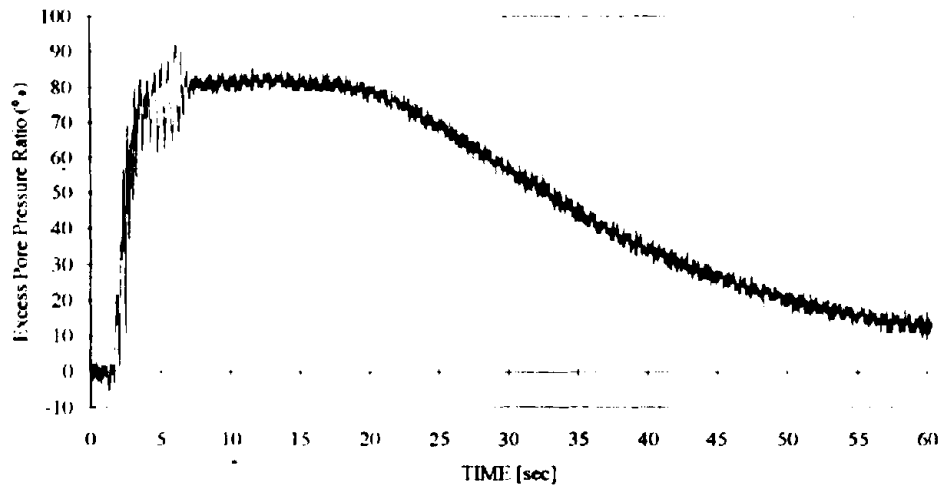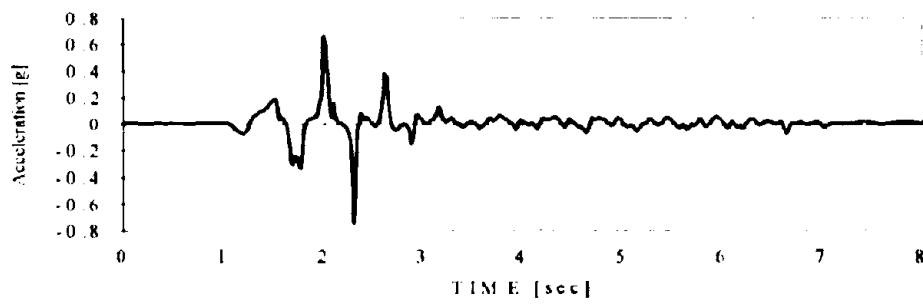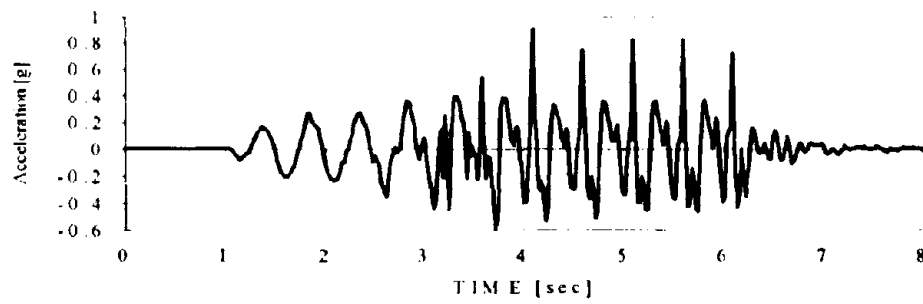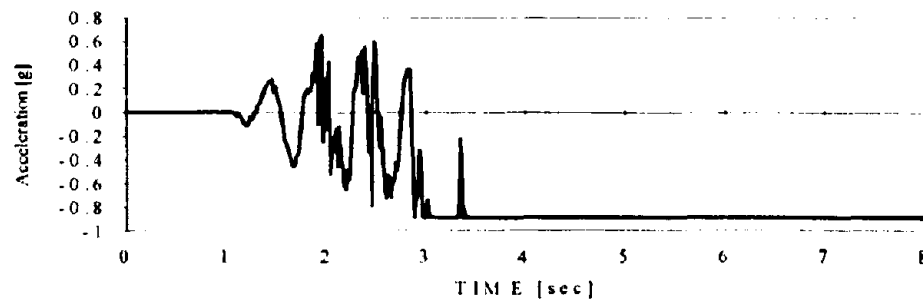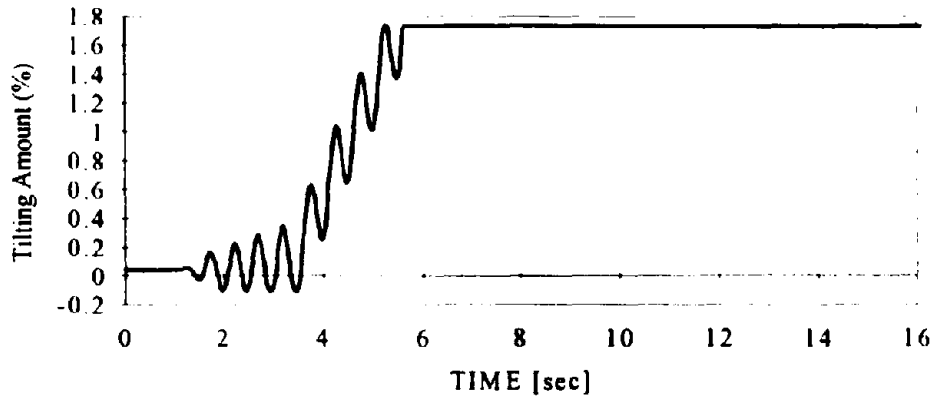Figure B.3: Excess pore pressure data in Test 1a

277
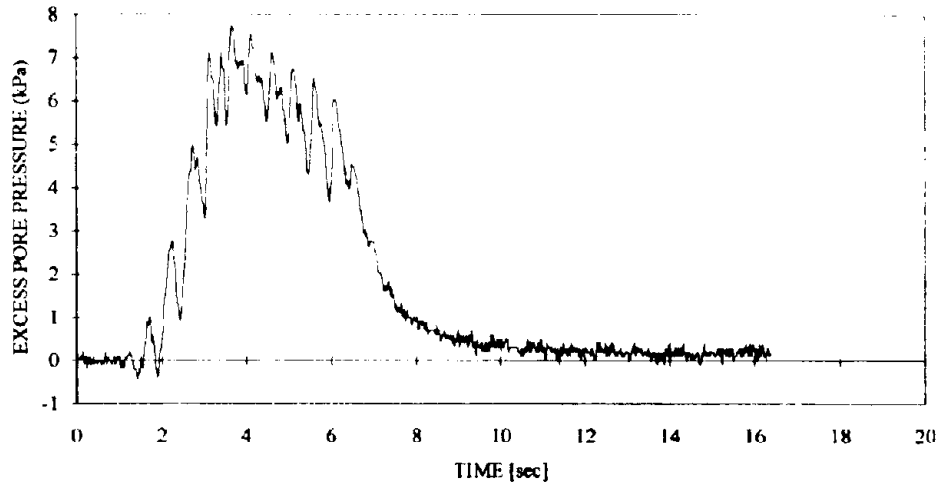
(d)   P5
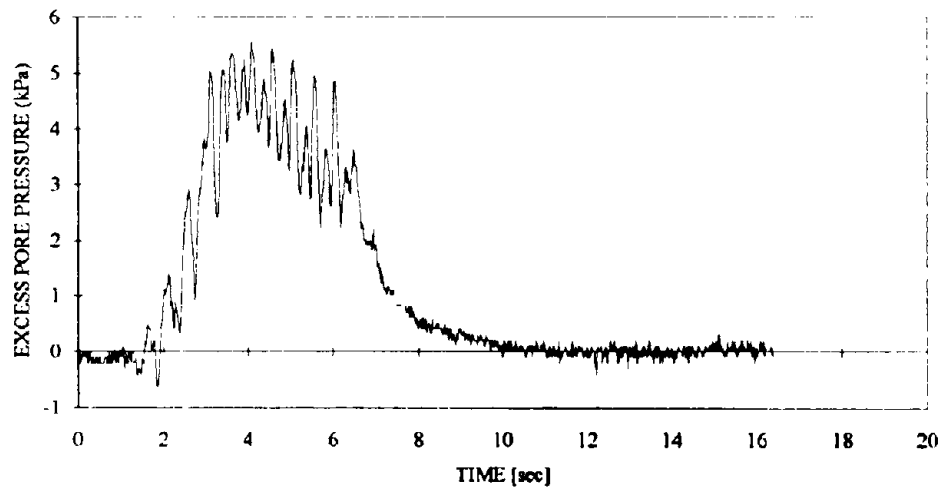
(e)   P6

Figure B.3: Excess pore pressure data in Test 1a
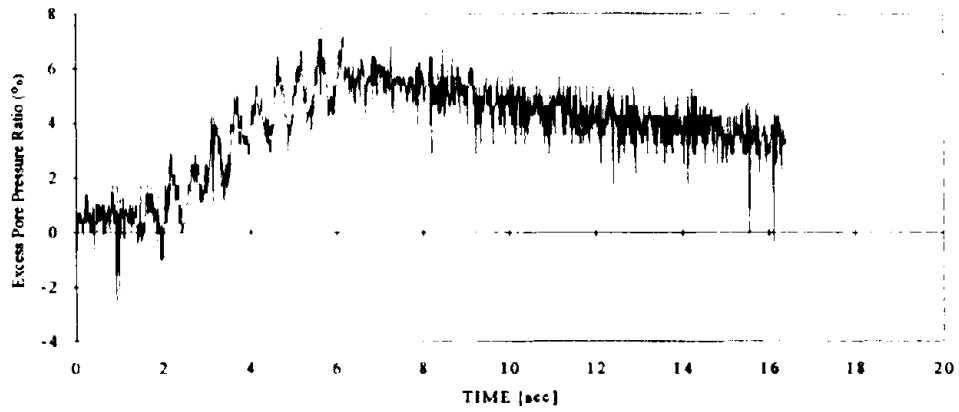
(a)   P1
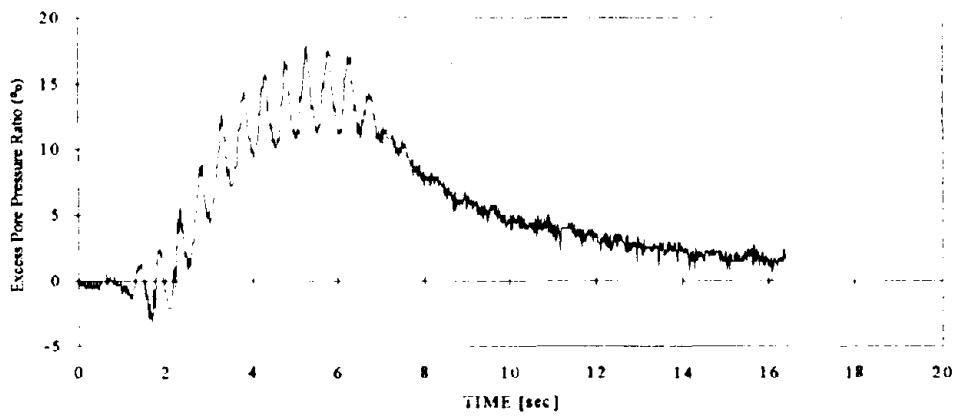
(b)   P2
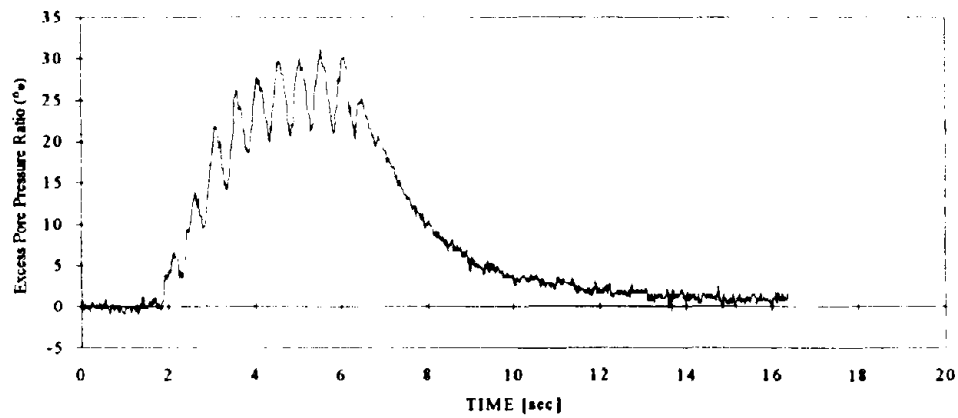
(c)   P4

Figure B.4: Excess pore pressure ratios in Test 1a

279
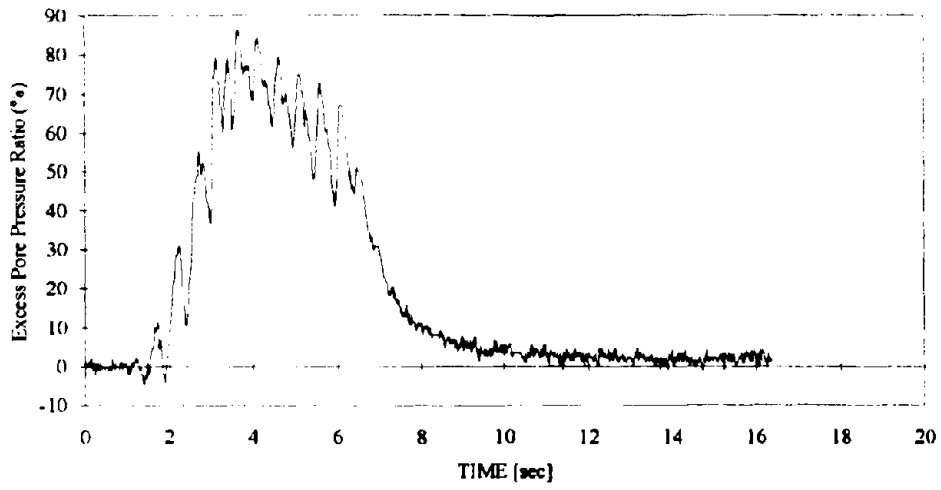
(d)   P5
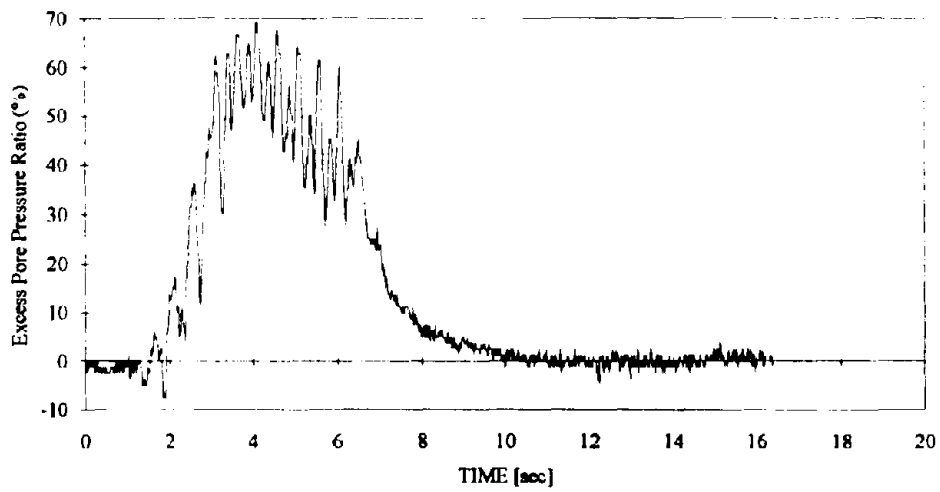
(e)   P6

Figure B.4: Excess pore pressure ratios in Test 1a

280
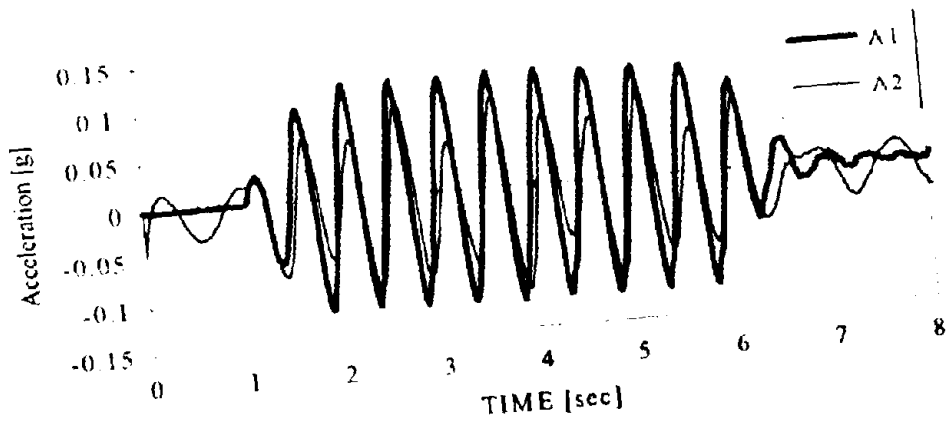
(a)   A1 and A2
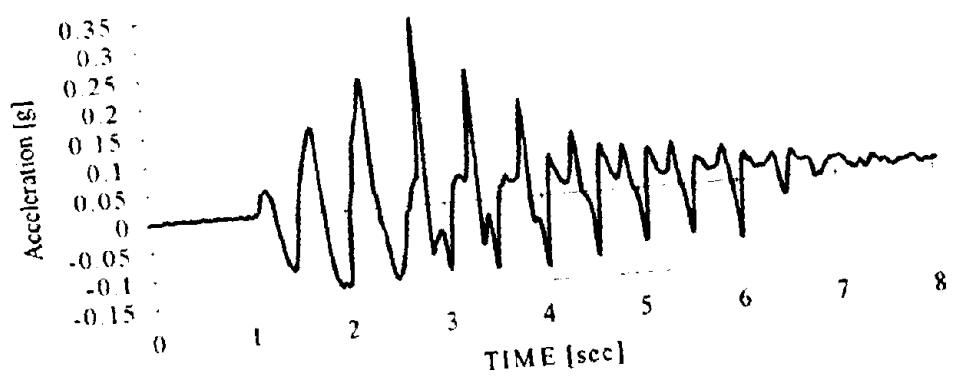
(b)   A3
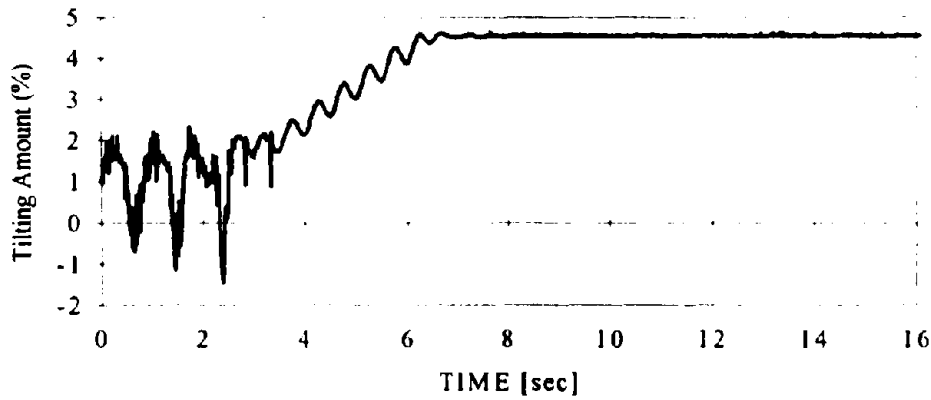
Figure B.5: Acceleration data in Test 1b
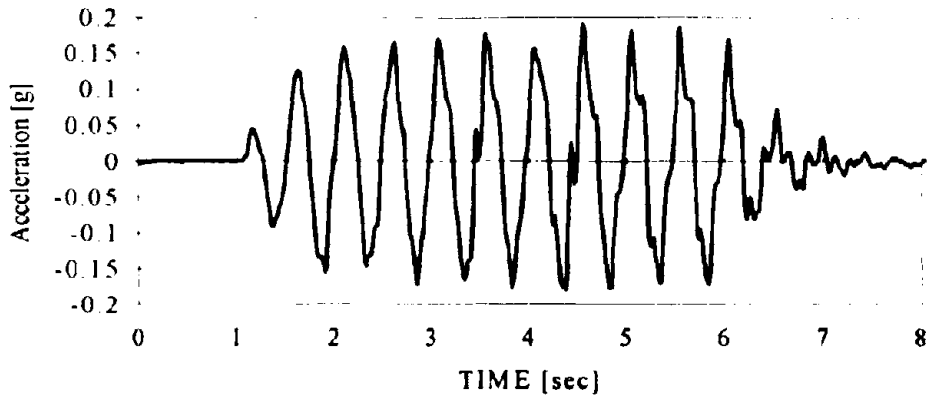
(c)   A4
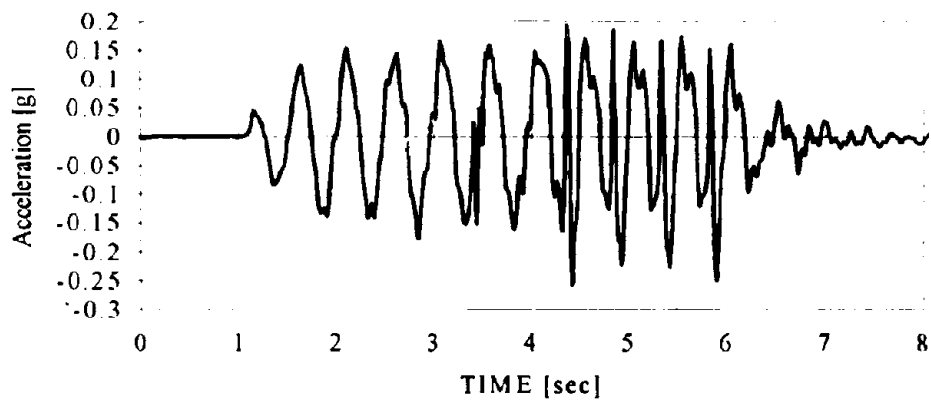
(d)   A5
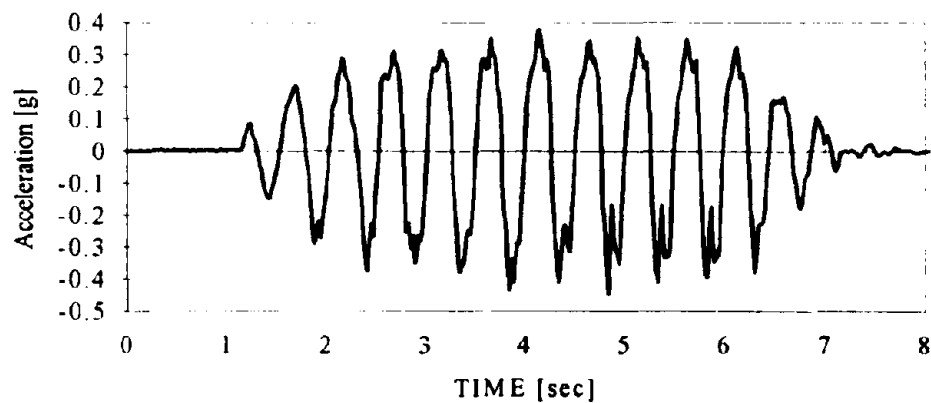
(e)   A6

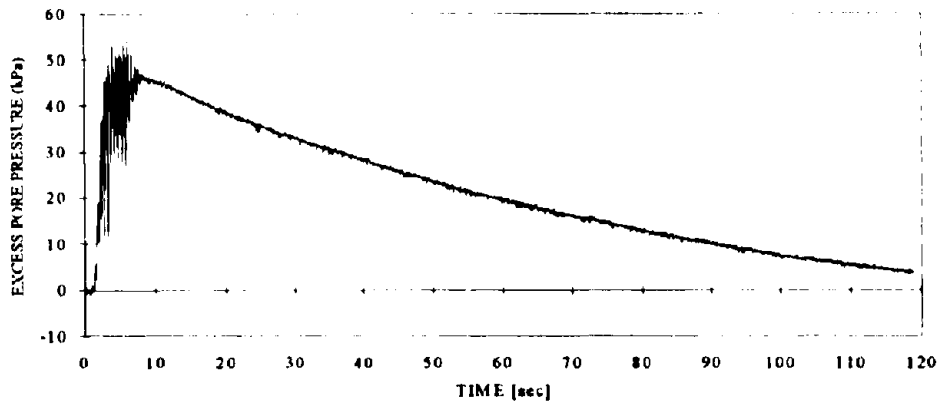Figure B.5: Acceleration data in Test 1b

282
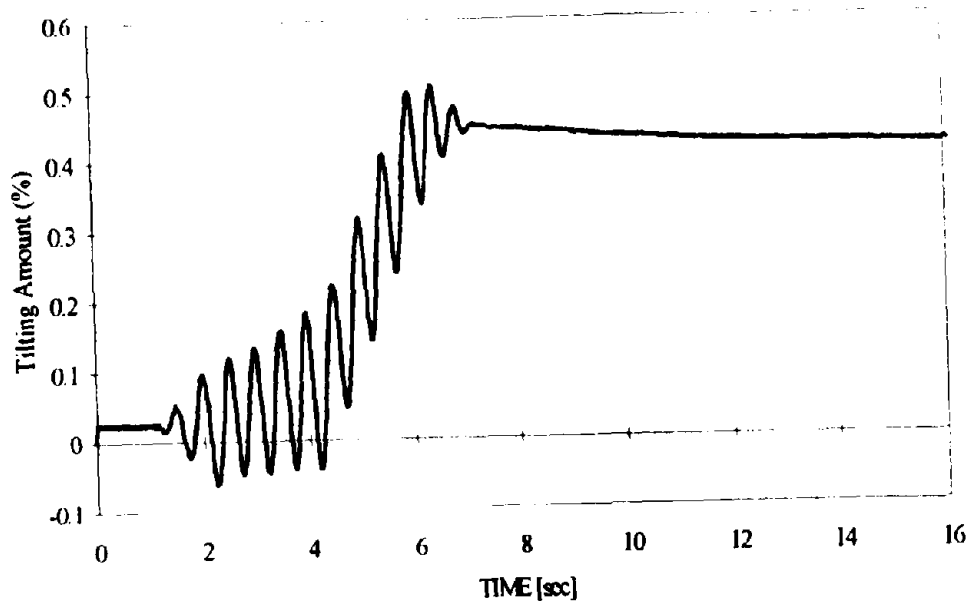
(a) Amount of tilt in wall (δ/H) - data of D3
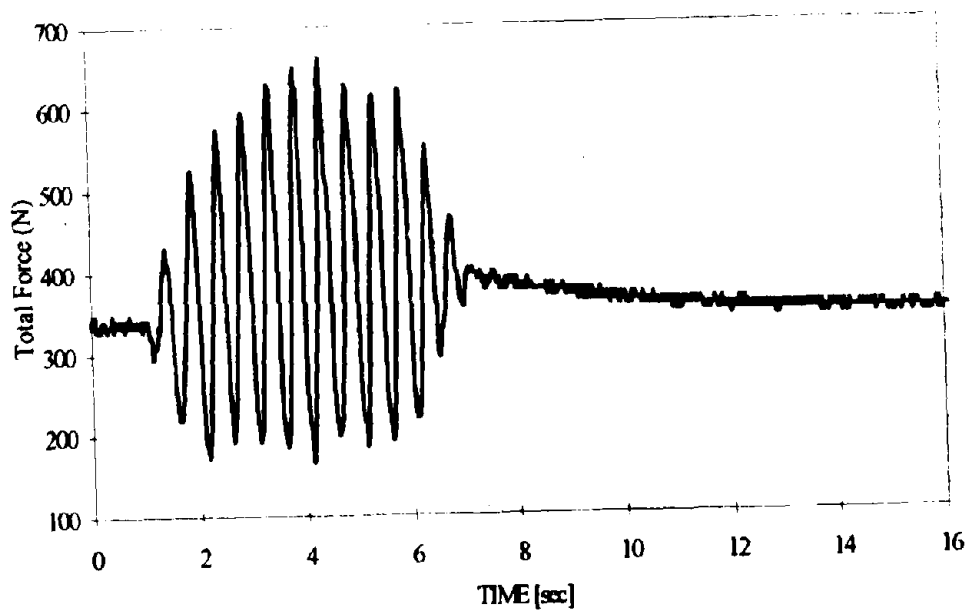
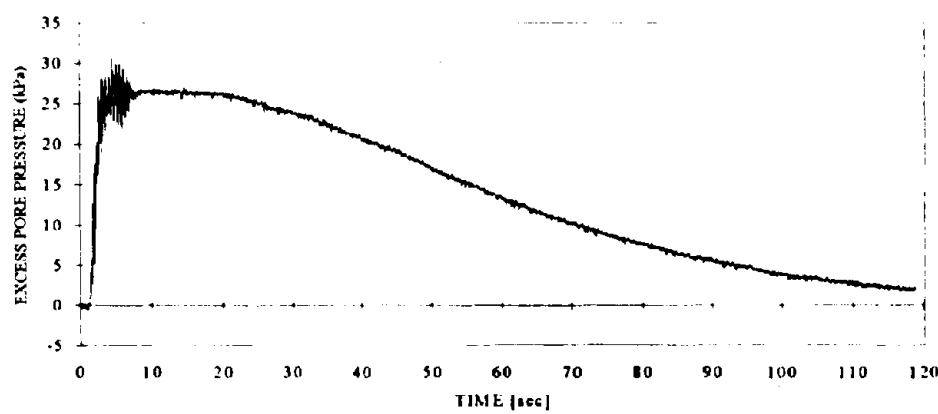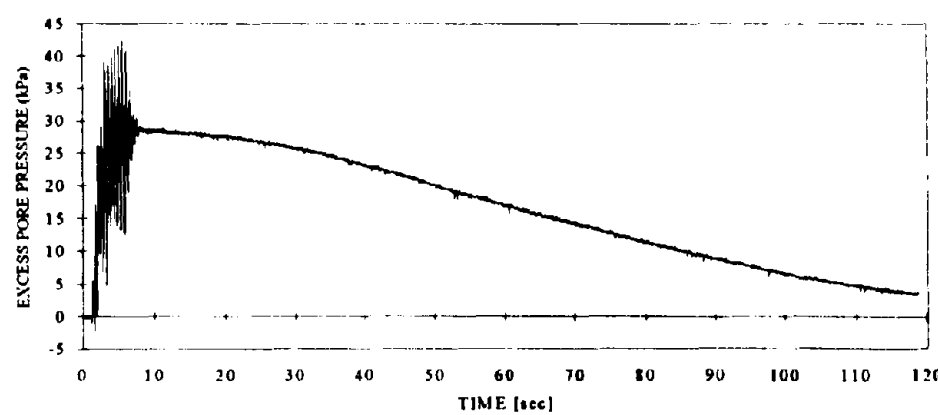(b) Load data (in model scale)

Figure B.6: Displacement and load data in Test 1b
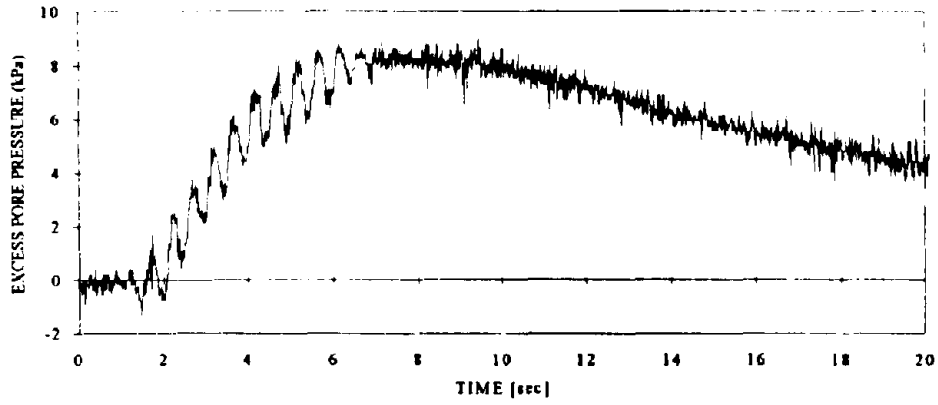
(a)   P1
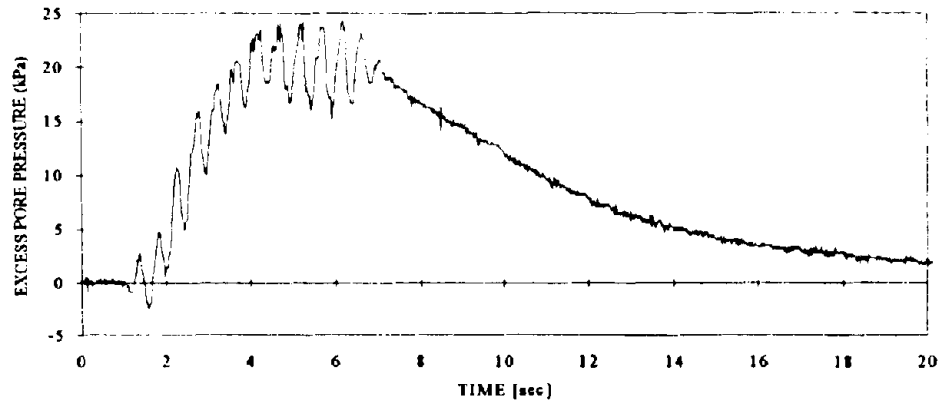
(b)   P2
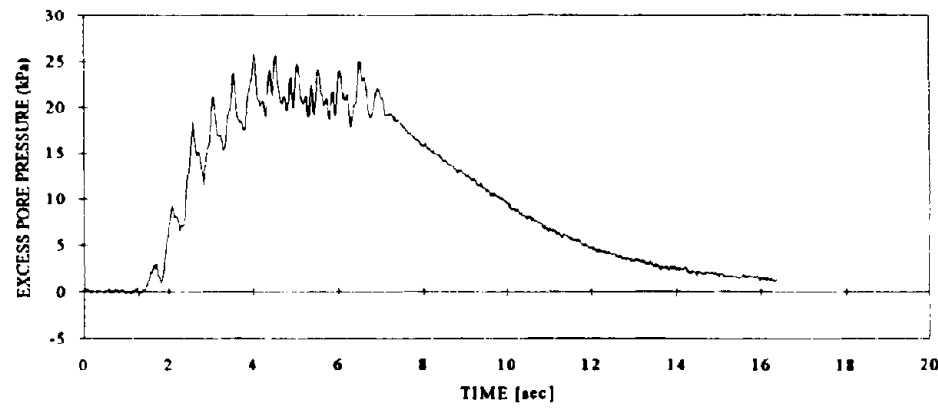
(c)   P4

Figure B.7: Excess pore pressure data in Test 1b

284
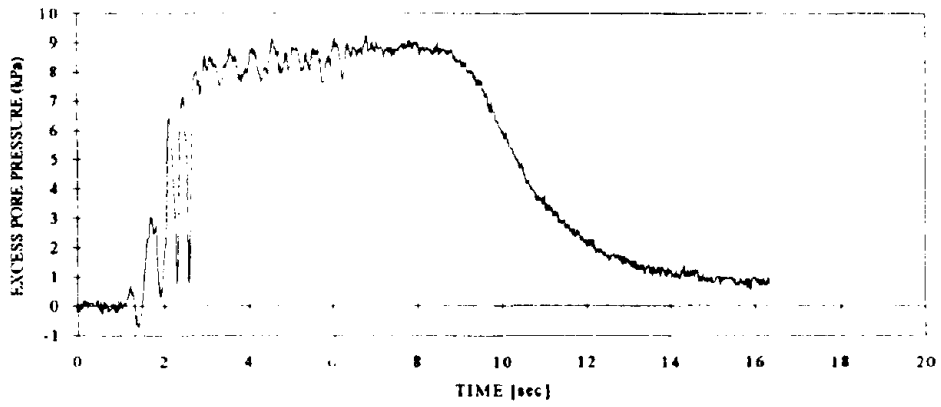
(d)   P5
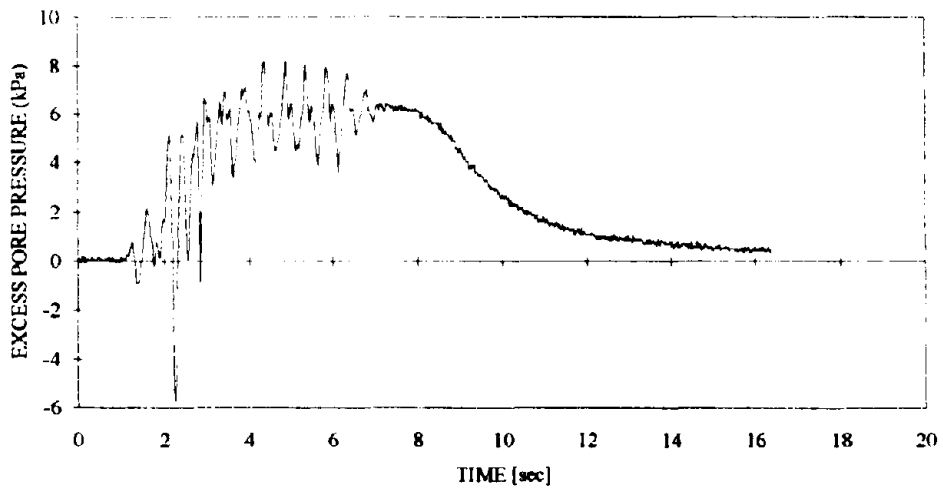
(e)   P6

Figure B.7: Excess pore pressure data in Test 1b
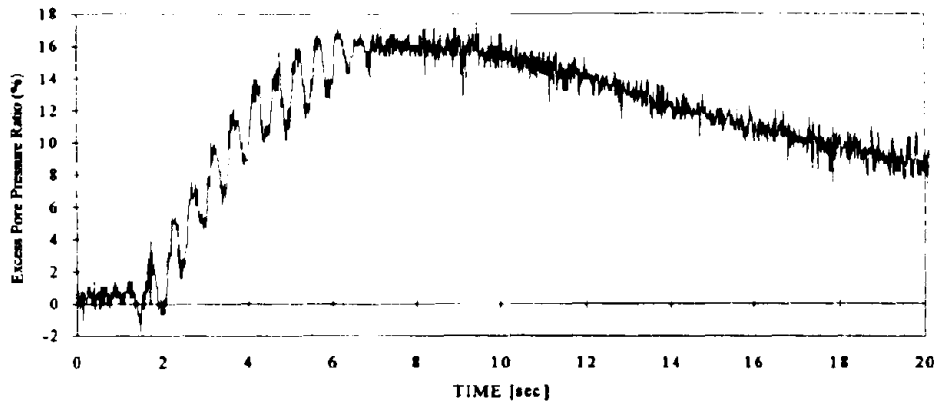
(a)   P1
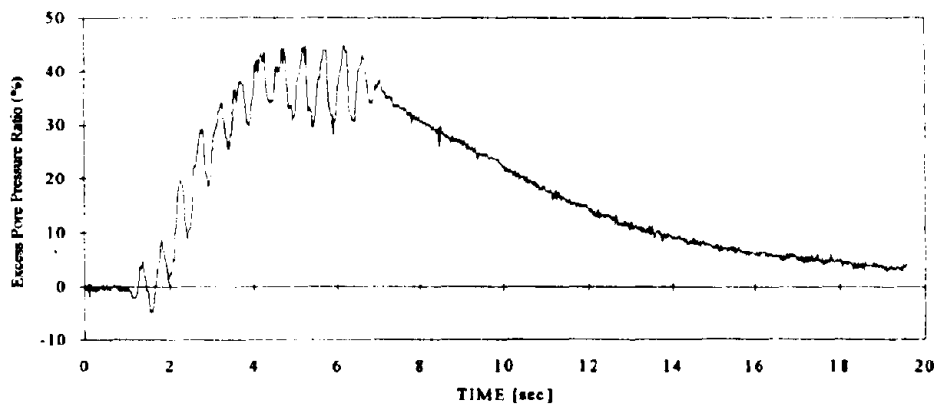
(b)   P2
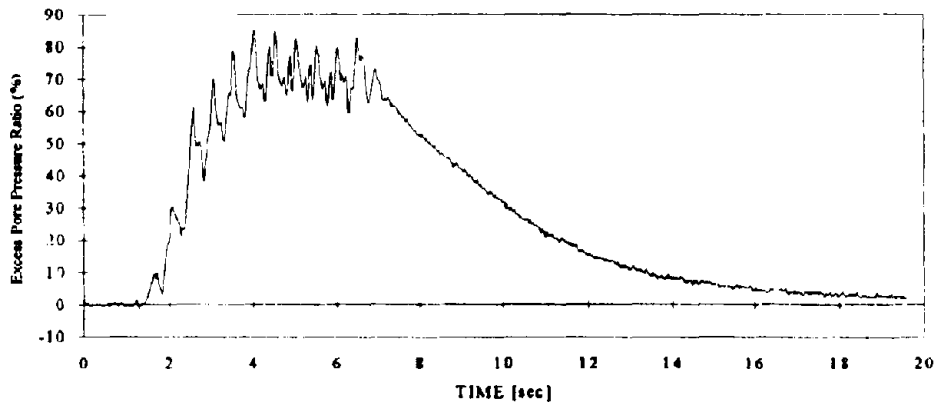
(c)   P4

Figure B.8: Excess pore pressure ratios in Test 1b
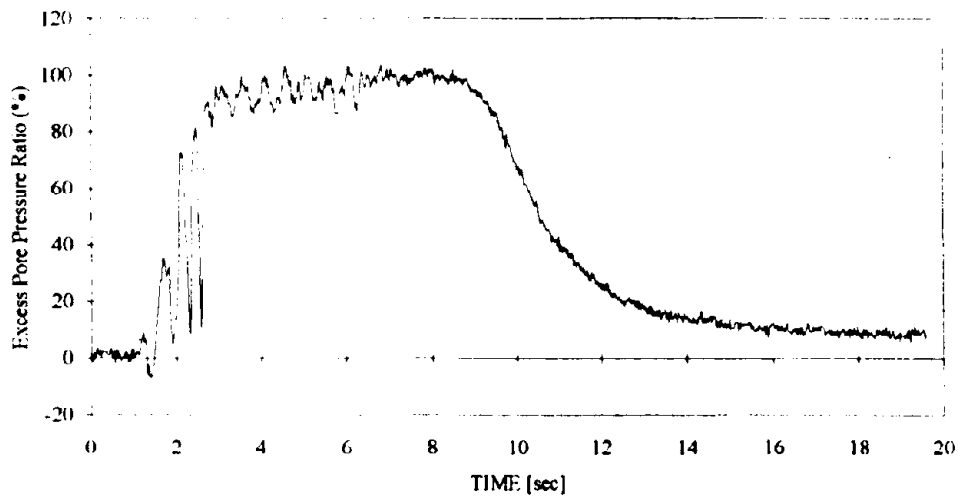
(d) P5
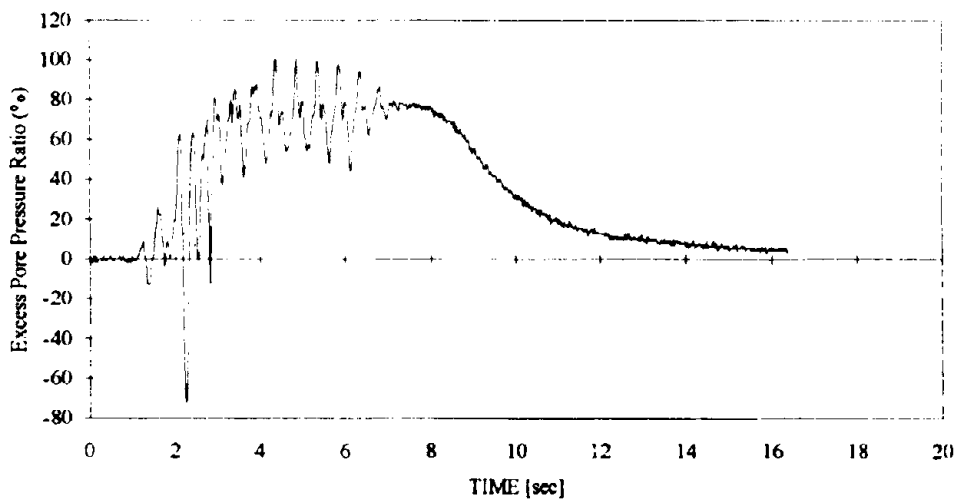
(e) P6

Figure B.8: Excess pore pressure ratios in Test 1b

287
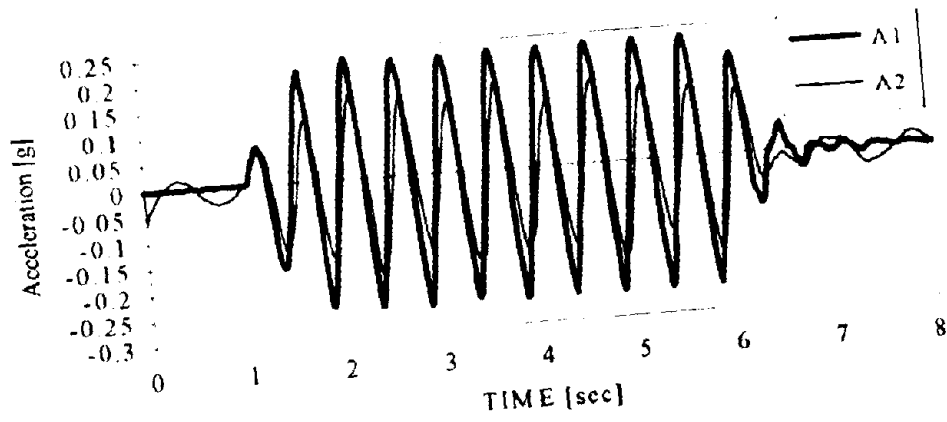
(a)   Al and A2
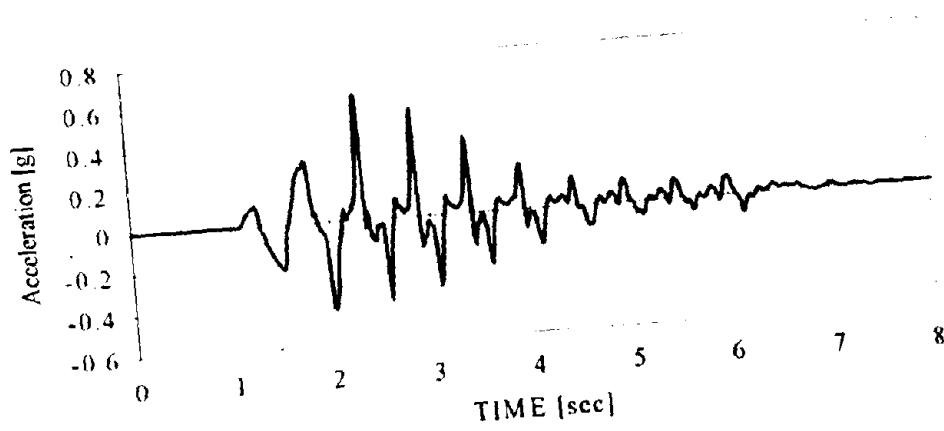
(b)   A3

Figure B.9: Acceleration data in Test 1c
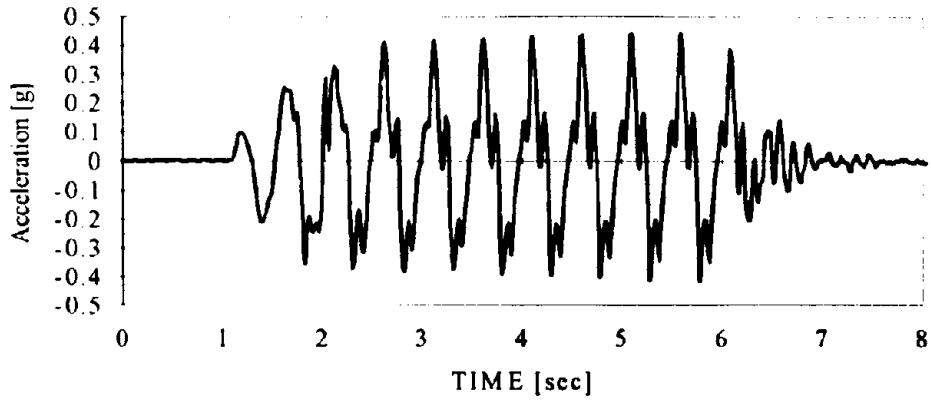
(c)   A4
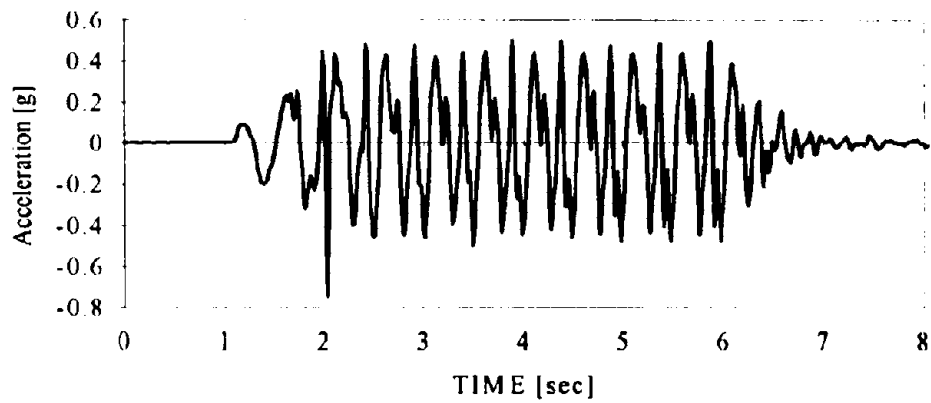
(d)   A5
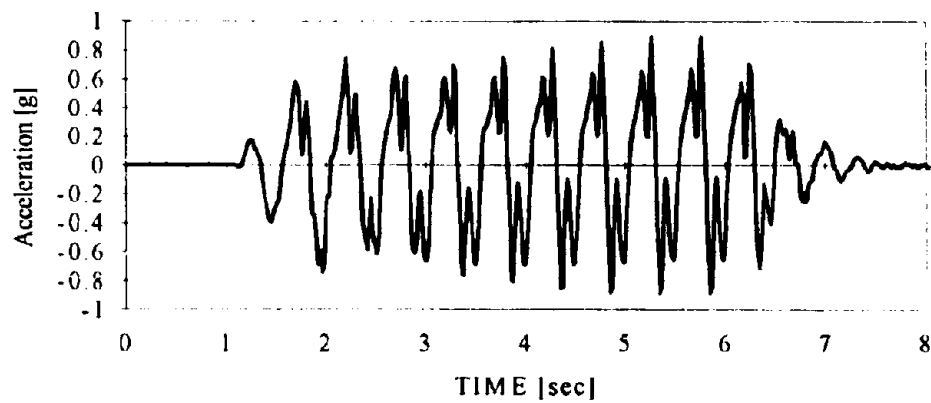
(e)   A6

Figure B.9: Acceleration data in Test 1c

289
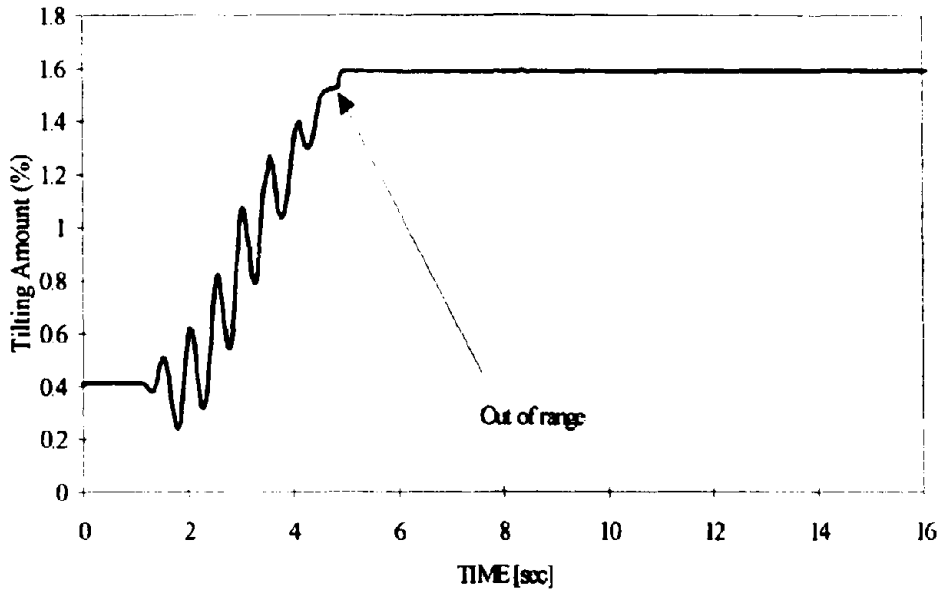
(a) Amount of tilt in wall (δ/H) - data of D3
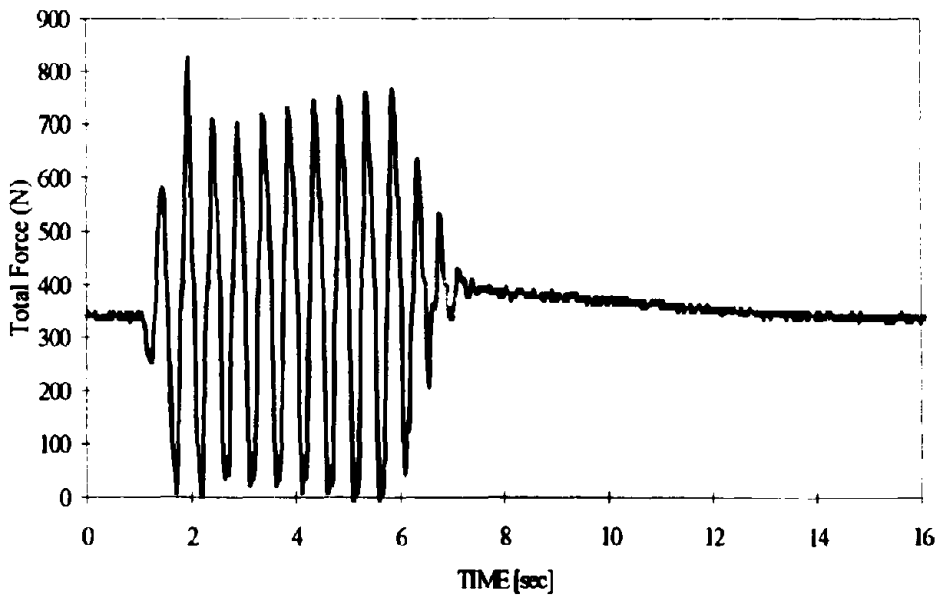
(b) Load data (in model scale)

Figure B.10: Displacement and load data in Test 1c
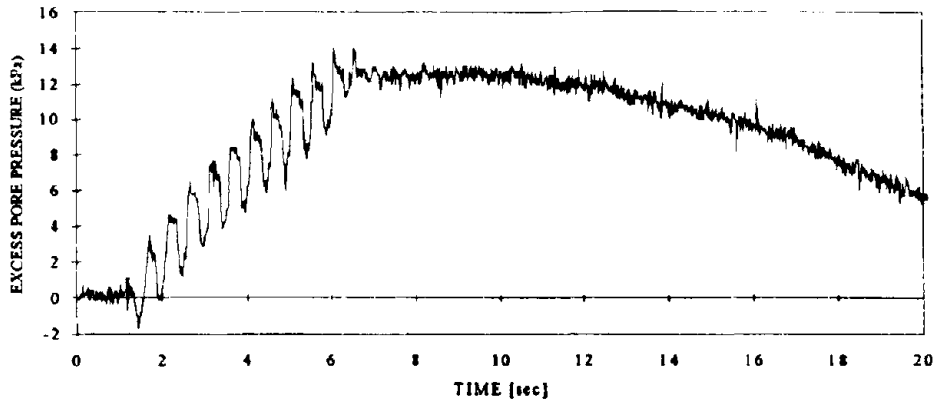
(a)   P1
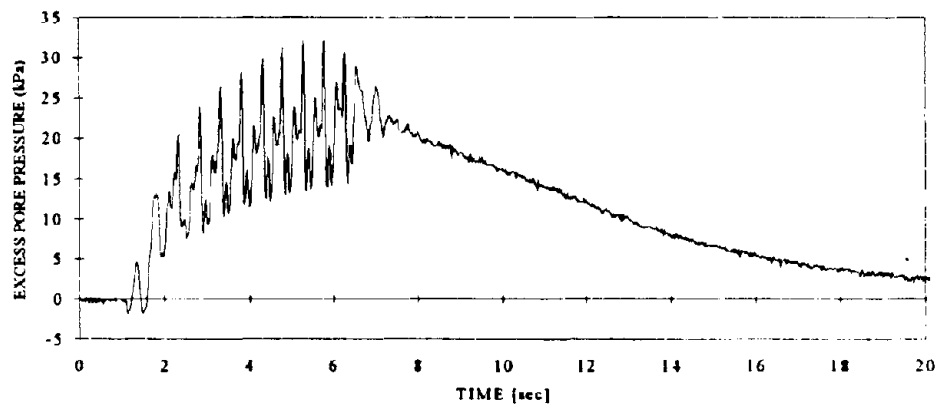
(b)   P2
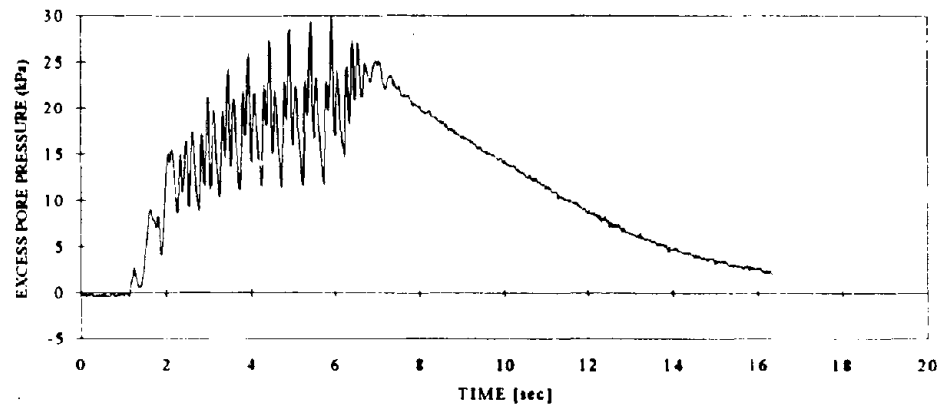
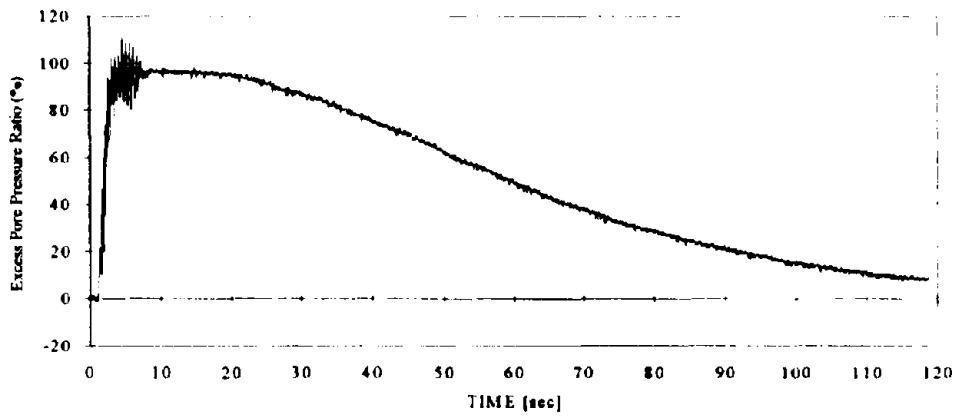(c)   P4

Figure B.11: Excess pore pressure data in Test 1c

291
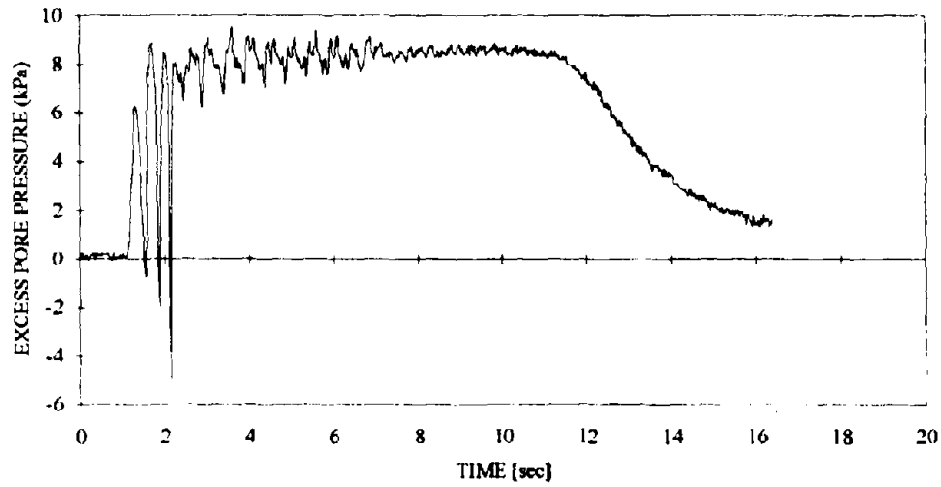
(d)   P5
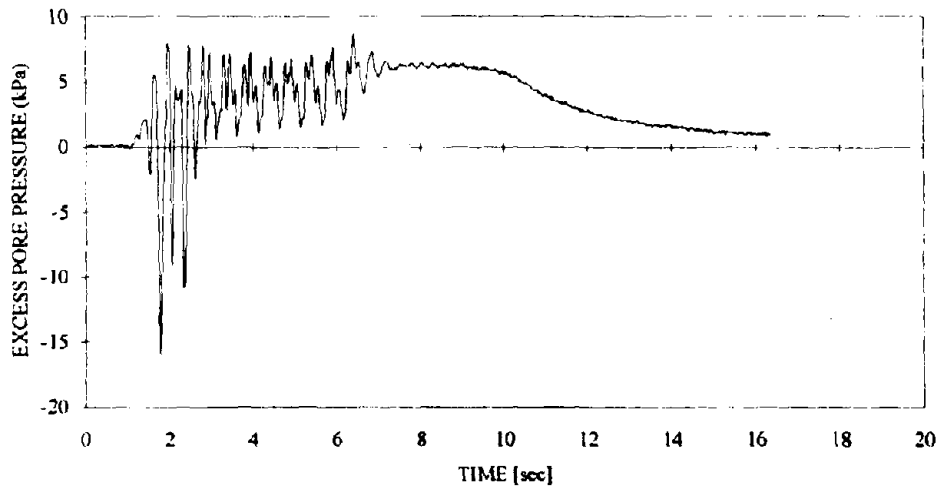

(e)   P6

Figure B.11: Excess pore pressure data in Test 1c

292

(a)   Pl
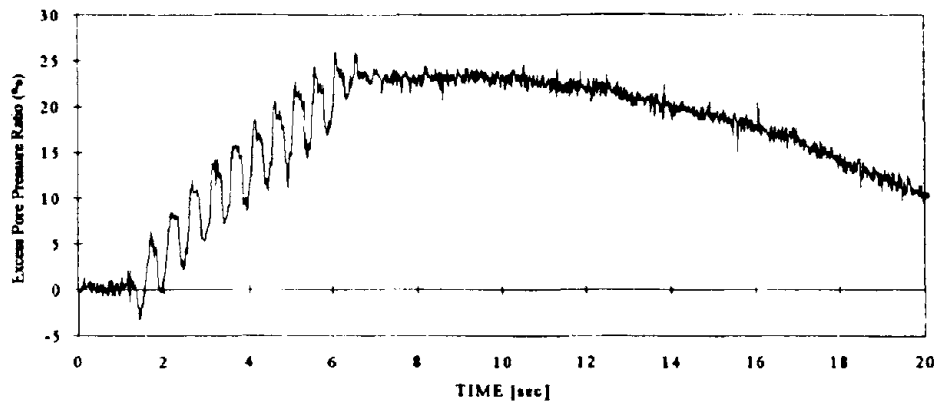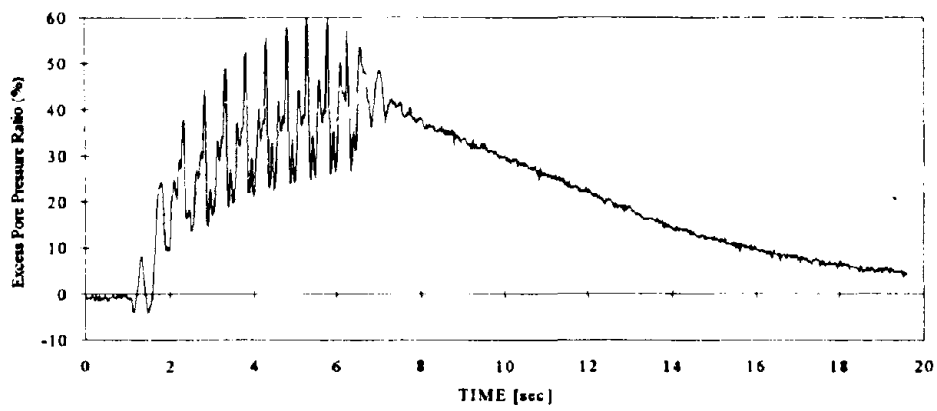
(b)   P2
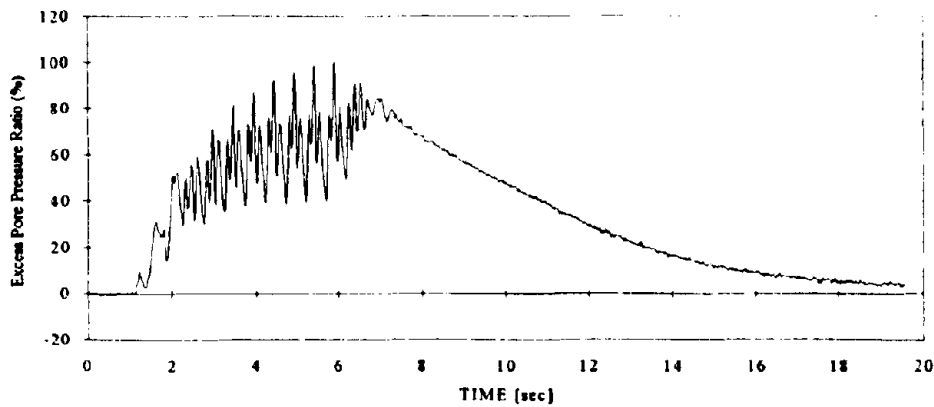
(c)   P4

Figure B.12: Excess pore pressure ratios in Test 1c

293
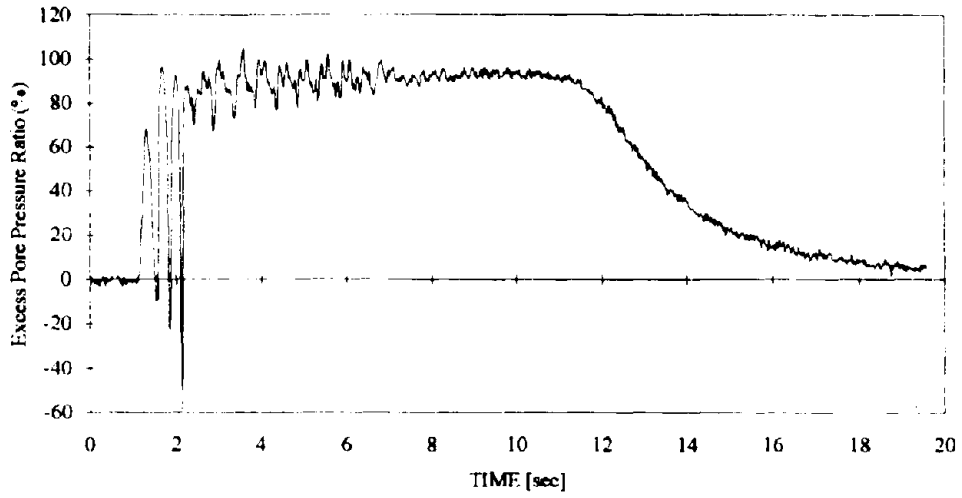
(d)   P5
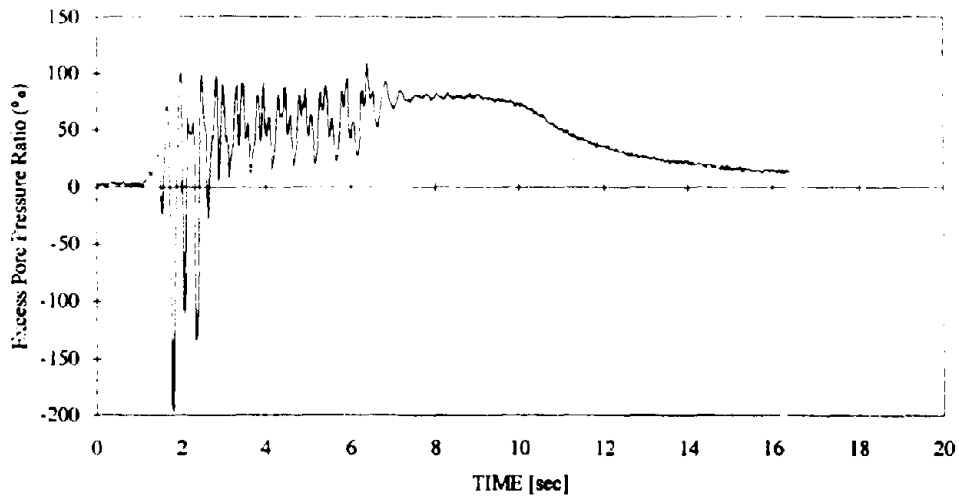
(e)   P6

Figure B.12: Excess pore pressure ratios in Test 1c

294

(a)   Al and A2

(b)   A3

(c)   A5

(d)   A6
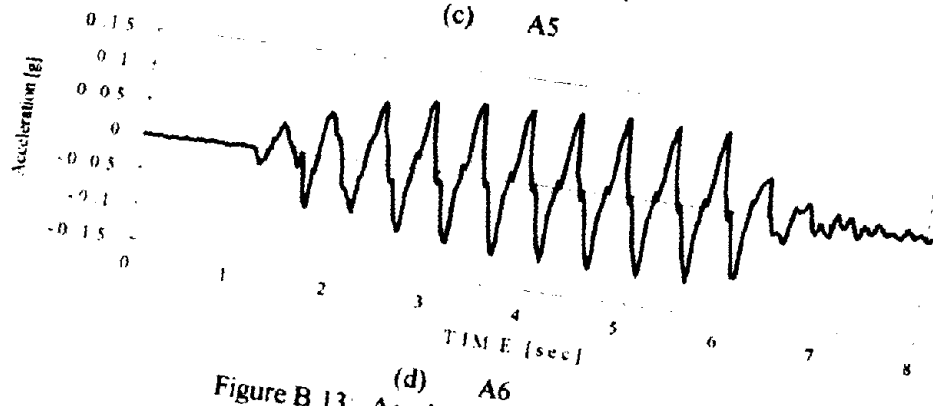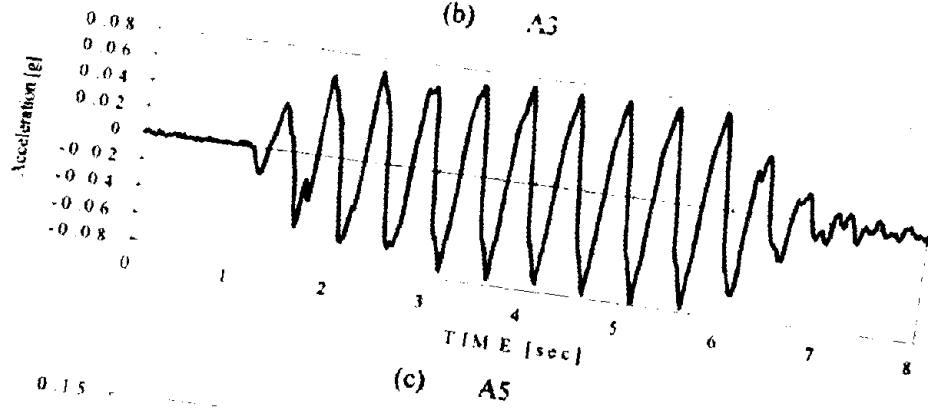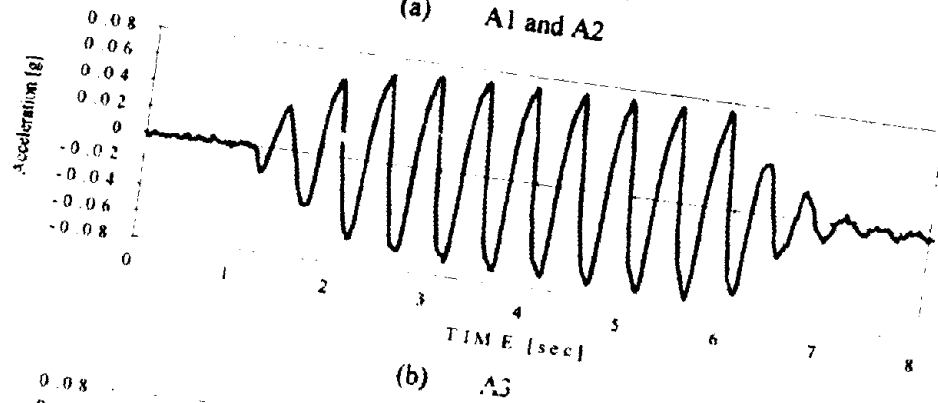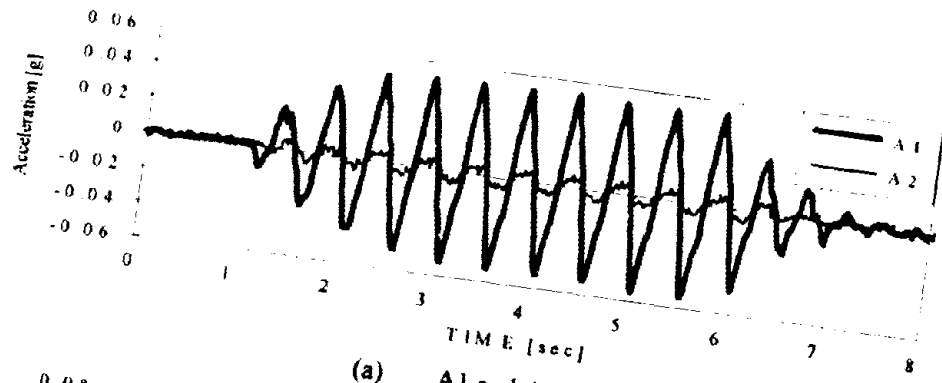
Figure B.13: Acceleration data in Test 2a
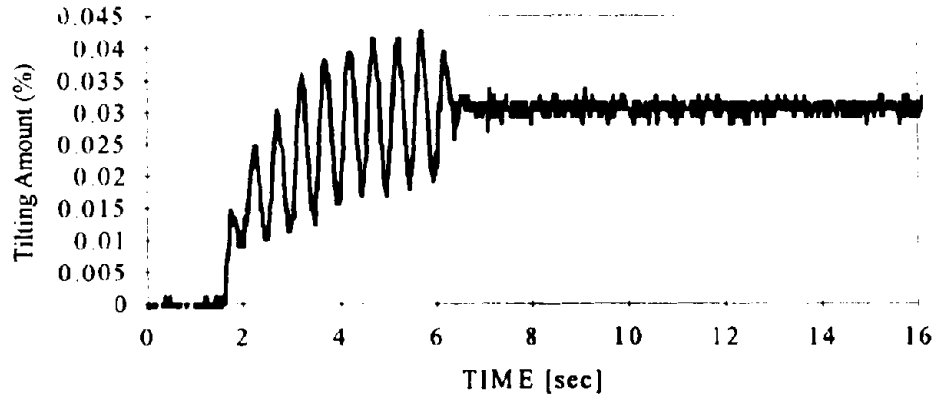
295

(a) Amount of tilt in wall (δ/H) - data of D3

Bad record
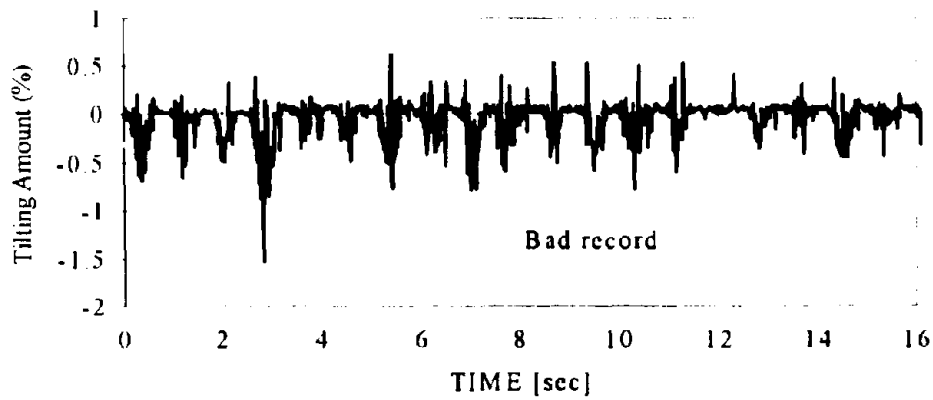
(b) Amount of tilt in wall (δ/H) - data of D4
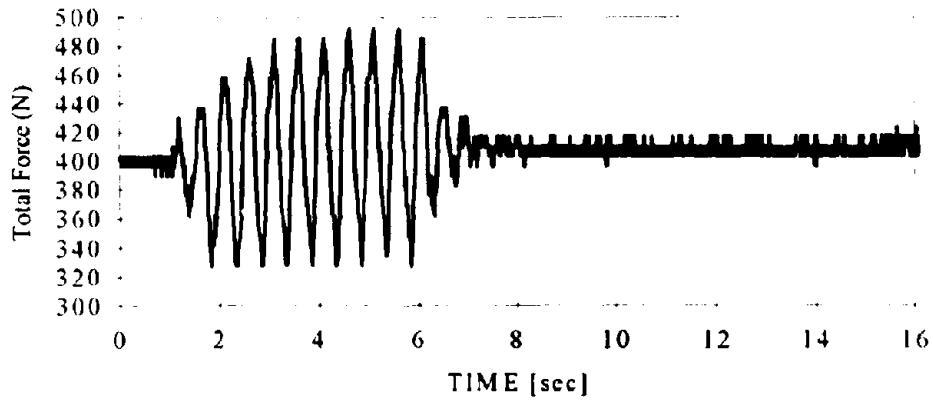
(c) Load data (in model scale)

Figure B.14: Displacement and load data in Test 2a

296
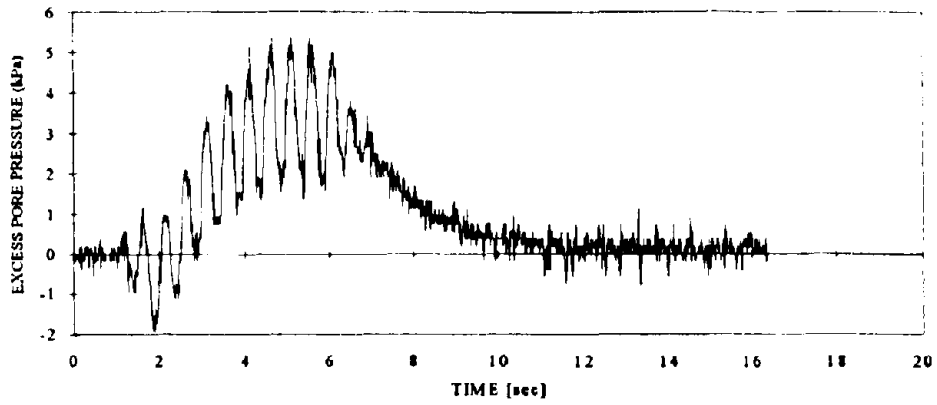
(a) P2
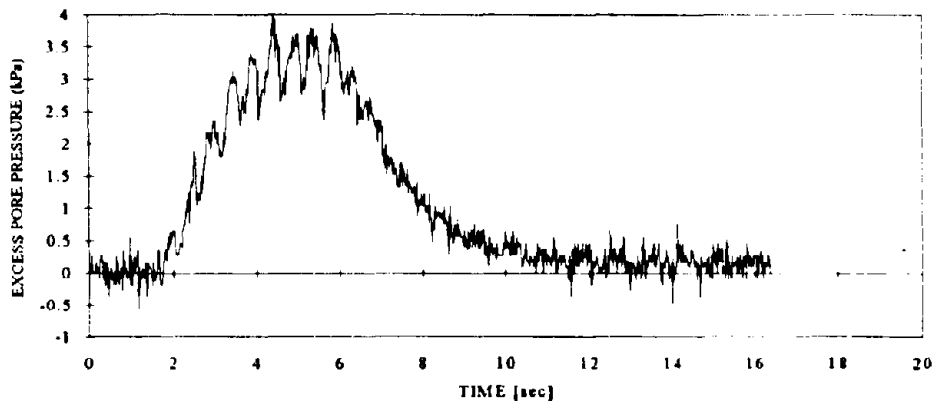
(b) P3
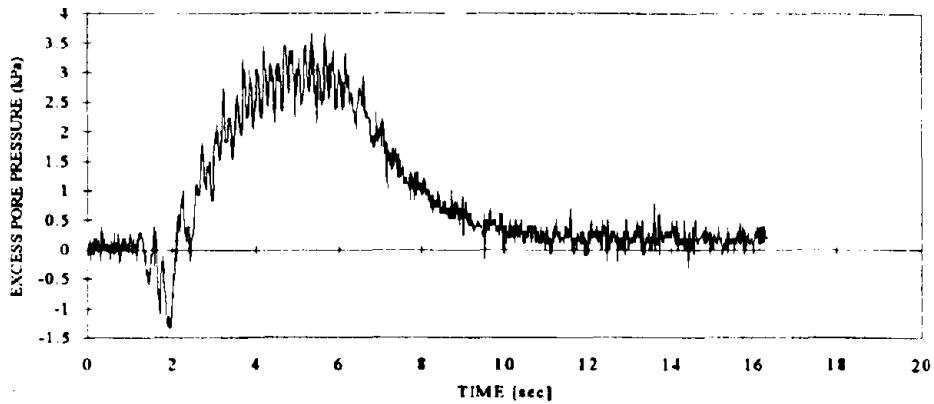
(c) P4

Figure B.15: Excess pore pressure data in Test 2a

297
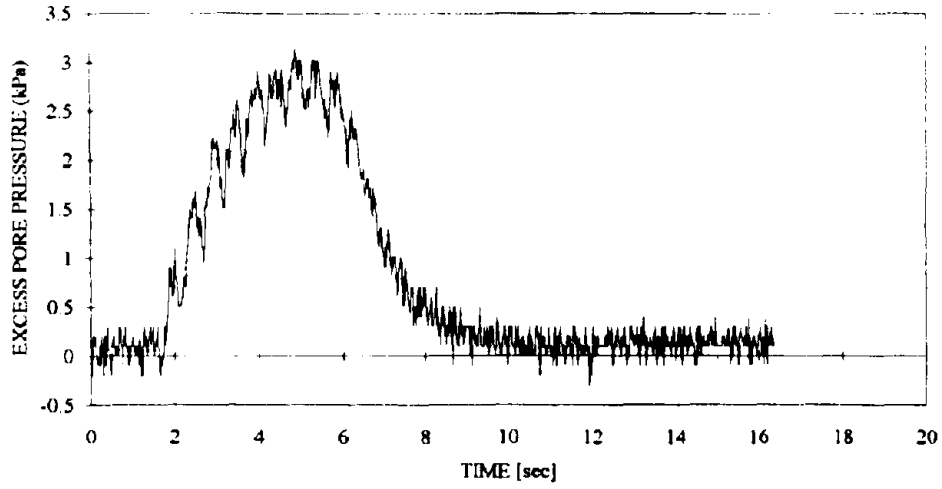
(d)   P5
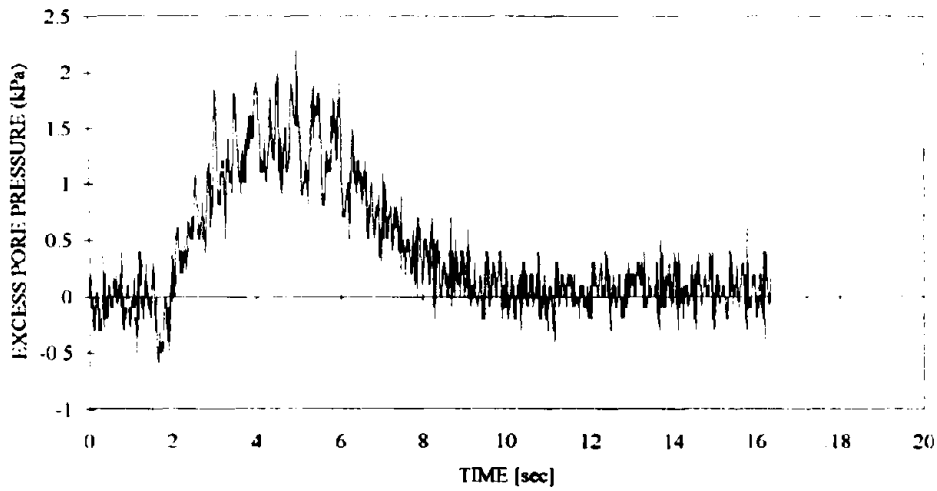
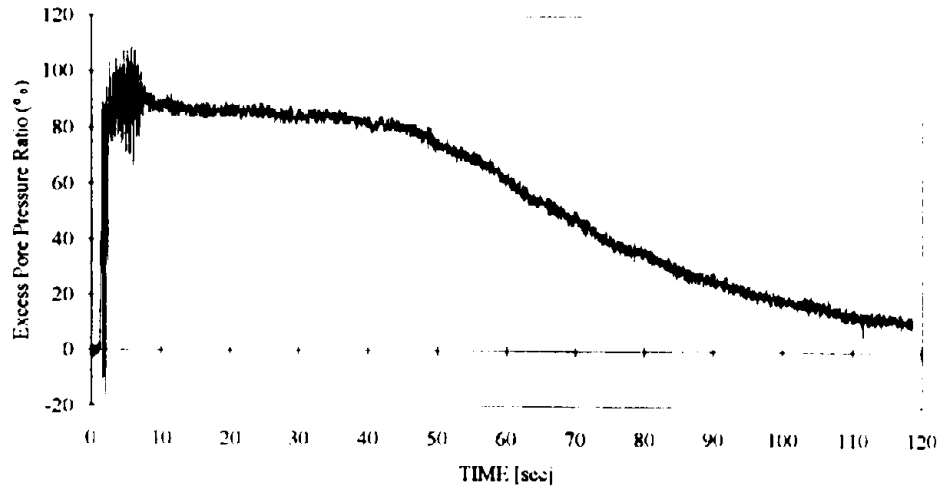

(e)   P6

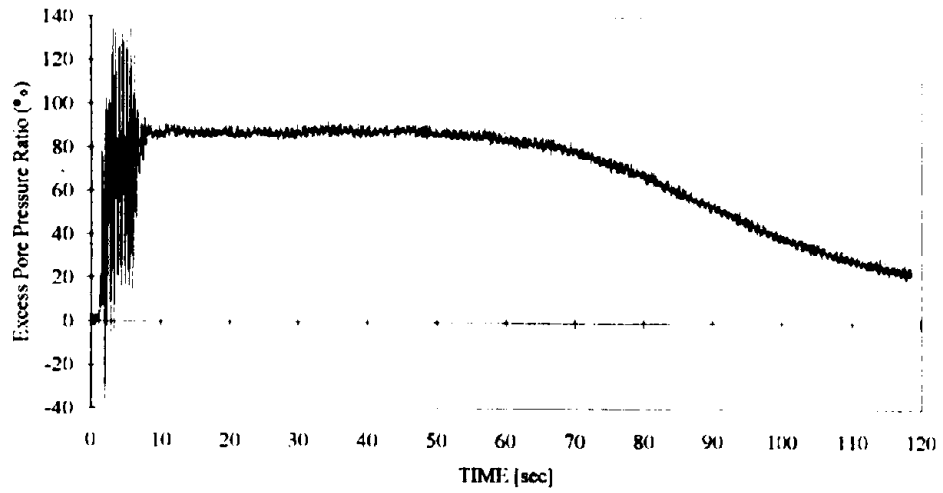Figure B.15: Excess pore pressure data in Test 2a

298
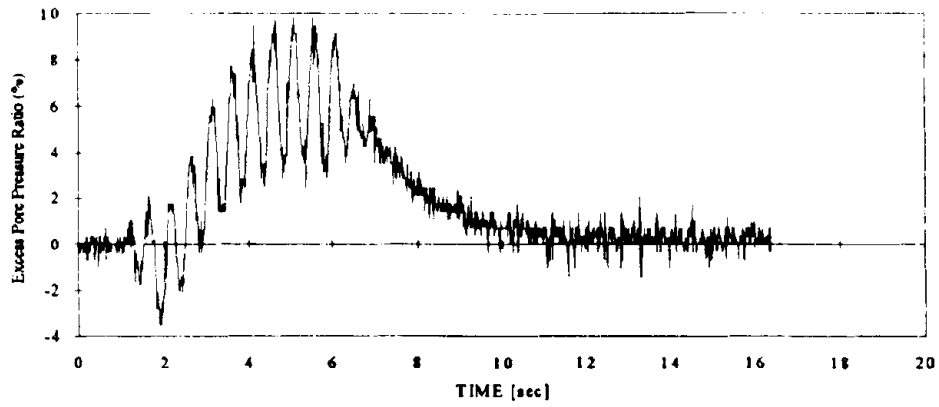
(a)   P2
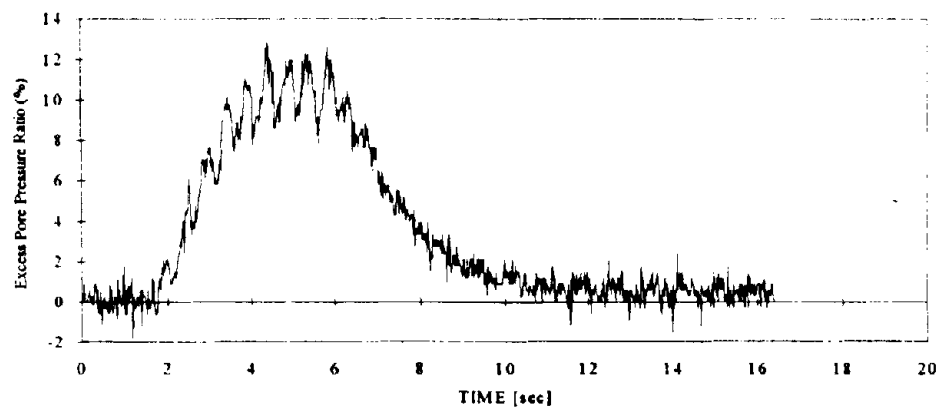
(b)   P3
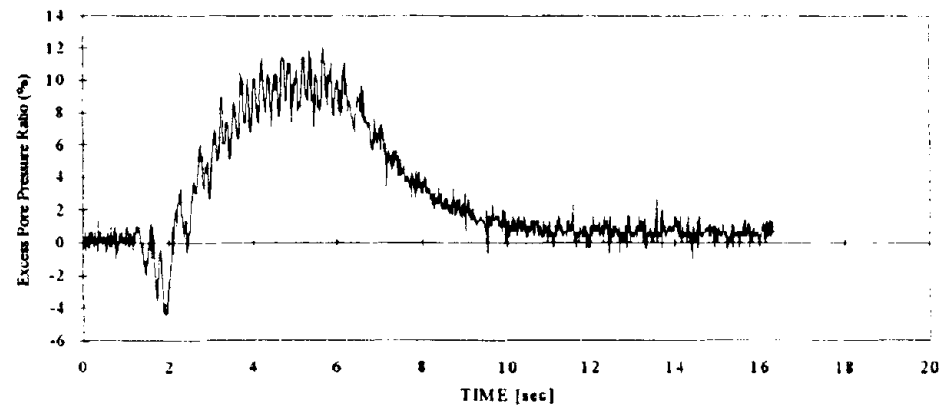
(c)   P4

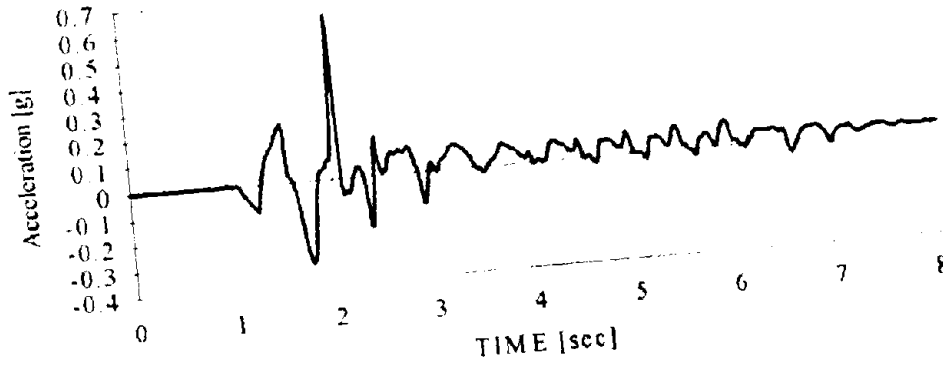Figure B.16: Excess pore pressure ratio in Test 2a

299
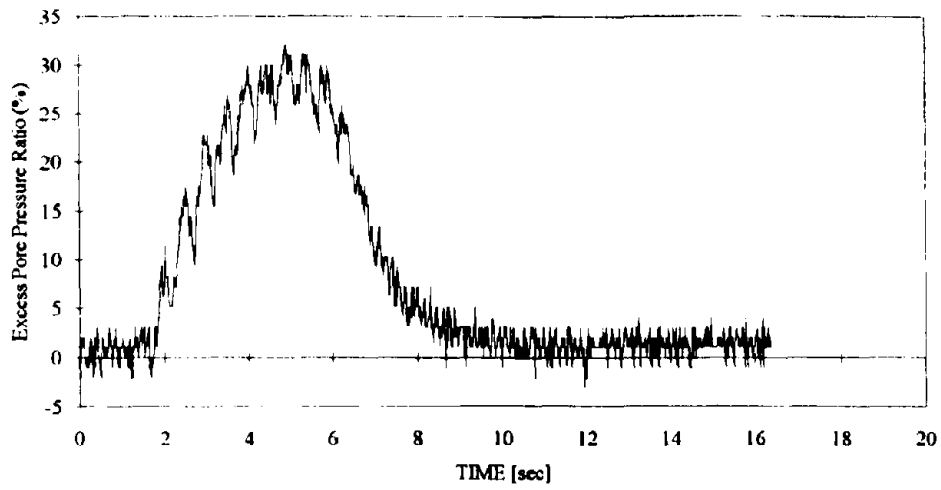
(d)   **P5**
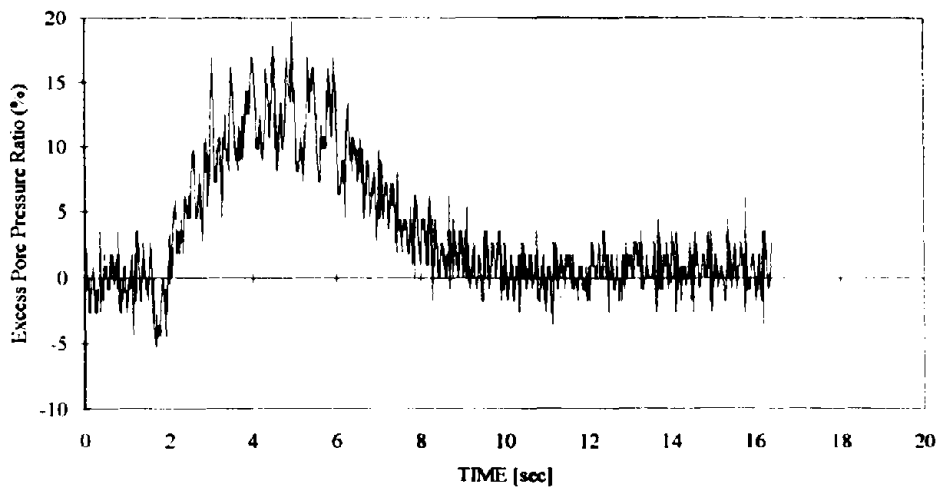
(e)   **P6**

Figure B.16: Excess pore pressure ratio in Test 2a
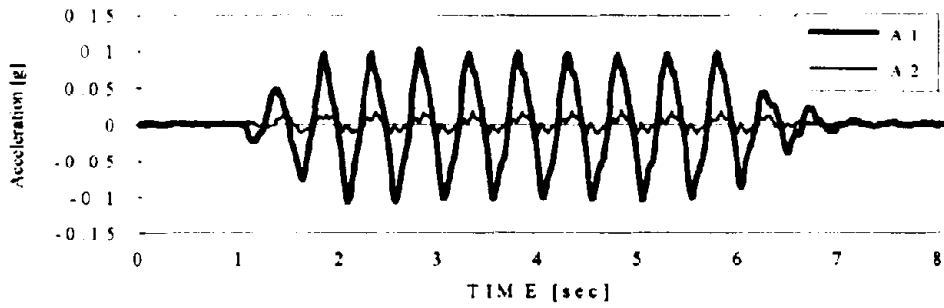
(a)   A1 and A2
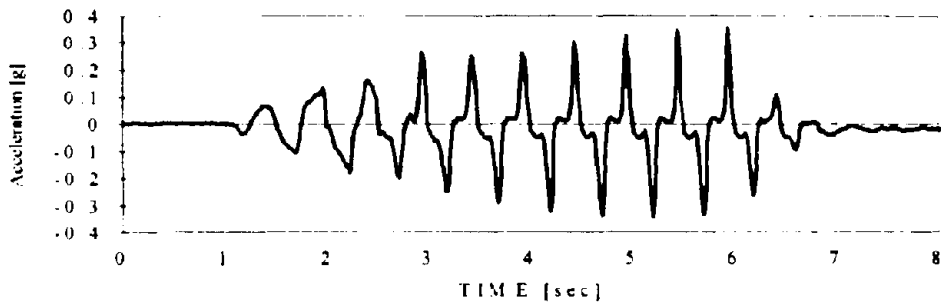
(b)   A3
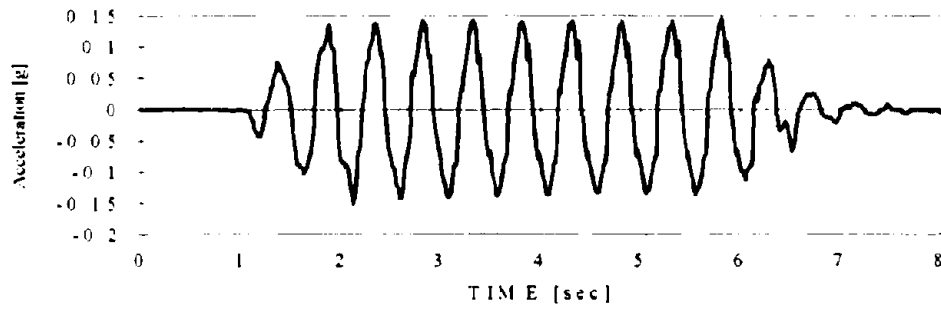
(c)   A5
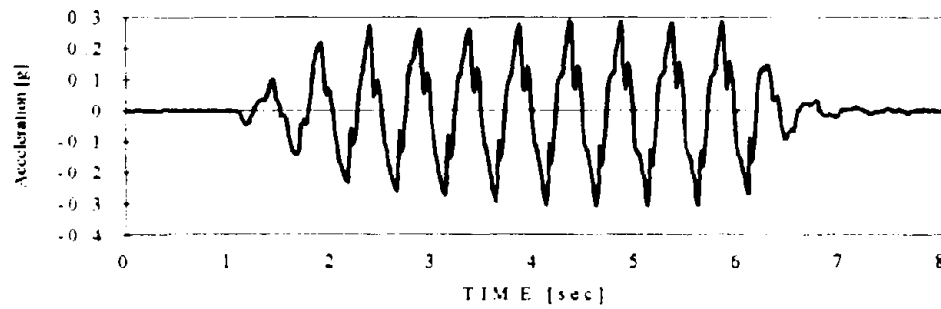
(d)   A6

Figure B.17 Acceleration data in Test 2b
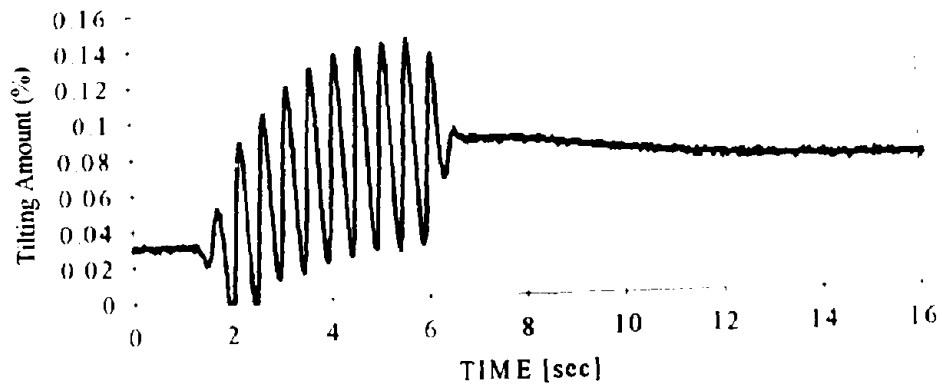
(a) Amount of tilt in wall (δ/H) - data of D3

Bad record
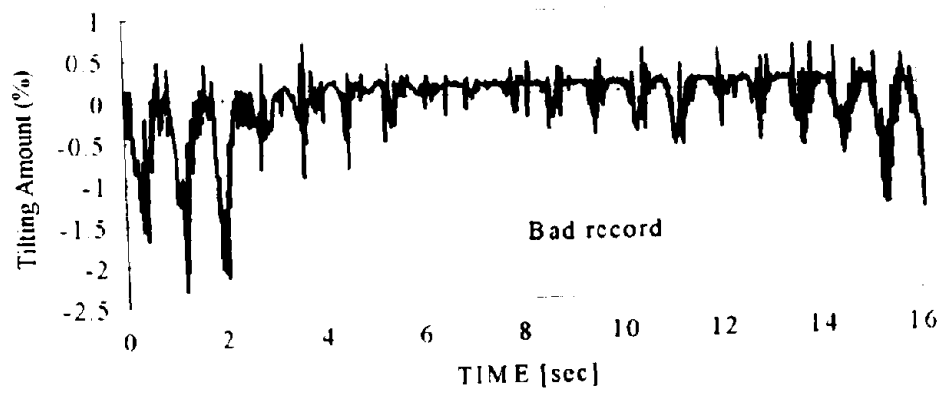
(b) Amount of tilt in wall (δ/H) - data of D4
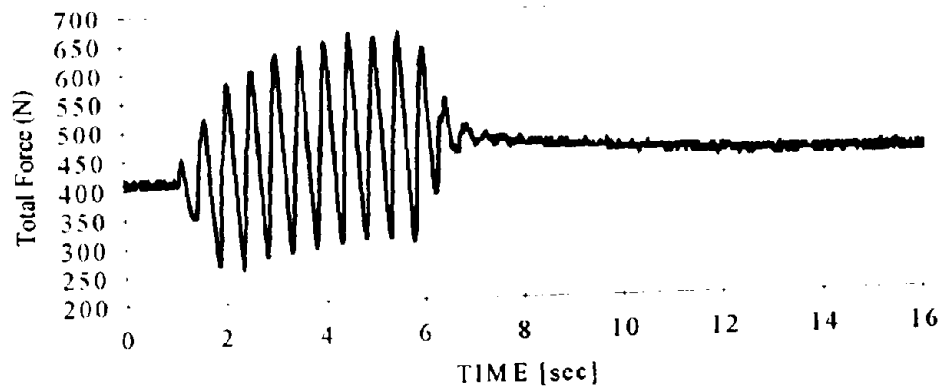
(c) Load data (in model scale)

Figure B.18: Displacement and load data in Test 2b

302
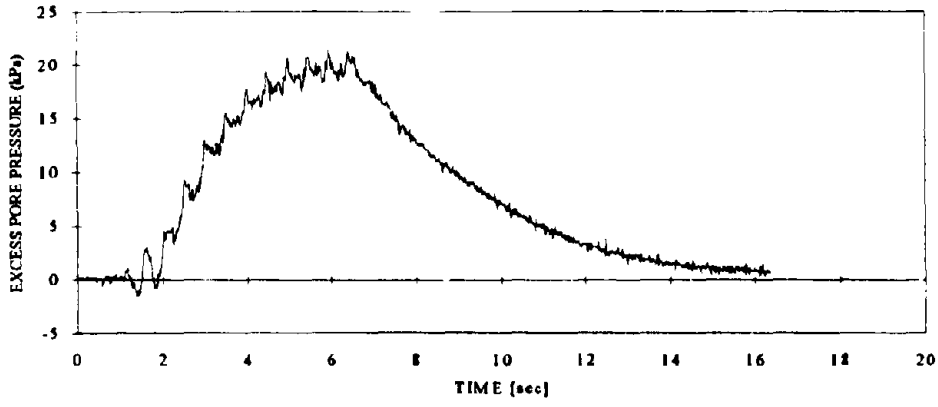
(a)   P2
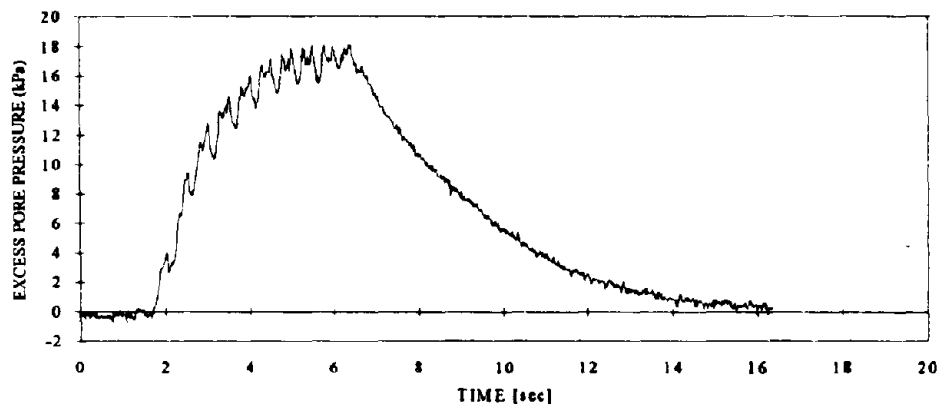
(b)   P3
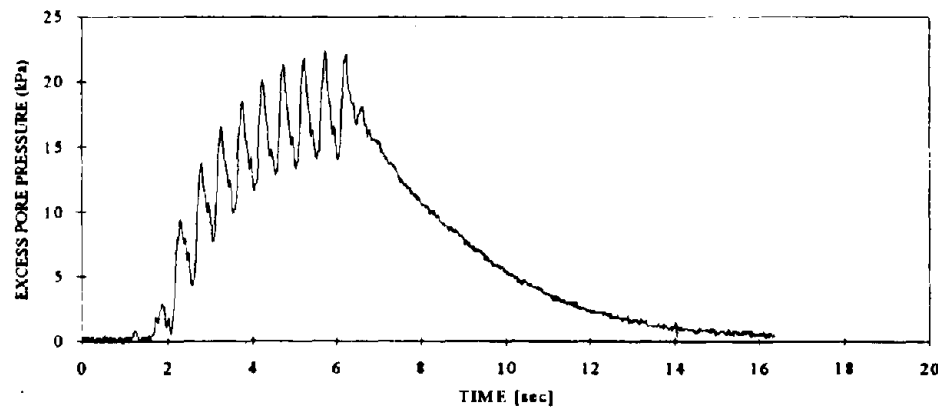
(c)   P4

Figure B.19: Excess pore pressure data in Test 2b

303
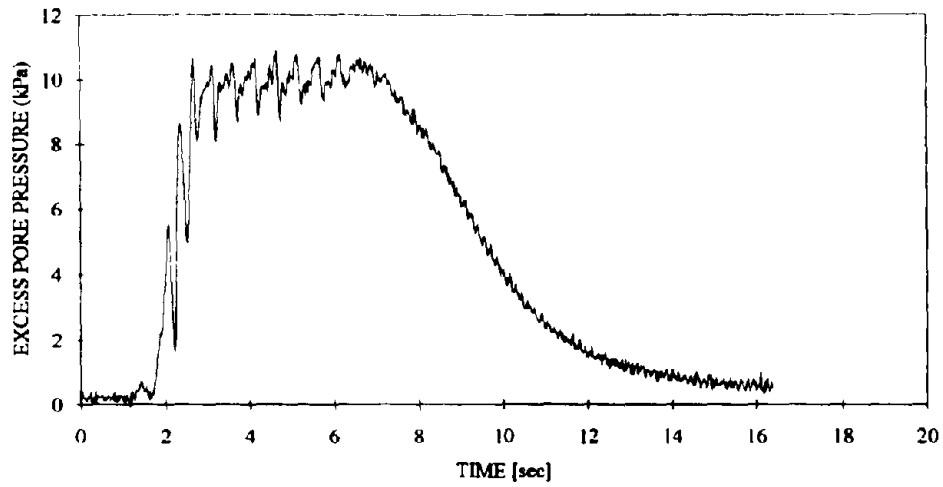
(d)   P5
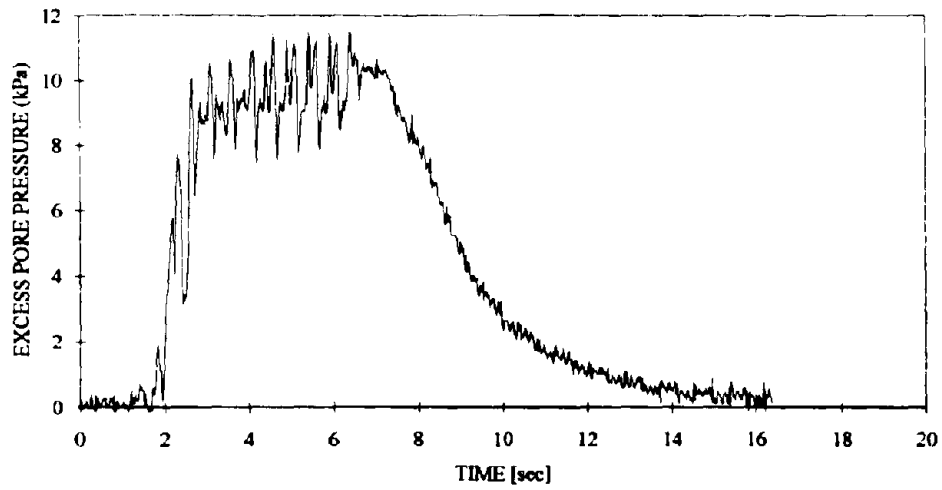
(e)   P6

Figure B.19: Excess pore pressure data in Test 2b
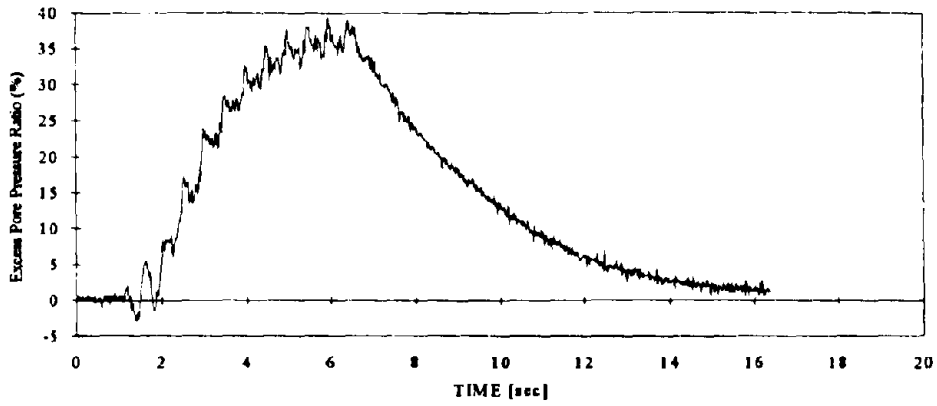
(a)   P2
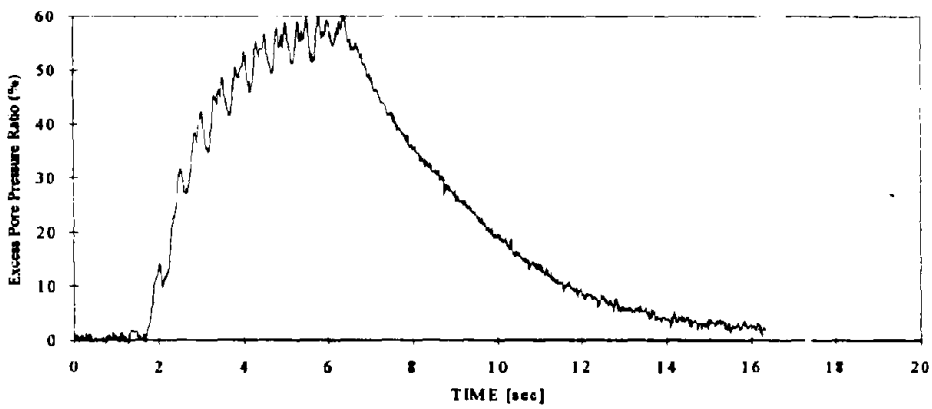
(b)   P3
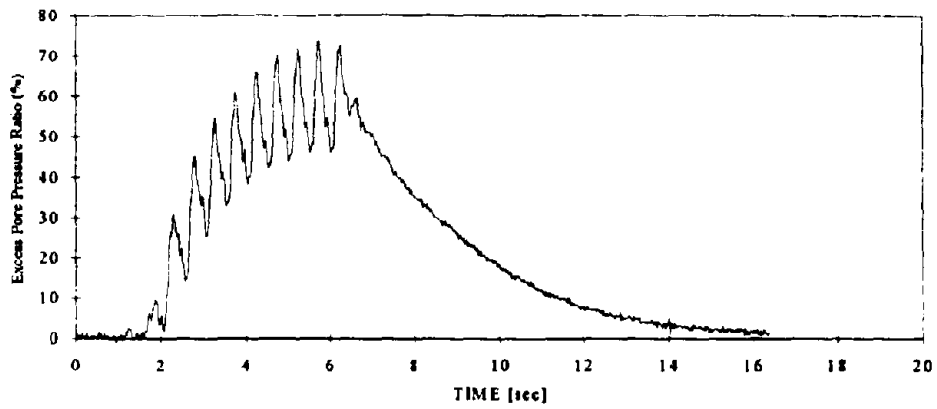
(c)   P4

Figure B.20: Excess pore pressure ratio in Test 2b

305
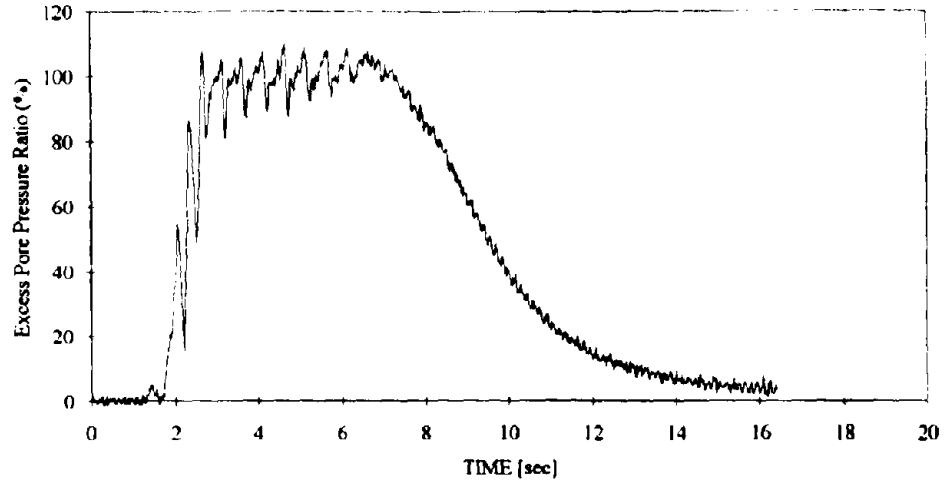
(d)   P5
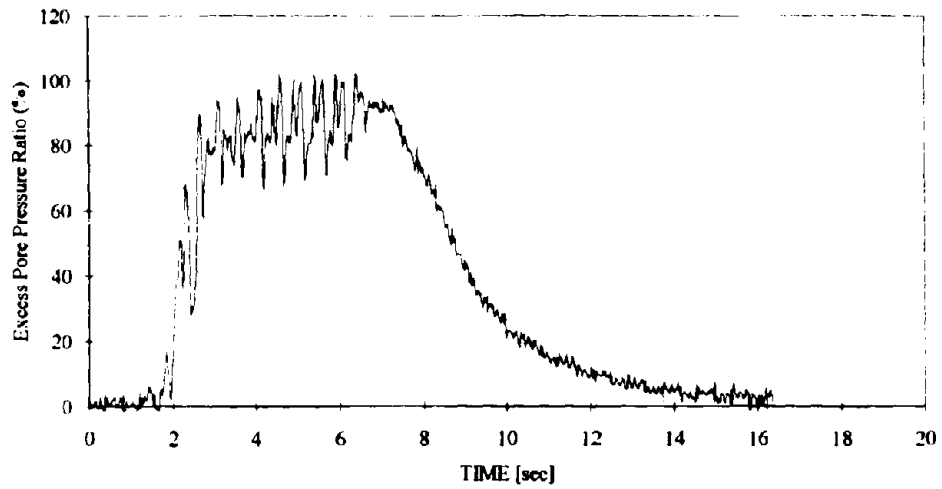
(e)   P6

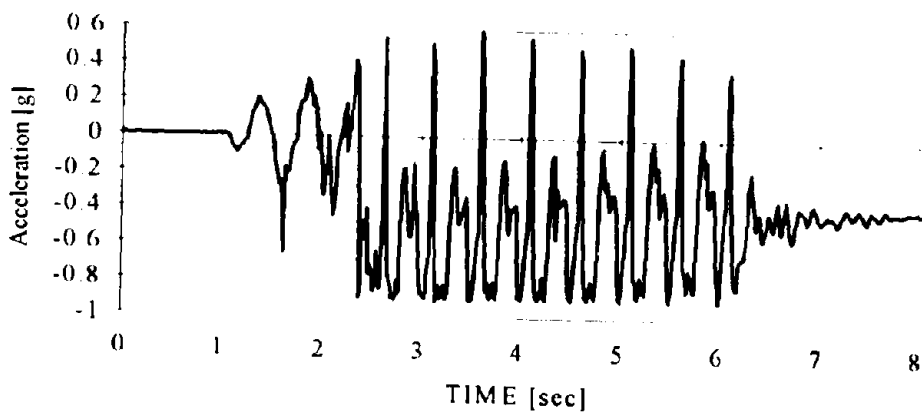Figure B.20: Excess pore pressure ratio in Test 2b
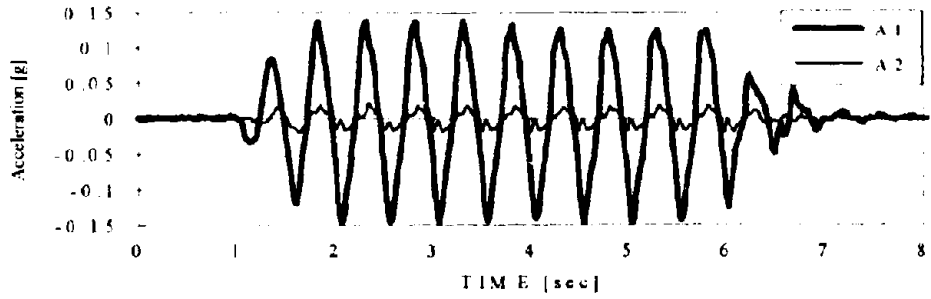
(a)   A1 and A2
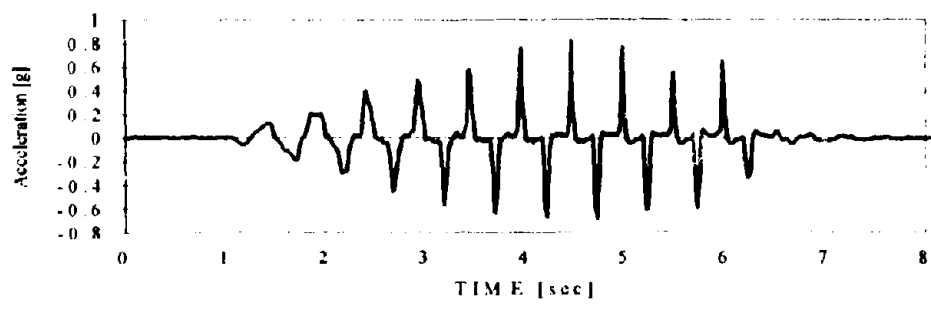
(b)   A3
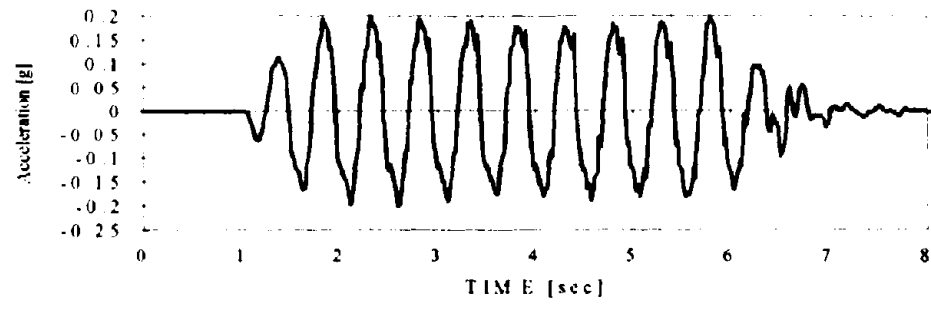
(c)   A5
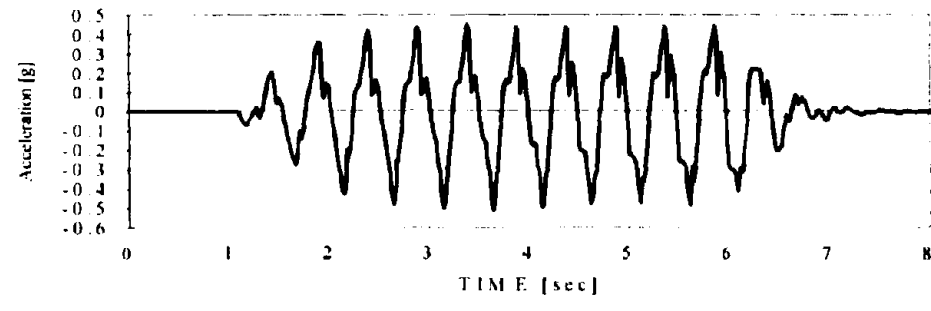
(d)   A6

Figure B.21 Acceleration data in Test 2c
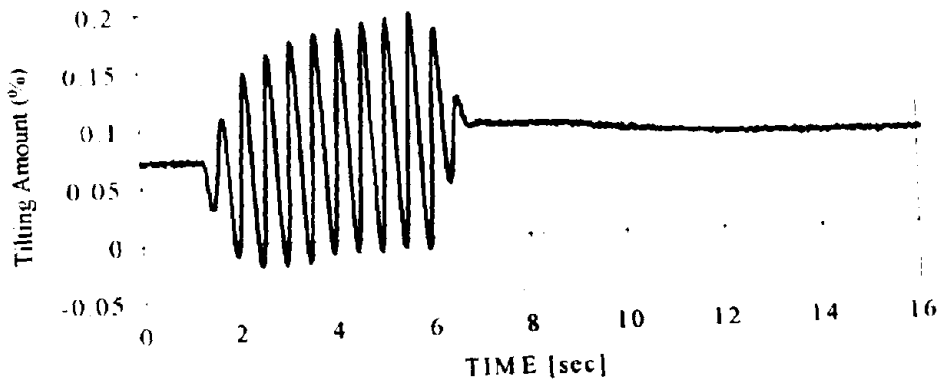
307

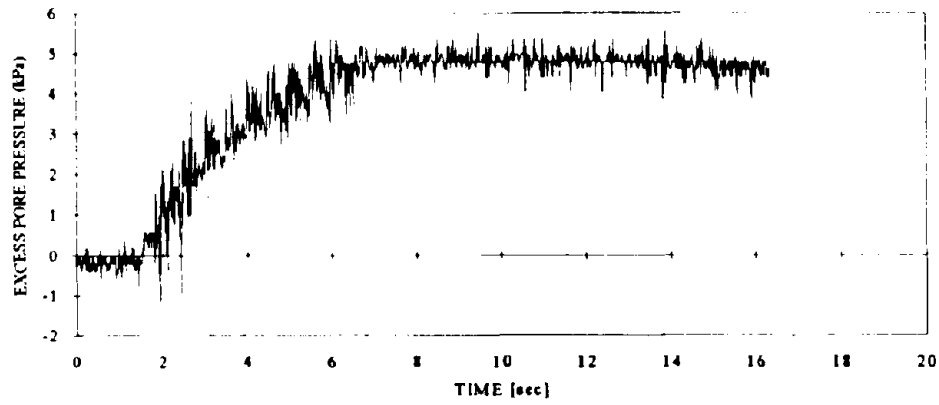(a) Amount of tilt in wall (δ/H) - data of D3

Bad record
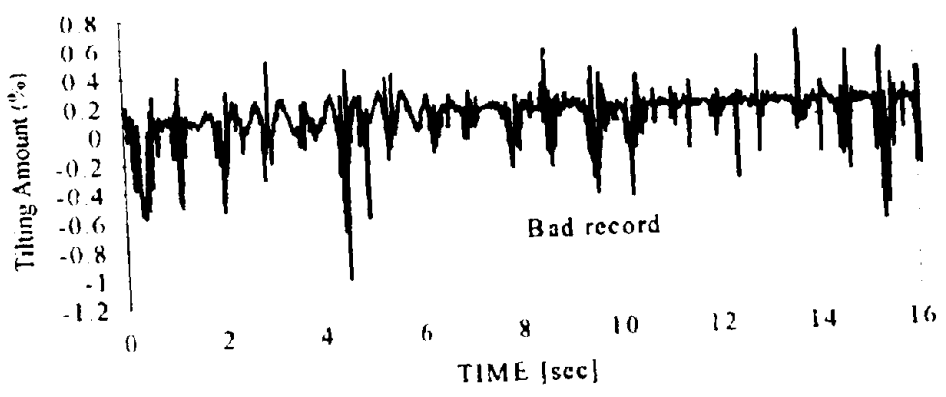
(b) Amount of tilt in wall (δ/H) - data of D4
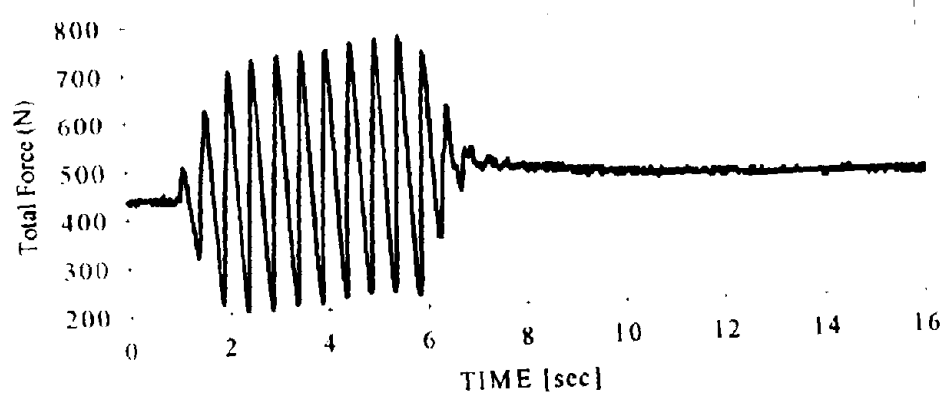
(c) Load data (in model scale)

Figure B.22: Displacement and load data in Test 2c

308
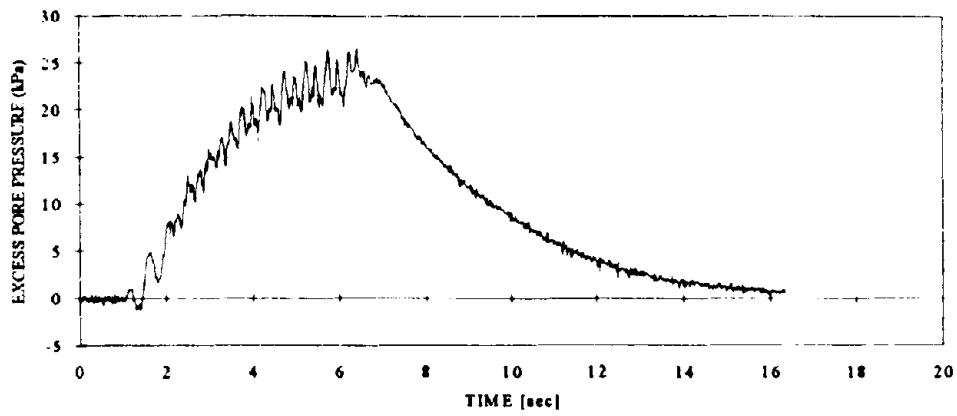
(a) P2
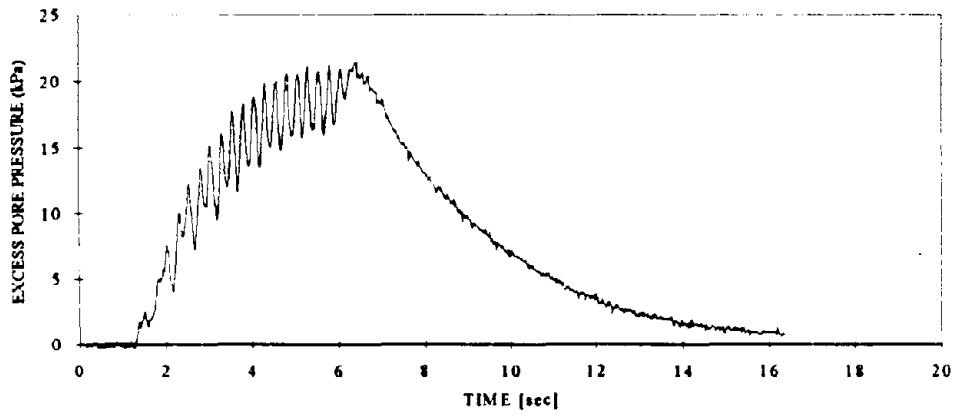
(b) P3

(c) P4

Figure B.23: Excess pore pressure data in Test 2c
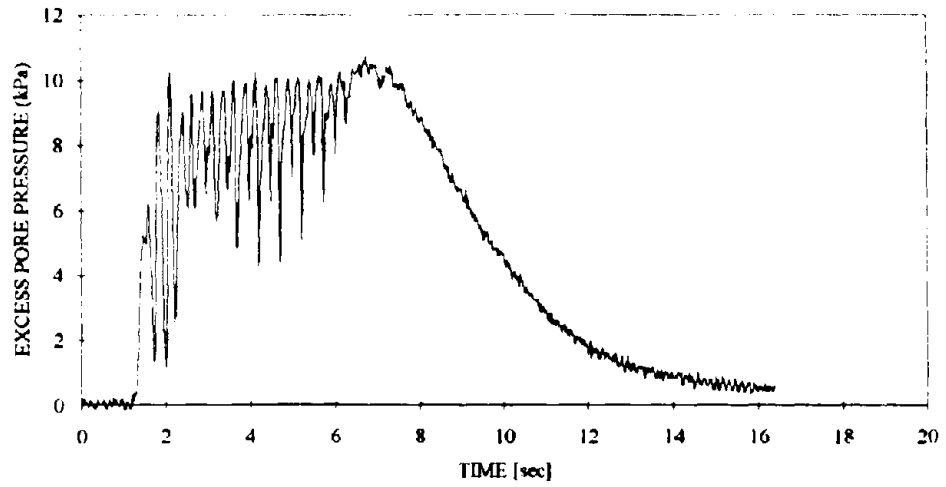
(d)   P5
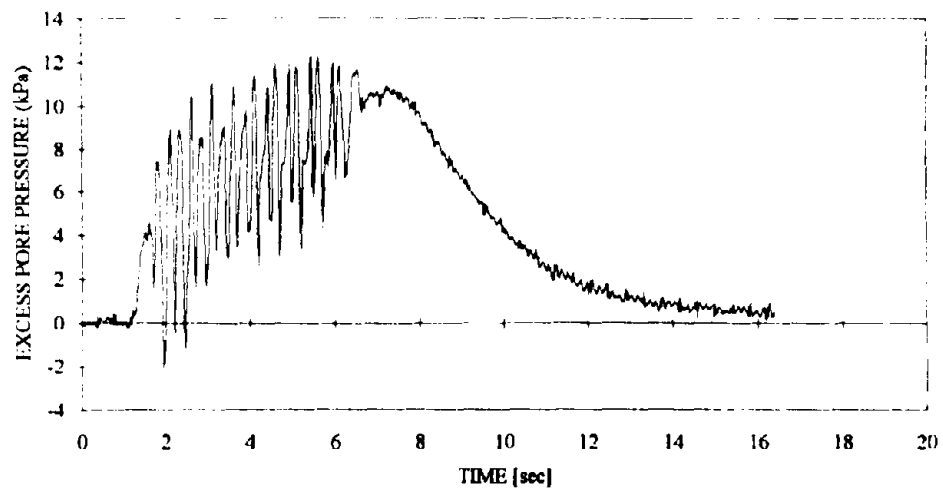
(e)   P6

Figure B.23: Excess pore pressure data in Test 2c
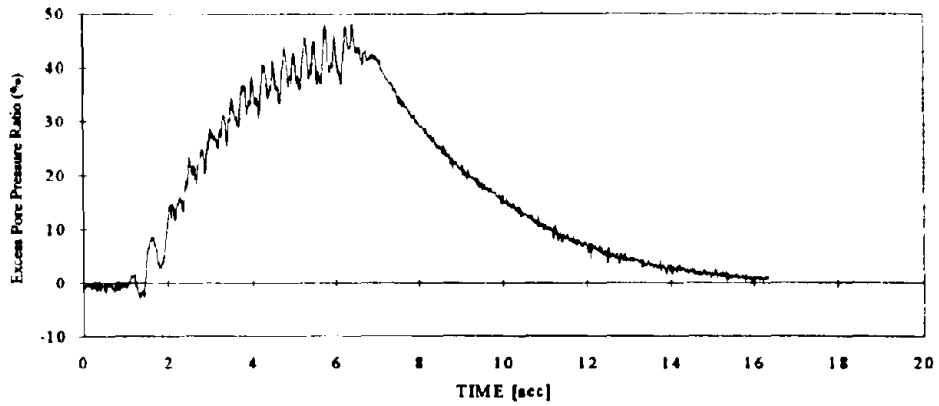
(a)   P2
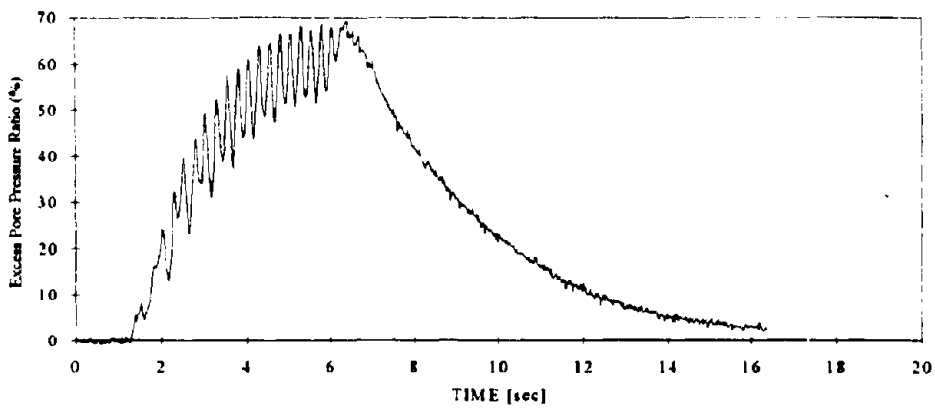
(b)   P3
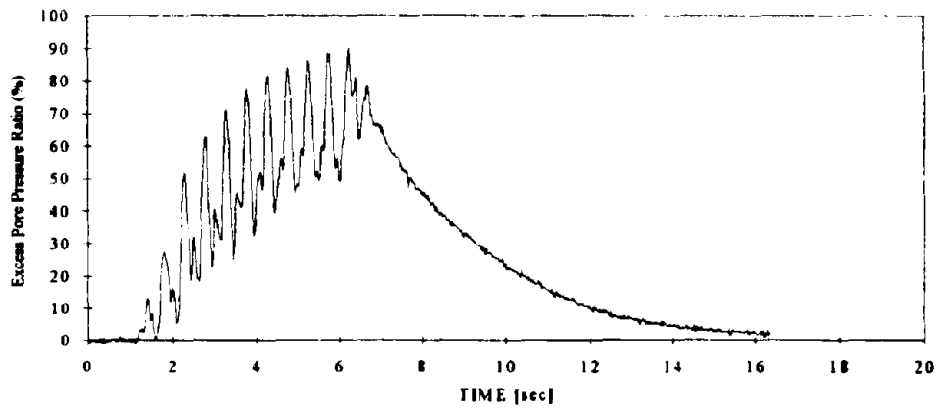
(c)   P4

Figure B.24: Excess pore pressure ratio in Test 2c

311
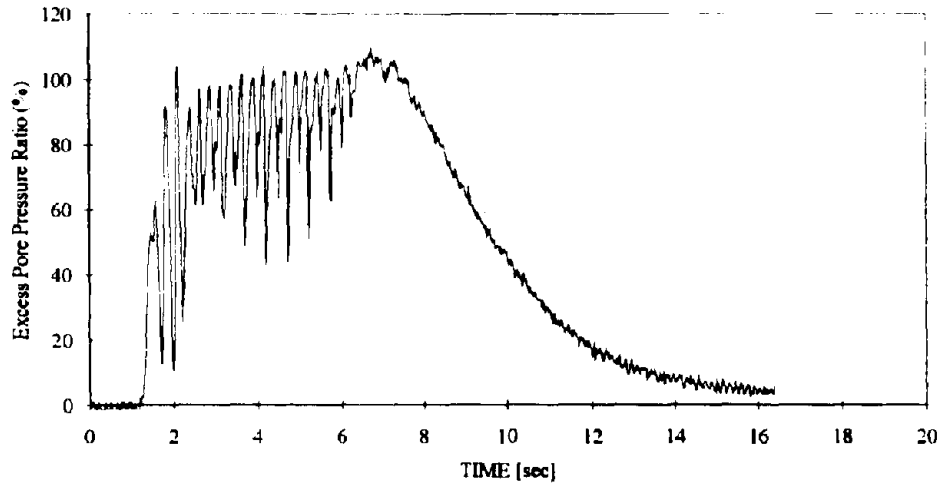
(d)   P5
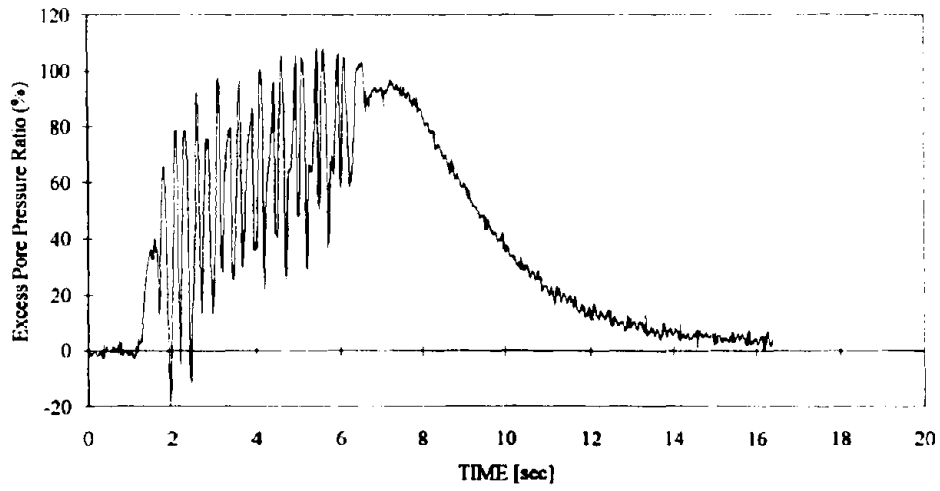
(e)   P6

Figure B.24: Excess pore pressure ratio in Test 2c

312
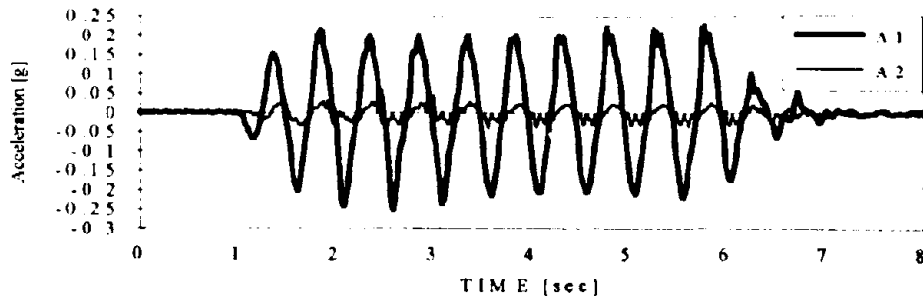
(a)   A1 and A2
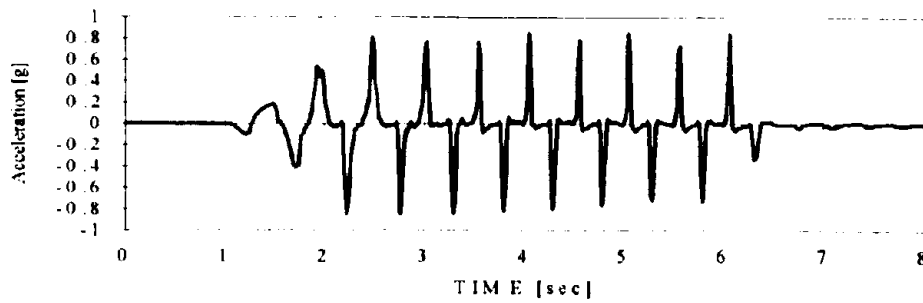
(b)   A3
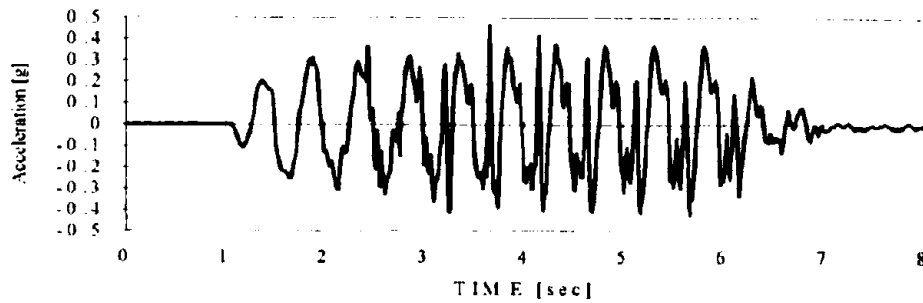
(c)   A5
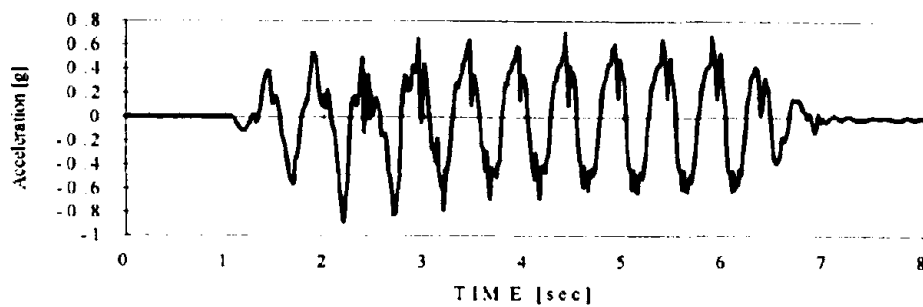
(d)   A6

Figure B 25: Acceleration data in Test 2d
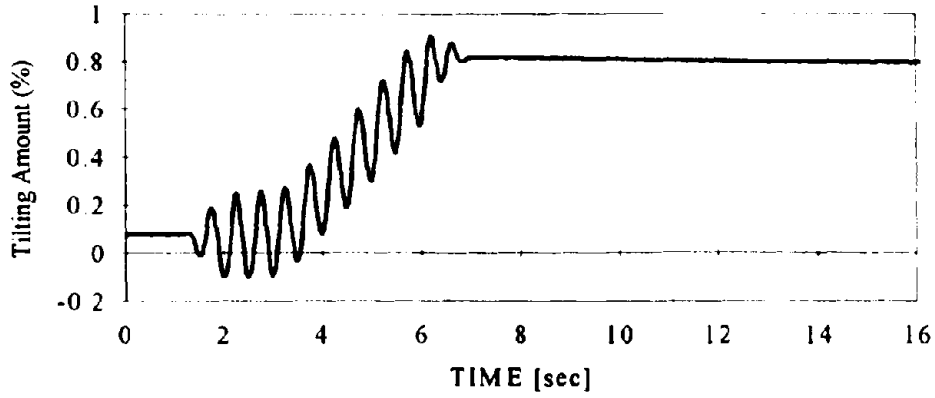
313

(a) Amount of tilt in wall (δ/H) - data of D3
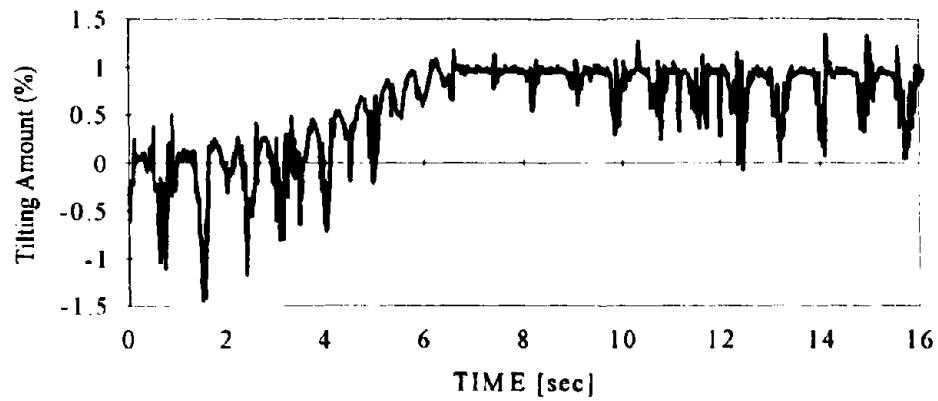
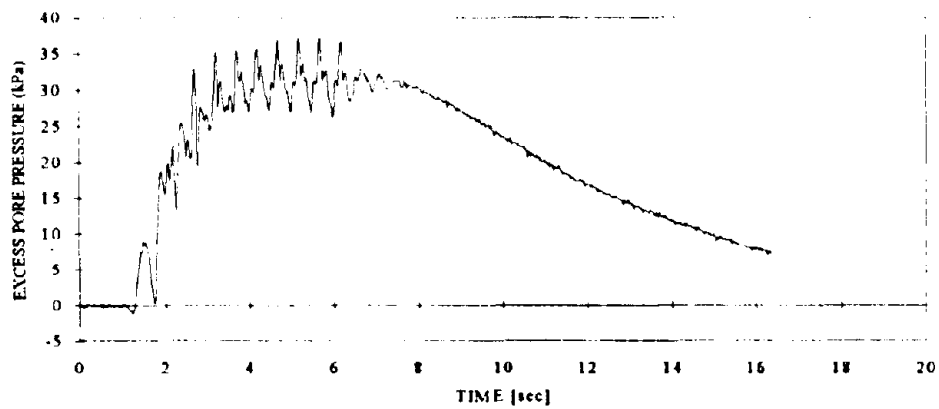(b) Amount of tilt in wall (δ/H) - data of D4
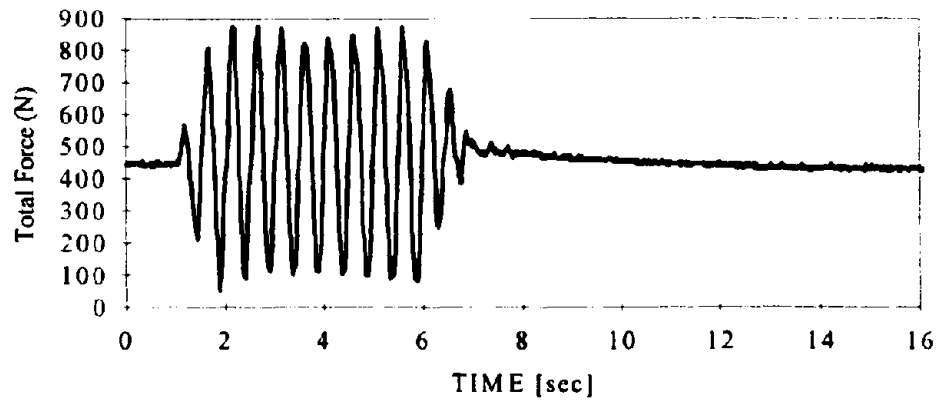
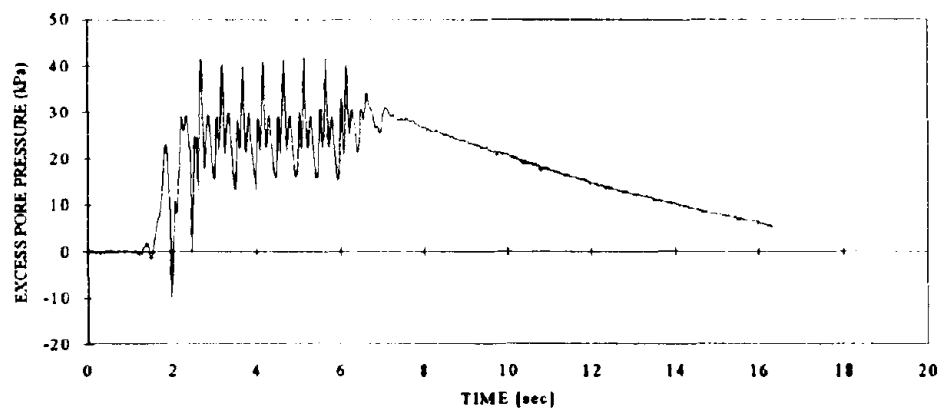
(c) Load data (in model scale)

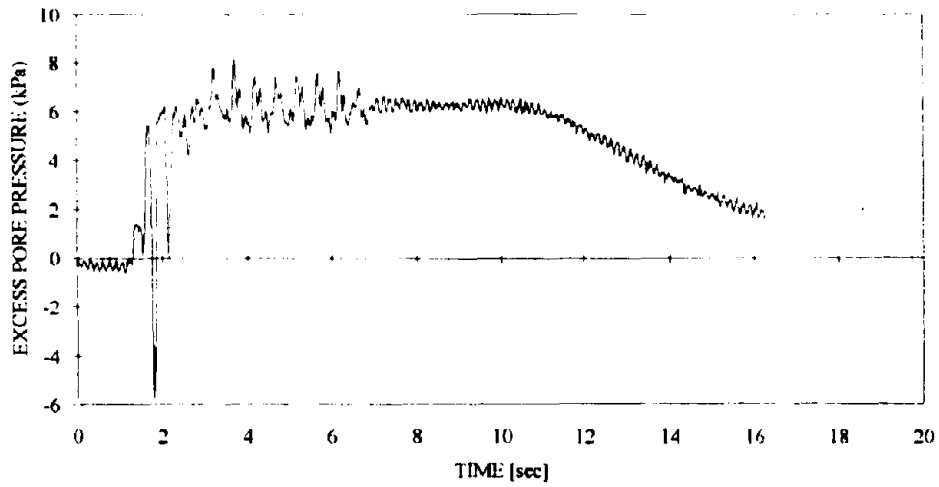Figure B.26: Displacement and load data in Test 2D
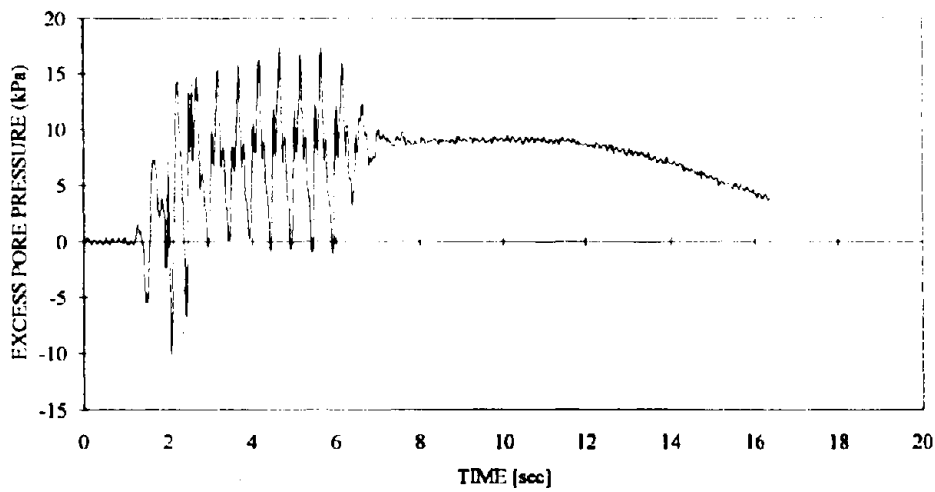
314
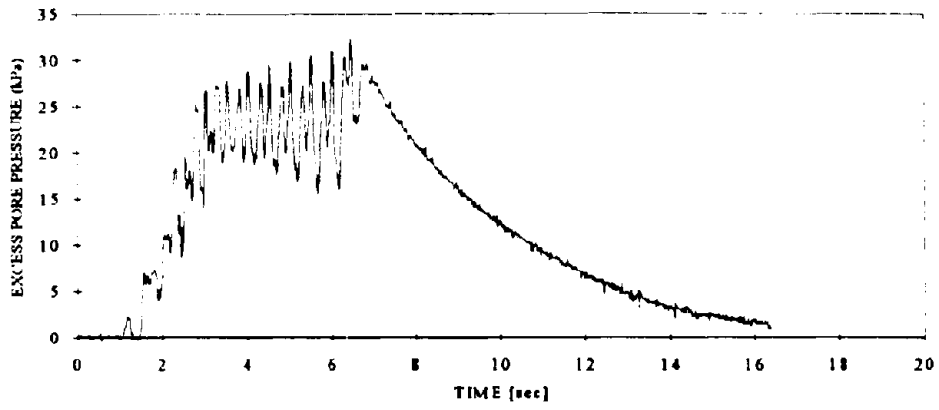
(a)   P2
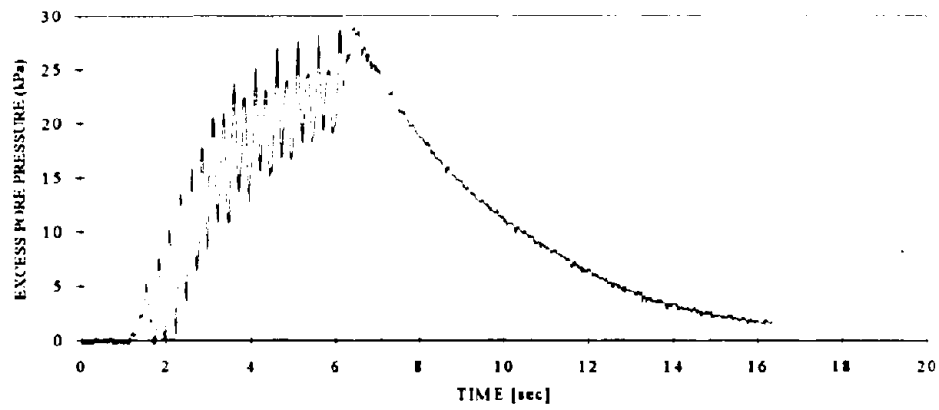
(b)   P3
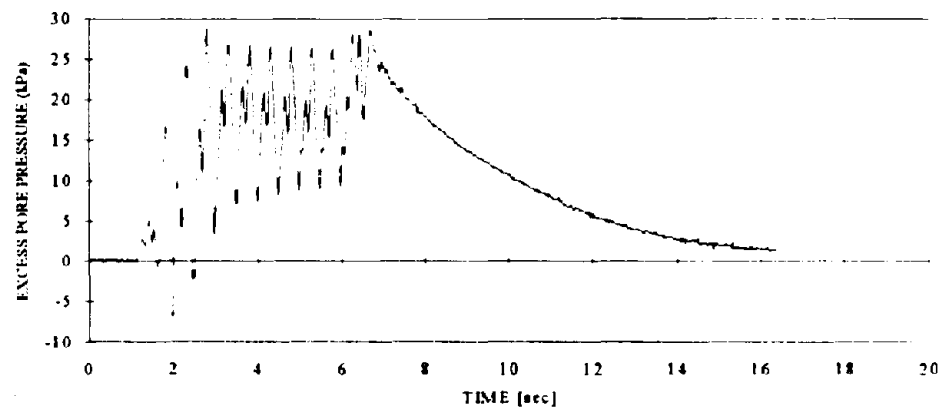
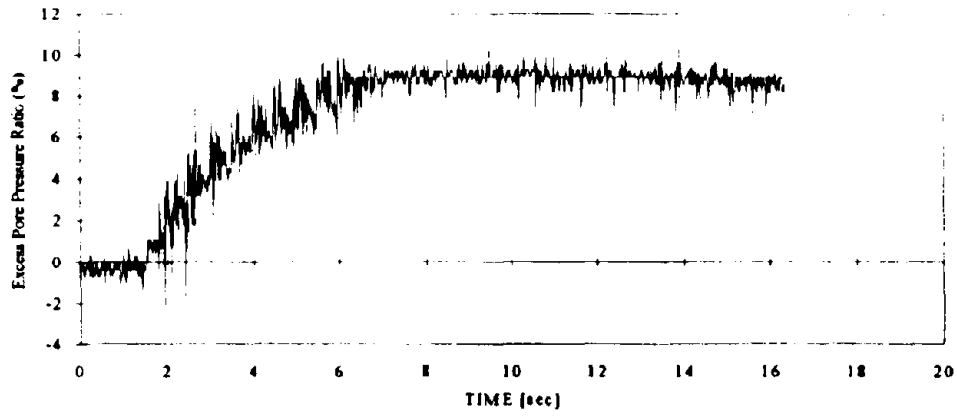(c)   P4

Figure B.27: Excess pore pressure data in Test 2d

315
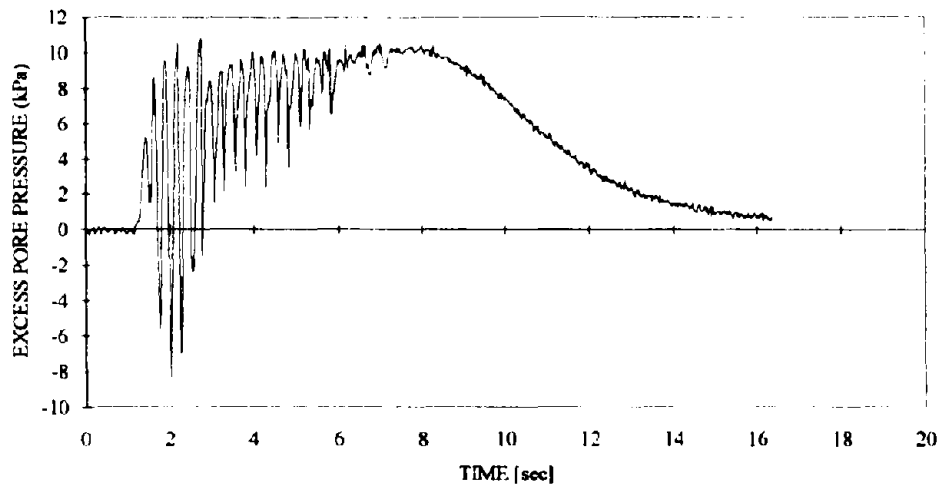
(d)   P5
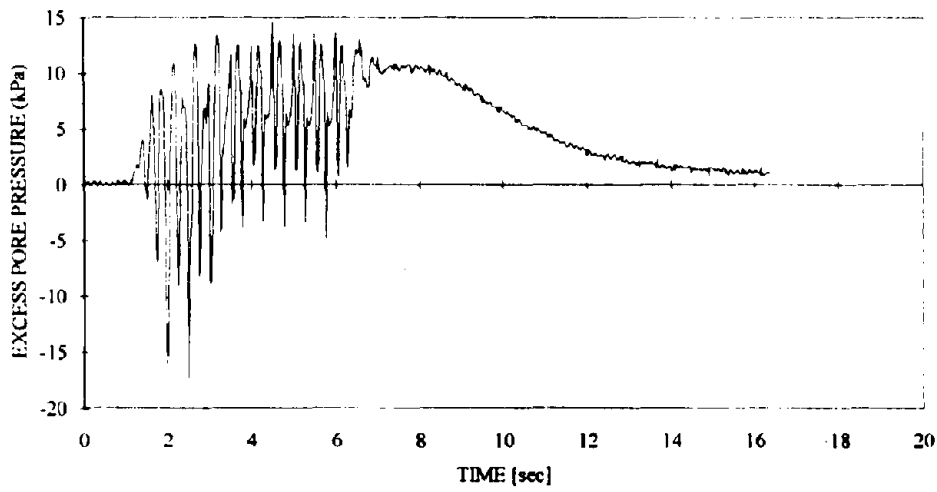
(e)   P6

Figure B.27: Excess pore pressure data in Test 2d

316
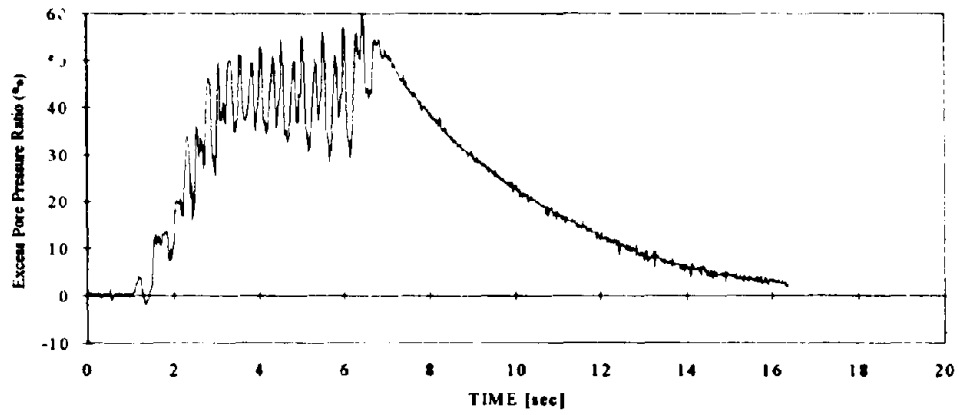
(a)   P2
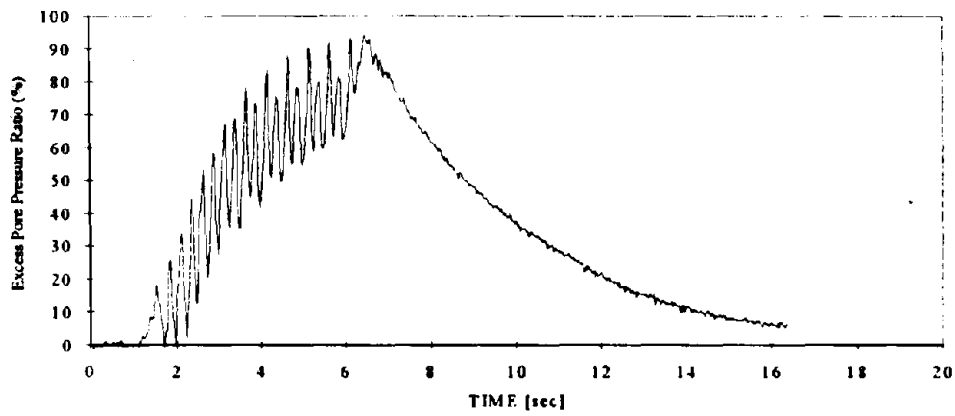
(b)   P3
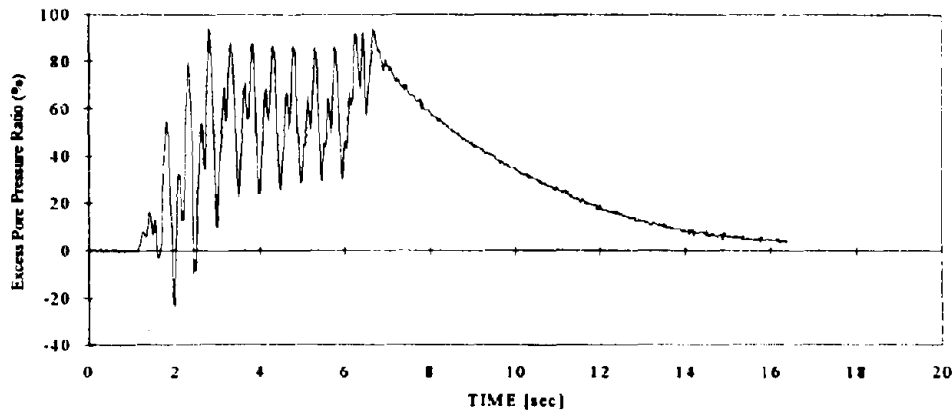
(c)   P4

Figure B.28: Excess pore pressure ratio in Test 2d

317
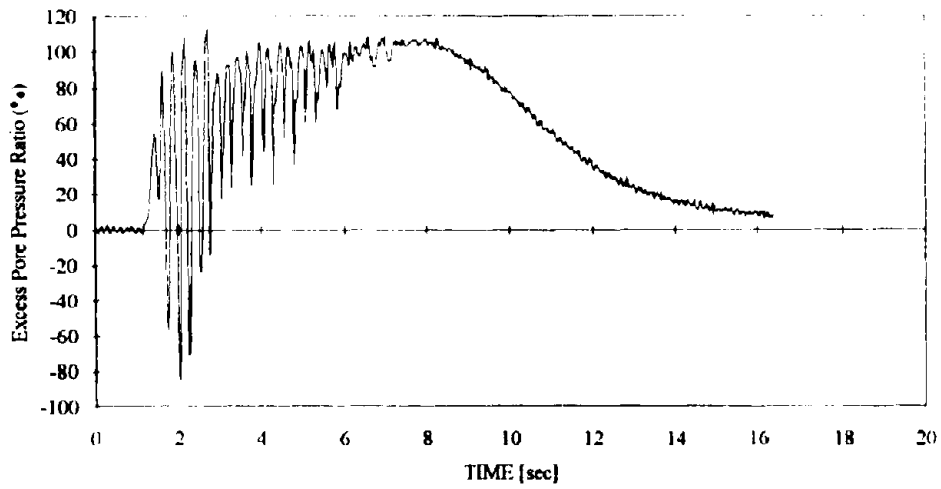
(d)   P5
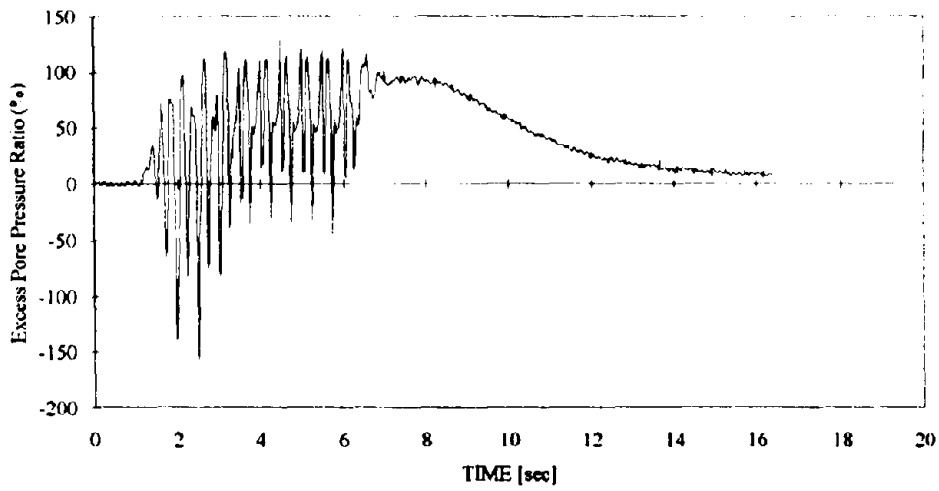
(e)   P6

Figure B.28: Excess pore pressure ratio in Test 2d

318
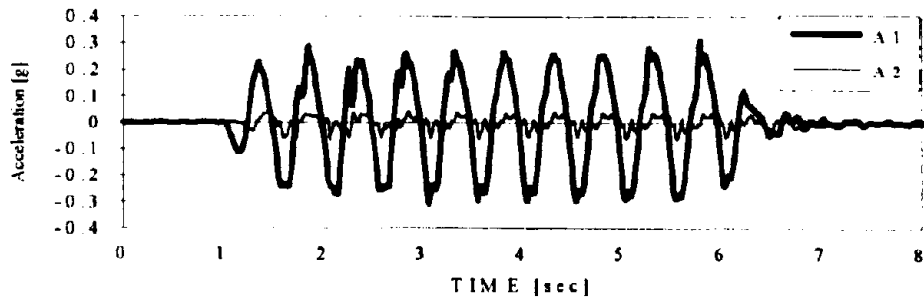
(a) A1 and A2
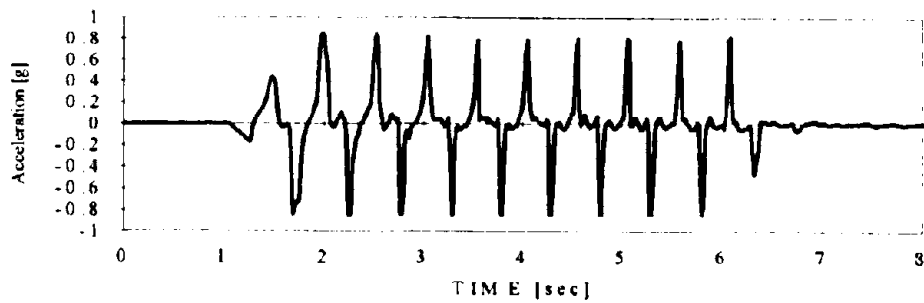
(b) A3
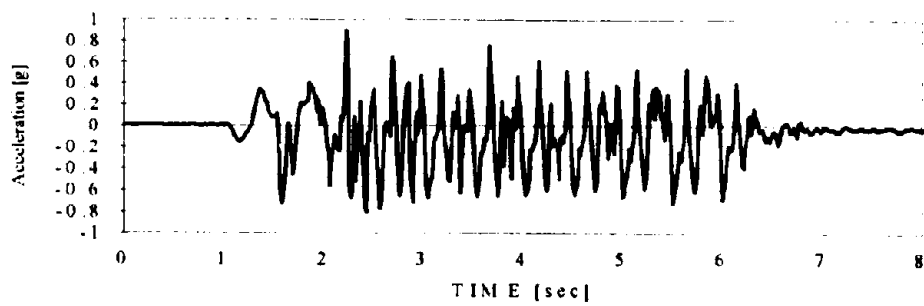
(c) A5
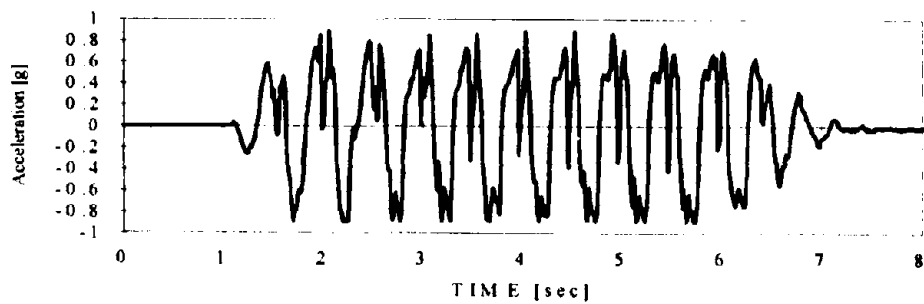
(d) A6

Figure B.29: Acceleration data in Test 2e
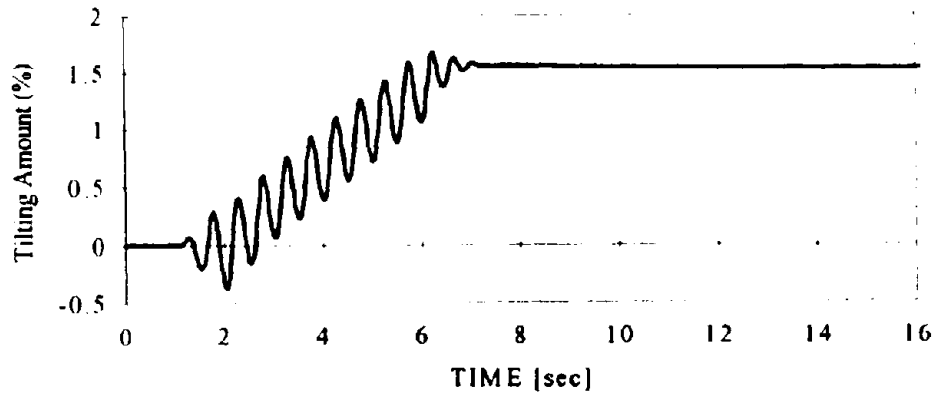
319

(a) Amount of tilt in wall (δ/H) - data of D3
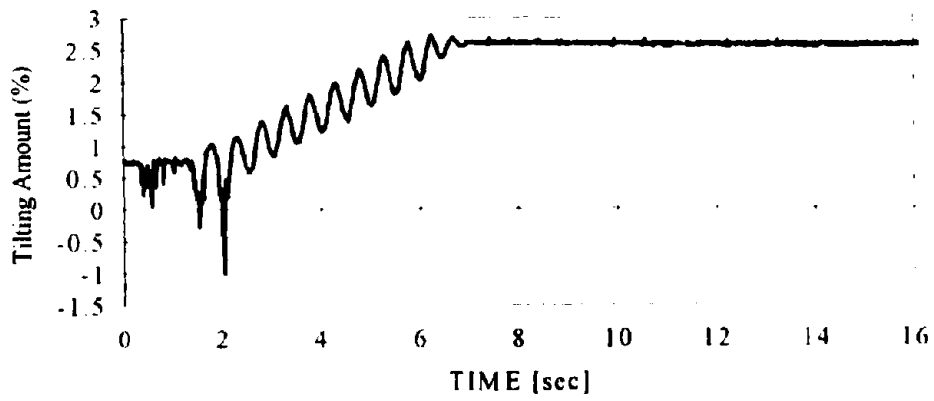
(b) Amount of tilt in wall (δ/H) - data of D4
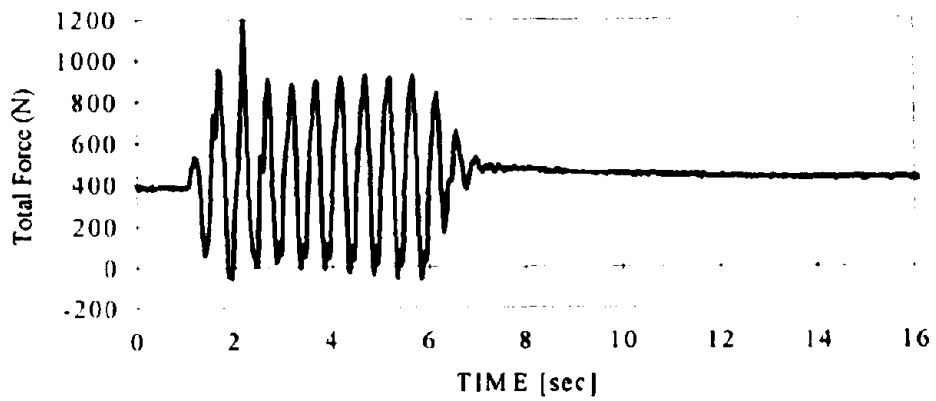
(c) Load data (in model scale)

Figure B.30 Displacement and load data in Test 2e

320
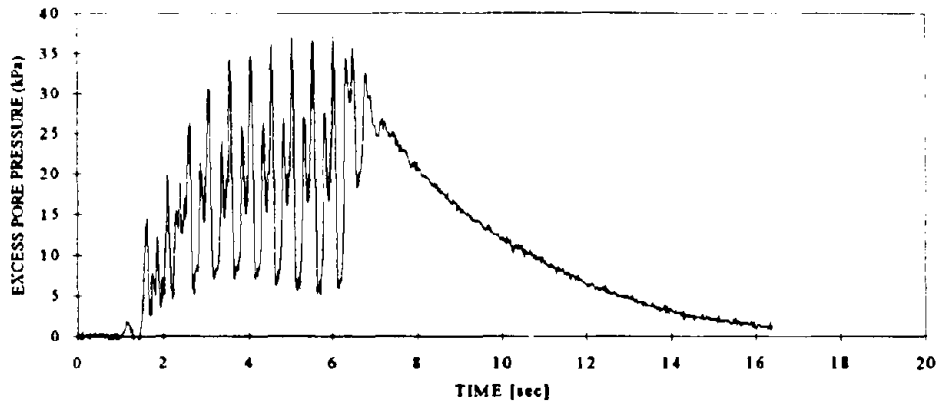
(a)   P2
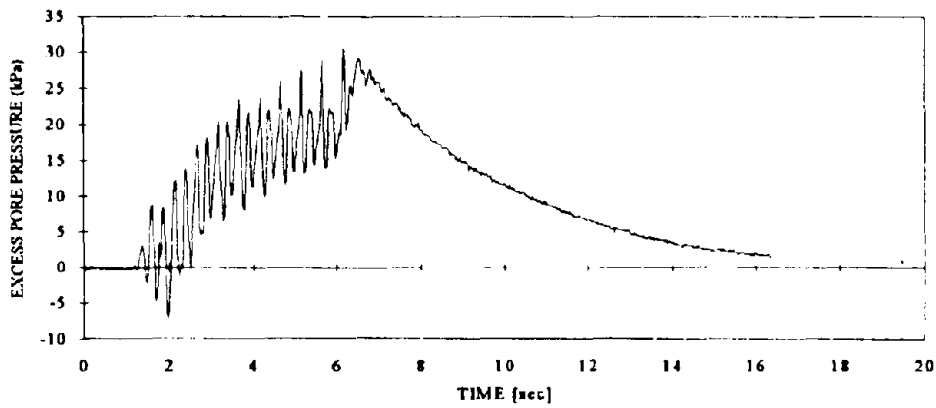
(b)   P3
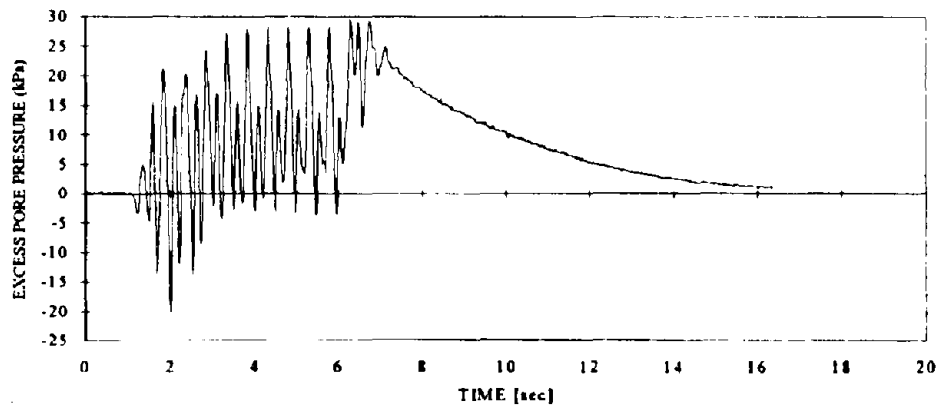
(c)   P4

Figure B.31: Excess pore pressure data in Test 2e
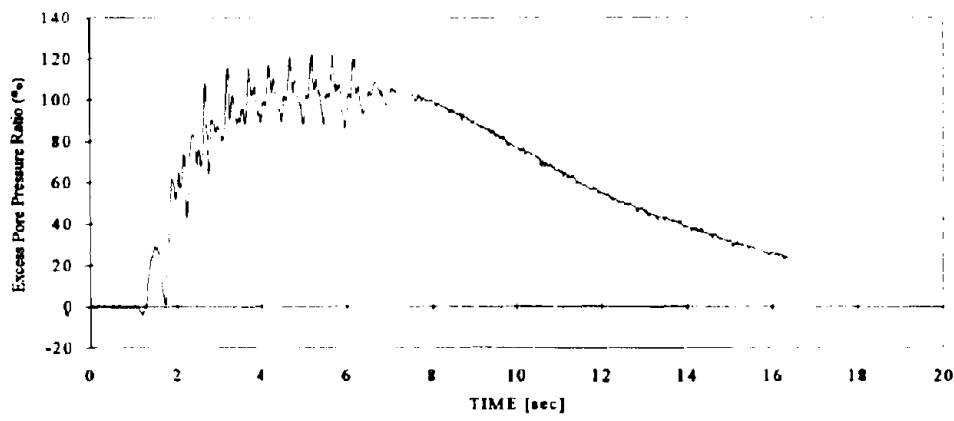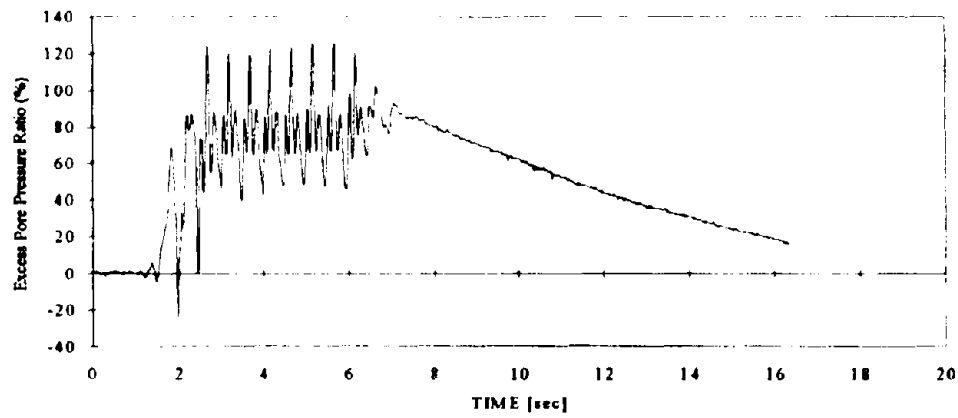
321
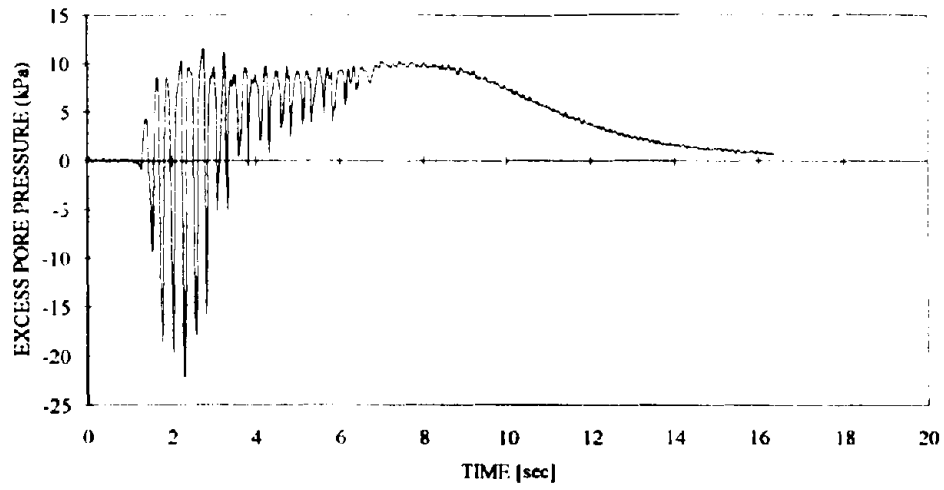
(d)   P5
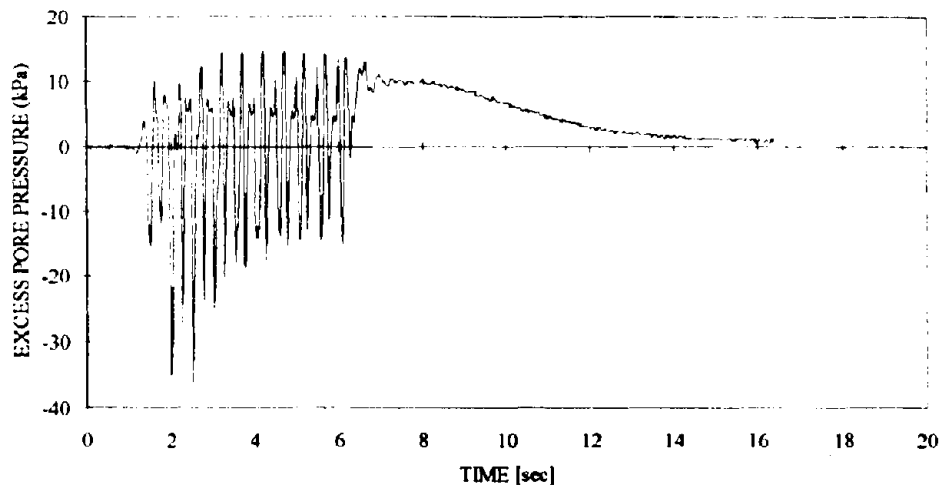
(e)   P6

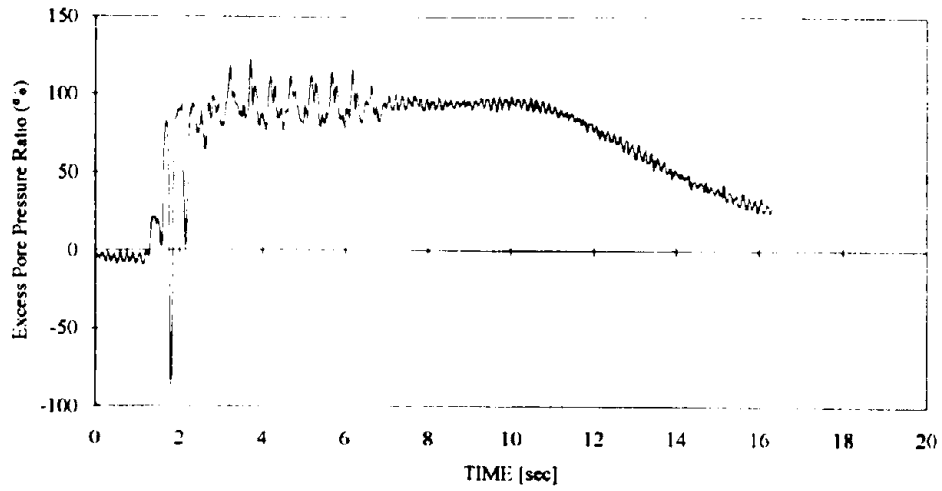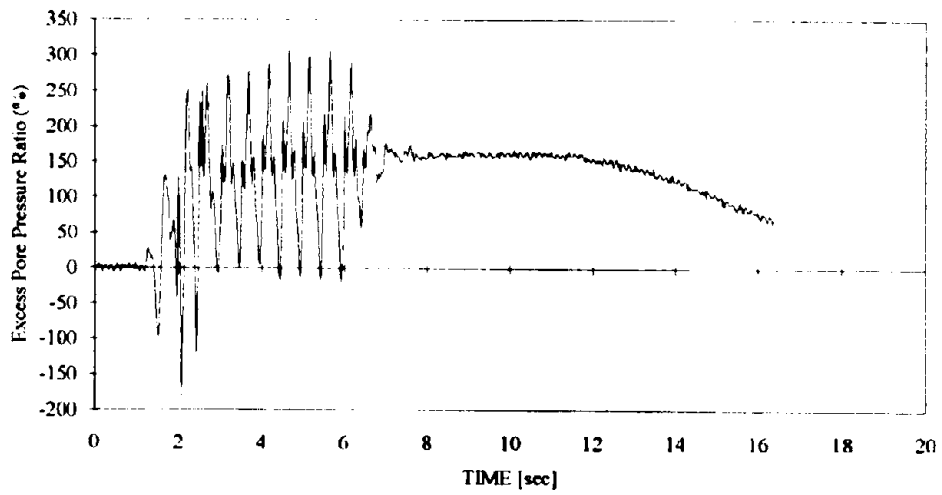Figure B.31: Excess pore pressure data in Test 2e
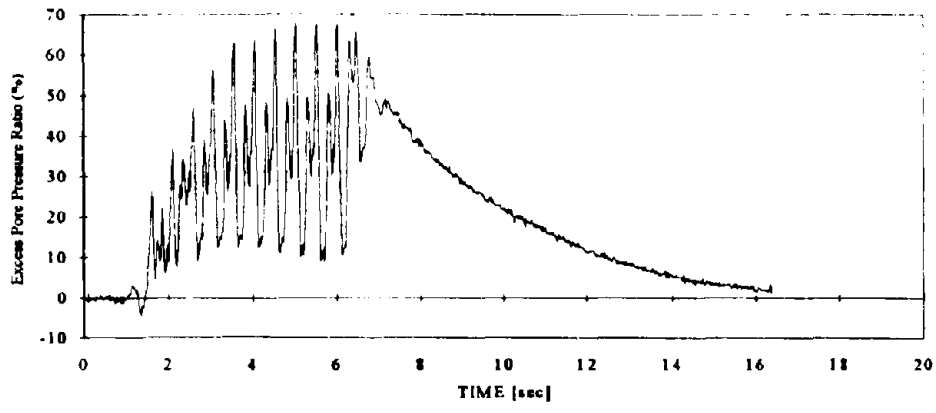
(a) P2
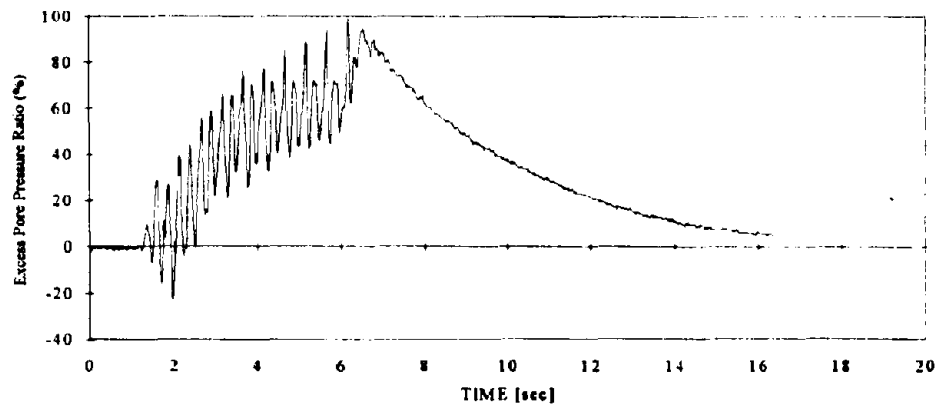
(b) P3
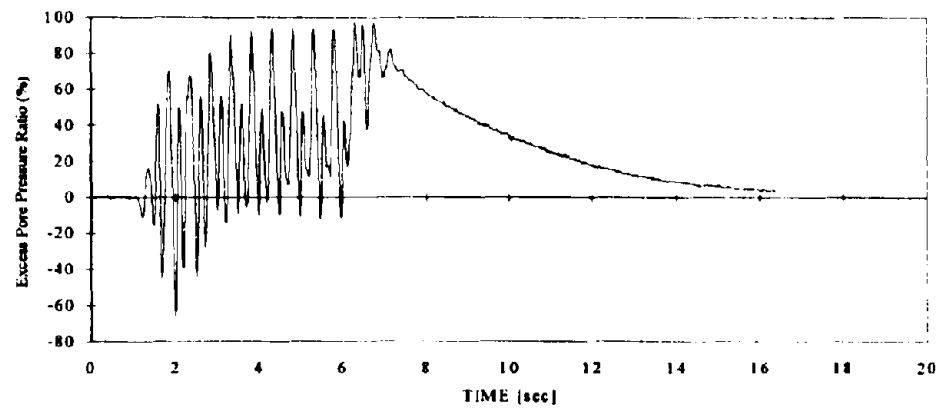
(c) P4

Figure B.32: Excess pore pressure ratio in Test 2e
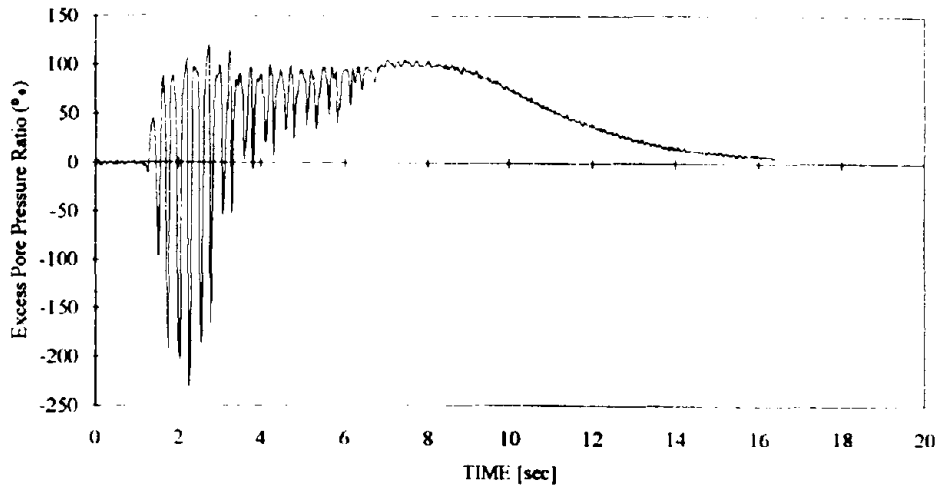
(d)   P5
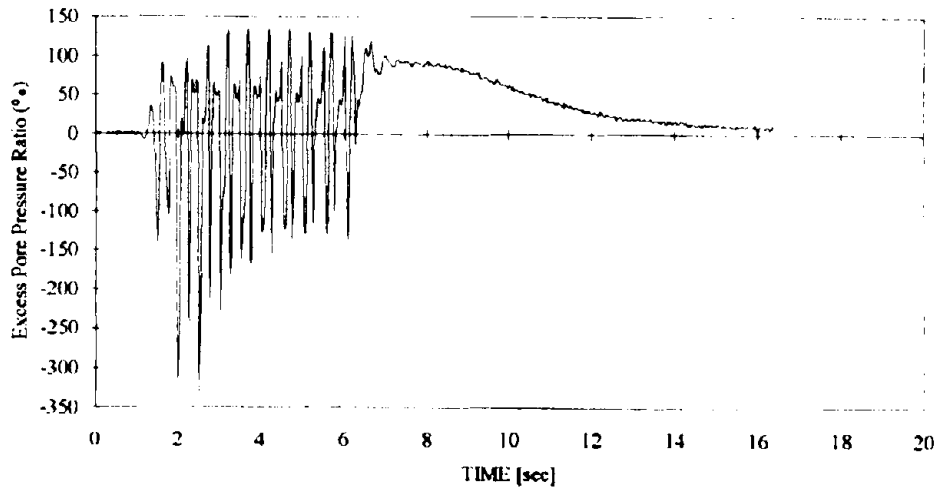
(e)   P6

Figure B.32: Excess pore pressure ratio in Test 2e

324
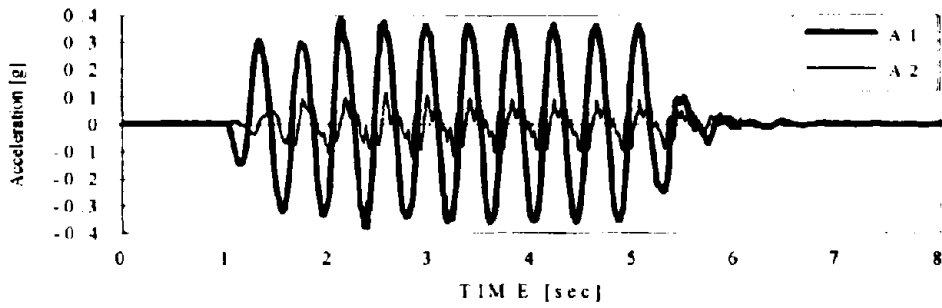
(a)   A1 and A2
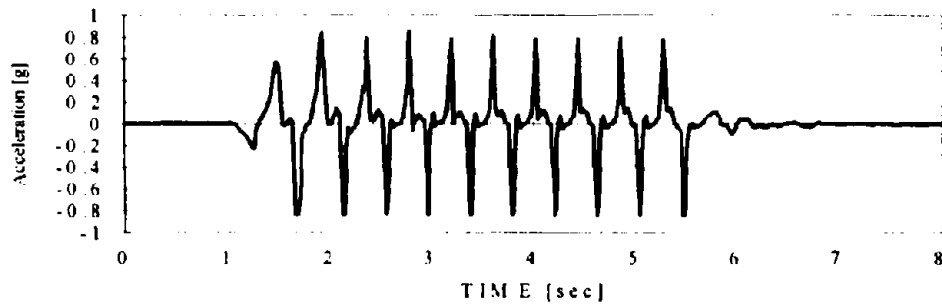
(b)   A3
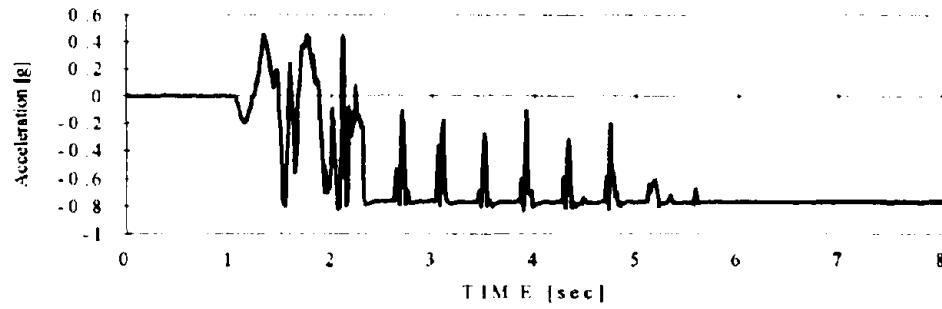
(c)   A5
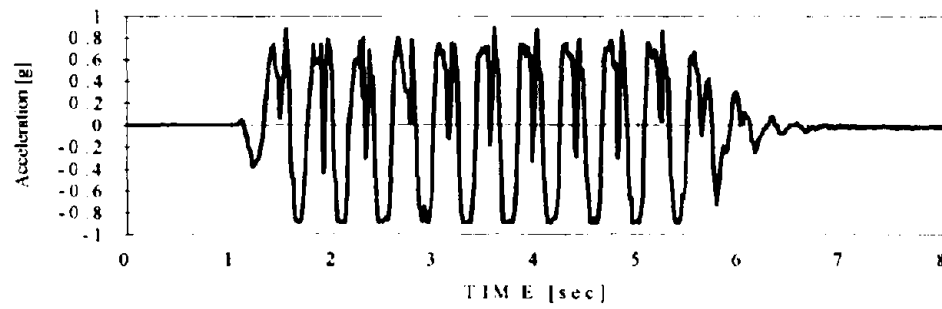
(d)   A6

Figure B.33: Acceleration data in Test 2f
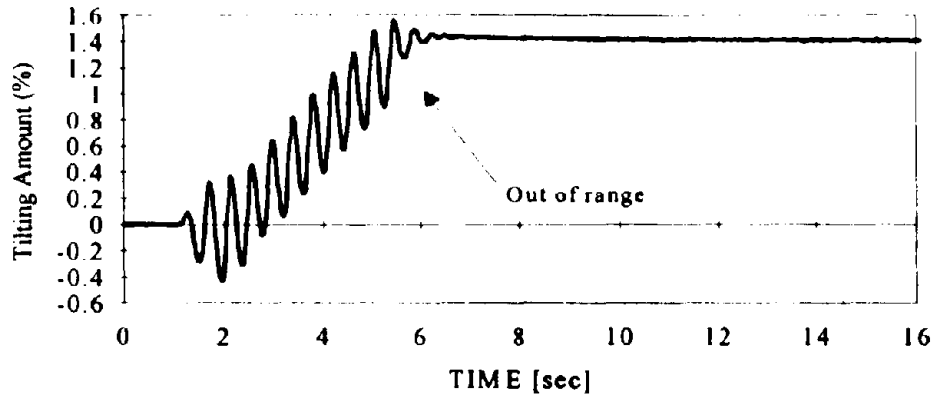
325

(a) Amount of tilt in wall (δ/H) - data of D3
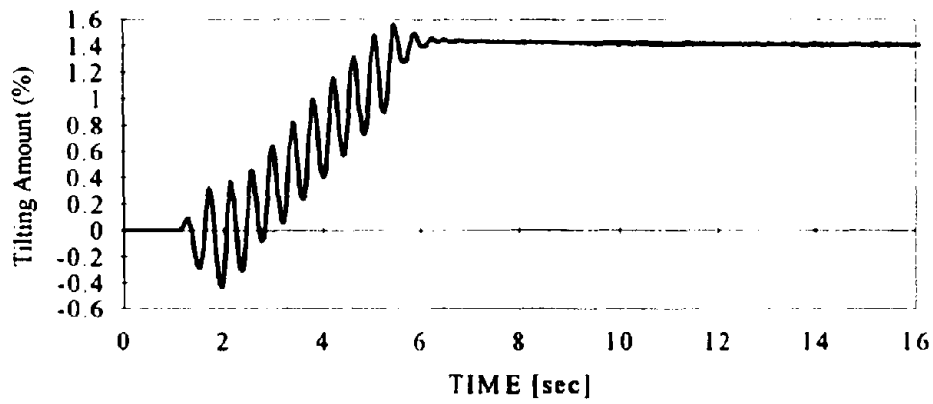
(b) Amount of tilt in wall (δ/H) - data of D4
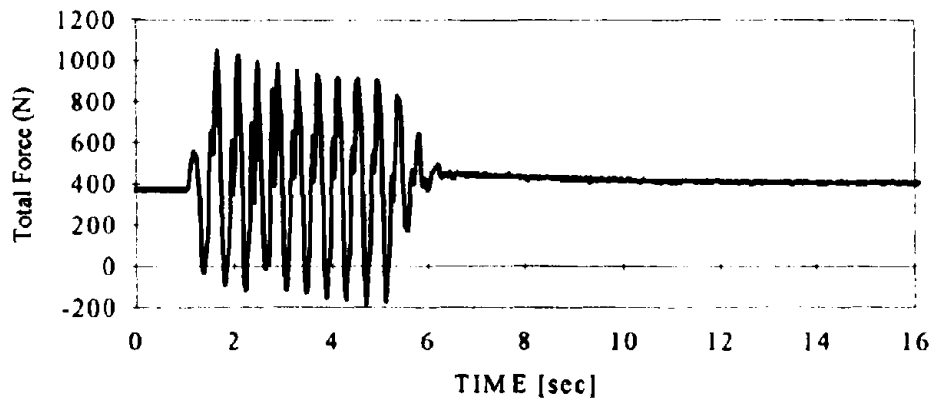
(c) Load data (in model scale)

Figure B.34: Displacement and load data in Test 2f

326
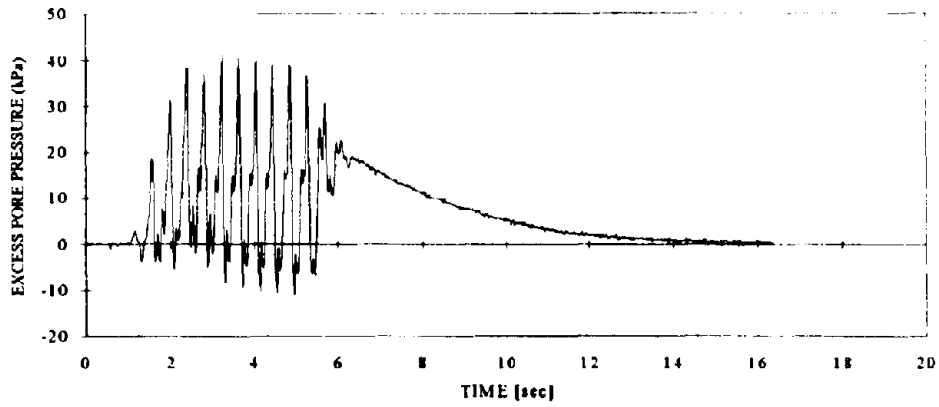
(a)　　P2
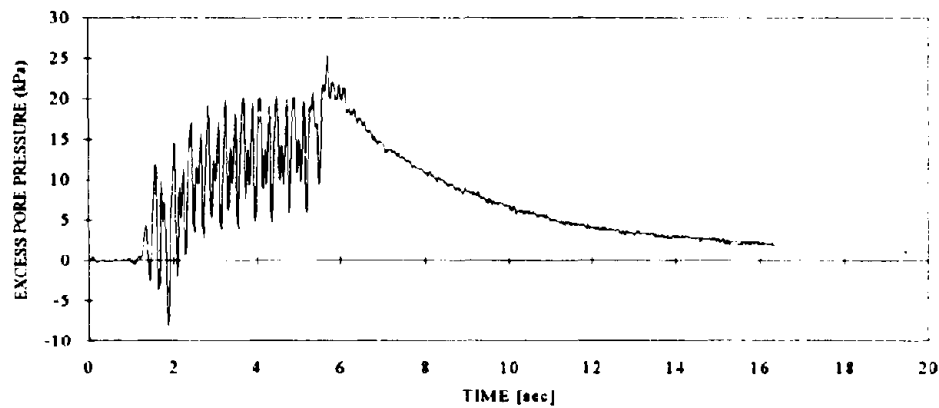
(b)　　P3

(c)　　P4

Figure B.35: Excess pore pressure data in Test 2f

327
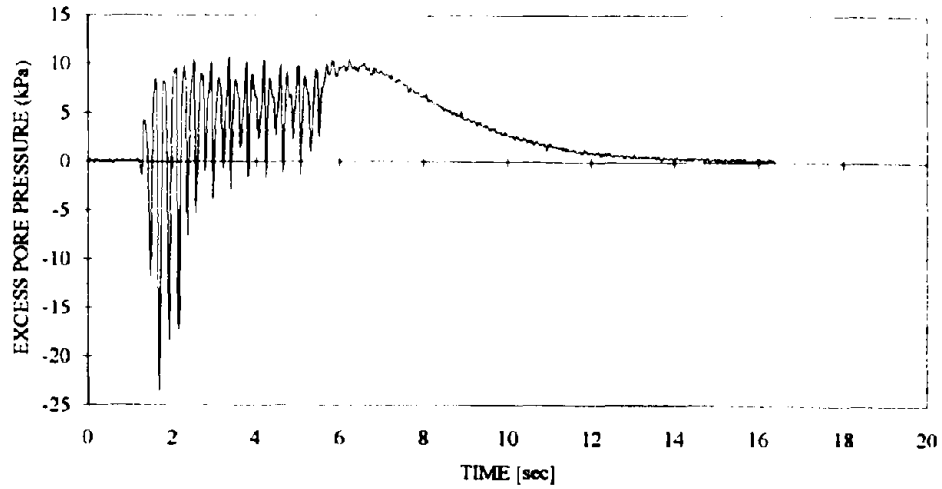
(d)   P5
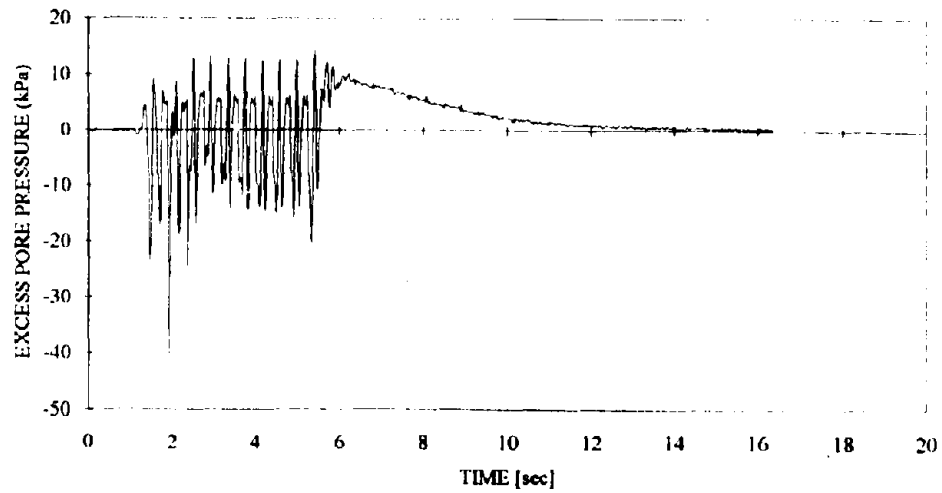
(e)   P6

Figure B.35: Excess pore pressure data in Test 2f
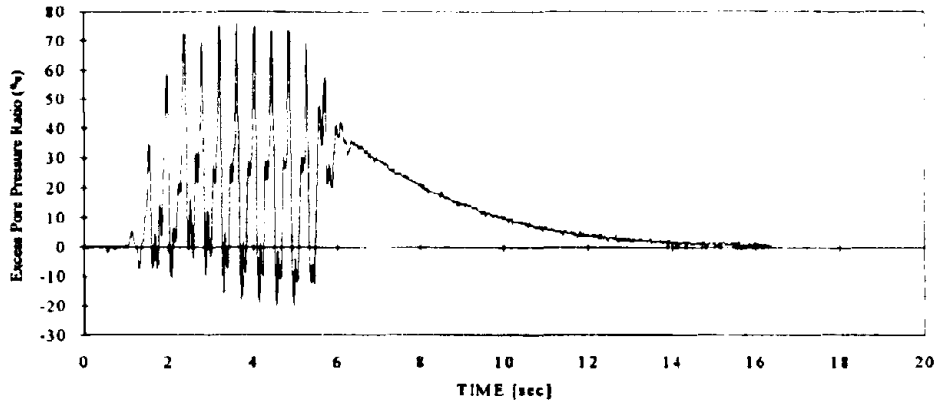
(a)   P2
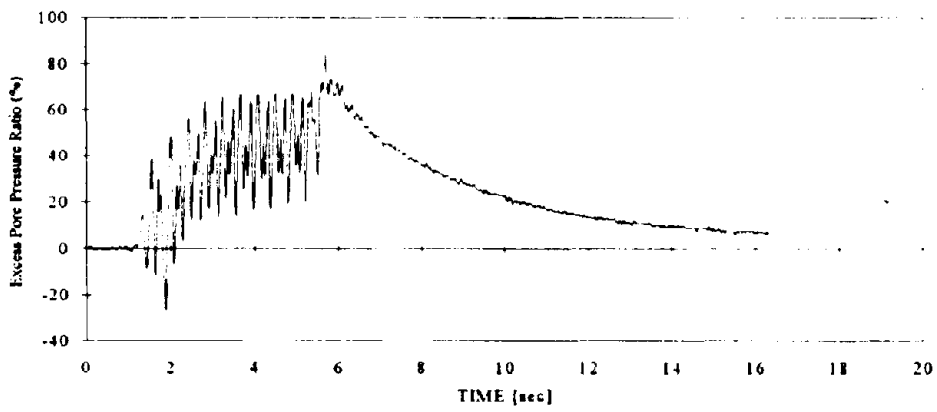
(b)   P3
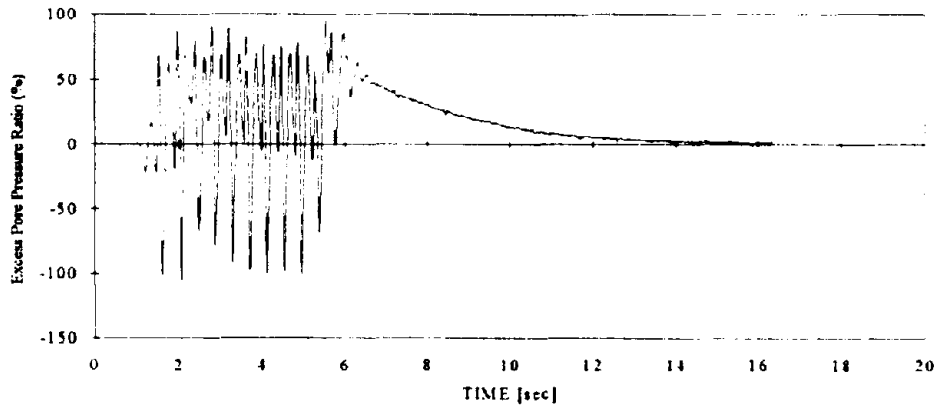
(c)   P4

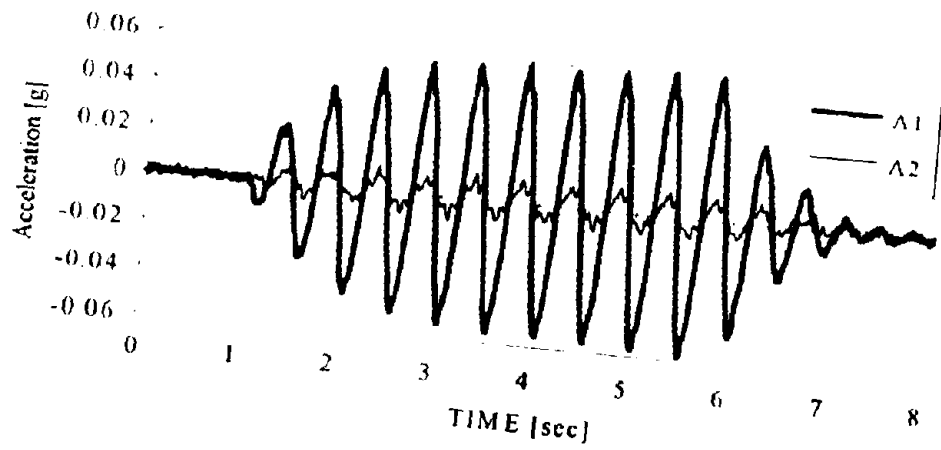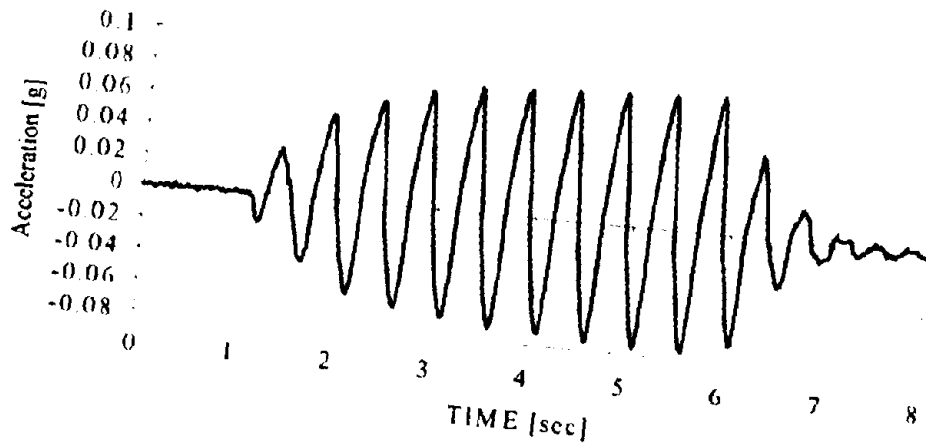Figure B.36 Excess pore pressure ratio in Test 2f

329
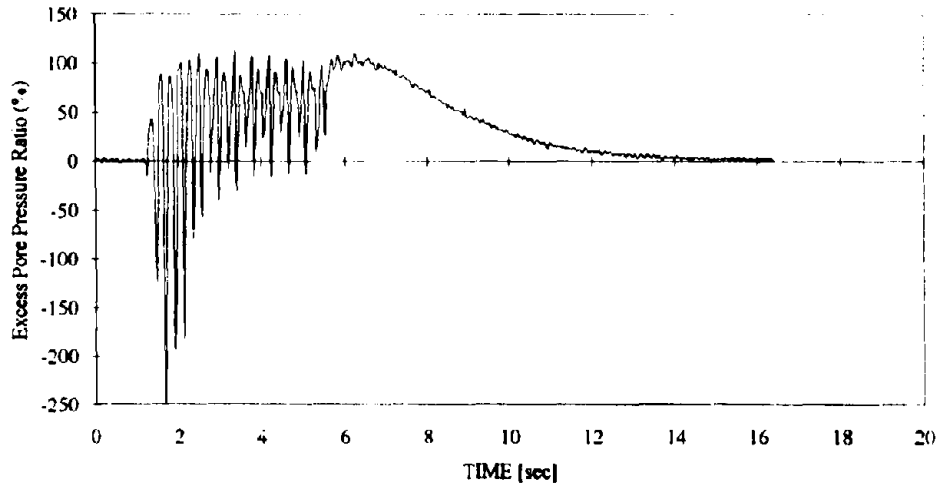
(d)   P5
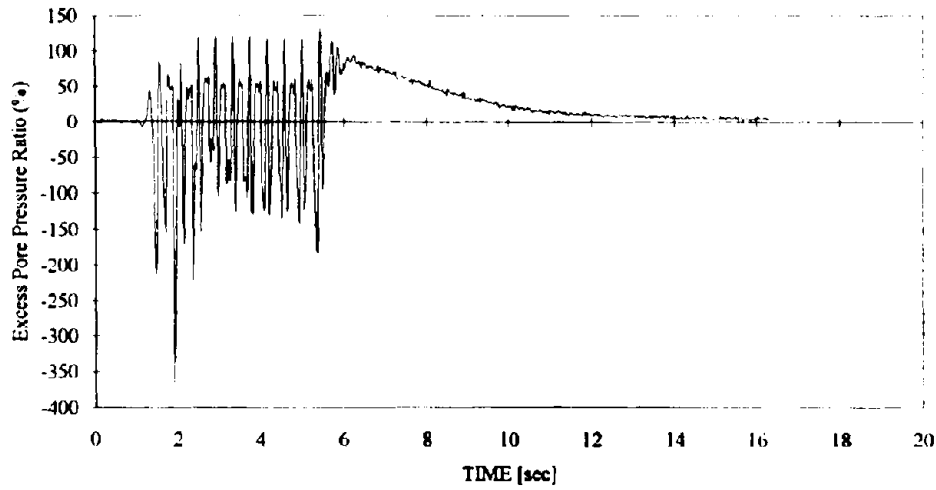
(e)   P6

Figure B.36: Excess pore pressure ratio in Test 2f
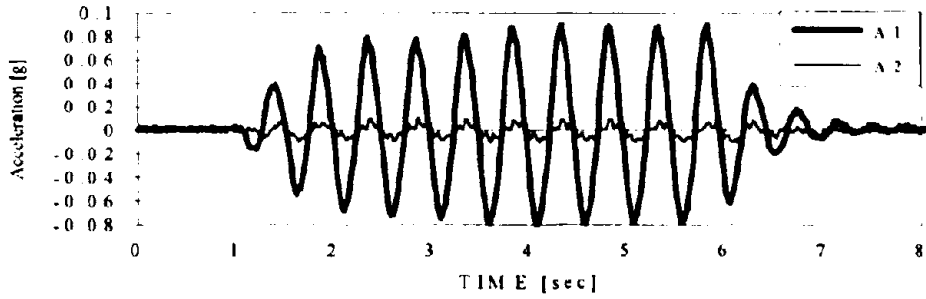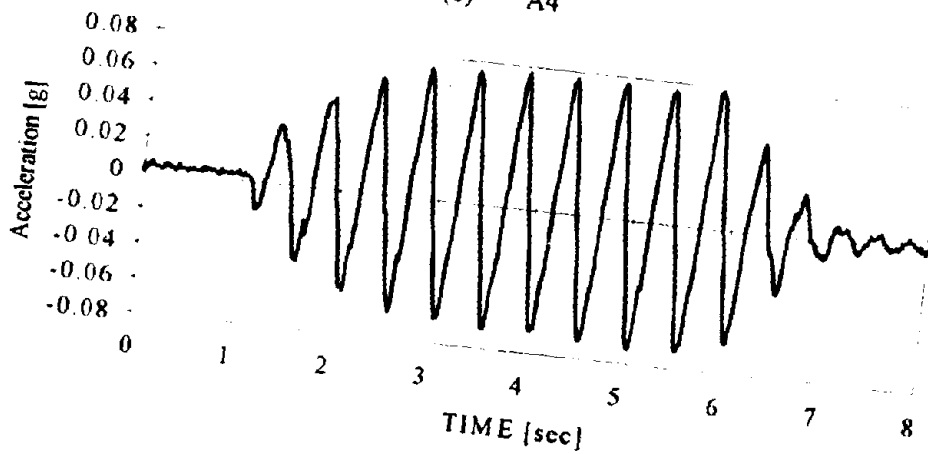
(a)   A1 and A2
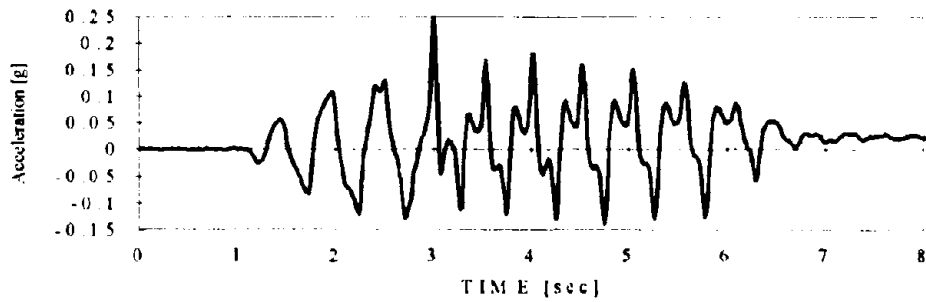
(b)   A3
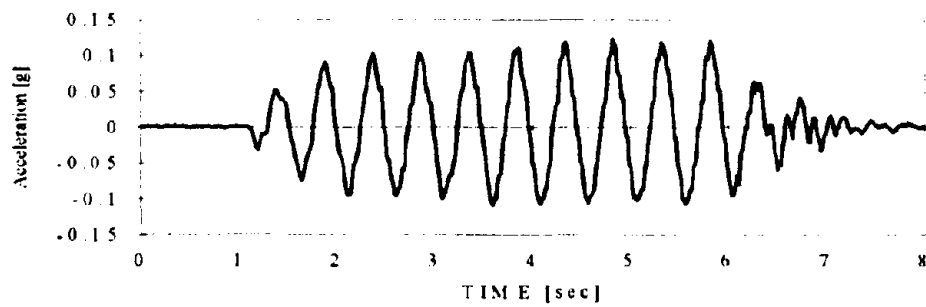
(c)   A5
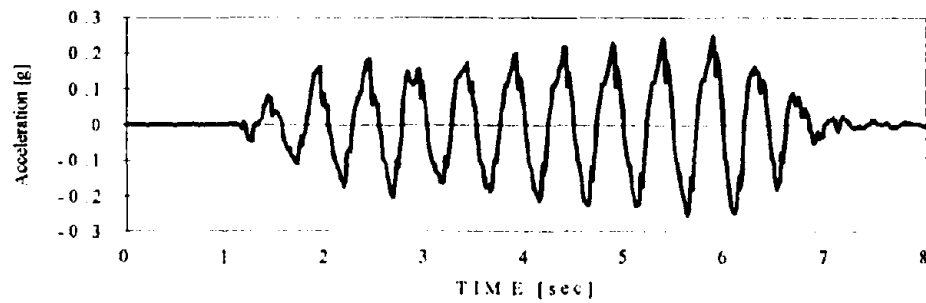
(d)   A6

Figure B.37: Acceleration data in Test 3a
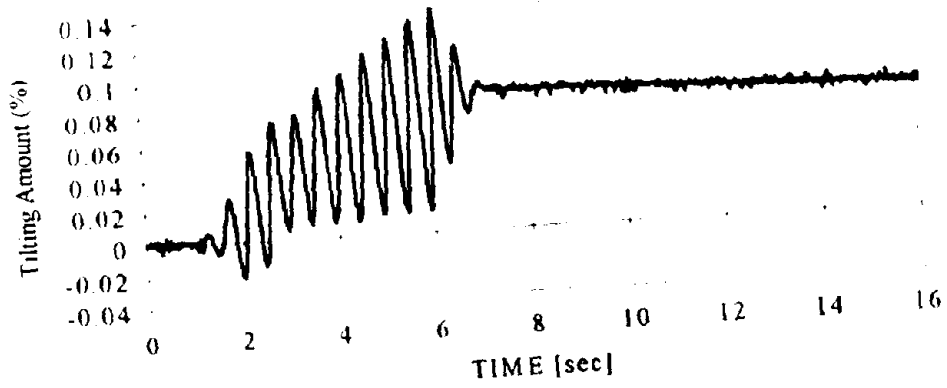
(a) Amount of tilt in wall (δ/H) - data of D3
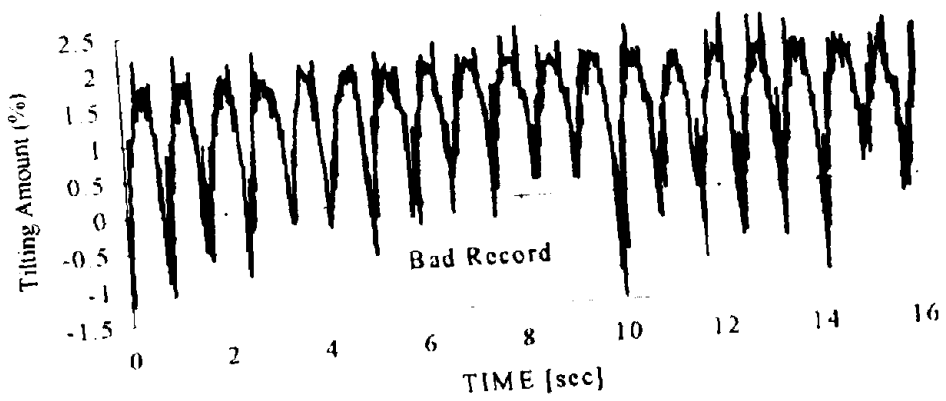
(b) Amount of tilt in wall (δ/H) - data of D4
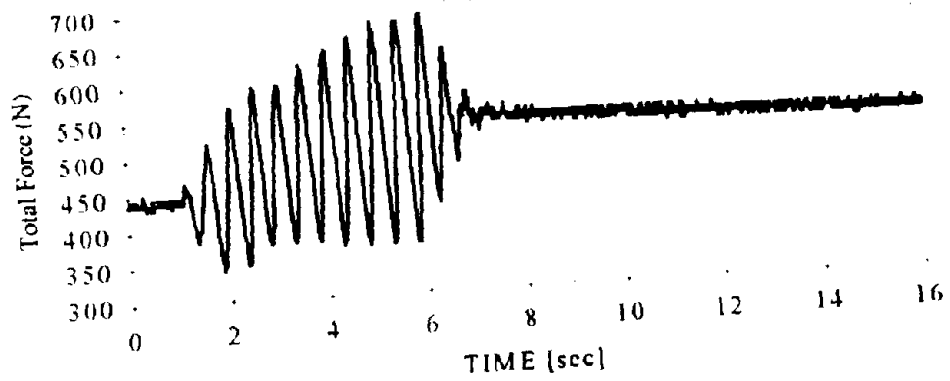
(c) Load data (in model scale)

Figure B 38: Displacement and load data in Test 3a

332
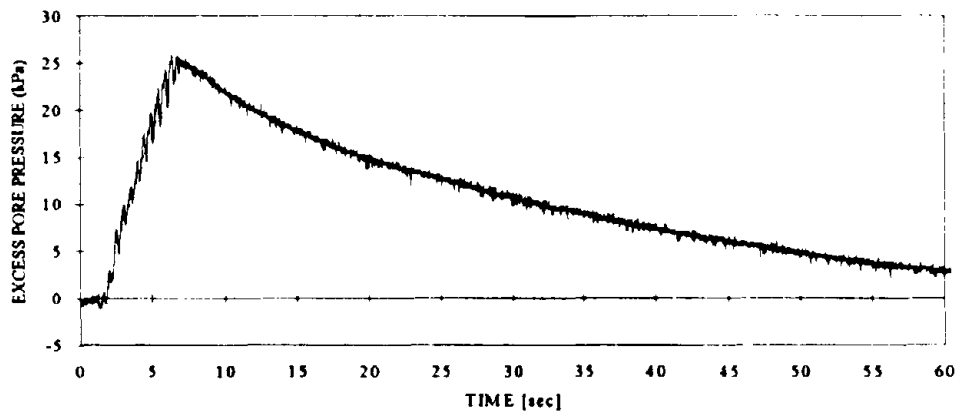
(a)   P2
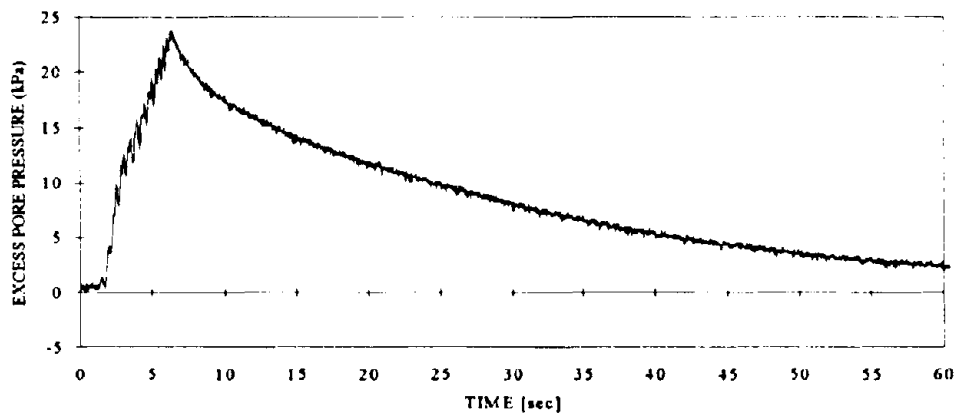
(b)   P3

(c)   P4

Figure B.39: Excess pore pressure data in Test 3a

333
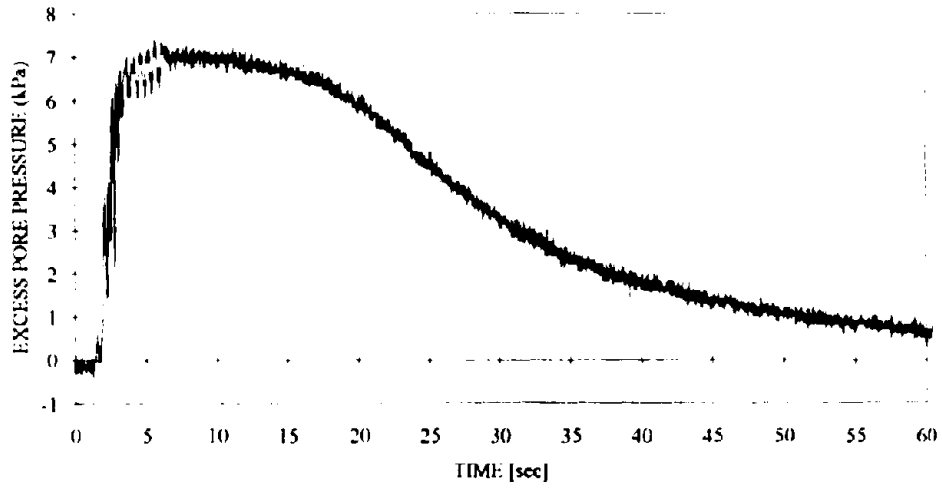
(d)   P5
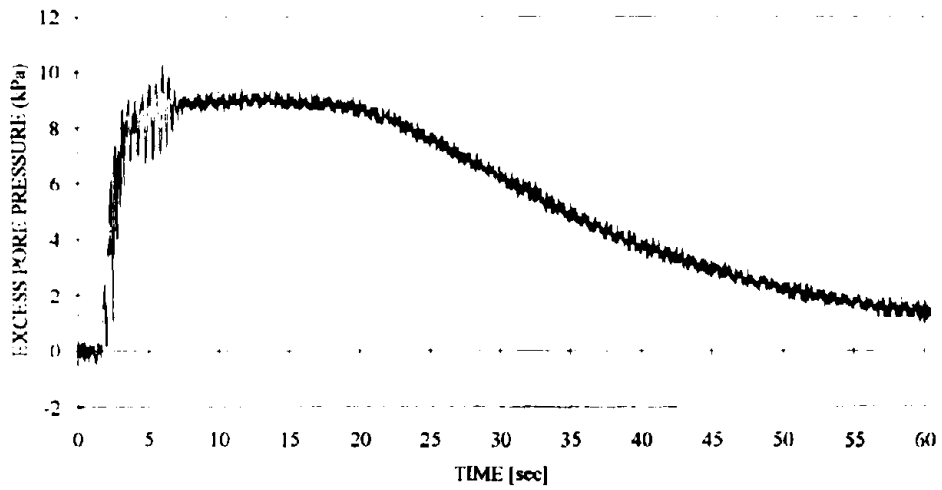
(e)   P6

Figure B 39: Excess pore pressure data in Test 3a
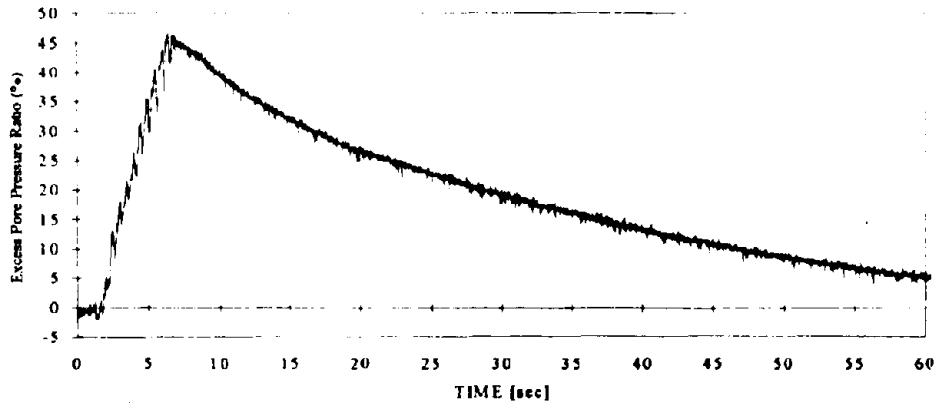
(a)   P2

(b)   P3

(c)   P4

Figure B.40: Excess pore pressure ratio in Test 3a

(d)   P5

(e)   P6

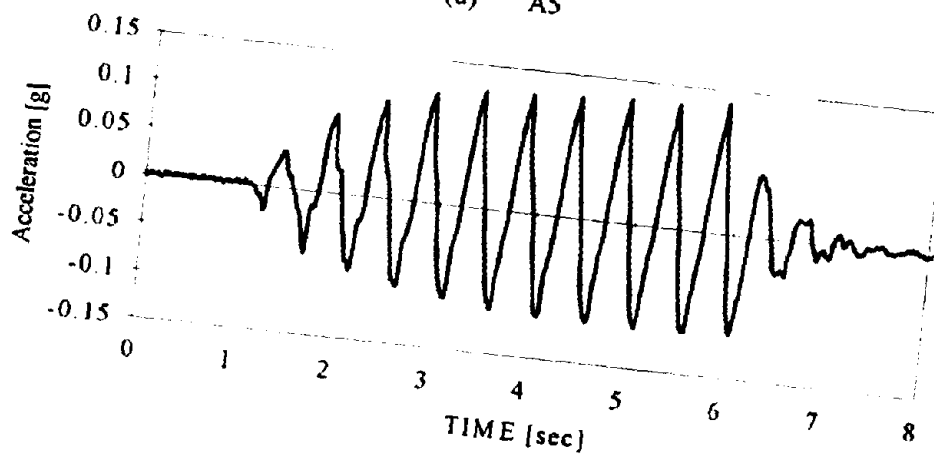Figure B.40 Excess pore pressure ratio in Test 3a
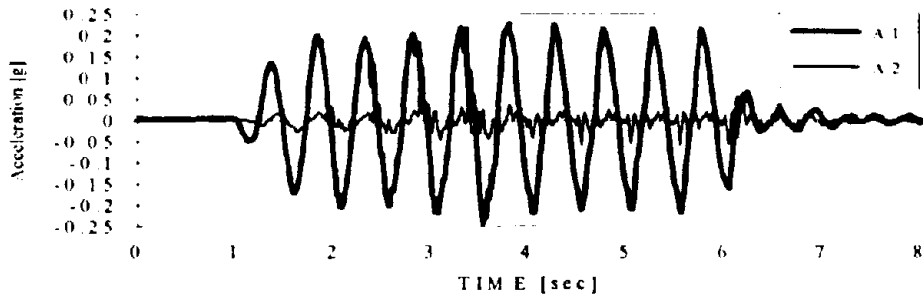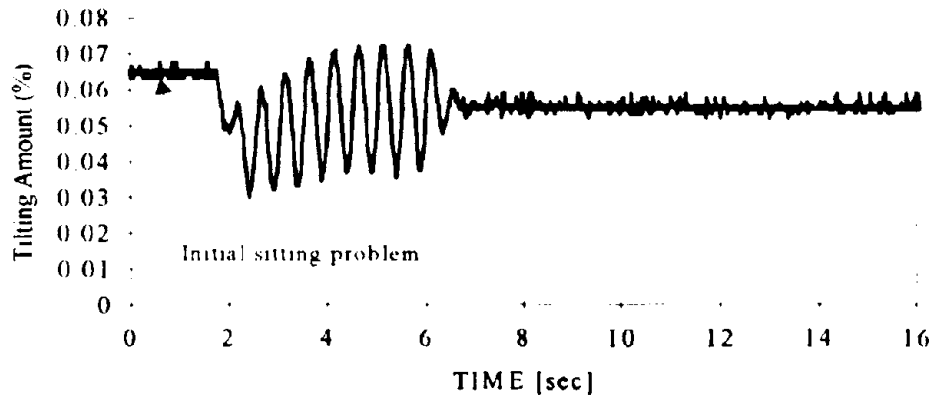
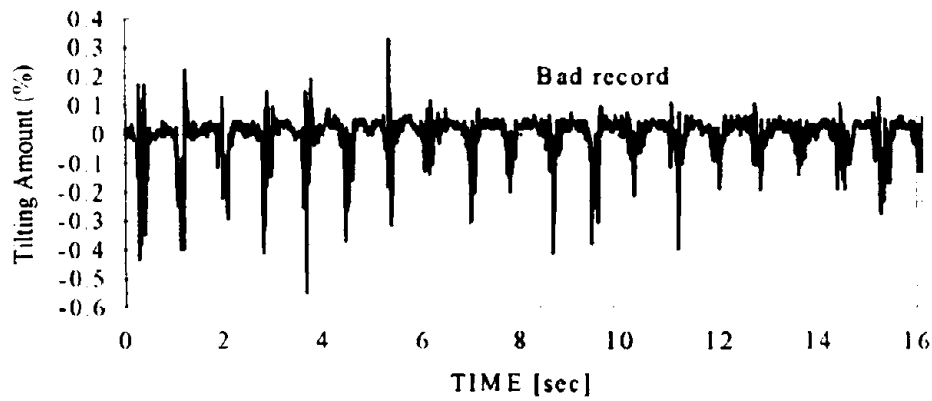(a)   A1 and A2

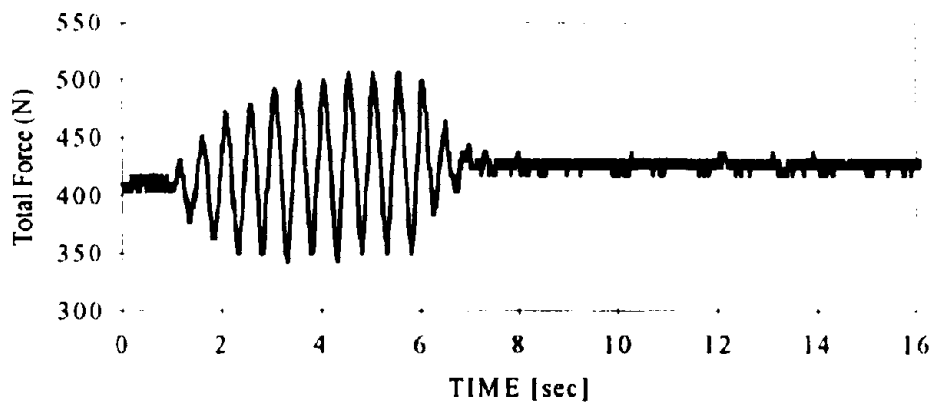(b)   A3

(c)   A5

(d)   A6

Figure B.41: Acceleration data in Test 3b

337

(a) Amount of tilt in wall (δ/H) - data of D3
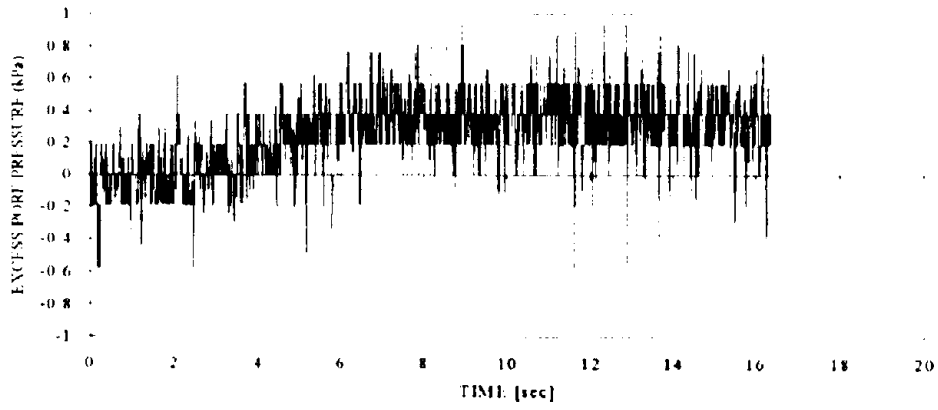

(b) Amount of tilt in wall (δ/H) - data of D4
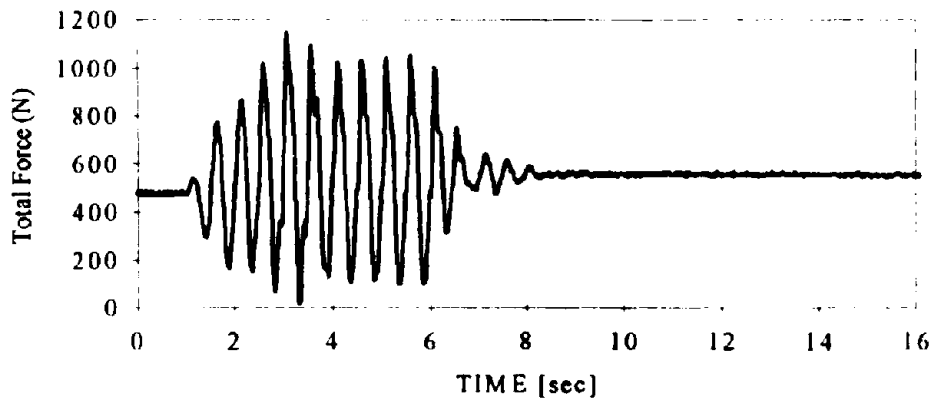
(c) Load data (in model scale)

Figure B.42: Displacement and load data in Test 3b

338

(a)   P2

(b)   P3

(c)   P4

Figure B.43: Excess pore pressure data in Test 3b

339
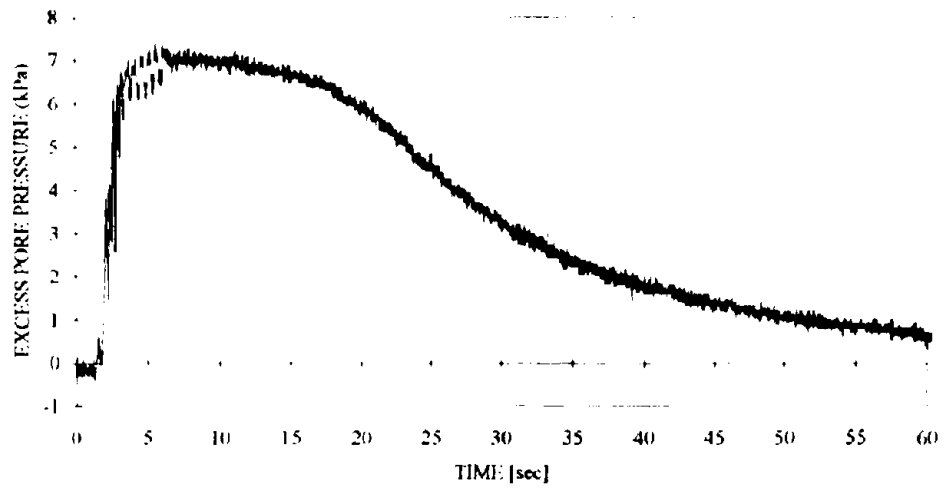
(d)   P5
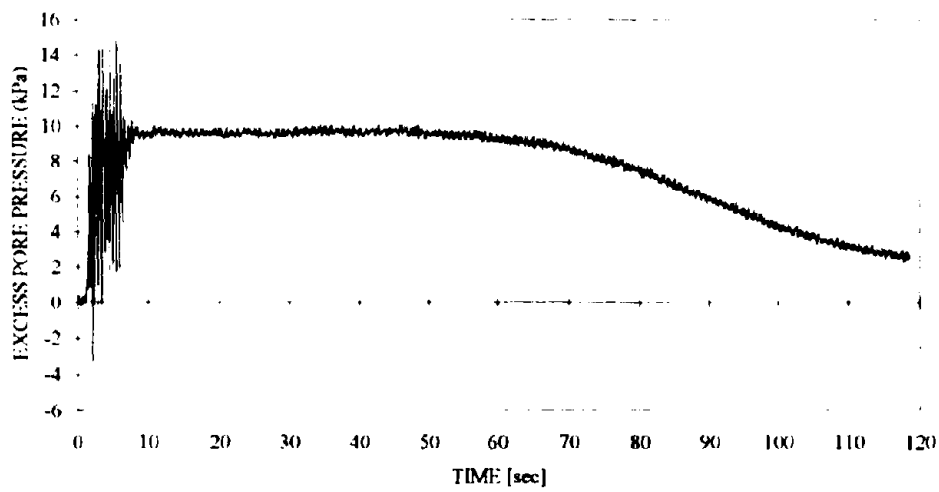
(e)   P6

Figure B.43: Excess pore pressure data in Test 3b

340
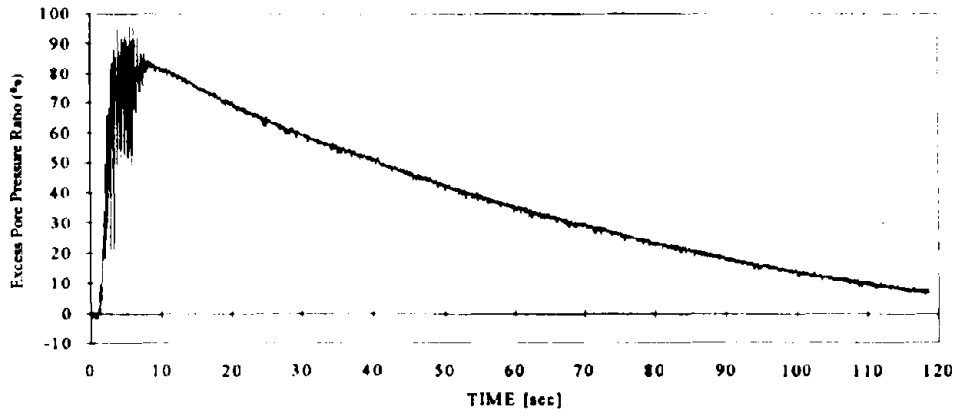
(a)   P2

(b)   P3
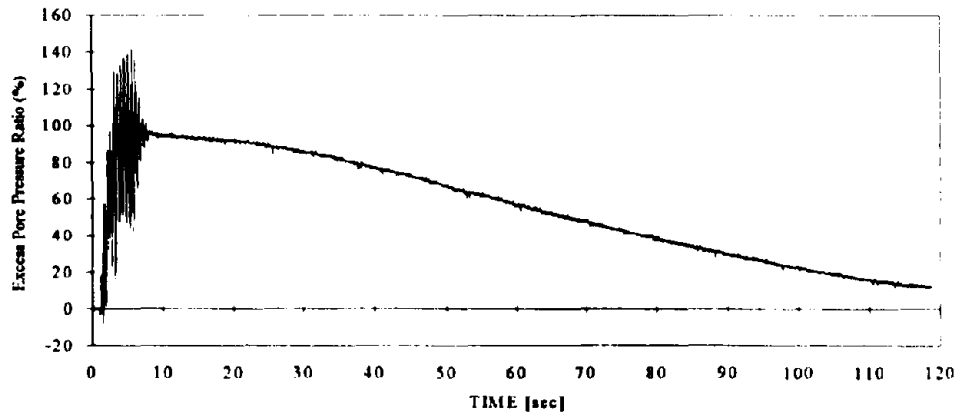
(c)   P4

Figure B.44: Excess pore pressure ratio in Test 3b

341

(d)   P5

(e)   P6

Figure B.44. Excess pore pressure ratio in Test 3b

342
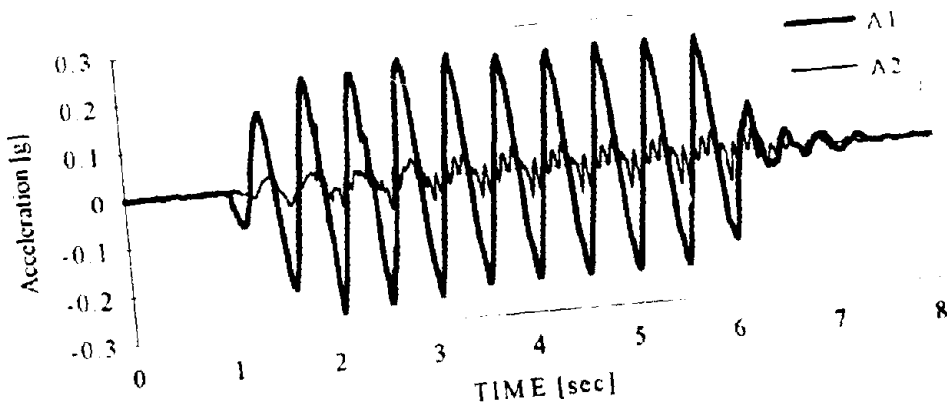
(a)   A1 and A2

(b)   A3

Figure B.45 Acceleration data in Test 4a
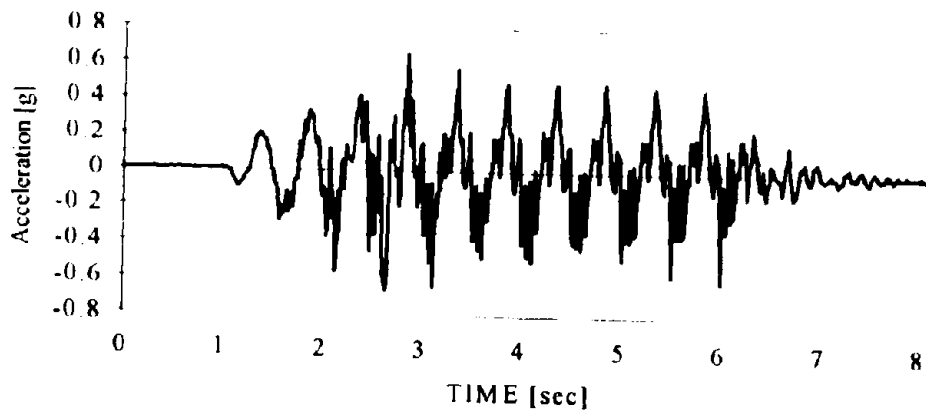
(c) A4

(d) A5
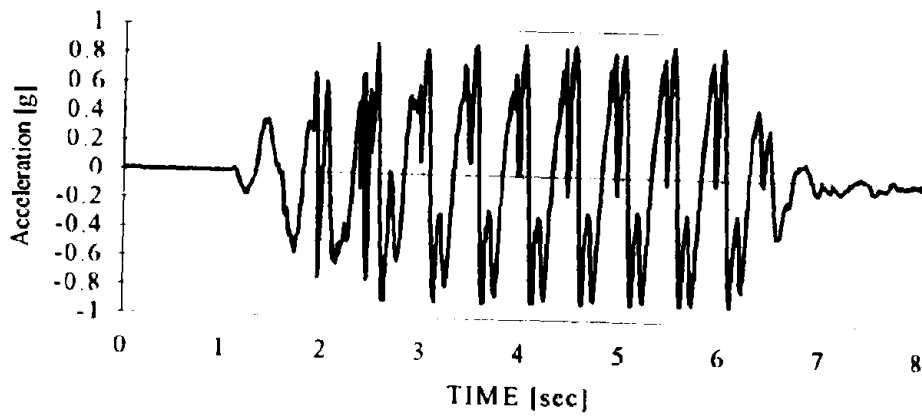
(e) A6

Figure B 45 Acceleration data in Test 4a
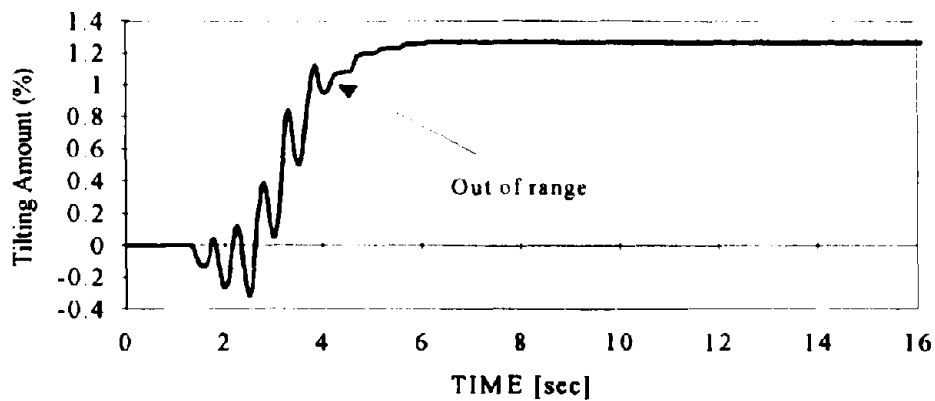
344

(a) Amount of tilt in wall (δ/H) - data of D3
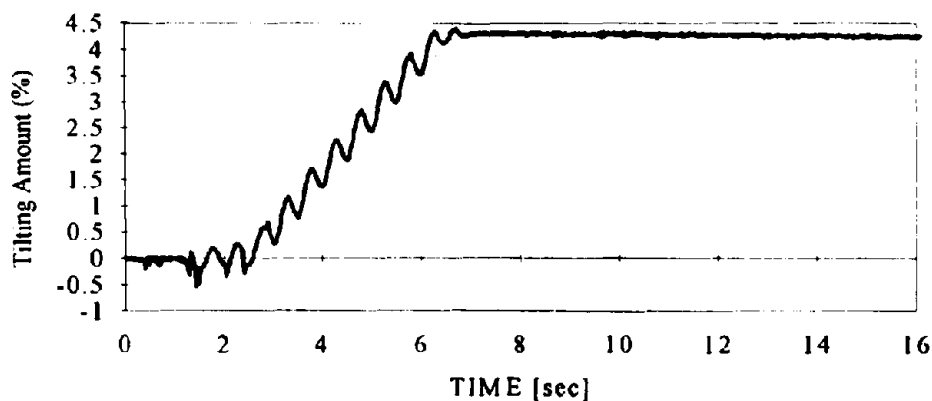
(b) Amount of tilt in wall (δ/H) - data of D4
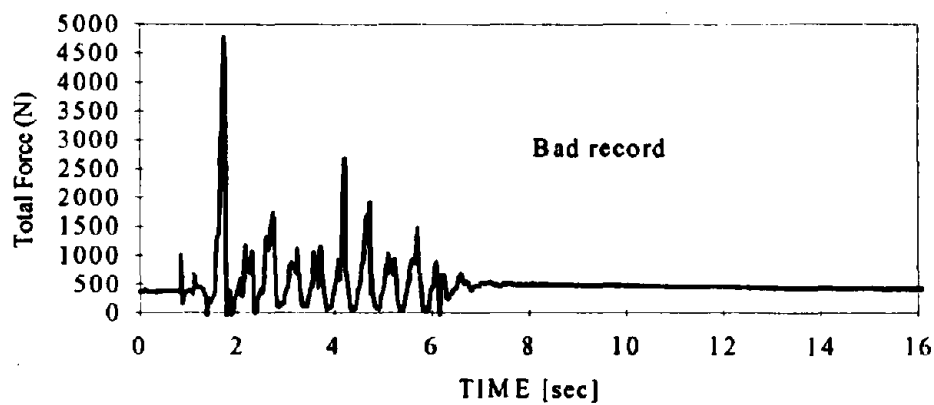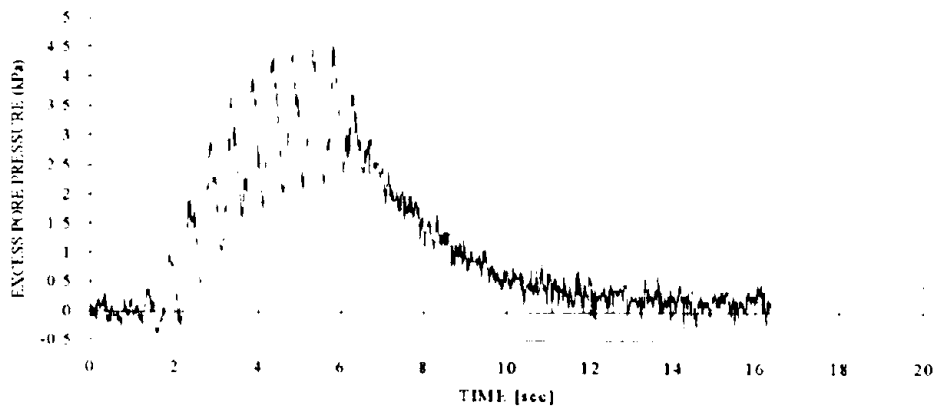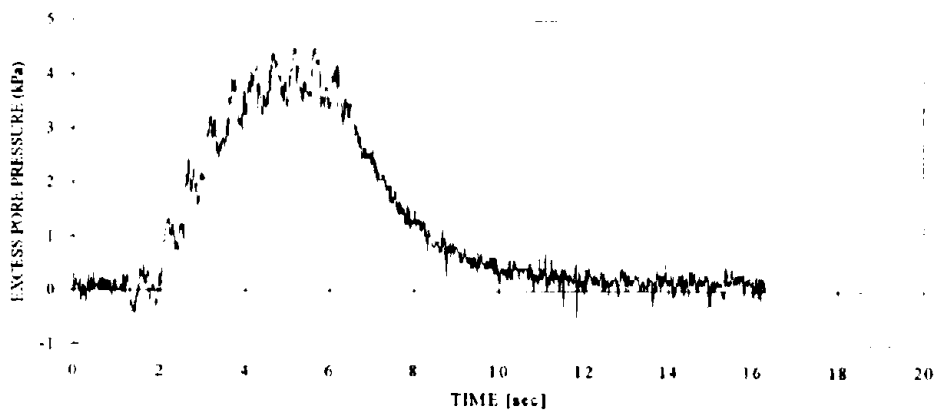

(c) Load data (in model scale)
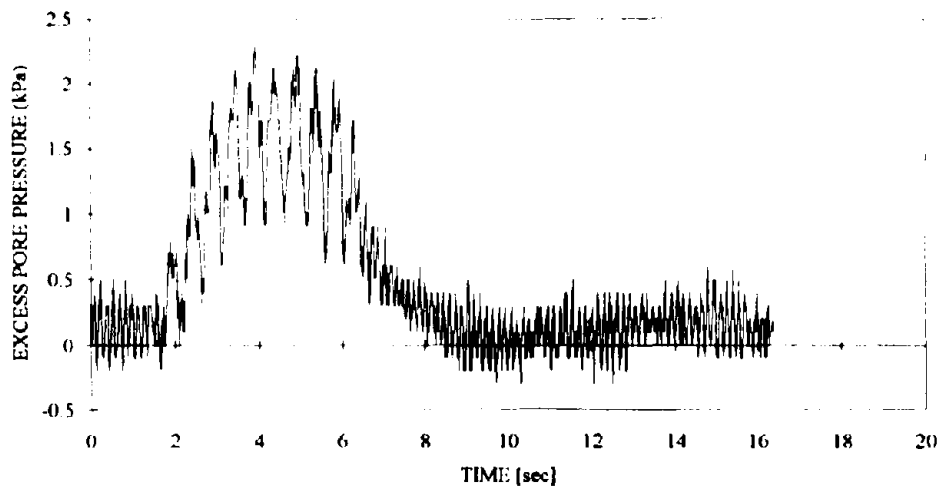Figure B.46: Displacement and load data in Test 4a
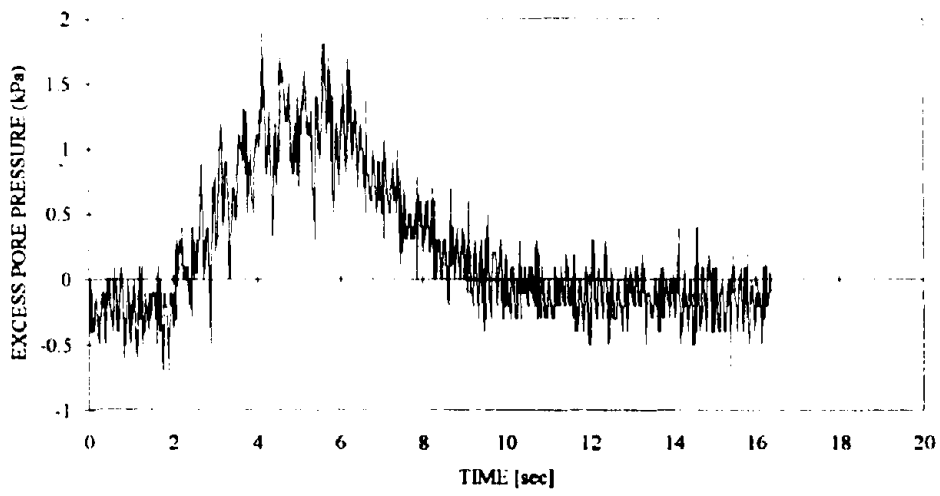
345

(a) P2

(b) P3
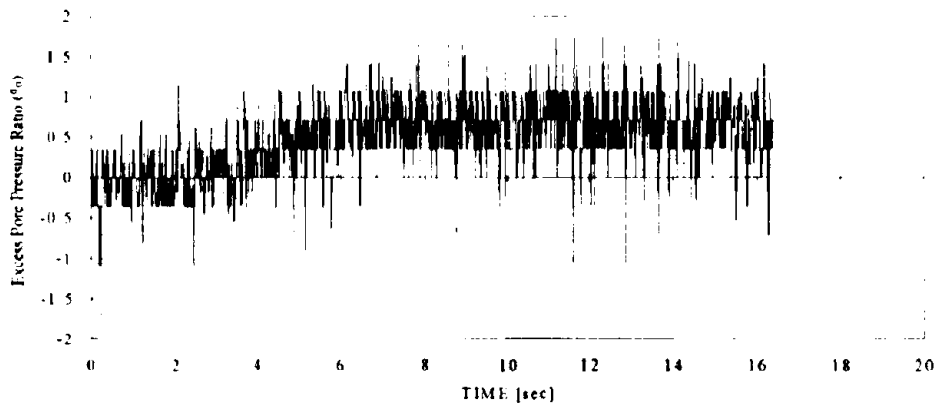
(c) P4

Figure B.47: Excess pore pressure data in Test 4a

(d)   P5

(e)   P6

Figure B.47: Excess pore pressure data in Test 4a

347

(a)   P2

(b)   P3

(c)   P4

Figure B.48: Excess pore pressure ratio in Test 4a

(d)   P5

(e)   P6

Figure B.48: Excess pore pressure ratio in Test 4a

349

(a)   A1 and A2

(b)   A3

Figure B.49 Acceleration data in Test 4b
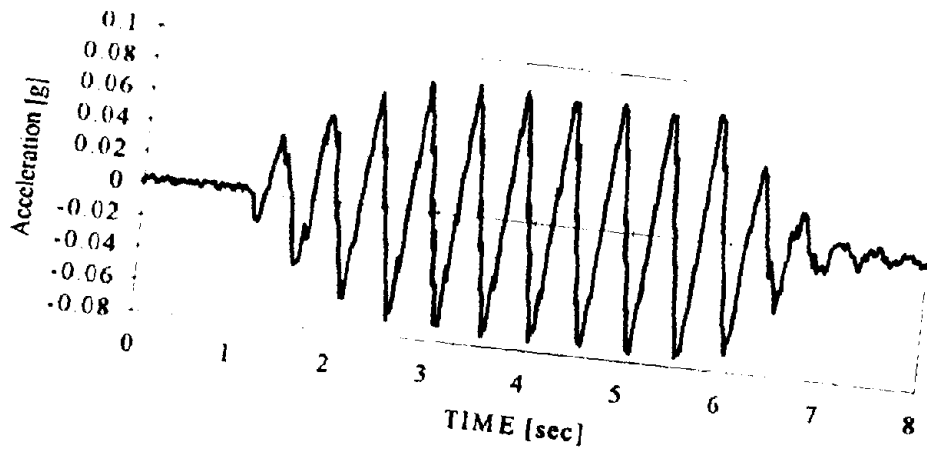
(c)   A4

(d)   A5

(e)   A6

Figure B.49: Acceleration data in Test 4b

351

(a) Amount of tilt in wall (δ/H) - data of D3

(b) Amount of tilt in wall (δ/H) - data of D4

(c) Load data (in model scale)

Figure B.50: Displacement and load data in Test 4b

352

(a)   P2

(b)   P3

(c)   P4
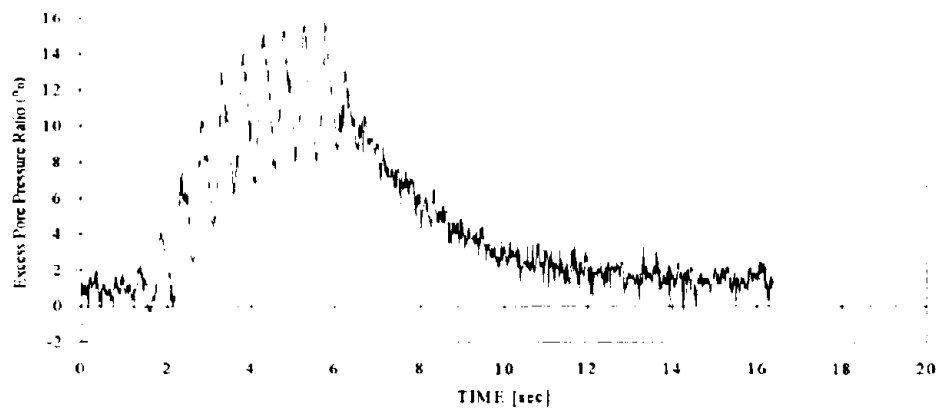
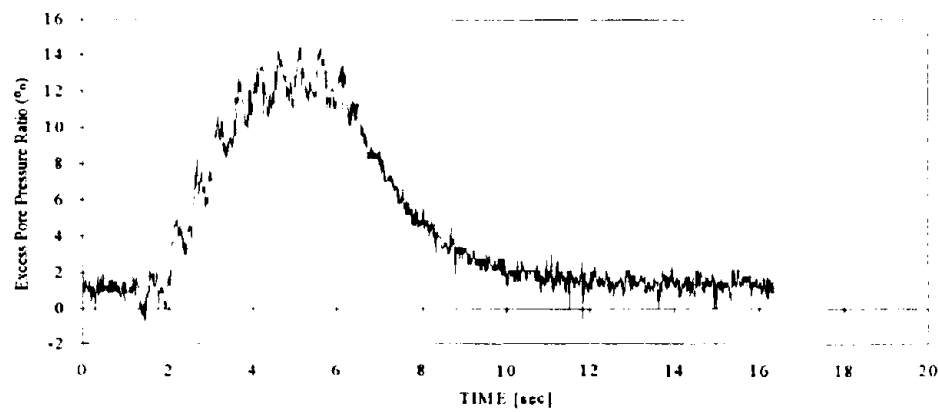Figure B.51   Excess pore pressure data in Test 4b

(d)   P5

(e)   P6

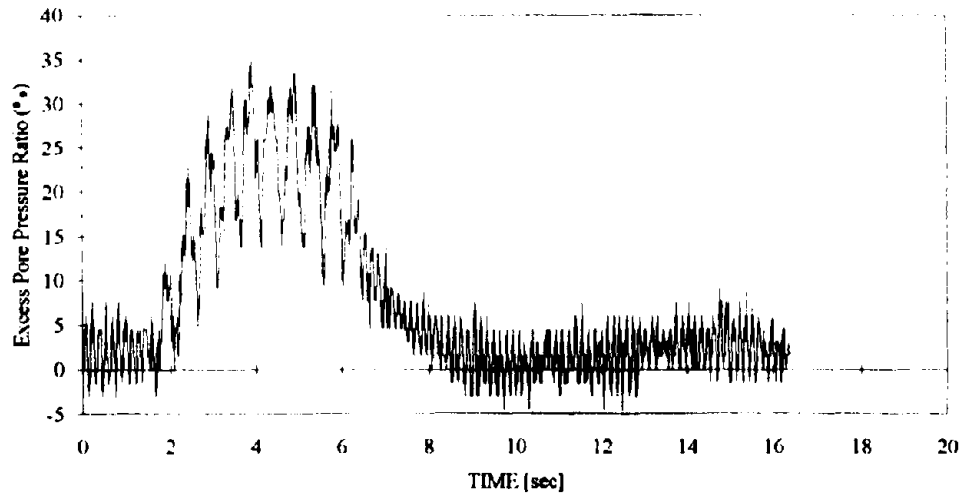Figure B.51: Excess pore pressure data in Test 4b
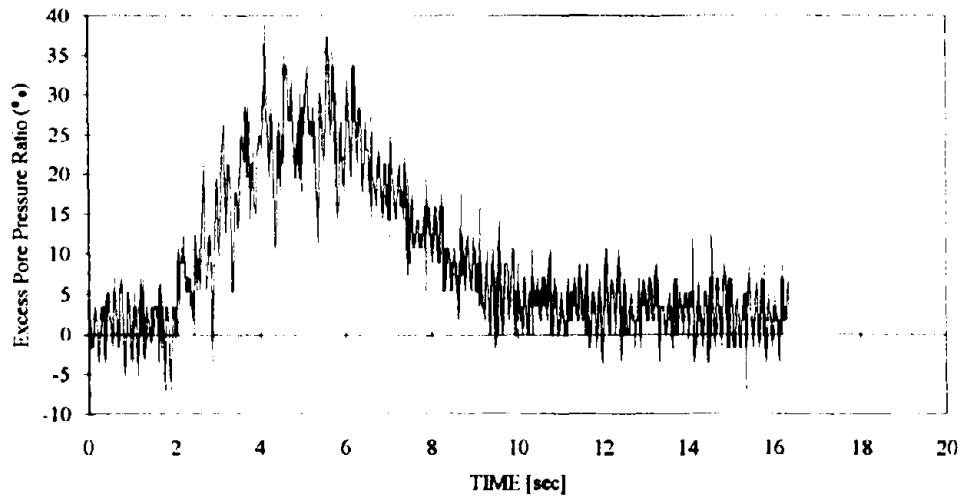
354

(a)   P2

(b)   P3

(c)   P4

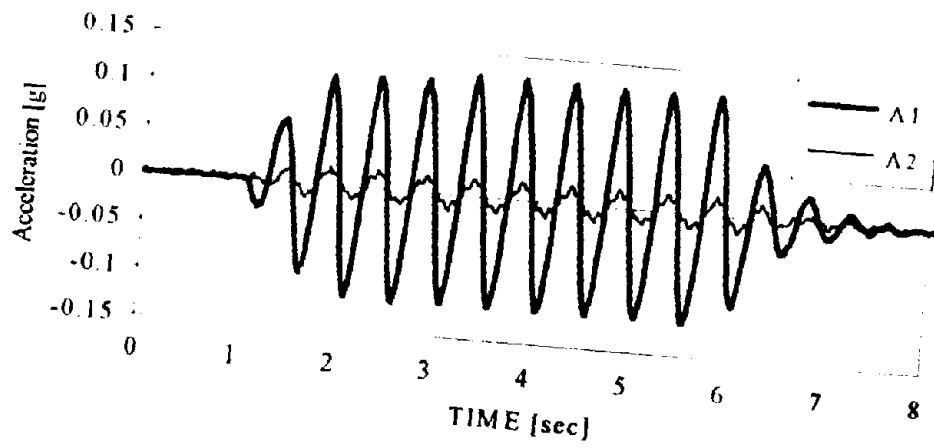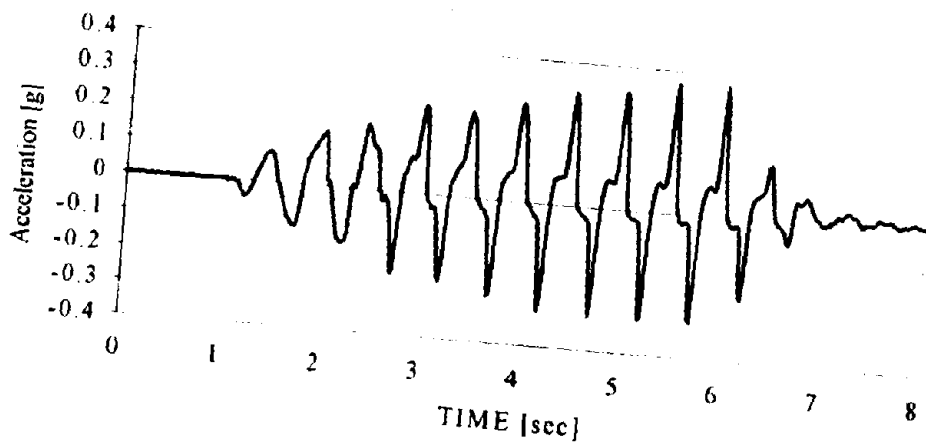Figure B.52 Excess pore pressure ratio in Test 4b

(d)   P5

(e)   P6

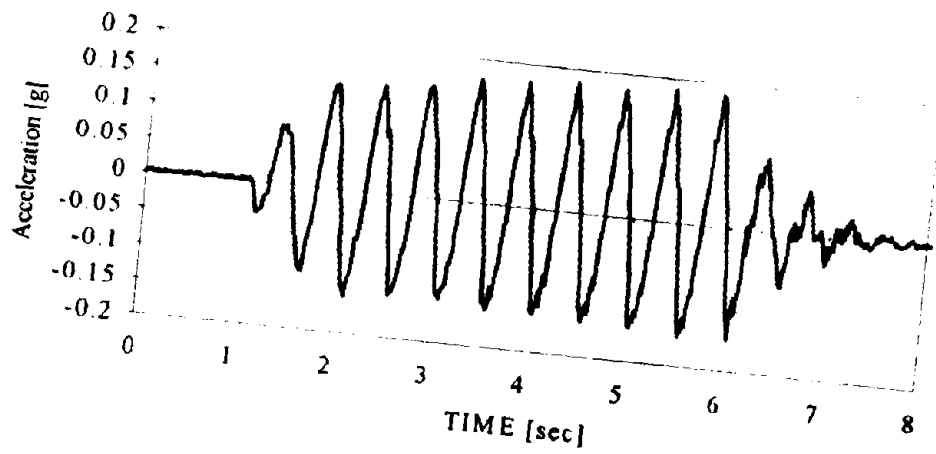Figure B.52: Excess pore pressure ratio in Test 4b

(a)   A1 and A2

(b)   A3
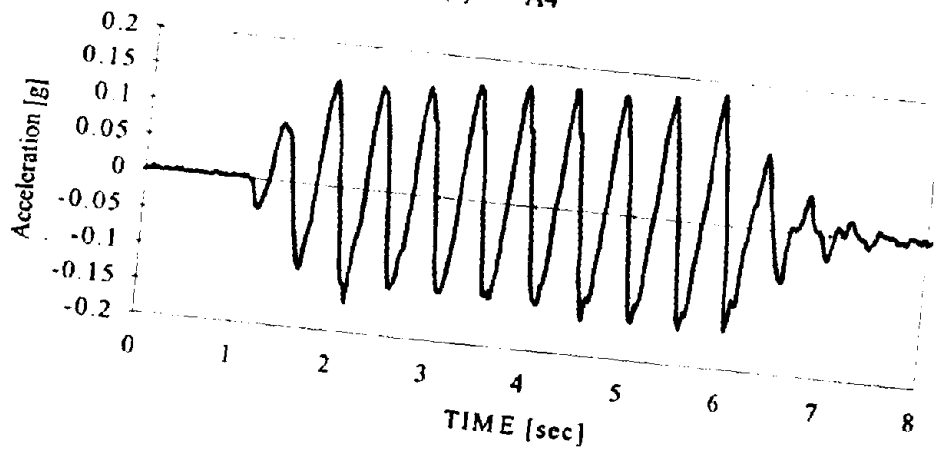
Figure B.53: Acceleration data in Test 4c

357

(c)   A4

(d)   A5

(e)   A6

Figure B.53: Acceleration data in Test 4c

358

(a) Amount of tilt in wall (δ/H) - data of D3

(b) Amount of tilt in wall (δ/H) - data of D4

(c) Load data (in model scale)

Figure B.54: Displacement and load data in Test 4c

(a)   P2

(b)   P3

(c)   P4

Figure B.55: Excess pore pressure data in Test 4c

(d)   P5
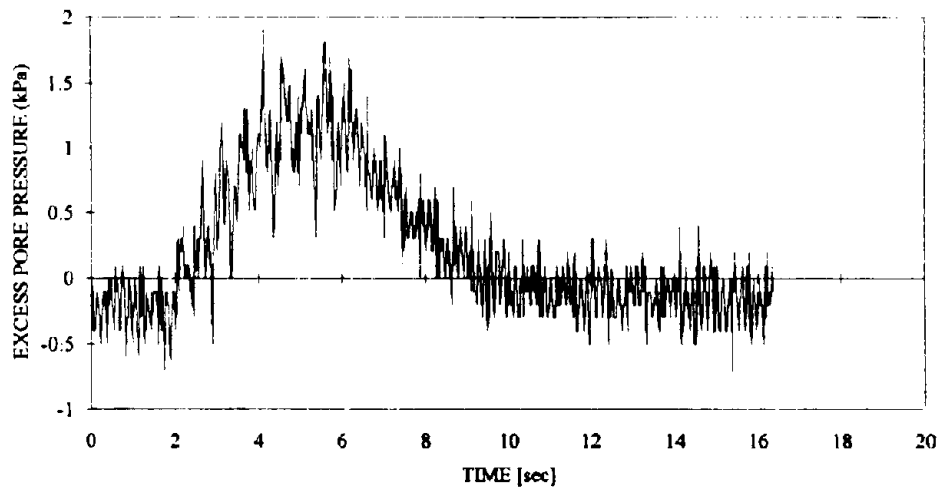
(e)   P6

Figure B.55: Excess pore pressure data in Test 4c

361

(a)　　P2

(b)　　P3

(c)　　P4

Figure B.56: Excess pore pressure ratio in Test 4c

362

(d)   P5

(e)   P6

Figure B.56: Excess pore pressure ratio in Test 4c
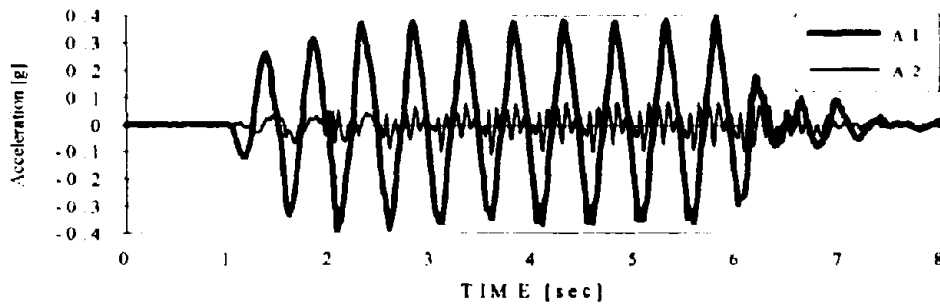
(a) A1 and A2
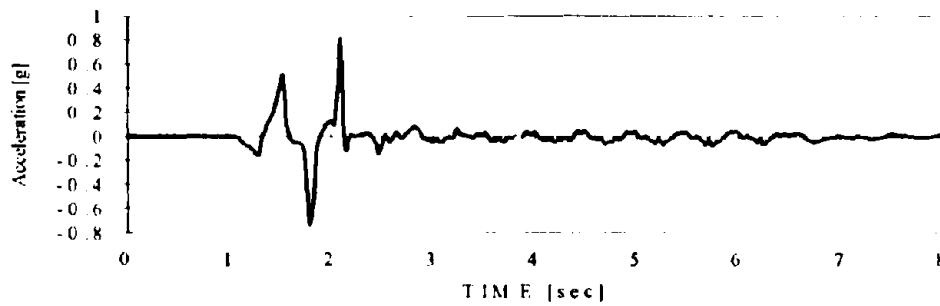
(b) A3
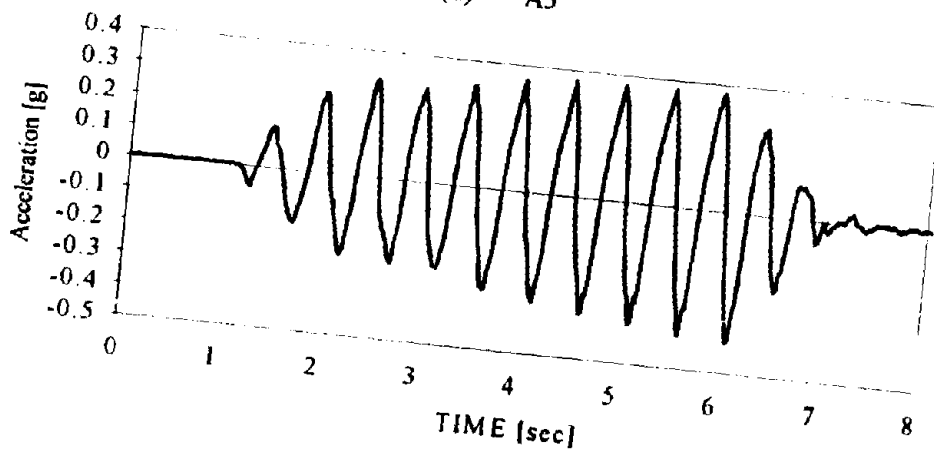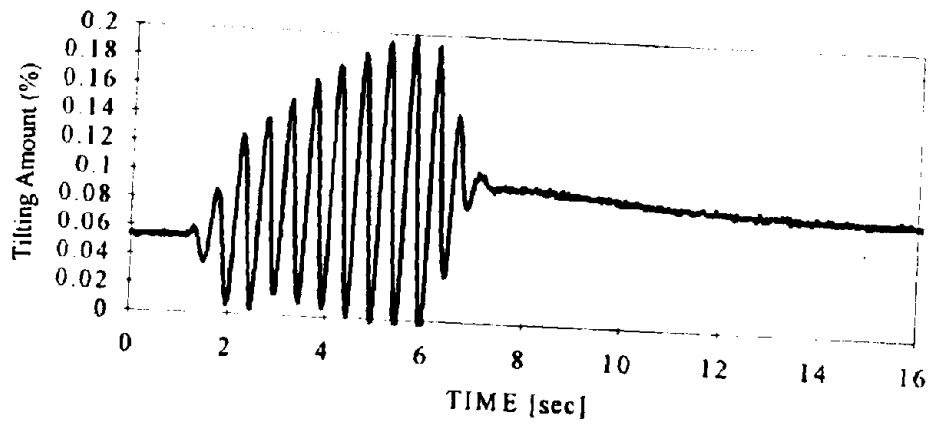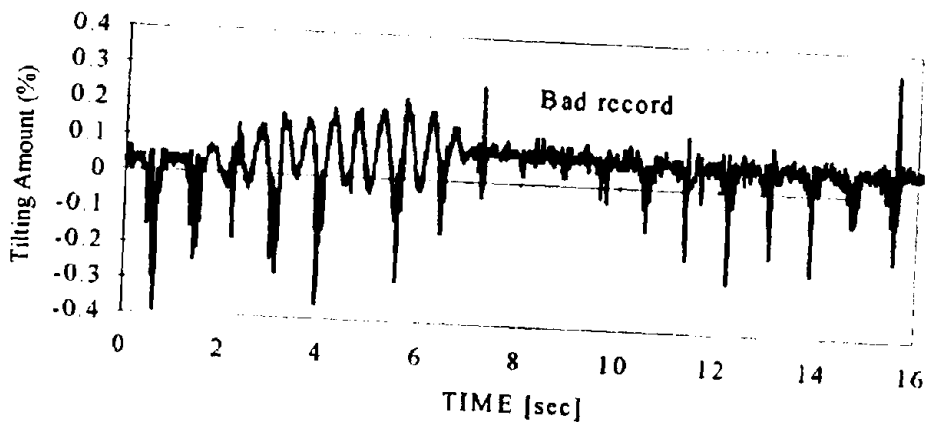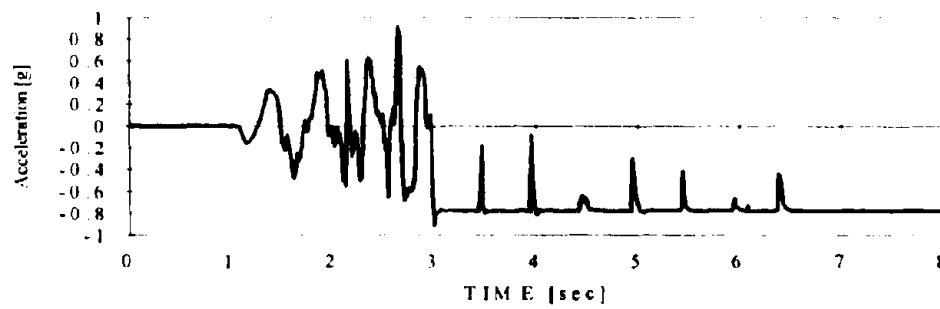
(c) A5
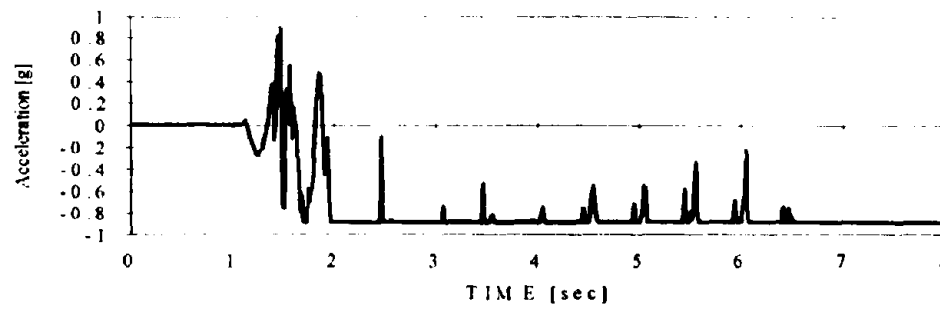
(d) A6

Figure B.57: Acceleration data in Test 5a
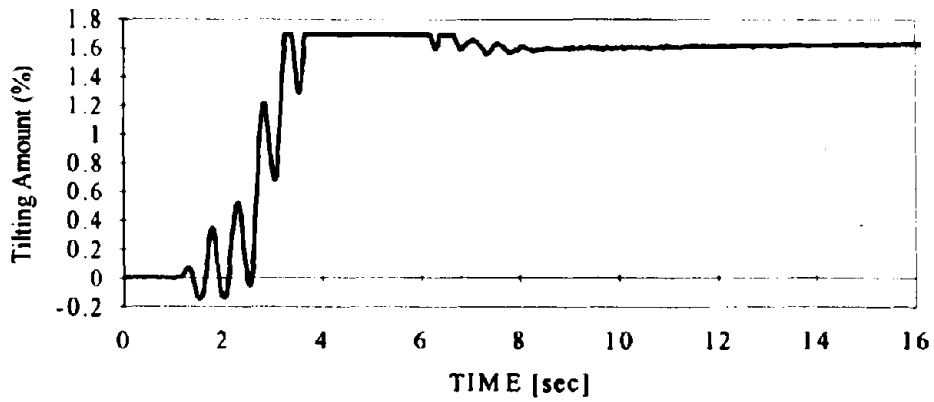
364

(a) Amount of tilt in wall (δ/H) - data of D3

(b) Amount of tilt in wall (δ/H) - data of D4

(c) Load data (in model scale)

Figure B.58 Displacement and load data in Test 5a
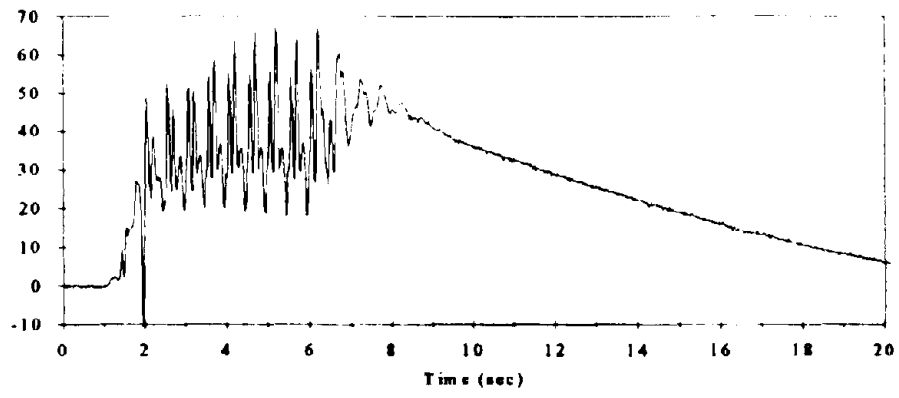
(a)   P2
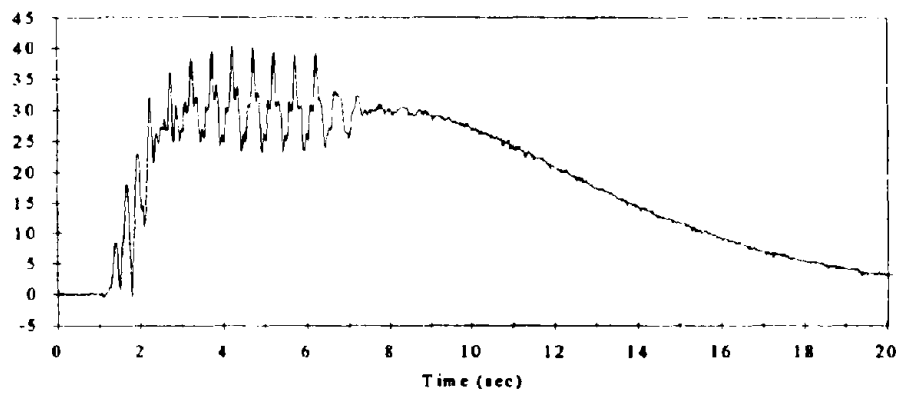
(b)   P3
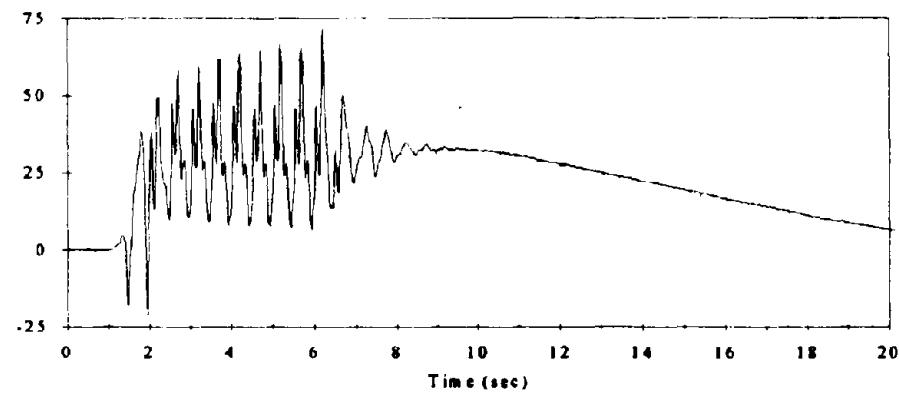
(c)   P4

Figure B.59: Excess pore pressure data in Test 5a
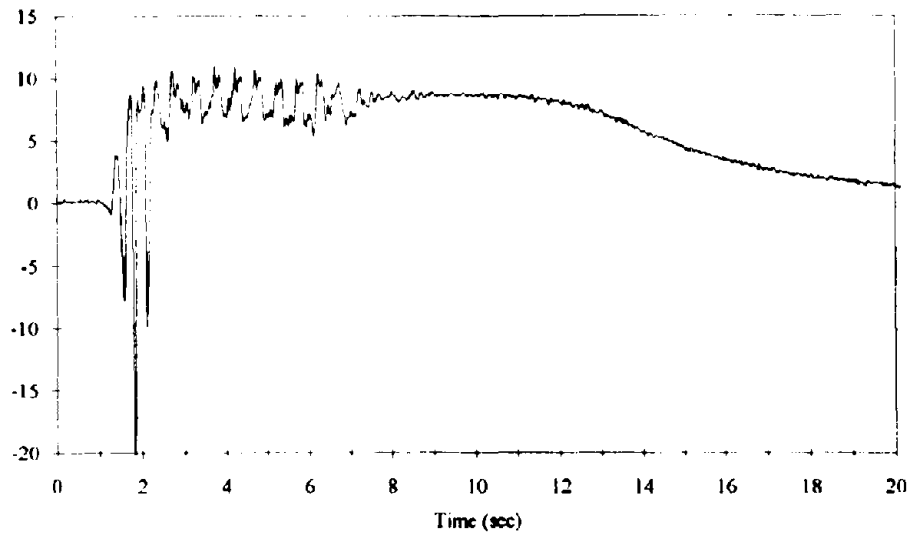
(d)   P5
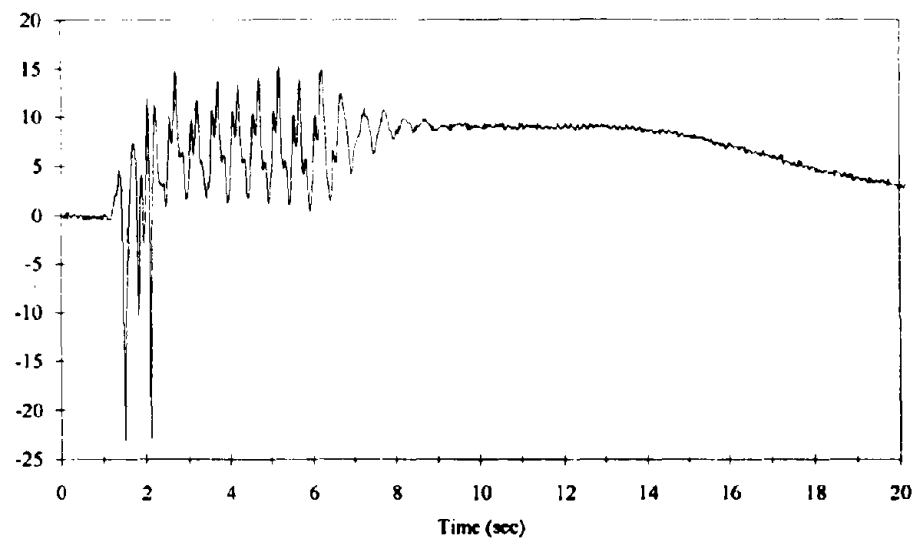
(e)   P6

Figure B.59: Excess pore pressure data in Test 5a
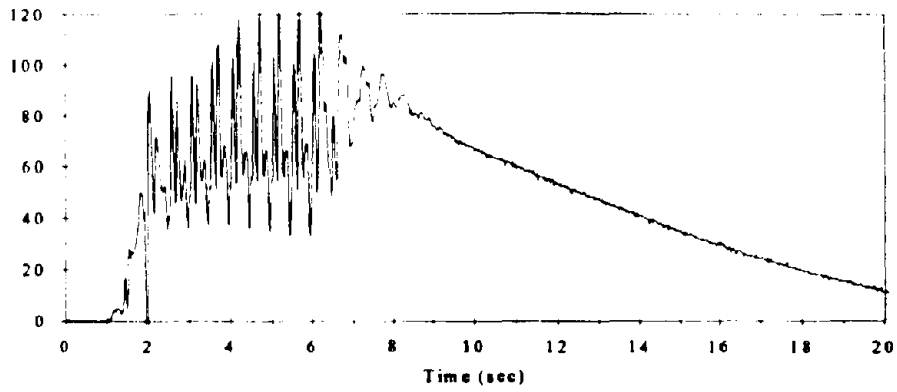
(a)   P2
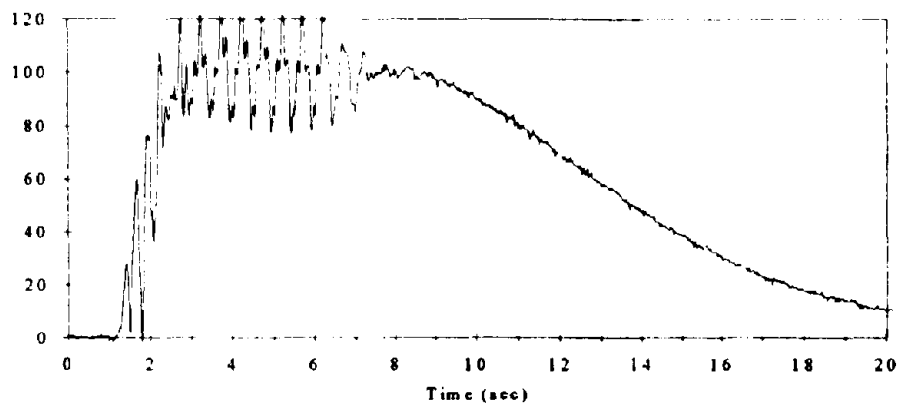
(b)   P3
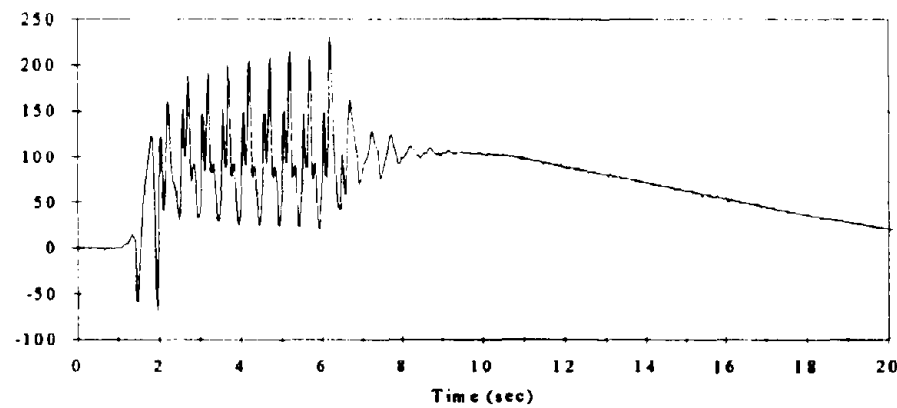
(c)   P4

Figure B.60: Excess pore pressure ratios in Test 5a

368
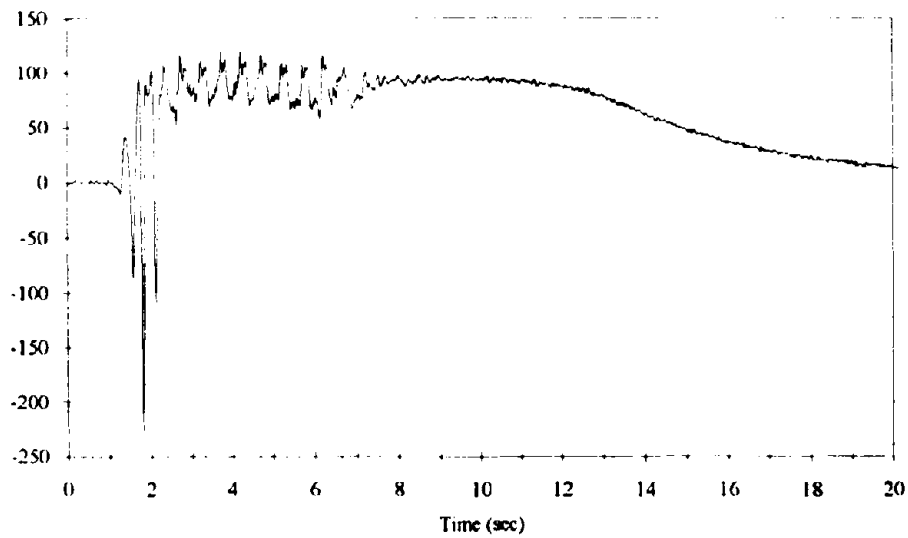
(d) P5
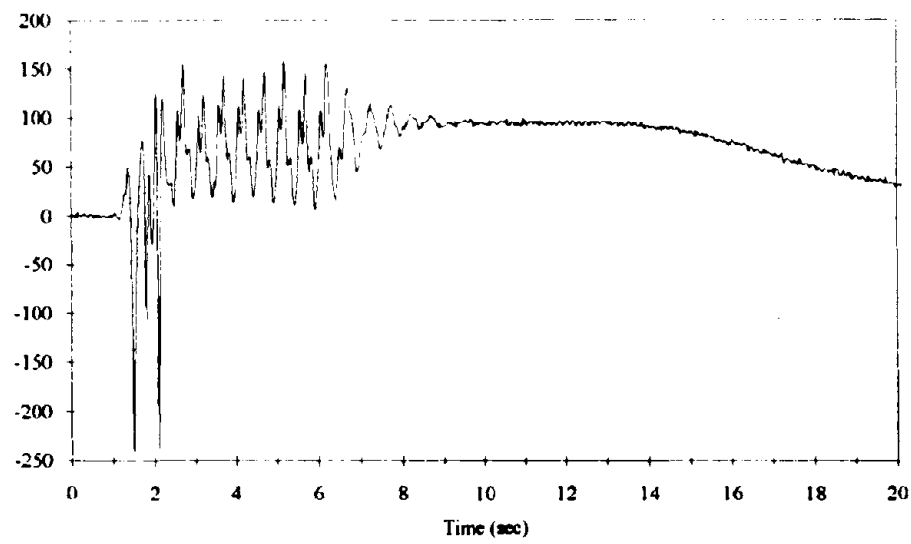
(e) P6

Figure B.60: Excess pore pressure ratios in Test 5a
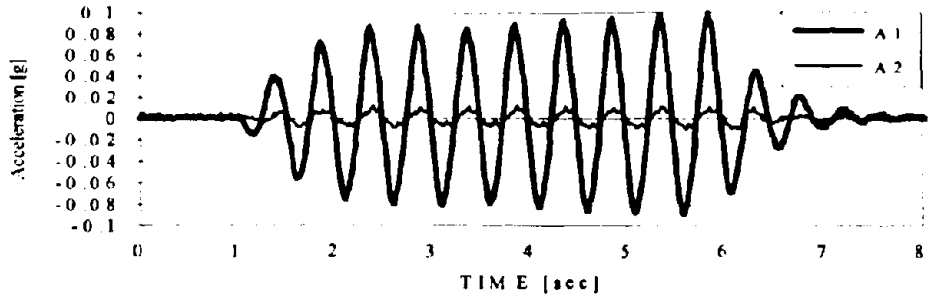
(a)   A1 and A2
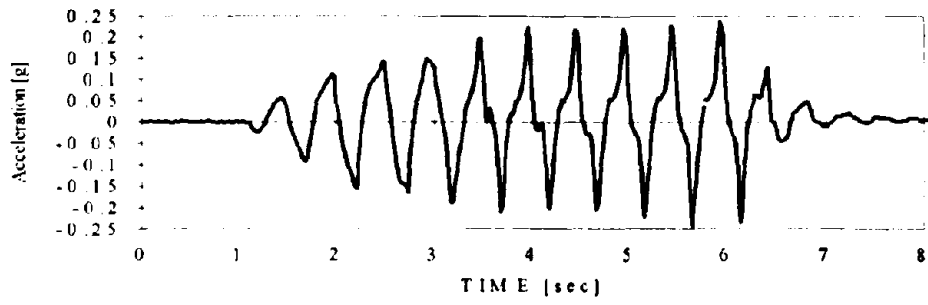
(b)   A3
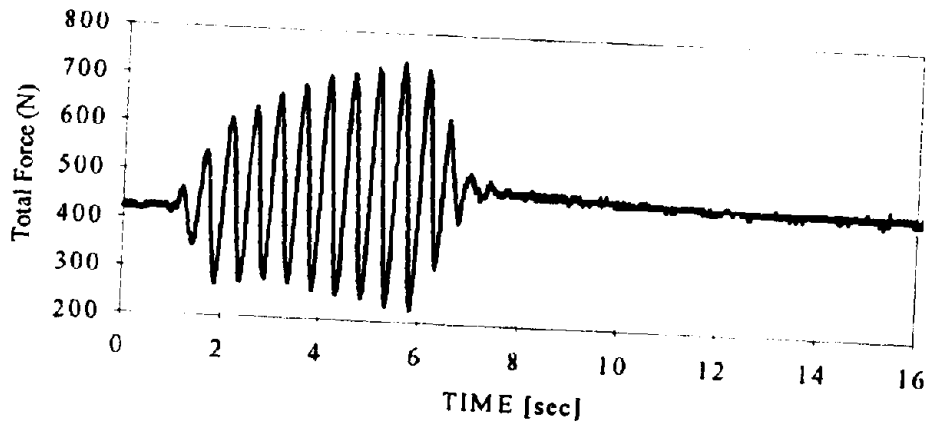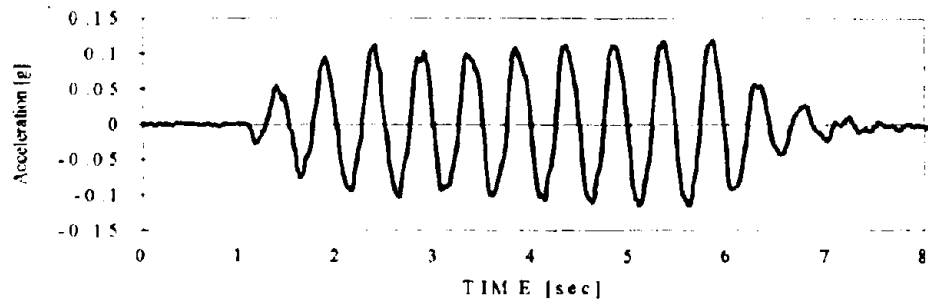

(c)   A5
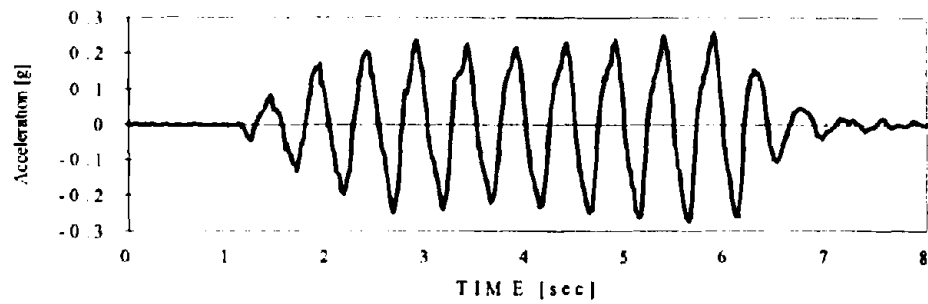
(d)   A6

Figure B.61: Acceleration data in Test 5a
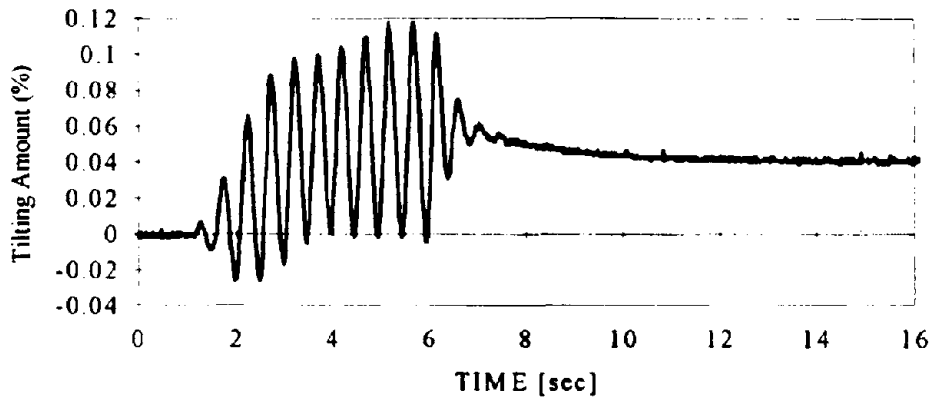
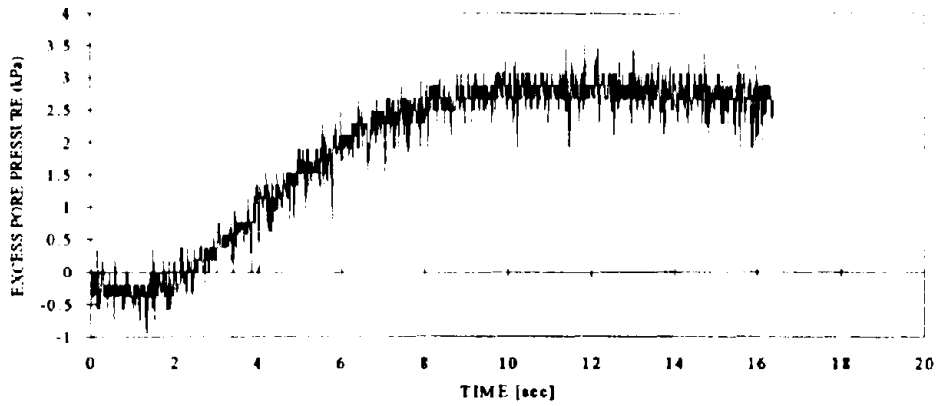(a) Amount of tilt in wall (δ/H) - data of D3
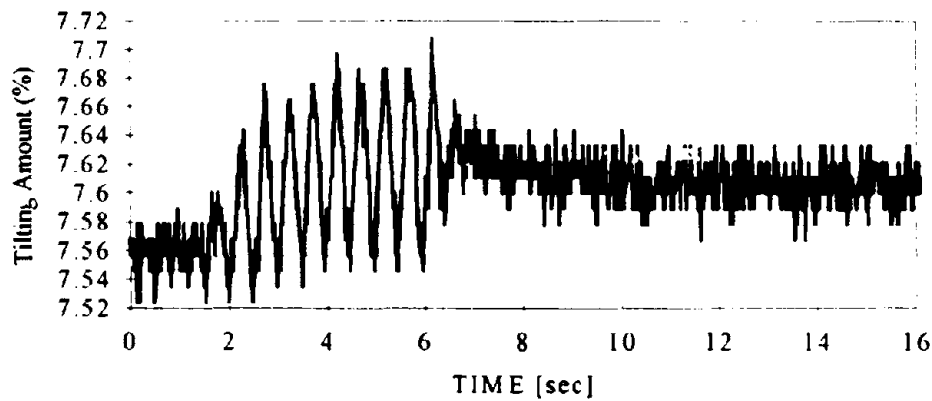
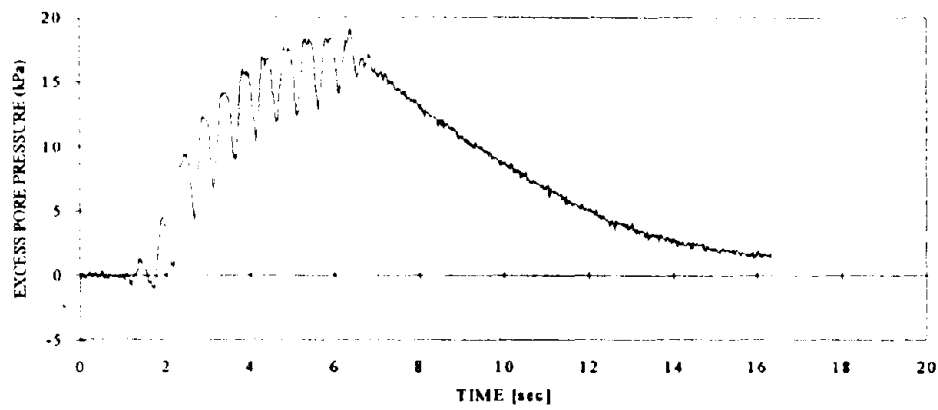(b) Amount of tilt in wall (δ/H) - data of D4
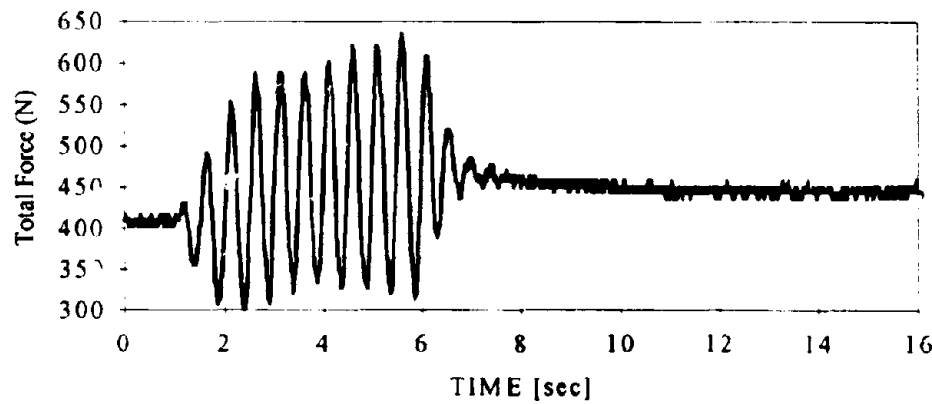
(c) Load data (in model scale)

Figure B.62: Displacement and load data in Test 5b
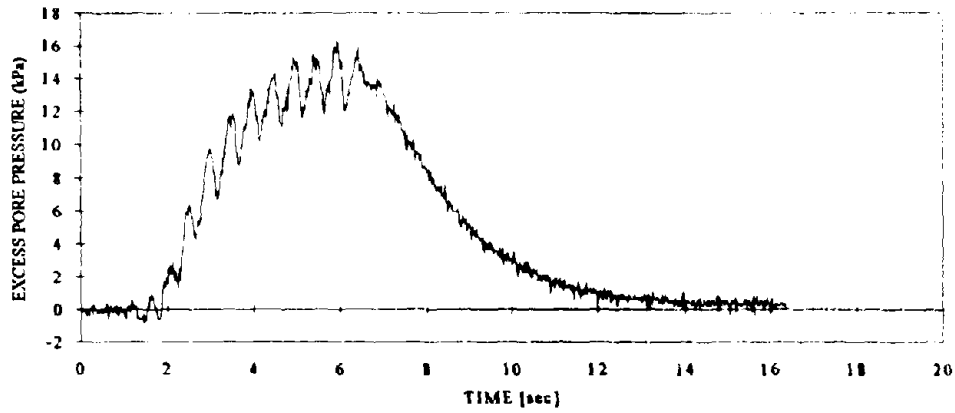
(a)   P2
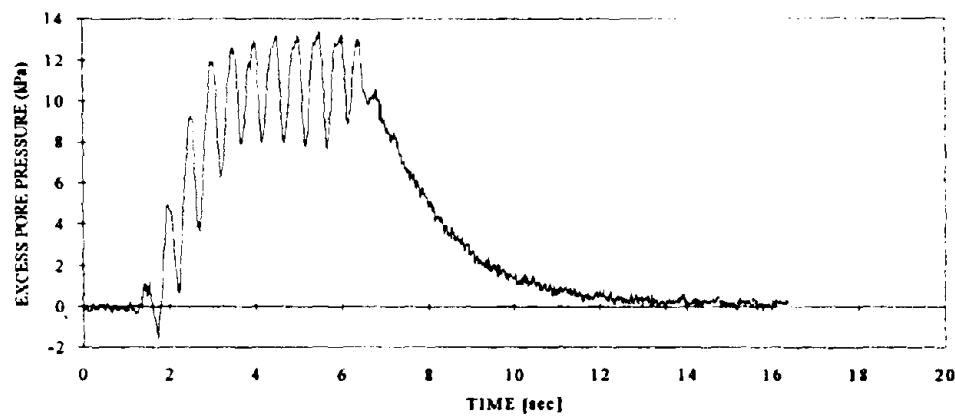
(b)   P3
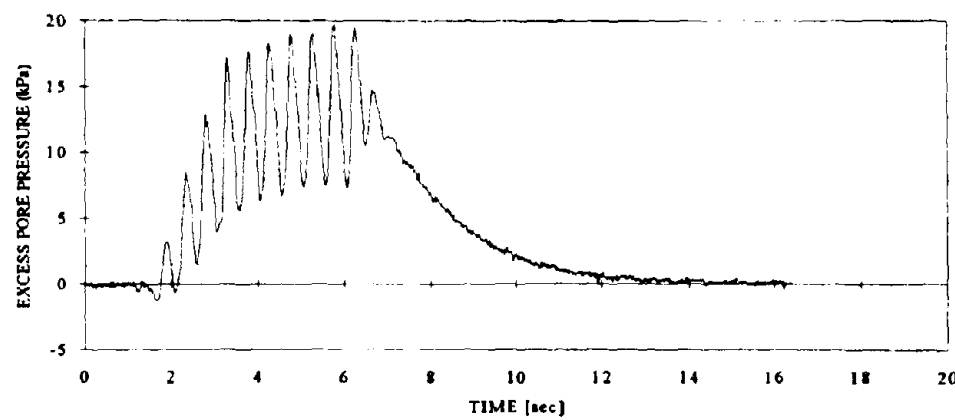
(c)   P4

Figure B.63: Excess pore pressure data in Test 5b

372
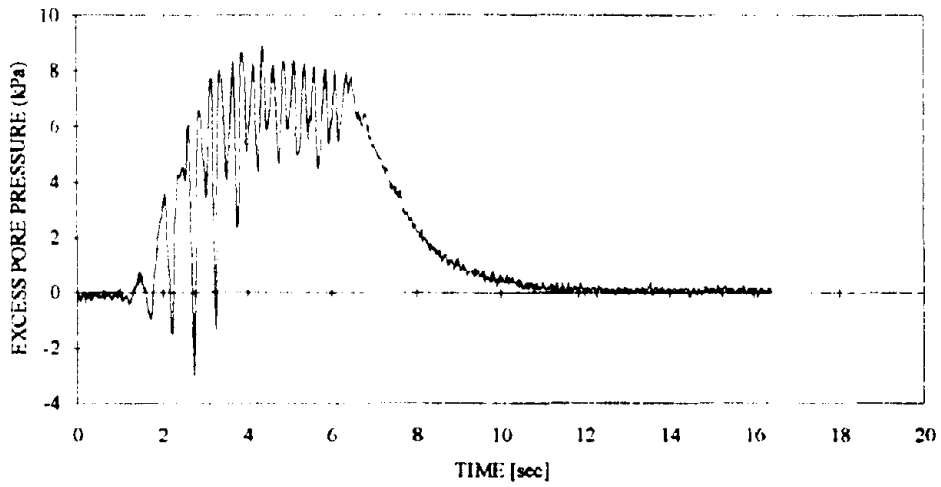
(d) P5
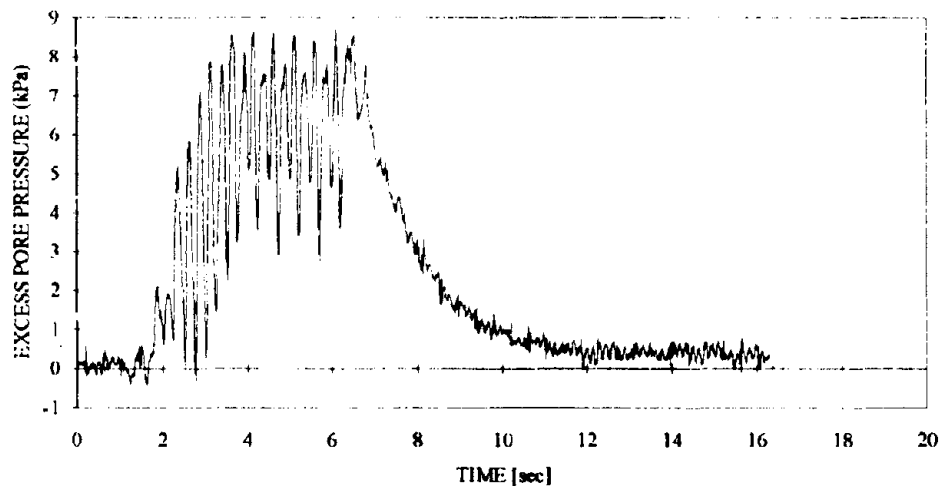
(e) P6

Figure B.63: Excess pore pressure data in Test 5b

373
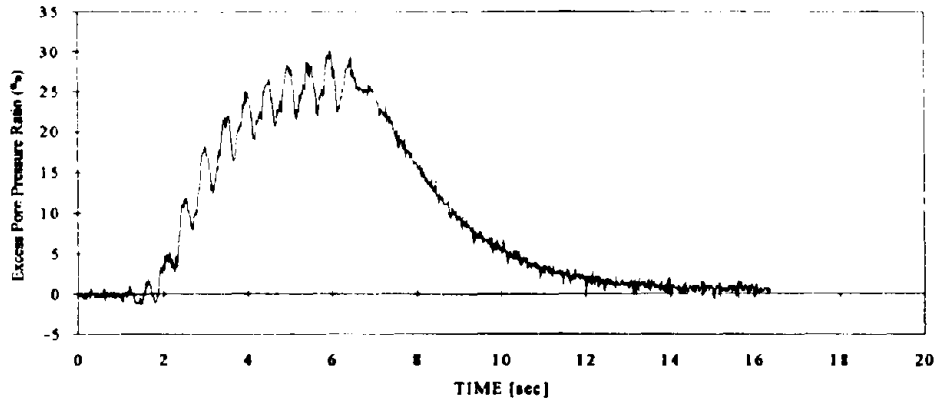
(a)   P2
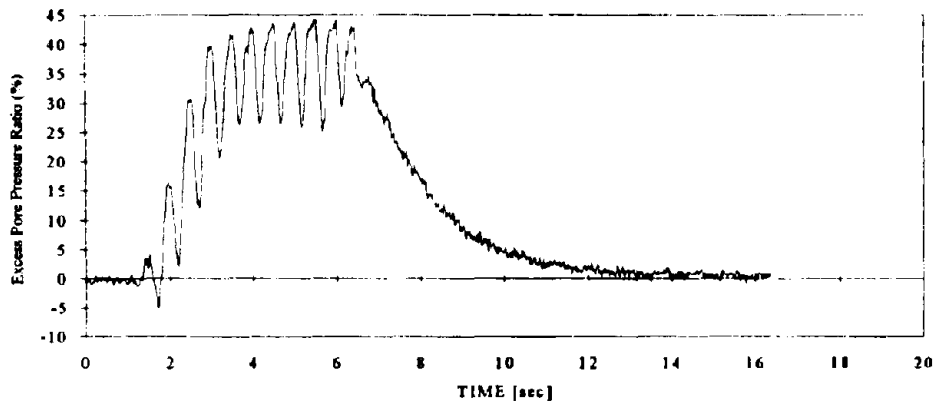
(b)   P3
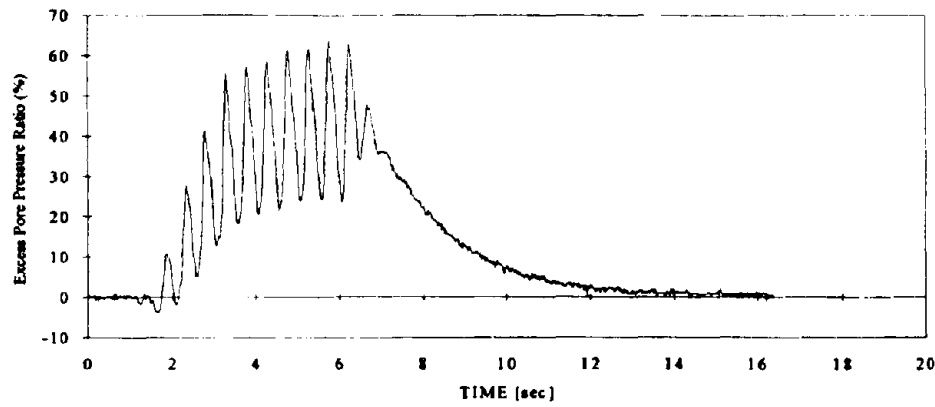
(c)   P4

Figure B.64: Excess pore pressure ratio in Test 5b

374
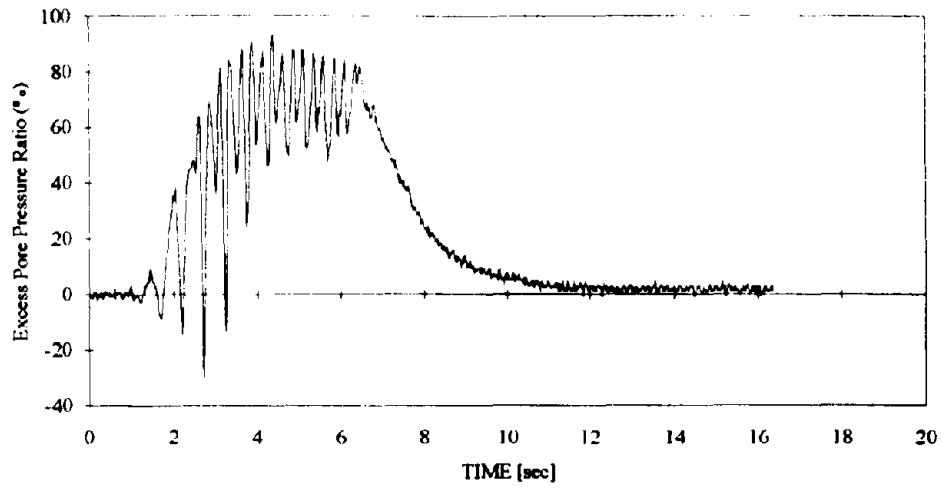
(d)   P5
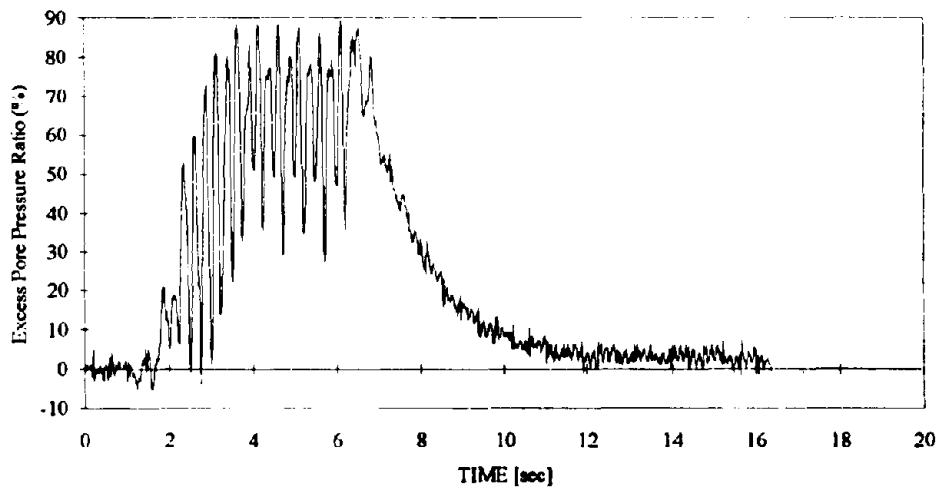
(e)   P6

Figure B.64: Excess pore pressure ratio in Test 5b
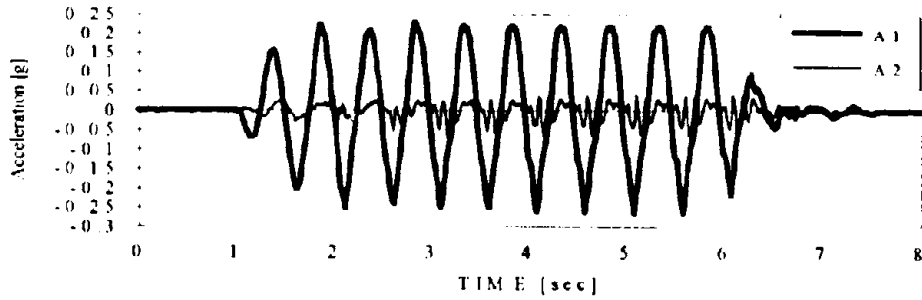
(a)   A1 and A2
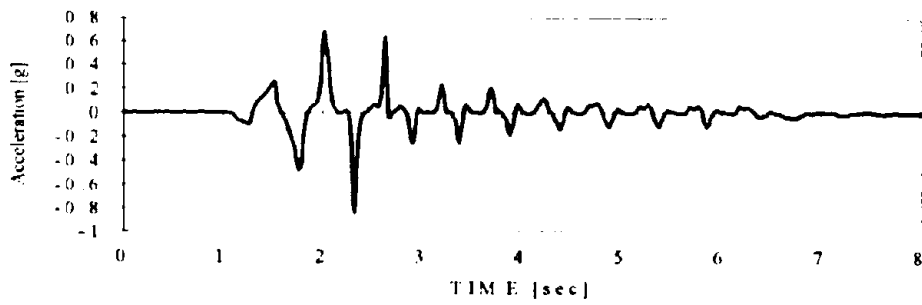
(b)   A3
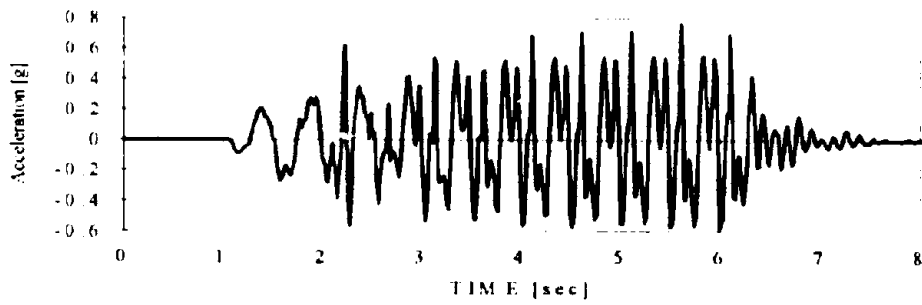
(c)   A5
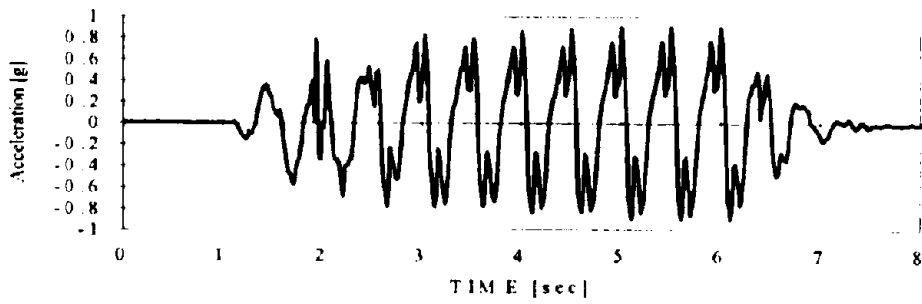
(d)   A6

Figure B.65 Acceleration data in Test 6a
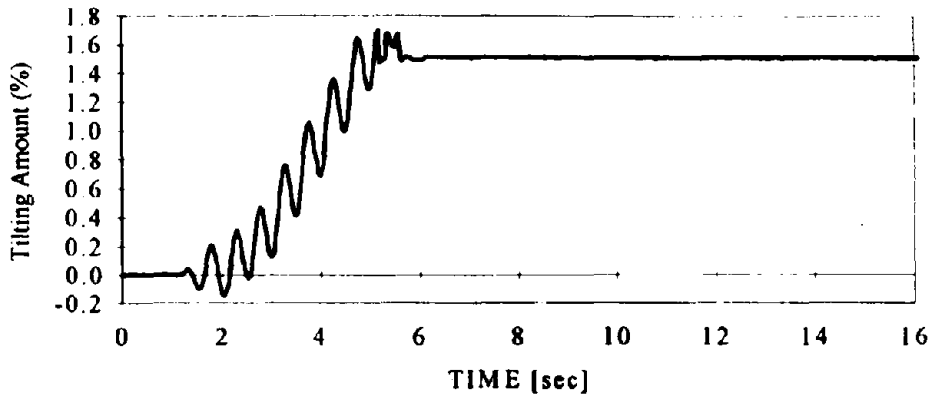
(a) Amount of tilt in wall (δ/H) - data of D3
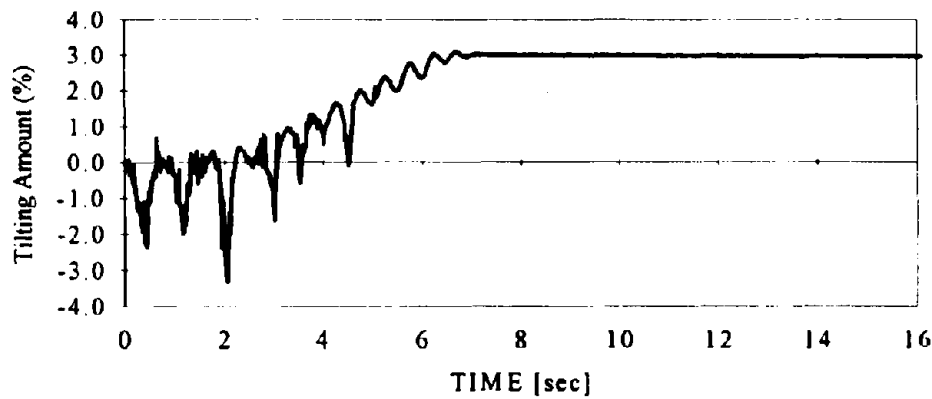
(b) Amount of tilt in wall (δ/H) - data of D4
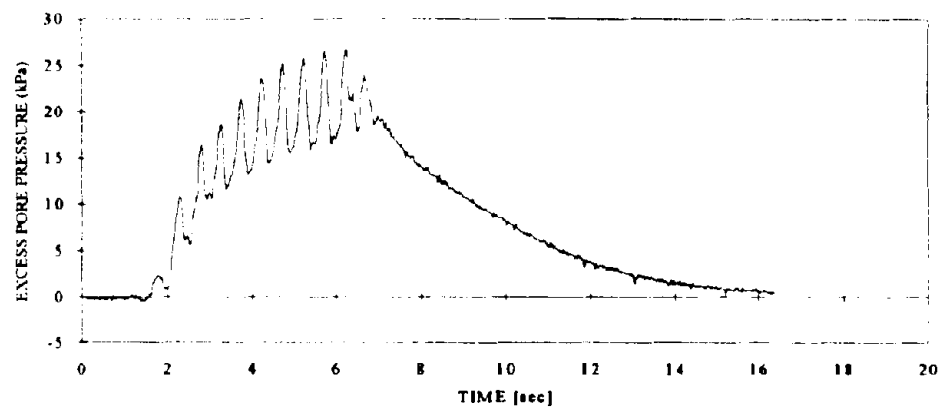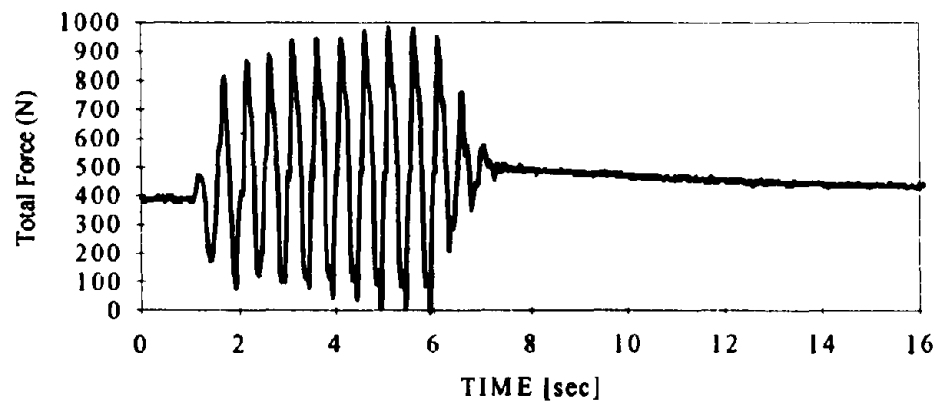

(c) Load data (in model scale)

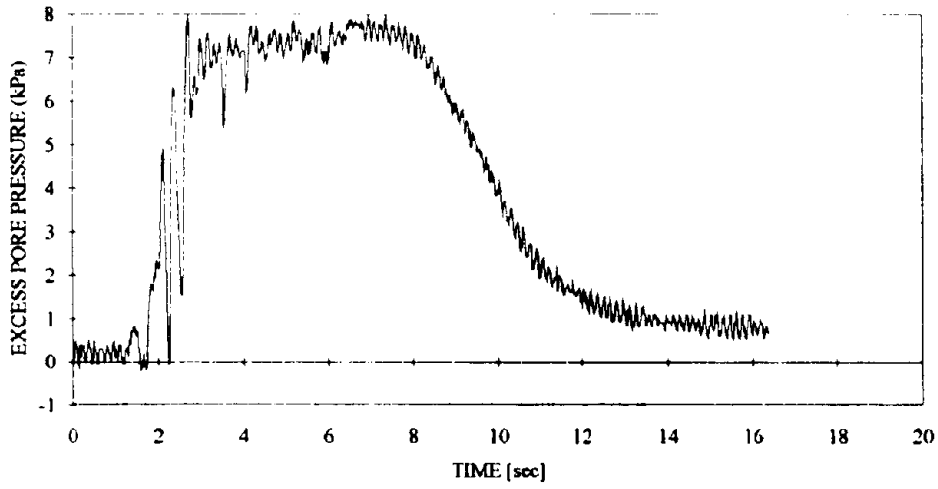Figure B.66: Displacement and load data in Test 6a

377
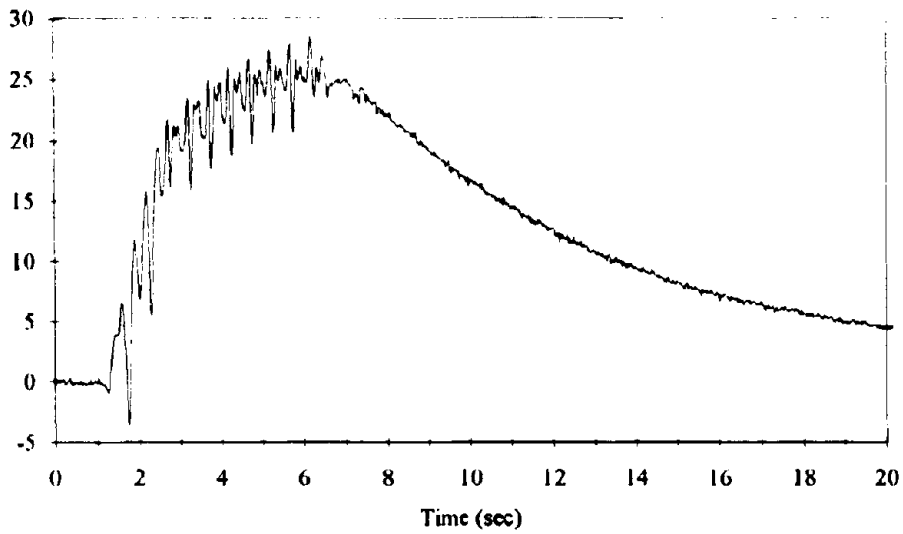
(a)   P3
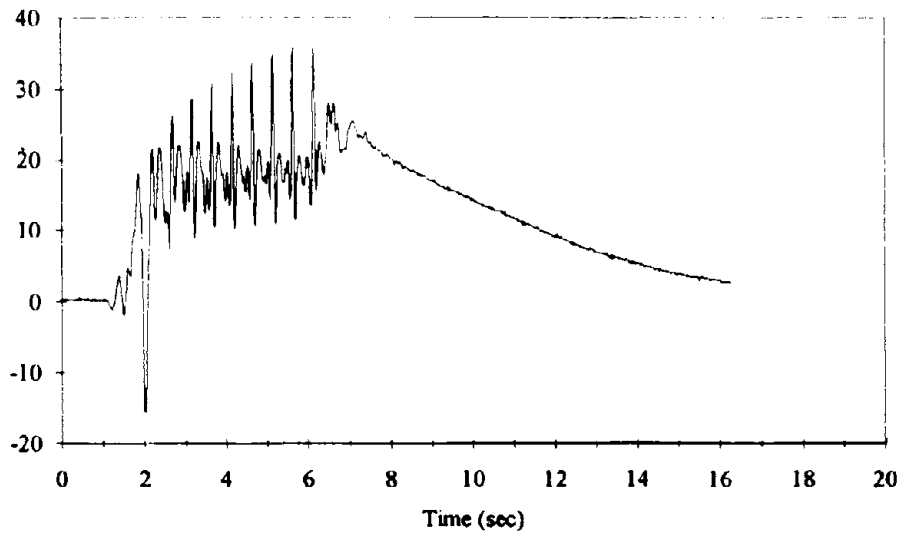
(b)   P4

Figure B.67: Excess pore pressure data in Test 6a

378
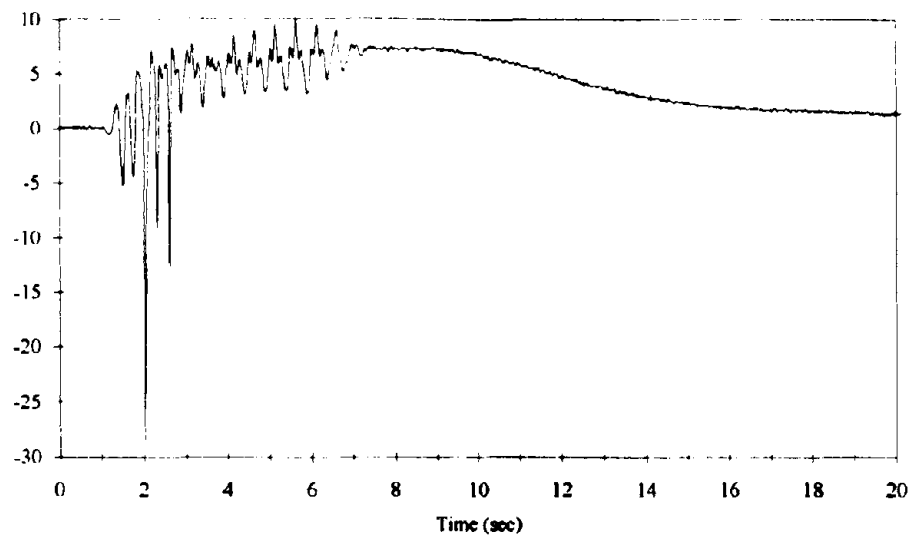
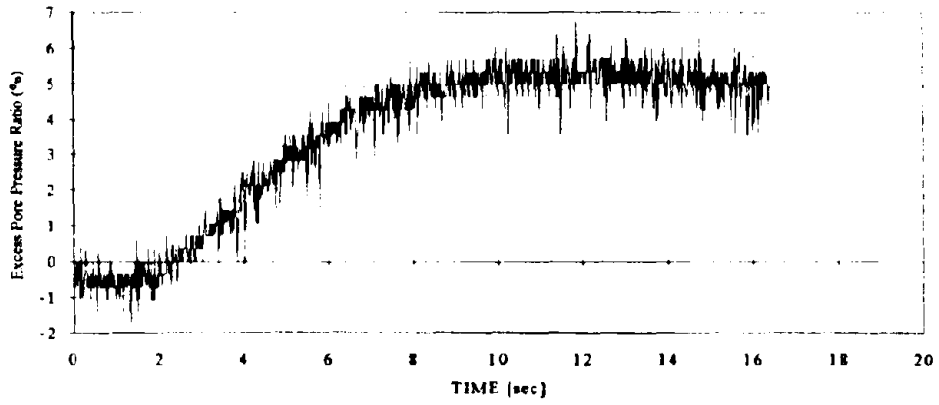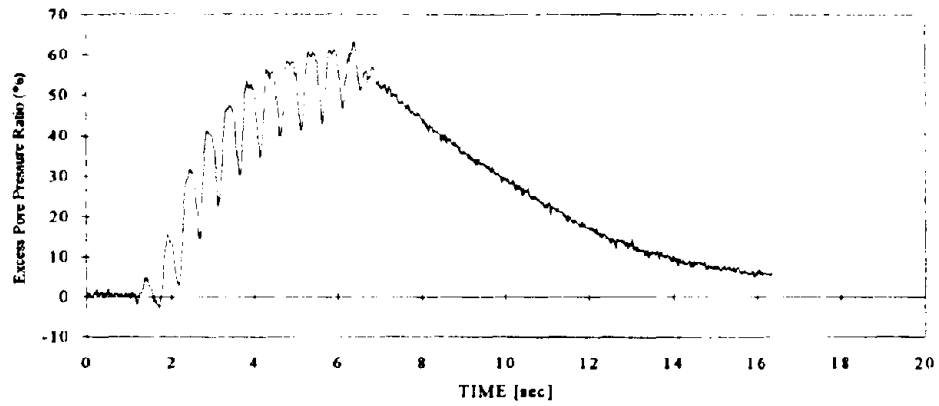(c) P5
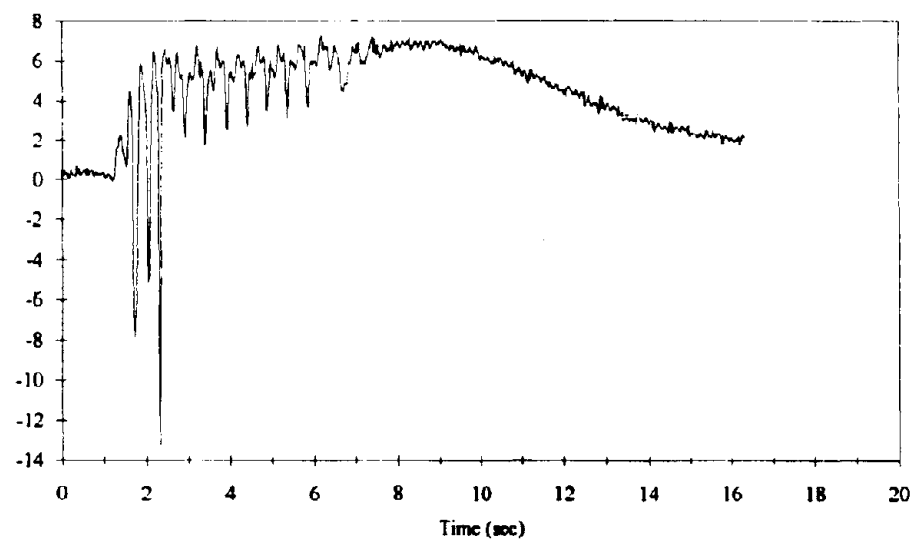
(d) P6

Figure B.67: Excess pore pressure data in Test 6a

379
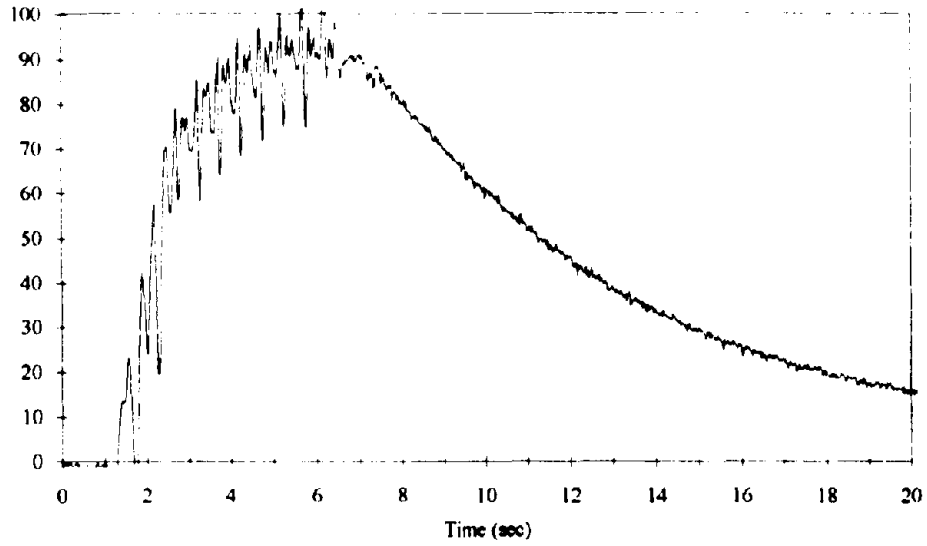
(a)   P3
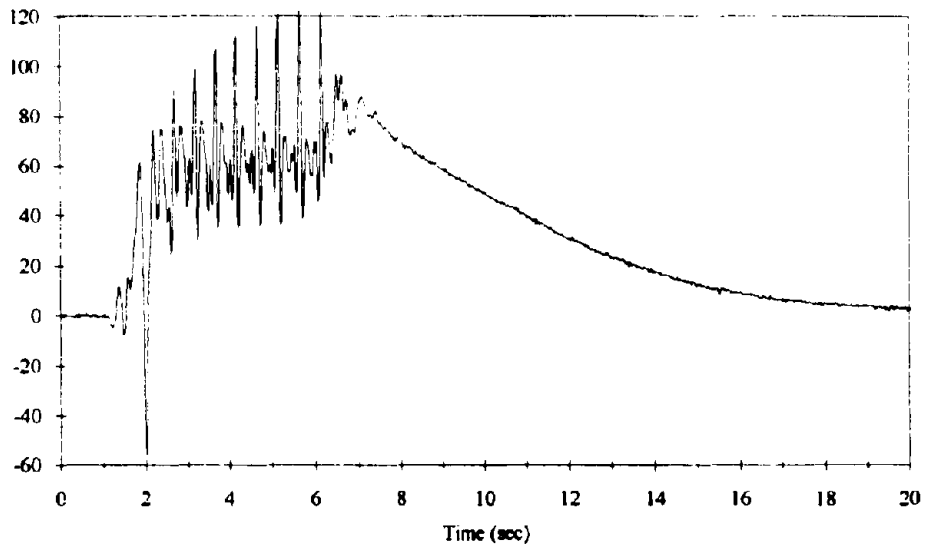
(b)   P4

Figure B.68: Excess pore pressure ratios in Test 6a

380
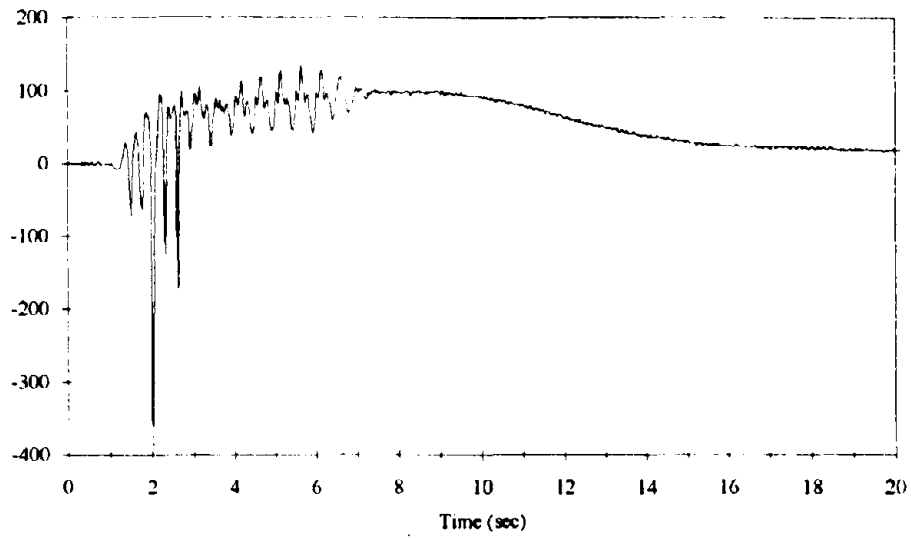
(c)   P5
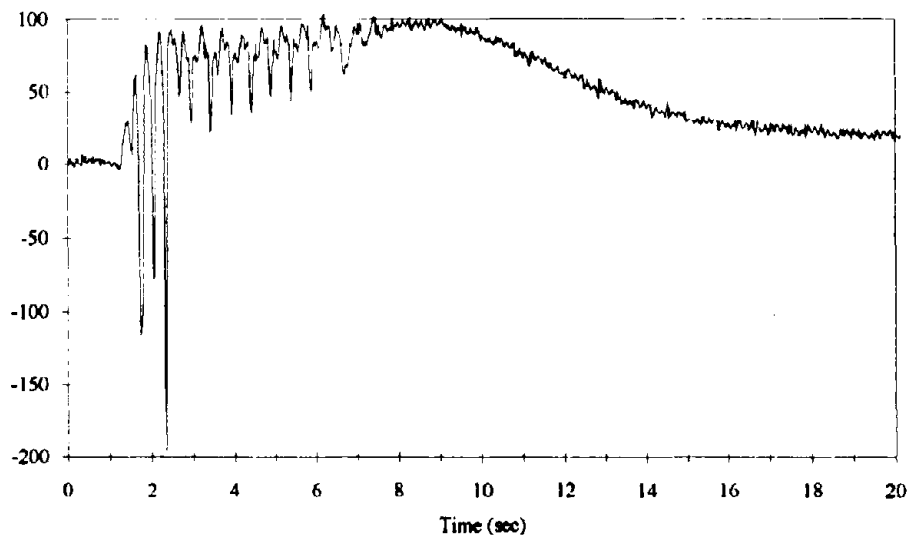
(d)   P6

Figure B.68 Excess pore pressure ratios in Test 6a

381
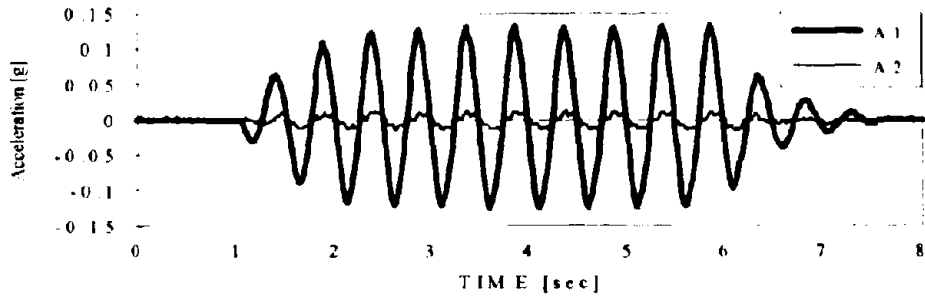
(a)   A1 and A2
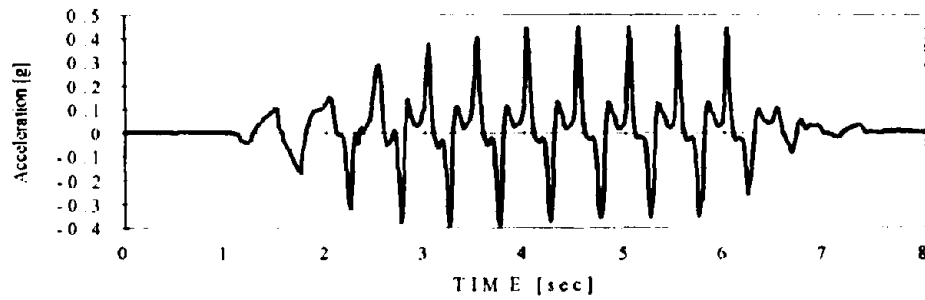
(b)   A3
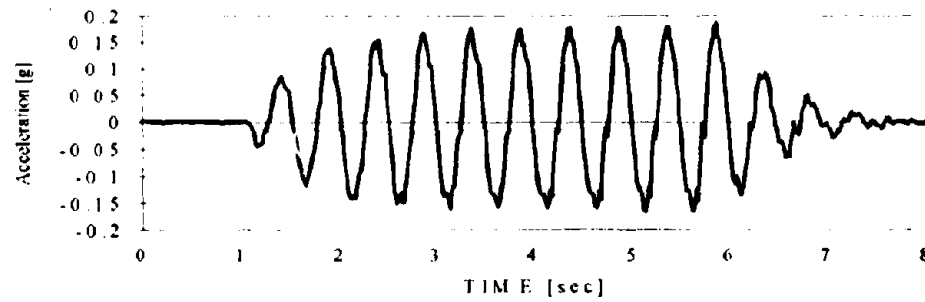
(c)   A5
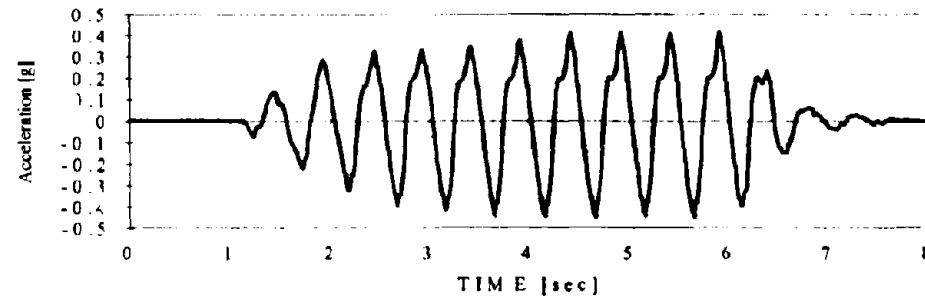
(d)   A6

Figure B.69 Acceleration data in Test 6b
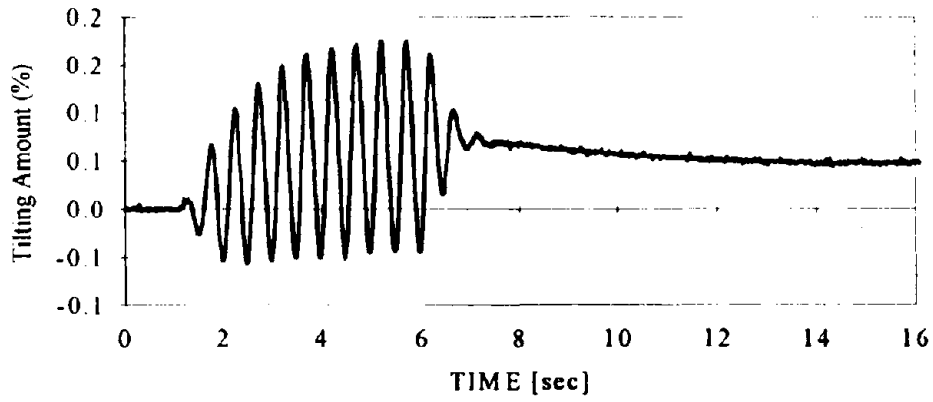
382

(a) Amount of tilt in wall (δ/H) - data of D3
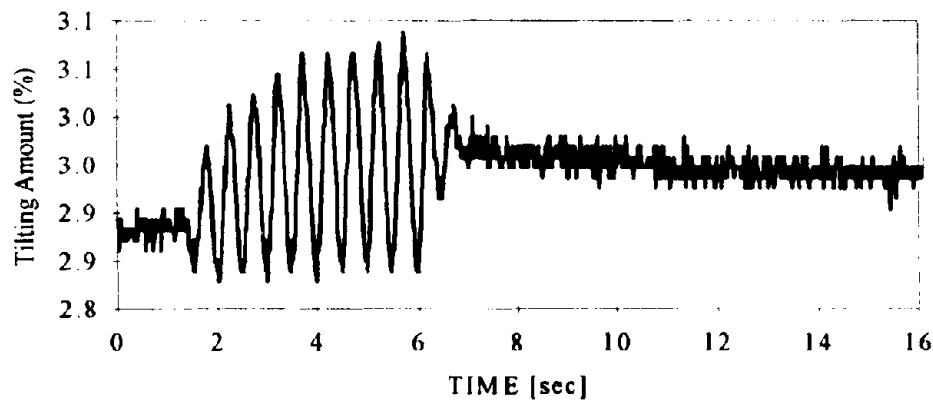
(b) Amount of tilt in wall (δ/H) - data of D4
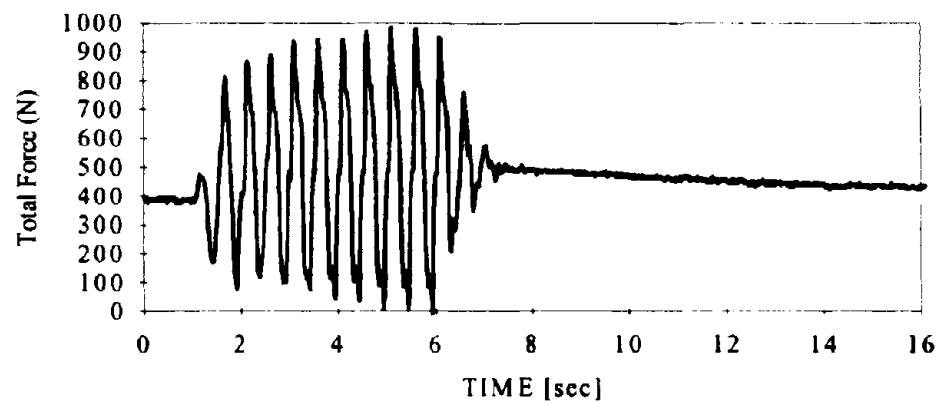
(c) Load data (in model scale)

Figure B.70: Displacement and load data in Test 6b

383
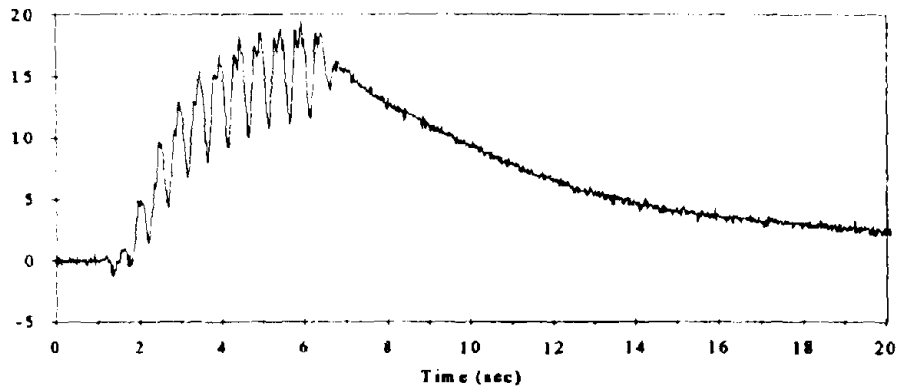
(a)   P2
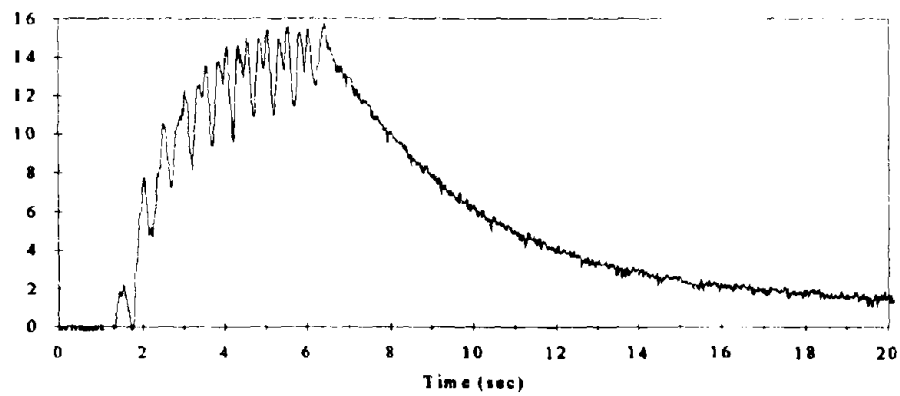
(b)   P3
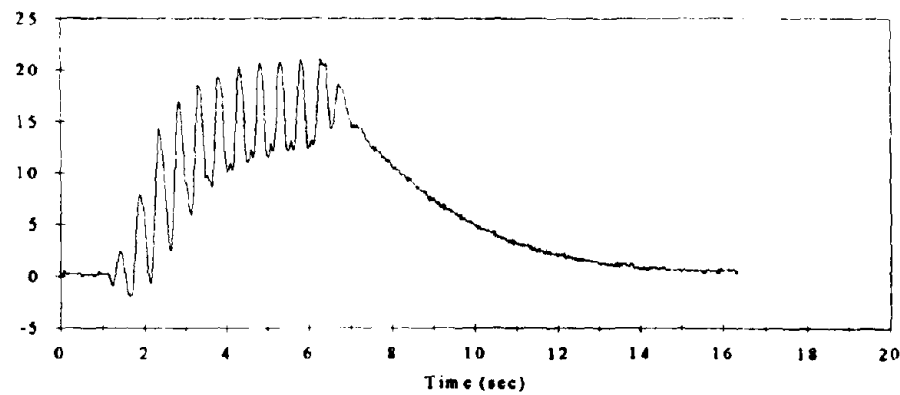
(c)   P4

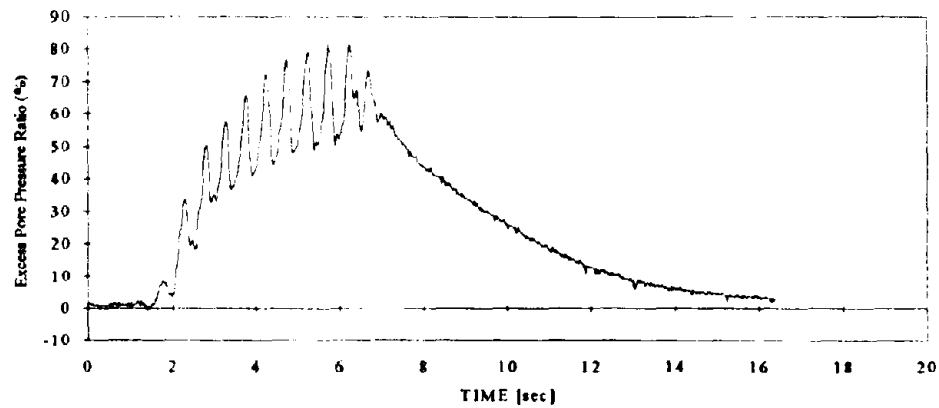Figure B.71: Excess pore pressure data in Test 6b

384
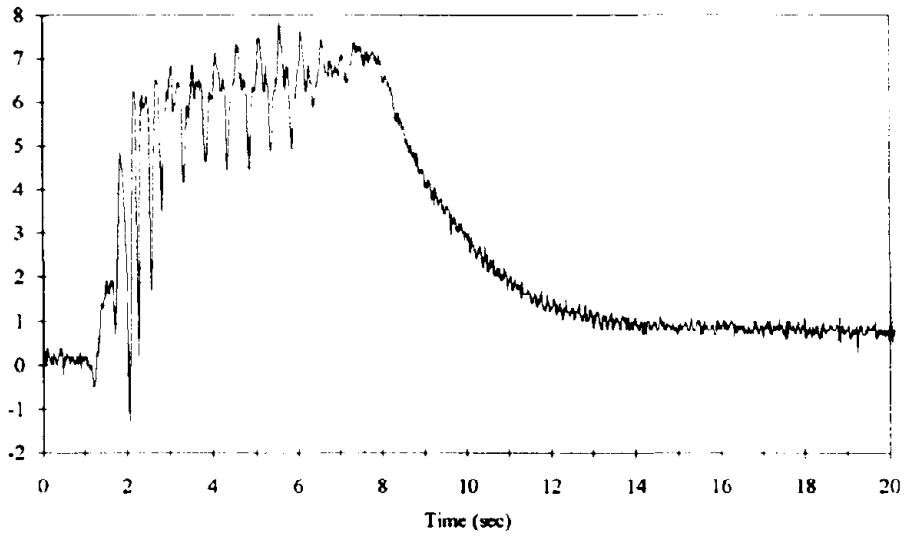
(d)   P5
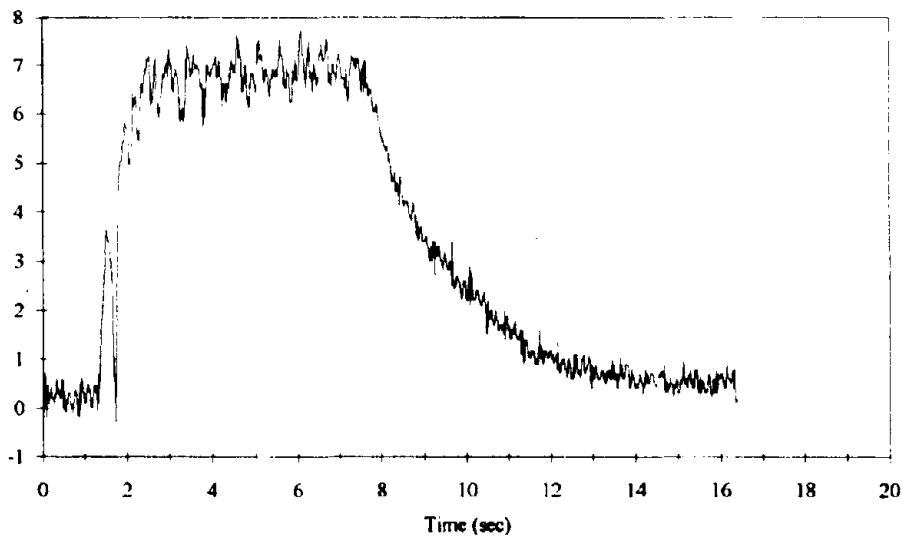
(e)   P6

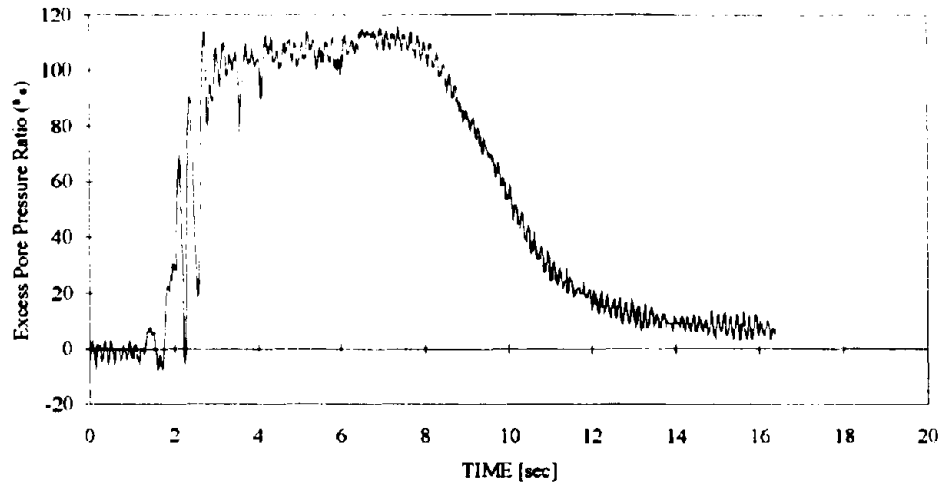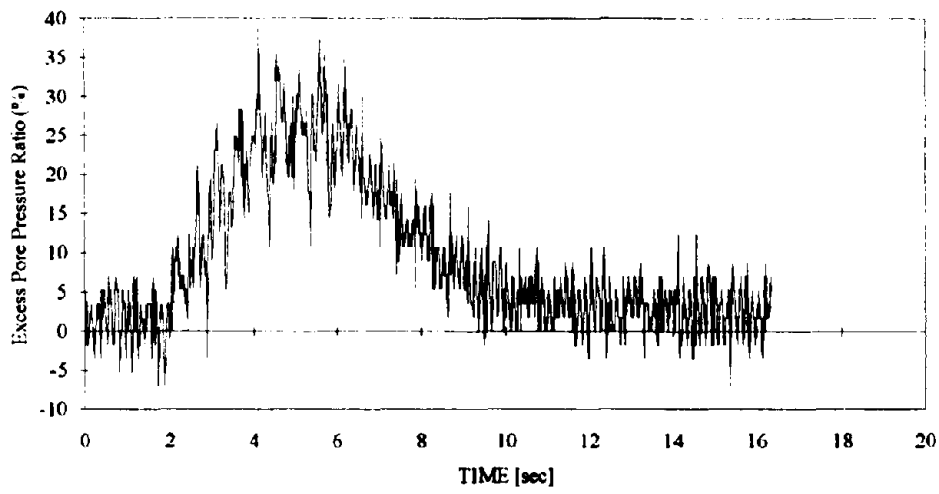Figure B.71: Excess pore pressure data in Test 6b

385
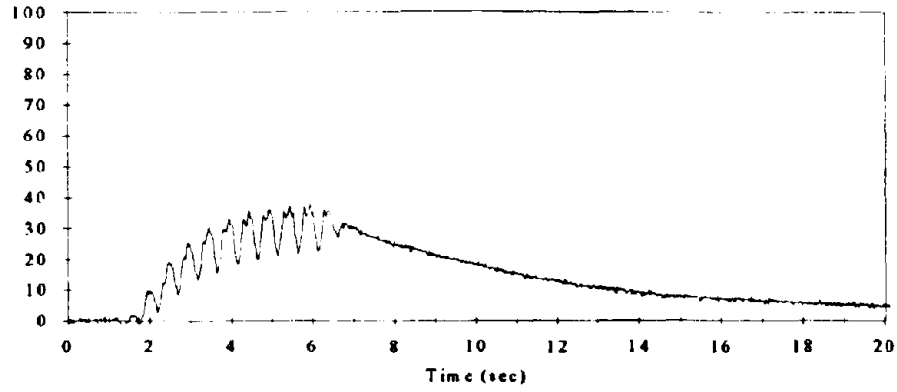
(a)   P2
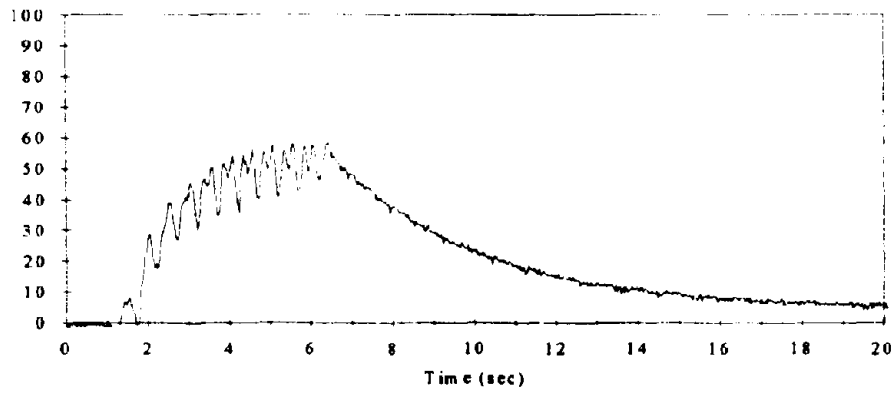
(b)   P3
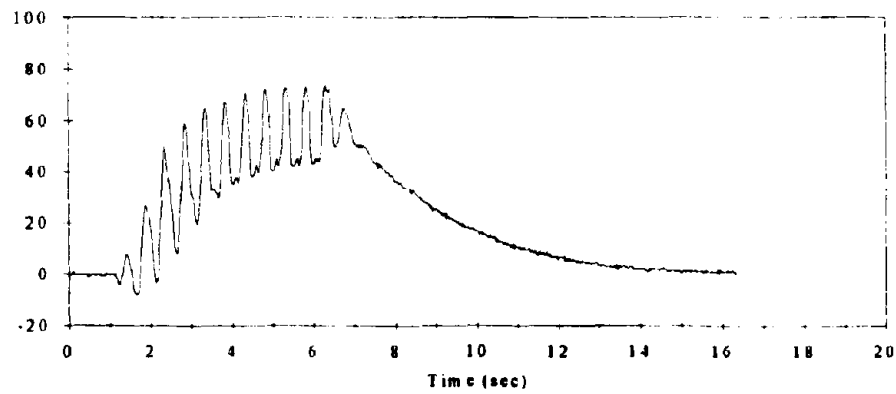
(c)   P4

Figure B.72 Excess pore pressure ratios in Test 6b

386
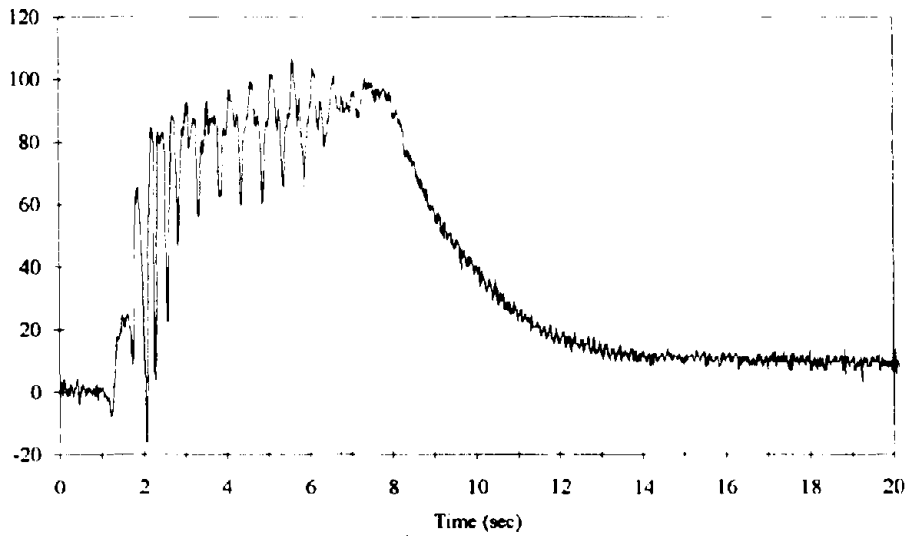
(d) P5
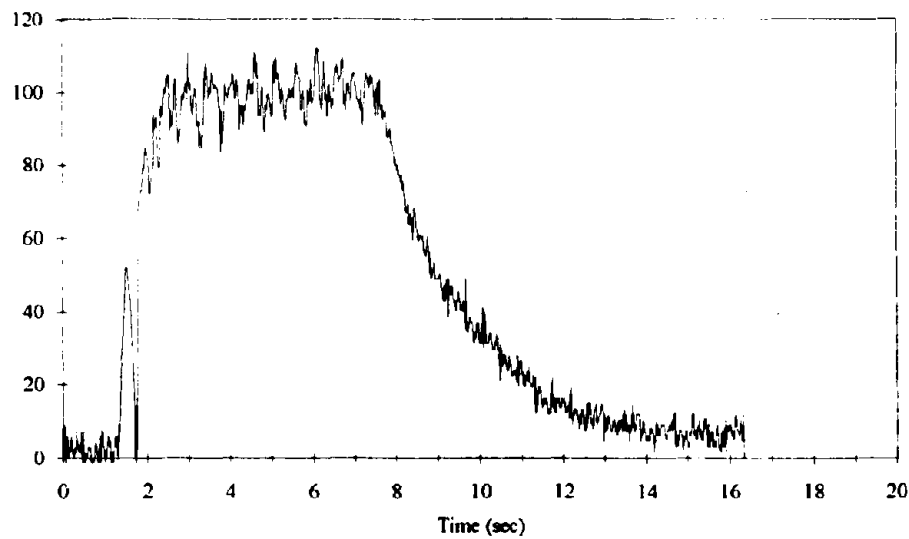
(e) P6

Figure B.72: Excess pore pressure ratios in Test 6b

387

Page Intentionally Left Blank

APPENDIX C

DETERMINATION OF MODEL PARAMETERS

The Earth Technology Corporation (1992) performed extensive series of laboratory tests on Nevada sands with two relative densities: 40% and 60%. The types of the laboratories tests include:

1. General index tests
   - specific gravity
   - maximum and minimum dry densities (minimum and maximum void ratios)
   - grain size distribution
   - permeability test
2. Resonant column test
3. Monotonic triaxial and DSS tests
4. Stress-controlled cyclic triaxial and DSS tests

Information from the first three types of laboratory tests were applied to determine some parameters of the Residual Strain Method. The cyclic test data failed to provide adequate information regarding the cyclic behavior of the Nevada sand since the cyclic tests were stress-controlled[1]. The task here is to choose best possible values for the model parameters based upon the really inadequate data.

---

[1] We really need strain-controlled cyclic test data to know the cyclic behavior of soils.

C.1 DETERMINATION OF PARAMETERS FROM OTHER SANDS

Because of the inadequate data of the Nevada sand, procedures were taken to evaluate the model parameters. One way to determine the parameters is to use typical values for other sands which are similar to the Nevada sand. Comprehensive tests had been carried out on Oosterschelde and Leighton-Buzzard Sands for determination of RSM model parameters (Bouckovalas, 1982; Pahwa et al., 1986). Nevada sand is similar to the above sands in some basic characteristics (see Section 5.2.1). The determination of some model parameters associated with Nevada sand are based upon information obtained from Oosterschelde and Leighton-Buzzard Sands.

Parameters C_2, c_5

The determination of these parameters requires the information of the shear strains (e_{v1}) at various shear stress ratios (Q) in cyclic triaxial tests. Available laboratory test data were not appropriate to determine the effect of Q on e_{v1}. The parameters from Oosterschelde and Leighton-Buzzard Sands are adopted here.

$$C_2 = 12$$
$$c_5 = 3.0$$

Parameters C_1 ($D_r = 40\%$) and α

C_1 equals 0.00685 at void ratio e being 0.74 and 0.75 for Oosterschelde and Leighton-Buzzard Sands respectively. For Nevada sand with 40% relative density ($e = 0.73$), it is reasonable to assume $C_1 = 0.00685$ (Dr = 40%). The parameter for denser sands (Dr = 60% and 75%) is to be determined based upon additional information. Details will be presented later.

390

Parameter α is equal to 0.5 for many sands. It is assumed to be 0.5 for Nevada sand at this time. Further confirmation will be presented shortly.

C.2   DETERMINATION OF PARAMETERS FROM LABORATORY TESTS

Parameters may be obtained from various laboratory test data from the Earth Technology Report. The data involve results from sieve testing, monotonic drained/undrained triaxial tests, cyclic triaxial and DSS tests and resonant column tests.

C.2.1   MAXIMUM FRICTION ANGLE (ϕ_{max}) AND FRICTION ANGLE AT THE PHASE TRANSFORMATION LINE (ϕ_{CT})

The friction angles ϕ_{max} and ϕ_{CT} can be obtained from static triaxial tests (Bouckovalas, 1982). The friction angles of Nevada sand obtained from both drained and undrained monotonic triaxial tests are plotted against porosity in Figure C.1. The results are presented with the average and the range of one standard deviation of the angles. Due to limited test data, the friction angles of Oosterschelde sand are used to help drawing the shape of the curves through the data of Nevada sand. The dashed lines, representing the friction angles of Nevada sand, are established based on the test data, and the solid lines of Oosterschelde sand as reference.

C.2.2 COMPUTATION OF G_0 FROM RESONANT COLUMN TESTS
-- Parameter B_c

The cyclic shear modulus at very small strain is expressed by Eq (5.11) as

$$G_0 = B_c P_a \frac{(2.973-e)^2}{1+e} \sqrt{\frac{\sigma'_{oct}}{P_a}} \qquad (5.11)$$

The Earth Technology Corporation (1992) performed a series of resonant column tests on Nevada sand (with Dr = 40% and 60%) to obtain the shear modulus at various confining pressures. The parameter B_c is calculated from the data of these tests. Table C.1 summarizes the test data. B_c = 265, averaged from the data, will be used as the input model parameter for CYCON.

C.2.3 DETERMINATION OF PARAMETERS FROM CYCLIC TRIAXIAL TESTS

C.2.3.1 Parameters From Cyclic Drained Triaxial Tests - (C_1, c_1, c_2 AND c_3)

Limited drained cyclic triaxial data are available from the laboratory test report by the Earth Technology Corporation. Excess pore pressure data from undrained tests are adopted to be an alternative of the volumetric strain in determining model parameters. Theoretical basis for this substitution is presented as follows.

From Eq.(5.1), the volumetric strain in undrained tests is equal to zero, thus

$$d\varepsilon_{vol} = d\sigma'_{oct}/K^t + d\varepsilon_{vol}^o = 0 \qquad (C.1)$$

For cyclic tests, the total stress does not change at the end of each cycle, i.e., $d\sigma_{oct} = 0$. Therefore,

$$d\sigma_{oct}' = d\sigma_{oct} - du = -du \qquad (C.2)$$

Substitute (C.2) into (C.1), then

$$du = K^t \, d\varepsilon_{vol}^o \qquad (C.3)$$

For the first cycle,

$$\Delta u^1 = K^t \, (\Delta\varepsilon_{vol}^o)^1 \qquad (C.4)$$

As c_1 is large and Q less than 1, Eq.(5.6) is reduced, at the end of the first cycle, into

$$(\Delta\varepsilon_{vol}^o)^1 = C_1 \, \gamma_{cyc}^{C_2} \qquad (C.5)$$

Substitute (C.4) and (C.5) into (5.3),

$$\Delta u^1 = (A \, C_1) \, P_a \, (\sigma_{oct}'/P_a)^\alpha \, \gamma_{cyc}^{C_2} \qquad (C.6)$$

Since A, C_1 and α are constant parameters, C_2 can be obtained from the cyclic triaxial test data plot of $\Delta u^1/(AC_1)P_a(\sigma_{oct}'/P_a)^\alpha$ against γ_{cyc} in logarithm scales. Figure C.2 presents the determination of C_2 for Nevada sand with 40% and 60% relative densities. The parameter C_2 is found to be 1.26 for Nevada sand. This is consistent with that of the Oosterschelde and Leighton-Buzzard sands.

Confirmation of the assumption of α being 0.5 follows the determination of C_2. Figure C.3 shows the confirmation.

With the excess pore pressure at the end of each cycle representing the volumetric strain, by substituting (C.3) into (5.6), the effect of number of cycles N can be obtained. Figure C.4 shows the results of undrained cyclic triaxial tests performed on isotropically-consoildated ($\sigma_{vo}'=\sigma_{ho}'$) samples (The Earth Tech. Corp. Report, 1992). The data lables denote the test No. of various triaxial tests. In this figure, the data curves concave upward

393

with an initial slope (c_3). This feature is similar to what had been observed in the data of triaxial tests on Oosterschelde sand by Lambe and Associates (1977). Lambe and Associates (1977) also showed that the $\log \dfrac{\Delta u}{\Delta u^I}$ (or $\log \dfrac{\Delta \varepsilon_v}{\Delta \varepsilon_v^I}$) versus $\log N$ curves, based on results of undrained cyclic triaxial tests on anisotropically-consolidated Oosterschelde sand samples $(\sigma'_{vo} > \sigma'_{ho})$, concave downward with a same initial slope as in the cases of isotropically-consolidated Oosterschelde sands. The $\log \dfrac{\Delta u}{\Delta u^I}$ versus $\log N$ curve of drained cyclic triaxial tests on Oosterschelde sands is straight with a slope equal to the initial slope in the above two types of undrained cyclic triaxial tests. This slope is the parameter c_3 of Oosterschelde sand. Therefore, based on the available cyclic triaxial test data of Nevada sand (undrained cyclic triaxial test on isotropically-consolidated samples), the parameter c_3 is found to be 0.40 (by drawing the initial slope of these data curves).

Tables C.2 and C.3 summarize the cyclic triaxial tests and the calculations involved in the above figures for Nevada sand with 40% and 60% relative densities. Some tests other than listed in the tables were not applicable for describing the cyclic behaviors -- owing to the poor cyclic pore pressure data.

C.2.3.2   Effect of Cyclic Strain -- Parameter β_c

The effect of cyclic strain γ_{cyc} is expressed in Eq.(5.10). Define the yield factor $R = 2^{\tau_{cyc}} \Big/ q_f$ and elastic strain as $\gamma_{el} = {\tau_{cyc}} \Big/ G_o$. Then,

$$\frac{\gamma_{el}}{\gamma_{cyc}} = 1 - R^{\beta_c} \qquad\qquad (C.7)$$

Thus, $R^{\beta_c} = 1 - \dfrac{\gamma_{el}}{\gamma_{cyc}}$ (C.8)

and $\beta_c = \dfrac{\log\left(1 - \gamma_{el}/\gamma_{cyc}\right)}{\log R}$ (C.9)

Tables C.4 and C.5 summarize the calculations for the parameter β_c from the data of cyclic triaxial tests on Nevada sand with relative densities 40% and 60%, respectively. Since these tests were stress-controlled, it was difficult to quantify the cyclic stress-strain relationship effectively from these data, especially when strain is small. In addition, the strain data was not precise enough - only to 0.015% (one-third of the strain in test No. 40-114). By omitting the outliers, the values of β_c are 0.69 ± 0.16 and 0.93 ± 0.11 in Tables C.4 and C.5. It was determined to use 0.70 and 0.90 as the values of β_c for Nevada sand with Dr of 40% and 60% respectively.

C.2.3.3 Tangent Bulk Modulus — Parameters A

The coupled effect of parameters A and C_1 is included in Eq.(C.6). After rearranging, (C.6) becomes

$$A\,C_1 = \Delta u^1 / P_a(\sigma_{oct}'/P_a)^{\alpha}\gamma_{cyc}{}^{C_2}$$ (C.10)

This coupled effect (AC_1) is 1.61 and 1.70 (averaged from several tests) for Nevada sand with Dr of 40% and 60% respectively. The calculations from each test are listed in Tables C.2 and C.3.

The parameter C_1 had been assumed to be 0.00685 for Nevada sand with Dr = 40%. The parameter A for this sand is determined to be 235, i.e., $A_{40\%}$ = 1.61/0.00685 = 235.

As A is proportional to $(2.97-e)^2/(1+e)$,

$$A_{60\%} = A_{40\%} \times 1.12 = 263,$$

and $C_1 = (AC_1)_{60\%} / A = 1.70 / 263 = 0.00646.$

C.2.3.4   Tangent Shear Modulus -- Parameter B_s

The relationship between the coefficient of earth pressure at rest (K_0) and overconsolidation ratio is expressed by Mayne and Kulhawy (1982) as

$$K_o^{OC} = K_o^{NC} OCR^{\sin\phi} \qquad (C.11)$$

where OCR is the ratio of preconsolidation pressure (σ'_{pc}) and present vertical effective stress (σ'_v). Substitute the stresses into the above relationship, it becomes

$$\frac{\sigma'_h}{\sigma'_v} = K_o^{OC} \left(\frac{\sigma'_{pc}}{\sigma'_v} \right)^{\sin\phi} \qquad (C.12)$$

and, $\sigma'_h = K_o^{NC} \left(\sigma'_{pc}\right)^{\sin\phi} (\sigma'_v)^{1-\sin\phi}$ \qquad (C.13)

$$d\sigma'_h = K_o^{NC} \left(\sigma'_{pc}\right)^{\sin\phi} \left[(1-\sin\phi)(\sigma'_v)^{-\sin\phi}\right] d\sigma'_v \qquad (C.14)$$

$$= (1-\sin\phi)K_o^{NC} OCR^{\sin\phi} d\sigma'_v$$

$$= \left(K_o^{NC}\right)^2 OCR^{\sin\phi} d\sigma'_v$$

Then the relationship between shear stress, $dq = d\sigma_v - d\sigma_h$, and the coefficient of earth pressure at rest can be expressed as

$$\frac{dq}{d\sigma_{oct}} = \frac{3}{2}\frac{d\sigma_v - d\sigma_h}{d\sigma_v + 2d\sigma_h} = \frac{3}{2}\frac{1 - \dfrac{d\sigma_h}{d\sigma_v}}{1 + 2\dfrac{d\sigma_h}{d\sigma_v}} = \frac{2}{3}\frac{1 - K_o^2}{1 + K_o^2} \qquad (C.15)$$

Cyclic simple shear tests involves an increase in pore pressure, and therefore an decrease of σ'_v. The stress path of this process in cyclic DSS tests is similar to that for one dimensional unloading. Therefore,

$$\left(\frac{dq}{d\sigma_{oct}}\right)_{cyclic} = \left(\frac{dq}{d\sigma_{oct}}\right)_{1-D} \qquad (C.16)$$

and, $\qquad \dfrac{1}{2}\dfrac{G^t}{K^t}\dfrac{d\varepsilon_v^o}{d\varepsilon_{vol}^o} = \dfrac{3}{2}\dfrac{1 - K_o^2}{1 + 2K_o^2} \qquad (C.17)$

Substitute the parameters obtained previously ($C_2 = 12$ and $c_5 = 3$) into Eq.(5.7) and (C.17), the ratio of tangent shear to bulk moduli is obtained as

$$\frac{G^t}{K^t} = 3\frac{1 - K_o^2}{1 + 2K_o^2}\frac{d\varepsilon_v^o}{d\varepsilon_{vol}^o} = 3\frac{1 - K_o^2}{1 + 2K_o^2}\frac{1}{12Q^3} = \frac{1}{4}\frac{1 - K_o^2}{1 + 2K_o^2}\frac{1}{Q^3} \qquad (C.18)$$

For Nevada sand with 40% relative density ($e = 0.73$, $\phi_{max} = 33^o$ and $\phi_{CT} = 28^o$), the earth pressure coefficient K_o is 0.455, the slope of the characteristic threshold line M is 0.557. Then the shear stress ratio is obtained as

$$Q = \frac{q}{\sigma_{oct}} = \frac{3}{2}\frac{1 - K_o^2}{1 + 2K_o^2}\frac{1}{M} = \frac{0.43}{0.557} = 0.77$$

Substitute Q into Eq.(C.18), the shear to bulk moduli ratio is calculated as

$$\left(\frac{G^t}{K^t}\right)_{Dr=40\%} = 0.25 \times 0.56 \times 0.77^{-3} = 0.307$$

Let $\qquad \mu = P_a\left(\dfrac{\sigma_{oct}}{P_a}\right)^\alpha$,

then $\quad K^1_{Dr=40\%} = \dfrac{G^1}{0.307}$,

and $\quad A_{Dr=40\%} = 265\mu \dfrac{(2.973-0.73)^2}{1+0.73} / 0.307 = 2550\mu$.

Follow the same procedures,

$$\left(\dfrac{G^1}{K^1}\right)_{Dr=60\%} = 0.25 \times 0.62 \times 0.87^{-3} = 0.235 \text{ , and } A_{Dr=40\%} = 3328\mu.$$

It is concluded to use $B_S = 265\mu$ and $A = 3000\mu$ for all densities. Therefore,

$B_S = 265/3000 \times A = 0.08833A = 22$ (Dr = 40%) or 23 (Dr = 60%).

C.2.3.5   Verification of Parameters Obtained From Cyclic Triaxial Tests

An independent program SANDMOD was written to predict the characteristics of cyclic triaxial (or DSS) tests with residual strain method. This program requires same input model parameters as for CYCON. The parameters obtained from cyclic triaxial tests were verified with SANDMOD. Predicted results are compared to the laboratory test results.

The comparisons are summarized in Figures C.8 through C.10. Comparisons are generally reasonable, although some comparisons look somewhat scattered. The scattered comparisons results from the scattered laboratory test results The parameters obtained from the available cyclic triaxial test results are claimed reasonable. Further adjustment for these parameters for better predictions would require a more comprehensive series of laboratory tests.

398

C.2.4 DETERMINATION AND VERIFICATION OF PARAMETERS FROM CYCLIC DIRECT SIMPLE SHEAR (DSS) TESTS

The behavior of soil may vary with the mode of shearing. Section 5.3.1 discusses the shearing mode (triaxial or DSS) and the location of the soil element within the backfill.

Most of the parameters obtained previously are associated with the properties of the soil. Only few parameters dependents on the modes of shearing associated with the type of laboratory testing. These shearing mode dependent parameters are related to the tangent bulk and shear moduli (K^t and G^t). That is, the previously obtained parameters B_s and A from cyclic triaxial test data need to be adjusted for the cyclic DSS tests.

Since the cyclic DSS tests were stress-controlled, the best information from the test data is the relationship between the cyclic shear stress and N_f (the number of shearing cycles to failure). This information was used to evaluate the model parameters B_s and A associated with the DSS mode of shearing. Table C.6 summarizes the information of the cyclic shear stress level ($\frac{q}{\sigma'_{vc}}$) and N_f from the cyclic DSS test data. These data are summarized in Figure C.8. The prediction for DSS tests with SANDMOD using the parameters obtained from triaxial test results is superimposed in Figure C.8, with a dashed line, as a comparison (Dr = 60%). After adjustment, the tangent moduli for DSS mode of shearing are concluded to be twice as large as for triaxial mode of shearing. The predicted results are presented in Figure C.8 by the solid line and the dotted line for Nevada sand with relative densities of 60% and 40%, respectively.

399

C.3 EVALUATION OF MODEL PARAMETERS OF DENSE NEVADA SAND (D_r = 75%) FOR PROGRAM CYCON

The model parameters of mid-dense Nevada sands (Dr = 40% and 60%) for using the program CYCON were obtained from both Triaxial and DSS tests performed by The Earth Technology Corporation. These parameters are listed in Table C.7. Since there are no lab test data of dense Nevada sand with 75% relative density, the model parameters are evaluated from those of the sands with 40% and 60% relative densities. However, most of these parameters remain same as those for the looser sands, only seven parameters need to evaluated. These parameters are highlighted by bold font and underlining in Table C.7. The key parameter is the void ratio e. All the other parameters are evaluated from the parameters of the looser sands based the void ratio. The procedures of evaluating these parameters are described as follows.

1. Void Ratio (e)

The void ratio of the 75% r.d. sand (= 0.595) is calculated from the maximum and minimum void ratios of Nevada sand, 0.833 and 0.50 respectively.

2. ϕ_{max} and ϕ_{CT}

The friction angles are obtained from Figure C.1. Note that the angles are presented by radians in Table C.7 and in degrees in Figure C.1.

3. C_1

This parameter is related to the volumetric strain by Eq. (5.6).:

400

$$\Delta\varepsilon_{vol}^{o} = C_1 (1 - Q^{c1}) \gamma_{cyc}^{c2} N^{c3} \tag{5.6}$$

Therefore, C_1 is proportional to the compressibility of the sand. Thus, $\frac{1}{C_1} \propto \frac{\Delta p}{\Delta e}$, where p

is the octahedral effective stress. Assume the void ratio is linearly related to **log** p. The relation is expressed by Eq. (C.19):

$$\frac{\Delta e}{\Delta \log p} = -C_c \tag{C.19}$$

where C_c is the coefficient of compression

The parameter C_1 for the sand with 75% relative density is obtained to be 0.00616 by extrapolating the C_1's for sands with 40% and 60% relative densities. The procedures are presented in Table C.8.

4. A

This parameter is the magnitude constant for the tangent bulk modulus as a function of octahedral effective stress(σ_{oct}'). This function is expressed in Eq. (5.3).

$$K^t = A P_a \left(\frac{\sigma_{oct}'}{P_a} \right)^{\alpha} \tag{5.3}$$

where the superscript t indicates that the L.H.S. of the above equation is the tangent bulk modulus. Under a certain octahedral stress, the modulus is function of void ratio. It was decided to link the modulus and void ratio by the strength (q_f) at a certain octahedral stress. The relation is expressed by Eq. (C.20).

$$\frac{K_1^t}{K_2^t} \left(= \frac{A_1}{A_2} \right) = \left(\frac{M_1}{M_2} \right)^{\eta} \tag{C.20}$$

401

The parameter M^2 is the slope of strength envelop on a *q-p* plot. Based on the friction angles of Nevada sand at three relative densities ($\phi_{40\%}$ = 0.576, $\phi_{60\%}$ = 0.628, $\phi_{75\%}$ = 0.689), the values of parameter M are: $M_{40\%}$= 1.331; $M_{60\%}$= 1.461; and $M_{75\%}$= 1.614. The index η in Eq. (C.20) is found to be 0.8 based on the values of A and M of the sand with relative densities of 40% and 60%. The parameter A is found to be 572 from the above information for the sand with 75% relative density.

5. B_s

This parameter is the magnitude constant for the shear modulus at small strain (G_0) as a function of void ratio and stress level. Eq. (5.5) expresses this function.

$$G_0 = B_s P_a \frac{(2.973-e)^2}{1+e} \sqrt{\frac{\sigma_{oct}}{P_a}} \qquad (5.5)$$

Using a similar procedure as obtaining the parameter A for the dense sand, the parameter B_s is found to be 46 for the sand with 75% relative density. It is similar to that of the sand with 60% relative density. This is due to the effect of void ratio in Eq. (5.5) more or less counterbalances the effect of M. Therefore, B_s is generally invariant with relative density.

6. β_c

This parameter adjusts the curvature of hyperbolic relationship between cyclic shear stresses(τ_{cyc}) and cyclic strains(γ_{cyc}). We expect smaller cyclic strain in denser sand under a certain cyclic stress. The cyclic stress-strain relation is described in Eq. (C.21).

---

[2] $M=6\sin\phi/(3-\sin\phi)$

$$\gamma_{cyc} = \frac{\tau_{cyc}}{G_o} \frac{1}{1 - \left(\frac{\tau_{cyc}}{q_f}\right)^{\beta_c}} \qquad (C.21)$$

where q_f is the shear strength.

The extrapolating the parameter β_c are based on the cyclic strain ratios for sands with different relative densities at same stress conditions. The procedures are described as follows:

1. Calculate the values of M for the three relative densities.

2. Calculate the ratio R ($= \tau_{cyc}/q_f$) based on the values of M, assuming that q_f is proportional to M.

3. Calculate the ratio of $\gamma_{cyc}/\gamma_{cyc,40\%}$ based on different values of β_c.

4. Estimate $\gamma_{cyc,75\%}/\gamma_{cyc,40\%}$ based on the ratio of shear modulus G_o.

Table C.9 presents the results of the above calculations. It is found that

$\left(\dfrac{\gamma_{cyc,60\%}}{\gamma_{cyc,40\%}}\right) \propto \left(\dfrac{G_{o,60\%}}{G_{o,40\%}}\right)^{-3.5}$; therefore, $\left(\dfrac{\gamma_{cyc,75\%}}{\gamma_{cyc,40\%}}\right)$ is assumed to be proportional to

$\left(\dfrac{G_{o,75\%}}{G_{o,40\%}}\right)^{-3.5}$ and is estimated to be 0.5. The value of β_c corresponding to it will be about

1.13. However, any value of β_c larger than 1.0 is unusual. Hence, the value of β_c for the 75% r.d. sand is judged to be 1.0.

Table C.1: Determination of B_c from resonant column tests

(from The Earth Technology Corp. Report, 1992)

Test No. 40-76
Dr = 40%
e = 0.732

σ'_{oct} (kPa)	G_0 (MPa)	B_c
40	44.64	243
80	63.35	244
160	91.98	251
320	128.51	248

Average = 247

Test No. 40-77
Dr = 40%
e = 0.738

σ'_{oct} (kPa)	G_0 (MPa)	B_c
40	48.69	268
80	70.48	274
160	97.29	268
320	137.7	268

Average = 269

Test No. 60-41
Dr = 60%
e = 0.659

σ'_{oct} (kPa)	G_0 (MPa)	B_c
40	53.72	263
80	85.71	297
160	119.03	292
320	161.21	279

Average = 283

Test No. 60-43
Dr = 60%
e = 0.659

σ'_{oct} (kPa)	G_0 (MPa)	B_c
40	-	-
80	73.45	254
160	106.2	260
320	149.29	259

Average = 258

Average of the average: $B_c = 265$

404

Table C.2: Computation of vertical strain in undrained cyclic triaxial tests -- Dr = 40%

(from The Earth Tech. Corp., 1992)

Test No.	Dr (%)	e	q_0 (kPa)	σ'_{oct} (kPa)	q_0/σ'_{oct}	Q	γ_{cyc}	Δu^1 (kPa)	$\Delta u^1/\sigma'_{oct}$	$\frac{\Delta u}{P_v,\sigma',\bar{P}}$	v (%)	$\frac{\Delta u^1}{P_a \gamma_{cyc}^{126}}$	$\frac{\varepsilon_v^1}{P_a \gamma_{cyc}^{126}}$	$\frac{I_{ver}}{I_{vol}}$	AC_1
40-115	41.6	0.731	0	40	0	0	0.135	8.95	0.2237	0.1415	0.0385	1.1158	0.4800	0.7007	1.7642
40-69	40.3	0.736	3.9	40	0.0975	0.08784	0.12	11.27	0.2818	0.1782	-0.0149	1.6299	-0.2159	-0.3152	2.5771
40-68	41	0.733	6.3	40	0.1575	0.14189	0.165	8.413	0.2103	0.1330	-0.0073	0.8146	-0.0706	-0.1030	1.2879
40-114	42.4	0.728	0	80	0	0	0.195	20.34	0.2543	0.2274	0.0574	1.5955	0.4504	0.6576	1.7839
40-71	42	0.729	17	80	0.2125	0.19144	0.075	4.425	0.0553	0.0495	0.0100	1.1570	0.2615	0.3817	1.2936
40-73	43.1	0.725	25.3	80	0.3163	0.28491	0.15	13.79	0.1724	0.1542	0.0683	1.5055	0.7459	1.0889	1.6832
40-50	42.8	0.727	20.7	160	0.1294	0.11655	0.105	12.74	0.0796	0.1007	0.0260	2.1801	0.4449	0.6495	1.7235

Table C.3: Computation of vertical strain in undrained cyclic triaxial tests -- Dr = 60%
(from The Earth Tech. Corp., 1992)

Test No.	Dr (%)	e	q_o (kPa)	σ'_{oct} (kPa)	q_o/σ'_{oct}	Q	γ_{cyc}	Δu^1 (kPa)	$\Delta u^1/\sigma'_{oct}$	$\frac{\Delta u^1}{P_a \sigma'_{oct} P_a}$	ε_v (%)	$\frac{\Delta u^1}{P_a \gamma_{cyc}^{126}}$	$\frac{\varepsilon_v^1}{P_a \gamma_{cyc}^{126}}$	$\frac{\varepsilon_{ver}^1}{\varepsilon_{vol}^1}$	AC_1
60-25	61.5	0.656	5.5	40	0.1375	0.1238	0.06	3.689	0.0922	0.0583	-0.0229	1.2777	-0.7928	-1.2086	2.0203
60-32	62	0.654	5.8	40	0.145	0.1306	0.06	4.94	0.1235	0.0781	-0.0200	1.7110	-0.6927	-1.0560	2.7054
60-34	62.2	0.653	8.6	40	0.215	0.1937	0.12	5.38	0.1345	0.0851	-0.0200	0.7781	-0.2892	-0.4409	1.2302
60-35	61.2	0.657	8.3	40	0.2075	0.1869	0.12	2.96	0.0740	0.0468	-0.0180	0.4281	-0.2603	-0.3968	0.6769
60-36	61.6	0.656	7.5	80	0.0938	0.0845	0.075	8.6	0.1075	0.0962	0.0038	2.2486	0.0994	0.1515	2.5141
60-24	60.5	0.66	7.8	80	0.0975	0.0878	0.045	2.15	0.0269	0.0240	0.0100	1.0700	0.4977	0.7587	1.1963
60-38	61.5	0.656	11.2	80	0.14	0.1261	0.285	29.3	0.3663	0.3270	-0.0495	1.4248	0.2408	0.3671	1.5930
60-37	63.1	0.65	11.4	80	0.1425	0.1284	0.105	11.75	0.1469	0.1314	-0.0010	2.0107	-0.0168	-0.0256	2.2480
60-31	62.4	0.653	47.5	160	0.2969	0.2675	0.435	98.95	0.6184	0.7823	0.1912	2.8244	0.5457	0.8319	2.2328

406

Table C.4: Determination of β_c from cyclic strain -- Dr = 40%

(from The Earth Tech. Corp., 1992)

Test No.	q_{cyc} (kPa)	q_o (kPa)	q_{CT} (kPa)	q_f (kPa)	R	G_o (kPa)	γ_{el} (%)	γ_{cyc} (%)	γ_{el}/γ_{cyc}	β_c
40-115	18.6	0	44.4	71.9	0.5174	48610	0.038	0.135	0.281	0.502
40-69	18.4	3.9	44.4	75.6	0.4868	48610	0.038	0.12	0.317	0.529
40-68	26.9	6.3	44.4	86.5	0.622	48610	0.055	0.165	0.333	0.854
40-114	28.8	0	88.8	135.3	0.4257	68745	0.042	0.195	0.215	0.284
40-71	29.4	17	88.8	152.9	0.3846	68745	0.043	0.075	0.573	0.891
40-73	43.1	25.3	88.8	174.9	0.4929	68745	0.063	0.15	0.420	0.770
40-50	48.4	20.7	177.6	282.2	0.343	97220	0.05	0.105	0.476	0.604

$\beta_c = 0.69 \pm 0.16$

Table C.5: Determination of β_c from cyclic strain -- Dr = 60%

(from The Earth Tech. Corp., 1992)

Test No.	q_{cyc} (kPa)	q_o (kPa)	q_{CT} (kPa)	q_f (kPa)	R	G_o (kPa)	γ_{el} (%)	γ_{cyc} (%)	γ_{el}/γ_{cyc}	β_c
60-25	17.9	5.5	44.4	81.8	0.4377	54672	0.033	0.06	0.55	0.97
60-32	18	5.8	44.4	82.2	0.438	54672	0.033	0.06	0.55	0.97
60-34	26	8.6	44.4	93	0.5591	54672	0.048	0.12	0.40	0.88
60-35	26.5	8.3	44.4	93.2	0.5687	54672	0.048	0.12	0.40	0.90
60-36	29.6	7.5	88.8	154.7	0.3827	77318	0.038	0.075	0.51	0.74
60-24	29.6	7.8	88.8	155	0.3819	77318	0.038	0.045	0.84	~~1.03~~
60-38	44.4	11.2	88.8	173.2	0.5127	77318	0.057	0.285	0.20	~~0.33~~
60-37	43	11.4	88.8	172	0.5	77318	0.056	0.105	0.53	1.10

$\beta_c = 0.93 \pm 0.11$

408

Table C.6: Summary of undrained cyclic DSS test data

(from the Earth Tech Report, 1992)

Test	Dr (%)	σ'_{vo} (kPa)	q_o (kPa)	$(u/\tau'_{vo})_{max}$	N_f	τ_{cyc}/σ'_{vc}
4009	40	80	0	1	7.5	0.0925
4008	40	80	0	1.005	3	0.1884
4007	40	160	0	0.9465	7	0.0713
4006	40	160	0	0.9375	4	0.1344
4010	40	156	3.1	0.99	10	0.0737
4011	40	156	3.3	0.976	8	0.0750
6005	60	80	0	1.008	9	0.1500
6004	60	80	0	1.026	2.5	0.2950
6007	60	160	0	0.9	56	0.0838
6006	60	160	0	0.88	5	0.1631
6008	60	160	0	0.98	5	0.1638
6009	60	160	5.9	0.98	18	0.0856

Table C.7: Model Parameters of Nevada Sand for Program CYCON

Dr	40%	60%	75%
ϕmax	0.576	0.628	**0.6894**
c	0.0	0.0	0.0
ϕ_{CT}	0.488	0.488	0.488
Su	10000	10000	10000
e	0.73	0.656	**0.595**
e_{min}	0.50	0.50	0.50
Pa	100	100	100
Bc	265	265	265
βc	0.70	0.90	**1.05**
Bs	---	46	**46**
βs	40	40	40
A	490	526	**572**
α	0.50	0.50	0.50
c_1	11	11	11
C_1	0.00685	0.00646	**0.00616**
c_3	0.40	0.40	0.40
c_2	1.26	1.26	1.26
C_2	12	12	12
c_5	3	3	3

410

Table C.8 Procedures for Evaluation of C_1

Dr	40%	60%	75%
e	0.73	0.656	0.595
C_1	0.00685	0.00646	**0.00616**
	B	**B**	↑
$1/100C_1$	1.46	1.548	1.6232
	B	**B**	↑
$ln(1+1/100C_1)^*$	0.9	0.9353	0.9644**
	→	→	↑

Note
* $\Delta ln(p)=ln(1+1/100C_1)-ln(1)=ln(1+1/100C_1)$
** from $\Delta e/\Delta ln(p)=-(1.548-1.46)/(0.9353-0.9)$

Table C.9 Extrapolation of β_c based on γ_{cyc} ratios

D_r	M	R	$G_{0,40\%}/G_0$	β_c	$\gamma_{cyc}/\gamma_{cyc,40\%}$
40%	1.33	0.5*	1.0	0.7	1.0
60%	1.46	0.4555	0.897	0.9	0.68
75%	1.61	0.413	0.820	0.9	0.575
				1.0	0.537
				1.1	0.507
				1.2	0.482

* An arbitrary ratio set for reference, R ranges between 0.3 and 0.6 in triaxial tests

411
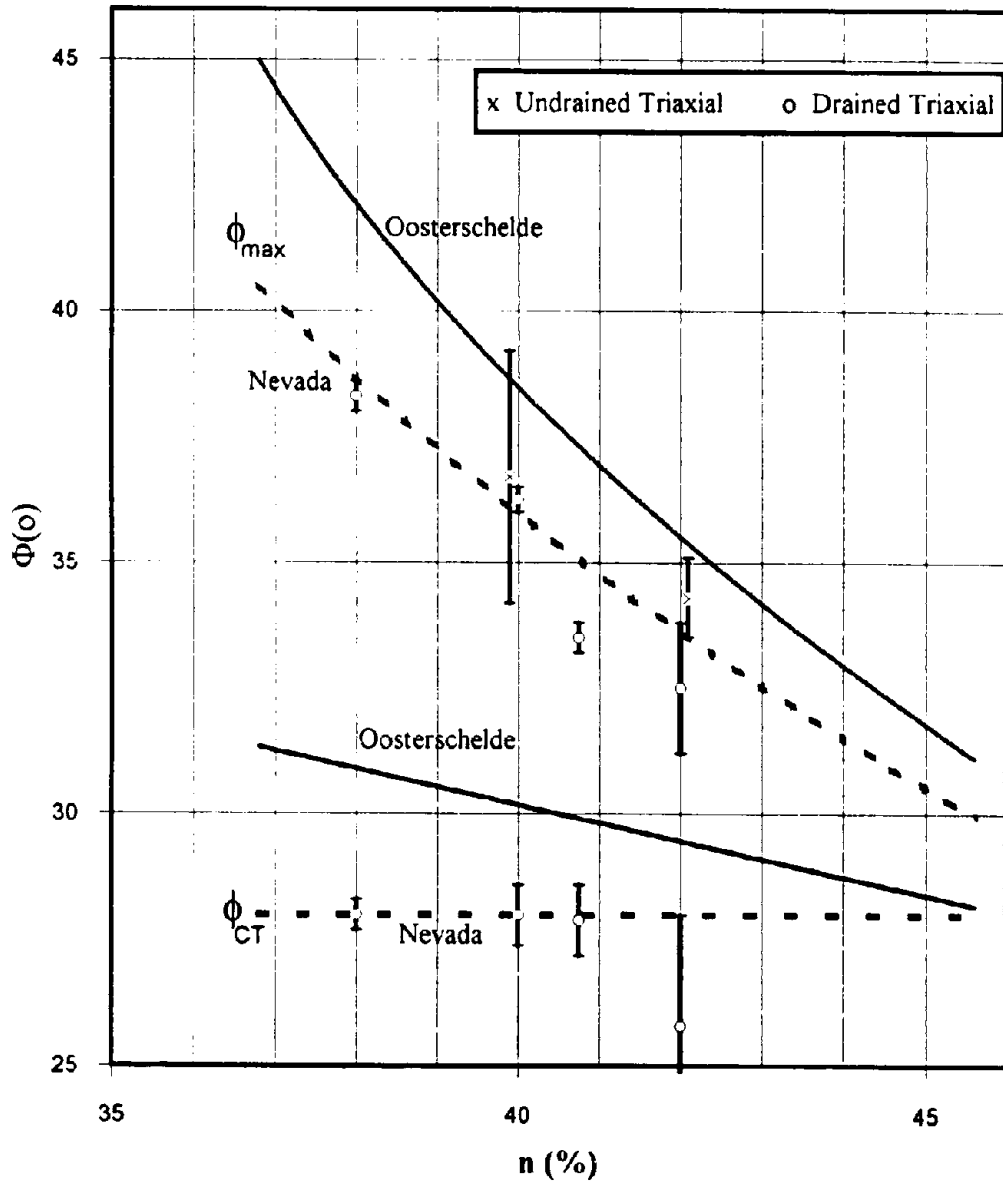
Figure C.1: Frictions Angles of Nevada Sand and Oosterschelde Sand
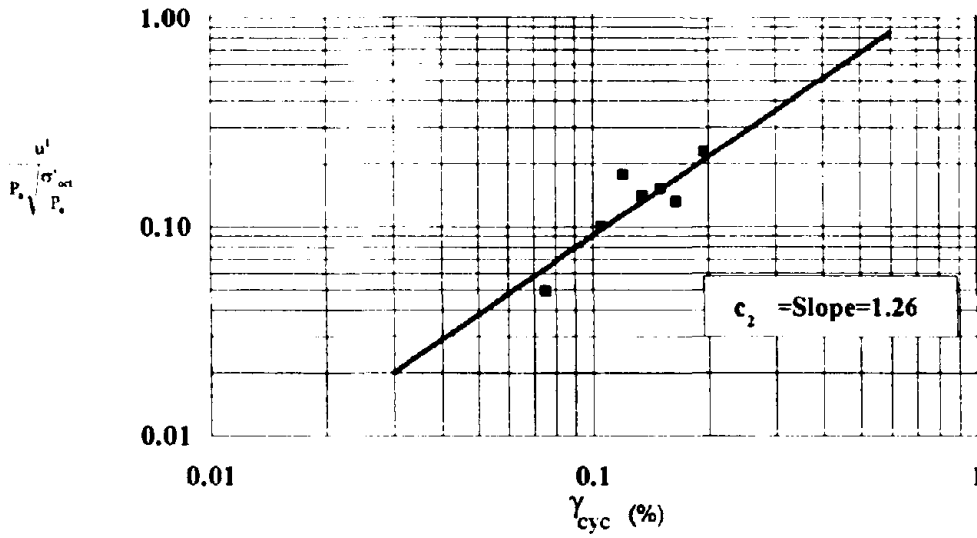
(a) Dr = 40%
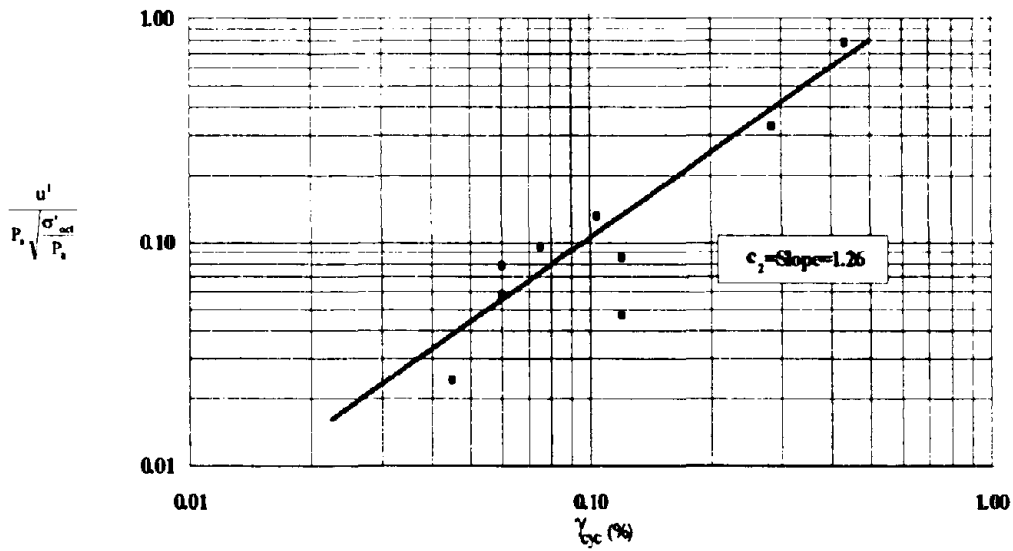
(b) Dr = 60%

Figure C.2: Determination for the parameter c_2
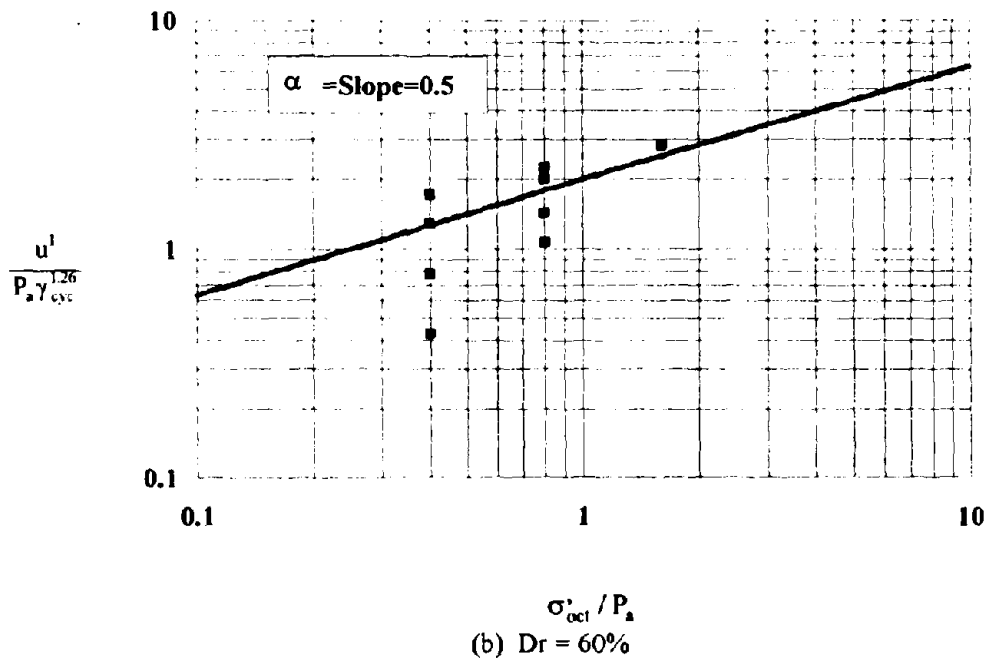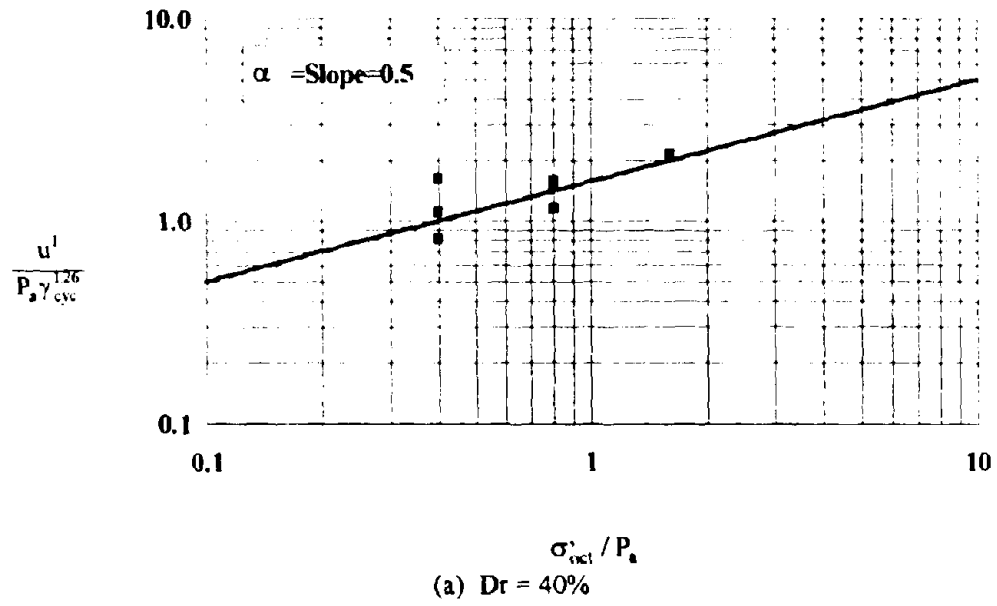
(a) Dr = 40%

(b) Dr = 60%

Figure C.3: Determination of the factor α
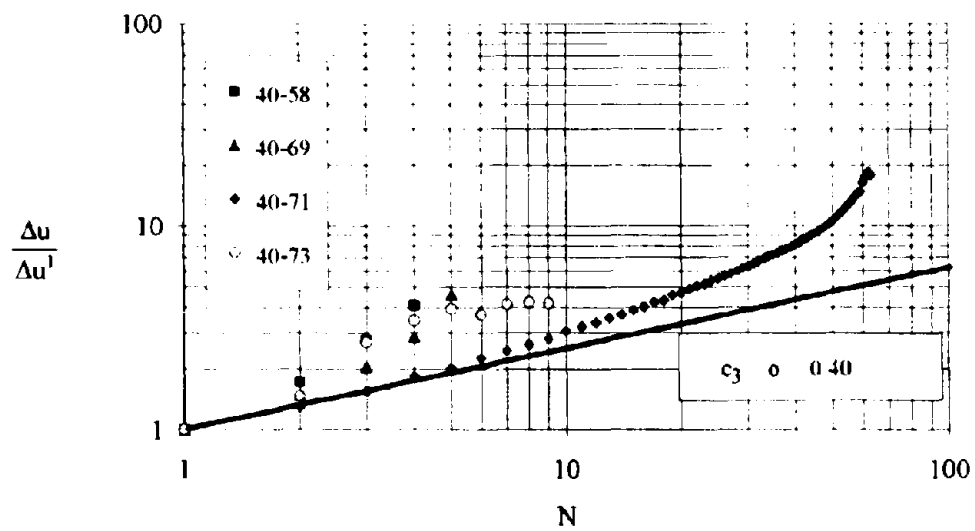
(a) Dr = 40%
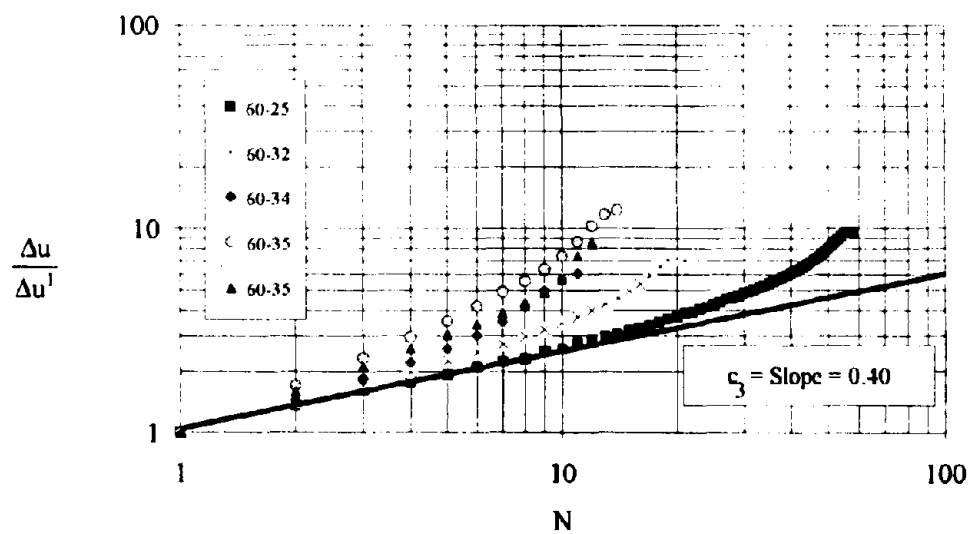
(b) Dr = 60%

Figure C.4: Determination of the parameter c_3

415
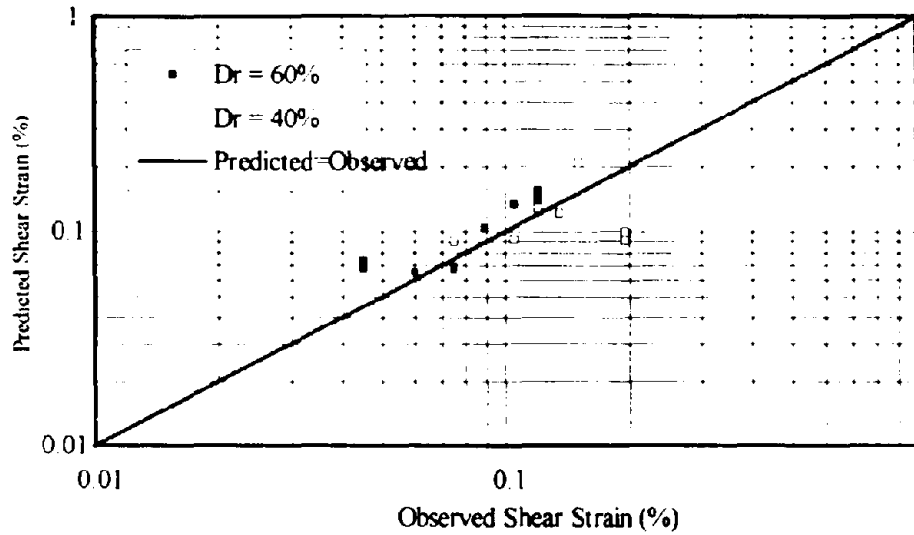
Figure C.5 Comparison of predicted shear strain and test data
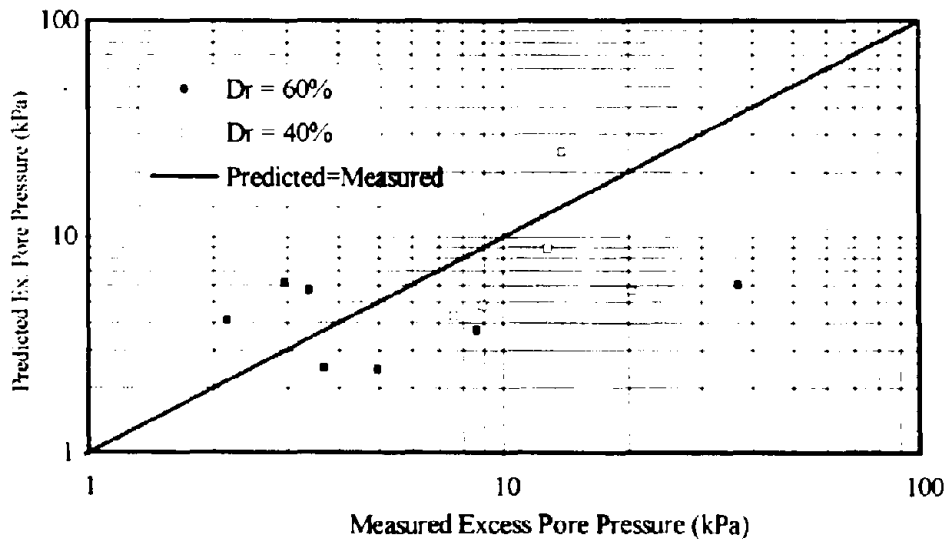
Figure C.6 Comparison of measured excess pore pressure at the end of first cycle and predictions
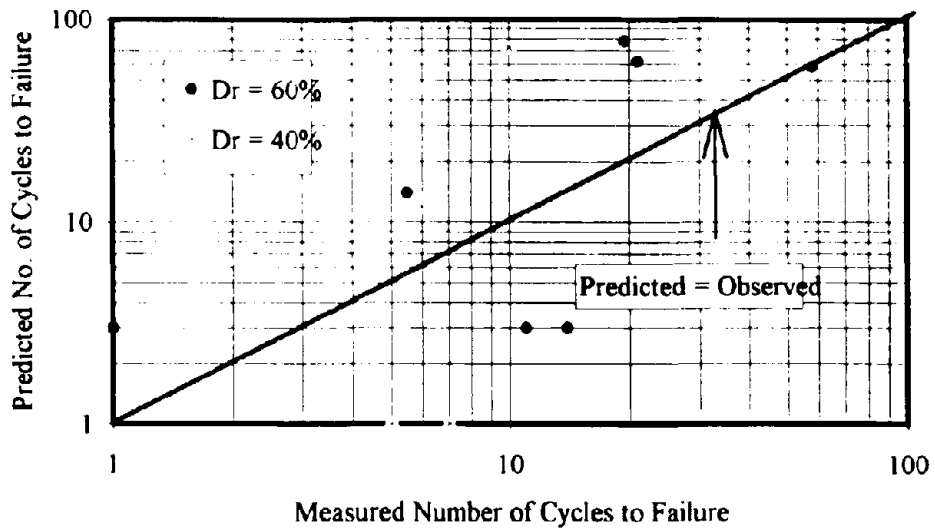
Figure C.7: Comparison of predicted and observed number of cycles to failure in cyclic triaxial tests
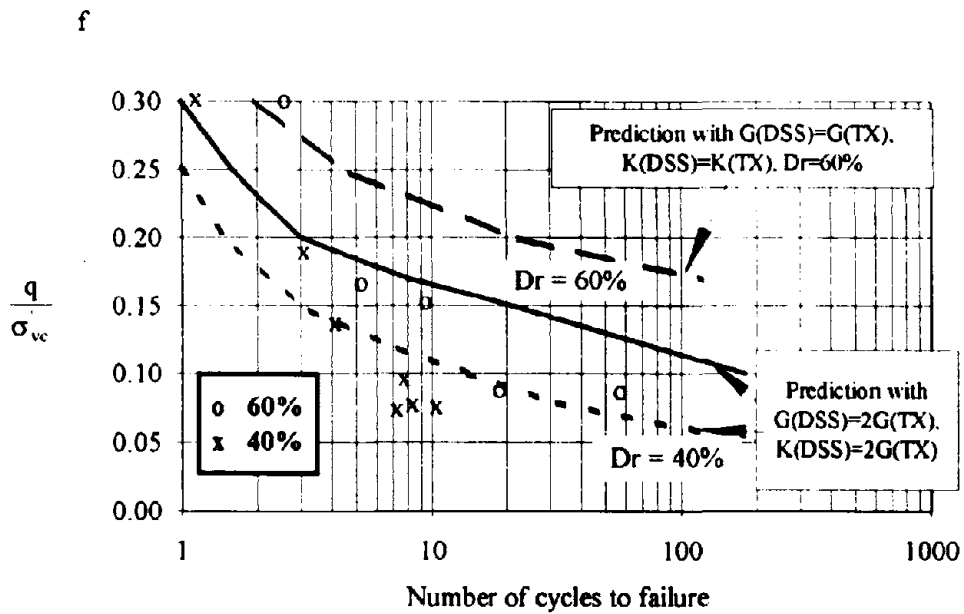
Figure C.8: Cyclic DSS test data and predictions

417

Page Intentionally Left Blank

Appendix D

INPUT FILES FOR FEM PROGRAMS

ABAQUS AND CYCON

D.1 INPUT FILE FOR ABAQUS

```
*HEADING
 SOLID SECTION - CHECKING STRESSES
*NODE
 701,0.,0.
 707,0.,-1.5
 709,0.,-3.
 713,0.,-7.
 901,-.03,0.
 907,-.03,-1.5
 909,-.03,-3.
 913,-.03,-7.
 1101,-1.25,0.
 1107,-1.25,-1.5
 1109,-1.25,-3.
 1113,-1.25,-7.
 1701,-5.,0.
 1707,-5.,-1.5
 1709,-5.,-3.
 1713,-5.,-7.
 2101,-9.,0.
 2107,-9.,-1.5
 2109,-9.,-3.
 2113,-9.,-7.
 2701,-18.,0.
 2707,-18.,-1.5
 2709,-18.,-3.
 2713,-18.,-7.
*NGEN,NSET=NULHS
 2701,2707,1
*NGEN,NSET=NMLHS
 2707,2709,1
*NGEN,NSET=NLLHS
 2709,2713,1
*NGEN,NSET=NURHS
 701,707,1
*NGEN,NSET=NMRHS
 707,709,1
*NGEN,NSET=NLRHS
 709,713,1
*NGEN,NSET=NU900
 901,907,1
*NGEN,NSET=NM900
 907,909,1
*NGEN,NSET=NL900
 909,913,1
*NGEN,NSET=NU1100
 1101,1107,1
*NGEN,NSET=NM1100
 1107,1109,1
*NGEN,NSET=NL1100
 1109,1113,1
*NGEN,NSET=NU1700
 1701,1707,1
*NGEN,NSET=NM1700
 1707,1709,1
*NGEN,NSET=NL1700
 1709,1713,1
*NGEN,NSET=NU2100
 2101,2107,1
*NGEN,NSET=NM2100
 2107,2109,1
*NGEN,NSET=NL2100
 2109,2113,1
*NSET,NSET=NSANDLHS
 2701,2713,1
*NSET,NSET=NSANDRHS
```

```
 701,713,1
**
*NFILL
 NURHS,NU900,2,100
*NFILL
 NMRHS,NM900,2,100
*NFILL
 NLRHS,NL900,2,100
*NFILL
 NU900,NU1100,2,100
*NFILL
 NM900,NM1100,2,100
*NFILL
 NL900,NL1100,2,100
*NFILL
 NU1100,NU1700,6,100
*NFILL
 NM1100,NM1700,6,100
*NFILL
 NL1100,NL1700,6,100
*NFILL
 NU1700,NU2100,4,100
*NFILL
 NM1700,NM2100,4,100
*NFILL
 NL1700,NL2100,4,100
*NFILL
 NU2100,NULHS,6,100
*NFILL
 NM2100,NMLHS,6,100
*NFILL
 NL2100,NLLHS,6,100
**
*NSET,NSET=NLHS,GENERATE
 701,713,1
*NSET,NSET=NRHS,GENERATE
 2701,2713,1
**NSET,NSET=NSAND,GENERATE
** NRHS,NLHS,100
*NSET,NSET=NTOP,GENERATE
 701,2701,100
*NSET,NSET=NBOT,GENERATE
 713,2713,100
**
**   ELEMENT INPUT
**
*ELEMENT,TYPE=CPE8
 11,901,903,703,701,902,803,702,801
*ELGEN,ELSET=SAND
 11,6,2,1,10,200,6
*ELSET, ELSET=INTRFACE
*SOLID SECTION, ELSET=SAND, MATERIAL=M1
*MATERIAL, NAME=M1
*ELASTIC, DEPENDENCIES=1
     10.0,  0.495,  0.,0.
  64293.8,  0.495,  0.,0.5
  90925.2,  0.495,  0.,1.0
 111360.2,  0.495,  0.,1.5
 128587.6,  0.495,  0.,2.0
 143765.6,  0.495,  0.,2.5
 157487.1,  0.495,  0.,3.0
 170105.5,  0.495,  0.,3.5
 181850.4,  0.495,  0.,4.0
 192881.5,  0.495,  0.,4.5
 203314.9,  0.495,  0.,5.0
 213238.5,  0.495,  0.,5.5
```

```
222720.4, 0.495, 0.,6.0
231814.7, 0.495, 0.,6.5
 240565.5, 0.495, 0.,7.
*DENSITY
 20.3
*BOUNDARY
NLHS,1
NRHS,1
NBOT,1,2
*STEP
 STEP 2 - APPLY BODY FORCE
*STATIC,PTOL=0.01
*FIELD, VARIABLE=1
 NTOP, 0.0
 NBOT, 7.0
*DLOAD
SAND,BXNU
*EL PRINT, POSITION=CENTROIDAL
 COORD,S11,S12,S22,PRIN3,PRIN2,PRIN1
** S11,S12,PRS12
*NODE PRINT
U,RF
*END STEP
**
**      ASSUME A 50% LARGER ACCELERATION AT LOAD CELL
**      WHICH IS A 33% INCREASE AT SOIL SURFACE
**
*USER SUBROUTINES
        SUBROUTINE DLOAD (F,KSTEP,KINC,TIME,NOEL,NPT,COORDS,JLTYP)
        IMPLICIT DOUBLE PRECISION(A-H,O-Z)
        DIMENSION COORDS(3)
        F=coords(2)*.18857143+5.38
        RETURN
        END
```

D.2 INPUT FILE FOR CYCON (for Test 1a)

FEAP ***** ANALYSIS OF CENTRIFUGE TEST 1A ******
253 70 4 2 3 8 0

NOPR
COOR

1	1	1.5	4.		67	1	-0.03	-1.5
3	0	1.5	3.		69	1	-0.03	-3.
4	0	1.25	4.		73	0	-0.03	-7.
5	0	1.25	3.		74	0	-0.64	0.
6	1	1.00	4.		77	1	-0.64	-1.5
8	0	1.00	3.		78	1	-0.64	-3.0
9	0	0.75	4.		80	0	-0.64	-7.0
10	0	0.75	3.		81	1	-1.25	0.
11	1	0.5	4.		87	1	-1.25	-1.5
13	1	0.5	3.		89	1	-1.25	-3.0
15	1	0.5	0.		93	0	-1.25	-7.0
21	1	0.5	-1.5		94	1	-1.875	0.
23	1	0.5	-3.0		97	1	-1.875	-1.5
27	0	0.5	-7.		98	1	-1.875	-3.0
28	0	0.25	4.		100	0	-1.875	-7.0
29	0	0.25	3.		101	1	-2.5	0.0
30	1	0.25	0.		107	1	-2.5	-1.5
33	0	0.25	-1.50		109	1	-2.5	-1.
34	1	0.25	-3.0		113	0	-2.5	-7.0
36	0	0.25	-7.0		114	0	-3.125	0.
37	1	0.0	4.0		117	0	-3.125	-1.5
39	1	0.0	3.0		118	1	-3.125	-3.00
41	1	0	0.		120	0	-3.125	-7.
47	1	0	-1.5		121	1	-3.75	0.
49	1	0	-3.0		127	1	-3.75	-1.5
53	0	0	-7.		129	1	-3.75	-3.
54	1	-0.015	0		133	0	-3.75	-7.00
57	0	-0.015	-1.5		134	1	-4.3	0.
58	1	-0.015	-3.0		137	0	-4.3	-1.5
60	0	-0.015	-7.		138	1	-4.3	-3.0
61	1	-0.03	0.		140	0	-4.3	-7.0
					141	1	-5.	0
					147	1	-5.	-1.5
					149	1	-5.	-3.
					153	0	-5.	-7.
					154	1	-6.	0

247	1	-18.	-1.5
249	1	-18.	-3.
253	0	-18.	-7.0

BOUN

1	1	-1	0	0	-1
3	0	1	0	1	-1
4	1	0	0	0	-1
41	0	0	0	1	-1
42	2	0	0	0	-1
52	0	0	1	0	-1
53	0	1	0	1	0
54	1	0	1	0	-1
60	0	1	1	1	-1
61	0	0	1	1	-1
62	2	0	0	0	-1
72	0	1	1	1	-1
73	0	0	1	0	0
74	1	1	0	0	-1
80	0	0	1	1	-1
81	0	0	0	0	-1
82	2	0	0	0	-1
92	0	1	1	1	-1
93	0	0	1	0	-1
94	1	0	0	1	-1
100	0	1	0	1	1
101	0	0	1	1	-1
102	2	0	0	0	-1
112	0	0	1	1	0
113	0	1	0	1	1
114	1	0	0	0	-1
120	0	1	1	1	-1
121	0	0	1	0	-1
122	2	0	0	0	-1
132	0	0	0	0	1
133	0	1	1	1	0

157	0	-6.	-1.5
158	1	-6.	-3.
160	0	-6.	-7.
161	1	-7.	0.
167	1	-7.	-1.5
169	0	-7.	-3.
173	1	-7.	-7.
174	0	-8.	0.
177	1	-8.	-1.5
178	0	-8.	-3.
180	1	-8.	-7.
181	0	-9.	0.
187	1	-9.	-1.5
189	1	-9.	-3.
193	0	-9.	-7.
194	1	-10.50	0.
197	0	-10.5	-1.5
198	1	-10.5	-3.
200	0	-10.5	-7.
201	1	-12.	0.
207	1	-12.	-1.5
209	1	-12.	-3.
213	0	-12.	-7.
214	1	-13.5	0.
217	0	-13.5	-1.5
218	1	-13.5	-3.
220	0	-13.5	-7.
221	1	-15.	0.
227	1	-15.	-1.5
229	1	-15.	-3.
233	0	-15.	-7.0
234	1	-16.5	0.
237	0	-16.5	-1.5
238	1	-16.5	-3.
240	0	-16.5	-7.
241	1	-18.	0.

426

ELEM									
1	1	8	3	1	6	5	2	4	7	0
2	1	13	8	6	11	10	7	9	12	0
3	2	39	13	11	37	29	12	28	38	0
4	2	41	15	13	39	30	14	29	40	0
5	2	43	17	15	41	31	16	30	42	0
6	2	45	19	17	43	32	18	31	44	0
7	2	47	21	19	45	33	20	32	46	0
8	2	49	23	21	47	34	22	33	48	0
9	2	51	25	23	49	35	24	34	50	0
10	2	53	27	25	51	36	26	35	52	0
11	3	63	43	41	61	55	42	54	62	0
12	3	65	45	43	63	56	44	55	64	0
13	3	67	47	45	65	57	46	56	66	0
14	3	69	49	47	67	58	48	57	68	0
15	3	71	51	49	69	59	50	58	70	0
16	3	73	53	51	71	60	52	59	72	0
17	4	83	63	61	81	75	62	74	82	0
18	4	85	65	63	83	76	64	75	84	0
19	4	87	67	65	85	77	66	76	86	0
20	4	89	69	67	87	78	68	77	88	0
21	4	91	71	69	89	79	70	78	90	0
22	4	93	73	71	91	80	72	79	92	0
23	4	103	83	81	101	95	82	94	102	0
24	4	105	85	83	103	96	84	95	104	0
25	4	107	87	85	105	97	86	96	106	0
26	4	109	89	87	107	98	88	97	108	0
27	4	111	91	89	109	99	90	98	110	0
28	4	113	93	91	111	100	92	99	112	0
29	4	123	103	101	121	115	102	114	122	0
30	4	125	105	103	123	116	104	115	124	0
31	4	127	107	105	125	117	106	116	126	0
32	4	129	109	107	127	118	108	117	128	0
33	4	131	111	109	129	119	110	118	130	0
34	4	133	113	111	131	120	112	119	132	0

ELEM			
134	1	0	0
140	-1	1	1
141	1	1	0
142	1	0	0
152	-1	0	2
153	1	0	0
154	0	1	0
160	-1	0	1
161	1	1	0
162	1	0	0
172	-1	0	2
173	1	0	0
174	0	1	0
180	-1	0	1
181	1	1	0
182	1	0	0
192	-1	0	2
193	1	0	0
194	0	1	0
200	-1	0	1
201	1	1	0
202	1	0	0
212	-1	0	2
213	1	0	0
214	0	1	0
220	-1	0	1
221	1	1	0
222	1	0	0
232	-1	0	2
233	1	0	0
234	0	1	0
240	-1	0	1
241	1	1	2
253	1	0	0
242	-1	0	2
252	1	0	0

```
35  4  143 121 141 135 122 134 142  0
36  4  145 123 143 136 124 135 144  0
37  4  147 125 145 137 126 136 146  0
38  4  149 127 147 138 128 137 148  0
39  4  151 129 149 139 130 138 150  0
40  4  153 131 151 140 132 139 152  0
41  4  163 141 161 155 142 154 162  0
42  4  165 143 163 156 144 155 164  0
43  4  167 145 165 157 146 156 166  0
44  4  169 147 167 158 148 157 168  0
45  4  171 149 169 159 150 158 170  0
46  4  173 151 171 160 152 159 172  0
47  4  183 161 181 175 162 174 182  0
48  4  185 163 183 176 164 175 184  0
49  4  187 165 185 177 166 176 186  0
50  4  189 167 187 178 168 177 188  0
51  4  191 169 189 179 170 178 190  0
52  4  193 171 191 180 172 179 192  0
53  4  203 181 201 195 182 194 202  0
54  4  205 183 203 196 184 195 204  0
55  4  207 185 205 197 186 196 206  0
56  4  209 187 207 198 188 197 208  0
57  4  211 189 209 199 190 198 210  0
58  4  213 191 211 200 192 199 212  0
59  4  223 201 221 215 202 214 222  0
60  4  225 203 223 216 204 215 224  0
61  4  227 205 225 217 206 216 226  0
62  4  229 207 227 218 208 217 228  0
63  4  231 209 229 219 210 218 230  0
64  4  233 211 231 220 212 219 232  0
65  4  243 221 241 235 222 234 242  0
66  4  245 223 243 236 224 235 244  0
67  4  247 225 245 237 226 236 246  0
68  4  249 227 247 238 228 237 248  0
69  4  251 229 249 239 230 238 250  0
70  4  253 231 251 240 232 239 252  0
```

```
MATE
  1  1 SOIL CUSHION
0.0,0.3,285.71,3,1,0,0,0
1.50,0.0,1.40,100.00,1,0,0.9
100,0.2.5215,0.9,1.750,40.0,2,2707557
0.5,11.0,0.00,0.40,1.26,0.00
0.00,9.80,12.0,3,0.0,0
  2 -1 ALUMINUM WALL
999999999. 0.0,26.46,3,1,0,0,0
0.0,0.0,0,0,0.0,0,0
100.0.0.0..0.0,0.0,0.0
0.00,0.0,0.00,0.0,0.0,0.0,0.00
0.00,9.8,0.0,0.0,0.0
  3  1 WALL-SOIL INTERFACE - Dr = 60%
999999999. 0,6.10.3.3,1,0,0,0
0.628,0.0,0.488,1000,0.0,656,0.50
100,0.265,0.0,9.23,0.40,0.263.0
0.5,11.0,0.006,46.0,40,1.26,0.0028
0.0028,9.80,12.0,3,0.0,0
  4  1 SAND - Dr = 60%
0.0,0.3,10.3,3,1,0,0,0
0.628,0.0,0.488,1000,0.0,656,0.50
100,0.265,0.0,9.23,0.40,0.263.0
0.5,11.0,0.006,46.0,40,1.26,0.0028
0.0028,9.80,12.0,3,0.0,0

END

MACRO
STRE   1.0    0.0    7.0
STRE   1.0           8.0
TIME                 0.5
SCAL   0.0909
LOOP          5.
DT     0.05   1.0    0.5
```

```
TANG
FORM
SOLV
STRE        7.0
TIME        0.5
DISP    5.0
STRE    5.0 4.0
NEXT
SCAL 2.0000
LOOP     5.
DT   0.05 1.0
TANG
FORM
SOLV
STRE        7.0
TIME        0.5
DISP    5.0
STRE    5.0 4.0
NEXT
SCAL 1.5000
LOOP     5.
DT   0.05 1.0
TANG
FORM
SOLV
STRE        7.0
TIME        0.5
DISP    5.0
STRE    5.0 4.0
NEXT
SCAL 1.1000
LOOP     5.
DT   0.05 1.0
TANG
FORM
SOLV
```

```
STRE        7.0
TIME        0.5
DISP    5.0
STRE    5.0 4.0
NEXT
SCAL 1.0000
LOOP      90.
DT   0.05 1.0 0.5
TANG
FORM
SOLV
STRE        7.0
TIME        0.5
DISP    10.0
STRE    10.0 4.0
NEXT
SCAL 0.2424
LOOP      10.
DT   0.05 1.0 0.5
TANG
FORM
SOLV
STRE        7.0
TIME        0.5
DISP    10.0
STRE    10.0 4.0
NEXT
SCAL  0.0
LOOP      10.
DT   0.5 1.0 5.0
TANG
FORM
SOLV
STRE        7.0
TIME    2.0 5.0
DISP
```

STRE
NEXT
END   10.0   4.0

1	1	-1.2500	3.5000	-.1000E+04	.0000E+00	-.1000E+04	-.1000E+04	.00
2	1	-.7500	3.5000	-.1000E+04	.0000E+00	-.1000E+04	-.1000E+04	.00
3	2	-.2500	3.5000	.0000E+00	.0000E+00	-.3395E+02	-.3395E+02	.00
4	2	-.2500	1.5000	.0000E+00	.0000E+00	-.1455E+02	-.1455E+02	.00
5	2	-.2500	-.2500	.0000E+00	.0000E+00	-.2425E+01	-.2425E+01	.00
6	2	-.2500	-.7500	.0000E+00	.0000E+00	-.7275E+01	-.7275E+01	.00
7	2	-.2500	-1.2500	.0000E+00	.0000E+00	-.1213E+02	-.1213E+02	.00
8	2	-.2500	-2.2500	.0000E+00	.0000E+00	-.2182E+02	-.2182E+02	.00
9	2	-.2500	-4.0000	.0000E+00	.0000E+00	-.3880E+02	-.3880E+02	.00
10	2	-.2500	-6.0000	.0000E+00	.0000E+00	-.5820E+02	-.5820E+02	.00
11	3	.0150	-.2500	-.1104E+01	.0000E+00	-.2575E+01	-.2575E+01	.00
12	3	.0150	-.7500	-.3311E+01	.0000E+00	-.7725E+01	-.7725E+01	.00
13	3	.0150	-1.2500	-.5518E+01	.0000E+00	-.1288E+02	-.1288E+02	.00
14	3	.0150	-2.2500	-.9932E+01	.0000E+00	-.2318E+02	-.2318E+02	.00
15	3	.0150	-4.0000	-.1766E+02	.0000E+00	-.4120E+02	-.4120E+02	.00
16	3	.0150	-6.0000	-.2649E+02	.0000E+00	-.6180E+02	-.6180E+02	.00
17	4	.6400	-.2500	-.1104E+01	.0000E+00	-.2575E+01	-.2575E+01	.00
18	4	.6400	-.7500	-.3311E+01	.0000E+00	-.7725E+01	-.7725E+01	.00
19	4	.6400	-1.2500	-.5518E+01	.0000E+00	-.1288E+02	-.1288E+02	.00
20	4	.6400	-2.2500	-.9932E+01	.0000E+00	-.2318E+02	-.2318E+02	.00
21	4	.6400	-4.0000	-.1766E+02	.0000E+00	-.4120E+02	-.4120E+02	.00
22	4	.6400	-6.0000	-.2649E+02	.0000E+00	-.6180E+02	-.6180E+02	.00
23	4	1.8750	-.2500	-.1104E+01	.0000E+00	-.2575E+01	-.2575E+01	.00
24	4	1.8750	-.7500	-.3311E+01	.0000E+00	-.7725E+01	-.7725E+01	.00
25	4	1.8750	-1.2500	-.5518E+01	.0000E+00	-.1288E+02	-.1288E+02	.00
26	4	1.8750	-2.2500	-.9932E+01	.0000E+00	-.2318E+02	-.2318E+02	.00
27	4	1.8750	-4.0000	-.1766E+02	.0000E+00	-.4120E+02	-.4120E+02	.00
28	4	1.8750	-6.0000	-.2649E+02	.0000E+00	-.6180E+02	-.6180E+02	.00
29	4	3.1250	-.2500	-.1104E+01	.0000E+00	-.2575E+01	-.2575E+01	.00

30	4	3.1250	-.7500	-.3311E+01	.0000E+00	-.7725E+01	-.3311E+01	-.7725E+01	.00
31	4	3.1250	-1.2500	-.5518E+01	.0000E+00	-.1288E+02	-.5518E+01	-.1288E+02	.00
32	4	3.1250	-2.2500	-.9932E+01	.0000E+00	-.2318E+02	-.9932E+01	-.2318E+02	.00
33	4	3.1250	-4.0000	-.1766E+02	.0000E+00	-.4120E+02	-.1766E+02	-.4120E+02	.00
34	4	3.1250	-6.0000	-.2649E+02	.0000E+00	-.6180E+02	-.2649E+02	-.6180E+02	.00
35	4	4.3000	-.2500	-.1104E+01	.0000E+00	-.2575E+01	-.1104E+01	-.2575E+01	.00
36	4	4.3000	-.7500	-.3311E+01	.0000E+00	-.7725E+01	-.3311E+01	-.7725E+01	.00
37	4	4.3000	-1.2500	-.5518E+01	.0000E+00	-.1288E+02	-.5518E+01	-.1288E+02	.00
38	4	4.3000	-2.2500	-.9932E+01	.0000E+00	-.2318E+02	-.9932E+01	-.2318E+02	.00
39	4	4.3000	-4.0000	-.1766E+02	.0000E+00	-.4120E+02	-.1766E+02	-.4120E+02	.00
40	4	4.3000	-6.0000	-.2649E+02	.0000E+00	-.6180E+02	-.2649E+02	-.6180E+02	.00
41	4	6.0000	-.2500	-.1104E+01	.0000E+00	-.2575E+01	-.1104E+01	-.2575E+01	.00
42	4	6.0000	-.7500	-.3311E+01	.0000E+00	-.7725E+01	-.3311E+01	-.7725E+01	.00
43	4	6.0000	-1.2500	-.5518E+01	.0000E+00	-.1288E+02	-.5518E+01	-.1288E+02	.00
44	4	6.0000	-2.2500	-.9932E+01	.0000E+00	-.2318E+02	-.9932E+01	-.2318E+02	.00
45	4	6.0000	-4.0000	-.1766E+02	.0000E+00	-.4120E+02	-.1766E+02	-.4120E+02	.00
46	4	6.0000	-6.0000	-.2649E+02	.0000E+00	-.6180E+02	-.2649E+02	-.6180E+02	.00
47	4	8.0000	-.2500	-.1104E+01	.0000E+00	-.2575E+01	-.1104E+01	-.2575E+01	.00
48	4	8.0000	-.7500	-.3311E+01	.0000E+00	-.7725E+01	-.3311E+01	-.7725E+01	.00
49	4	8.0000	-1.2500	-.5518E+01	.0000E+00	-.1288E+02	-.5518E+01	-.1288E+02	.00
50	4	8.0000	-2.2500	-.9932E+01	.0000E+00	-.2318E+02	-.9932E+01	-.2318E+02	.00
51	4	8.0000	-4.0000	-.1766E+02	.0000E+00	-.4120E+02	-.1766E+02	-.4120E+02	.00
52	4	8.0000	-6.0000	-.2649E+02	.0000E+00	-.6180E+02	-.2649E+02	-.6180E+02	.00
53	4	10.5000	-.2500	-.1104E+01	.0000E+00	-.2575E+01	-.1104E+01	-.2575E+01	.00
54	4	10.5000	-.7500	-.3311E+01	.0000E+00	-.7725E+01	-.3311E+01	-.7725E+01	.00
55	4	10.5000	-1.2500	-.5518E+01	.0000E+00	-.1288E+02	-.5518E+01	-.1288E+02	.00
56	4	10.5000	-2.2500	-.9932E+01	.0000E+00	-.2318E+02	-.9932E+01	-.2318E+02	.00
57	4	10.5000	-4.0000	-.1766E+02	.0000E+00	-.4120E+02	-.1766E+02	-.4120E+02	.00
58	4	10.5000	-6.0000	-.2649E+02	.0000E+00	-.6180E+02	-.2649E+02	-.6180E+02	.00
59	4	13.5000	-.2500	-.1104E+01	.0000E+00	-.2575E+01	-.1104E+01	-.2575E+01	.00
60	4	13.5000	-.7500	-.3311E+01	.0000E+00	-.7725E+01	-.3311E+01	-.7725E+01	.00
61	4	13.5000	-1.2500	-.5518E+01	.0000E+00	-.1288E+02	-.5518E+01	-.1288E+02	.00

62	4	13.5000	-2.2500	-.9932E+01	.0000E+00	-.2318E+02	-.9932E+01	-.2318E+02	.00
63	4	13.5000	-4.0000	-.1766E+02	.0000E+00	-.4120E+02	-.1766E+02	-.4120E+02	.00
64	4	13.5000	-6.0000	-.2649E+02	.0000E+00	-.6180E+02	-.2649E+02	-.6180E+02	.00
65	4	16.5000	-.2500	-.1104E+01	.0000E+00	-.2575E+01	-.1104E+01	-.2575E+01	.00
66	4	16.5000	-.7500	-.3311E+01	.0000E+00	-.7725E+01	-.3311E+01	-.7725E+01	.00
67	4	16.5000	-1.2500	-.5518E+01	.0000E+00	-.1288E+02	-.5518E+01	-.1288E+02	.00
68	4	16.5000	-2.2500	-.9932E+01	.0000E+00	-.2318E+02	-.9932E+01	-.2318E+02	.00
69	4	16.5000	-4.0000	-.1766E+02	.0000E+00	-.4120E+02	-.1766E+02	-.4120E+02	.00
70	4	16.5000	-6.0000	-.2649E+02	.0000E+00	-.6180E+02	-.2649E+02	-.6180E+02	.00

1	1	0.75	3.5	0.0	0.0	0.0	0.0	0.0	0.0	
2	1	0.75	3.5	0.0	0.0	0.0	0.0	0.0	0.0	
3	2	0.25	3.5	0.0	0.0	0.0	0.0	0.0	0.0	
4	2	0.25	1.5	0.0	0.0	0.0	0.0	0.0	0.0	
5	2	0.25	-0.25	0.0	0.0	0.0	0.0	0.0	0.0	
6	2	0.25	-0.75	0.0	0.0	0.0	0.0	0.0	0.0	
7	2	0.25	-1.25	0.0	0.0	0.0	0.0	0.0	0.0	
8	2	0.25	-2.25	0.0	0.0	0.0	0.0	0.0	0.0	
9	2	0.25	-4	0.0	0.0	0.0	0.0	0.0	0.0	
10	2	0.25	-6	0.0	0.0	0.0	0.0	0.0	0.0	
11	3	-0.015	-0.25	-30.9	0.082401	-5.472	-5.472	-18.01	-30.9	0.0
12	3	-0.015	-0.75	-31.49	0.026795	-3.784	-3.784	-17.46	-31.49	0.0
13	3	-0.015	-1.25	-31.71	0.027907	-4.238	-4.238	-17.79	-31.71	0.0
14	3	-0.015	-2.25	-35.15	0.042927	-11.2	-11.2	-22.94	-35.15	0.0
15	3	-0.015	-4	-31.14	0.07077	-20.29	-20.29	-25.46	-31.14	0.0
16	3	-0.015	-6	-41.7	-0.051433	-29.37	-29.37	-35.18	-41.7	0.0
17	4	-0.64	-0.25	-25.79	0.6647	-1.901	-1.883	-13.71	-25.81	0.0
18	4	-0.64	-0.75	-26.63	1.229	-0.8469	-0.7884	-13.6	-26.68	0.0
19	4	-0.64	-1.25	-26.56	1.302	-0.5966	-0.5315	-13.44	-26.63	0.0
20	4	-0.64	-2.25	-30.06	1.266	-7.019	-6.949	-18.35	-30.13	0.0
21	4	-0.64	-4	-27.02	1.643	-16.37	-16.12	-21.48	-27.27	0.0
22	4	-0.64	-6	-40.81	6.361	-28.86	-26.11	-34.49	-43.56	0.0
23	4	-1.875	-0.25	-21.04	0.7522	-0.3678	-0.3404	-10.6	-21.07	0.0

432

24	4	-1.875	-0.75	-21.92	1.873	-0.5293	-0.3666	-11.11	-22.08	0.0
25	4	-1.875	-1.25	-22.27	2.522	-0.6595	-0.3691	-11.35	-22.56	0.0
26	4	-1.875	-2.25	-25.5	3.159	-5.934	-5.437	-15.56	-26	0.0
27	4	-1.875	-4	-22.45	4.597	-13.22	-11.32	-17.65	-24.35	0.0
28	4	-1.875	-6	-25.06	17.08	-14.01	-1.588	-19.34	-37.48	0.0
29	4	-3.125	-0.25	-17.26	0.6537	0.1034	0.1279	-8.494	-17.29	0.0
30	4	-3.125	-0.75	-17.45	1.818	-0.2503	-0.060176	-8.764	-17.64	0.0
31	4	-3.125	-1.25	-17.47	2.756	-0.5335	-0.096103	-8.909	-17.9	0.0
32	4	-3.125	-2.25	-20.15	4.199	-4.957	-3.874	-12.43	-21.24	0.0
33	4	-3.125	-4	-17.75	6.972	-10.56	-6.313	-14.02	-22	0.0
34	4	-3.125	-6	-19.34	25.06	-10.59	10.47	-14.82	-40.4	0.0
35	4	-4.375	-0.25	-13.7	0.611	0.073658	0.1007	-6.743	-13.72	0.0
36	4	-4.375	-0.75	-13.49	1.754	-0.1758	0.051426	-6.766	-13.72	0.0
37	4	-4.375	-1.25	-13.22	2.819	-0.4154	0.1778	-6.748	-13.81	0.0
38	4	-4.375	-2.25	-15	4.785	-3.84	-2.069	-9.325	-16.77	0.0
39	4	-4.375	-4	-13.09	8.687	-7.92	-1.441	-10.4	-19.57	0.0
40	4	-4.375	-6	-14.19	30.56	-7.98	19.63	-10.97	-41.8	0.0
41	4	-6	-0.25	-8.977	0.5901	-0.081544	-0.042573	-4.484	-9.016	0.0
42	4	-6	-0.75	-8.709	1.757	-0.2303	0.1194	-4.425	-9.059	0.0
43	4	-6	-1.25	-8.427	2.921	-0.4167	0.5354	-4.378	-9.38	0.0
44	4	-6	-2.25	-9.38	5.3	-2.621	0.2857	-5.94	-12.29	0.0
45	4	-6	-4	-8.063	10.12	-5.034	3.683	-6.483	-16.78	0.0
46	4	-6	-6	-8.71	34.88	-5.273	27.93	-6.922	-41.91	0.0
47	4	-8	-0.25	-3.001	0.5899	-0.052178	0.061458	-1.511	-3.114	0.0
48	4	-8	-0.75	-2.878	1.792	-0.085174	0.7901	-1.467	-3.753	0.0
49	4	-8	-1.25	-2.804	3.035	-0.1958	1.803	-1.485	-4.803	0.0
50	4	-8	-2.25	-3.143	5.663	-0.9886	3.699	-2.045	-7.83	0.0
51	4	-8	-4	-2.495	10.96	-1.557	8.946	-2.006	-13	0.0
52	4	-8	-6	-3.582	37.36	-2.588	34.28	-3.054	-40.45	0.0
53	4	-10.5	-0.25	4.513	0.5772	0.05079	4.587	2.259	-0.022666	0.0
54	4	-10.5	-0.75	4.373	1.786	0.1668	5.029	2.247	-0.4895	0.0
55	4	-10.5	-1.25	4.132	3.008	0.2134	5.763	2.151	-1.417	0.0

56	4	-10.5	-2.25	4.521	5.594	1.296	8.73	2.88	-2.913	0.0
57	4	-10.5	-4	4.24	10.85	2.819	14.4	3.494	-7.341	0.0
58	4	-10.5	-6	3.699	36.88	2.222	39.8	-5	2.93	0.0
59	4	-13.5	-0.25	13.36	0.6558	0.049637	13.39	6.638	0.017403	0.0
60	4	-13.5	-0.75	13.19	1.784	0.227	13.43	6.643	-0.013987	0.0
61	4	-13.5	-1.25	13.3	2.851	0.7235	13.91	6.94	0.1072	0.0
62	4	-13.5	-2.25	15.28	4.852	4.208	17.11	9.646	2.382	0.0
63	4	-13.5	-4	13.06	8.826	7.926	19.68	10.39	1.302	0.0
64	4	-13.5	-6	8.818	30.68	2.457	36.48	5.581	-25.21	0.0
65	4	-16.5	-0.25	22.39	0.6521	0.7107	22.41	11.44	0.6911	0.0
66	4	-16.5	-0.75	22.82	1.649	0.07476	22.94	11.33	-0.044114	0.0
67	4	-16.5	-1.25	22.44	2.144	-0.393	22.64	10.91	-0.5927	0.0
68	4	-16.5	-2.25	25.15	2.598	4.729	25.47	14.79	4.404	0.0
69	4	-16.5	-4	21.54	3.706	11.98	22.81	16.59	10.71	0.0
70	4	-16.5	-6	35.44	12.86	24.47	43.93	29.65	15.97	0.0

STOP

Appendix E

CYCON PREDICTIONS

AND

TEST RESULTS
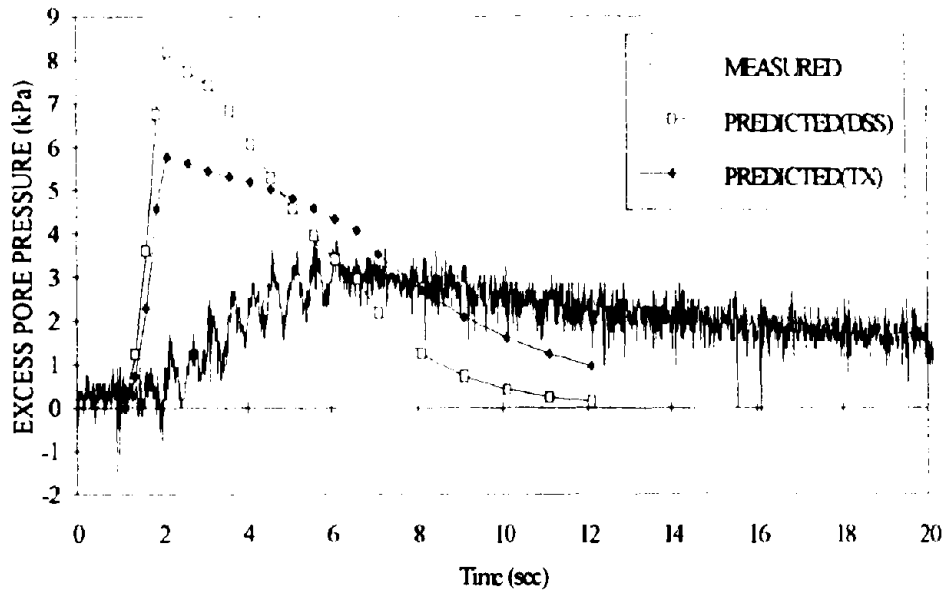
(a) Excess pore pressure at P1
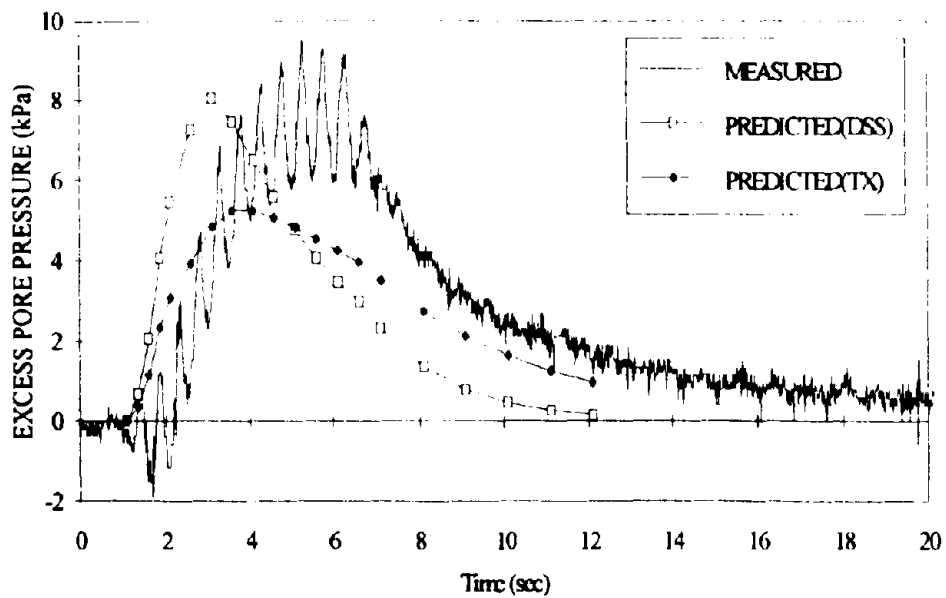
(b) Excess pore pressure at P2

Figure E.1: Predicted and observed excess pressrues in Test 1a

436
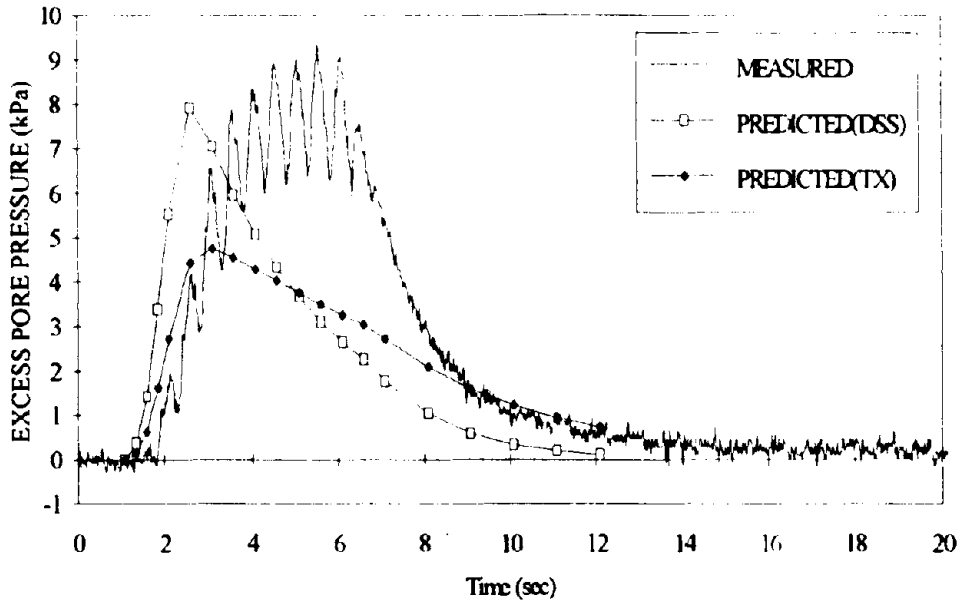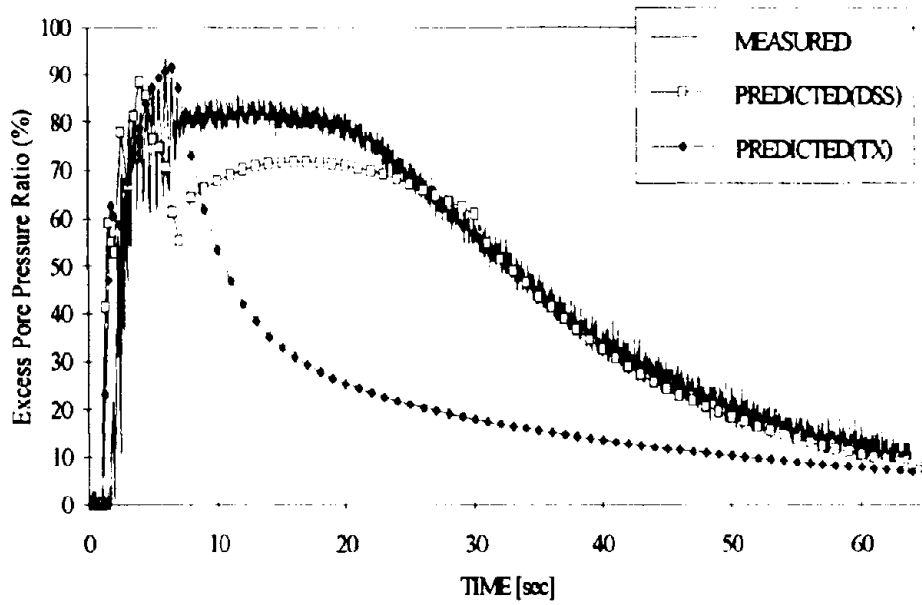
(c) Excess pore pressure at P4
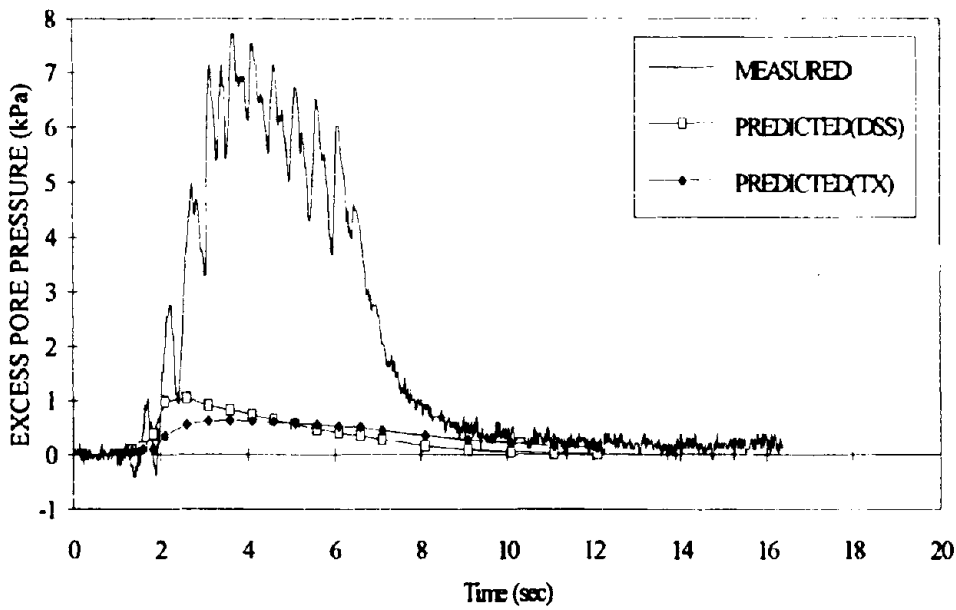
(d) Excess pore pressure at P5

Figure E.1: Predicted and observed excess pore pressrues in Test 1a
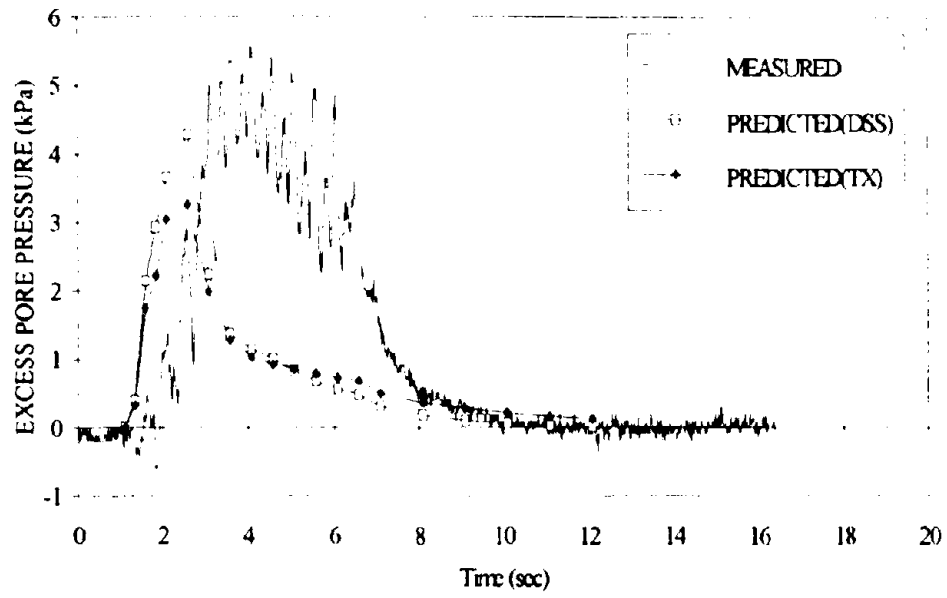
(e) Excess pore pressure ratio at P6

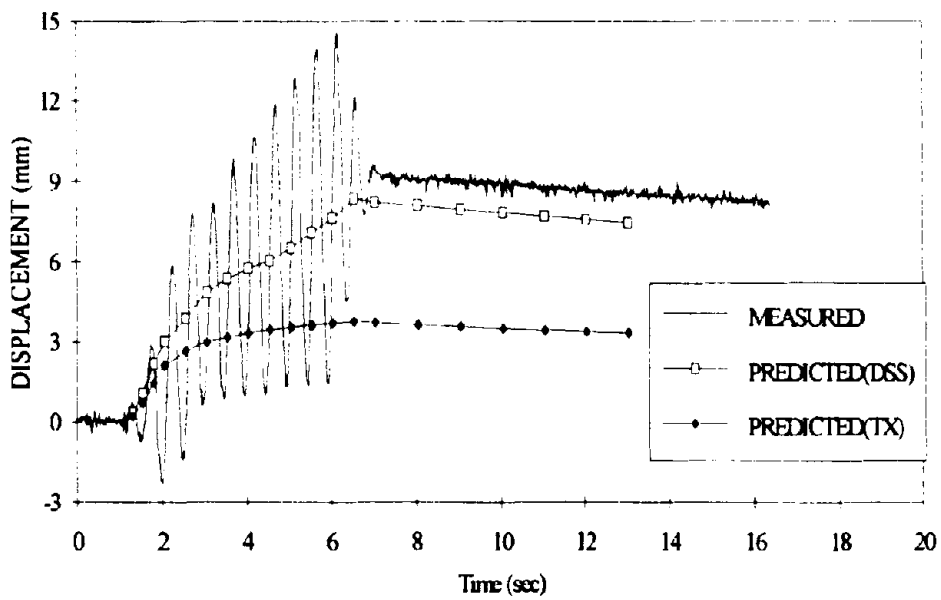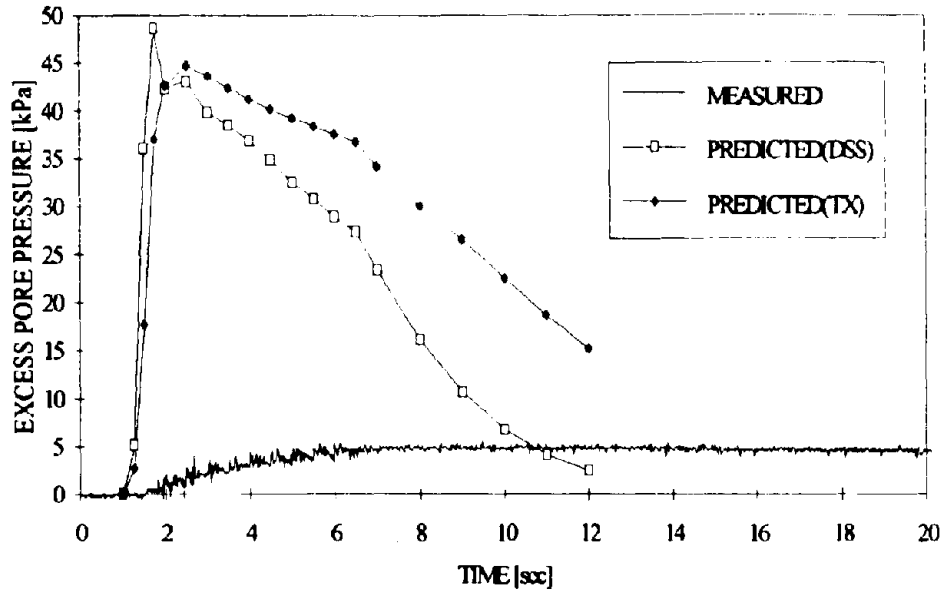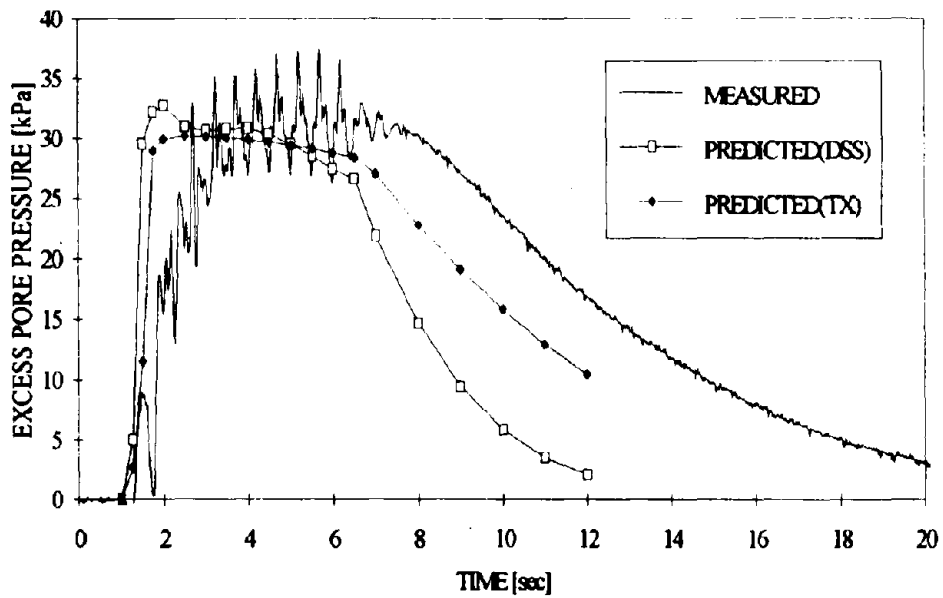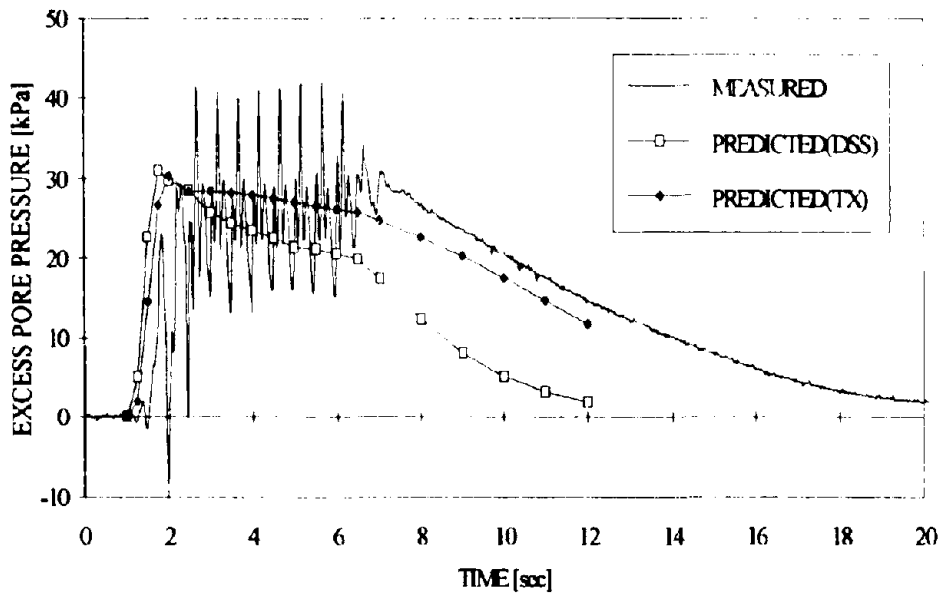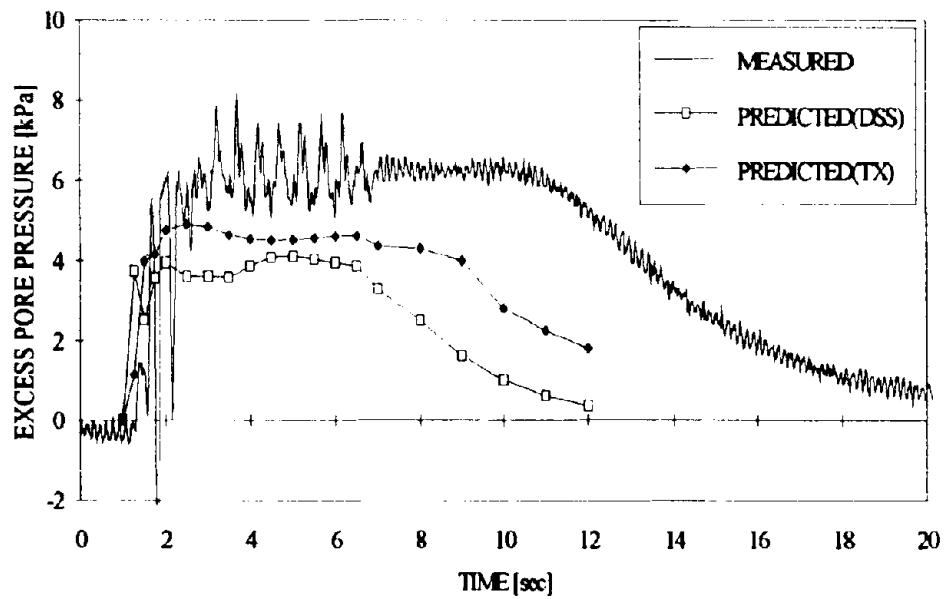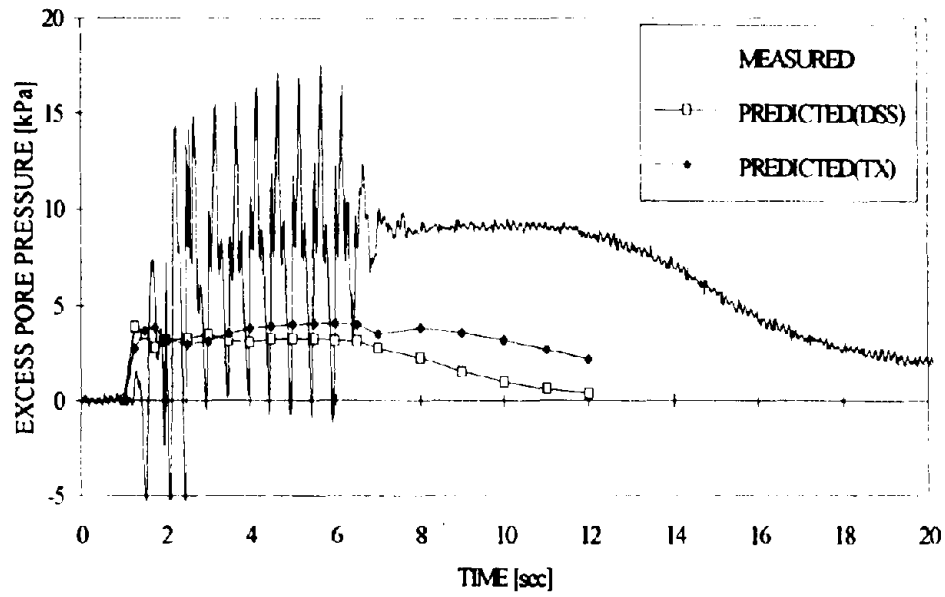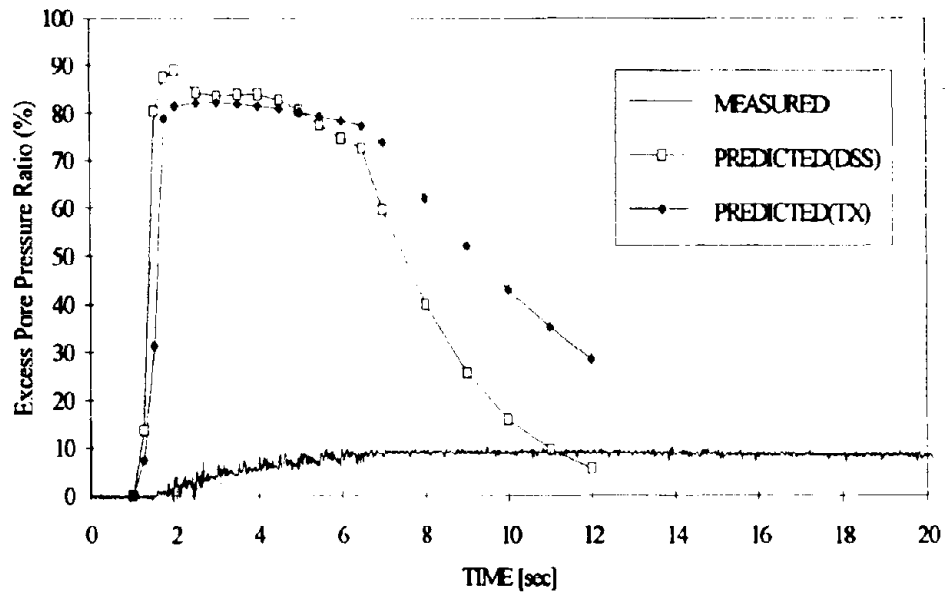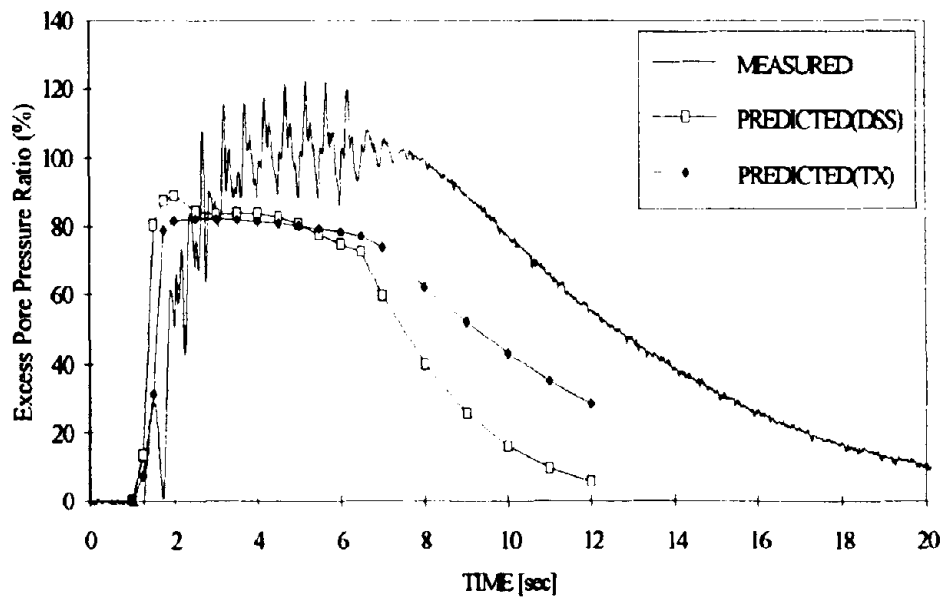Figure E.1: Predicted and observed excess pore pressrues in Test 1a
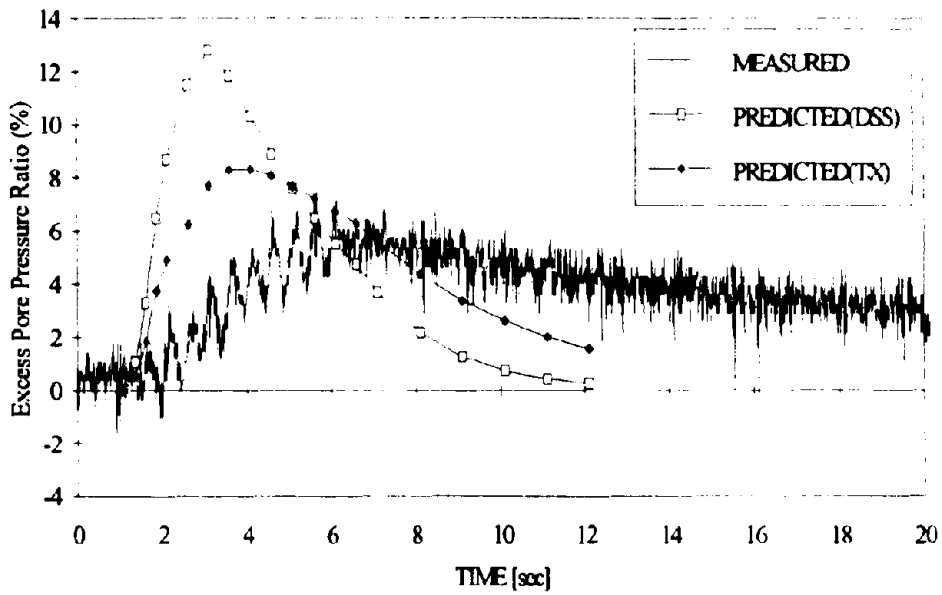
(a) Excess pore pressure ratio at P1
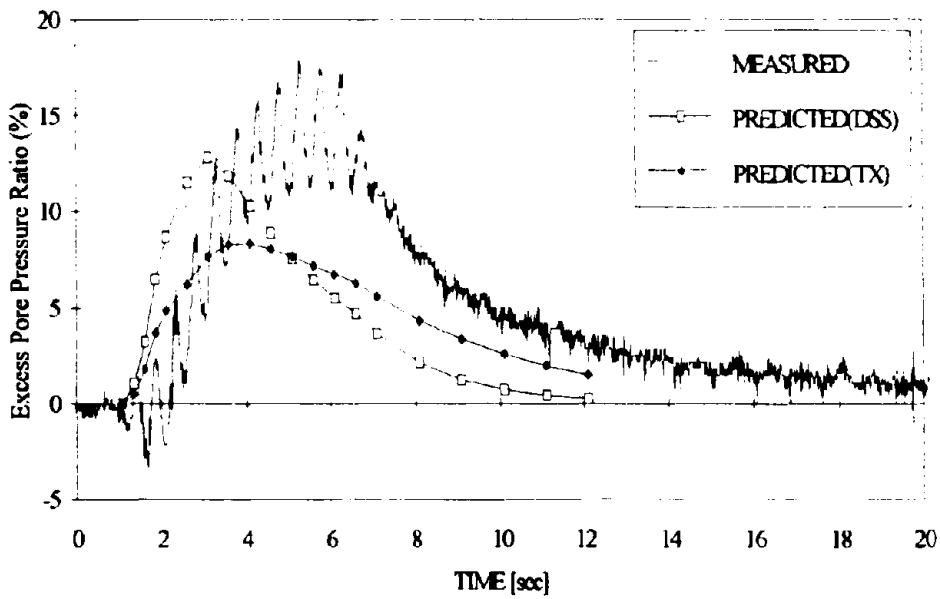
(b) Excess pore pressure ratio at P2

Figure E.2: Predicted and observed excess pore pressrue ratios in Test 1a

439
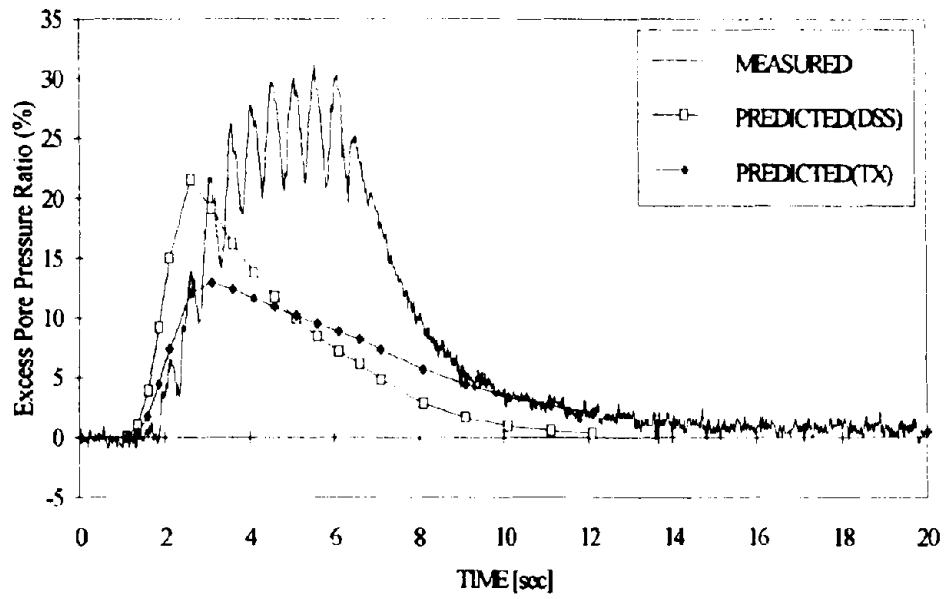
(c) Excess pore pressure ratio at P4
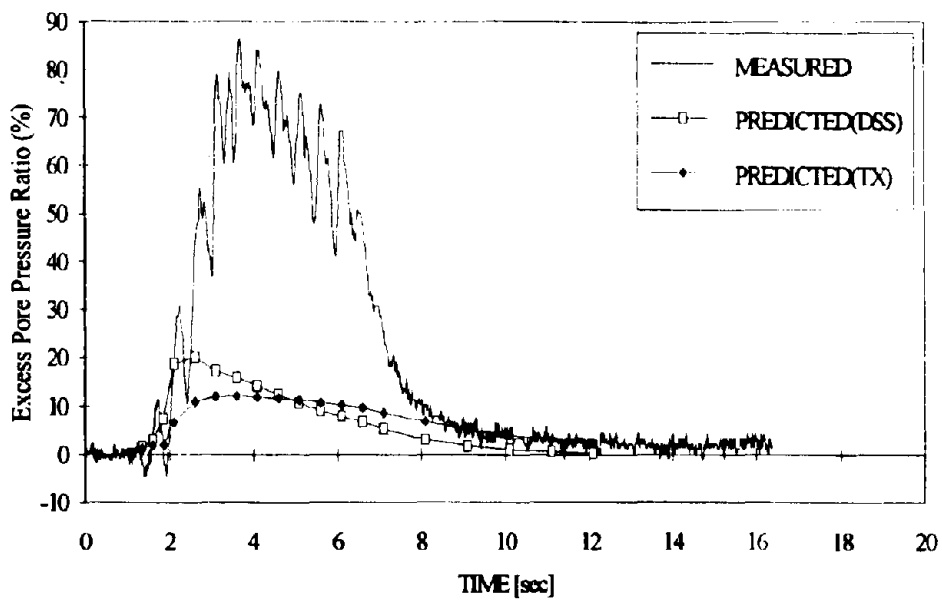
(d) Excess pore pressure ratio at P5

Figure E.2: Predicted and observed excess pore pressrue ratios in Test 1a
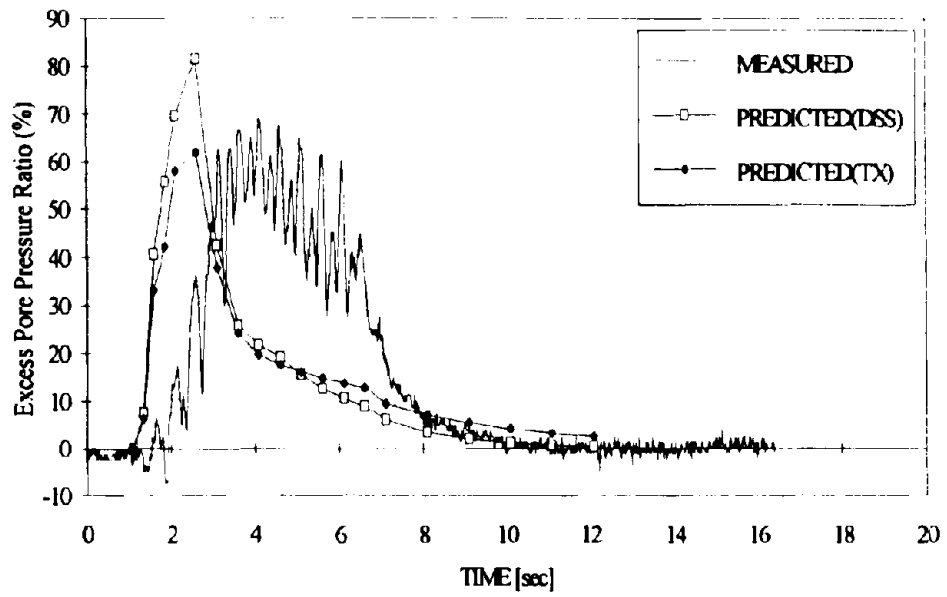
(e) Excess pore pressure ratio at P6

Figure E.2: Predicted and observed excess pore pressrue ratios in Test 1a
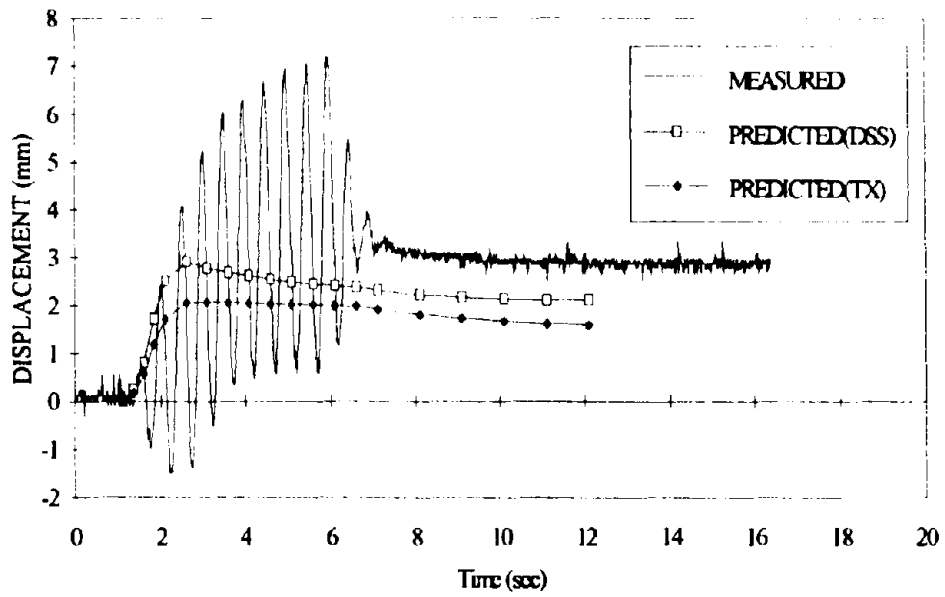
Figure E.3: Predicted and observed horizontal wall top displacement in Test 1a
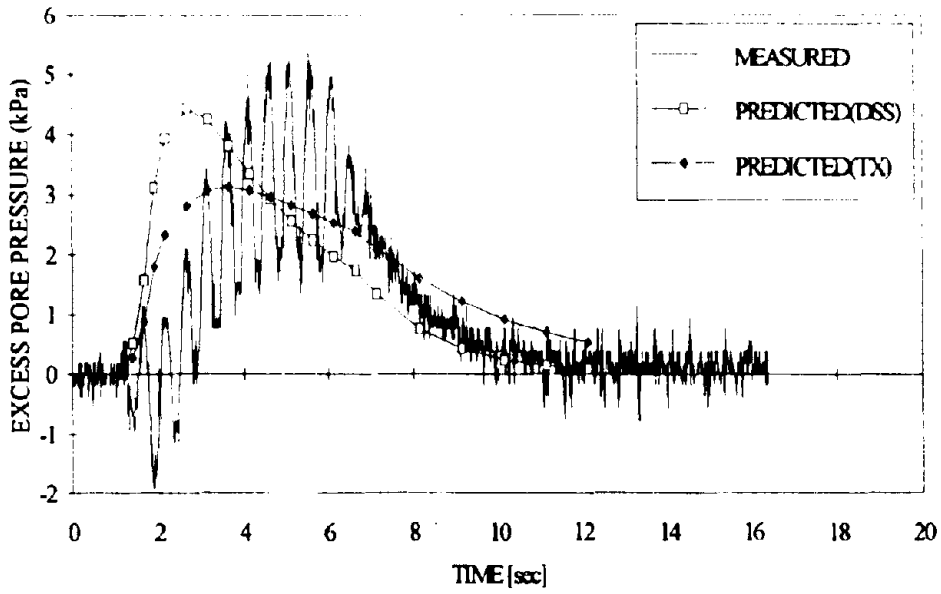
(a) Excess pore pressure at P2
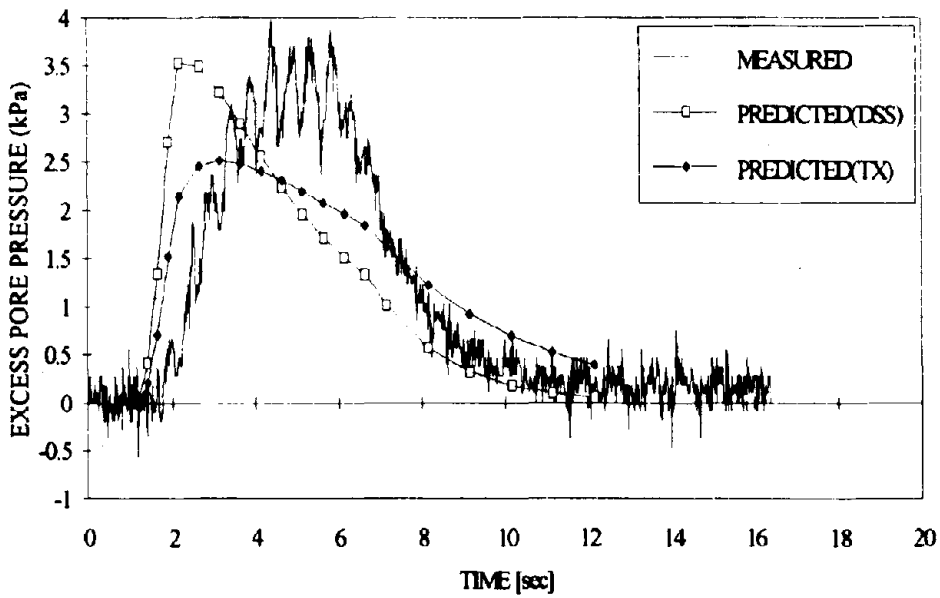
(b) Excess pore pressure at P3

Figure E.4: Predicted and observed excess pore pressrues in Test 2a
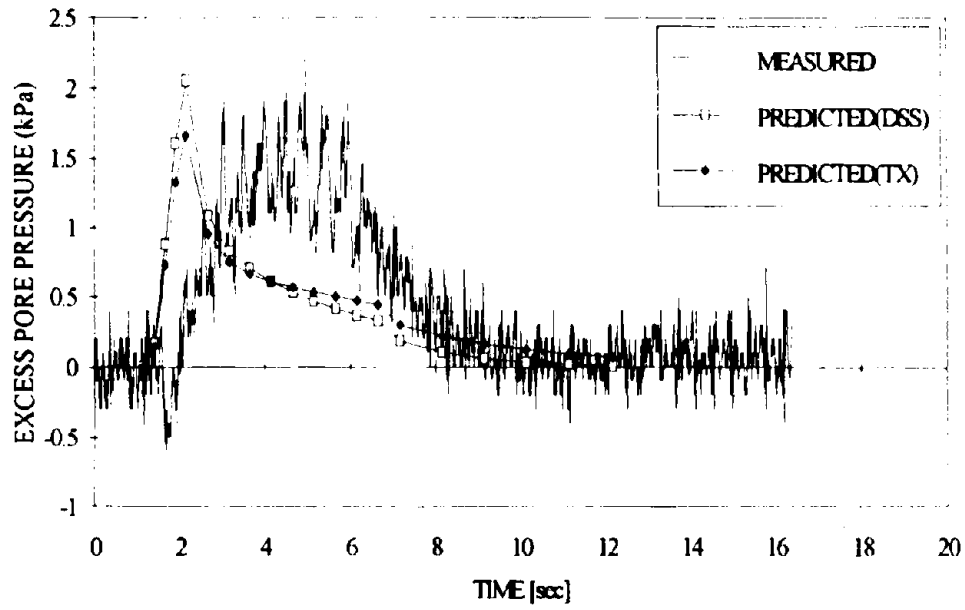
(e) Excess pore pressure ratio at P6

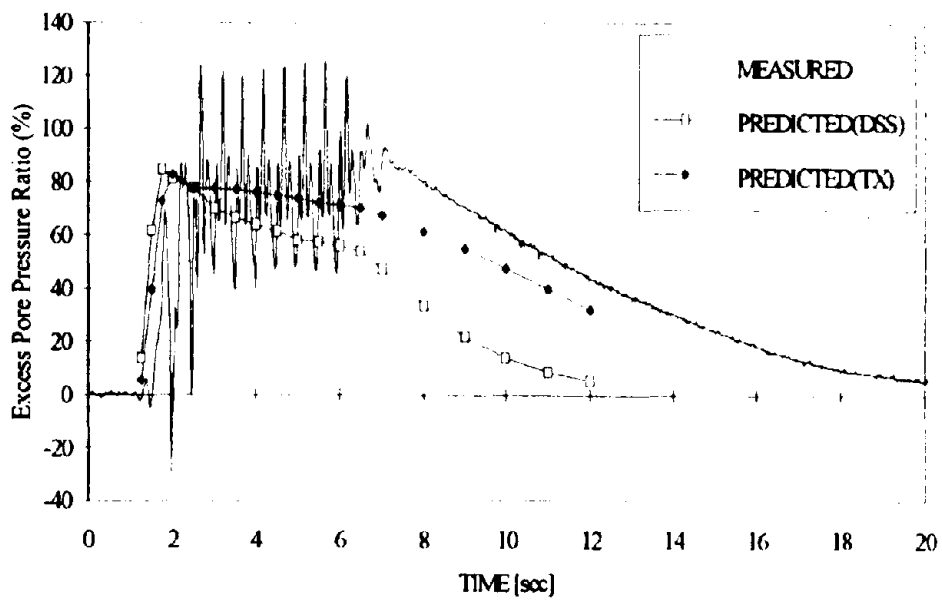Figure E.4: Predicted and observed excess pore pressrues in Test 2a
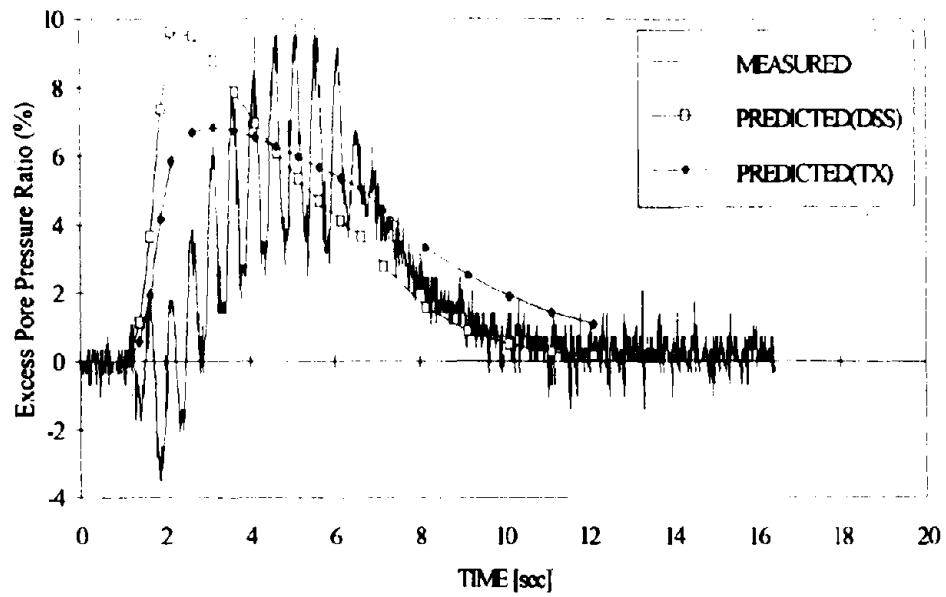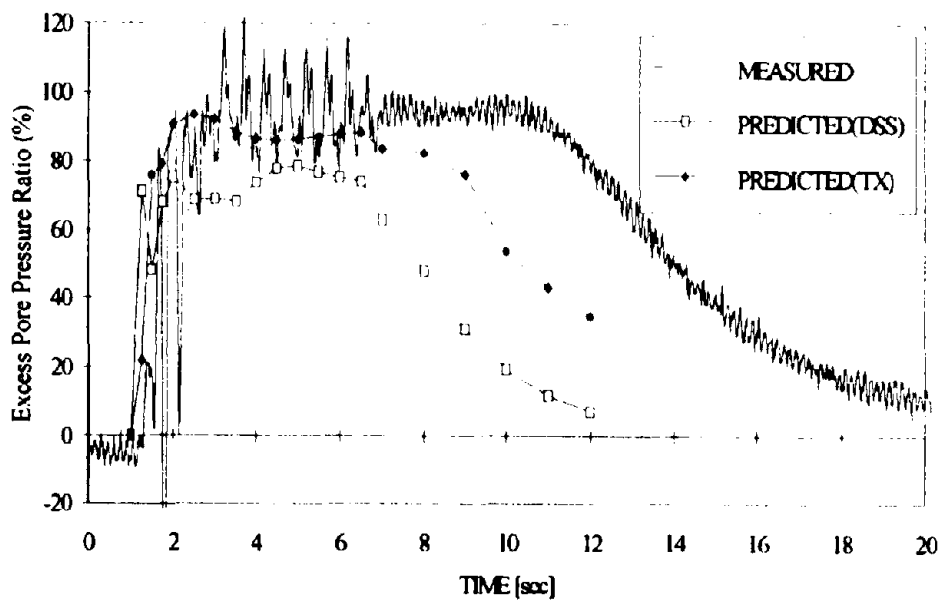
(a) Excess pore pressure ratio at P2
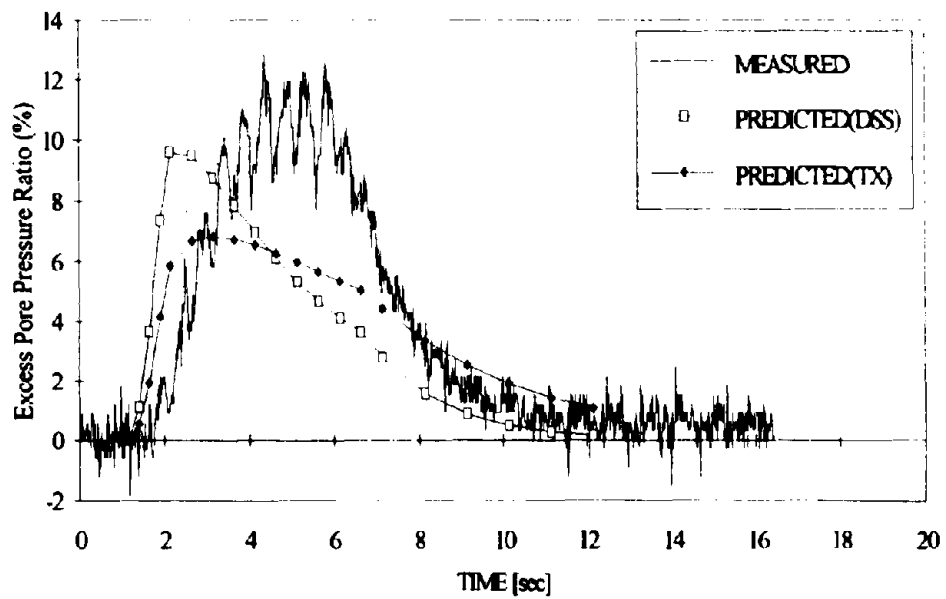
(b) Excess pore pressure ratio at P3

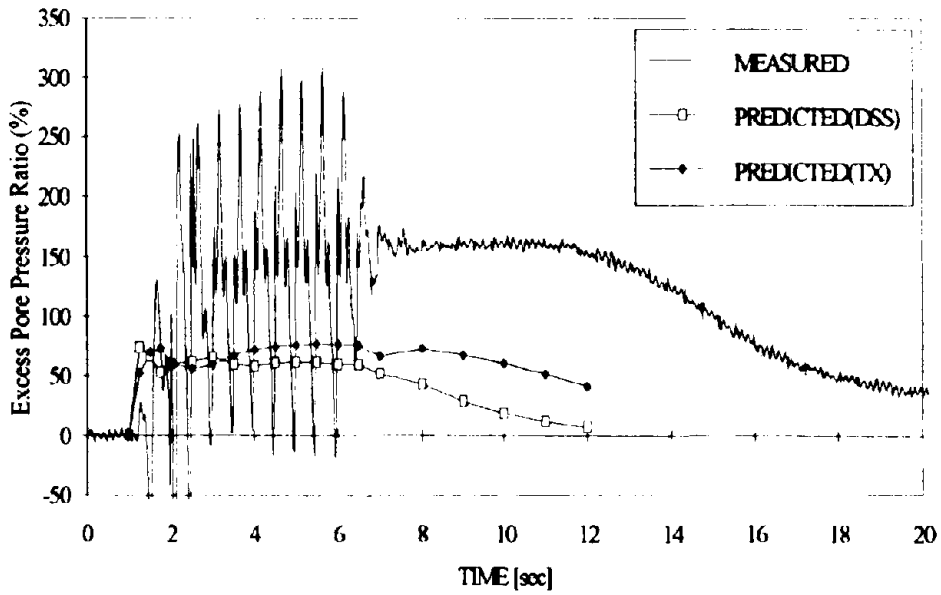Figure E.5: Predicted and observed excess pore pressrue ratios in Test 2a
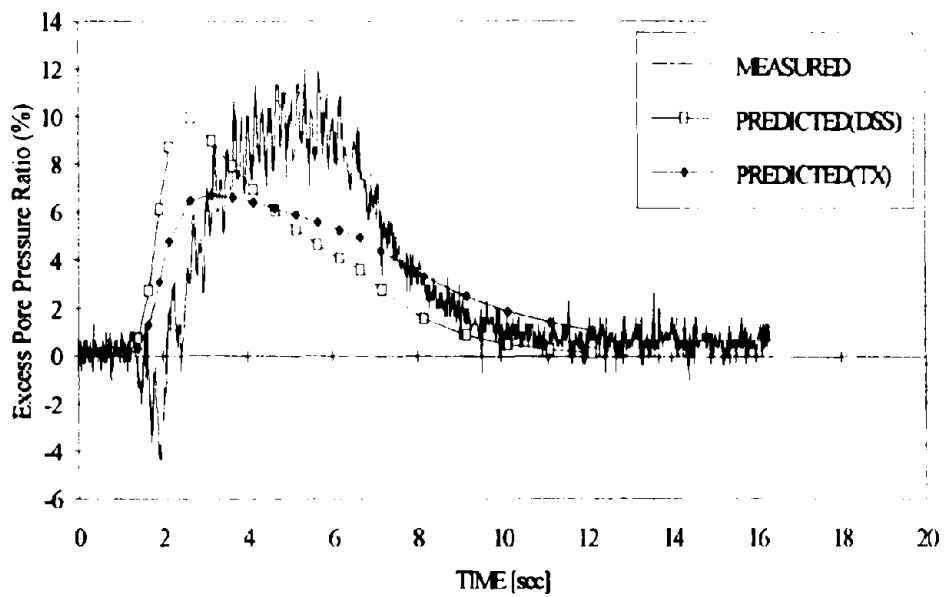
(c) Excess pore pressure ratio at P4
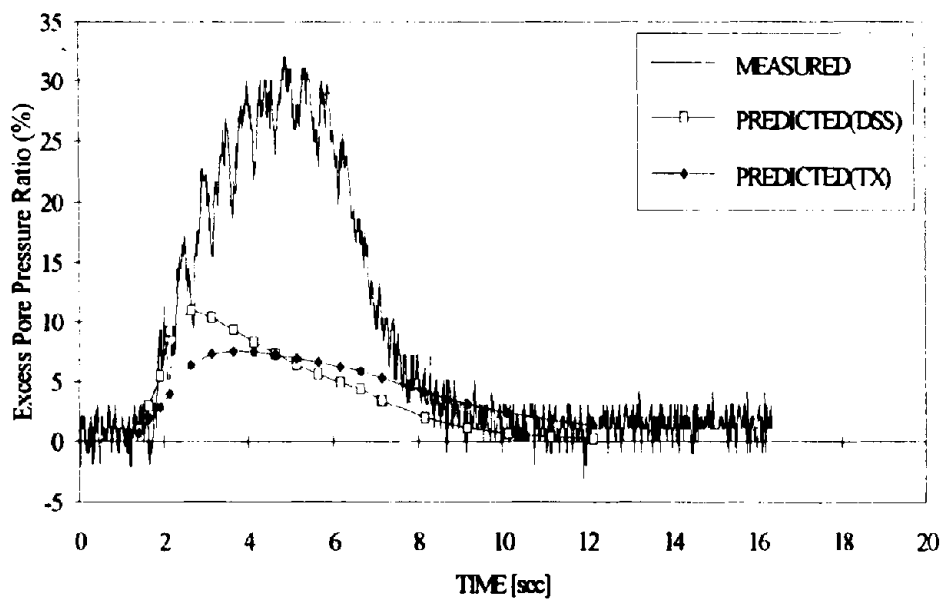
(d) Excess pore pressure ratio at P5

Figure E.5: Predicted and observed excess pore pressrue ratios in Test 2a

446
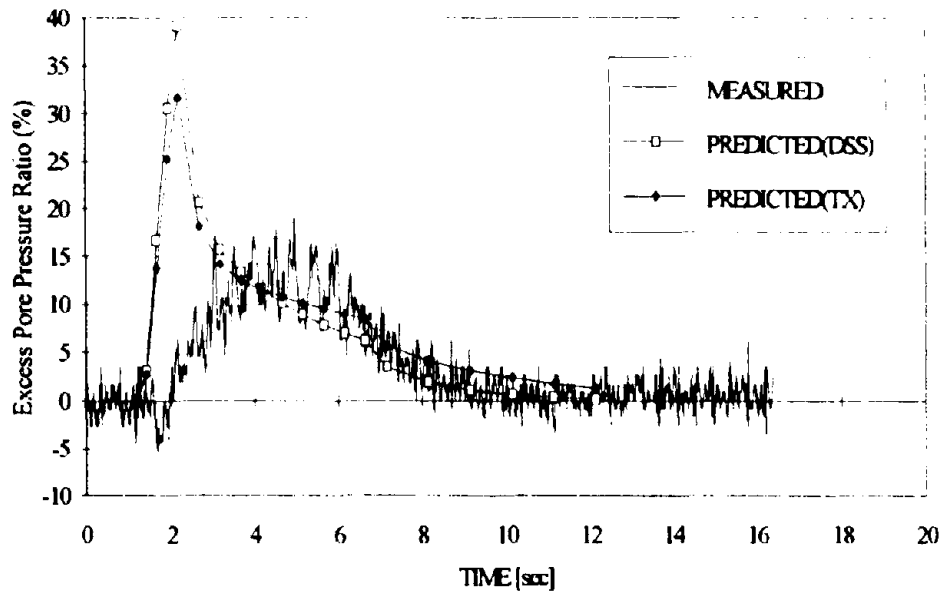
(e) Excess pore pressure ratio at P6

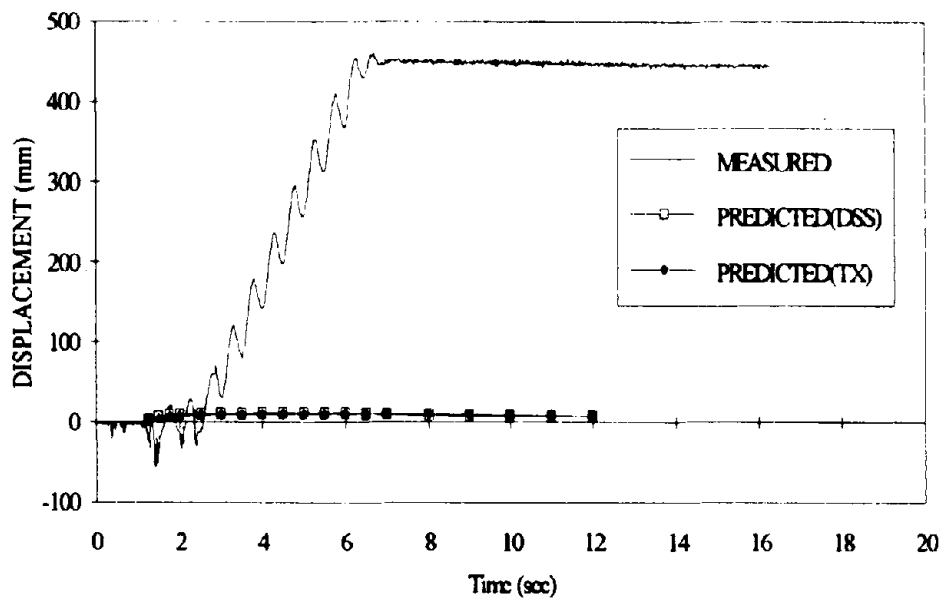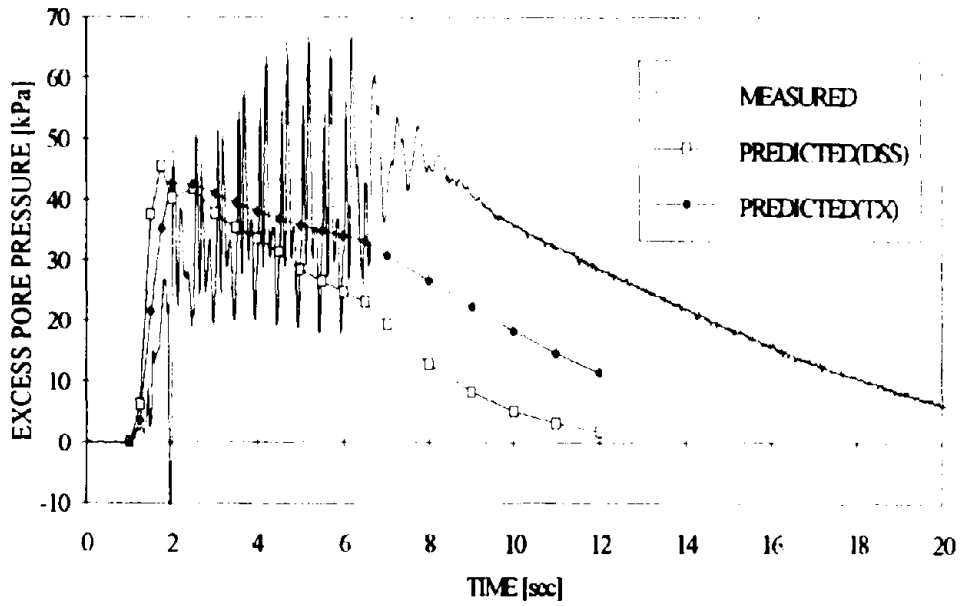Figure E.5: Predicted and observed excess pressrue ratios in Test 2a
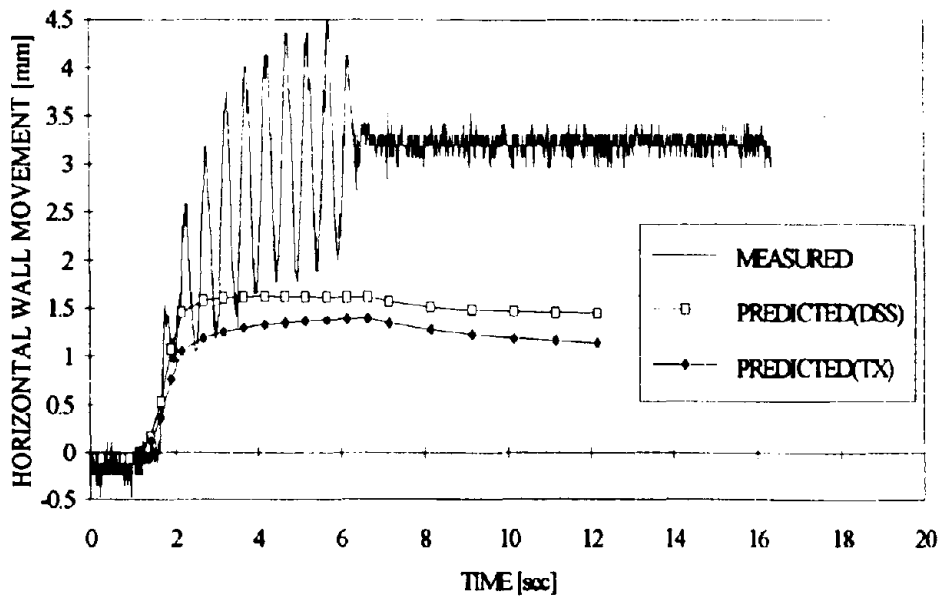
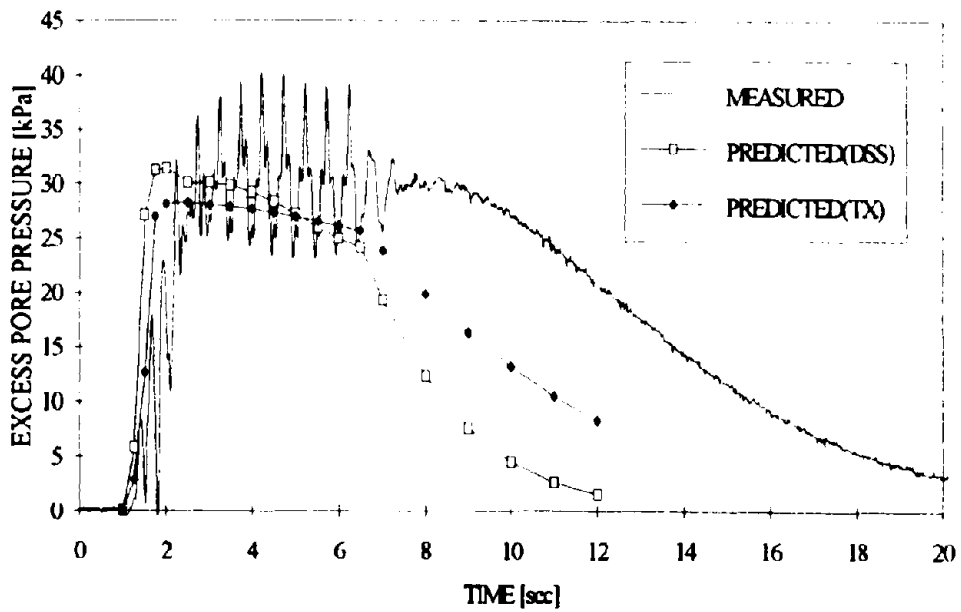Figure E.6: Predicted and observed horizontal wall top displacement in Test 2a
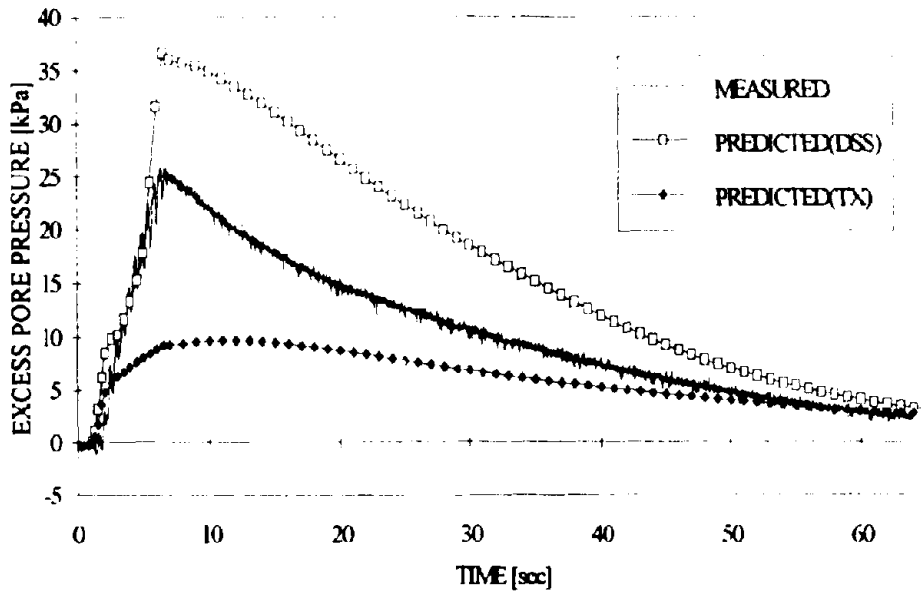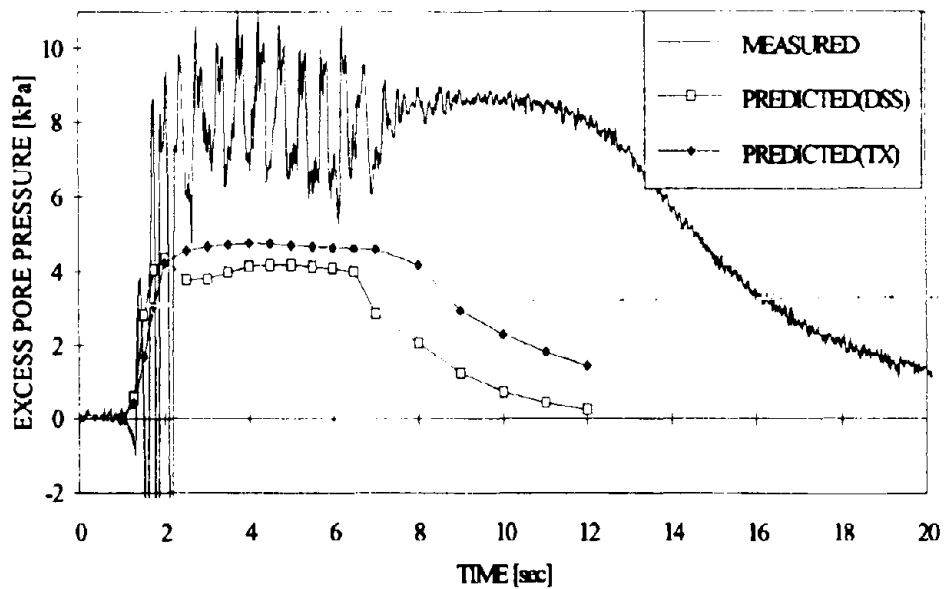
(a) Excess pore pressure at P2
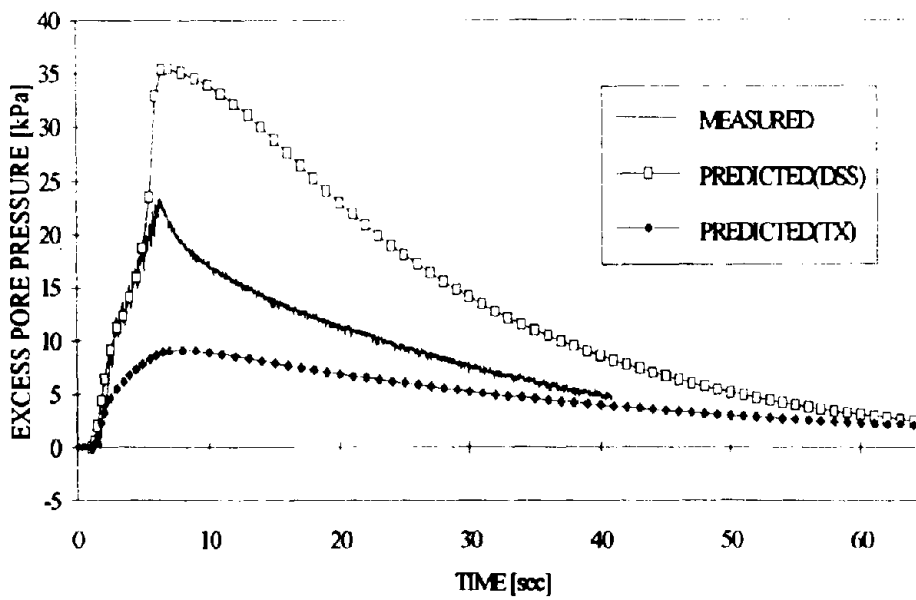
(b) Excess pore pressure at P3

Figure E.7: Predicted and observed excess pressrues in Test 3a
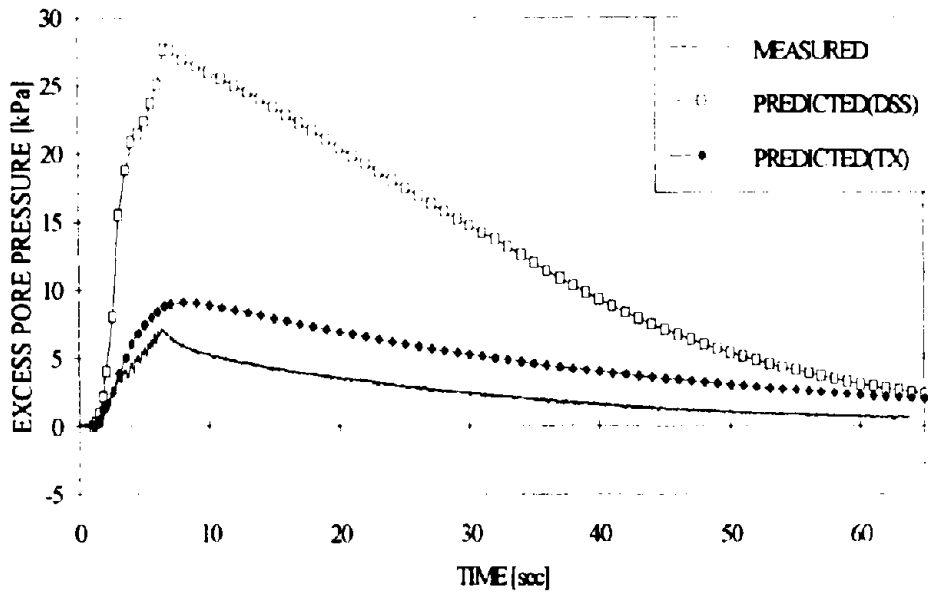
(c) Excess pore pressure at P4
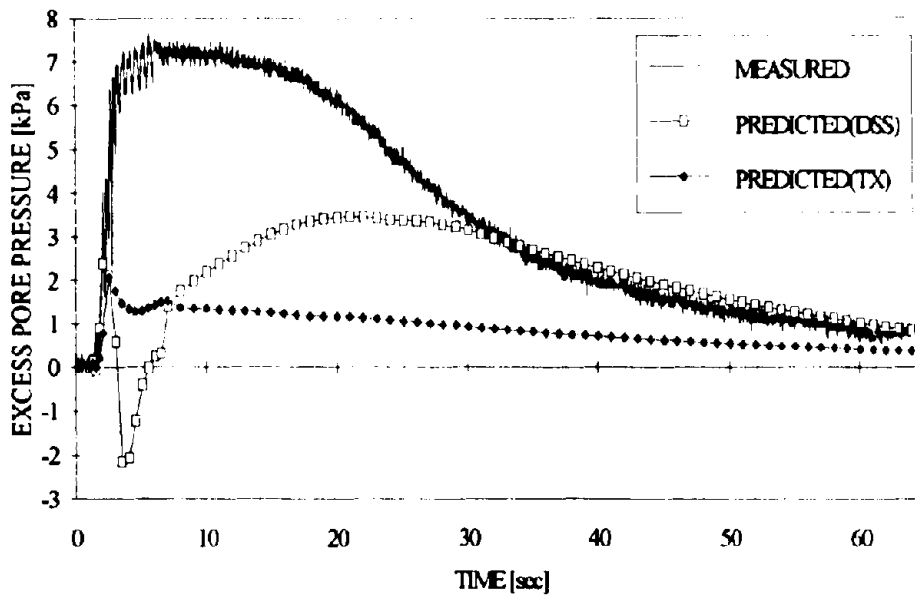
(d) Excess pore pressure at P5

Figure E.7: Predicted and observed excess pore pressrues in Test 3a

449
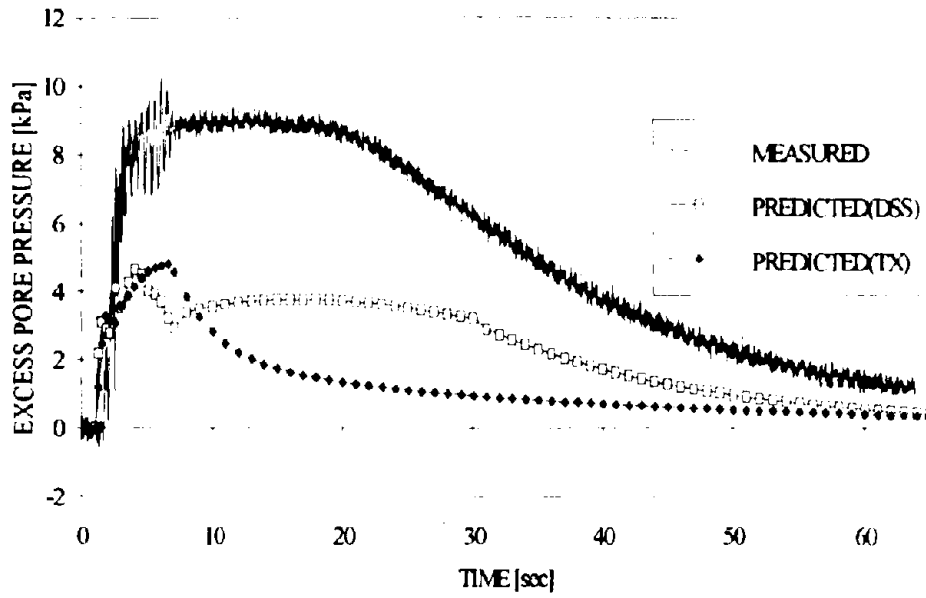
(e) Excess pore pressure ratio at P6

Figure E.7: Predicted and observed excess pore pressrues in Test 3a
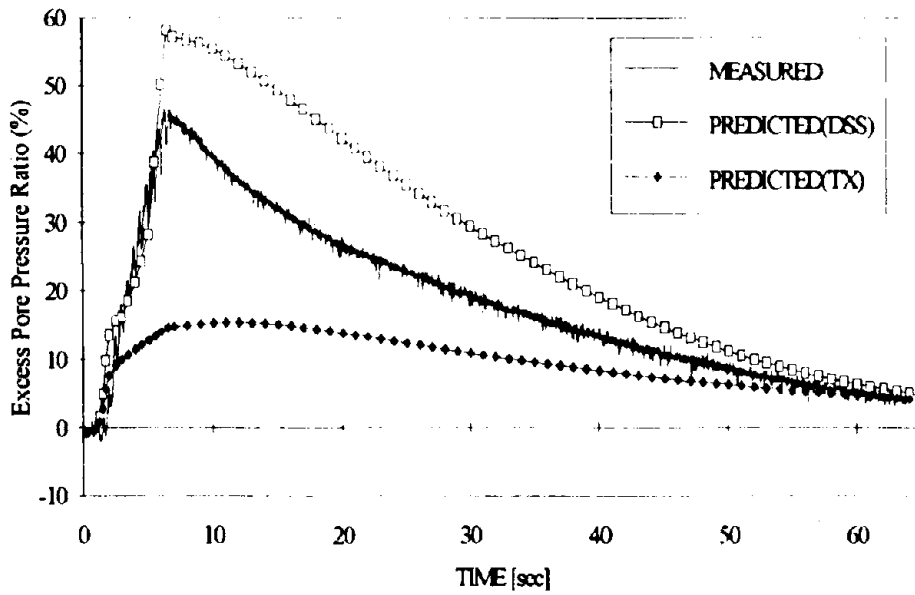
(a) Excess pore pressure ratio at P2
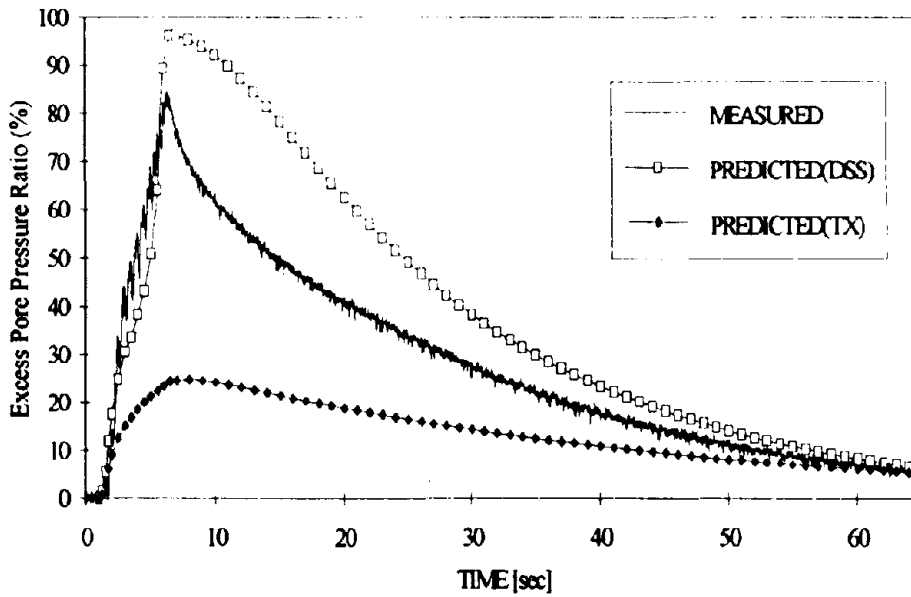
(b) Excess pore pressure ratio at P3

Figure E.8: Predicted and observed excess pore pressrue ratios in Test 3a
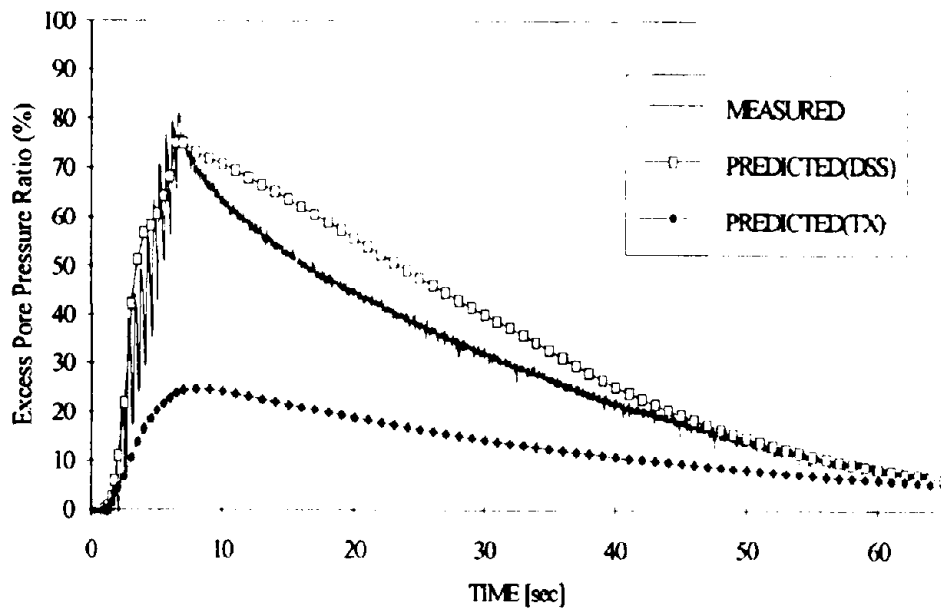
(c) Excess pore pressure ratio at P4
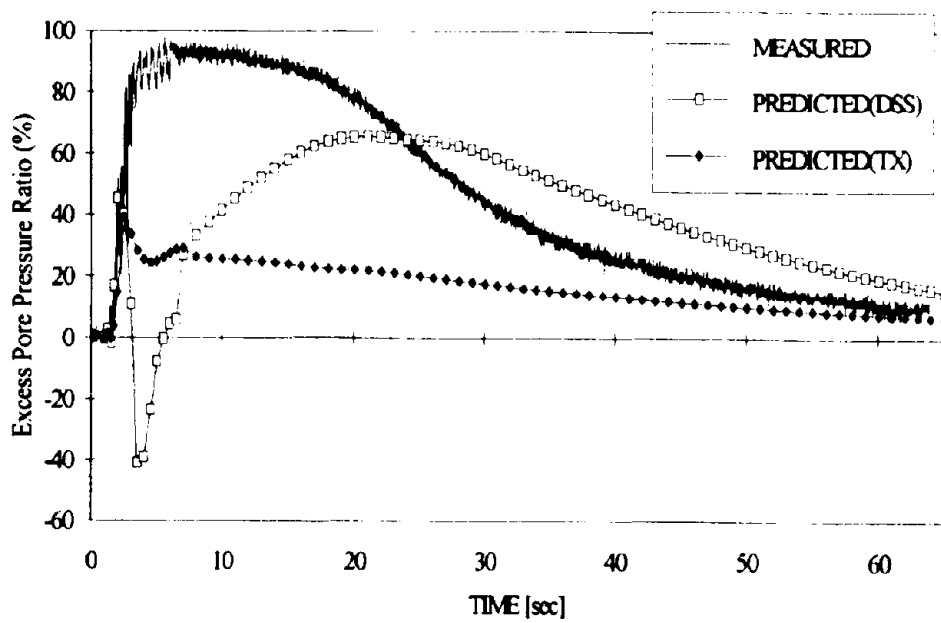
(d) Excess pore pressure ratio at P5

Figure E.8: Predicted and observed excess pore pressrue ratios in Test 3a

452

(e) Excess pore pressure ratio at P6

Figure E.8: Predicted and observed excess pore pressrue ratios in Test 3a

Figure E.9: Predicted and observed horizontal wall top displacement in Test 3a

(a) Excess pore pressure at P2

(b) Excess pore pressure at P3

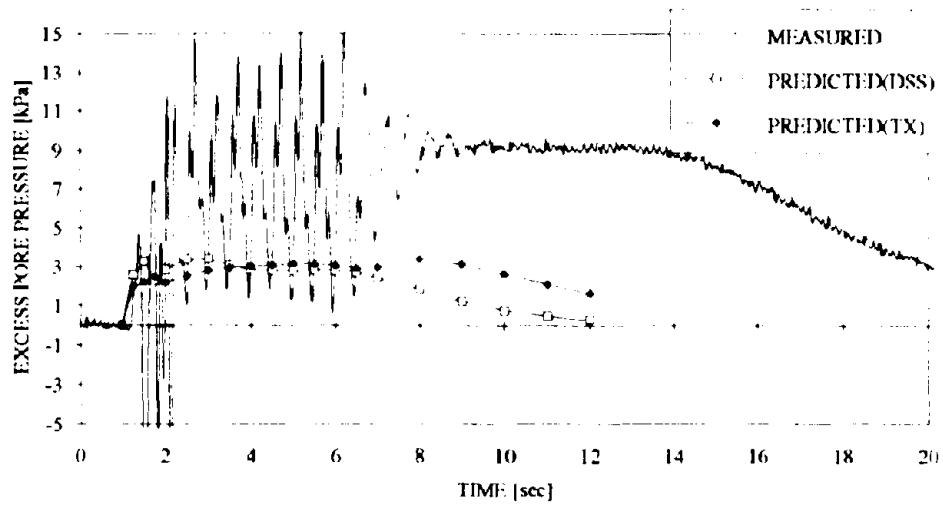Figure E.10: Predicted and observed excess pore pressrues in Test 4a
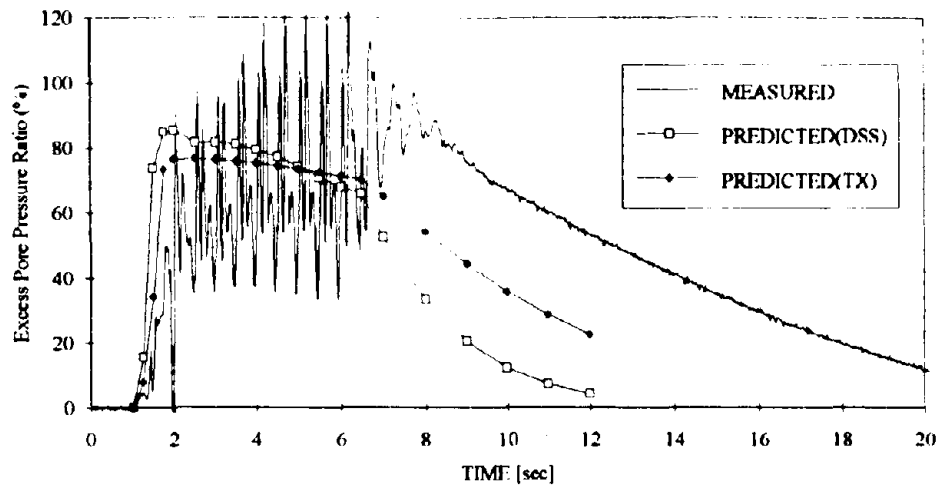
(c) Excess pore pressure at P4

(d) Excess pore pressure at P5

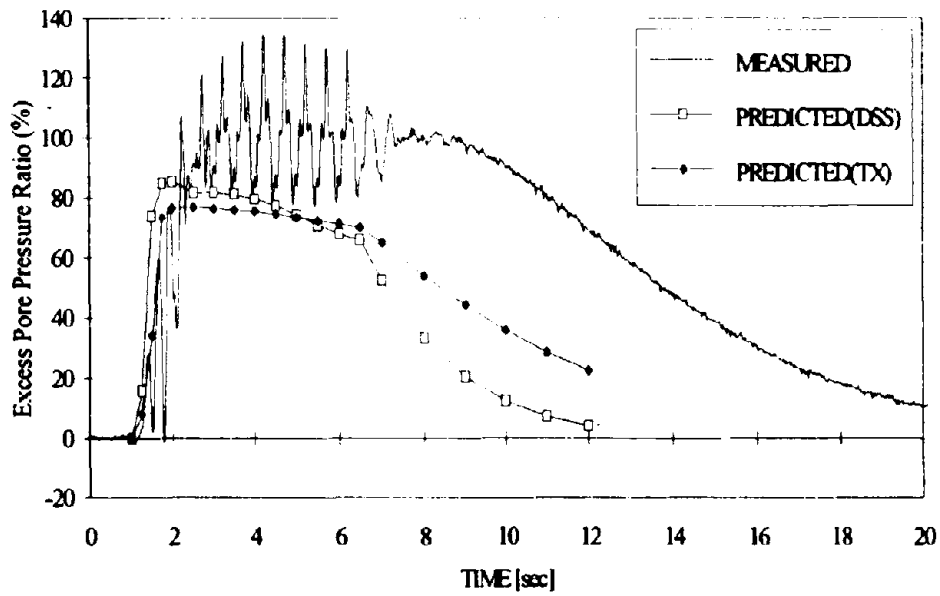Figure E.10: Predicted and observed excess pore pressrues in Test 4a

455

(e) Excess pore pressure ratio at P6

Figure E.10: Predicted and observed excess pore pressrues in Test 4a
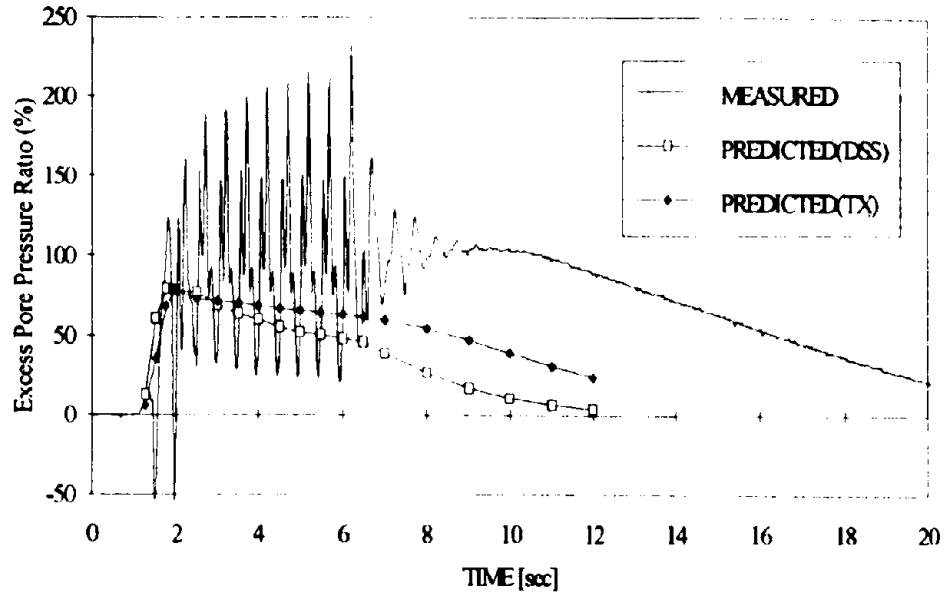
(a) Excess pore pressure ratio at P2

(b) Excess pore pressure ratio at P3

Figure E.11: Predicted and observed excess pore pressrue ratios in Test 4a

457

(c) Excess pore pressure ratio at P4
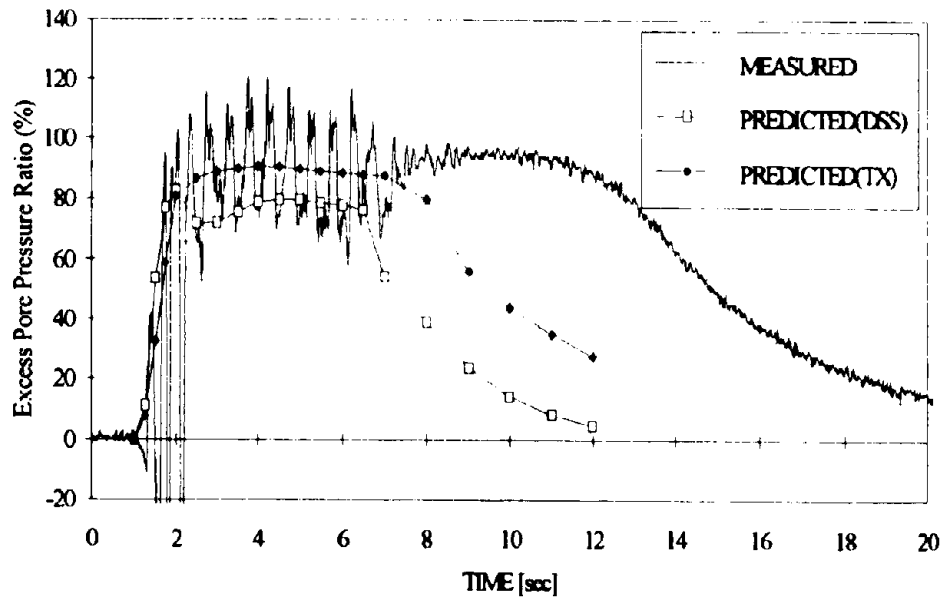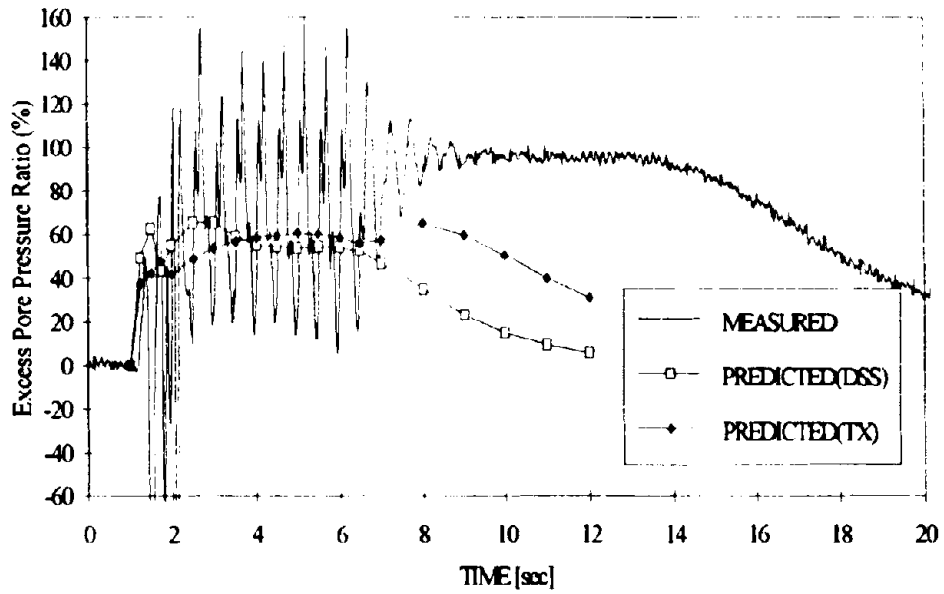

(d) Excess pore pressure ratio at P5

Figure E.11: Predicted and observed excess pore pressrue ratios in Test 4a

(e) Excess pore pressure ratio at P6

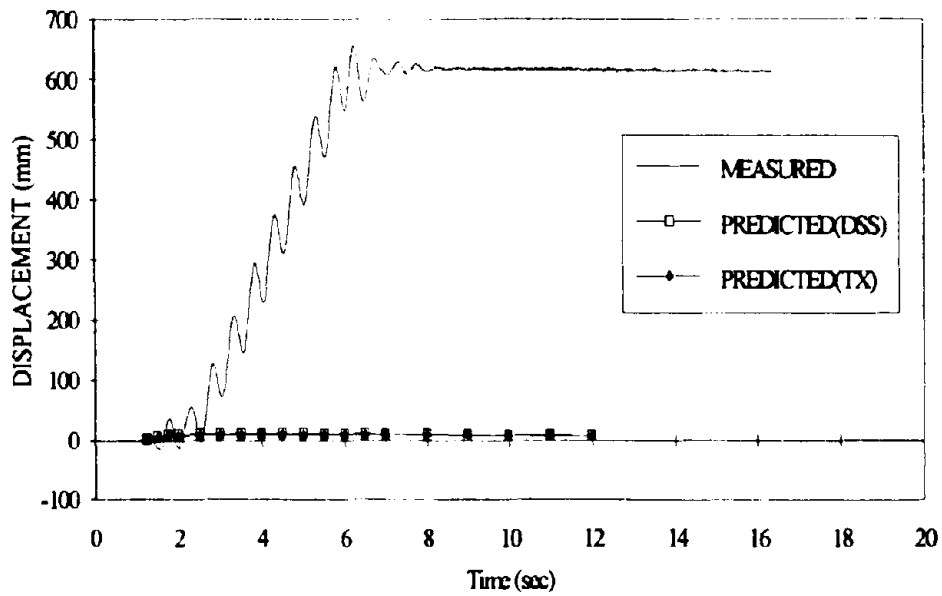Figure E.11: Predicted and observed excess pore pressrue ratios in Test 4a
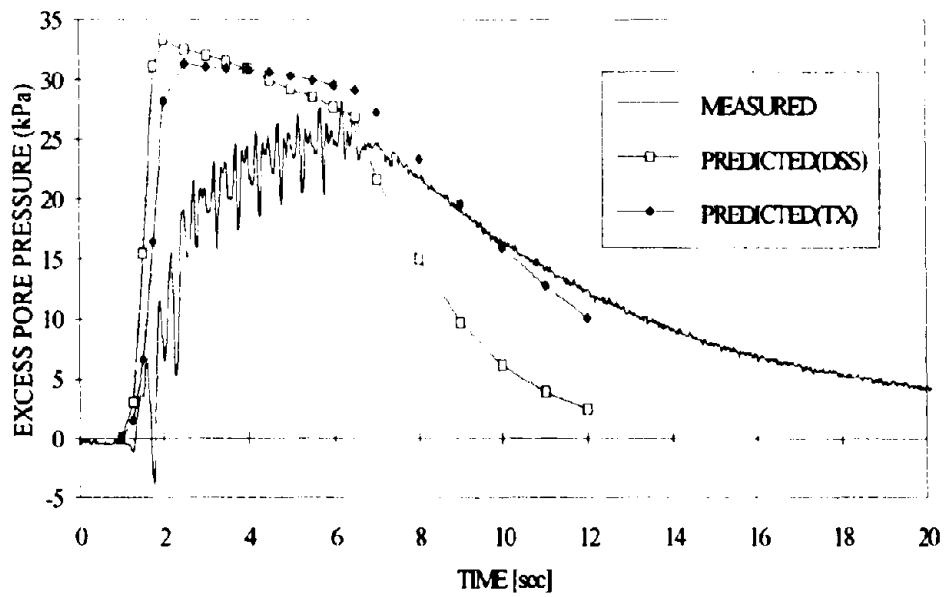

Figure E.12: Predicted and observed horizontal wall top displacement in Test 4a

459

(a) Excess pore pressure at P2

(b) Excess pore pressure at P3

Figure E.13: Predicted and observed excess pore pressrues in Test 5a

460
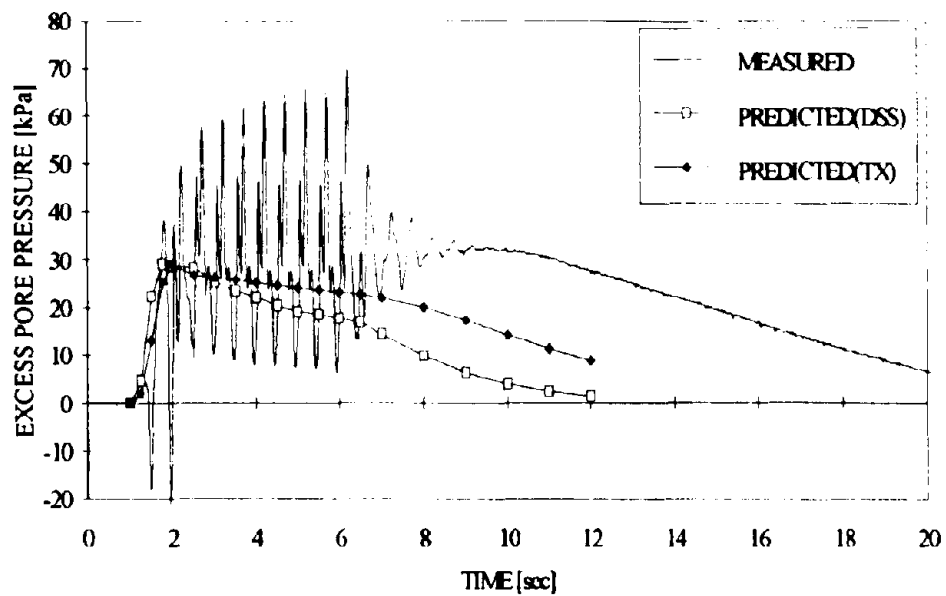
(c) Excess pore pressure at P4

(d) Excess pore pressure at P5

Figure E.13: Predicted and observed excess pore pressrues in Test 5a

461

(e) Excess pore pressure ratio at P6

Figure E 13: Predicted and observed excess pore pressrues in Test 5a

(a) Excess pore pressure ratio at P2

(b) Excess pore pressure ratio at P3

Figure E.14: Predicted and observed excess pore pressrue ratios in Test 5a

(c) Excess pore pressure ratio at P4

(d) Excess pore pressure ratio at P5

Figure E.14: Predicted and observed excess pore pressrue ratios in Test 5a

464

(e) Excess pore pressure ratio at P6

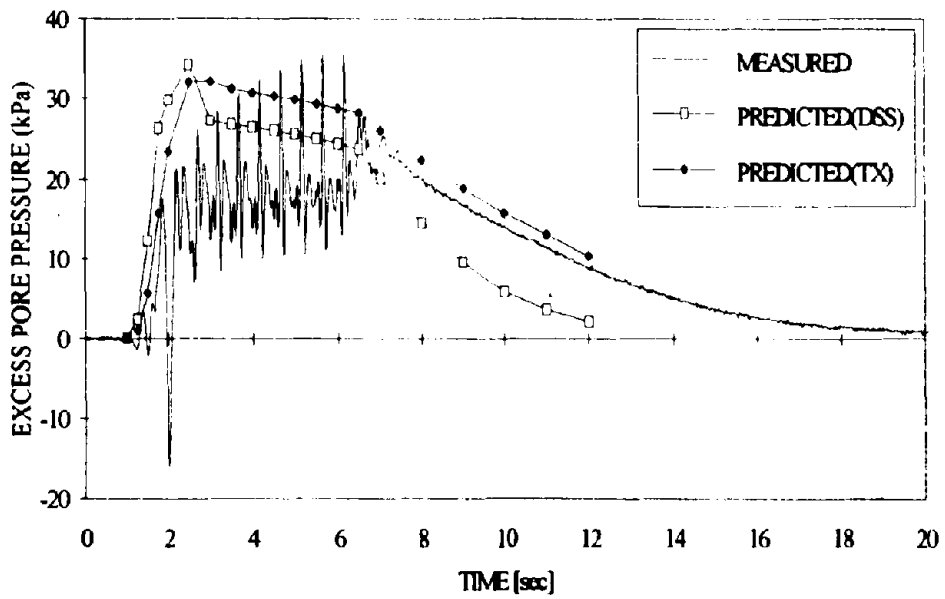Figure E.14: Predicted and observed excess pore pressrue ratios in Test 5a

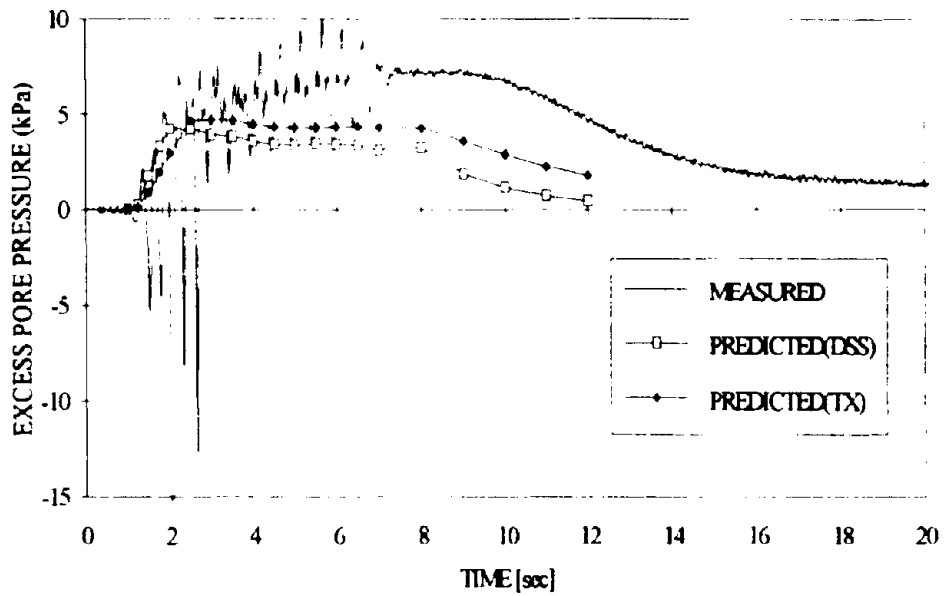Figure E.15: Predicted and observed horizontal wall top displacement in Test 5a

465
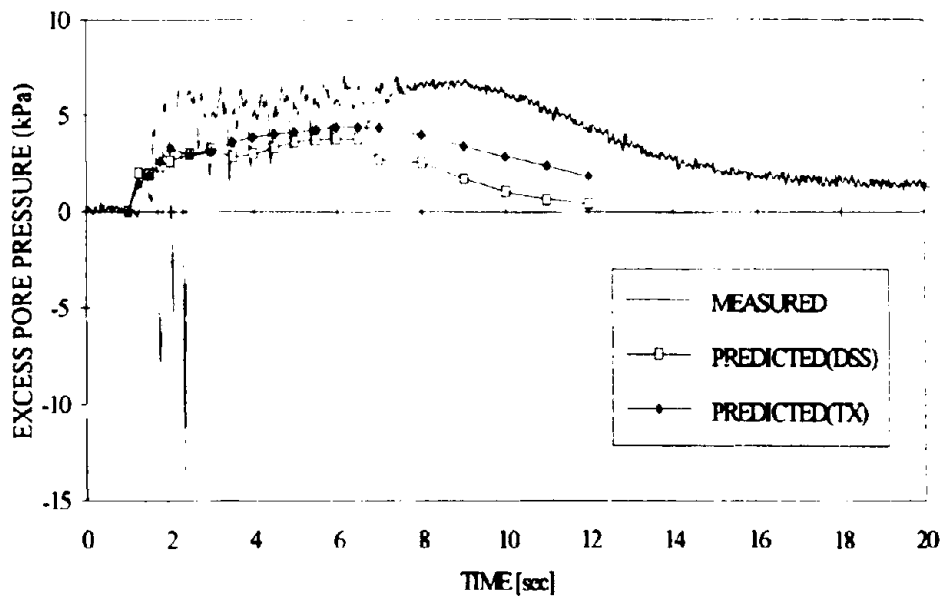
(a) Excess pore pressure at P3

(b) Excess pore pressure at P4

Figure E.16 Predicted and observed excess pore pressrues in Test 6a
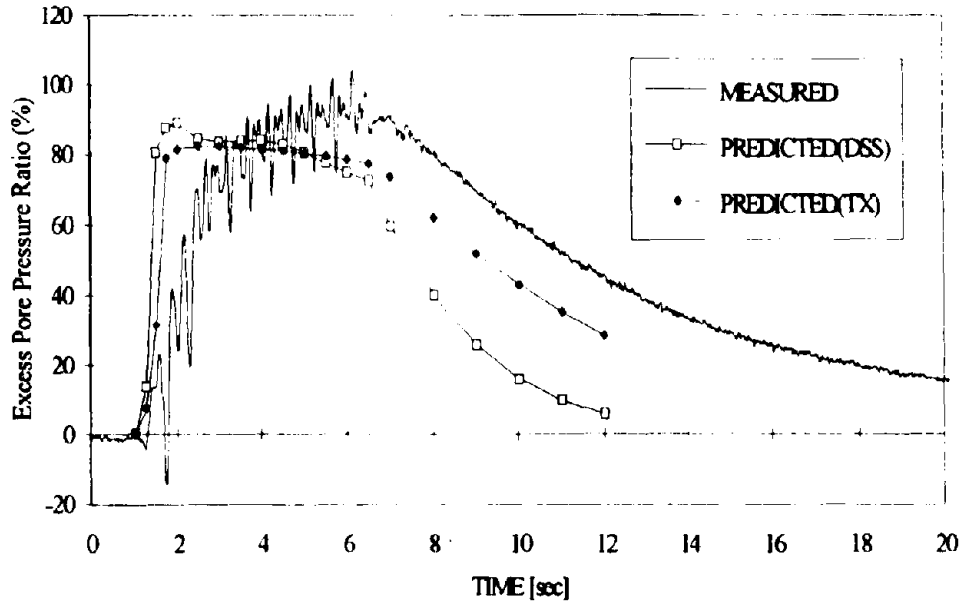
466

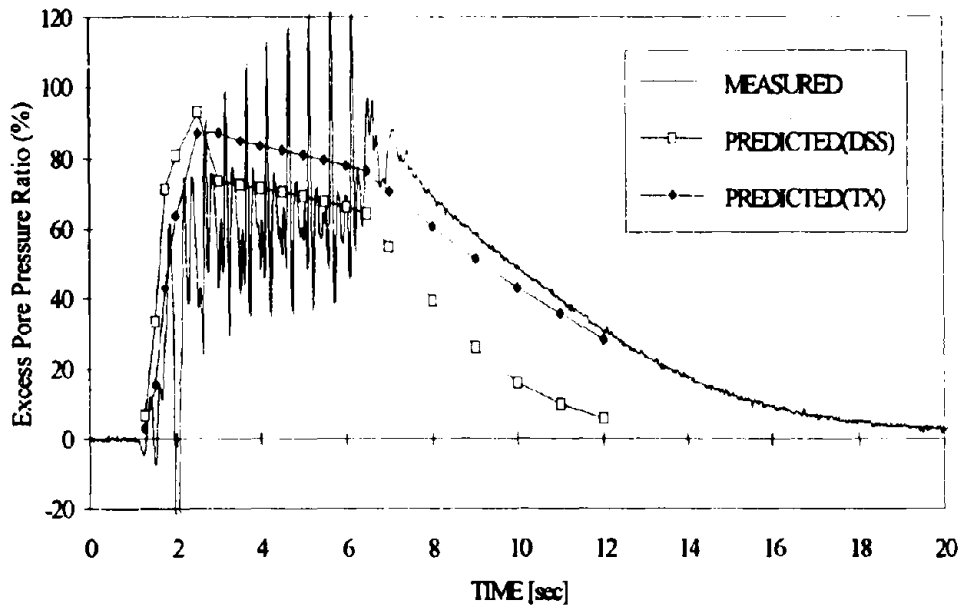(c) Excess pore pressure at P5

(d) Excess pore pressure at P6

Figure E.16: Predicted and observed excess pore pressrues in Test 6a

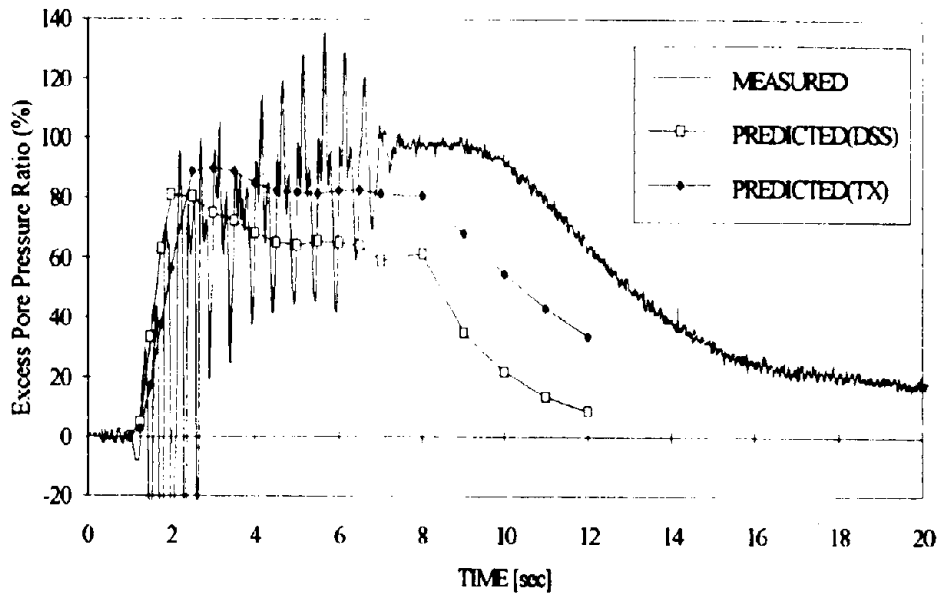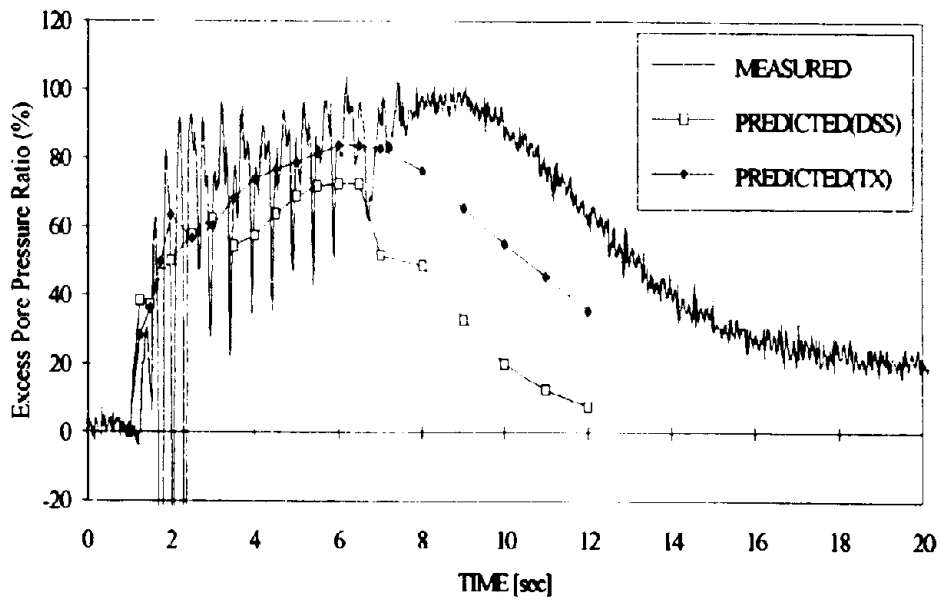(a) Excess pore pressure ratio at P3

(b) Excess pore pressure ratio at P4

Figure E.17: Predicted and observed excess pore pressrue ratios in Test 6a

468

(c) Excess pore pressure ratio at P5

(d) Excess pore pressure ratio at P6

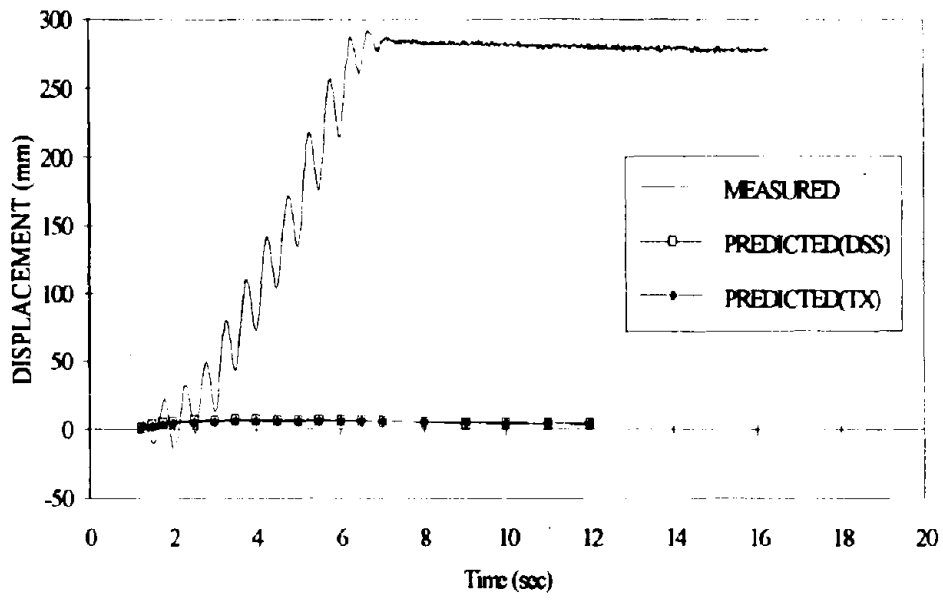Figure E.17: Predicted and observed excess pore pressrue ratios in Test 6a

Figure E.18: Predicted and observed horizontal wall top displacement in Test 6a

APPENDIX F

SPRING CONSTANT OF NEVADA SAND IN THE CENTRIFUGE MODEL

Scott (1973) proposed a method to estimate the spring constant of a soil stratum behind a retaining wall with a shear beam-Winkler model shown in Figure F.1. The Winkler spring constant k of this model is

$$k = \frac{8G(1-v)}{L(1-2v)} \tag{F.1}$$

The Earth Technology Corporation (1992) performed a series of resonant column tests. The shear modulus at various effective confining pressures are summarized in Table C.1.

The initial vertical effective stress is zero at the surface and 73.5 kPa at the bottom. The vertical effective stress decreases to about 30 to 40 kPa at the bottom[1] after 5 cycles of shaking during the tests with slip. In the tests with slip, the liquefaction front[2] is at about 3.6m (0.072m in the model) above the base. Therefore, assuming a vertical effective stress of 35 kPa at the bottom, the effective confining pressure is

---

[1] According to the pore pressure measured at P2. The time-wise average of the execss pore pressure in these tests were about 30 ~ 45 kPa.
[2] Above this front, the soil is liquefied.

$$\sigma_c^{'} = \frac{1+2K_o}{3}\sigma_v^{'} = \frac{1+2\times0.4}{3}35 = 21(kPa) \qquad (F.2)[3]$$

The shear modulus is proportional to $\sqrt{\sigma_c^{'}}$. Thus, the effective confining pressure for calculating the average shear modulus through the thickness (3.6m in prototype scale) of the soil in which the soil did not liquefy was about $\frac{2}{3}$ x 21 = 14 (kPa). The shear modulus at small strains can be estimated using Eq. (5.5).

$$G_0 = B_c P_a \frac{(2.973-e)^2}{1+e}\sqrt{\frac{\sigma_{oct}^{'}}{P_a}} \qquad (5.5)$$

where B_c = 265 for Nevada sand is determined in Appendix C (see Table C.7). The void ratio (e) is equal to 0.656 and 0.595 for Nevada sand with relative densities of 60% and 75% (Table C.7). Therefore,

$$G_0 = 32144 \text{ kPa} \qquad (Dr = 60\%)$$
$$G_0 = 35154 \text{ kPa} \qquad (Dr = 75\%)$$

For estimating the Winkler spring constant, the average G_0 (=33650 kPa = 33.65 MPa) is used.

The average Winkler type spring constant (at small strains) is

$$k_o = \frac{8G(1-v)}{L(1-2v)} = \frac{8\times33.65(1-v)}{0.36(1-2v)} = 740\frac{(1-v)}{(1-2v)} \text{ MPa/m} \qquad (F.3)$$

where v is the Poisson's ratio; L is the length of the sand stratum. Assuming v = 1/3, then the average Winkler spring constant (k_o) is about 1480 MPa/m (model scale) from Eq. (F.4).

---

[3] The frictional angle of the Nevada sand is about 37°. The lateral stress ratio at rest, K_o, is about $1 - \sin 37^o = 0.4$.

The spring constant k_I in the Lumped-Mass-Sliding-Block model in Chapter 7 is at its maximum value when the cyclic shear strain is small. It can be estimated from the Winkler spring constant k_O as follows.

$$(k_1)_{max} = k_o wH' \frac{0.4H'}{H_{tie-back}}$$ \hfill (F.5)

where H' (= 0.08 m in model scale or 4 m in prototype scale) is the thickness of soil with non-zero vertical effective stress. Therefore,

$$(k_1)_{max} = k_o \times 0.19 \times 0.08 \times \frac{0.4 \times 0.08}{0.21} = 3.4 \text{ MN/m} = 3400 \text{ kN/m}$$
$$\text{(in model scale)}$$

When the cyclic shear strain is large, the spring constant should be smaller, because of the reduction in shear modulus according to the large stain. From the modified displacement data[4], the "observed" cyclic shear strain was about 0.1% ~ 0.2% in most of the non-slip centrifuge model tests and was about 0.2% ~ 0.5% in the slip tests. These strains were large enough to reduce the shear modulus and the spring constant to their residual values in these tests. The back calculated spring constant k_I of 723 kN/m in Chapter 7 is about 21% of the maximum value at small stains ($(k_1)/(k_1)_{max}$ = 723/3400 = 21%). This percentage is a reasonable reduction ratio for the residual shear modulus of Nevada sand in this study.

The uncertainties in estimating the spring constant for a soil is generally large, especially for a partially liquefied soil. Therefore, the above analysis should be used with caution. Nevertheless, the above estimations do verify the back-calculated spring constant k_I (= 723 kPa) in Chapter 7 is a reasonable value.

---

[4] The cyclic amplitude of the data of wall displacement (at the tie-back level) is amplified by a factor of 1.67 (= 1 / 60%) according to the frequency response of the displacement transducer.
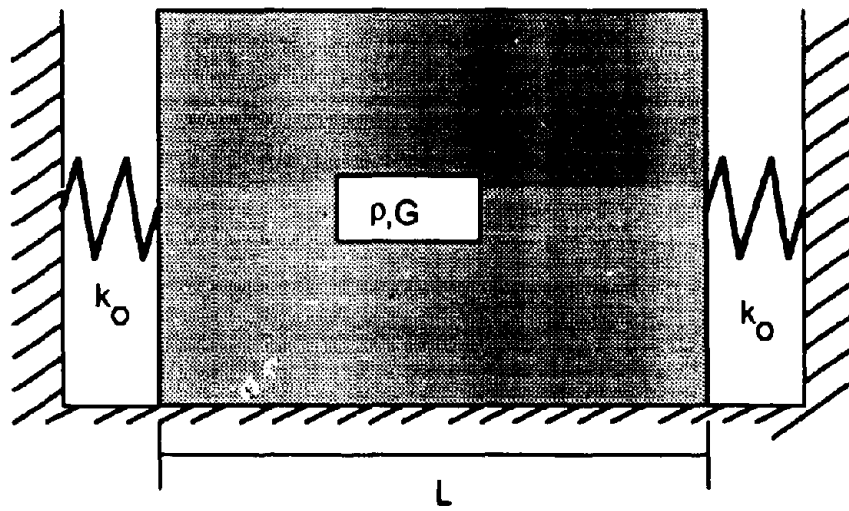
Figure F.1: Continuous Shear Beam Model for soil backfill (*from* Scott, 1973)